12-2003

Irradiation Induced Order-Dis Order Transformations in Ni-Mo Alloys

Ovidiu F. Toader
Western Michigan University

IRRADIATION INDUCED ORDER-DISORDER TRANSFORMATIONS IN Ni-Mo ALLOYS

by

Ovidiu F. Toader

A Dissertation
Submitted to the
Faculty of The Graduate College
in partial fulfillment of the
requirements for the
Degree of Doctor of Philosophy
Department of Physics

Western Michigan University
Kalamazoo, Michigan
December 2003

INFORMATION TO USERS

The quality of this reproduction is dependent upon the quality of the copy submitted. Broken or indistinct print, colored or poor quality illustrations and photographs, print bleed-through, substandard margins, and improper alignment can adversely affect reproduction.

In the unlikely event that the author did not send a complete manuscript and there are missing pages, these will be noted. Also, if unauthorized copyright material had to be removed, a note will indicate the deletion.

ProQuest Information and Learning Company
300 North Zeeb Road
P.O. Box 1346
Ann Arbor, MI 48106-1346

To my family

ACKNOWLEDGMENTS

First, I wish to express my appreciation to my advisor, Dr. Pnina Ari-Gur for the guidance and the encouragement in the course of the work. I am very grateful to Dr. Giora Kimmel who inspired my research and provided help and advice when I needed it.

I would like to express my thanks to all the professors in the Physics department who agreed to serve on my committee, and to all who helped with the completion of my education. My gratitude to Professor Halderson, Professor Rosenthal, Professor McGurn and Professor Chung who took their time while I was a graduate student, to explain with patience and to make difficult concepts and principles easier to understand. I also want to thank Dr. Pancella who agreed to sit on my committee.

My thanks go to Professor Shamu, who opened his home to me the first day I set foot in Kalamazoo and who gave me great advice all the years I have known him. I wish to express thanks to Dr. Nora Berrah and Dr. Burkhart Langer as the first people at WMU who initiated me with diligence in the art of Physics research. Many thanks to Lori Krum, from the Physics Department, who helped me a lot with the difficult world of the paperwork and to Barbara Shouse, from the International Student Office, that went above and beyond in order to help me.

Michigan Ion Beam Laboratory for Surface Modification and Analysis at the University of Michigan is acknowledged for the use of facilities. Special thanks to

the Director of the laboratory, Professor Gary Was without whose approval nothing could have been done. I wish to acknowledge the lab manager, my friend and my colleague Dr. Victor Rotberg for his encouragement and support during all the time I worked on my research. I wish to thank to all the other people who gave me advice and assistance during my long days and nights of work: Dr. Bogdan Alexandreanu, Dr. Jeremy Busby, Bill Cook, Ying Qi as well as Dr. John Mansfield at the Electron Micro-Beam Laboratory.

I would also like to express all my gratitude to my family's dear friend, Barbara Chaiken who was always there for us.

Last, but certainly not least, I would like to thank my family. To my wife Liliana, for the support and encouragement in the difficult moments, who was with me from the beginning to the end of my journey. To my children, Andreea and Andrew, who allowed me to take some time off from being a father (but only on the condition that I give them a big rain-check) and to the rest of my family across the seven seas.

Ovidiu F. Toader

TABLE OF CONTENTS

LIST OF TABLES

LIST OF FIGURES

CHAPTER 1

INTRODUCTION

1.1 Order-Disorder Transformations

Many solid solutions undergo long range ordering (LRO) below a critical temperature [1, 2, 3, 4 and 5]. In a LRO state, the component atoms of the alloy system occupy specific sets of sites in the lattice; the arrangement of atoms is regular and long range periodical in three dimensions. This type of order occurs at simple stoichiometric compositions. In contrast, in a short range ordered state (SRO), the structure is neither completely random nor long range ordered; rather non-random atomic arrangements occur statistically throughout the lattice [1, 6 and 7]. The formation of LRO is accompanied by an increase in the lattice constant, creating a lower symmetry of the unit cell. The fact that the symmetry of the occupied positions of the ordered phases decreases, creates an additional split in the energy levels of the crystal, which in turn may provide the extra energy required by the stabilization of the superstructures [8]. These transition processes produce a change in the mutual arrangement of the atoms over the sites of the original crystal lattice inducing the change in symmetry and a change in LRO parameter. Changes occur also in the two, three and many particle correlation functions. The distance dependence and the number of neighbors vary according to the particular type of superstructure created ([9, 10, 11 and 12]. By finding the ordering parameters and

the ordering energy, we can further determine the entropy of an alloy and the part of the energy that depends on these order parameters. The LRO parameter is unique for the phase transition and is correlated with the behavior of the other parameters.

The quantum theory of the ordered phases can explain the limited role played by the pair interactions in alloys and the consideration of three particle contributions to the total energy. Ordered phases in a binary alloy can form by crystallization from a liquid phase or from a solid phase under certain conditions. Phases with the ordered arrangements of atoms sometimes called superstructures (due to the increase in periodicity distance) can be observed in the phase diagram of the metallic systems that exhibit order-disorder. The binary ordered phases show most of the time a (nearly) stoichiometric ratio of the atoms like the compositions of AB, AB_2, AB_3 and AB_4. In the structure of these alloys there are partially ordered arrangements of atoms divided into different sublattices as seen in Figure 1.1.1.

1.2 Irradiation Induced Transformations

Random displacement of atoms and replacement collision sequences are known to be important mechanisms for inducing disorder in an ordered alloy under irradiation. At the same time, enhanced diffusion due to radiation induced point defect may cause restoration of order under certain conditions [15, 16, 17, 18, 19, 20, 21, 22, 24 and 25]. The fact that an order-disorder transformation can be induced both ways by suitably altering the dose rate and temperature has been established for a while [23, 26 and 28]. Radiation can be used as a tool to induce and understand phase transformations [03, 11

and 17]. Bombarding by heavy particles simulates the process of radiation damage in nuclear fuel without the inconvenience of nuclear reactions, which is accompanied by the accumulation of radioactive hazardous materials. In nuclear fuel, the radiation damage is an unavoidable phenomenon. The investigations related to radiation damage have as one of the goals the study of the kinetics of the development of radiation damage in conditions similar to those of the materials in nuclear reactors. For example, U_3Si was found to have a 5% increase its volume after irradiation in a very low flux [29, 30]. X-ray diffraction found that an amorphous structure was formed, a fact also confirmed by Transmission Electron Microscopy (TEM) [29 and 31]. This amorphous and brittle structure recovers at a relatively low-temperature annealing (300^0C) forming a very fine polycrystalline ductile U_3Si structure. A possible explanation is that U_3Si is a product of a peritectoid transformation and each radiation-damage event associated with local heating results in the decomposition of U_3Si to U and U_3Si_2. The phase mixture is quenched back to room temperature by the rest of the material surrounding the irradiated area. The low flux allows preservation of low temperature of the entire bulk material. After some time the sample turns into a mixture of nano crystals of U and U_3Si_2 with a 5% specific volume increase compared with U_3Si. The main process here is the destruction of the initial material structure, transforming a coarse structure to a fine one.

Disordering under irradiation is not very obvious at higher irradiation temperatures because vacancies can move very fast. These effects are observed in two-phase alloys in the formation of precipitates [22 and 32]. The defects can dissolve in some regions near point defect sinks, but can grow in size in other regions. Irradiation increases the ordering kinetics via the increased vacancy concentration, but can also cause

disorder in an ordered alloy. Schulson proposed that disordering produced by atomic rearrangements can occur in: (a) thermal spikes, (b) replacement collision sequences, (c) collapse of cascade to vacancy loops and (d) random vacancy-interstitial recombination [22]. He suggested that (a) and (b) dominate disordering caused by cascade producing irradiation, while the others two dominate when cascades are not produced. Wilkes et al. [33] modeled mathematically the disordering process and Dienes [48] modeled mathematically the ordering rates. Dienes modified the ordering rates to include the increased vacancy concentrations resulting from irradiation. Liou and Wilkes proposed a model of phase stability during irradiation, but that was limited to the $L1_2$ ordered phase [35]. During irradiation, particle size distributions characterized by a size larger than the steady-state size is expected to decrease and the distributions that are smaller are expected to increase. Banerjee [26 and 32] showed that in the case of Ni irradiations on Ni_4Mo samples, the steady state structure was independent of the initial state of order. In the process of transition of Ni_3Mo from SRO to LRO it is very likely that there is a concentration of clusters of DO_{22} type and a mixture of $D1_a$ (Ni_4Mo) and Pt_2Mo type clusters (Ni_2Mo). It is accepted that close to the transition temperature, dramatic changes occur in the order parameter due to a large concentration of vacant lattice sites, and high atomic mobility. More details about the irradiation effects are given in section 2.2.

1.3 Objectives and Approach of the Dissertation Research

The main objectives of the present study were to introduce low irradiation flux in order to transform a large grain alloy to a fine grain structure and to observe radiation induced order-disorder transformations in a Ni-Mo alloy. The Ni_4Mo is a good candidate for the study because it is a peritectoid compound formed at a critical temperature $T_c = 868^0$ C in a slow ordering process from a high temperature disordered structure. Above T_c, the structure is phase face centered cubic (fcc) solid solution. Ordered Ni_3Mo forms peritectoidally at the transition temperature $T_c = 910^0$ C. Ni-Mo system may potentially offer the solution concerning the generality of the micro-domain concept of LRO and SRO. The Ni-20 at. % Mo (Ni_4Mo) and Ni-25 at. % Mo (Ni_3Mo) alloys are known for their corrosion resistance in non-oxidizing, acid chloride environments [34] used in chemical processing industry. There are several commercially available alloys based on this composition [30]. One example, Hastelloy B has the composition given in Table 1.1

Ni	Mo	Fe	Co	Cr	Mn	Si	C
Balance	26-30	2.0	1.0	1.0	1.0	1.0	0.02

Table 1.1 Chemical composition of commercially available Hastelloy Ni-Mo alloy. The units are in weight percent.

If our idea is correct then the process of decomposition under irradiation is: $Ni_4Mo \rightarrow Ni_3Mo + FCC\ solid\ solution$. This process consists of two stages: (a) decomposition and (b) peritectoid reaction. If the temperature is too high, even below the

peritectoid point, the local hot spots from the radiation reach the solid solution zone and there will be no decomposition, just disordered single-phase FCC solution. When the material would cool, it would go through an ordering process without the peritectoid reaction. This project was aimed at finding a solution of this problem by irradiating samples at room temperature, followed by low temperature annealing at about 300^0 C. Because Ni_4Mo would form not by recrystalization but by peritectoid reaction: $Ni_3Mo + Ni \rightarrow Ni_4Mo$, a formation of a fine grain structure of Ni_4Mo with long-range order was expected. After the irradiation, the material was annealed in low temperature, where the growth rate is slow but due to the irradiation, there will be a high density of nucleation sites. This condition favors the formation of fine grain new Ni_4Mo structure.

In this way, we wanted to obtain a correlation between the annealing temperature and the final grain size. In principle, we can end up with any desired grain size, depending on the recovery temperature. The goal is to obtain fine grain surface that enables better finishing (polishing, coating, painting), better wear resistance and delay fatigue failure.

After casting and homogenization, large grains of FCC structure are formed. X-ray diffraction will show preferred orientation. Ordering process at lower temperature (below the peritectoid point) forms multi-domain coarse ordered structure. Any attempt to obtain finer structure by lowering the temperature of the thermal treatments will be associated with major slowing of the process of homogenization and ordering.

The validation of the effectiveness and the degree of control of the irradiation procedure and parameters was made by the in-depth examination of the irradiated

samples. Order-disorder reactions are suited for this work because they are a well-studied phenomenon with a developed mathematical and physical model. Irradiations were performed mainly with two different ion beams: H^+ and Ni^+ at low temperature (less than 100^0 C for H^+ and less than 50^0 C for Ni^+) with doses from 0.01 to 1 dpa. A few irradiations were also performed with He beam for comparison effect comparison.

Although the systematic study of order-disorder transformations was undertaken mainly to demonstrate the efficacy of the irradiation technique, the results provided a great deal of information into the grain boundary structure and grain size of the Ni-Mo alloys after various irradiation conditions. The results complement irradiation experiments from previously published results [1, 4, 6, 11, 15, 22, 24, 27, 32, 33, 35, 36, 37, 38, 39, and 40] and generated experimental data for further understanding of order-disorder transformations in particular and of phase transformation in general.

In the next chapters will be presented the behavior of Ni_3Mo and Ni_4Mo under irradiation conditions. Some of the irradiated samples were also subject to annealing as a post irradiation process. Chapter two will first discuss background material pertinent to the present work with a presentation of the Ni-Mo alloys and their behavior under different thermal or irradiation conditions. This is followed by a theoretical description of the analysis methods that were employed and their application and benefits to the present study. Chapter three will give a detailed presentation of the experimental procedures and apparatus. Chapter four will present the results obtained with the X-ray diffraction analysis, Scanning Electron Microscopy (SEM), Orientation Imaging Microscopy (OIM), Rutherford backscattering and hardness testing. Chapter five will discuss the results in terms of their support for the hypothesis of the irradiation induced

order-disorder transformation in Ni-Mo. In addition, the final remarks, recommendations and future directions of the work will be given also in this section.

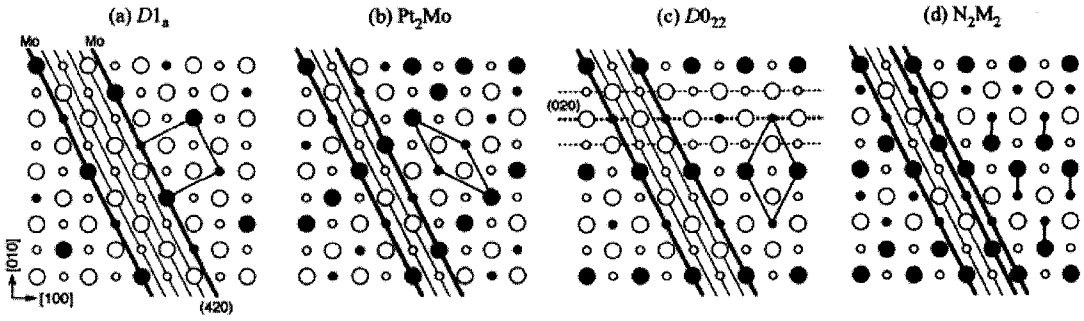

Figure 1.1.1 [001] cross section of ordered structures relevant to the FCC based Ni-Mo system: (a) D1a corresponding to Ni_4Mo, (b) Ni_2Mo (of type Pt_2Mo), (c) $D0_{22}$ is corresponding to Ni_3Mo and (d) Ni_2Mo_2. Open and closed circles denote Ni and Mo atoms, and large and small circles indicate the location of z=0 and z=1/2 planes, respectively [59].

CHAPTER 2

BACKGROUND

2.1 Solid-Solid Phase Transformations

Phase Transformations are the basis of much of our current materials technology. Many advances made during the last decades in high-temperature and electronic technologies have increased the demands for more sophisticated materials and have lead to the development of many novel processes and materials based on our understanding of the thermodynamics and kinetics of the transformations. The ability to work effectively with materials depends on our understanding of the basic principles of phase transformations and the methods of analysis.

The stability of a system is determined by its thermodynamic characteristics. In a closed system for constant temperature and pressure, the phase for which the Gibbs free energy is the lowest, is stable. A phase transformation starts when a system is no longer stable. Temperature, crystal defects like vacancies, dislocations and interphase interfaces alter the stability. The atomic mechanism of the transformation is related to many atomic processes, which must occur in a material during a transformation. The exact nature of these processes is not exactly known, but there is a strong dependence on temperature.

This classification of phase transformation is based on the successive differentiation of a thermodynamic potential, usually the Gibbs free energy with respect to an external variable such as the temperature or the pressure [41]. The order of the transformation is given by the lowest derivative that exhibits discontinuity. In the fully ordered binary alloys, the two kinds of atoms each occupy clearly defined sets of positions, and the unit cell constants are propagated throughout the crystal by exact lattice translations. In the fully disordered state, the atomic site occupancy is random with average composition corresponding to the bulk alloy. Two microscopic modes of transformation in materials have been identified [42]:

A: Reconstructive transformations are initiated by the appearance of microscopically small volumes of the product phase at identifiable locations in the initial phase, a process called nucleation. Heterogeneous nucleation can occur at quenched-in crystal defects or foreign particles. The rate of nucleation is temperature dependent. When atomic configurations act as nuclei for the process, the nucleation becomes homogenous. Progress of the transformation occurs by the migration of the interface between the nuclei of the product base and the untransformed parent phase. This process is known as growth. One type of growth is found in solid-solid transformations, is temperature dependent and it may involve short-range and long-range diffusion and transfer processes at the interface. At any time during such a transformation, a part of the system has transformed while the rest has not.

B: There is another type of growth that yields a rate independent of temperature, which is called displacive transformation. These transformations occur over the entire

volume of the system simultaneously. The entire system changes and approaches the final equilibrium state.

A phase transformation is a change in the macrostate of an assembly of interacting atoms or molecules as a result of some variation in the external conditions [42]. This must lead to an increase of the entropy and a variation of the thermodynamic functions of the closed assembly. The study of phase transformations is of interest to physicists, chemists, geologists, metallurgists and other scientists interested in states of aggregation. The physicists are interested in the phenomena near the critical points or lambda points of single-component fluids, superfluid or magnetic system that undergo continuous or higher order transformations. Material scientists are concerned with changes in spatial configuration of atoms as specified by the crystal structure, by the chemical composition and by the long range and short-range order.

The structure of states with intermediate order and the nature of order-disorder phase transitions are of considerable interest for the science of materials and practical applications.

2.1.1 The Free Energy of the Phase Transitions

Thermodynamically, a compound is characterized by its Gibbs free energy G. Irreversible decompositions are characterized by a discontinuity in G. Reversible phase changes are characterized by $dG = 0$ and may be classified in terms of the lowest-order

partial derivative of G that exhibit discontinuity at Tc [43]. A first order phase change shows discontinuities in the entropy:

$$S = -(\frac{\partial G}{\partial T})p \tag{2.1}$$

and volume

$$V = -(\frac{\partial G}{\partial P})_T \tag{2.2}$$

where P is the pressure. First order phase changes have a latent heat given by:

$$L = T_c(S^h - S^l) \tag{2.3}$$

where the superscripts h and l refer to the high-temperature and low-temperature states. Higher order phase transitions have continuous first derivatives of G, so there is no discontinuity in S or V and no latent heat associated with the transition. The latent heat of first order phase change provides a means of maintaining a constant temperature reservoir or a way to store energy. Changes in volume at first order phase change govern the pressure dependence of the transition through Clapeyron's equation. For second order transitions, Ehrenfest equation [43] gives us:

$$\frac{dP}{dT} = \frac{(c_p{}^h - c_p{}^l)}{TV(g^h - g^l)} = \frac{(g^h - g^l)}{(K^h - K^l)} \tag{2.4}$$

where:

$Cp = T(\frac{\partial S}{\partial T})_p$ is the specific heat

$\alpha = V^{-1}(\frac{\partial V}{\partial T})_p$ is the thermal expansion coefficient

$K = -V^{-1}(\frac{\partial V}{\partial P})_T$ is the compressibility.

Volume changes also introduce thermal hysteresis at a first-order transition. If the nucleation energy for the new phase is large, the thermal hysteresis can be tens to hundreds of degrees wide. Problems can be created in metamagnets for example, which exhibit antiferromagnetic-to-ferromagnetic transitions [42].

The change in Bravais lattice symmetry at a first order transition often produces small changes in absolute lattice constants and in atomic positions. In the case of second order phase transitions, the point group of lower symmetry must be the subgroup of the higher symmetry point group with small atomic displacements.

2.1.2. Lattice Wave Description of Phase Transformations

An arbitrary disturbance in a crystalline solid solution can be described as a sum of lattice plane wave modulations. In metallic systems, the wave amplitude generally refers to atomic displacements or to atomic replacements. The properties of crystalline solid solutions can be studied by examining the response of the ideal solution to a lattice wave modulation or perturbation of the type:

$$A_j(k)\exp(i\mathbf{kx}) \tag{2.5}$$

where **x** is the lattice vector, **k** is the wave vector giving the direction and inverse of wavelength of the modulation, A is the amplitude of the perturbation and j denotes the polarization of the wave. The specification of the wave vector k, the polarization j and

the sublattice determines the mode of the lattice wave. The nature of the amplitude A determines the physical properties of the wave: **A (k)** can represent a Fourier component of a local compositional field, a displacement field or an electric or magnetic field. A phase transition occurs when the parent structure is unstable with respect to a particular wave or combination of harmonic excitations. Table 2.1 shows a simple classification of phase transformations based on the nature of the least stable wave: (long-wave denotes a **k** vector near the center of Brilloiuin zone, short-wave denotes a **k** vector near or on the Brillouin zone boundary) [39].

Nature of wave	**Long wave**	**Short wave**
Replacive	Clustering	Order-disorder
Displacive (acoustive)	Martensitic	Omega-phase
Electric	Ferroelectric	Antiferroelectric
Magnetic	Ferromagnetic	Antiferromagnetic

Table 2.1 A simple classification of phase transformation based on the nature of the waves.

The lattice wave formalism may be used as a convenient description of the configuration of structural defects in the crystal. The **k**-space description is useful when interpreting X-ray, neutron or electron diffraction data that are recorded in the same space. The energy of a defect structure may be given in terms of lattice waves in an appropriate **k**-space representation [44] as shown in Figures 2.2.1 and 2.2.2.

2.2 Irradiation Effects on Materials

Microstructural changes occur with progressive doses of irradiation under cascade forming heavy ion irradiation. Random displacements of atoms and replacement collision sequences are known to be important mechanisms for inducing disorder in an ordered alloy. In contrast, enhanced diffusion due to irradiation induced point defects causes restoration of order at temperature where defects become mobile. Order-disorder can be induced with irradiation in both ways [23, 26 and 32]. From the state diagrams we can determine where ordering and disordering regimes dominate. The state diagrams are expected to be strongly dominated by the nature of irradiation. Irradiation strongly affects the hardness of materials, but no generally accepted mechanism has been formulated for this observed increase in hardness [45]. Any type of radiation will produce hardening, but it does not appear feasible to strengthen materials by irradiation to any greater extent that can be accomplished by conventional techniques. Radiation effects can be annealed out of metals and alloys by suitable post irradiation thermal treatment. The reverse of property changes usually occurs in the same temperature region as recovery of cold-working effects [9].

The radiation-induced changes in electrical properties are generally less thermally stable and can be removed easier than changes in mechanical properties. Because an interstitial atom has greater mobility than other defects, it is expected to have major effect on annealing at low temperatures. Vacancy migration of some type may occur at room temperature. Above this temperature, the migration is in the accepted mode and at about

600 K self-diffusion processes dominate. A classification of irradiation effects on materials is given by Dienes [34]. Most physical properties of a material are affected:

- ***Electrical properties*** from the introduction of defects and by the variation of the number of current carriers. For conductors, there is an increase in resistivity due to the increase in electron scattering on the newly created defects. For binary alloys the change in resistivity is due to the change in the degree of short range order (SRO) or long range order (LRO), and not only by the creation of new defects.
- ***Thermal conductivity*** is affected by imperfections in the crystal structure as the thermal waves and phonons are scattered by the lattice imperfections.
- ***Stored energy*** is the energy increase of the lattice due to irradiation. Knowing the total stored energy, and calculating the energy of the formation of defects, we could estimate the total number of defects after the irradiation.
- ***Hardness*** changes are observed in most of the irradiated materials. The hardness of the binary alloys can be varied by changing the phase or the degree of SRO or LRO.

Prior to the apparition of nuclear energy, the interests of materials engineer were concentrated with the improvement of mechanical and physical properties, increasing the applicability of materials for higher temperatures, devising means to create corrosion resistant materials and to predict behavior of a material from its basic structure. Today, a nuclear engineer must add the study of the effect on properties of the bombardment of

materials with energetic beams of particles. From the point of view of a nuclear scientist, the following effects of radiation on materials could be considered [45]:

A. Creation of vacancies from a primary collision of an energetic particle with an atom (PKA or primary knocked-on atoms). An energetic particle can knock on more atoms before stopping. The first knocked-on atom can knock-on more atoms until looses all its energy and comes to rest in an interstitial position in the lattice. Hence, vacancies and interstitials are formed in the collision process.

B. A secondary effect of irradiation is a change in structure caused by "Thermal Spikes" [21]. These changes occur when the energy of the knocked-on atoms dissipates locally as a thermal pulse. This pulse can produce extremely high temperatures for a very short period of time [41 and 50]. The area affected by such a "spike" could contain interstitial vacancies, miss-oriented regions or dislocation loops (Fig. 2.2.5).

Russell [47] suggests the following processes as mechanisms for irradiation-induced phase change:

A. Enhanced diffusion. At lower temperatures, with respect to phase change temperature, the irradiation produces vacancies and interstitials much more rapid then they can diffuse to dislocations, grain boundaries and other defects. Vacancy concentrations are many orders of magnitude greater then the equilibrium value. In Figure 2.2.3, we can see the effect of the irradiation on the diffusion coefficient in an alloy. The irradiation will have little effect on D at high temperatures due to thermal vacancy production. The activation energy for diffusion is the sum of the energies of vacancy formation and migration. At intermediate temperatures, D takes a relative

constant value of about 10^{-16} cm^2/s, that is enough to produce a significant atomic mixing. By studying the kinetics of the domain growth [38], was found that it was analogous to metallurgical grain growth and could be described by the expression:

$$D^n = kt \tag{2.4.2}$$

where D is the average domain size, t is the aging time, k is the rate constant and the exponent n is the slope of the Log (D) vs. log (t) plot as seen in Figure 2.2.3. The value of n changes with temperature from 2.0 between 800^0 and 850^0 C to 2.9 between 600^0 and 700^0 C. Many research papers investigate the variation of diffusion coefficient with the temperature [1, 15, 23, 39 and 48].

B. Solute Segregation. The solute flux may be induced by solute. A vacancy flux gives rise to a solute flux with the slow diffusing species going to the defect sink. [49 and 50]. In alloys under irradiation, permanent fluxes of point defects are sustained towards sinks such as free surfaces and interfaces. The coupling between these point defect fluxes may induce a modification of the composition field as demonstrated by Okamoto and Wiedersich [24]. In austenitic stainless steels, this would lead to chromium depletion at the grain boundaries, and this is the main suspect in stress corrosion cracking in Pressurized Water Reactors (PWR).

C. Defect Recombination at the Particle Mix Interface. Cauvin and Martin [51] developed a theory for the effect of excess vacancies and interstitials on the nucleation of coherent particles, where point defects are trapped at the particle-matrix interface, as opposed to being absorbed. The effect of point defect trapping is the increase in

recombination at the particle-matrix interface that results in an influx of solute. This way the particle stability is enhanced.

D. Ordering and disordering. Like presented earlier, the effect of irradiation on ordered alloy phases can be described as a balance between two conflicting processes: the disordering produced by the atomic replacements during cascade and defect production, and the ordering facilitated by the migration of vacancies and interstitials. According to Liou and Wilkes [35], the rate of change of the order parameter S, is the sum of the irradiation disordering and irradiation enhanced thermal ordering rates. Under constant flux and temperature, S will achieve a steady state. The model presented by Banerjee and Urban [32] is consistent with Bragg-Williams solid solution model. Most of these theories predict that irradiation disordering will prevail at low temperatures, with some form of order being present at intermediate temperatures. Complete disordering would follow at temperatures higher than the critical temperature Tc.

E. Amorphization. It seems that excess vacancies may alter the phase equilibrium by acting as a thermodynamic component in the solid solution. Irradiation of an equilibrium alloy of two solid phases at a temperature T could raise the effective temperature of T_1' where the irradiated alloy would be composed of amorphous and crystalline phases of different compositions or even to T_2' to produce a uniform amorphous-like alloy presented in Figure 2.2.4 [15 and 105].

F. Recoil resolution. Energetic atoms may strike atoms in precipitate particles and propel them into the surrounding lattice. Crystals are predicted to approach an equilibrium radius from larger to smaller sizes, smaller particles being more stable than

larger ones [3 and 33]. This would be accompanied by an enrichment of the undersize component at the surface and a depletion of the oversize solutes near irradiated surfaces [39].

2.3 Temperature Effects on Ordering in Binary Alloys

In the study of irradiation effects in metals and alloys, perhaps the most important single variable is the temperature. This is because the temperature will determine whether the effects caused by irradiation will have sufficient mobility to interact and bring about additional secondary effects. Thermal and mechanical properties of materials are influenced by to the induced defects and are dependent on the amount of dislocations [42]. The lattice waves are scattered by defects, decreasing the thermal conductivity of the material. Dislocations can move or can be pinned because of irradiation. Pinning is generally attributed to interstitials interacting with dislocations. The interstitials are the only type of defect expected to have sufficient mobility to account for the observed results in thermal properties at low temperatures [52]. Point defects can be a factor too as the periodic structure is disturbed for several atomic distances around it, affecting this way the thermal, electrical and mechanical properties [38 and 53]. Another thermal effect is the energy stored in Frenkel pairs (pairs of lattice vacancies and interstitial atoms). When the temperature of the irradiated specimen is raised, these defects can recombine and release their stored energy of about 5 eV per pair [54].

Upon heating, some alloys go through a phase transformation. When this happens in a furnace, the alloy will return to its room-temperature phase with coarse microstructure. When instead, heating is very local (as in the case of an irradiated sample, when the bulk acts as a heat sink), the resulting microstructure will be very fine [55]. The conditions required for the process to occur are: (a) the radiation is strong enough to heat the spot to above the transformation temperature and (b) the rest of the sample is kept cold enough to induce quench-like conditions on the heated zone.

Due to the presence of several competing ordering processes Ni_4Mo and Ni_3Mo have been in the attention of a few research groups [13, 26, 32 and 56]. Okamoto and Thomas [13] and Spruielli and Stansbury [56] aged Ni_4Mo at different temperatures and looked at the electron diffraction patterns. They observed that for an alloy initially quenched from 1000^0 C and then aged at 750^0 C, the ordering reaction takes place at the surface and very fast. The intensity of the {1 1/2 0} peaks are still present but a lot weaker than at 650^0 C and they disappear after a longer ageing time. Work by Tanner et al. [57 and 58] has shown that in bulk samples the LRO $D1_a$ structure does not develop even after annealing for 550 h at 300^0 C. All the experiments done with Ni-Mo alloys emphasize how critical the temperature is in the absence of other factors (irradiation effects) in the order-disorder process.

Figure 2.3.1 presents the temperature evolution of Ni_4Mo and Ni_3Mo by means of electron diffraction [59]. The images were obtain by TEM and indicate that the ordering process is present in Ni_4Mo and Ni_3Mo specimens at temperatures a little under the

critical temperature, but not above it. In addition, Banerjee [1] has determined the stability ranges as depending on the temperature for the Ni-Mo alloys. This dependence is presented in the Figure 2.4.6. In the plot of SRO and LRO vs. the temperature, we can see the temperature ranges where each of the processes is dominant.

2.4 Ni-Mo Type Alloys

Nickel and Nickel based alloys have shown potential as structural and containment materials in nuclear reactors. The increasing demand for high operating temperatures and new reactor concepts created a demand for a structural material that has strength at high temperatures and is resistant to certain media. Some examples are Inconel-X, Hastelloy-X and Hastelloy C. Unalloyed nickel has very little use as a construction material for reactors. However, it has been used in investigations to study the mechanism of irradiation damage and irradiation hardening [60 and 61]. The effects were evaluated based on changes in ultimate tensile strength, lower yield points and ductility as measured by elongation at fracture [62]. The experimenters attempted to separate and evaluate the effect of lattice displacement and dislocation locking as they may have been related to irradiation hardening. They found that the lattice hardening of pure Ni was dependent upon total neutron exposure in the following manner:

$$\sigma_i = \sqrt{A(1-e^{-B\Phi})} \qquad (2.4.1)$$

where:

σ_i = lattice friction stress

Φ= particle flux (/ cm^2)

A = constant

B = constant

Makin et al. [62] observed that low exposures to irradiation (8x 10^{17}) part/cm^{-2} produced a noticeable increase in the yield strength and a decrease in total elongation at fracture, but very little change was found in the ultimate strength. However, after a dose of 5x10^{19} part/cm^2, a 100% increase in the yield strength was noticed. A similar study was made by Wilsdorf [63] with irradiation up to a dose of 10^{19} part/cm^2. He noticed that the increased yield strength reported is not the result of vacancies and vacancy clusters but is due to anchoring of dislocations by loops and kinks, which are nucleated at vacancies. He also observed that once slip has occurred along a few slip planes, a large number of existing vacancies have been eliminated from between the slip planes. The slip path is then clear and deformation can occur quite readily. Hence, a low rate of work hardening can be expected for irradiated materials.

Many Ni based alloys can be strengthened by fine dispersions of second phase ordered precipitates [18 and 64]. Future breeder reactors and second or third generation fusion reactors may rely heavily on these two-phase material for their construction. The increase in strength caused by the precipitates will allow reductions in the mass of some structural components and thus improve reactor performance (by increasing breeding efficiency for example). However, the long term strength and integrity of these two phase material depend on the precipitate morphology and that can be drastically altered by the irradiation environment. In reactors, the service temperatures may well exceed 400^0 C.

Ordered compounds, specifically of the type Ni_3X, will remain ordered at these temperatures and at the 10^{-6} dpa/s damage rate anticipated. However, other microstructural modifications can occur at these temperatures, such as void swelling, dislocation loops and network formation. The microstructure of the precipitated phase, i.e. the size distribution, shape, number density and volume fraction characterizing the precipitates, may be altered by irradiation. These alterations are referred to as precipitate restructuring. They can be: irradiation enhanced coarsening of precipitates, spatial redistribution of precipitates and precipitate renucleation [65].

Some Ni-Mo alloys upon exposure to elevated temperatures in the range 600^0-800^0 C, suffer an almost complete loss of room temperature ductility as a result of LRO [18]. It is very important to elucidate the embrittlement of ordered Ni_4Mo and Ni_3Mo in order to better use these and similar alloys.

The structure of the disordered primary Ni-Mo solution is fcc. Diffraction patterns of this phase exhibit diffuse peaks in all equivalent {1 1/2 0} positions in the fcc reciprocal lattice over a wide range of compositions (8-33 at % Mo). Within this range, several ordered structures have also been observed. In addition to the β phase (Ni_4Mo) and gamma-phase (Ni_3Mo), a metastable phase Ni_2Mo has been observed in the (β + γ) region, possessing a Pt_2Mo superlattice (Figure 2.4.1). None of these ordered phases produces superlattice reflections at the {1 1/2 0} positions. The phase diagram of Ni-Mo alloy is presented in Figure 2.4.1 and the alloys researched in the present paper are given in Table 2.2 with their symmetry characteristics.

Type	Alloy	Structure Struchturberiht	Structure Schonfliss	Structure International	Characteristic stars	Unit cell content
A_4B	Ni_4Mo	D1a	C_{4h}^5	I4/m	4/5 (1/2 1 0)	2
A_3B	Ni_3Mo	DO_{22}	D_{4h}^{17}	I4/mmm	1 0 0 ; 1 0 ½	2
A_2B	Ni_2Mo	-	D_{2h}^{25}	Immm	1/3 (2 2 0)	2
AB	NiMo	$I1_0$	D_{4h}^1	P4/mmm	0 0 1	1

Table 2.2 Crystallography of Ni-Mo alloys.

The structures of Ni_4Mo, Ni_3Mo and Ni_2Mo belong to the family of {1 1/2 0} of fcc based structures in that they owe their stability to the minimum of the reciprocal space (k-space) potential energy function V (k) in the point <1 1/2 0> [88]. Such a minimum would imply a tendency for like atoms to be the third nearest neighbors (separated by <1 1/2 > fcc vectors). This would lead to a stabilization of a geometry sketched in Figure 2.4.3. The Mo atoms at the corners of these tiles are separated only by the third nearest neighbor vectors [9 and 10]. In the as quenched fcc Ni-Mo alloys (and some Au-Cr, Au-V alloys) the minimum in the V(k) function at <1 1/2 0> points is characterized by intensity maxima at <1 1/2 0> and equivalent in the reciprocal space of fcc [66].

2.4.1 Ni_4Mo

The Ni-20 at% Mo alloy is well known for its corrosion resistance in non-oxidizing, acid chloride environments. There are several commercial alloys based on this composition [18]. The Ni_4Mo exists as Short Range Ordered (SRO) face centered cubic (fcc), α-phase above 868^0 C (1140 K). The lattice parameter of the disordered fcc phase

of the composition Ni 20 at. % Mo is a $_{fcc}$ = 3.6086 A. After the ordering transformation, the lattice dimensions of the initial α–phase are preserved with only a 1.16 % contraction in the c axis and 0.4 % expansion along a and b axes. The Long Range Ordered (LRO) structure is body centered tetragonal (bct.) $D1_a$ (β-phase) with lattice dimensions a= 0.5731 nm, c = 0.3571 nm, and c/a = 0.623. In the ordered phase, Ni_4Mo exhibits a range of physical and mechanical properties that correlate well with the internal structure [9]. The two competing superlattice structures in Ni_4Mo are associated with the wave vectors <1 1/2 0> and 1/5<4 2 0>. The corresponding structures can be described in terms of stacking {420} planes of all Ni (N) and all Mo (M) in the stacking sequence MNNNNM. The ordering process of an fcc alloy with <1 1/2 0> wave vector fulfill the symmetry criteria for a second order transition while the 1/5<420> ordering is a first order transition to a $D1_a$ type structure [26 and 44]. Bellon and Martin [3] were able to calculate the free energies associated with these two structures as functions of their respective order parameters. The $D1_a$ ordering process as a first order transition occurs by nucleation of microdomains followed by their growth. The (001) plane of ordered phase is parallel to the {001} planes of the fcc parent which allows six unique variants of domains from a single fcc orientation, and two possible orientations of the bct lattice in any one of the {001} planes. This creates three types of domain interfaces as determined by Ruedl et al. [8]. In increasing order of surface energy, these are: antiphase boundaries (APB) (Figure 2.4.13), antiparallel twin boundary (APTB) and perpendicular twin boundary (PTB). The APB occurs when two neighboring domains having parallel c-axes are related by a translation mismatch. The PTB separates two domains for which rows of molybdenum

atoms enclose an angle of 2 arctn (1/3). The structures are mirror images, twin related and the c-axes are antiparallel. The PT results when the c-axes in adjacent domains are perpendicular.

LeFevre at al. [67] and Okamoto [13] pointed to the fact that LRO and SRO structures of Ni_4Mo are characterized by the occupancy of every fifth {420} fcc plane by molybdenum atoms with the intervening planes occupied by nickel atoms. The consequence is that superlattice reflections occur at every 1/5{420} position in reciprocal space.

The primary driving force for the coarsening reaction in the ordered Ni_4Mo is the reduction in interfacial energy of the system obtained by the elimination of the APB between the small domains [9]. The heterogeneous grain boundary product consists of groups of large domains separated by APB on planes of low energy {110} α-phase [13]. The initial difference in the degree of order between the coarse grain boundary domains and the fine intragrain domains provides a small driving force. Thus, the progression of the coarsening reaction has the advantage of lowering the energy of the system by eliminating the extra interfacial energy of the intragrain APB while simultaneously causing a small increase in the degree of order. It is a process that resembles secondary recrystalization. This coarsening mechanism in Ni_2V was discussed by Tanner [57] and is very similar to the reaction observed in Ni_4Mo. Ni_2V is isotypic with Ni_2Mo [68], and is also classified as a [420] alloy. It was observed that the growing domains carry the original incoherent grain boundary ahead [57]. Since the transfer of atoms require less energy at grain boundary, this interface provides a substrate of rapid diffusion, which in

turn, results in rapid growth. Tanner assumed the grain surface composed of ledges and that the migration process is related to variations in the movement of atoms on these ledges [58].

Irradiations using 1 MeV electron beam have clearly shown a continuous transition from <1 1/2 0> ordered state to the $D1_a$ state [8] (Figures 2.4.2, 2.4.3 and 2.4.5). In the low temperature range when T < (- 50^0) C) both SRO and LRO are destroyed. In the intermediate ranges (-50^0) - (+150^0) C, the structures can be maintained to a certain level. For T > 150^0 C, LRO cannot be fully destroyed and SRO does not build up. For high temperatures (200^0 -500^0 C), a sample originally in LRO will remain in LRO with a slight reduction in LRO parameter and a mixture of LRO and SRO states will develop in the SRO sample. In the 500^0-850^0 C range, only the LRO structure persists (Figure 2.4.6). For electron irradiation, Meulanere et al. [112] propose the following mechanisms:

1. Points defects are created

2. The point defects cluster together creating an ordered or a random defect pattern, depending on the irradiation conditions

3. Upon further irradiation, these clusters grow to form visible defects establishing a stable pattern.

Under 300 KeV Ni^+ irradiations, there are no mixed SRO - LRO states observed [8]. The steady state structures are independent of the initial set of ordering (Figure 2.4.6). Ni^+ irradiations performed by Sundararaman et al. [144] yielded similar results. Samples initially in the SRO state and irradiated at temperatures below 550^0 C do not

show any tendency towards LRO. Only at the temperatures above 750^0 C spots for the 1/5{420} reflections start showing up. For the samples initially in LRO, the $D1_a$ structure disappears completely in the 20^0 – 200^0 C range. For the 750^0 – 850^0 C range, there is no significant difference in the diffraction pattern between the irradiated samples and the as-quenched alloys from that temperature. At temperatures around 750^0 C LRO is not affected by irradiation. Mixed states of LRO and SRO are observed by Bellon at all. [15] at intermediate temperatures for samples initially in LRO state and irradiated with He^+ and Ne^+ beams. These beams produce a smaller amount of cascades as compared with electron irradiation [32]. This means that no reasonable conclusion can be reached on the influence of the dose rate in case of electron and alpha irradiations due to the difference in collision mechanisms.

2.4.2. Ni_3Mo

This alloy exhibits a SRO state characterized by diffraction intensities at {1 1/2 0} positions above the critical temperature point [68]. A complete extinction of the intensities of {1 1/2 0} positions of the reciprocal space is noticed below the critical temperature. Progressive ordering in the Ni-Mo binary alloy in the vicinity of the composition for Ni_3Mo has shown that the Ni_2Mo and the Ni_4Mo phases nucleate during the early stages of the transformation. The evolution of order in Ni_3Mo has been studied in a wider temperature ranges under electron irradiation with a displacement rate of about $5x10^{-3}$ dpa/s [9]. Ni_3Mo decomposes peritectoidally at 910^0 C to α-phase + NiMo.

Quenching fast from higher temperatures the decomposition of Ni_3Mo to NiMo can be suppressed [66]. Progressive changes in the [1 0 0] diffraction pattern at two temperatures in electron irradiations are shown in Figure 2.4.2. Here a diffuse intensity distribution develops connecting the {1 1/2 0} spots with a change towards the 1/3{4 2 0} and the 1/5{4 2 0} positions which are the superlattice reflections of Ni_2Mo and Ni_4Mo. This can also be seen from the steady state structure developing as a function of temperature (Figure 2.4.6). After heating above 950^0 C and then slowly cooling, van Tendeloo [66] observed the diffraction patterns specific to the $D0_{22}$ superlattice spots, and then at about 800^0 C he noticed the formations of Ni_4Mo and Ni_2Mo. The intermediate phases, Ni_2Mo, Ni_4Mo and Ni_3Mo ($D0_{22}$) are based on a cubic close-packed stacking and are the direct superstructure of the disordered fcc matrix.

2.4.3 Ni_2Mo

Ni_2Mo has a base-centered-orthogonal (bco) structure and like the $D1_a$ structure of Ni_4Mo, the Ni_2Mo structure can be described by stacking atoms on either {420} or {220} planes where every third plane contains all Mo and in between al Ni atoms. This way, the reciprocal lattice can be constructed from the original fcc lattice where the superlattice reflections will appear at every 1/3(220) or 1/3(420) reciprocal lattice vectors [68]. This will give rise to six orientation variants of Ni_2Mo corresponding to the six variants of {220}[13].

2.4.4 NiMo

According to Jin [71], NiMo alloy, also known as the δ-NiMo phase, has a primitive unit cell with a = b = 0.9108 nm, c = 0.8852 nm and $\alpha = \beta = \gamma = 90^{0}$. The crystal can be viewed as tetragonal and belonging to the space group P4/mmm. A SEM picture of the surface of this phase and a surface analysis is presented in Figure 2.4.9 where areas of the δ-phase are seen enclosed by the Ni matrix. NiMo is one of the decomposition product of Ni_3Mo and Ni_4Mo.

2.5 Mechanisms of order-disorder transformations

The order-disorder transformation has been the subject of numerous theoretical and experimental investigations since the early part of this century as many solid solution exhibit LRO below a critical temperature and SRO above. Perfect LRO is an abstraction valid at 0 K, and perfect stoichiometry. Any deviation from perfection may be characterized in terms of crystalline defects such as periodic distribution of antiphase boundaries (APB) in case of long period superlattice. Statistical thermodynamic treatments of ordering can account for diffuse scattering distribution without recourse to any particular structural features, so they may not be essential for a description of the equation of a disordered state. In a long range ordered state (LRO) the component atoms of the alloy system occupy specific sets of sites in the lattice making the arrangement of atoms regular and periodic in three dimensions. This type of ordering usually occurs at

simple stoichiometric compositions. In a short range ordered (SRO) state, the structure is neither completely random nor long range ordered, rather non-random atomic arrangements occur statistically throughout the lattice.

There are numerous other alloys undergoing a phase change from a cubic to a non-cubic phase, like Cu-Au, Cu-Pt, Ni_2V and Ni_3V. In alloys undergoing a symmetry change upon ordering, self-deformation of the alloy, arising from volume and shape changes of the unit cell, has a decisive effect upon strength. This is in addition to factors such as composition, domain size and melting temperature, which also determine the strength of a cubic superstructure.

The transformation of the high temperature phase to the lower temperature phase involves segregation of atoms of each component of the alloy to specific sites in the array of atomic positions of the high-temperature phase. The low-temperature ordered phase is generated in this manner from the high temperature disordered phase. In such an order-disorder transformation, a random distribution of atoms on a given array of atomic sites changes into an ordered distribution leaving the array of atomic sites unaffected [72].

During an ordering reaction, the like atoms generally tend to remain as far apart as possible from one another such that the number of unlike atomic bonds in the ordered phase is increased. Landau and Lifshitz were the first ones to introduce mathematically based interesting concepts regarding the process of phase transitions [73]. Initially, their theories have made little waves into the world of materials science literature, mainly because they were loaded with numerous abstract group theory terms. The physicists working in the filed of phase transformations were more interested in the mathematical

model created by Ising and Khachaturyan. The mean field model suggested by Khachaturyan [74] is in fact a Bragg-Williams model with an arbitrary number of long-range order parameters. In this model, the free energy is Taylor and Fourier expanded with the essential distinction between harmonic and anharmonic terms emphasized.

2.5.1 Mean Field Free Energy Model

We start with an fcc or bcc lattice where each site s can be occupied by an atom of type A or B, and with a region consisting of N = Ni x N2 x N3 unit cells. Next we set up a microcanonical ensemble with N lattice sides [78]. We assume that in a point s the occupation number is 1 if there is a B atom and 0 if not. If we sum the occupation number at all points and divide by the number of systems in the ensemble we get the fractional occupancy or the concentration:

$$0 \leq f(s) \leq 1 \tag{2.5.1}$$

with the overall concentration:

$$c_B = c = \frac{1}{N}\sum c(p) \tag{2.5.2}$$

$$c_A = 1 - c^{-p} \tag{2.5.3}$$

where the summation over p is over the N lattice points of the crystal. This is the same as subdividing the original lattice into N equivalent sublattices (with N large). In the first (zero) approximation, the internal energy of the crystal is obtained by assuming that the atoms interact with pairwise forces and that the partition function can be factored into independent vibrational and configurational parts. This function can be obtained by

taking random distribution of A and B atoms. Considering the Helmholtz free energy [74]:

$$F = F_A + F_B + F_M \tag{2.5.4}$$

F_A = energy of pure A crystal including vibrational energy

F_B = energy of pure B crystal including vibrational energy

F_M = configurational free energy of mixing

$$F_M = N_{v0} q_0 + \frac{1}{2}\sum v(p - p_0)\xi(p)\xi(p_0) + r\sum\{c(p)\ln c(p) + [1 - c(p)\ln(1 - c(p))]\} \tag{2.5.5}$$

where

$\xi(p) = c(p) - c$ is the concentration deviation and p is the pair interaction parameter

$v_{AB}(r)$ is the pair energy of a pair separated by the lattice vector **x**(r)

We will also use:

$q_0 = c_A c_B = c(1-c)$

$v_0 = -\sum v(p)$

$\tau = k_B T$, k_B is Boltzman constant, T the absolute temperature.

Using eq. 2.5.5 Khachaturyan showed that the minimalization of free energy leads to a Fermi-Dirac distribution law for c(p) [74]. In our simple mean field theory there are no singularities for the free energy so we can do a Taylor expansion about the homogenous state c(p) = c

If :

$$F_M = Nc_0 \tag{2.5.6}$$

with the expansion coefficients for c(p) given by:

$$f_0 = v_0 c_A c_B + T(c_A \ln c_A + c_B \ln c_B)$$

$$f_0(r \neq 0) = 2v(r)$$

$$f_1 = -\frac{r(c_{A2} - c_{B2})}{q_{02}}$$

$$f_2 = \frac{2T(c_{A3} - c_{B3})}{q_{03}}$$

The zeroth order term is the regular solution model. The second order term depends only on local concentration. If we assume c_B to be less than 1/2 without loosing generality (1/4 for Ni_4Mo) then the third order coefficient is always negative and the forth always positive. If we put the condition that the free energy is minimum with respect with N configuration variables c (p), then we obtain the equilibrium configuration and the average concentration. The situation can be simplified by grouping sites into a small number of sublattices according to perfect ordering at stoichiometric compositions[75]. We can define a long-range order parameter (LRO) as a combination of concentration deviations:

$$\eta = \sum Y(p)\xi(p) \qquad (2.5.7)$$

where γ (p) are the coefficients of lattice grouping and η is an homogeneous function that must vanish above the transition temperature Tc.

$\xi(p) = 0$ is a homogenous state and a solution of the minimization of the free energy [2.5.6] at high temperatures. A phase transition of the second kind is one for which the order parameter goes to zero as the temperature approaches the critical temperature from below [78]. Having a non-vanishing third order term in expression

(2.5.6), F is an asymmetrical function of η and $\xi(p)$ thus producing a phase transition of the first order.

In the ordered phase of Ni_4Mo and Ni_3Mo, only Ni atoms are the nearest neighbors of Mo atoms. Therefore the number of unlike Mo-Ni atomic bonds in the ordered structure is much higher than in the disordered structure. The Ni-Mo bond energy may be estimated from the enthalpy of formation of the alloy and is negative. Hence, the presence of a large number of Ni-Mo bonds in the ordered phase reduces the free energy and renders the ordered phase more stable than the disordered phase. During an ordering reaction, the like atoms generally tend to remain as far apart as possible from one another so that the number of unlike bonds in the ordered phase is increased.

Ordering in the fcc lattice can be described as four interpenetrating simple cubic sublattices of equal size. The lattice points at the cube corners of the fcc unit cell constitute one sublattice and each pair of points at the center of two opposite faces generate one sublattice in combination with similar lattice points on the neighboring unit cells.

2.5.2 Antiphase Domains

The ordering process within each grain of the disordered phase may start at a number of locations on any one of the sublattices. Considering the two-dimensional lattice in Figure 2.4.13, we can assume that ordering in region I starts with the black atoms occupying the sublattice marked by the dashed lines, and in the region II starts with

the black atoms occupying the sublattice marked by full lines. When these regions grow and meet they are out of step at the boundary because the same sublattice contains different atoms on both sides. Since nearest neighbors of an atom are located on another sublattice, the same kind of atoms face each other across the boundary and the boundary is associated with a positive energy. Such boundaries are known as antiphase domain boundaries (APB) and the ordered regions on both sides of the boundary are called antiphase domains. A shift or translation of the atomic arrangement on one side of the boundary in a certain crystallographic direction in the crystal can eliminate the misalignment across the boundary and hence the boundary itself. The domain boundary is specified by stating the translation vector (p vector) and the plane on which the boundary lies.

The presence of APB at regular intervals stabilizes the ordered structure. This stability can be attributed to the decrease in electronic energy of the phase due to the periodic presence of the antiphase domain boundaries[76]. The APB can be identified by TEM on the basis of the relation between their contrast characteristics and specimen orientations [77].

2.5.3 Short Range Order

Above the critical temperature (T_C) the LRO does not disappear completely and suddenly. For temperatures not too distant from T_C, one can still observe superlattice lines or spots in the diffraction figures. This condition is called short range order (SRO).

An alloy can be "frozen" in this condition by heating it above T_C and then rapidly quenching it to room temperature [13 and 68]. For example, in the ordered Ni_3Mo, a Mo atom located at (000) or at the origin, is surrounded by 12 Ni atoms at (1/2 1/2 0) and equivalent positions. Any given Ni atom is surrounded by 8 Ni atoms and 4 Mo atoms. Above T_C this arrangement breaks down, because a Mo atom can be found either at the corner or in the center of a face. This kind of behavior is observed in many solid solutions [78 and 79]. There is also a tendency of like atoms to be close neighbors – effect known as clustering [69]. All solid solutions may exhibit SRO or clustering in a lower or higher degree just because they are composed of unlike atoms with specific forces operating between them.

In ordered as well as disordered structures, each atom is surrounded by a certain number of first, second and other higher order nearest neighbors. Out of these neighbors some are like atoms and some are unlike atoms. For example if the coordination number in an alloy, A-B containing 25%at B is twelve, the number of nearest neighbors of each atom becomes twelve. In the disordered structure each A atom will have on average three B atoms as nearest neighbors. If A atoms prefer B atoms as neighbors, the average number of B atoms, which are nearest atoms of atom A, will be greater than three. Such ordering may not extend beyond the first nearest neighbors. The number of A-B bonds in an alloy with SRO is greater than that in the random alloy. The short-range parameter σ may be defined as:

$$\sigma = \frac{q - q_r}{p_m - q_r} \tag{2.5.8}$$

where q is the number of A-B pairs, q_r is the average number of A-B pairs in the random arrangement, and q_m is the maximum possible number of A-B pairs.

The ordered phase contains a large number of unlike atom bonds, which reduces the bond energy and in some cases the electronic energy of the phase. At low temperatures the ordered phase is stabilized since the free energy of the ordered phase becomes lower than that of the disordered unity. Any decrease in the degree of order raises the bond energy but simultaneously increases the configurational entropy, which makes a negative contribution to the free energy. The entropy contribution (-TS) to the free energy becomes appreciable at high temperatures. Therefore the degree of order decreases with an increase in temperature. At a critical temperature, T_C, the long-range is completely destroyed and S becomes zero. The long-range order parameter usually changes discontinuously at T_C. The local segregation of atoms continues to exist above T_C, and the short-range order parameter continues to decrease above T_C with the increase in temperature. When an alloy that has SRO is quenched to a temperature Ta below T_C, the disordered structure with a short range order is retained at Ta. With an increase in holding time at Ta, the ordered phase nucleates and grows into an ordered domain, which tends to coalesce to produce larger domains. During this period, the degree of long-range order approaches unity. Four different processes are part of the order-disorder transformation: [1]

1. Formation of SRO above T_C
2. Nucleation and growth of the ordered phase at $Ta < T_C$
3. Increase in the degree of LRO of the ordered phase

4. Coalesce of the antiphase domains.

The degree of SRO increases with the increase in the number of A-B pairs, process that occurs homogenously. In general in an alloy, the atoms A and B change their position by diffusional motion. If the new position results in an increase in the number of A-B bonds, the free energy of the system is normally reduced and the atoms tend to spend a greater fraction of the time in the new position. Consequently the degree of SRO is increased. On the basis of this mechanism the rate of increase in the number of A-B bonds may be expected to be proportional to exp(-Q*/RT) and ($q_e - q$), where Q* is the activation enthalpy for diffusion and q_e is the equilibrium number of A-B pairs. Hence:

$$\frac{dq}{dt} = k_1 e^{-\frac{Q}{RT}}(q_e - q), \text{ where } k_1 \text{ is a constant.} \qquad (2.5.9)$$

$$\frac{d\sigma}{dt} = k_2(\sigma_e - \sigma) \qquad (2.5.10)$$

where k_2 is a constant and σ_e is the equilibrium short-range order parameter.

The applicability of this equation to SRO kinetics in alpha-brass has been verified by Damask [46]. The activation energy of 165 kJ/mole obtained for alpha-brass is close to the energy activation for the diffusion. However it is not easy to study the SRO kinetics. The measurement of σ by X-ray diffraction technique is tedious. The widely used resistivity measurements are difficult to interpret unambiguously since short-range ordering may either increase or decrease the resistivity. The disordered alloy quenched to a temperature below T_C generally contains SRO. SRO implies that ordering may extend up to a few neighbors. Therefore as illustrated in the Figure 2.5.1, a structure with SRO may be visualized as a disordered structure with very small ordered domains [74]. Such

ordered domains of supercritical size act as nuclei for the ordered phase. Thus the transformation is considered to be initiated by a constant number of nuclei N_0 that is initially present in the unit volume, and further nucleation may be taken as negligible.

There are a few good models for Short Range Ordering:

1. The statistical model: SRO is homogeneous. The occupation in any neighboring shell around a central atom of one type fluctuates around some value. With increasing distance of the neighboring shell the pair correlation function becomes the function of a statistically uncorrelated arrangement [80].

2. The model of disperse order: SRO is heterogeneous. The fluctuations in concentration and in the degree of order are no longer statistical. We can assume a less ordered matrix with dispersely distributed particles of a long range ordered phase [81 and 82].

3. The microdomain model: SRO is of a heterogeneous type, consisting of relatively well-defined and well-ordered regions (the microdomains – a few unit cells in size) embedded in a random matrix. Only the degree of freedom varies between the microdomains and the matrix, not the composition [83, 84 and 85].

We can distinguish two groups of reflection maxima in the diffraction spectra based on the positions of the diffuse maxima. One group of maxima located at the special points (Lifshitz points) of the first Brillouin zone, and the second group is located at any other position. Okamoto and Thomas [13] observed a close relationship of stable/metastable ordered structures in Ni-Mo alloys displaying the (1 1/2 0) diffuse maxima in SRO state. These structure are built by stacking (420) planes. Okamoto

suggested that SRO state consists of a mixture of microdomains ($D1_a$ and $D0_{22}$) [13]. Das determined that the structure of microdomains leading to (1 1/2 0) diffuse maxima does not necessarily correspond to a LRO structure [68]. The models of microdomains and concentration waves (real-space and reciprocal approach to the microstructure) were considered equivalent as the microdomains may represent the materialization of the concentration waves [86]. De Meulanere et al. [53 and 87] observed $D1_a$ and $D0_{22}$ as building elements for the SRO states. Investigation on transition stages between SRO and LRO are of special interest because the diffuse maxima and superlattice reflections are located differently.

2.5.4 Long-Range Order

The perfectly ordered arrangement of atoms can extend over the entire crystal. If there are faults in the ordered arrangements like those brought about by the exchange of positions of A and B atoms, the order is less than perfect. The parameter that measures the degree of order is designated as the degree of long-order S. If we consider a binary alloy with two types of atoms A and B, and two lattice positions α and β, in the ordered state in the ideal stoichiometry α-sites are occupied by A-atoms and β-sites by a B-type atoms. In terms of composition fractions we have:

$$x_A + x_B = 1$$

If N is the number of atoms in a sample we should have $N_A = x_A N$ and $N_B = x_B N$. Also lets consider y_α and y_β the fractions of α-sites and β-sites with $y_\alpha + y_\beta = 1$. Then the

number of each kind of site is given by $N_\alpha = y_\alpha N$, and $N_\beta = y_\beta N$. According to Warren[89] we can use the following parameters:

r_A = fraction of α-sites occupied by the right atom (A)

w_α = fraction of α-sites occupied by the wrong atom (B)

r_B = fraction of β -sites occupied by the right atom (B)

w_β = fraction of β-sites occupied by the wrong atom (A)

Then we can write:

$r_\alpha + w_\alpha = 1$ and $r_\beta + w_\beta = 1$.

The fraction of the sites occupied by A-atoms must equal the fraction of A-atoms, and same for B-atoms. Mathematically:

$$y_\alpha r_\alpha + y_\beta r_\beta = x_A \text{ and } y_\beta r_\beta + y_\alpha r_\alpha = x_B \tag{2.5.11}$$

The long-range order parameter used in section 2.1 can be defined for a random arrangement and is proportional to $(r_\alpha + r_\beta)$ with S = 0 for a completely disordered state, and S = 1 for stoichiometric composition $(r_\alpha = r_\beta = 1)$. Then we define:

$$S = a + b(r_\alpha + r_\beta)$$

Applying the two extreme conditions we obtain:

$$S = r_\alpha + r_\beta - 1 = r_\alpha - w_\beta = r_\beta - w_\alpha \tag{2.5.12}$$

Using the equations (2.5.11) and (2.5.12):

$$S = \frac{r_\alpha - x_A}{y_\beta} = \frac{r_\beta - x_B}{y_\alpha} \tag{2.5.13}$$

This way the parameter S can become 1 for a perfect stoichiometry and is going to be less than one for anything else. With this definition, the structure factors for the superstructure reflections would be proportional to S even for non-stoichiometric compositions. The structure factor can be written in a more elaborated way as a sum over the α and β position [89]:

$$F = \sum_{\alpha}(r_{\alpha}f_A + w_{\alpha}f_B)e^{2\pi i(hx_n+ky_n+lz_n)} + \sum_{\beta}(r_{\beta}f_B + w_{\beta}f_A)e^{2\pi i(hx_n+ky_n+lz_n)} \quad (2.5.14)$$

Change in composition may affect the state of order-disorder. Since the ratio of corner sites to face centered sites in Ni_3Mo must be exactly 1:3, then perfect order can be achieved only when the stoichiometry of the alloy is very near this composition. Same is true for Ni_4Mo alloy with a ratio of 1:4.

Banerjee et al. [11] determined experimentally the values for S under electron irradiation (Figure 2.5.2 – 2.5.3). He notes that the degree of order achieved after irradiation, seems to be independent on dose rate and temperature. Also in spite of the scatter in the measured values it is evident that the steady state value of S does not exceed 0.55 for the temperature ranges (350^0 C – 450^0 C) but gets as high as 0.85 in the ranges (500^0 C – 700^0 C). Mhatre et al. [12] looked at the value of S in the case of 100 MeV I^{9+} irradiation, when the LRO was induced in Ni_4Mo through electronic excitation loss and nuclear energy loss (Figure 2.5.5).

2.6 X-ray Diffraction Studies of Ni-Mo Alloys

X-ray diffraction (XRD) is one of the best techniques used to uniquely identify the crystalline phases present in materials and to measure the structural properties like grain size, phase composition, preferred orientation and defect structure of these phases. XRD also offers great accuracy in determining the atomic spacing. It is a nondestructive, no contact procedure and more sensitive to elements to higher Z since the diffracted intensity from these elements is larger than the intensity from elements with low Z. With the most available instruments a sensitivity of about 50 A can be achieved. One minor disadvantage is that XRD requires specimens to have at least a minimum square surface size of about 25 mm^2. The order-disorder transformation in binary substitutional alloys can be successfully studied with the help of XRD diffraction. This subject is treated in detail in a few of the reference books [88, 90 and 91]. In Figure 2.6.1 it is shown the basic setup for an X-ray experiment. The diffraction angle 2θ is the angle between the incident and the diffracted X-rays. In an XRD experiment, the diffracted intensity is measured as a function of 2θ and the orientation of the specimen, which yields a diffraction pattern. The X-ray wavelength is typically 0.7-2 A, corresponding to X-ray energies of 6 – 17 KeV.

2.6.1 Bragg Law

Crystals consist of planes of atoms spaced at a distance d apart (Figure 2.6.2). They can be resolved into many atomic planes each with different d-spacing. Miller indices are used to distinguish between the planes. They are the reciprocals of the plane intercepts with the three basic axes. So for a cubic crystal (Ni) with a_0 as the lattice constant:

$$d_{hkl} = \frac{a_0}{\sqrt{h^2 + k^2 + l^2}} \tag{2.6.1}$$

From Fig. 2.6.1 it is easy to find the Bragg's law:

$$\lambda = 2d_{hkl} \sin\theta_{hkl} \tag{2.6.2}$$

where θ_{hkl} is the angle between the atomic planes and the incident X-ray. The detector is placed at $(2\theta_{hkl})$ and the crystal must be oriented such that the normal to the diffracting plane is coplanar with the incident and the diffracted beams. The integrated X-ray intensities diffracted from the specimen are given by [158] :

$$I_{hkl} \propto |F_{hkl}| e^{-2M} V \tag{2.6.3}$$

where the factor e^{-2M} (Debye-Waller factor) accounts for the reduction in intensity due to the disorder in the crystal and V is the diffracting volume and depends on the absorption coefficient and the size of the sample. F_{hkl} is the structure factor for the (hkl) diffraction peak and is related to the atomic arrangements in the material. More exact is the Fourier transform of the positions of the atoms in one unit cell. Each atom is weighted by its form factor, which is equal to Z for small 2θ but decreases as 2θ increases.

2.6.2 Phase Identification

One of the strengths of the XRD method is the phase identification capability. This is done by comparing the d-spacing in the diffraction pattern and the integrated intensities with known standards. The JCPDS Powder Diffraction file (Joint Committee on Powder Diffraction Standards), provides data for random orientation. For specimens containing several phases, the proportion of each phase can be determined from the integrated intensities in the diffraction pattern. If there is specimen preferred orientation then intensities need to be integrated at many different orientations. Preferred orientation can make positive phase identification difficult. For random orientation the process is easier as the integrated intensities will give the desired information. The structural changes that accompany the isothermal ageing of Ni_4Mo can be revealed by XRD. (Figure 2.6.3 – 2.6.4). Ling et al. [92 and 93] points out that the gradual changes in some of the superlattice reflection could be traced with a careful XRD analysis. The behavior of the superlattice reflections observed in Figure 2.6.4 is due to the increase in the domain size and degree of order with ageing time. The broadening of the fundamental reflection is mainly attributed to the strain accompanying the ordering process as can be seen in Figure 2.6.5.

2.6.3 Determination of Strain and Grain Size

Diffraction peak positions are precisely measured with XRD. This can provide information on the type of strain, homogenous or in-homogenous in the material. Homogenous or uniform elastic strain will shift the peak position. In the (hkl) direction, the strain component will be:

$$\frac{(d_{hkl} - d_{0,hkl})}{d_{0,hkl}} \tag{2.6.4}$$

where $d_{0,hkl}$ is the unstrained spacing.

In-homogenous strain can vary from grain to grain or within a single grain. This will cause a broadening of the diffraction peak that increases with (sinθ). Peak broadening is also caused by the finite size of the grain but in this case there is no dependence on (sinθ). These two processes can be separated by a careful analysis of the peak shape at different orders. If there is no strain, the grain size L is estimated from the peak width ($\Delta 2\theta$) with the Scherrer formula:

$$L = \frac{\lambda}{(\Delta 2\theta)\cos\theta} \tag{2.6.5}$$

2.6.4 Determination of Preferred Orientation

The amount of preferred orientation can be estimated by comparing the integrated intensities with the values given by JCPDS, or using the expression for integrated intensity (Eq. 2.6.3). If the material has (hkl) texture then the (hkl) diffraction peak will

have a larger than expected intensity. For a more complete determination of the preferred orientation, the intensity of the (hkl) peak must be measured at different specimen orientations.

2.6.5 Detection of the Superlattice Lines

We consider now the case of Ni_3Mo and the equations 2.5.11 through 2.5.14. The atomic location for Mo is in the corners of the unit cell and for Ni in the center of the faces. There are on-average, 4 atoms in a unit cell, 3 of Ni and one of Mo and we can write:

$$\beta = 000;\ \alpha = \frac{1}{2}\frac{1}{2}0,\ 0\frac{1}{2}\frac{1}{2},\ \frac{1}{2}0\frac{1}{2},\ y_\alpha = \frac{3}{4}\ and\ y_\beta = \frac{1}{4}$$

F becomes:

$$F = (r_\alpha f_A + w_\alpha f_B)(e^{\pi i(h+k)} + e^{\pi i(l+k)} + e^{\pi i(h+l)}) + (r_\beta f_B + w_\beta f_A),\ hkl\ unmixed\ ,$$

$$F = 3(r_\alpha f_A + w_\alpha f_B) + (r_\beta f_B + w_\beta f_A) = 4(x_B f_B + x_A f_A),\ Fundamental,\ hkl\ mixed \qquad (2.6.1)$$

$$F = (r_\beta f_B + w_\beta f_A) - (r_\alpha f_A + w_\alpha f_B) = S(f_B - f_A),\ Superstructure \qquad (2.6.2)$$

For perfect order

$w_\beta = 0$ and

$w_\alpha = 0$, then:

$$F = (f_B + 3f_A),\ hkl\ unmixed \qquad (2.6.3)$$

$$F = (f_B - f_A),\ Fundamental,\ hkl\ mixed \qquad (2.6.4)$$

Comparing equations 2.6.1 – 2.6.4, we note that only the superlattice lines are strongly affected by the departure from the perfect order. This is because the intensity of a superlattice line is proportional to F^2 and therefore to S^2. For example a decrease in order from S = 1.00 to S=.50, would cause a decrease of intensity by about 75%. By comparing the integrated intensity ratios of a superlattice and of a fundamental line, we can determine S experimentally. In a random alloy, there should be a larger background extending over the range of the whole 2θ [90]. This diffuse scattering is due to the randomness of the crystals.

What are the detection limits for superlattice lines? For Ni_3Mo the relative integrated intensities of a superlattice and of a fundamental line are proportional to their $|F|^2$ values:

$$\frac{Intensity(Superlattice\,line)}{Intensity(Fundamental\,line)} \approx \frac{|F|_S^2}{|F|_f^2} = \frac{(f_{Mo} - f_{Ni})^2}{(f_{Mo} + 3f_{Ni})^2} \qquad (2.6.5)$$

For very low angles (close to zero) f ~ Z, the equation becomes:

$$\frac{I_S}{I_f} \approx \frac{(42-28)^2}{(42+3(28))^2} \approx 0.012$$

We can see that the superlattice lines are only about 1% of the fundamental lines, and they can be detected only because of their known location.

2.7 Rutherford Backscattering Spectrometry

Rutherford backscattering spectrometry (RBS) is extensively used for accurate determination of stoichiometry, elemental area density and concentration of implanted or impurity elements in materials and thin films. This is an ion beam based analytical technique that can give information on the atomic composition profile of the near surface region of materials. The physical processes involved in this technique are very well understood [94, 95 and 96]. Computer codes have been developed that provide efficient means of performing quantitative RBS analysis [91]. The limitations reside in the current knowledge of the stopping power of materials for α-particles of MeV energies. The shape of the RBS spectrum can provide the energy-depth relation and yield-composition relation but is dependent on the stopping power values.

2.7.1 The Physics of Backscattering

The backscattered spectrum (Figure 2.7.1) is determined by the energy analysis of the backscattered ions in the detection system. The energy of a backscattered particle detected at a given angle depends on the loss of the energy due to the transfer of momentum to the target atoms and loss due to the transmission through the target. There is a direct relationship between the channel number on the x axis and the energy of the ions. The elements in the spectrum appear either as peaks or, in the case of a mixture of elements, as peaks on top of other peaks. The peak widths are caused by energy loss in

the materials of the ions that are analyzed. Energy straggling (fluctuations in energy loss) limits the resolution of mass and depth in RBS. ^{4}He backscattering kinematic factor, is defined as the ratio of the projectile energies after and before the collision [96]:

$$K_{M2} = \left\{\frac{M_1 \cos\theta \sqrt{M_2^2 - M_1^2 \sin^2\theta}}{M_2 + M_1}\right\}^2; \text{ for } ^4\text{He}, M_1 = 4.003 \quad (2.7.1)$$

M_1 = atomic mass of the projectile

M_2 = atomic mass of the target atom

θ = scattering angle in the laboratory system

$K_{M2} = K_M = K$

At $\theta = 180^0$:

$$K_{M2} = \left\{\frac{M_2 - M_1}{M_2 + M_1}\right\}^2 \quad (2.7.2)$$

At $\theta = 90^0$:

$$K_{M2} = \frac{M_2 - M_1}{M_2 + M_1} \quad (2.7.3)$$

For a $\theta = 170^0$, a typical lab scattering angle, with a He beam, the kinematic factors for Nickel and Molybdenum are:

Mo: 0.8473

Ni: 0.7626

The differential cross section for scattering, in a given direction into a detecting solid angle, is defined for a target atom:

$$\left(\frac{d\sigma}{d\Omega}\right) d\Omega = \frac{number\ of\ particles\ scattered\ in\ the\ solid\ angle\ d\Omega}{number\ of\ incident\ particles\ per\ unit\ area}$$

This expression can be written based on the Rutherford scattering formulation transformed from center of mass to laboratory coordinates:

$$\frac{d\sigma}{d\Omega} = \left(\frac{Z_1 Z_2 e^2}{2E\sin^2\theta}\right)^2 \frac{\left\{\cos\theta + \left[1-\left(\frac{M_1 \sin\theta}{M_2}\right)^2\right]^{1/2}\right\}^2}{\left[1-\left(\frac{M^1 \sin\theta}{M^2}\right)^2\right]^{1/2}} \quad \text{(mb/str)} \qquad (2.7.4)$$

Z_1=atomic number of the projectile

Z_2 = atomic number of the target

e = electron charge

E= energy of the projectile immediately before scattering

The average scattering cross section σ is defined as:

$$\sigma = \frac{1}{\Omega}\int \frac{d\sigma}{d\Omega} d\Omega$$

Ω = finite detector's solid angle.

When we have compound targets, the additivity of stopping cross sections (Bragg's rule) must be applied in the molecular and atomic scale :

$$\varepsilon^{A_m B_n} = m\varepsilon^A + n\varepsilon^B \qquad (2.7.5)$$

AmBn = molecular form of a compound formed from m atoms of A and n atoms of B.

ε = the stopping cross section per atom.

ε_0 = the stopping cross section per atom for θ= 0.

$$\varepsilon \equiv \frac{1}{N}\frac{dE}{dx} \qquad (2.7.6)$$

with $\frac{dE}{dx}$ representing the energy loss and N the atom number in the target

$N = N_0\rho/M$,

N_0= Avogadro number

ρ = the density of target

M = mass number of the target.

The spectrum height (counts per channel) at the surface of the element to be studied is:

$$H = Q\sigma(E_0)\Omega N\delta x/\cos\theta_1 \tag{2.7.7}$$

where,

Q = total number of projectiles incident to the target

N = atomic density

δx = the thickness of the target for which backscattering into δE takes place.

If we consider:

$\delta E = [S_0]\,\delta x$, where $[S_0]$ is the backscattering energy loss factor near surface, then:

$$H = Q\sigma(E_0)\Omega N\delta E_1/[S_0] \tag{2.7.8}$$

$$H = Q\sigma(E_0)\Omega\delta E_1/[\varepsilon_0] \tag{2.7.9}$$

with E_1 the energy of one channel, and δE the channel width. If we have a mixture of elements X and Y and the concentration of each may vary with the depth, the spectrum may look something like in Figure 2.7.2. Using the above formulas we obtain:

$$H_A^{AB} = Q\sigma_A(E)\Omega N_A^{AB}\delta E_1/[S]_A^{AB} \tag{2.7.10}$$

$$H_A^{AB} = Q\sigma_A(E)\Omega\frac{\delta E_1}{[\varepsilon]_A^{AB}}\frac{N_A^{AB}}{N^{AB}} \tag{2.7.11}$$

where H_A^{AB} is the height of the energy spectrum of particles scattered from atom A in a mixture AB at the surface.

$$N^{AB} = N_A^{AB} + N_B^{AB} \tag{2.7.12}$$

where N^{AB} is the total concentration, N_B^{AB} and N_A^{AB} are the atomic concentrations of A and B in the mixture. The backscattering cross section for the mixture molecule could be written as:

$$\varepsilon^{AB} = \frac{N_A^{AB}}{N^{AB}}\varepsilon^A + \frac{N_B^{AB}}{N^{AB}}\varepsilon^B \tag{2.7.13}$$

where the additivity rule for Ni4Mo can be written as:

$$\varepsilon^{Ni_4Mo} = 4\varepsilon^{Ni} + \varepsilon^{Mo}$$

Then:

$$\frac{H_A^{AB}}{H_B^{AB}} = \frac{N_A^{AB}}{N_B^{AB}}\frac{\sigma_A}{\sigma_B}\frac{[\varepsilon]_B^{AB}}{[\varepsilon]_A^{AB}} \tag{2.7.14}$$

If we consider the partial concentration:

$$c_A = \frac{N_A^{AB}}{N^{AB}}$$

and the Bragg's rule for additivity:

$$\varepsilon^{AB} = c_A\varepsilon^A + c_B\varepsilon^B$$

Here, ε^{AB} is the weighted average stopping cross section per atom with weighting factor c_A and c_B in the mixture. Considering the relationship $([\varepsilon], \varepsilon)$ at $\theta = 0^0$:

$$[\varepsilon_0] = K\varepsilon(E_0) + \frac{1}{|\cos\theta|}\varepsilon(KE_0) \tag{2.7.15}$$

we obtain:

$$[\varepsilon]_A^{AB} = K_A\varepsilon^{AB}(E_0) + \frac{1}{|\cos\theta|}\varepsilon^{AB}(K_AE_0) \tag{2.7.16}$$

$$[S]_A^{AB} = N^{AB}[\varepsilon]_A^{AB} \tag{2.7.17}$$

We want to determine the atomic concentration from the height of the spectrum, or, if a standard pure element is available, from the ratios of the heights. From (2.7.9) the height of the spectrum for a pure element is :

$$H_A^A = Q\Omega\sigma_A \frac{\delta E_1}{[\varepsilon]_A^A} \tag{2.7.18}$$

From (2.7.11) and (2.7.18), we will be able to determine the height ratio:

$$\frac{H_A^{AB}}{H_A^A} = \frac{N_A^{AB}}{N^{AB}} \frac{[\varepsilon]_A^A}{[\varepsilon]_A^{AB}} = c_A \frac{[\varepsilon]_A^A}{[\varepsilon]_A^{AB}} \tag{2.7.19}$$

Then again from (2.7.11) we obtain the height ratio:

$$\frac{H_A^{AB}}{H_A^A} = \frac{N_A^{AB}}{N^{AB}} \frac{\sigma_A}{\sigma_B} \frac{[\varepsilon]_B^{AB}}{[\varepsilon]_A^{AB}} = \frac{c_A}{c_B} \frac{\sigma_A}{\sigma_B} \frac{[\varepsilon]_B^{AB}}{[\varepsilon]_A^{AB}} \tag{2.7.20}$$

The surface concentration can be determined form the equation 2.7.19. If we do an iteration of the surface analysis we should be able to determine the concentration of an element A contained in another element B. For this, we refer to the figure 2.7.2. The approximate formula:

$$\frac{H_A^{AB}(E_{1A})}{H_A^A(E_{1A}')} = c_A(x) \frac{[\varepsilon(E)]_A^A}{[\varepsilon(E)]_A^{AB}} \tag{2.7.21}$$

where:

E_{1A} is the energy E before a scattering event at the depth x

E_{1A}' is the same energy E before a scattering event at the depth x' for a pure element

$$\frac{H_A^{AB}(E_{1A})}{H_A^A(E_{1B})} = \frac{c_A(E)}{c_A(E)} \frac{[\varepsilon(E)]_B^{AB}}{[\varepsilon(E)]_A^{AB}} \frac{N_A^{AB}(x)}{N_B^{AB}(x)} \tag{2.7.22}$$

This equation differs from equation 2.7.20 in the fact that it is evaluated at energy E before scattering from A or B. The last two equations are approximations because the corrections due to the differences in energy width of windows inside and outside the target were not included. This would ad about 5% error. The accepted error in an RBS experiment is anywhere between 3 -10%.

2.7.2 Application to the Ni-Mo System

Using the tabulated values by Tesmer and Nastasi [96] for Helium, 2000 KeV we will have the following values for the electronic stopping cross sections:

$$\varepsilon_{Ni} = 68.03 \frac{eV cm^2}{10^{15}} atoms$$

$$\varepsilon_{Mo} = 91.09 \frac{eV cm^2}{10^{15}} atoms$$

Then we have for Ni_4Mo:

$$\varepsilon^{Ni_4Mo} = (4\times 68 + 1\times 91)\times 10^{-15} eV\, cm^2 = 363\times 10^{-15} eV\, cm^2$$

To find $(\frac{dE}{dx})^{Ni_4Mo}$ we have to calculate the molecular density

$$N^{Ni_4Mo} : N^{Ni_4Mo} = \frac{\rho N_0}{M} = \frac{9.158 \frac{g}{cm^3} \times 6.023\times 10^{23} \frac{molecules}{mole}}{327 \frac{g}{mole}} = 1.69\times 10^{23} \frac{Ni_4Mo}{cm^3}$$

We can obtain the stopping power using:

$$(\frac{dE}{dx})^{Ni_4Mo} = N^{Ni_4Mo} \varepsilon^{Ni_4Mo} = N_A^{AB} \varepsilon^A + N_B^{AB} \varepsilon^B = 363\times 10^{-15} \times 1.69\times 10^{23} = 613 \frac{eV}{\frac{0}{A}}$$

The same result could be obtained by calculating the atomic densities of each element in the molecule:

$$N_{Ni}^{Ni_4Mo} = 4\times 1.69\times 10^{23} = 6.76\times 10^{23}\frac{Ni}{cm^3}$$

$$N_{Mo}^{Ni_4Mo} = 1\times 1.69\times 10^{23} = 1.69\times 10^{23}\frac{Mo}{cm^3}$$

and:

$$(\frac{dE}{dx})^{Ni_4Mo} = N_{Ni}^{Ni_4Mo}\varepsilon^{Ni} + N_{Mo}^{Ni_4Mo}\varepsilon^{Mo} = 6.76\times 10^{23}\times 68.03\times 10^{-15} + 1.69\times 10^{23}\times 91.09\times 10^{-15} = 613\frac{eV}{\overset{0}{A}}$$

In previous RBS analysis of Ni-Mo alloy, Sarholtz et al. [98] found little difference between ordered and disordered alloys. However, they concluded that the domains and the size distribution of the domains are critically influenced by the annealing treatment. In their opinion, the conventional electropolishing treatment will leave the surface with an enriched molybdenum layer, while annealing of a mechanically polished crystal will produce an enriched Ni layer on the surface. A careful mechanical polishing is preferred versus a chemical treatment. Figure 2.7.3 shows the random and aligned spectra for implantation fluences of 10^{17} cm^{-2} and $4x10^{18}$ cm^{-2}. An interesting behavior is seen in the development of radiation damage with the increase in fluence. The radiation induced damage increases until about 10^{-18} cm^{-2} and then decreases a little and better channeling in Mo part of the spectrum is observed. But the damage for $4x10^{-18}$ $cm^{-2}$is the same as for $1x10^{-18}$ cm^{-2}. The explanation given by Sarholtz is that some sort of radiation induced re-crystallization mechanism takes place intermixed with radiation damage induced by ion bombardment [98]. I believe that they were actually seeing the beginning

of an ordering process in the Ni_4Mo surface similar to what was observed in our research. In the samples we irradiated, we were able to see in the RBS spectra, a slight change in surface stoichiometry with the change in irradiation dose.

2.8 Orientation Imaging Microscopy

OIM is a technique that employs the computer acquisition and indexing of electron backscatter patterns (EBSP) or Kikuchi patterns from an array of points to obtain orientations of a large number of grains in a specimen. Once the orientation and position of the grains are known, direct correlations between texture and other microstructural characteristics such as grain size and grain boundary character can be made through the creation of orientation maps. In OIM, electron backscattered patterns formed in a SEM are collected from points on the sample surface distributed over a regular grid and automatically indexed. From this data, a map can be constructed displaying changes in crystal orientation over the specimen surface. The orientation of each point in the microstructure is known and hence the location, line length and character of all grain boundaries. In principle, the orientation of each grain (crystal) with respect to an external reference system can be determined by the analysis of its diffraction pattern. When the electron beam of narrowly defined energy strikes the crystal, the electrons disperse beneath the surface and diffract in a systematic manner such that for each set of crystal planes there are two cones on which those diffracted electrons lie, one corresponding to the electrons incident on the *{hkl}* plane at angle θ_B and the other one corresponding to

the electrons incident to the *{hkl}* plane at angle $-\theta_B$. The interaction of the cones with a surface gives rise to lines, the Kikuchi lines. Each pair of lines forms a Kikuchi band. The collection of all Kikuchi bands formed as described constitutes the Kikuchi pattern, and the intersection of the Kikuchi bands designates the zone axes (Figure 2.8.1). To asses the image quality of the individual Kikuchi patterns, an image quality (IQ) parameter is recorded, that depends, among other factors on the OIM system parameters, the sample surface preparation or on the alloy's structure. The angular resolution in the determination of the grains' misorientation is about 1^0. In OIM, a grain is a set of connected points with similar orientations. The user defines a tolerance angle, the maximum misorientation two neighboring points in the same grain may have. The grain-defining algorithm then looks at the microstructure point by point. For each point in the microstructure, the neighboring points are checked and the misorientation is compared to the tolerance angle. If the misorientation between two neighboring points is greater than the tolerance angle, the two points are identified as belonging to two different grains. If it is less than the tolerance angle, they are identified as belonging to the same grain. The neighbors of these points are then checked, and so on until the set of connected points is bounded by points, which exceed the tolerance angle.

2.9 Hardness of the Ni-Mo Alloys

After thermal annealing or because of irradiation exposure, Ni-Mo alloys go through a process of strengthening and loss of ductility. The strengthening can be attributed to a combination of small domain size and coherency stress generated during the ordering stages [92 and 93].

Tawancy studied the ordering reactions that occur in Ni-Mo alloys and in Cr enriched Ni-Mo alloys [99]. He looked mainly at the thermal behavior of Ni_3Mo. Initially the specimens were heated to 1000^0 C. Then, to induce ordering in the specimens, they were heat treated for up to 16000 h at temperatures in the range of 500^0-800^0 C. Mechanical properties were determined from room temperature tensile tests. Electron diffraction patterns confirmed that the as cast alloys were displaying SRO. Order was induced in the Ni-Mo alloy after heat treatment at about 700^0 C. Figure 2.9.1 illustrates the effect of ordering. The yield strength nearly doubles and the loss of ductility was almost complete. Figure 2.9.1 illustrates the true tensile stress strain diagram. Ordering resulted in the formation of Ni_4Mo (D1a superlattice). In another set of experiments Tawancy, looked at two Ni-Mo alloys with the composition close to Hastelloy B2, (that is commercially available) that had stoichiometries close to the stoichiometry of Ni_3Mo and Ni_4Mo [99]. The results are shown in Figure 2.9.3 and we notice a considerable increase in yield strength and a decrease of ductility. Additional X-ray diffraction analysis done on both alloys showed that after 1000 h, the ordered phase of Ni_4Mo ($D1_a$ superstructure) and also traces of superlattice ($D0_{22}$) characteristic to the

ordering of Ni_3Mo were found in the alloy initially in Ni_3Mo configuration. In the $D1_a$ structure every fifth plane is occupied by Mo atoms producing superlattice reflections at 1/5<420>. For the $D0_{22}$ every forth plane is occupied by Mo atoms producing reflections at 1/4<420>. This is in agreement with the fact that during ordering to Ni_3Mo a superlattice $D1_a$ (Ni_4Mo) could also form as an intermediate transient phase [66]. Intergranular embrittlement associated with Ni_4Mo ordering could be related with discontinuous grain boundary ordering reaction [25, 33, and 101]. Earlier studies have shown that the strain energy associated with intragranular ordering could be minimized by self-generated or strain induced recrystalization resulting in a discontinuous ordering at the boundaries [9]. Tawancy found that the coexistence of $D1_a$ and $D0_{22}$ reduced the strain energy associated with intragranular ordering by suppressing the grain boundary reaction [99].

In another study of the variation of hardness with temperature, Ling et al. [94], showed that the microhardness increased with the ageing time (Figure 2.9.4 – 2.9.5). From X-ray calculations, Ling found that the domain size increased in three different directions (Figure 2.9.6) [93]. He concluded that the isothermal ordering in Ni_4Mo proceeded primarily by the homogenous process of short-range diffusion followed by domain growth and the elimination of domain boundaries. The order strengthening in the early stage was due to domain hardening and partial order. In the late stage, the interface strain and the dislocations that are generated from the interface and appear in large number strengthened the alloy.

El-Shanshoury et al. [100] looked at the influence of neutron irradiation on the ductility and tensile properties of Ni and some other Ni alloys including Ni-Mo. His results are presented in Figures 2.9.6-2.9.7. He concluded that the differences in ductility between un-irradiated and irradiated samples decreased with the increase in temperature reaching a minimum at the temperatures of complete recovery from irradiation effects. The difference in strength is removed at about 500^0 C and at higher temperatures the values of the strength of irradiated specimens are generally lower than those of the un-irradiated specimens.

In the present research, we investigated the effects of the irradiation with light and heavy ions on the hardness of Ni-Mo alloys. This work will complete the data that is now available on the hardness change of these alloys under thermal processing conditions. We decided to employ two separate ways to measure the hardness. First by microhardness using a Vickers indenter and second by nano-hardness using a nano-indenter. Nano-indents are in the in the submicron range depth. The reason to employ nano-hardness measurements to complement the microhardness testing was the Ni^+ irradiation. Due to the high damage rate, the path of Ni beam through the alloys is less than 2 μm. I was not able to locate in the literature any nano-indentation tests done on Ni-Mo alloys to be able to compare my results with. More details of the experimental setup for this procedure will be given in section 3.8.2.

2.10 Figures for Chapter 2

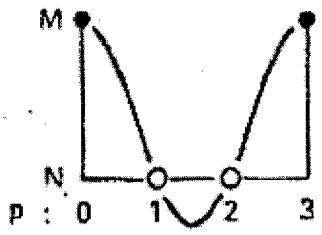

$$Ni_2Mo \quad c_p = \frac{1}{3} + \frac{2}{3}(\cos\frac{2\pi}{3}p)$$

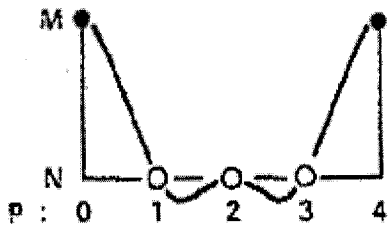

$$Ni_3Mo \quad c_p = \frac{1}{4} + \frac{1}{4}(2\cos\frac{\pi}{2}p + \cos\pi p)$$

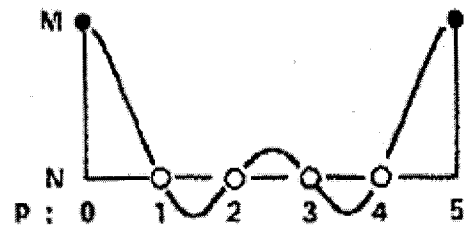

$$Ni_4Mo \quad c_p = \frac{1}{5} + \frac{2}{5}(\cos\frac{2\pi}{5}p + \cos\frac{4\pi}{5}p)$$

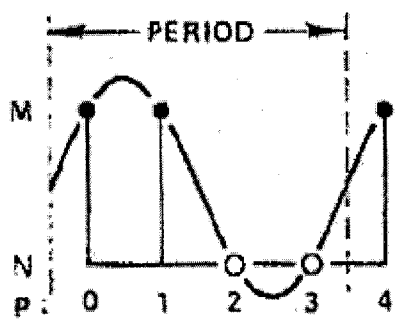

$$NiMo \quad c_p = \frac{1}{2} + \frac{\sqrt{2}}{2}(\sin\frac{\pi}{2}(p + \frac{1}{2}))$$

Figure 2.2.1 Concentration wave description of Ni_2Mo, Ni_3Mo Ni_4Mo and NiMo structures. The formulas are found by Fourier expansion of the concentration delta function c_p. [44].

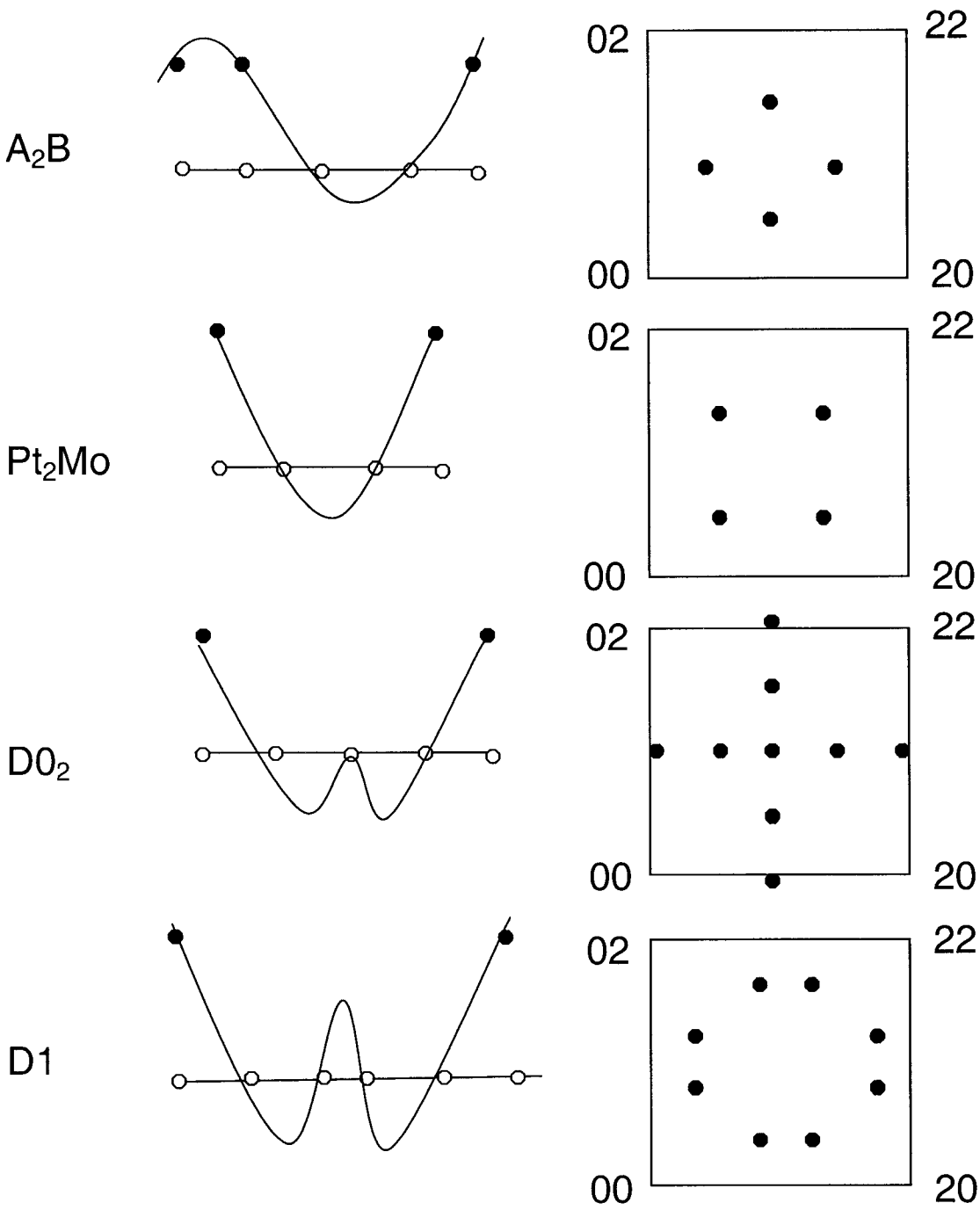

Figure 2.2.2 Crystal structures corresponding to Ni-Mo alloys, built on the basis of {420} concentration waves. Also shown are the positions of superstructure reflections in the (001) plane of reciprocal space.

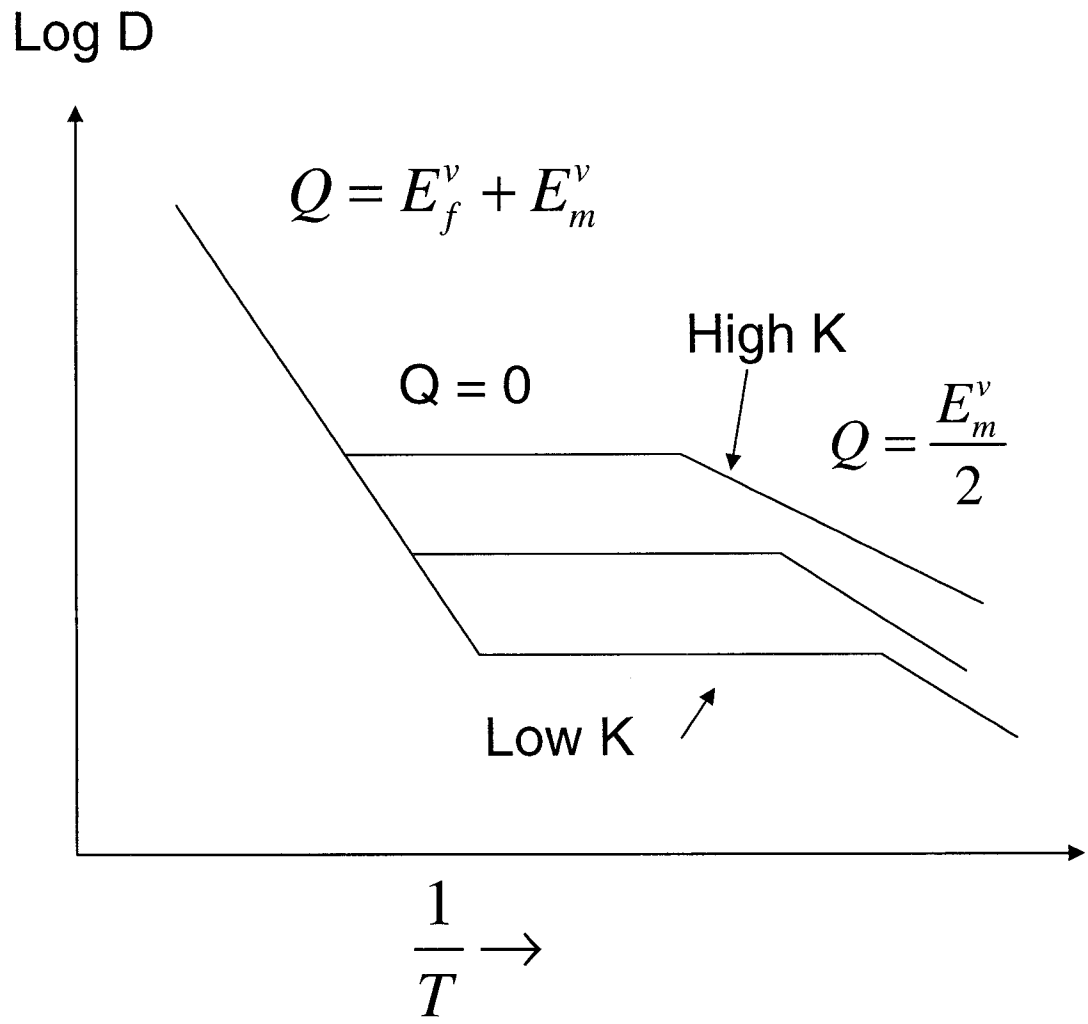

Figure 2.2.3 Schematic plot of the self-diffusion coefficient under irradiation. Increasing the displacement rate K, elevates the horizontal portion of the curve [47].

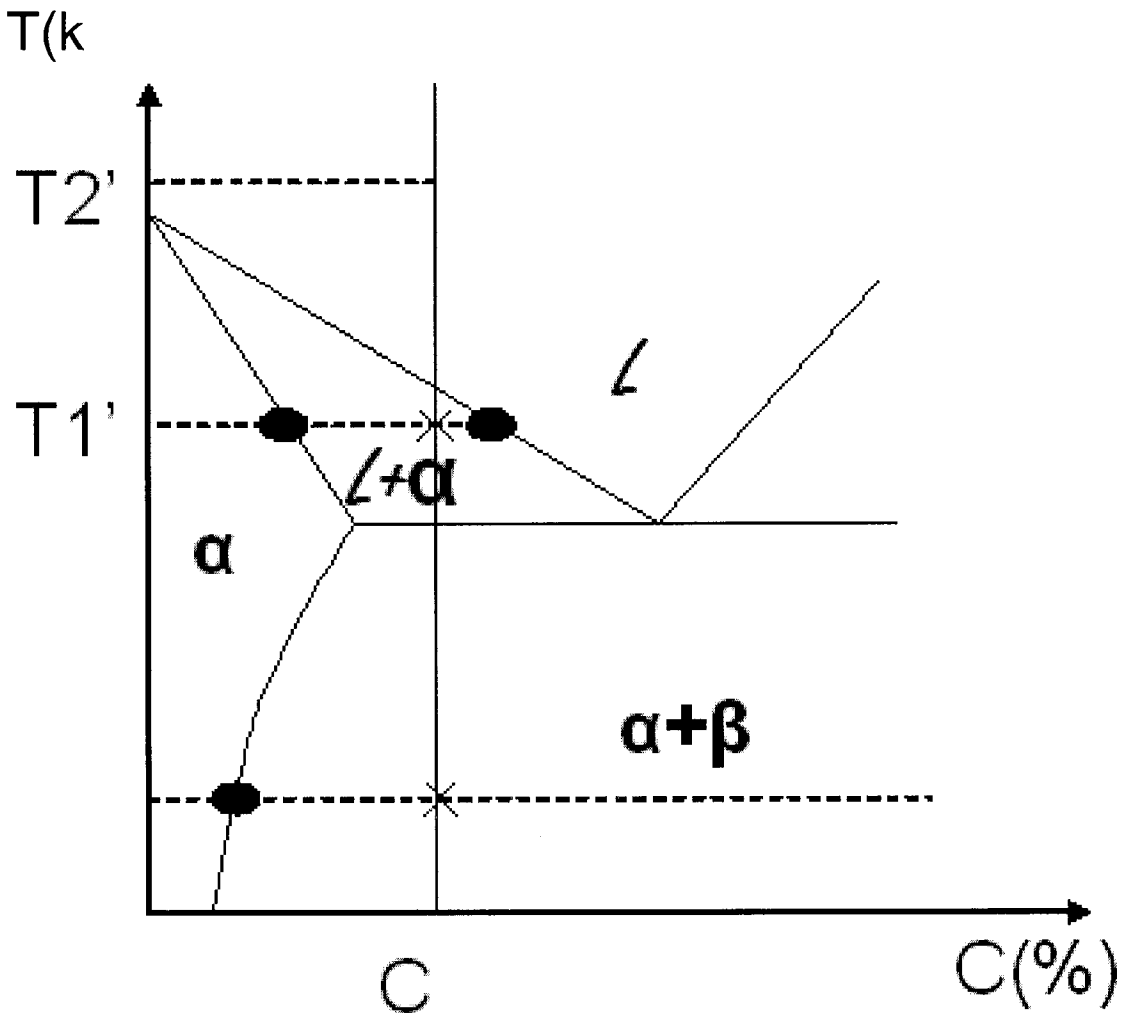

Figure 2.2.4 Irradiation of a two-phase alloy at temperature T may give a configuration found thermally at T1' or T2' [48].

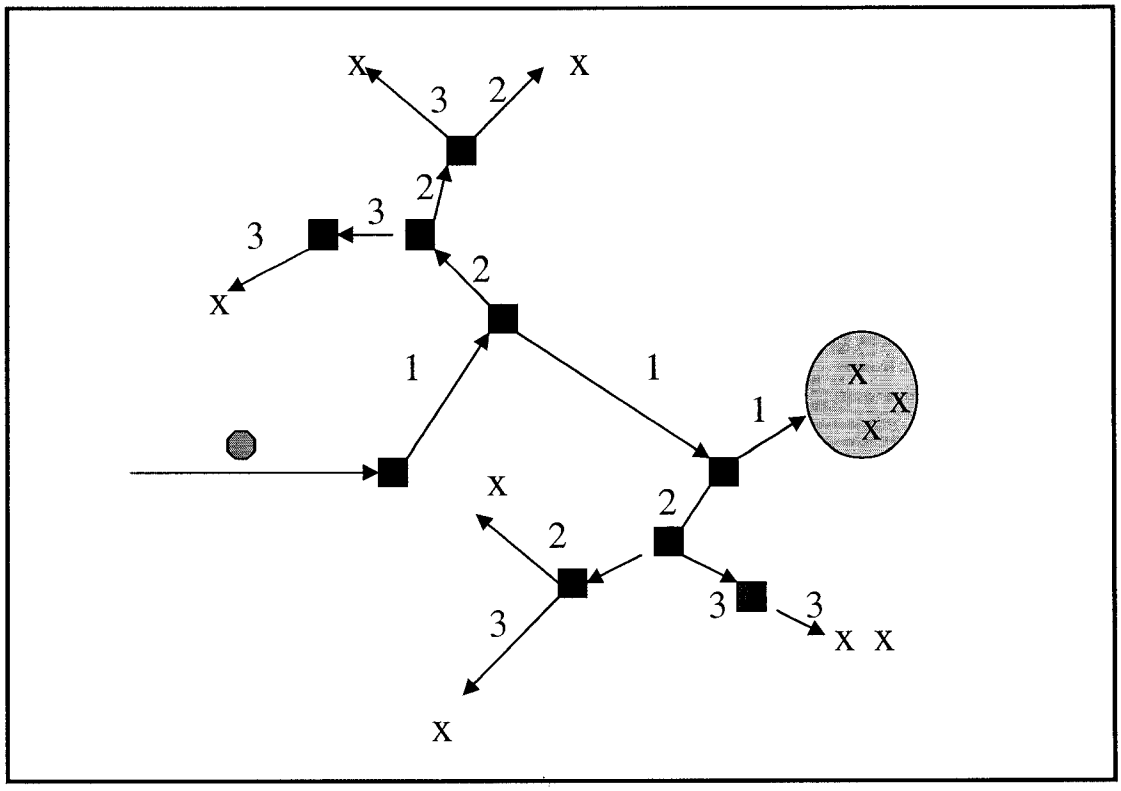

Figure 2.2.5 Mechanisms of irradiation effects [65].

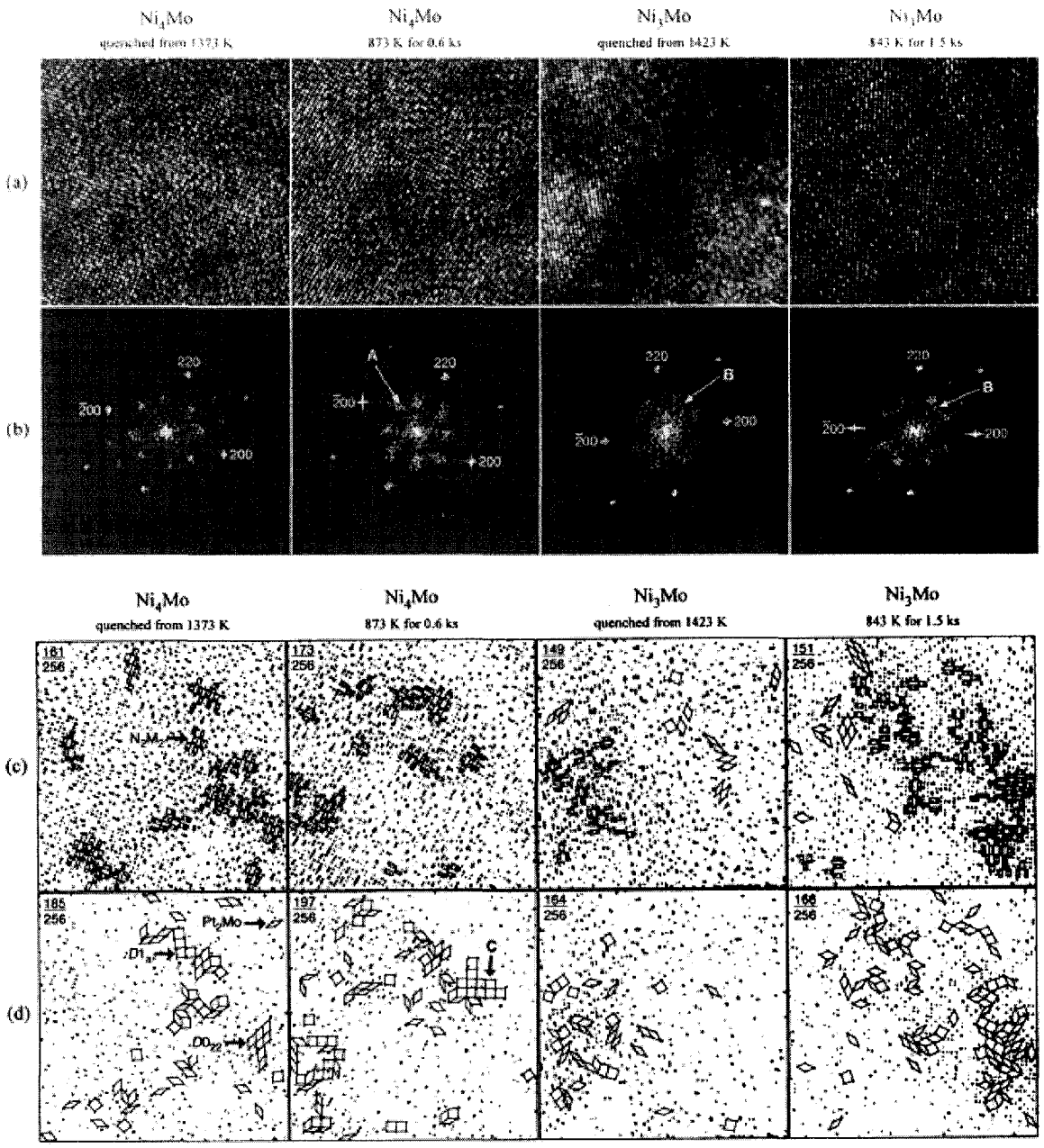

Figure 2.3.1 HRTEM images of: (a) Ni_4Mo and Ni_3Mo after different heat treatment (b) Fourier power spectra, (c) and (d): digitally processed images. The differences in diffuse intensity distribution among the specimens are pointed by arrows A and B. The fraction *p*/256 in each processed image denotes the threshold value for displaying the image contrast with 256 gray levels from 1 (black) to 256 (white). The preferential growth of $D1_a$ type domains is observed in Ni_4Mo as pointed by arrow C. The number of Pt_2Mo type clusters is larger in Ni_3Mo than in Ni_4Mo [59].

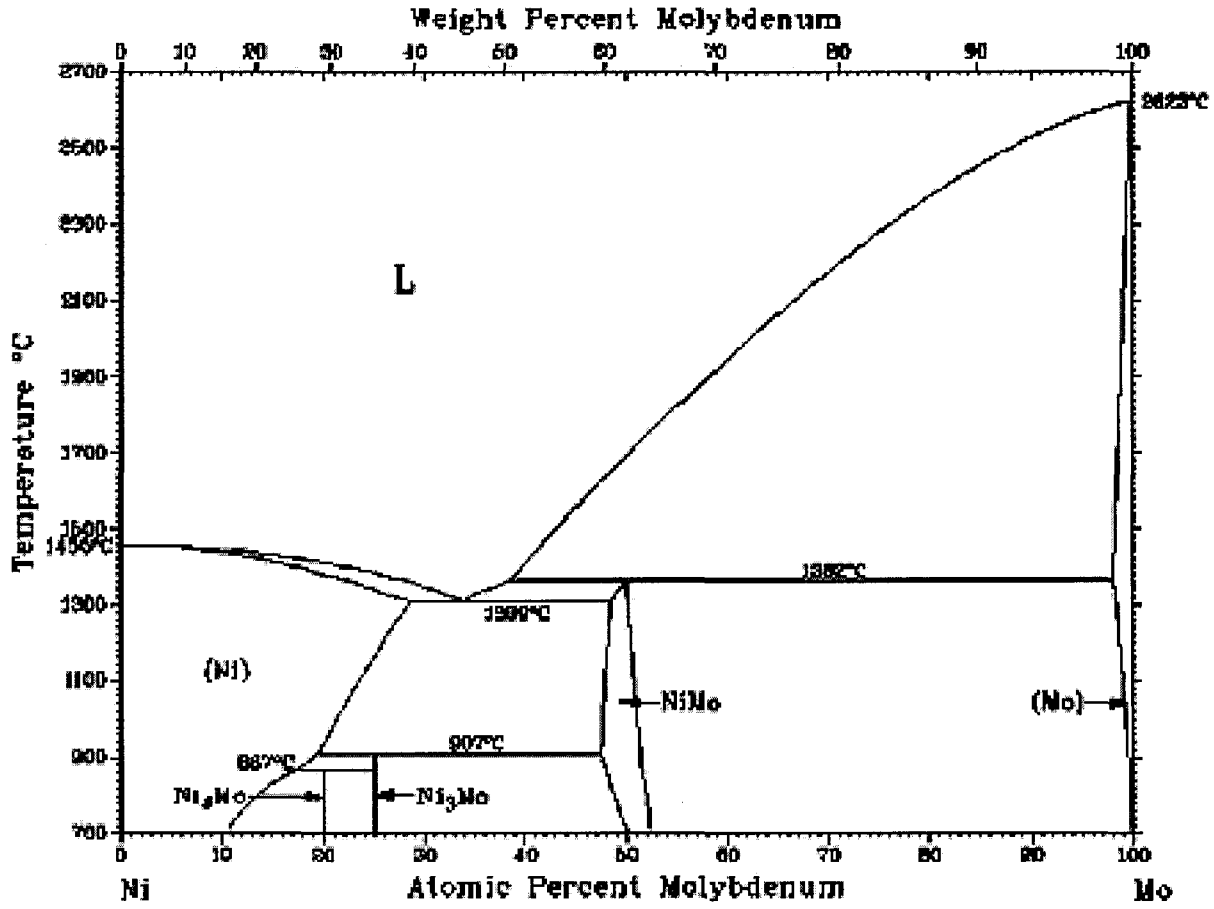

Figure 2.4.1 Phase Diagram for Ni-Mo.

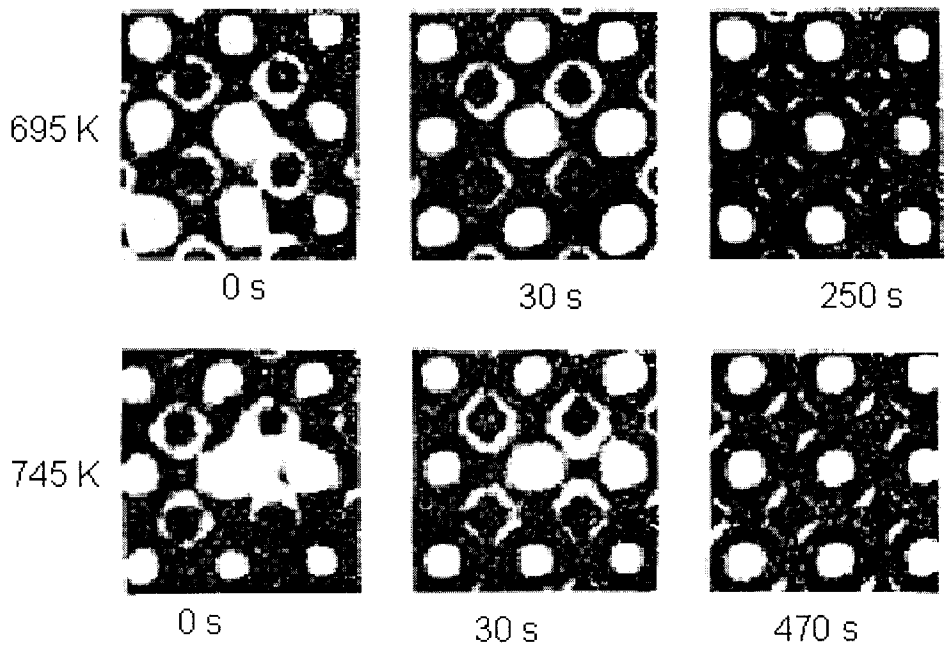

Figure 2.4.2 Sequence of diffraction patterns showing progressive changes from SRO to LRO at 695 K and 745 K under electron irradiation in Ni_4Mo [32].

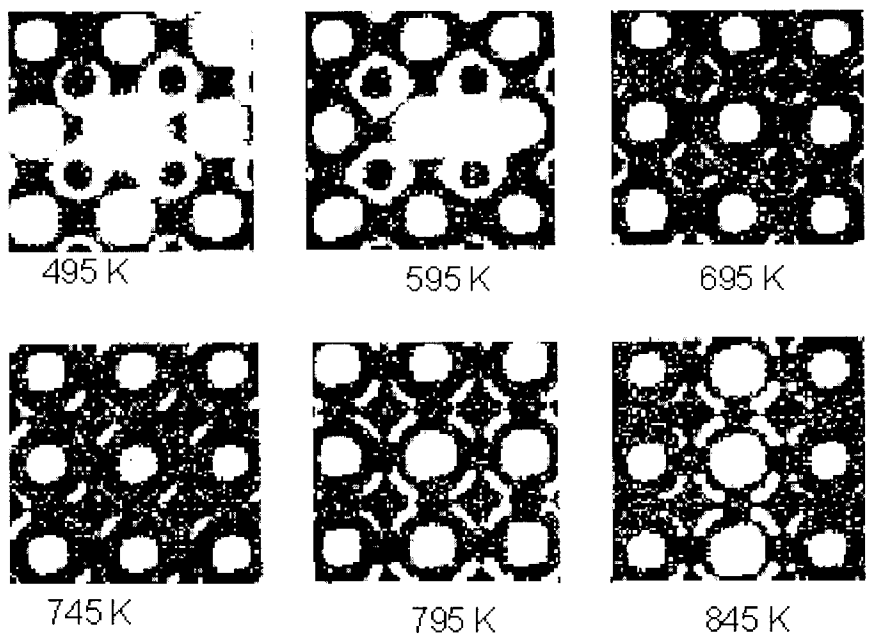

Figure 2.4.3 Steady state structures developed in Ni_3Mo at different temperatures under 1 MeV electron irradiation [26].

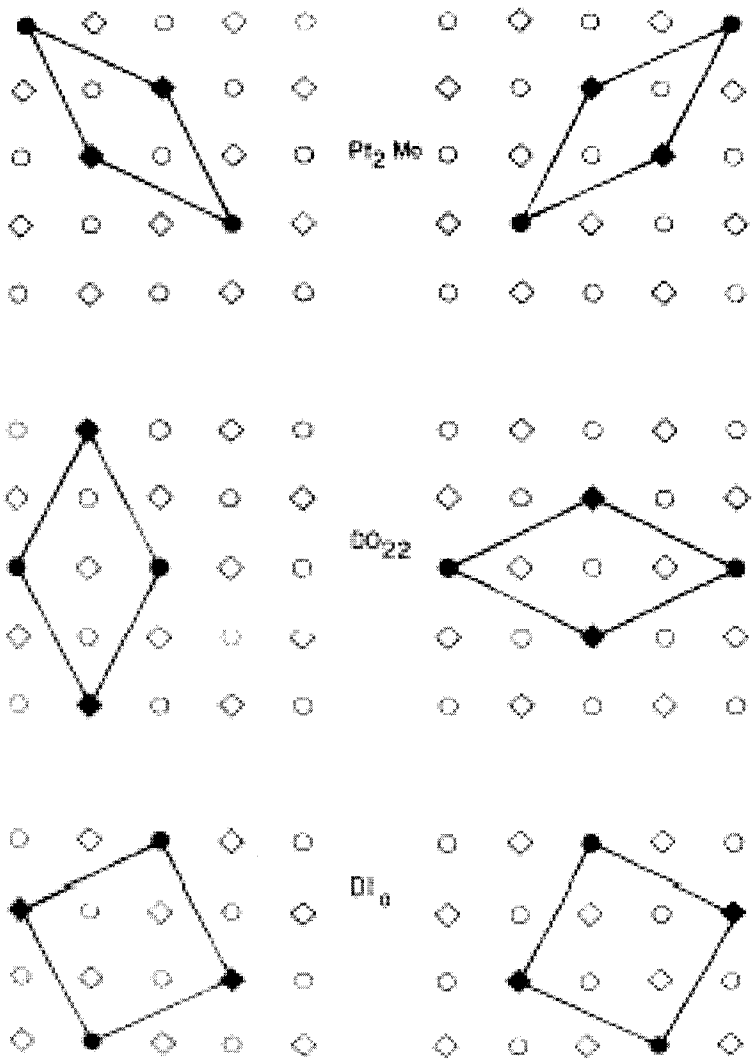

Figure 2.4.4 A view of the FCC structure showing uni-molecular subunit cell clusters of Ni_2Mo, Ni_3Mo (DO_{22}) and Ni_4Mo (D1a) in two different orientation variants. Diamonds and circles represent locations of atoms in the upper and lower layers respectively. Solid symbols represent Mo atoms. Open symbols represent Ni atoms [102].

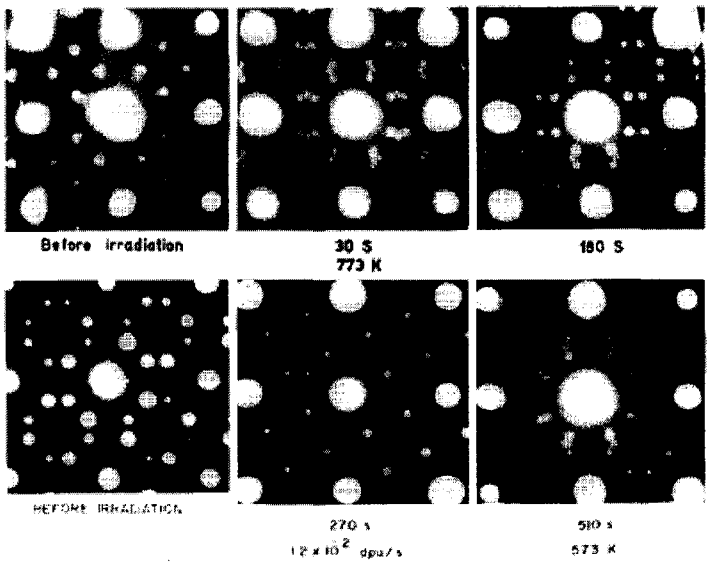

Figure 2.4.5 Series of patterns showing progressive changes in the state of order during electron irradiation. Top: the decay of SRO and gradual development of LRO at 773 K. Bottom: the destruction and subsequent development of SRO during irradiation at 570 K [32].

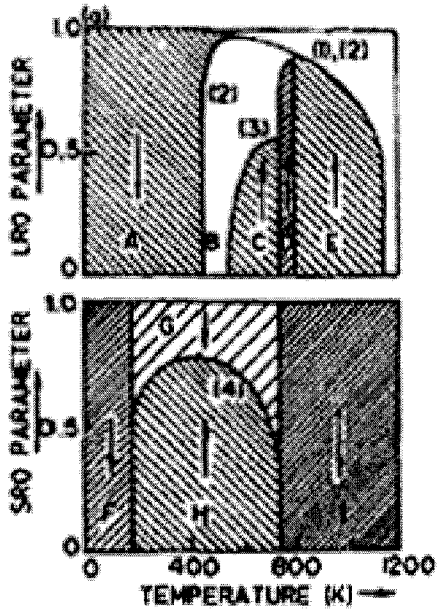

Figure 2.4.6 Steady state diagrams showing the stability ranges of SRO and LRO under electron irradiation at a dose rate of 10^{-3} dpa/s. (A): destruction of LRO; (B): no change; (C): continuous ordering SRO to LRO; (D): similar to (C) but LRO stronger; (E) nucleation and growth of D1a domains; (F) destruction of SRO; (G) transition SRO to LRO at higher temperatures; (H) development of SRO; (I) destruction of SRO and transition to LRO [32].

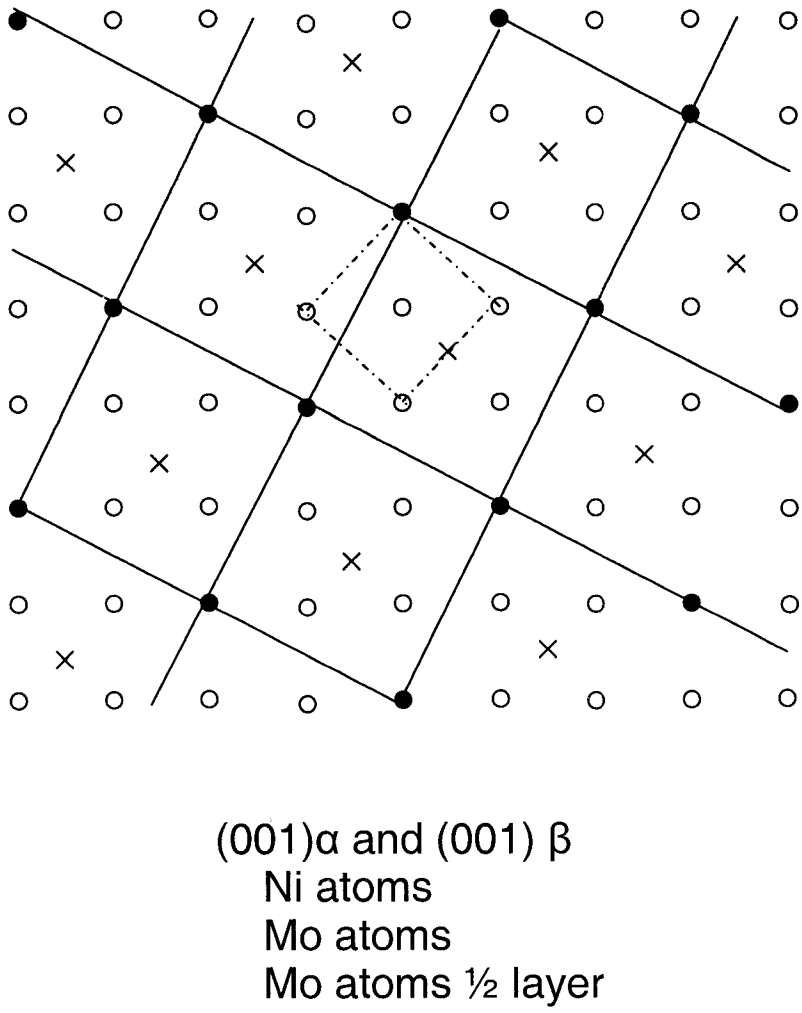

Figure 2.4.7 Arrangements of the Ni-Mo atoms in the ordered β-phase. Dashed lines are the fcc cells and the solid lines are the β-phase [102].

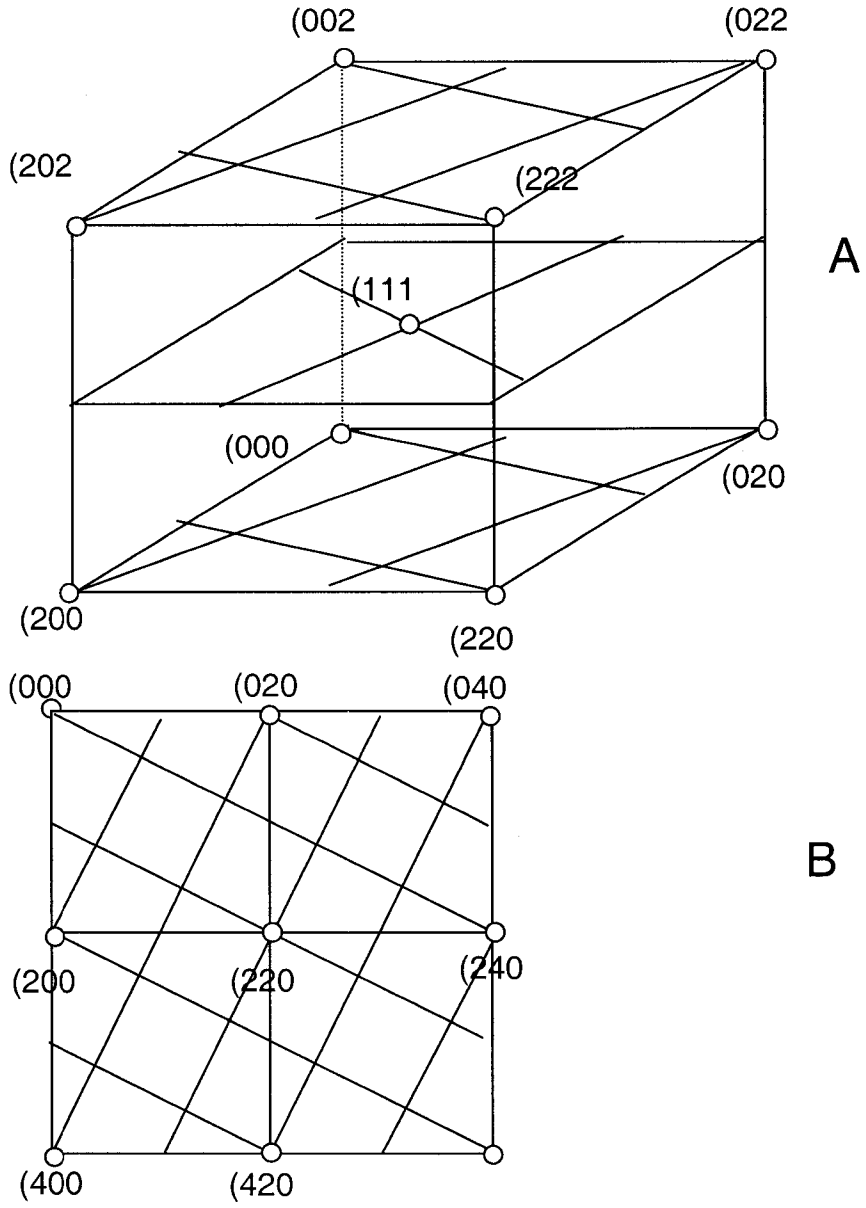

Figure 2.4.8 Reciprocal lattice of β-phase showing LRO spots. (A): 3D reciprocal lattice (B): (001) reciprocal plane.

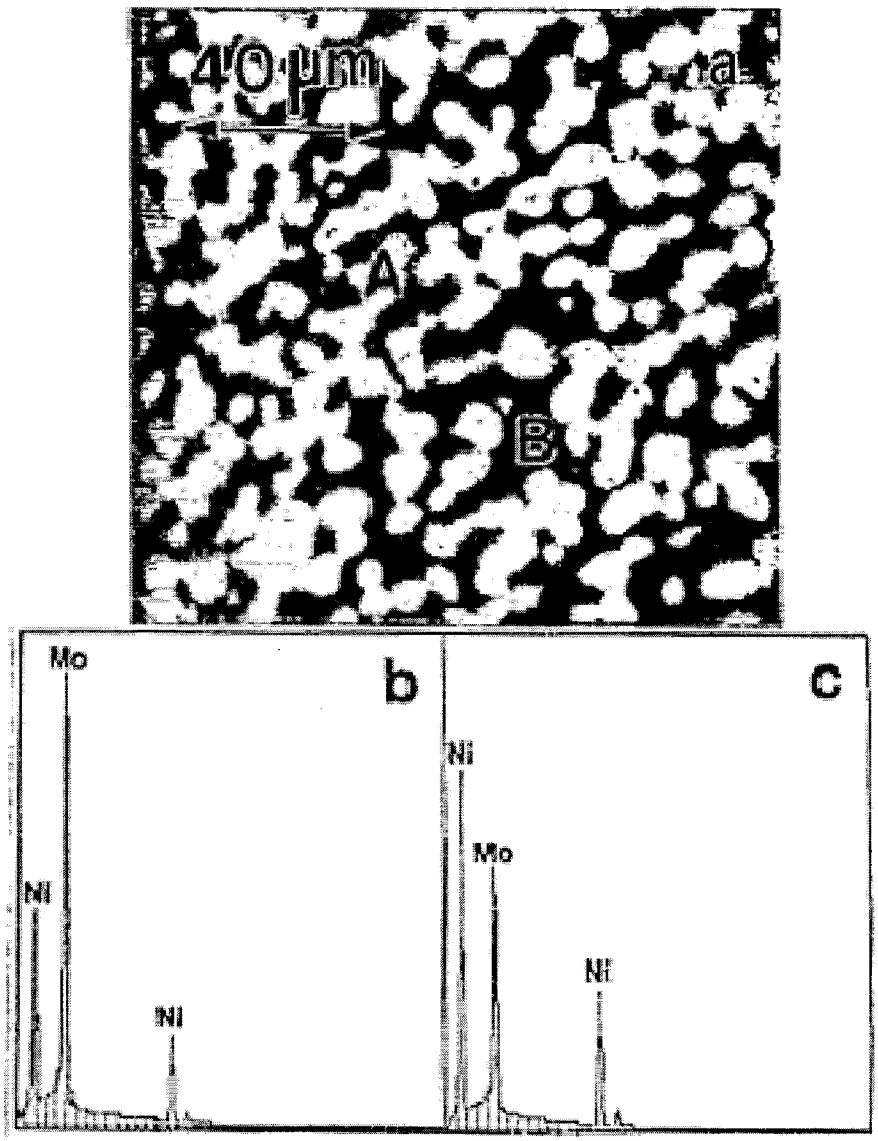

Figure 2.4.9 SEM picture of the NiMo alloy, where the bright spots are the δ-phase and the dark areas represent the Ni solid matrix. Energy dispersive spectra is presented in (b) and (c) of the δ-phase and Ni matrix respectively [19].

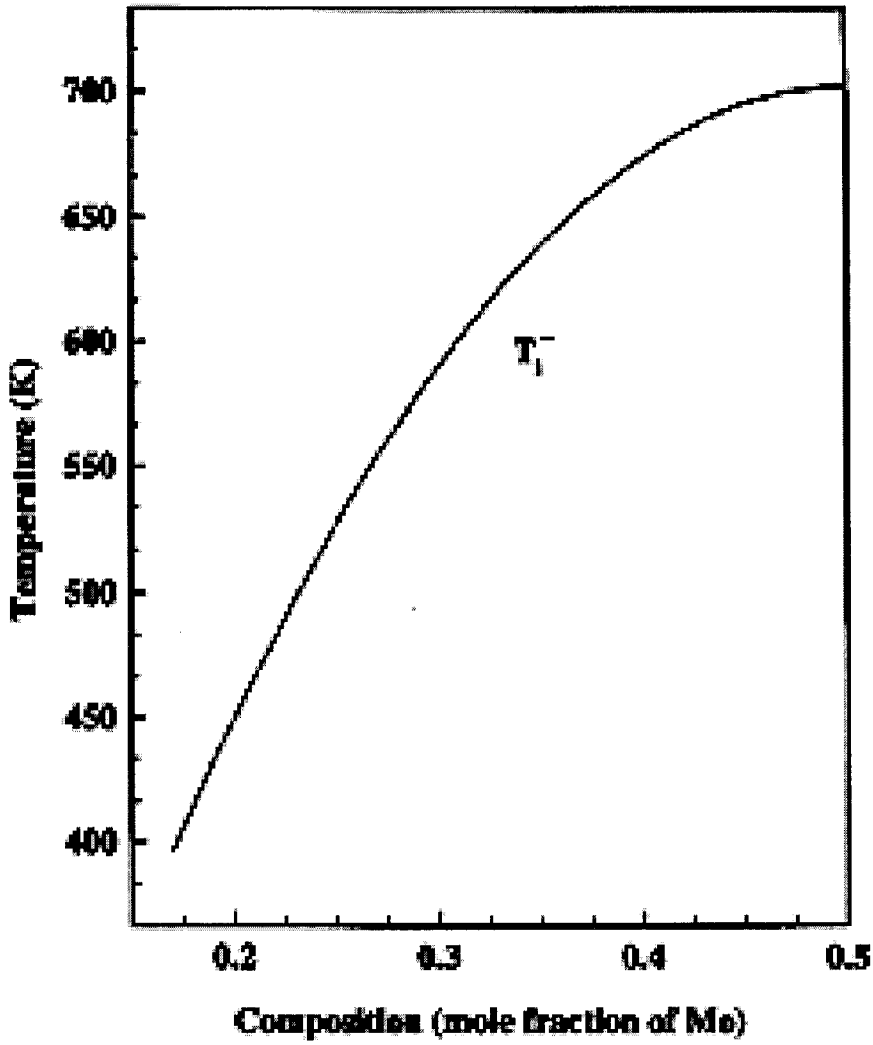

Figure 2.4.10 The ordering instability temperature T corresponding to onset of (1½0) ordering in a Ni-Mo alloy plotted as a function of the concentration of Mo [1].

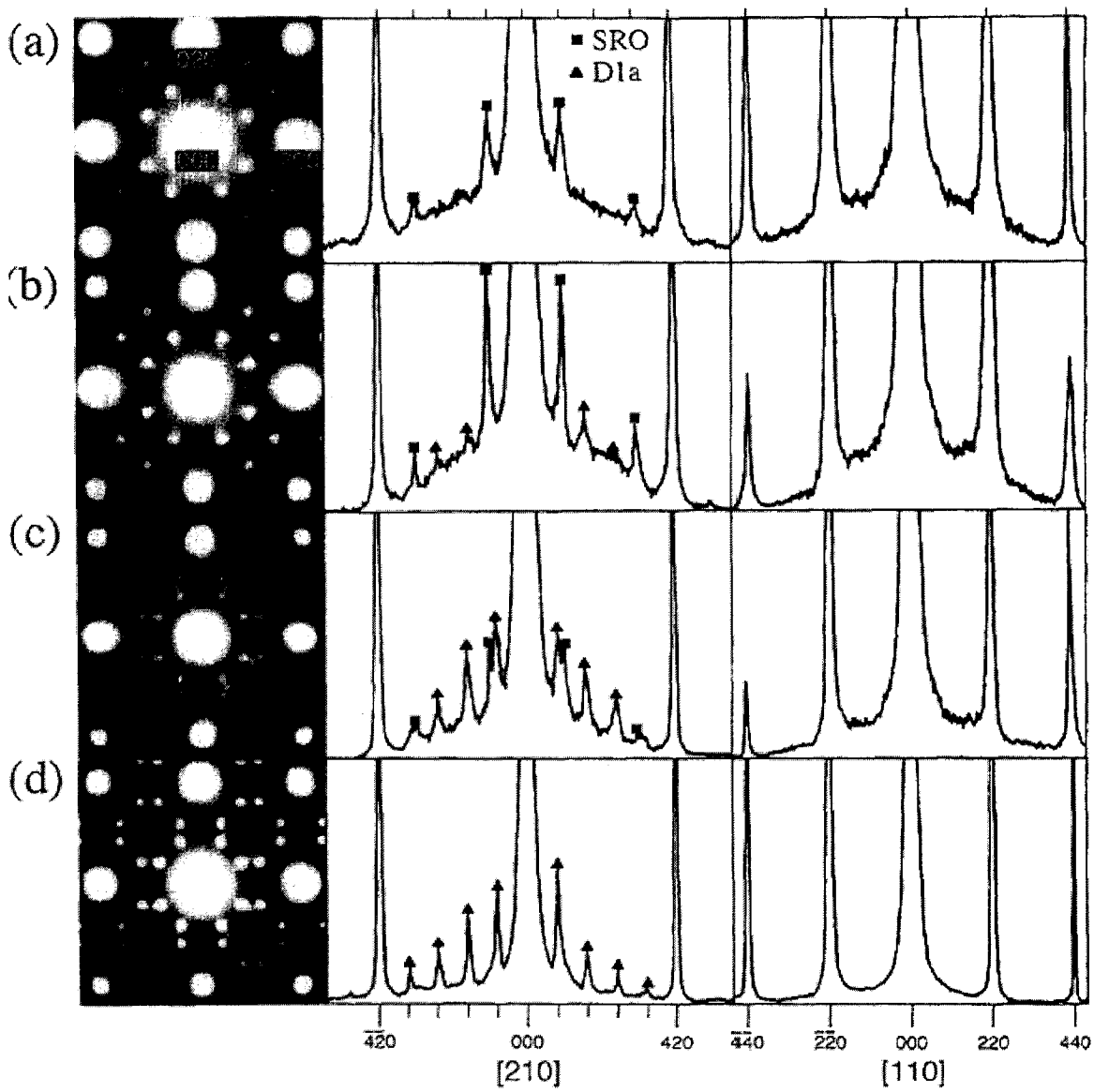

Figure 2.4.11 (001) Electron diffraction patterns of Ni_4Mo (left) and the diffraction intensity profiles in [210] (center) and [110] (right) direction. As quenched from 1000^0 C (a) and annealed at 600^0 C for 2 h. (b), 15 h (c), and 24 h (d). The positions of the diffuse intensity maxima shift from {1 ½ 0} to 1/5{4 2 0} with the progress of the ordering. The {1 ½ 0} reflections (marked with closed squares) are once intensified before their disappearance [103].

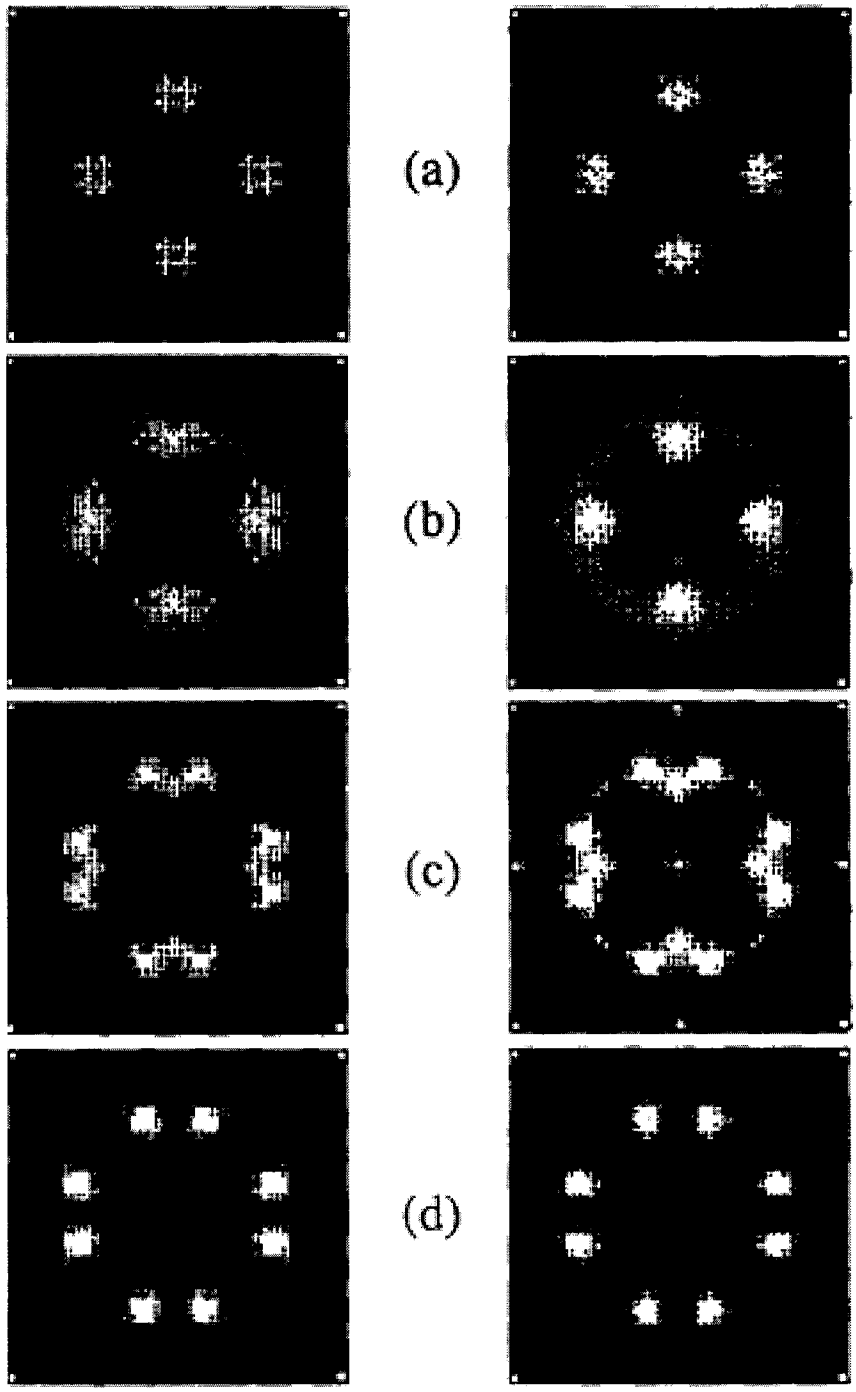

Figure 2.4.12 (001) Fourier power spectra of atomic arrangements during the ordering processes obtained by Monte Carlo simulations. The left case is a good agreement with the change of electron diffraction patterns shown in Figure 2.4.11 [101].

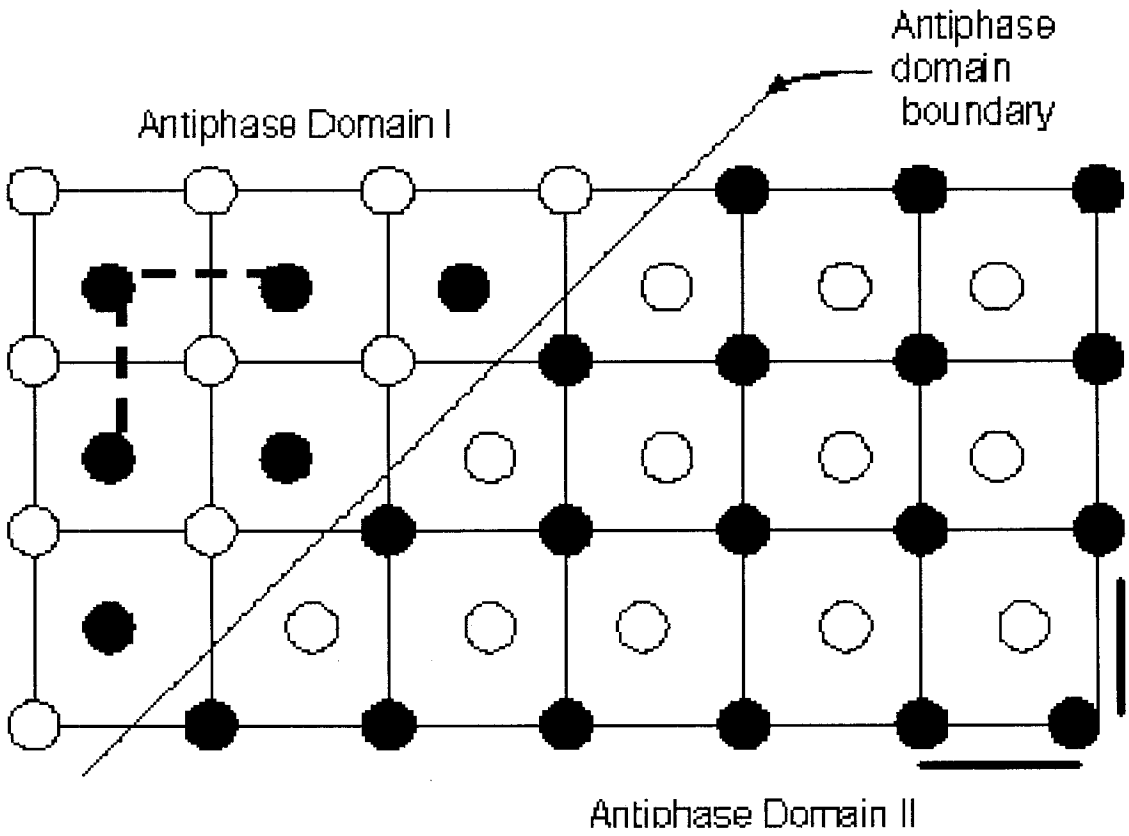

Figure 2.4.13 Antiphase boundaries.

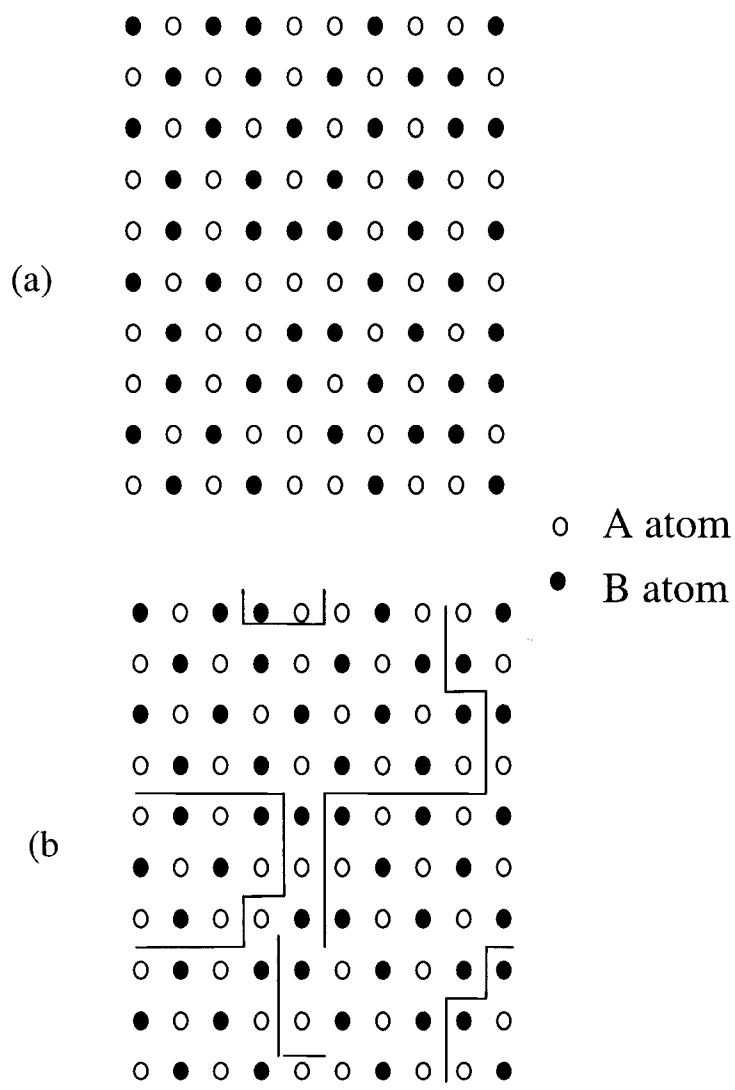

Figure 2.5.1 (a) - a solid solution A-50at% B with SRO. (b) regions of perfect order delineated in the solution shown in (a).

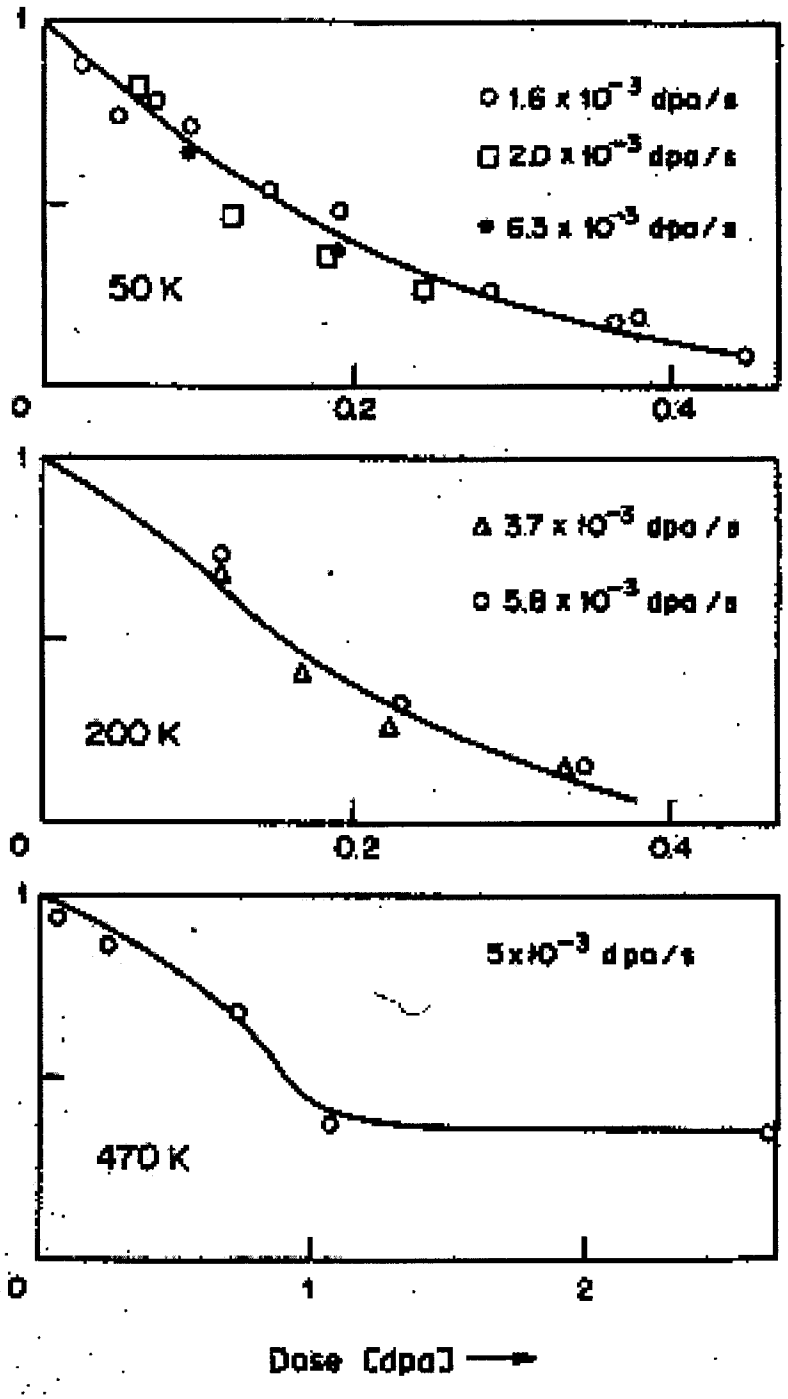

Figure 2.5.2 Long range order parameter S, as a function of irradiation dose at 50, 200 and 470 K [27].

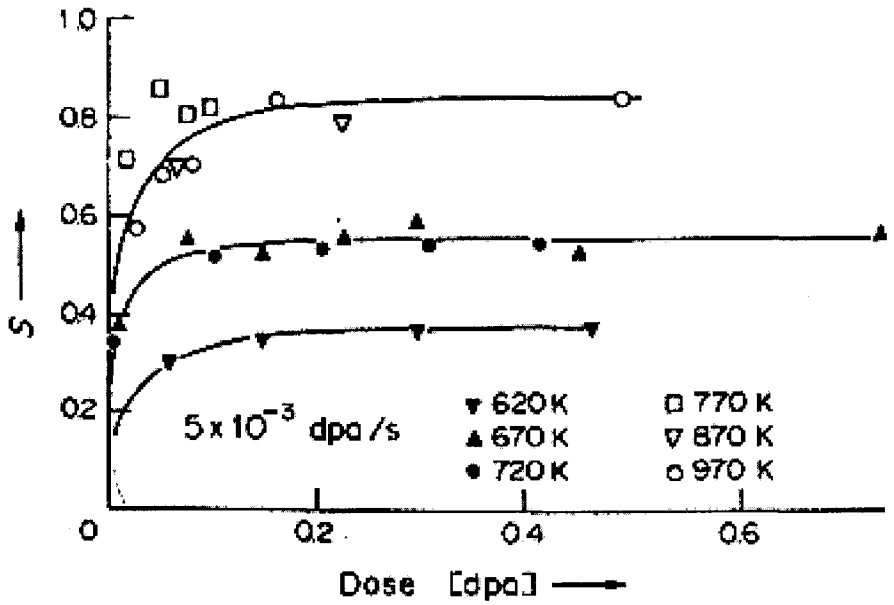

Figure 2.5.3 Long range order parameter as a function of irradiation dose [27].

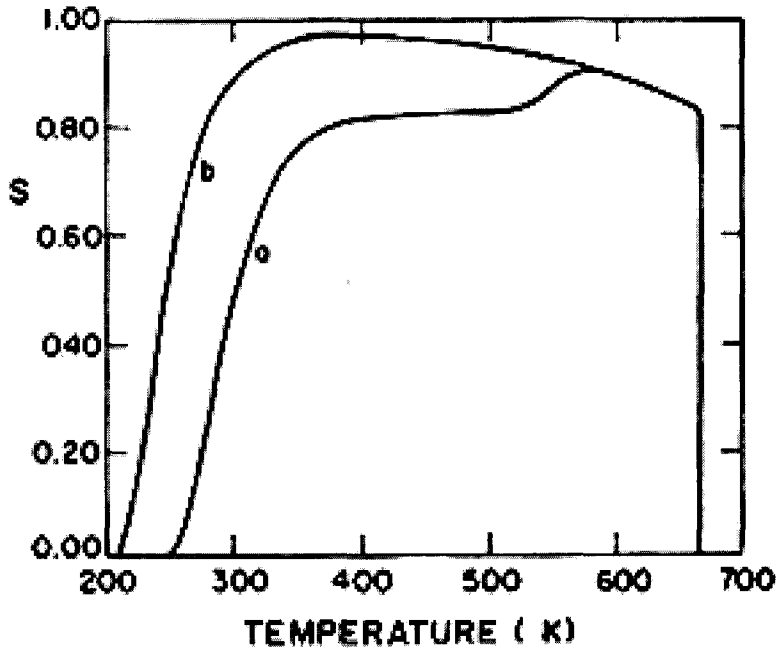

Figure 2.5.4 The steady state degree of order S as a function of temperature under neutron irradiation (a) fast neutrons, (b) thermal neutrons in Cu_3Au [25].

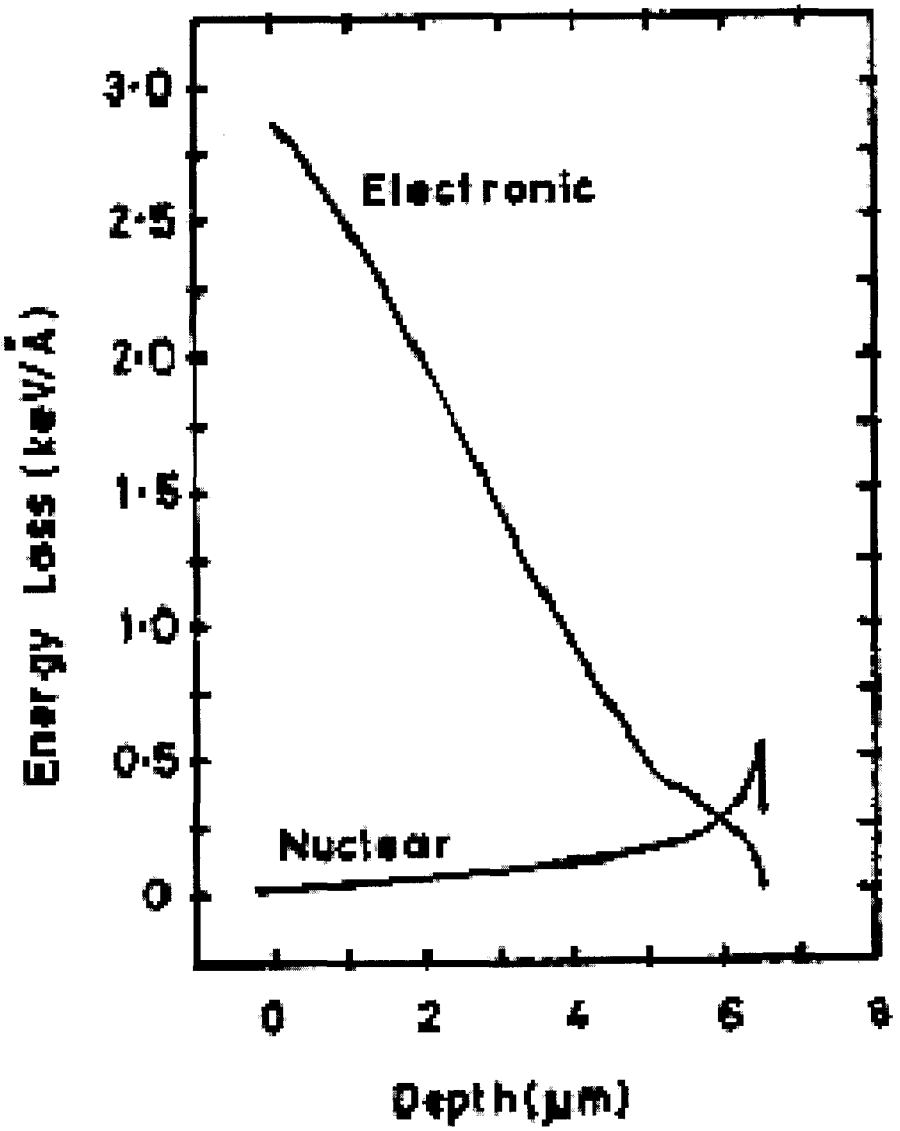

Figure 2.5.5 Se and Sn various depths for 100 MeV I^{9+} beam irradiation on Ni_4Mo [12].

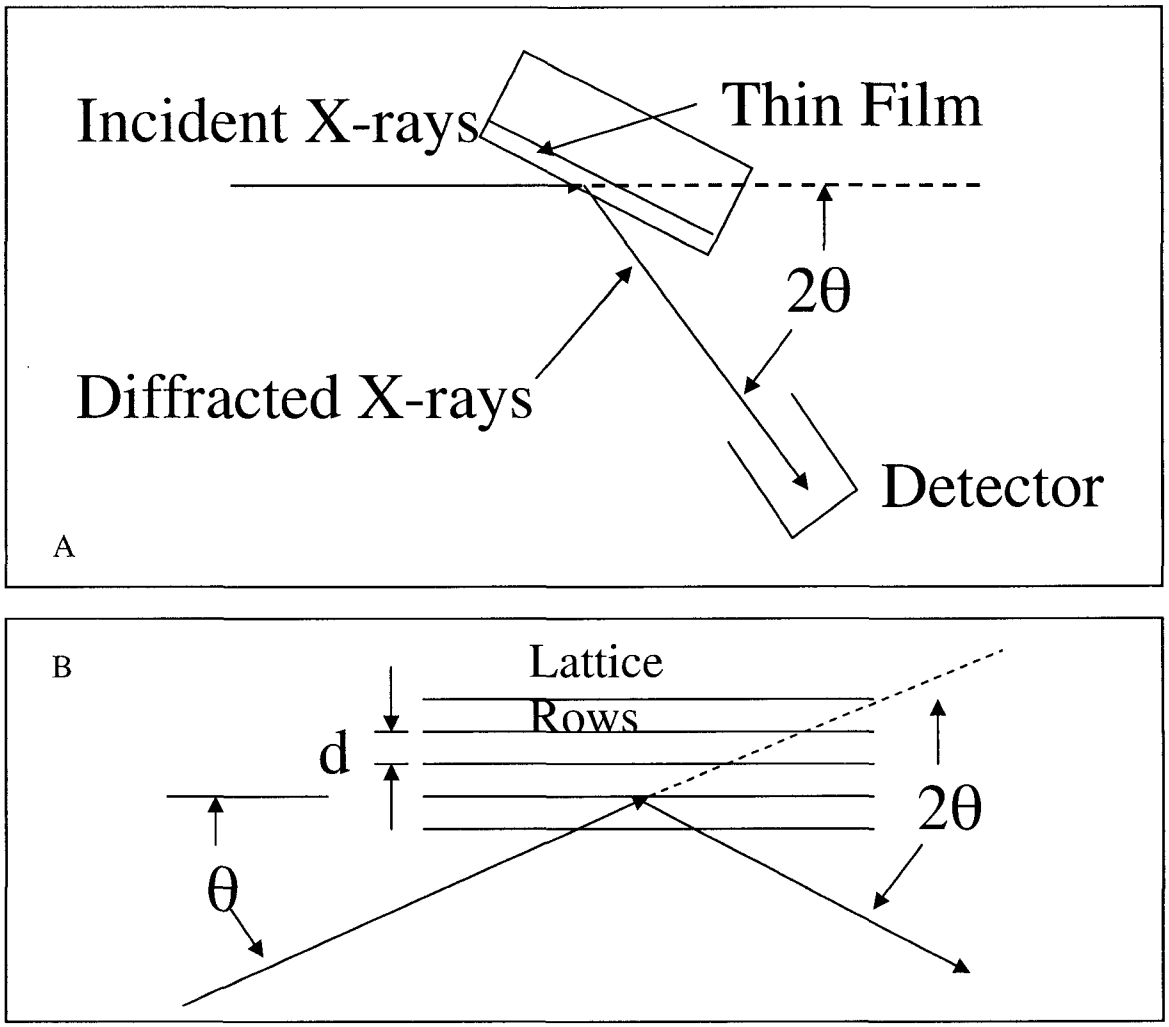

Figure 2.6.1 XRD setup. (A) shows geometry and the relative placement of the specimen and detector and (B) shows the path of the x-rays and the diffraction angle.

A

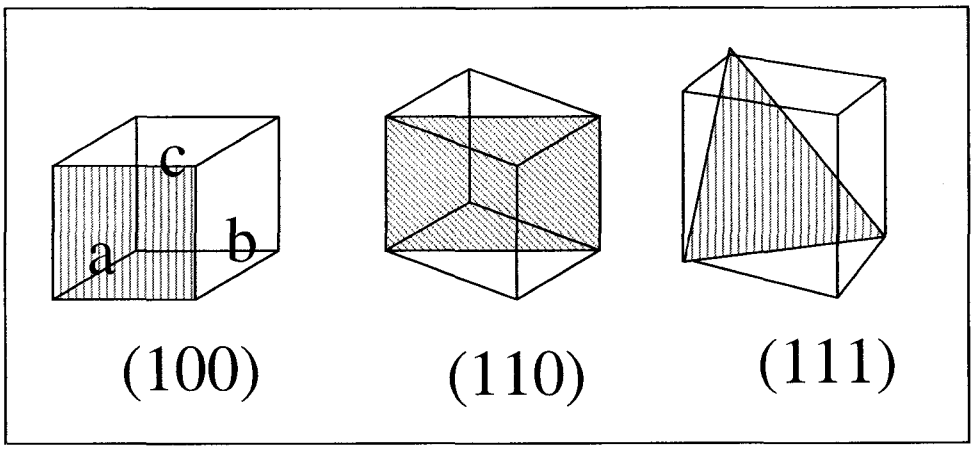

B

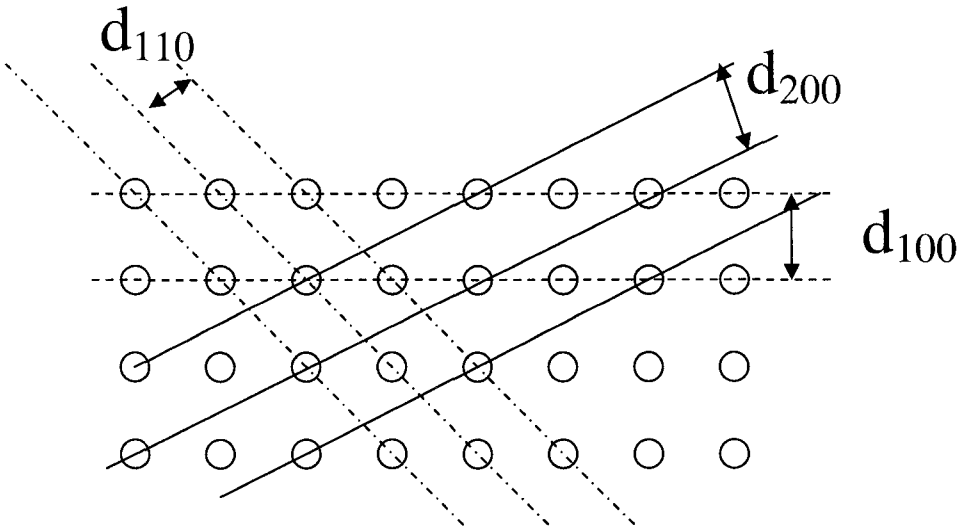

Figure 2.6.2 (A) Miller indices of atomic planes in a simple cubic crystal and (B) several atomic planes and their d-spacings in the same crystal system.

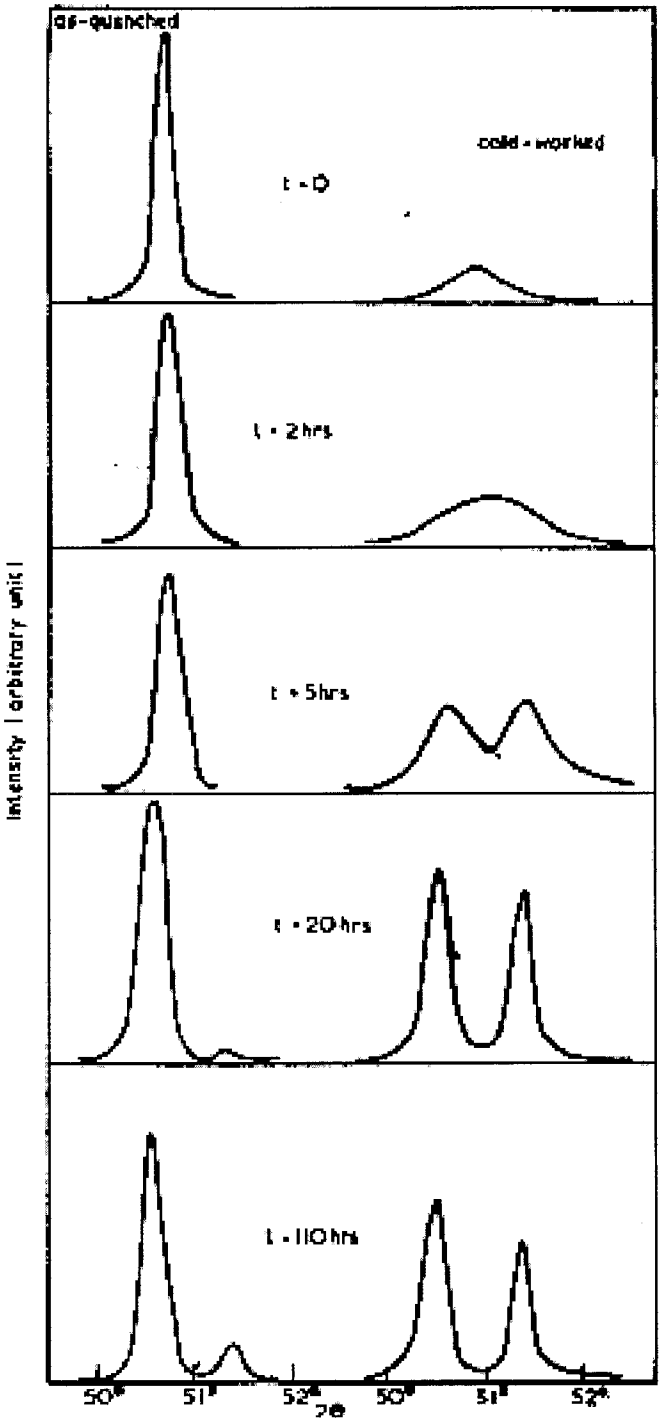

Figure 2.6.3 Changes in the line profiles of the (200) reflections for cold-worked and as quenched samples during progressive ordering at 700^0 C [92].

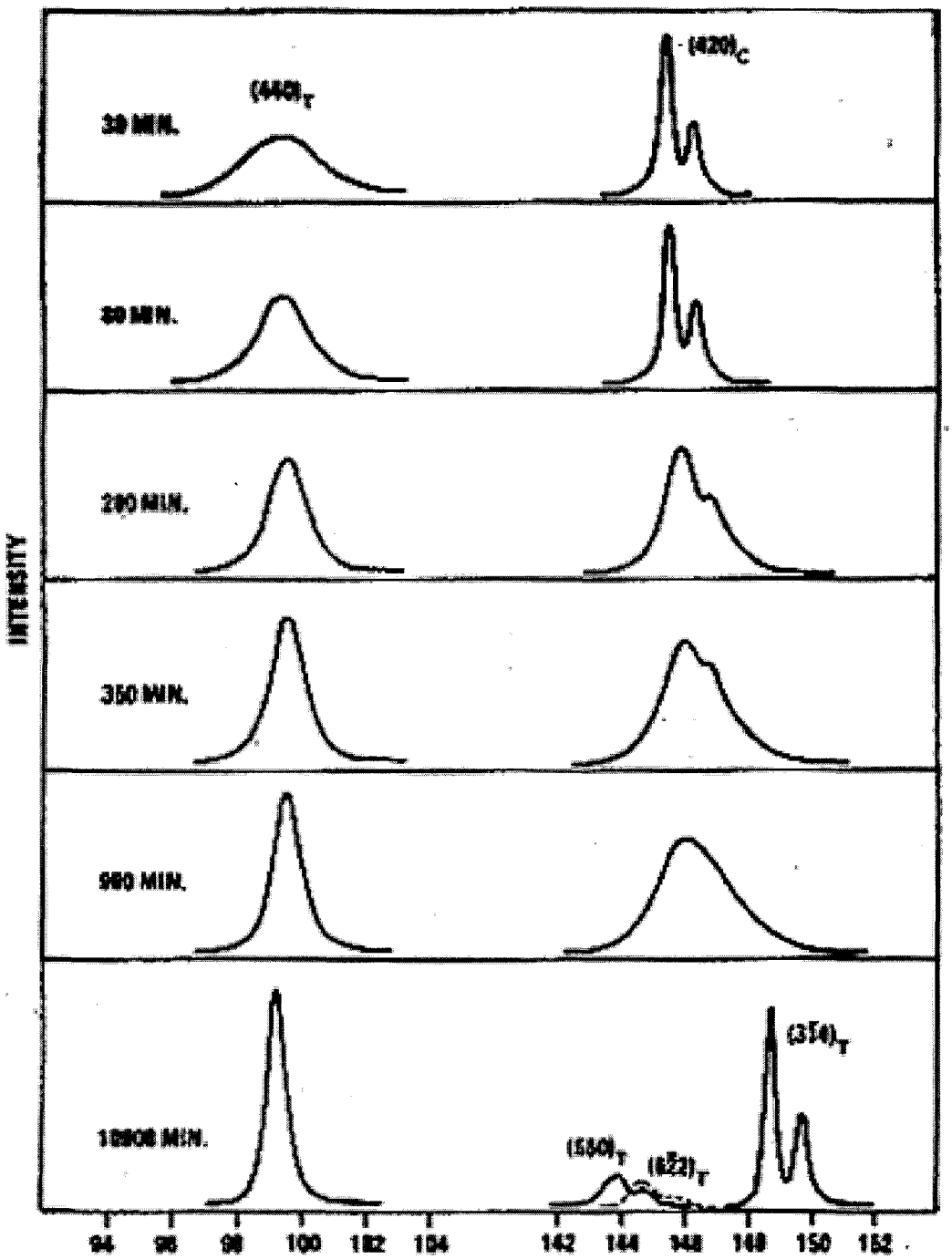

Figure 2.6.4 Change of the peak shape of a superlattice and a fundamental reflection during isothermal ageing at 700^0 C [93].

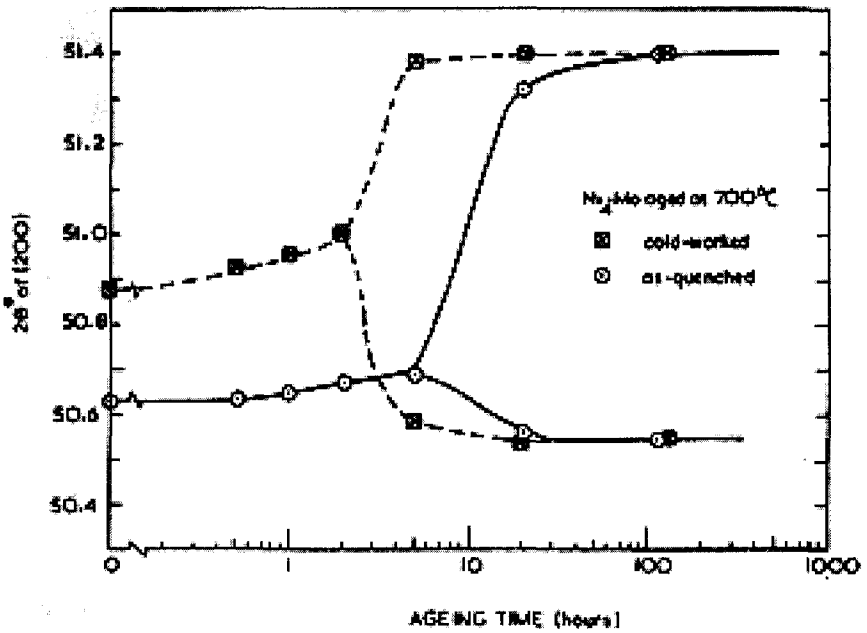

Figure 2.6.5 Position of the peak maxima of the (200) reflections as a function of annealing time at 700^0 C [92].

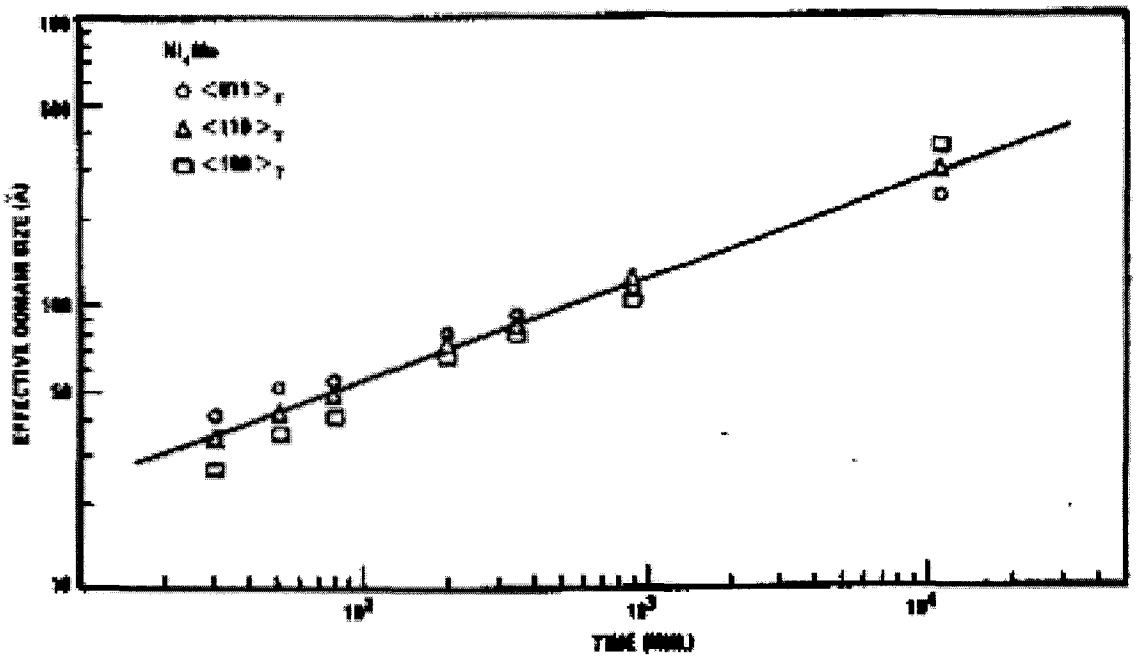

Figure 2.6.6 Natural logarithm of the domain size vs. logarithm of the ageing time for three crystallographic directions [82].

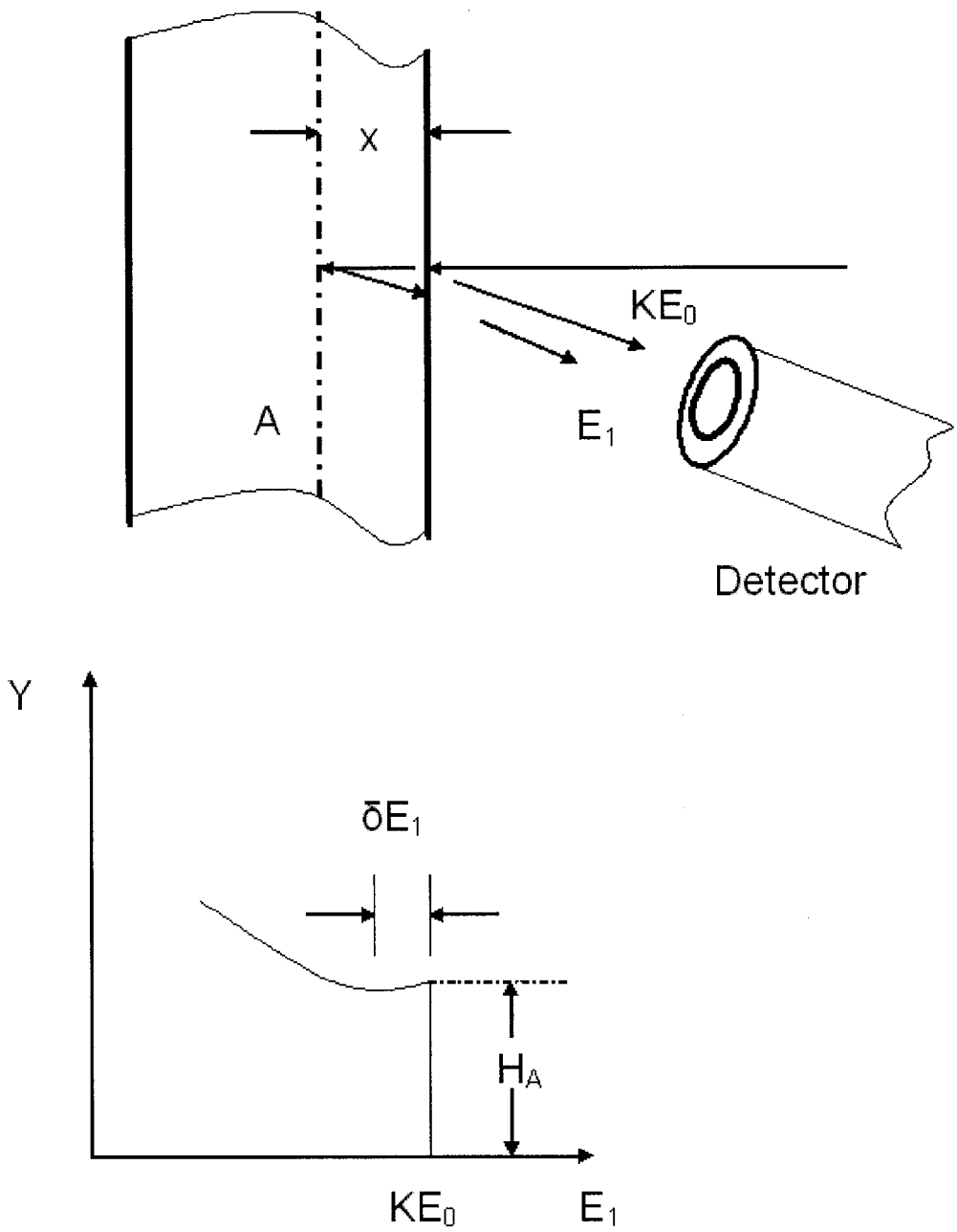

Figure 2.7.1 Detection setup and sample RBS spectrum at the surface of a one component material.

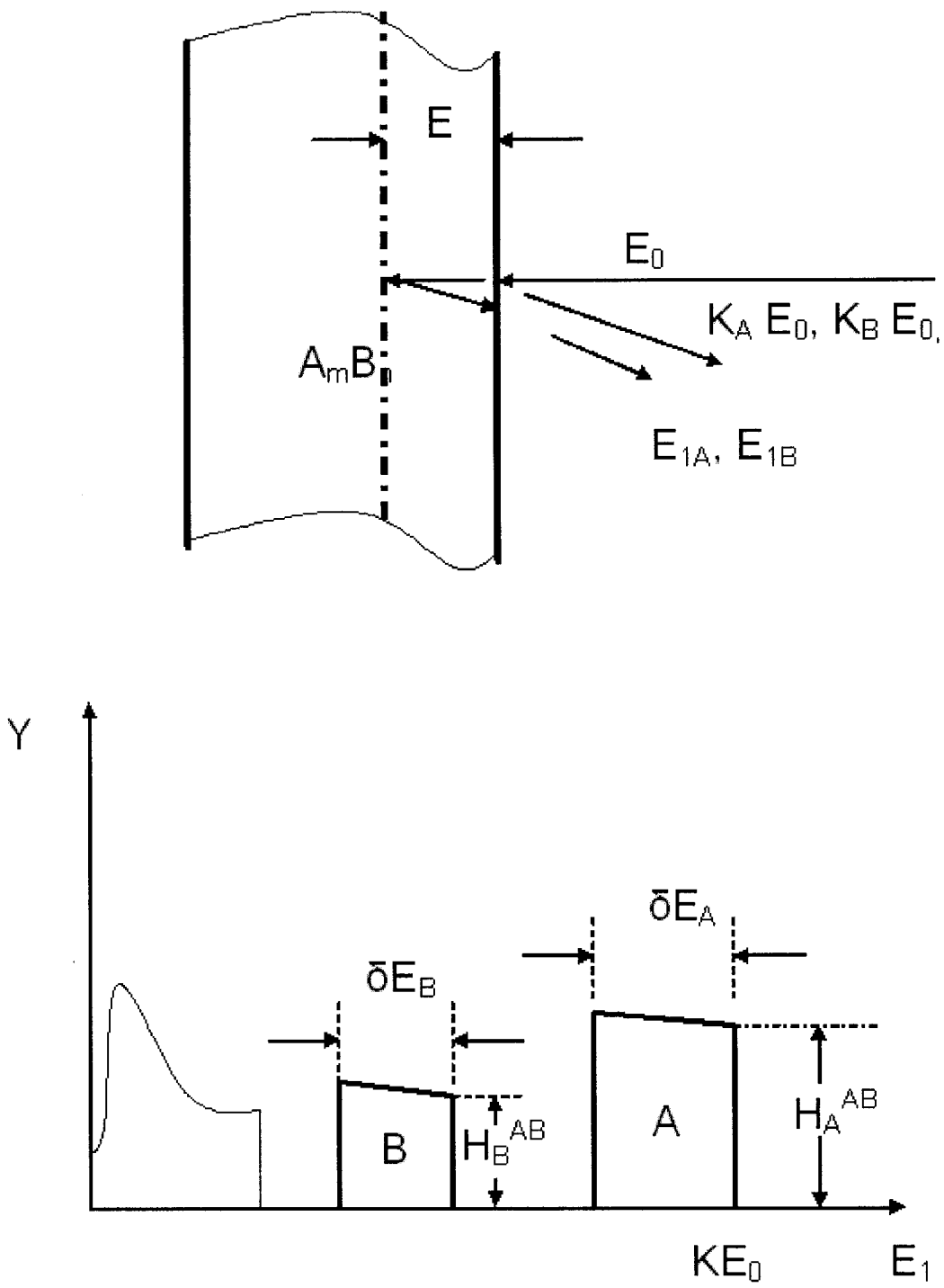

Figure 2.7.2 Sample RBS spectrum for a mixture with two components: AnBm.

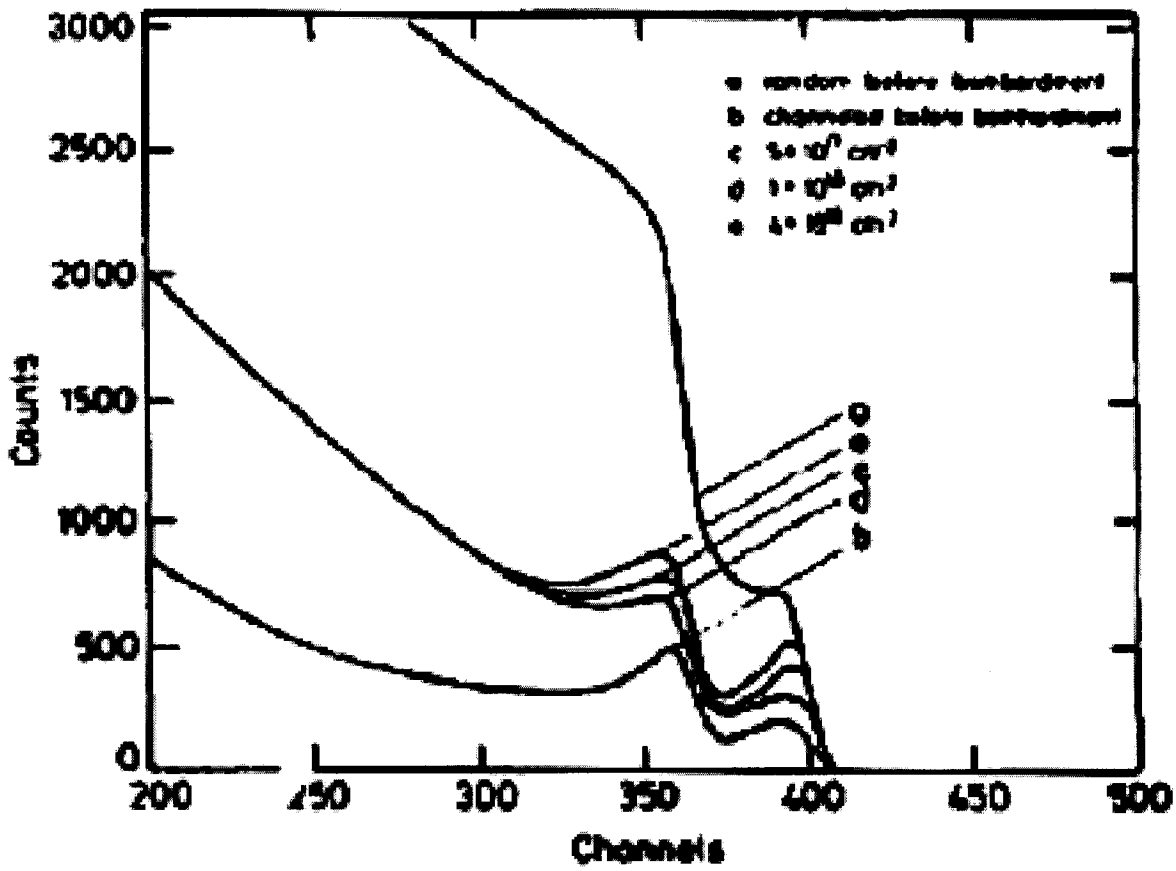

Figure 2.7.3 RBS spectra of Ni_4Mo bombarded along the (001) direction with different fluences of Ar+ beam [98].

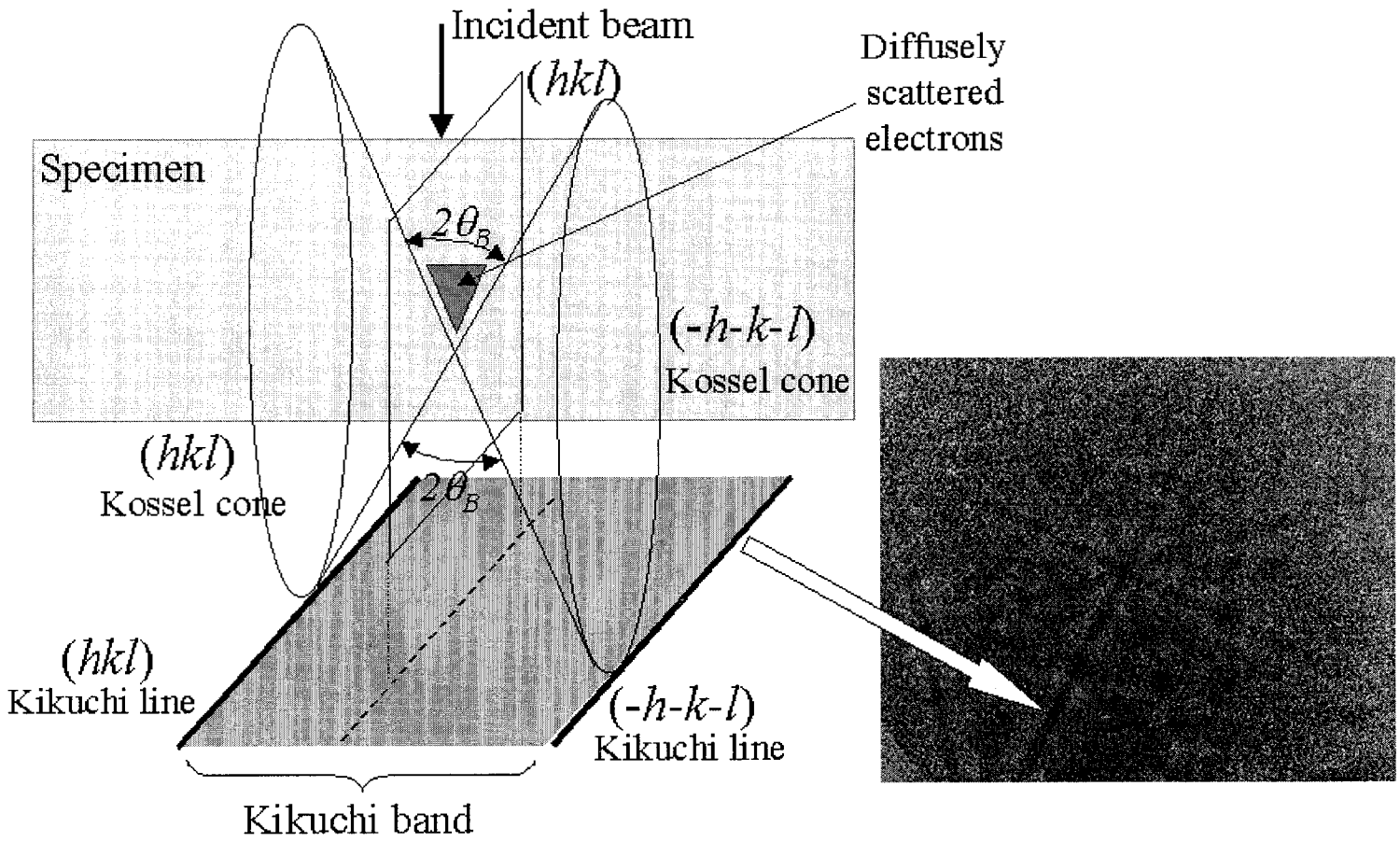

Figure 2.8.1 Formation of Kikuchi bands as a result of electron diffraction on the <hkl> family of planes

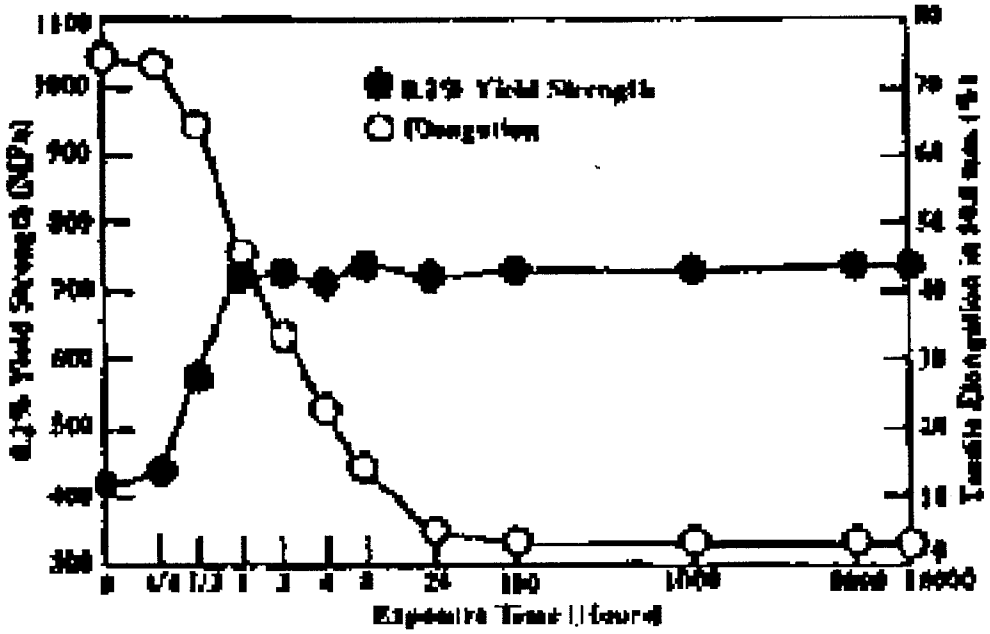

Figure 2.9.1 Effect of thermal exposure of Ni-Mo alloy (a) at 700^0 C and Ni-Mo-Cr alloy (b) at 550^0 C [99].

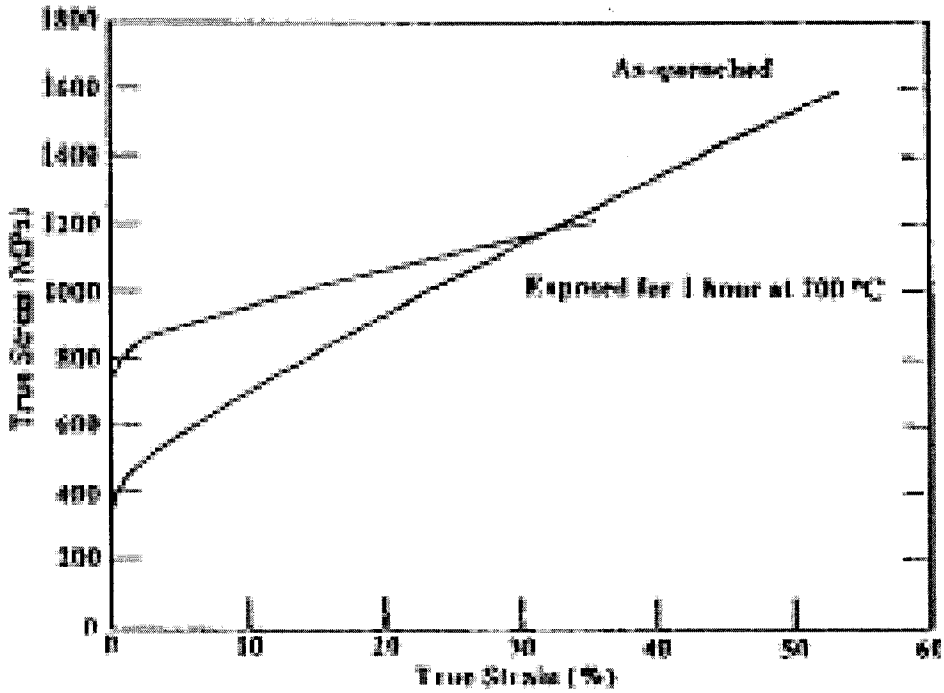

Figure 2.9.2 True tensile – stress diagrams for Ni_3Mo alloy [99].

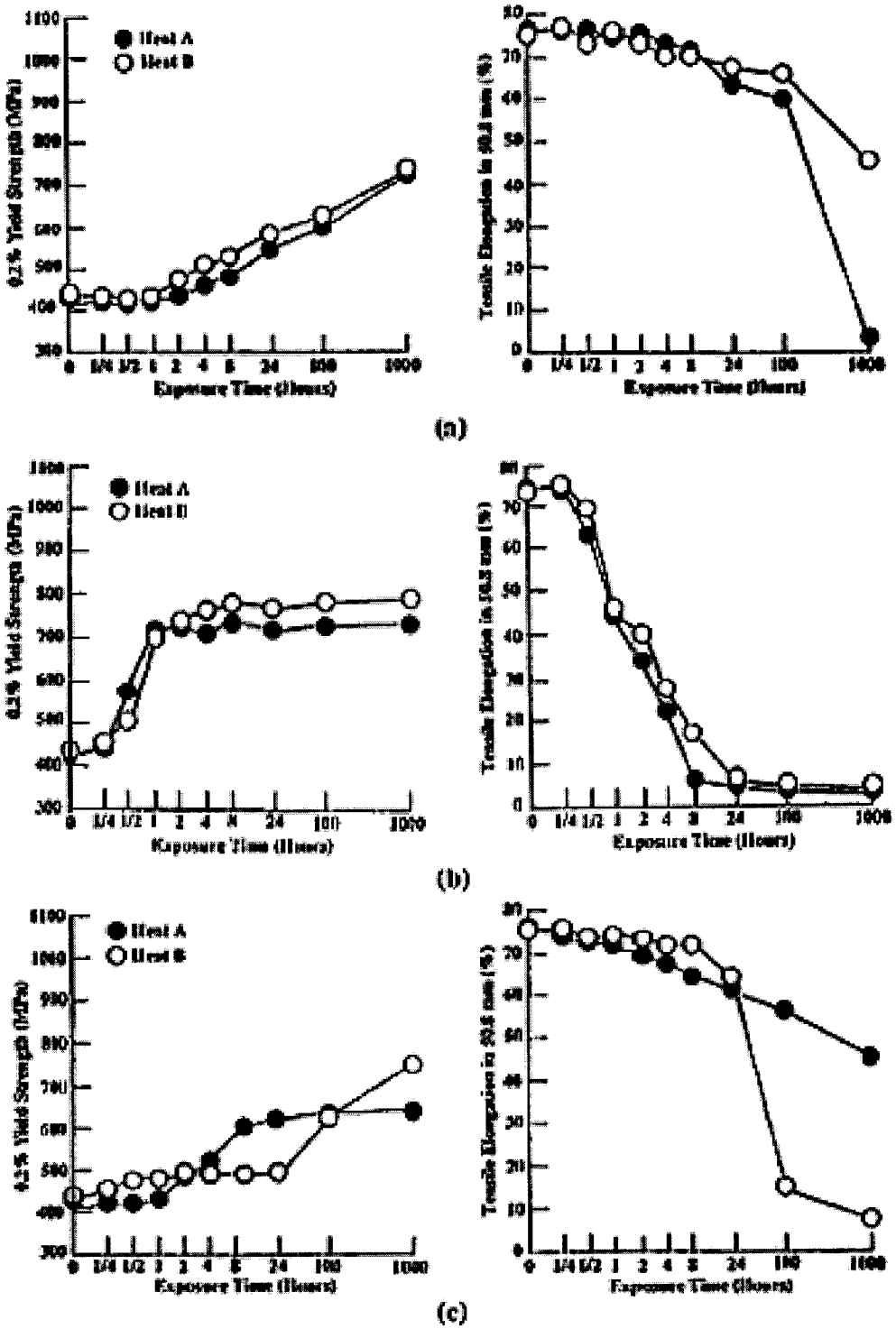

Figure 2.9.3 Effect of thermal exposure of two alloys. Set A: Ni26%Mo and Set B: Ni 29%Mo). Temperatures are (a) 600^0 C, (b) 700^0 C and (c) 800^0 C [98].

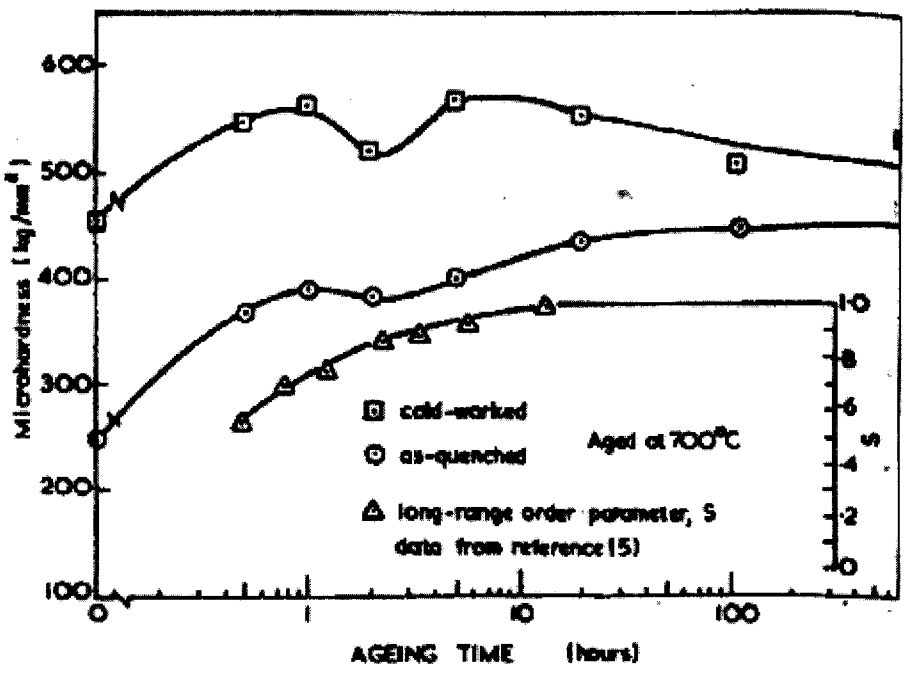

Figure 2.9.4 Microhardness variations as a function of ageing time for cold-worked and as quenched Ni_4Mo annealed at 700^0 C [98].

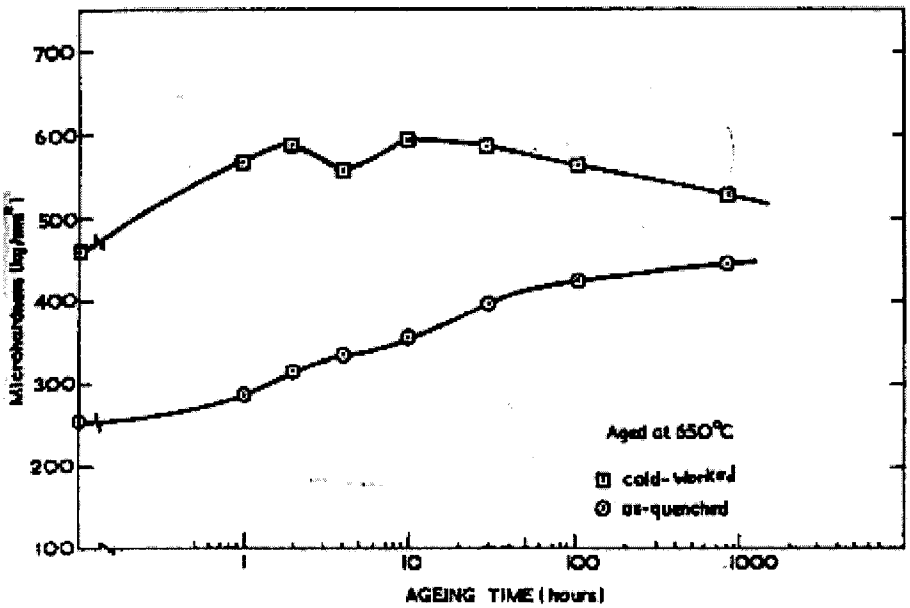

Figure 2.9.5 Microhardness variations as a function of ageing time for cold-worked and as quenched Ni_4Mo annealed at 650^0 C [98].

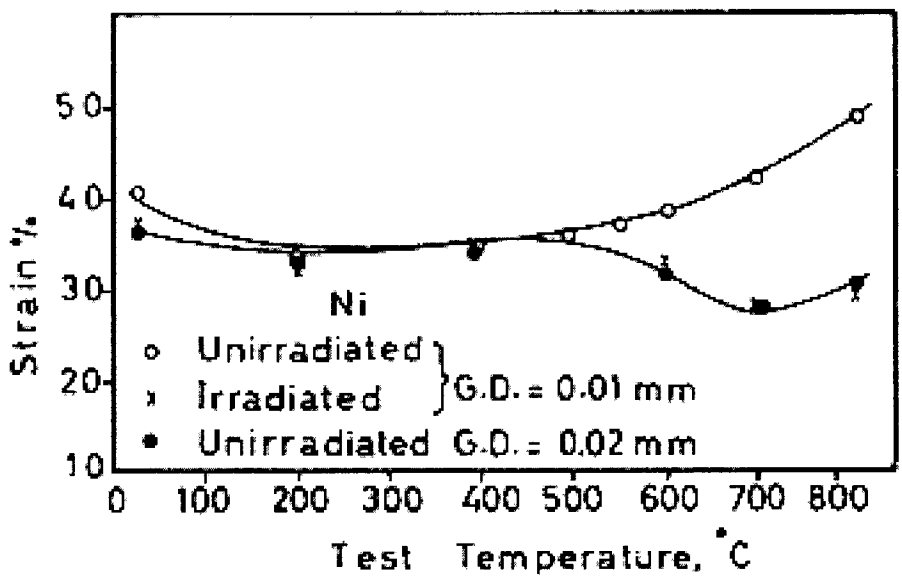

Figure 2.9.6 Effect of grain size and neutron irradiation ($7x10^{17}$ cm^{-2} and $2x10^{18}$ cm^{-2}) on the ductility of Ni [100].

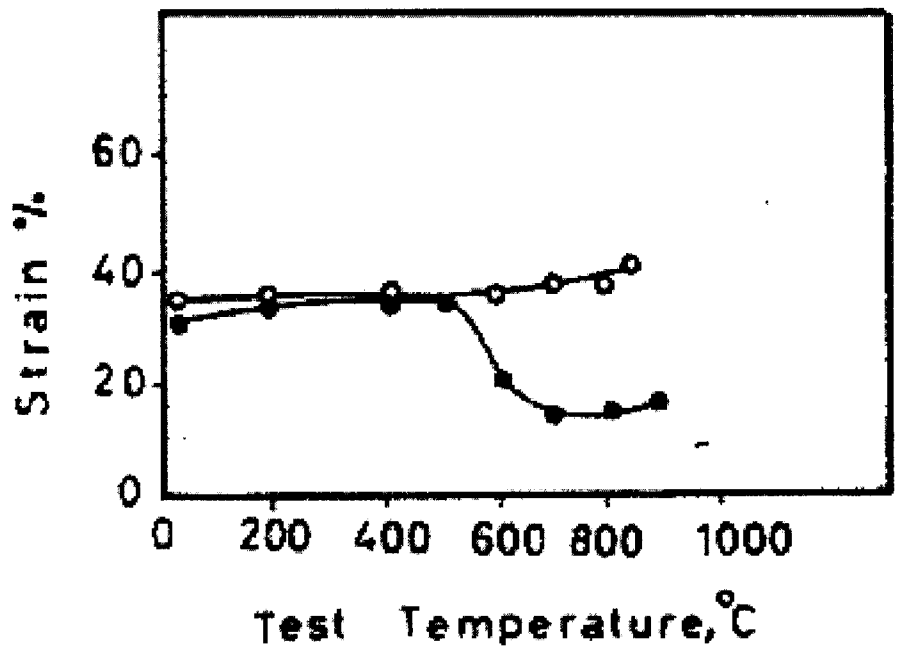

Figure 2.9.7 Effect of neutron irradiation ($7x10^{17}$ cm^{-2} and $2x10^{18}$ cm^{-2}) on the tensile properties of Ni_4Mo alloy [100].

CHAPTER 3

EXPERIMENTAL PROCEDURE

This experimental procedure covers the measurements of unirradiated (NoI), Ni irradiated, He irradiated, proton irradiated and post-irradiation annealed samples. The experimental procedures are described in the following sections:

1. Ni-Mo alloys and sample preparation
2. The Tandetron accelerator, the ion sources and the irradiation chamber
3. The sample irradiation process
4. Post annealing procedures
5. XRD setup and measurements
6. Scanning Electron Microscope (SEM) and Orientation Imaging Microscopy (OIM)
7. RBS data collection
8. Hardness testing

3.1 Alloys and Sample Preparation

The alloys used in this work were specifically chosen to perform a systematic analysis of the order-disorder transition under various irradiation conditions. As stated in the previous chapters Ni_4Mo and Ni_3Mo are very good candidates for this purpose

The Ni-Mo alloys (Ni_4Mo, Ni_3Mo, Ni_2Mo and NiMo) alloys were cast in an arc melting furnace (Figures 3.1.1 – 3.1.4) in the WMU Material Sciences Laboratory. First, the corresponding weight for each component was calculated (Table 3.1) and then the amount of Ni and Mo was determined within a .1 g precision. The purity of the materials was better than 99.5% and the components were procured from Alpha Aesar.

The preparation process consisted of arc melting of the two elements together in an Ar atmosphere. When both metals reached the liquid state, the arc was kept a little longer and was actually used to stir and better mix the liquid. Upon cooling, the cast was turned upside down and the process was repeated three or four times to ensure a complete homogenization of the alloys. Due to the high melting temperature of Mo, the higher the amount of Mo in an alloy, the more time it took to melt and homogenize the mixture. The final alloys were cast in a convex lens shape with a diameter of about 35 mm.

The next step was cutting the casts into smaller pieces about 2.5 mm thick using an electric discharge machine (EDM). The thickness affected by this process was about 10-20 μm. To ensure a surface without contamination, a layer of about 100 μm was removed with grinding paper. In this manner, the samples used for irradiation were in an identical condition to those unirradiated. Furthermore, to preserve the condition of the material, no heat or mechanical treatment was given to a first set of cast alloys. A second set of Ni_4Mo and Ni_3Mo specimens was annealed for 75 h at 800^0 C, close to the critical ordering temperature (LRO in Ni_4Mo). The third set of Ni_4Mo and Ni_3Mo was annealed for 75 h at 1000^0 C, above the critical temperature in order to achieve short range order (SRO) structure. The cast samples of Ni_2Mo and NiMo were not subject to any heat treatment. The samples prepared this way were wet polished using SiC grinding paper to

a final finish of 4000 grit. The process produced a mirror-like finish and was followed by electropolishing.

Different solutions were suggested in the literature for the electropolishing process of the Ni-Mo alloys. Tawancy [55] used a solution of 30% nitric acid in methanol at -30^0 C, Chakravati [101] used a solution composed of 2/3 sulfuric acid and 1/3 water at 0^0 C. Chevalier [72] used 53 ml of 60% chlorhidric acid, 53 ml of 40% hydrofluoric acid, 25 ml water and 367 ml ethyl cellosolve. Chen [42] suggested 225 ml nitric acid, 150 ml sulphuric acid, 100 ml water and 3 g NaCl and Cao [10] used one part nitric acid and three parts methanol at -30^0 C. All of the above were tried, but neither gave a good results such that the samples could be used for OIM. Chen's solution was slightly altered to 25% nitric acid, 25% sulphuric acid and 50% water and the results were satisfactory. If the samples were kept too long in the electrolyte, the etching effect became dominant.

3.2 The Tandetron Accelerator, the Ion Sources and the Irradiation Chambers

Specimen irradiations were performed using the General Ionex Tandetron accelerator at the Michigan Ion Beam Laboratory. The 1.7 MeV Tandetron accelerator (Figure 3.2.1) is a solid-state gas insulated, high frequency device, capable of operation between 0.2 and 1.7 MeV. The accelerator can operate with a duoplasmatron source (used for He^+ beam), a sputtering source (used for Ni^+ beam) and a high current Torvis-type source (for H^+ beam). A beam of protons of up to 300 uA can be produced with the

Torvis type ion source. The 15 degree beamline (measured with respect to the direction of the Tandetron) is dedicated to the implantation and the irradiation experiments. This beamline consists of a quadrupole for focusing, an analyzing magnet, a raster scanner and a steerer system (Figure 3.2.1). The second beamline is used for ion beam analysis. Each beamline is terminated with a target chamber. The radiation damage chamber (at the end of the 15 degree beamline) is cryopumped in the range 10^{-10} Torr regime and has attached on one of the ports, a temperature controlled heated sample stage for irradiation damage experiments. The second beamline contains an aperture system, a Faraday cup for charge collection, a beam viewer, a translation two-axis goniometer and detectors for backscattering and glancing angle measurements. It is turbo-pumped and equipped for rapid sample turn-around. Rutherford Backscattering (RBS), Nuclear Reaction Analysis (NRA), elastic recoil detection (ERD) and ion channeling are conducted in this chamber.

The Torvis source and the end-station data-collection system are interfaced and electronically controlled by computers running Microsoft Windows 2000 and Labview from National Instruments. The control/monitor program was entirely written at Michigan Ion Beam Laboratory (MIBL) and provides easy remote access via a web page (Figures 3.2.8 – 3.2.9). The data is streamed into a web site allowing remote users to control and read back the parameters. The Torvis source was built by National Electrostatic Corp. (NEC) (Figure 3.2.2). The interface between the controlling computer and the source is done via RS232 communication port through fiber optics. The source can deliver about 300 μA at the low energy side of the accelerator and in excess of 150 μA at the high energy end.

The Duoplasmatron IONEX Model 358 ion source generated the He+ beam. A low pressure arc-discharge in the gas to be ionized is electrostatically constricted by a funnel shaped intermediate electrode placed between the electron-emmitting cathode (hot filament) and the anode. The strong axial magnetic field, which develops between the intermediate electrode and anode, constricts the discharge to a narrow plasma beam along the axis of the exit aperture. For negative ions, the intermediate electrode is displaced with respect to the anode aperture axis with the help of an adjustable sliding seal located between these parts. In this way, displacements of up to 0.1 inch are possible. The duoplasmatron source is a high brightness ion source, capable of delivering about 500 nA of He current at the high energy end.

To produce the Ni beam, a sputter type source was used. Due to the fact that at the low energy end of the accelerator there are two ports at 30 degrees from the direction of the tube of accelerator, only two sources can be mounted at one time. The Torvis source can not be removed and replaced with ease, so the sputter source was interchanged with the duoplasmatron when the Ni irradiations were performed.

The irradiation stage that can be seen in Figure 3.2.5 was designed to control the temperature of the samples by controlling the temperature of the stage [105]. This is accomplished by flowing room temperature air through the cooling lines that penetrate the back of the stage. The surface of the stage is made of copper in order to provide good heat conduction away from the samples.

The temperature of the specimens was monitored using two techniques. Type J (iron/constantine) thermocouples were spot welded directly to the surface of the samples. Typically there were three or four thermocouples attached to the samples during any one

irradiation. Each of the four thermocouples is welded to a sample as close to the irradiated region as possible, outside the irradiated area of the samples. This is because charge from the ion beam may affect their behavior. The thermocouples are primarily used as a means to calibrate a thermal imager prior to the irradiation. Thermocouples also provide a secondary means of temperature measurement during irradiation. A separate thermocouple monitors the temperature at the back of the stage.

In addition to the thermocouples, a thermal imager (called Stinger), manufactured by IRCON is attached to one of the ports of the irradiation chamber. This instrument provides real time temperature monitoring during irradiation (Figures 3.2.3 – 3.2.4).

The irradiation stage is electrically isolated from the beam line. Four rectangular tantalum apertures are used to define the area on the samples that is irradiated with the proton beam. Prior to the irradiation, a benchtop laser is used to ensure that the aperture assembly is properly aligned. A misaligned aperture may result in either the left side sample or the rightmost side of the sample being partially shaded from the proton beam by the aperture. These samples would not receive a uniform irradiation and would not be useful in later analysis. A small laser pointer is mounted to a translating stage, which is attached to one end of a benchtop. The irradiation stage sits in a custom-built holder attached to the opposite end of the benchtop (approximately 20 feet away). The laser beam is positioned such that it is perpendicular to the sample surface on the irradiation stage. When the laser is located such that half of the laser beam hits the aperture with the other half of the beam hitting the samples behind the aperture, the alignment of the aperture can be checked. If the laser beam does not hit the entire sample, the aperture position is then corrected [105].

The approximately 3 mm diameter proton, helium and nickel beams are rastered across the stage so that about half the total beam current is deposited on the samples and half on the apertures. Additionally, each beam is centered by balancing the amount of beam current measured on each of the apertures. This rastering also ensures that samples at any position on the stage receive the same dose. The beam is rastered at high frequencies in both the horizontal and vertical directions (255 Hz and 2061 Hz, respectively). The length of one beam scanning cycle is 3.9 ms and is governed by the frequency in the x-direction. The ratio of these two frequencies is 8.08. Since this ratio is not an integer, the path that the beam follows will not be identical each cycle, which will lead to further spatial uniformity. When the actual size of the beam is considered, coverage of the samples is found to be 85% for each half-cycle and 100% for each full cycle. Thus, the entire sample surface is hit by the beam every 3.9 ms .

Experimental parameters are tracked continuously during the irradiation using a PC-based monitoring system. During the irradiation, experimental temperatures and beam current are monitored using an Pentium IV computer. Monitoring software, written in the Labview environment, tracks and records the stage current, aperture current, thermal imager temperature, and the temperature from up to five thermocouples. This system allows the operator to continuously monitor experimental parameters while also providing a comprehensive history of each irradiation. A sample screen shot of the GUI interface is shown in Figure 3.2.6 [106, 107]. A similar screen is available in real time for any web user logging in into the lab site (Figure 3.2.7). Also, alarms are available to alert the operator when experimental parameters have moved outside acceptable limits. Stage current is first fed into an analog meter and current integrator before being fed into

the monitoring computer. Aperture currents are linked directly to the computer monitor without an intermediate analog output. Sample temperature and stage current readings are also saved to a file during the irradiation. Following irradiation, the temperature and stage current histories can be plotted for future reference. During irradiation, we did not create any radioactive products due to the low energy of the proton beam below the threshold of Ni or Mo activation.

3.3 The Irradiation Procedure

The required doses and dose rates are calculated using SRIM2003 [108]. The damage profiles for the beams used in this experiment are illustrated in Figure 3.3.1 (3 MeV Ni^+) Figure 3.3.2 (2 MeV He^+) and Figure 3.3.3 (1 MeV protons).

Irradiation with 1 MeV protons results in a nearly uniform damage rate through the first 5 μm of the proton range. For a nominal beam intensity of 1 μA/cm^2 on the samples (the Tandetron accelerator can provide up to 25 μA/cm^2), the corresponding damage rate can be calculated. SRIM2003 simulations provide the average number of displacements generated per ion density per unit volume of material as a function of ion range. The results are given in units of Displacements/Angstrom/Ion as shown for example in Figure 3.2.5 in the Collision Events plot. This value can be converted to a displacement rate by using [105]:

$$displacement\ \ rate\ (dpa) = \frac{proton\ \ flux \times displacements / angstrom / ion}{atomic\ \ density}, \qquad (3.3.1)$$

where the theoretical atomic density of Ni_4Mo is 9.15 x 10^{22} atoms/cm^3 or 9.15 x 10^{14} atoms/cm^2/ Å. The number of ions/unit area/unit time can be converted from a current density to a particle flux using the factor 1 Amp = 1 Coulomb/s = 6.25 x 10^{18} electrons/s. Since the hydrogen ion is singly charged, a single electron is measured for each incident ion. Therefore, the proton flux is given as:

$$proton\ flux = 1.0\times10^{-6}\ \frac{A}{cm^2}\times 6.25\times10^{18}\ \frac{protons}{A} = 6.25\times10^{12}\ \frac{protons}{cm^2 s}. \quad (3.3.2)$$

Combining these results in Eq. (3.3.1),

$$displacement\ rate\ (dpa) = \frac{6.25\times10^{12}\ \frac{protons}{cm^2 s}\times 2.2\times10^{-4}\ \frac{displacements}{angstrom\cdot ion}}{9.15\times10^{14}\ \frac{atoms}{angstrom\cdot cm^2}} = 1.51\times10^{-6}\ \frac{dpa}{s}. \quad (3.3.3)$$

With a displacement rate of 1.51 x 10^{-6} dpa/s, a 1.0 dpa irradiation requires a total irradiation time of:

$$irradiation\ time = \frac{1.0\ dpa}{1.51\times10^{-6}\ \frac{dpa}{s}} = 6\times10^{5}\ s \approx 166\ hours. \quad (3.3.4)$$

Irradiation doses for H were as follows: 1, 0.5, 0.2, 0.1, 0.05 and 0.01, where the dpa number was calculated as described above, using SRIM2003 and a displacement energy, E_d, of 25 eV. Similar calculations made for He and Ni would give irradiations times as listed in Table 3.2.

Multiple samples can be irradiated simultaneously, providing duplicate samples for the same experimental conditions. On the irradiation stage where the temperature can be kept down with the air flown through the cooling lines, only two large samples can be irradiated in one batch. The following is the structure of a regular irradiation set:

- Ni
- Ni_3Mo no treatment

- Ni_3Mo pre-annealed at 800^0 C for 72 h
- Ni_3Mo pre-annealed at 1000^0 C for 72 h
- Ni_4Mo no treatment
- Ni_4Mo pre-annealed at 800^0 C for 72 h
- Ni_4Mo pre-annealed at 1000^0 C for 72 h

3.4 The Post-Irradiation Annealing

For the post-irradiation annealing treatment, a high vacuum furnace chamber was used (Figure 3.4.1). In order to reduce the chamber's contamination a sorption pump provided the initial rough vacuum. After a vacuum in the militorr range is achieved, a manual valve is opened and the samples are cryopumped. Annealing can proceed when vacuum is in the 10^{-8} torr range.

3.5 XRD Measurements

The XRD measurements were done at the University of Michigan in Materials Characterization Laboratory using a Rigaku Rotoflex RU-200 machine. The 2θ angle was varied between 20 and 100 degrees for all the spectra collected keeping constant all the other parameters.

3.6 Orientation Imaging Microscopy

The OIM system attached to the Philips XL30FEG SEM at the University of Michigan's Electron Microbeam Analysis Laboratory (EMAL) is also capable of distinguishing between different phases that may be present in the material. Measurements of crystallographic orientations along with microscopic observations are the basis of quantitative investigations of the microstructure of crystalline materials.

For the OIM analysis performed in this work, the SEM accelerating voltage was 25 kV and the spot size 5 at a magnification 500×. The SEM time is affected by two other parameters: step size and the number of patterns averaged at each point. The step size is usually dictated by the grain size of the structure to be mapped. For a 200 μm grain size, the step size was chosen to be between 5 and 10 μm, such that plenty of mapping points fall within each grain. However, in order to obtain the high quality EBSPs needed for an accurate analysis, a certain number of patterns must be averaged by the image processor. A large such number - usually dictated by the strain level in the sample and the quality of sample preparation - results in a proportionally large analyzing time/step. In the specific case of our Ni_4Mo and Ni_3Mo alloys samples, a number of 8 frames were averaged at each point, and in this way the analyzing time was kept at 0.5 sec/step. To perform OIM analysis, an area of interest on the sample is selected and the electron beam is driven automatically from point to point over this area, allowing for the resulting Kikuchi patterns to be collected on a phosphor screen. A schematic diagram of the OIM system in use at the University of Michigan is presented in Figure 3.6.1 [109].

In order to obtain intense Kikuchi patterns, the sample has to be steeply tilted to about 70° from the horizontal, i.e. 20° with respect to the incident electron beam. This specific angle of 70°, was chosen because in this configuration the calibration Si [001] crystal has the [114] zone axis, which serves as the pattern center, normal to the phosphor screen. The area to be mapped is then selected and the beam is collimated in "spot" mode. The EBSP image formed on the phosphor screen is captured by a silicon intensified target (SIT) camera and routed through a digital signal processor to the computer. Both camera and beam control units are interfaced to a PC. As the electron beam is driven from point to point on the analyzed area, the resulting patterns are displayed in a video window of the computer where they are analyzed and indexed automatically by the software. This procedure is illustrated in Figure 2.8.1. Based on the analysis of the Kikuchi pattern at each analysis point, the rotation matrix of the crystal with respect to the reference coordinate frame represented by the calibration Si [001] crystal, R, is calculated (Figure 3.6.3). The rotation matrix, R, is essentially the matrix of direction cosines, which maps the specimen crystal coordinate system into the reference coordinate system. In Figure 3.6.3, the two points to the left have the same rotation matrix R_1 with respect to the reference coordinate system, as they belong to the same grain. Once the grain boundary is crossed, the Kikuchi pattern changes and a new rotation matrix corresponding to the orientation of this grain to the reference, R_2, are calculated. Further, the misorientation of the two grains is calculated as:

$$M = R_2 R_1^{-1} \tag{3.6.1}$$

The data resulting from a scan (location, orientation and image quality of the pattern of

each point analyzed) can be processed to create orientation imaging micrographs, enabling a visual representation of the microstructure, as illustrated by the OIM map next to the SEM micrograph of Figure 3.6.3. The methodology for performing OIM analysis is described in detail in Appendix A2.

3.7 RBS Setup and Data Collection

In the RBS experiments, the backscattered particles were detected with an EGG Ortec surface barrier silicon charged particle detector at an angle of 170^0 (a solid angle Ω = 5 sr.) relative to the incident beam direction. The energy resolution of the detector is about 10 KeV. The RBS spectra were analyzed using the RUMP computer code [51] for simulation of backscattered alpha particles. Duoplasmatron ion source was used to generate He^4 ions and was the described in section 3.2. The current was about 100 nA on the target samples and about 300 nA at the low energy Faraday cup, before the acceleration through the Tandetron. The signals from the detectors were processed by an Ortec 428 bias power supply, and the current measured with a 428 Ortec Digital Current Integrator. The signal was also fed into a Brookhaven BIC charge integrator for direct count. The charge collected for each sample was about 100 μC in order to obtain good statistics. The data files collected needed to be converted from an ORTEC specific format with a program called ORFAST in order to be analyzed by RUMP and converted next to ASCII type files. These data files and the simulation files could be then displayed and manipulated with a program like Microsoft Excel. RUMP is a very helpful software tool that could be used to determine if the right stoichiometry is present in the bulk

material. It is also useful in determining if any changes occurred in the surface layers of the irradiated specimens. The simulations were performed on each spectrum acquired from the samples to be irradiated to confirm uniformity. The actual procedures used to obtain quantitative information are:

1. Construct a composition profile of the target based on available information
2. Simulate the RBS spectra using RUMP
3. Compare the simulated spectrum with the experimental spectrum
4. Reconstruct the simulated spectrum to fit the experimental spectrum
5. Repeat steps 2 - 4 until there is a good match between the two spectra.

In order to get accurate spectra with good statistics, sometimes the beam had to be reduced in intensity (to reduce the detector's dead time) but then the acquisition time increased.

3.8 Hardness testing

3.8.1 Nano-indentation procedure

The hardness measurements were performed using a Nano Instruments® II nanoindenter at the University of Michigan Electron Microbeam Analysis Laboratory (EMAL). A typical load vs. displacement curve is shown in Figure 3.8.1. Each indent consisted of three loading steps made under load control at a 10% rate up to 5 mN. In each loading step a hold segment was introduced to account for thermal drift during measurement, and an unloading segment was used to correct for elasticity. A hardness

value was calculated for each loading step by dividing the load by the contact area of the indenter using the following shape function describing the shape of the indenter tip:

$$A(d) = 24.5d^2 + 246.57d + 0.0037403d^{1/2} + 0.00035551d^{1/4} + 0.0070361d^{1/8} + \\ + 0.0034207d^{1/16} + 0.0021362d^{1/32} + 0.0084845d^{1/64} + 0.0013783d^{1/128} \quad (3.8.1)$$

where A is the projected area of the indenter tip and d is the plastic indent depth. The three hardness values resulting from each indent were averaged together to produce a single hardness/indent value.

In nano-hardness testing of poly-crystals, the indent size is usually much smaller than the grain size. Especially in the case of the deformed samples, several parameters may influence the outcome of the hardness measurements, and therefore, needed to be taken into consideration such as the grain orientation, the grain size, and the relative position of indents with respect to grain boundaries. An additional complication is brought about by the fact that some grains may be shallow, causing an effect on the measured hardness. Unfortunately, these cases are impossible to detect. To try to address these issues a large set of data points was selected for each sample in randomly chosen spots. Patterns of indents with spacing of either 20 μm or 40 μm were performed on randomly-selected areas on all samples (Figure 3.8.2). The average hardness of a sample was calculated by averaging all hardness values measured on that sample.

3.8.2 Micro-hardness procedure

The measurements were performed on the polished samples at room temperature using a Vickers micro-hardness tester with Vickers pyramidal indenter. The

microhardness instrument was first verified and calibrated using standard procedures with a stainless steel block. A load of 10 g was applied for 10 s, and the final value for hardness was averaged for at least 4 sets of 25 points taken at random on the surface of each sample. In the case that larger variations were observed more sets of data were collected. The choice of low load was selected for the fact that the irradiated depth in the case of Ni beam was less that 2 μm, so we wanted to ensure that the depth of the indent was within this range. The typical size of the diagonals in the indentation measurements (d1, d2) was about 11 μm. The depth of the indentation is 1/7 of this value and that would mean about 1.5 μm. On the average, the depth was well within the 1 μm range. Microhardness sample point data are shown in Figure 3.8.3.

There are several factors that may contribute to the micro-hardness variation: the solid solution hardening, the presence of different phases in the alloy and the size of the grains. The grain size is an important variable affecting the hardness and can be usually expressed by the Hall-Petch relationship: $H_v = H_0 + kd^{-1/2}$, where, H_v is the measured hardness, H_0 and k are constants and d is the average grain size. Part of the change in hardness with heat-treatment temperature or after irradiation exposure is caused by the disorder-order change in the structure, as verified by the X-ray diffraction results.

3.9 Tables for Chapter 3

Ni_4Mo		At. #	At. %	Wt. %
	Ni	28	80	70.9958
	Mo	42	20	29.0042
Ni_3Mo	Ni	28	75	64.7370
	Mo	42	25	35.2629
Ni_2Mo	Ni	28	66.7	55.0709
		42	33.3	44.9291
NiMo	Ni	28	50	37.9631
		42	50	62.0367

Table 3. 1 The calculation of the % weight of Ni and Mo to melt in the furnace in order to obtain the desired Ni-Mo alloys.

Beam	Dose (DPA)	Time (h)	Beam	Dose (DPA)	Time (s)
H	0.01	2	Ni	0.01	30
	0.05	9		0.05	60
	0.1	17		0.1	120
	0.2	33		0.2	240
	0.5	84		0.5	600
	1	166		1	1200
He	0.01	0.2			
	0.5	10			
	1	20			

Table 3.2 Irradiation time for H+, He+ and Ni+.

100 C followed by 250^0 C		
1 DPA NI	Ni_3Mo	Ni_4Mo
	Ni_3Mo 800^0 C	Ni_4Mo 800^0 C
	Ni_3Mo 1000^0 C	Ni_4Mo 1000^0 C
250^0 C		
0.05 DPA H	Ni_3Mo	Ni_4Mo
	Ni_3Mo 800^0 C	Ni_4Mo 800^0 C
	Ni_3Mo 1000^0 C	Ni_4Mo 1000^0 C
0.05 DPA Ni	Ni_3Mo	Ni_4Mo
	Ni_3Mo 800^0 C	Ni_4Mo 800^0 C
	Ni_3Mo 1000^0 C	Ni_4Mo 1000^0 C
0.1 DPA Ni	Ni_3Mo	Ni_4Mo
	Ni_3Mo 800^0 C	Ni_4Mo 800^0 C
	Ni_3Mo 1000^0 C	Ni_4Mo 1000^0 C
350^0 C		
0.5 DPA H	Ni_3Mo	Ni_4Mo
	Ni_3Mo 800^0 C	Ni_4Mo 800^0 C
	Ni_3Mo 1000^0 C	Ni_4Mo 1000^0 C
0.5 DPA Ni	Ni_3Mo	Ni_4Mo
	Ni_3Mo 800^0 C	Ni_4Mo 800^0 C
	Ni_3Mo 1000^0 C	Ni_4Mo 1000^0 C
450^0 C		
1 DPA NI	Ni_3Mo	Ni_4Mo
	Ni_3Mo 800^0 C	Ni_4Mo 800^0 C
	Ni_3Mo 1000^0 C	Ni_4Mo 1000^0 C

Table 3.3 Samples subject to post annealing treatment.

3.10 Figures for Chapter 3

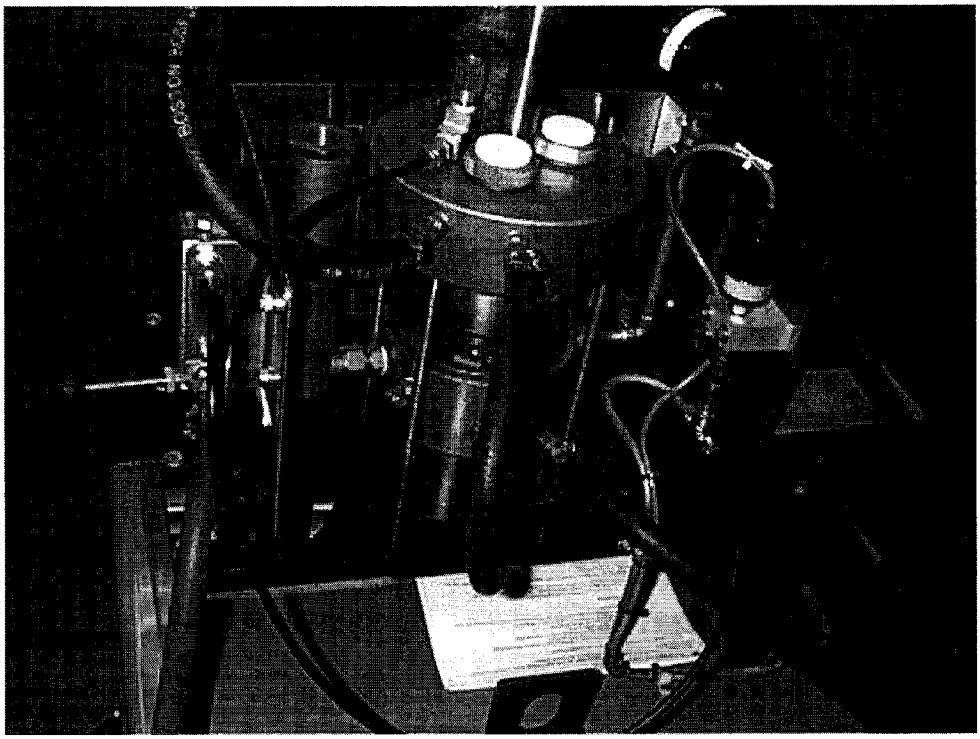

Figure 3.1.1 The arc melting furnace with Ni and Mo pieces loaded.

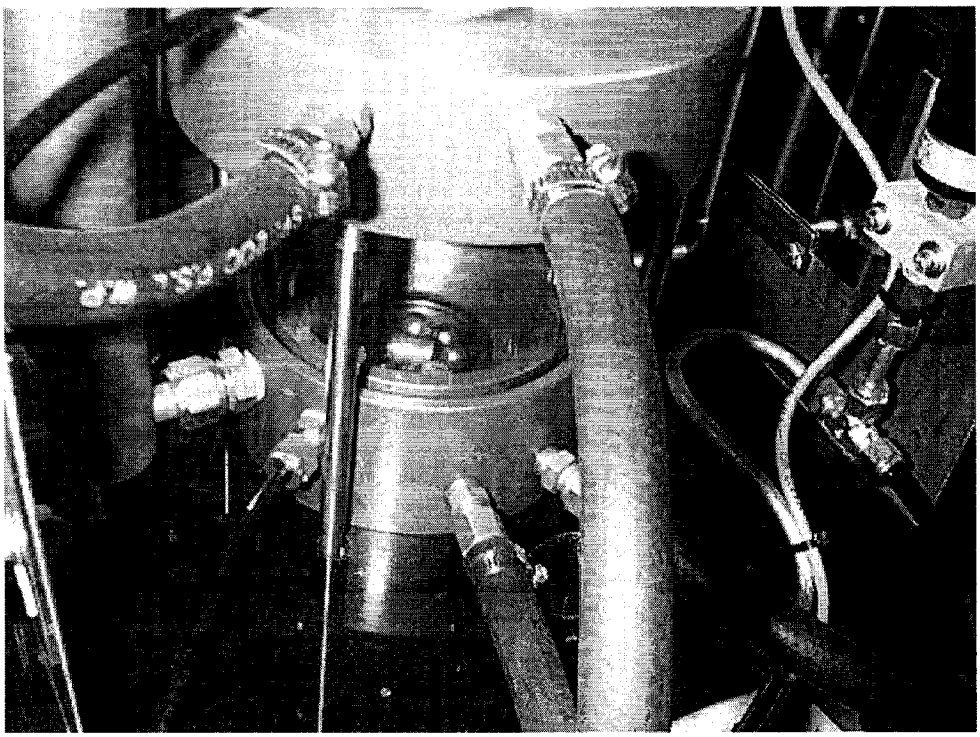

Figure 3.1.2 Close-up of the Ni and Mo in the loading cup.

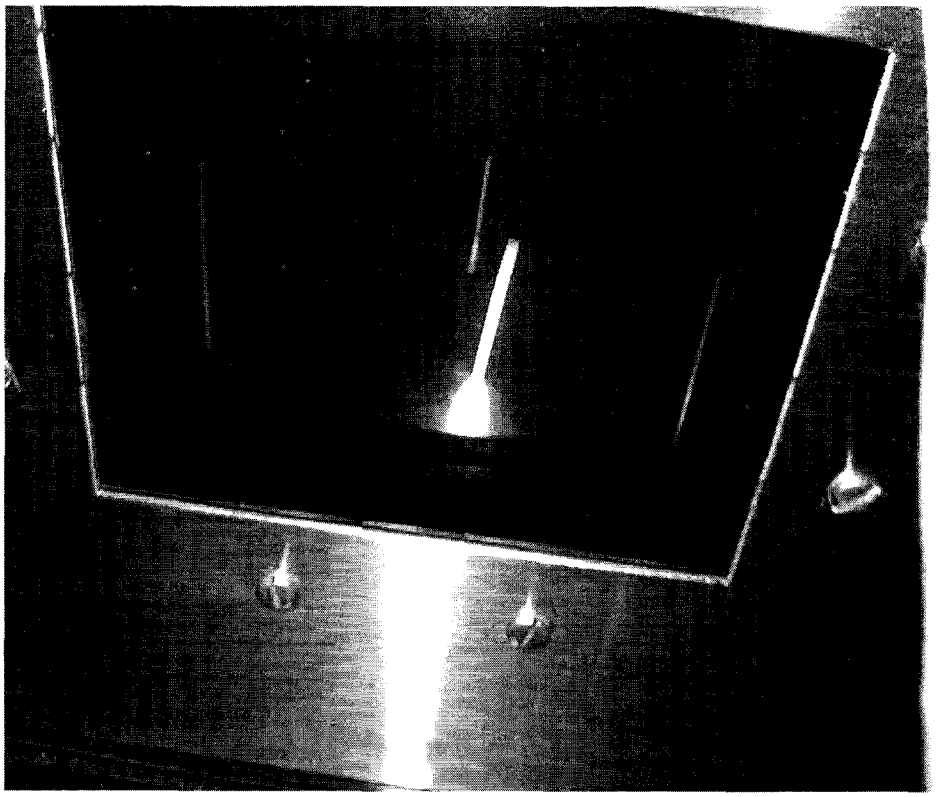

Figure 3.1.3 The arc melting process.

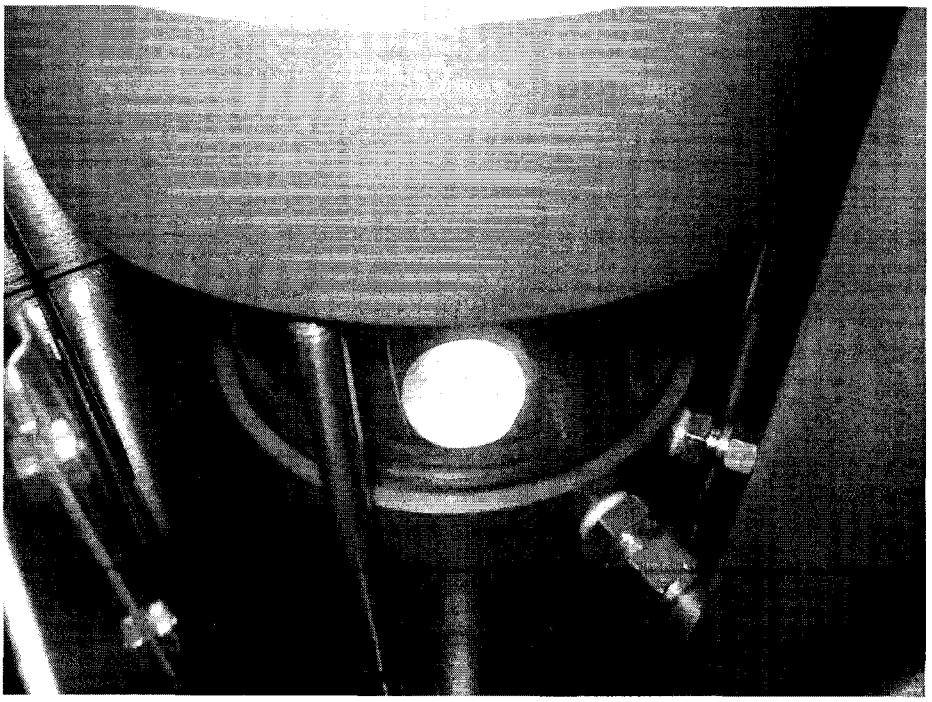

Figure 3.1.4 The Ni-Mo alloy in the initial stages of cooling.

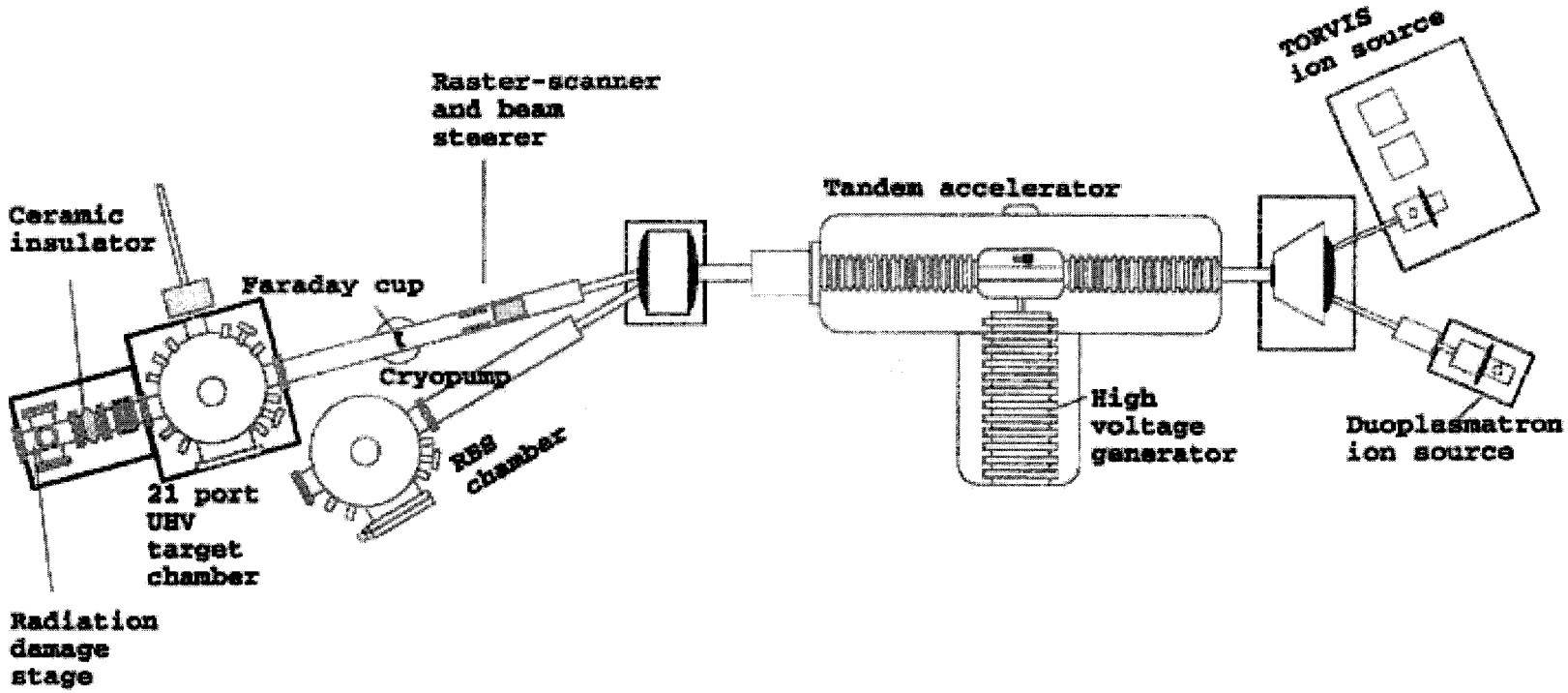

Fig. 3.2.1 1.7 MeV Tandetron accelerator

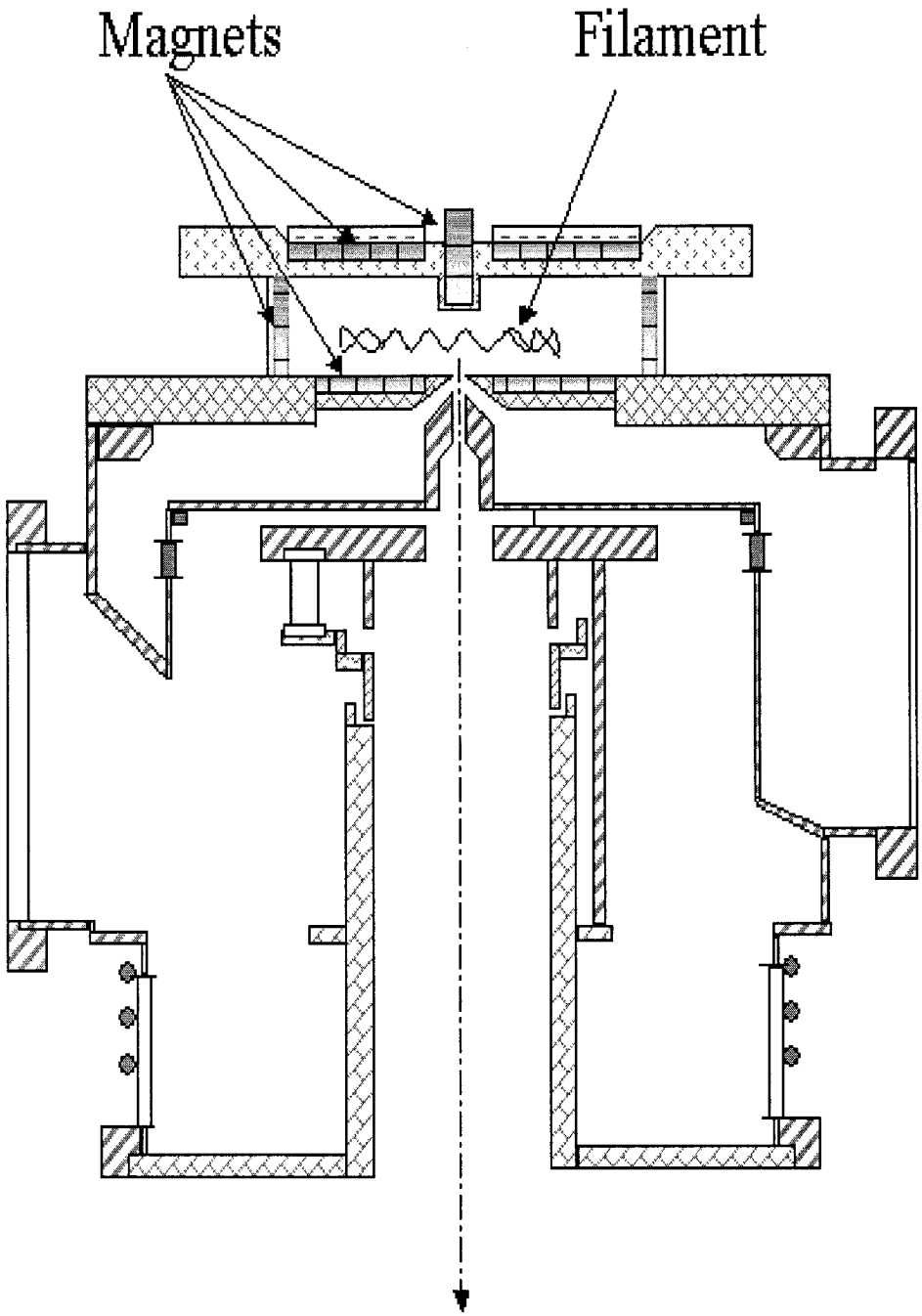

Figure 3.2.2 The Torvis source. The plasma chamber containing the filament and surrounded by magnets is on top, followed by the extractor and lens assembly. The two side ports are connected to high speed turbomolecular pumps.

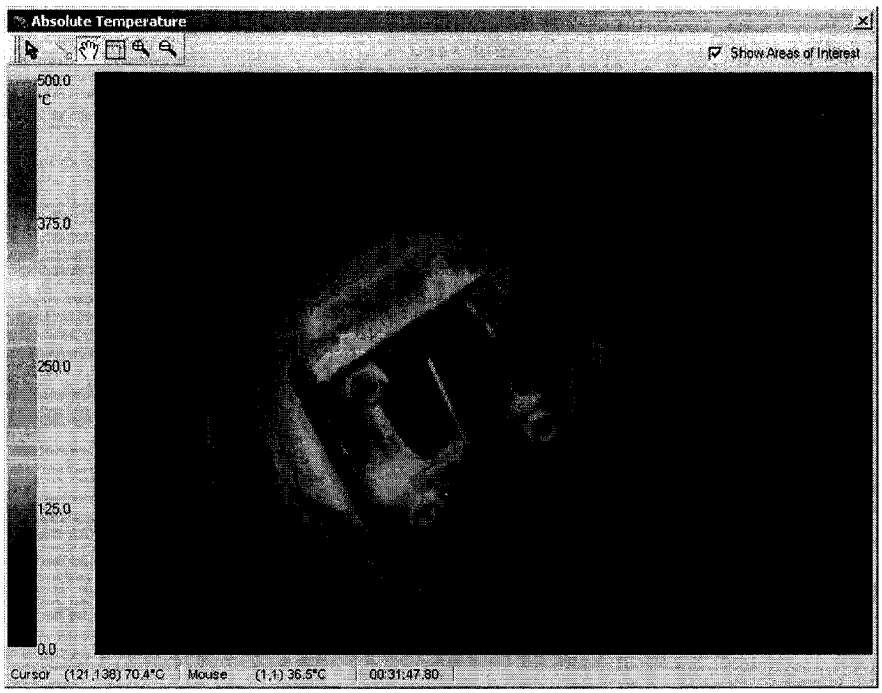

Figure 3.2.3 Stinger's thermal mapping of the samples during irradiation.

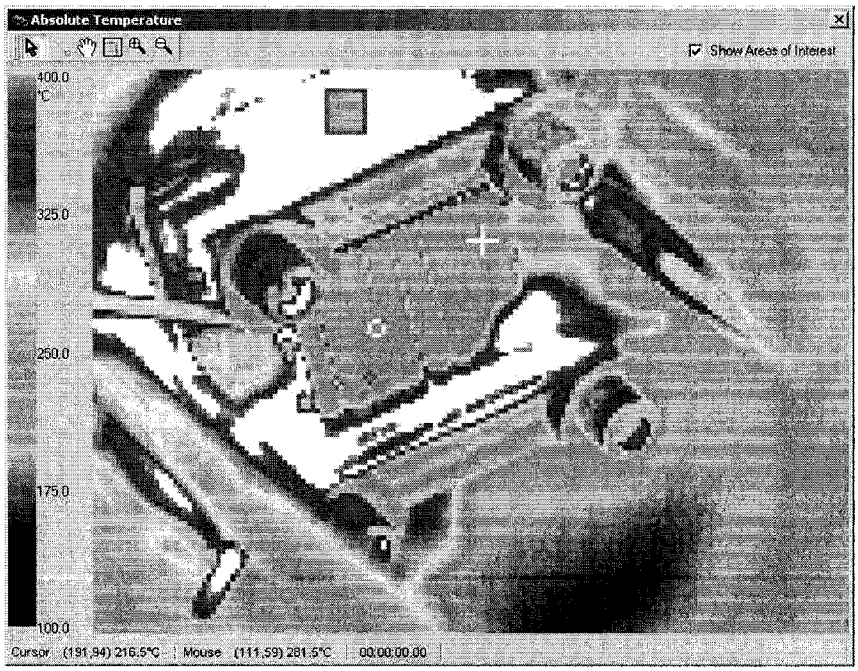

Figure 3.2.4 Thermal view of the samples cooling.

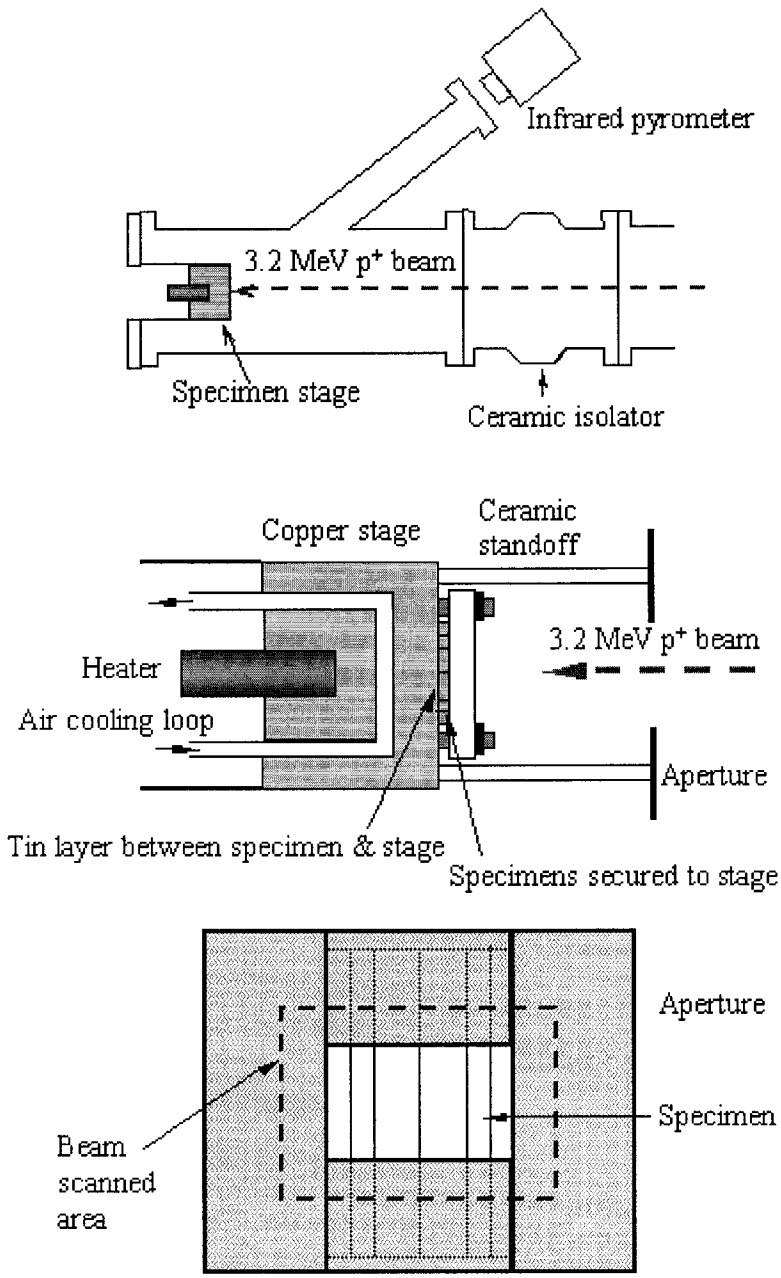

Figure 3.2.5 Irradiation stage on the beamline (top) showing the cooling loops (middle) and the system of apertures (bottom) used to monitor the distribution of current on the stage [105].

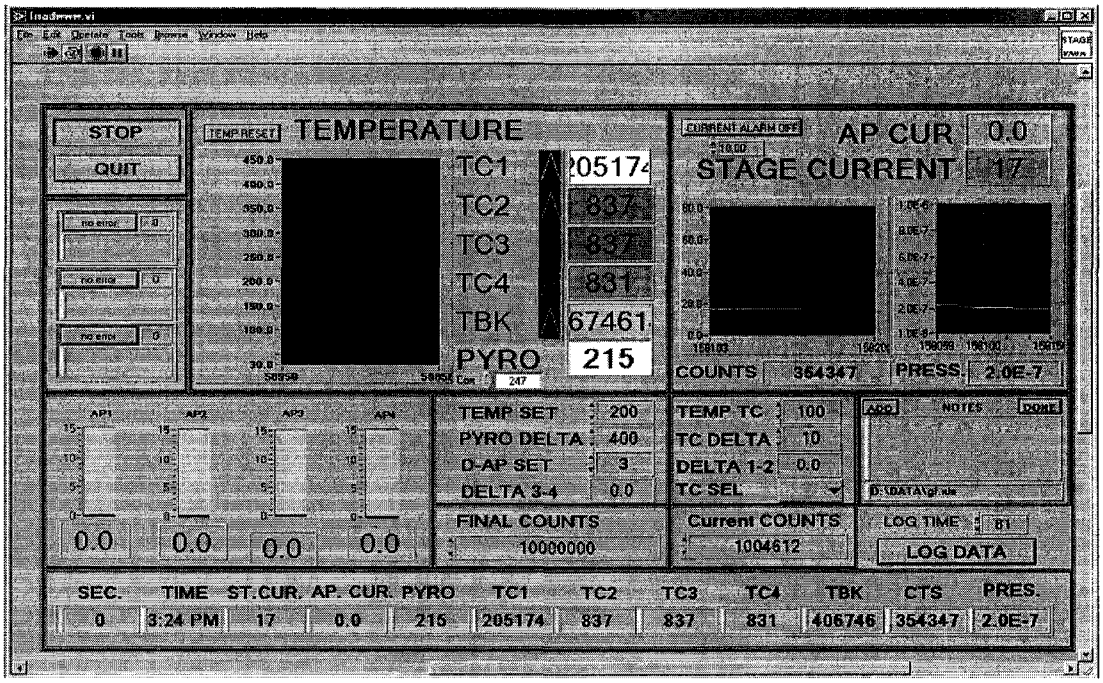

Figure 3.2.6 Graphical user interface (GUI) on the stage computer. All the parameters are monitored in real time and stored in a file once every minute.

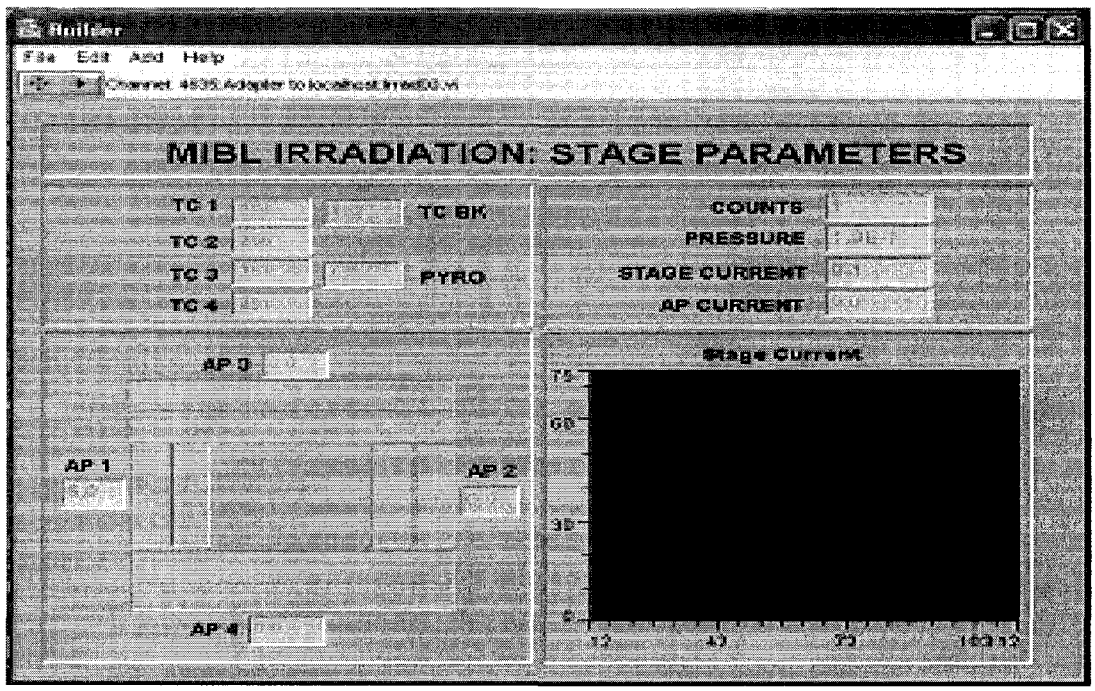

Figure 3.2.7 Remote interface of the GUI from the lab. This interface is available with real time data to a web page during the irradiations.

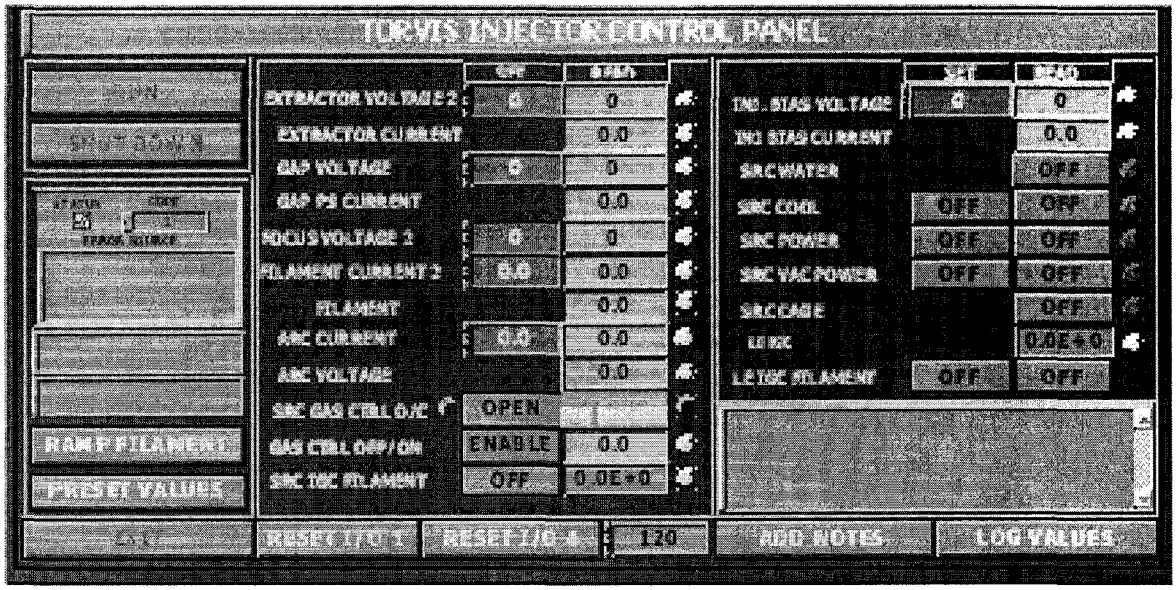

Figure 3.2.8 Graphical user interface for the Torvis source. All the control parameters are easy to change and monitor.

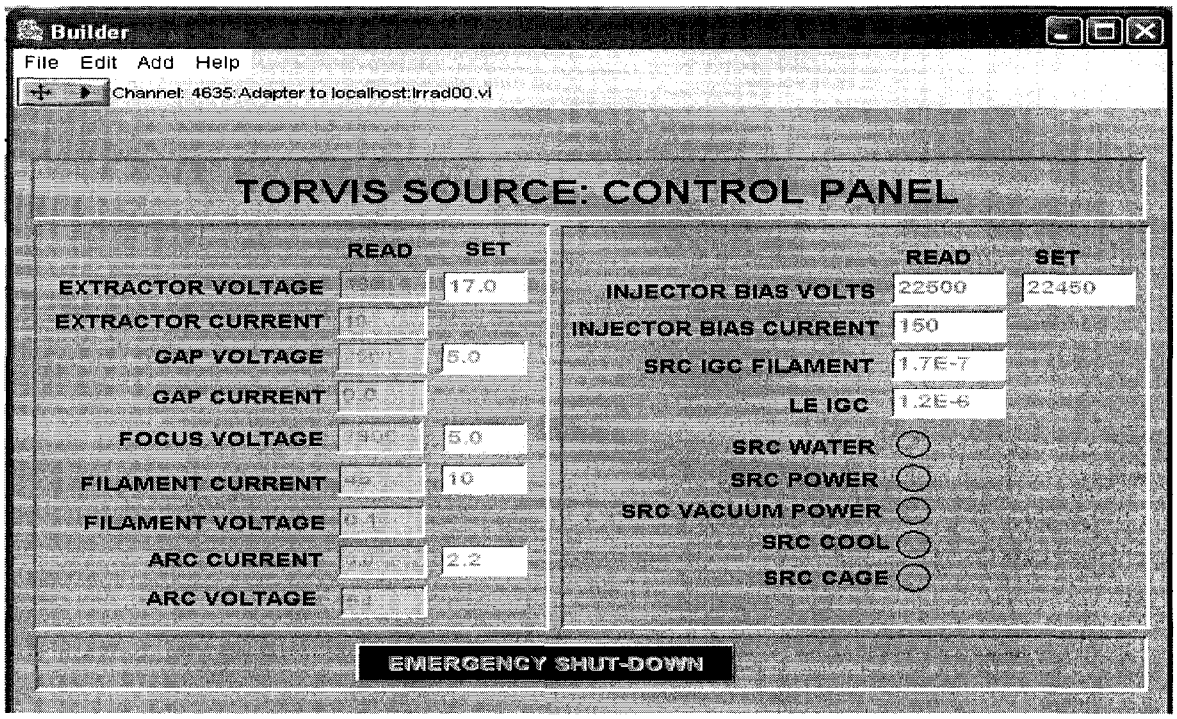

Figure 3.2.9 Remote graphical user interface. This panel is available on a web page during the use of the Torvis source.

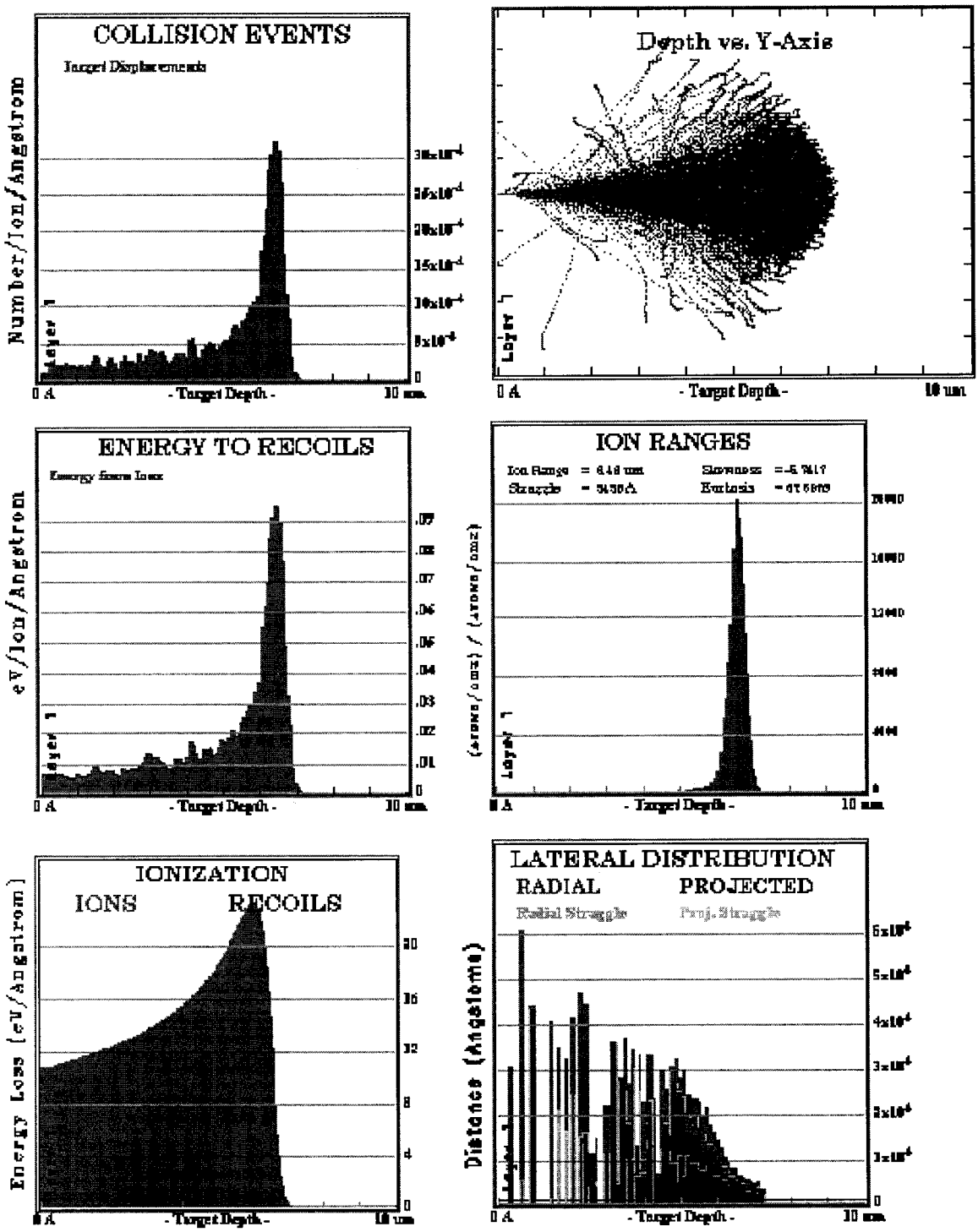

Figure 3.3.1 SRIM 2003 simulation plots for H at 1 MeV irradiation into Ni_4Mo.

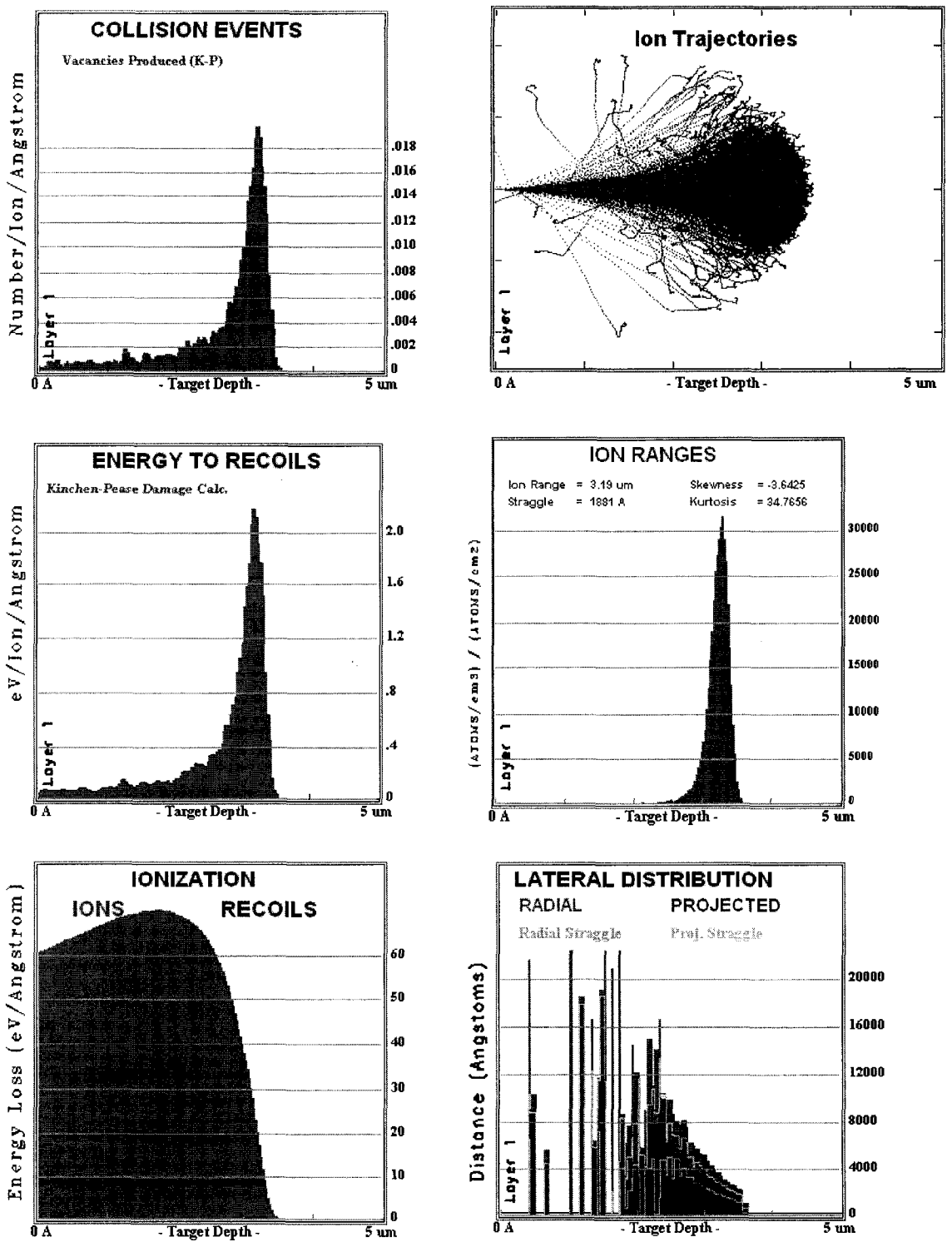

Figure 3.3.2 SRIM 2003 simulation plots for He at 2 MeV irradiation into Ni_4Mo.

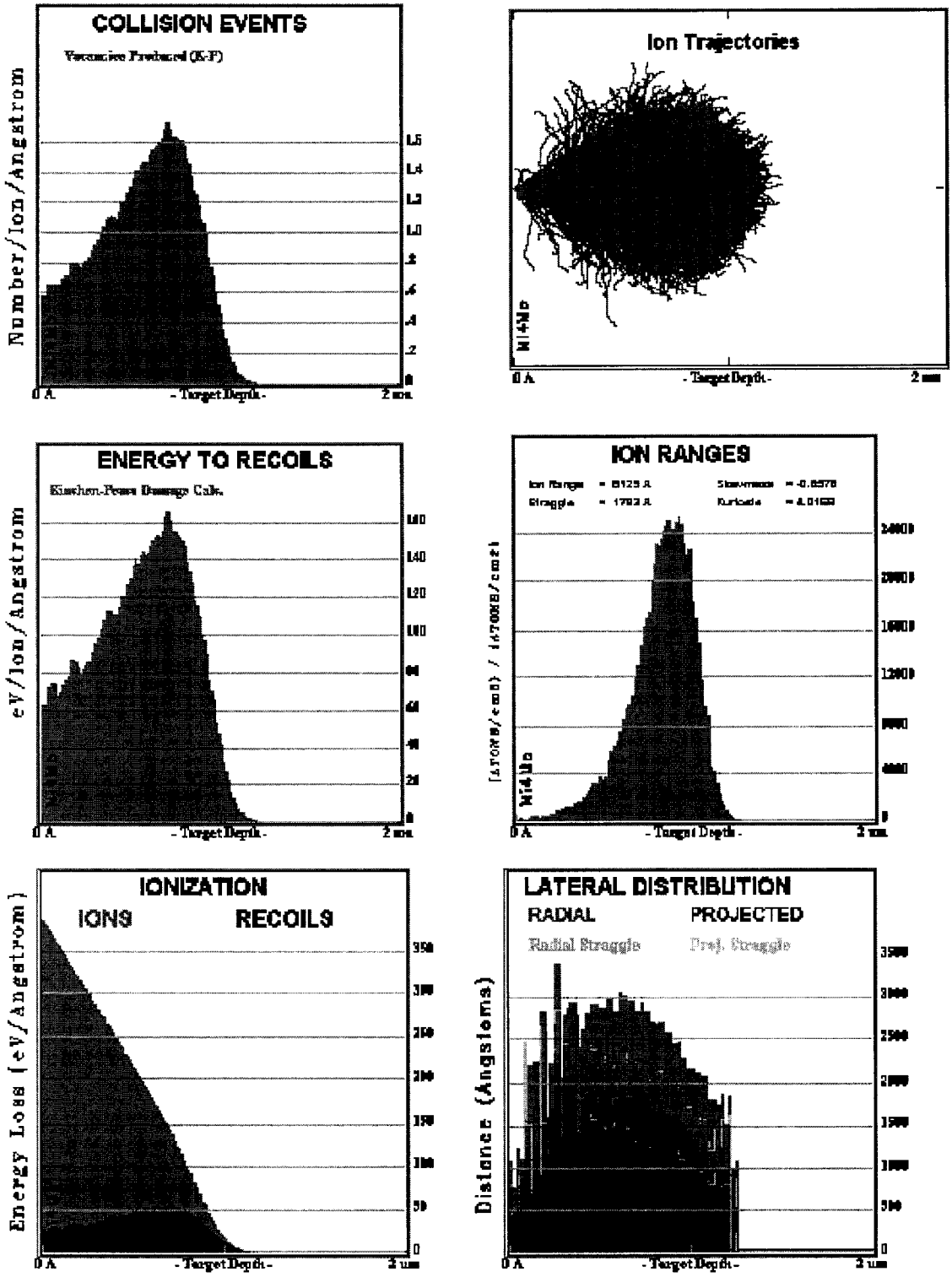

Figure 3.3.3 SRIM 2003 simulation plots for Ni at 3 MeV irradiation into Ni_4Mo.

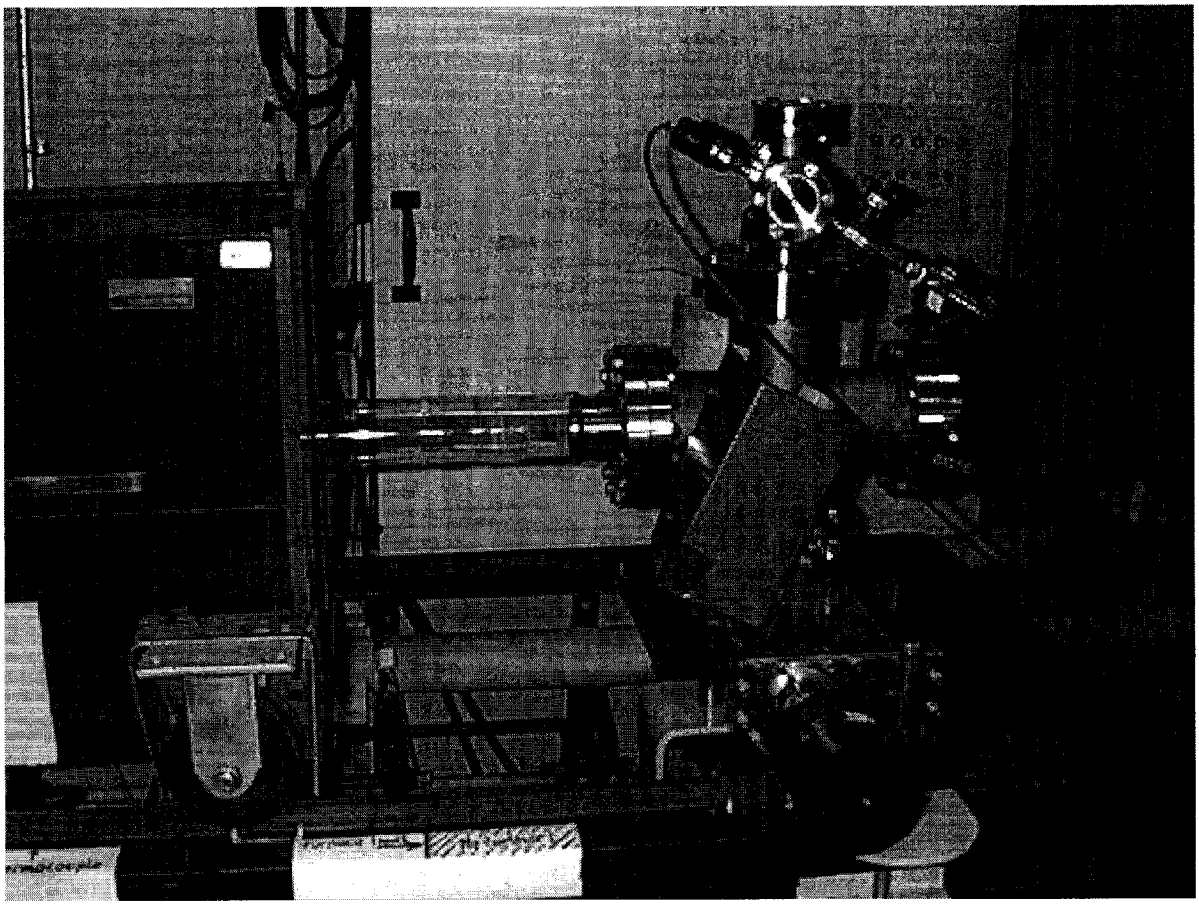

Figure 3.4.1 Post irradiation high vacuum annealing furnace.

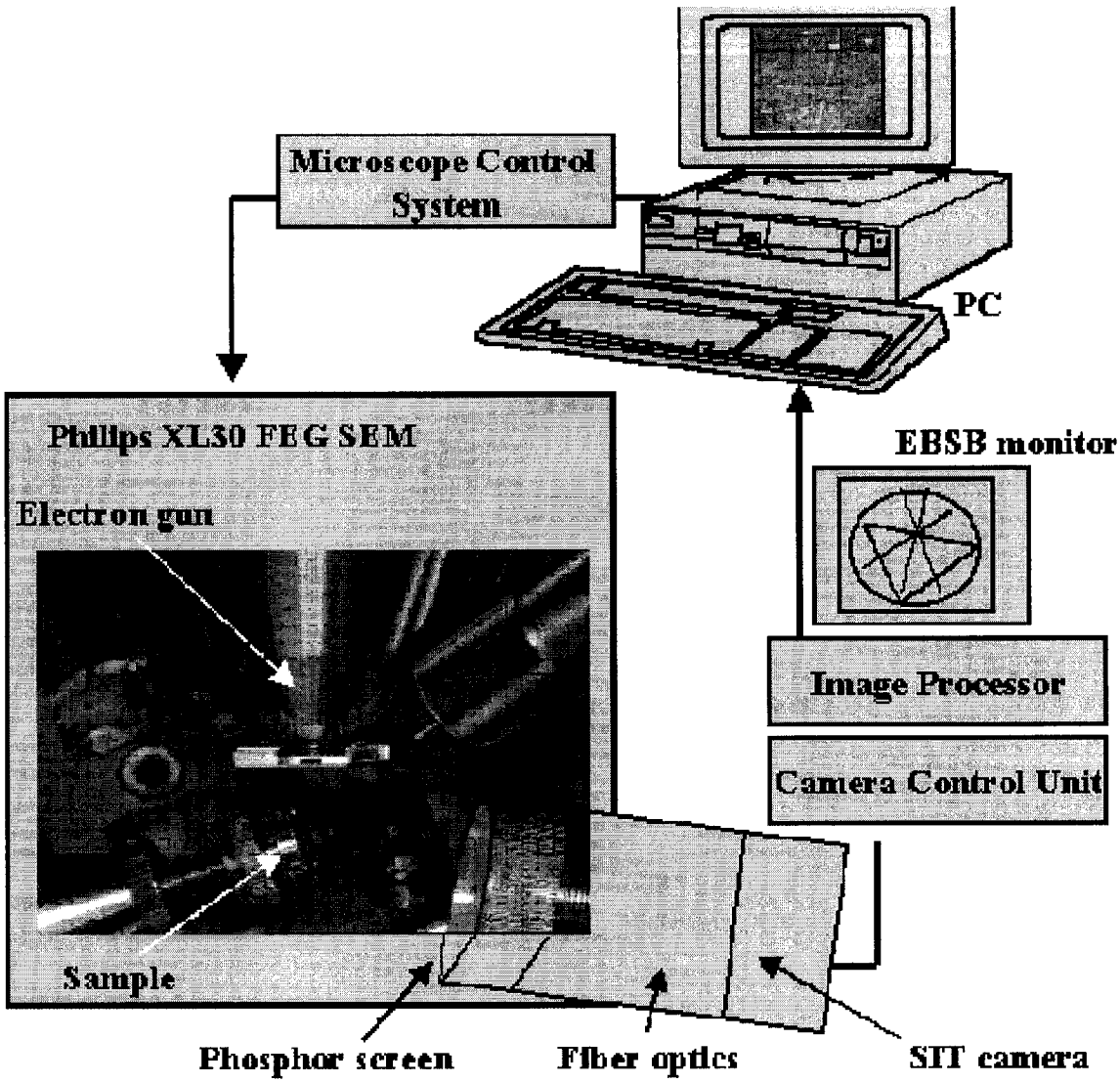

Figure 3.6.1 OIM and SEM setup at the University of Michigan EMAL.

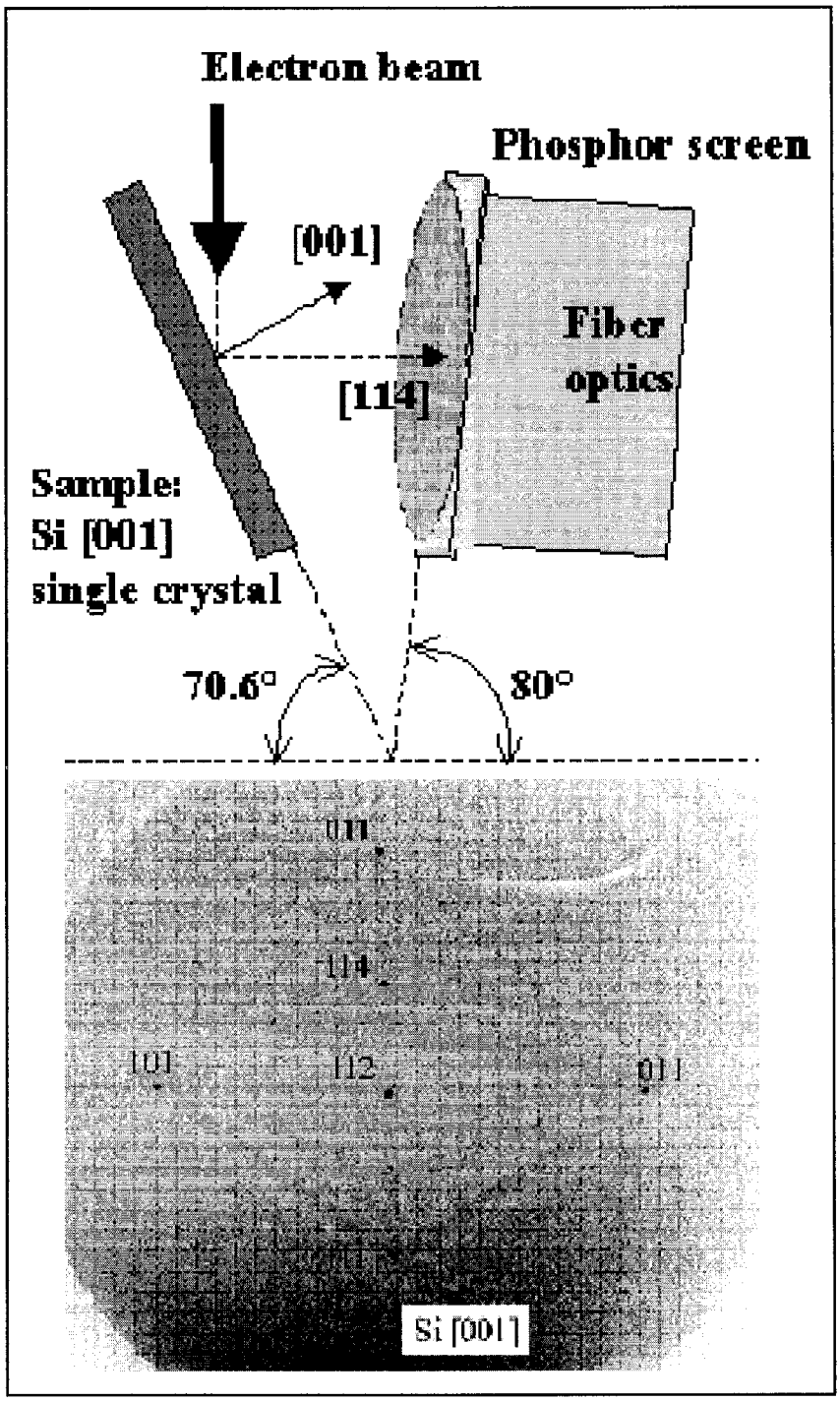

Figure 3.6.2 Detail of the OIM process.

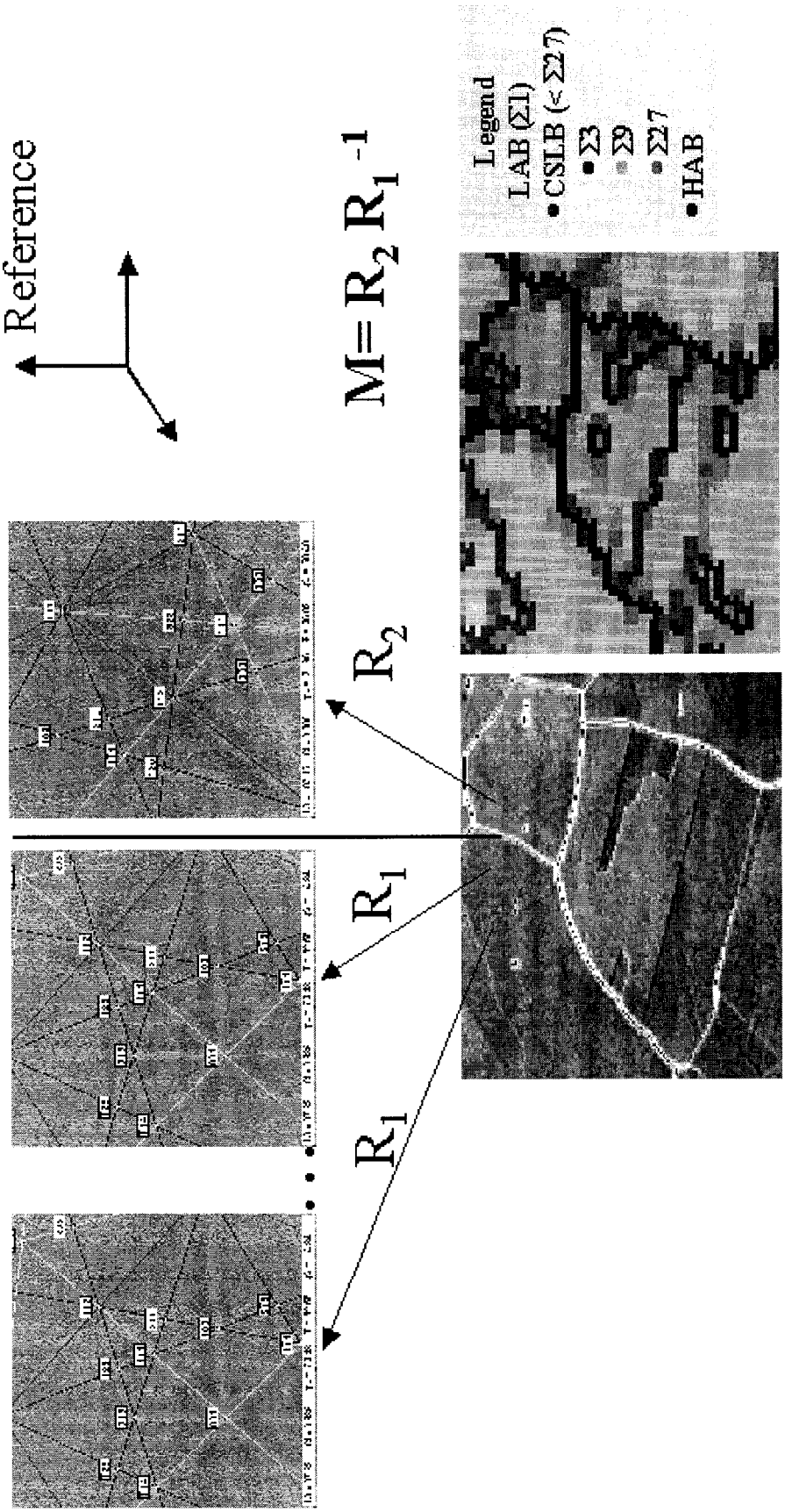

3.6.3 Principle of grain boundary mapping via OIM.

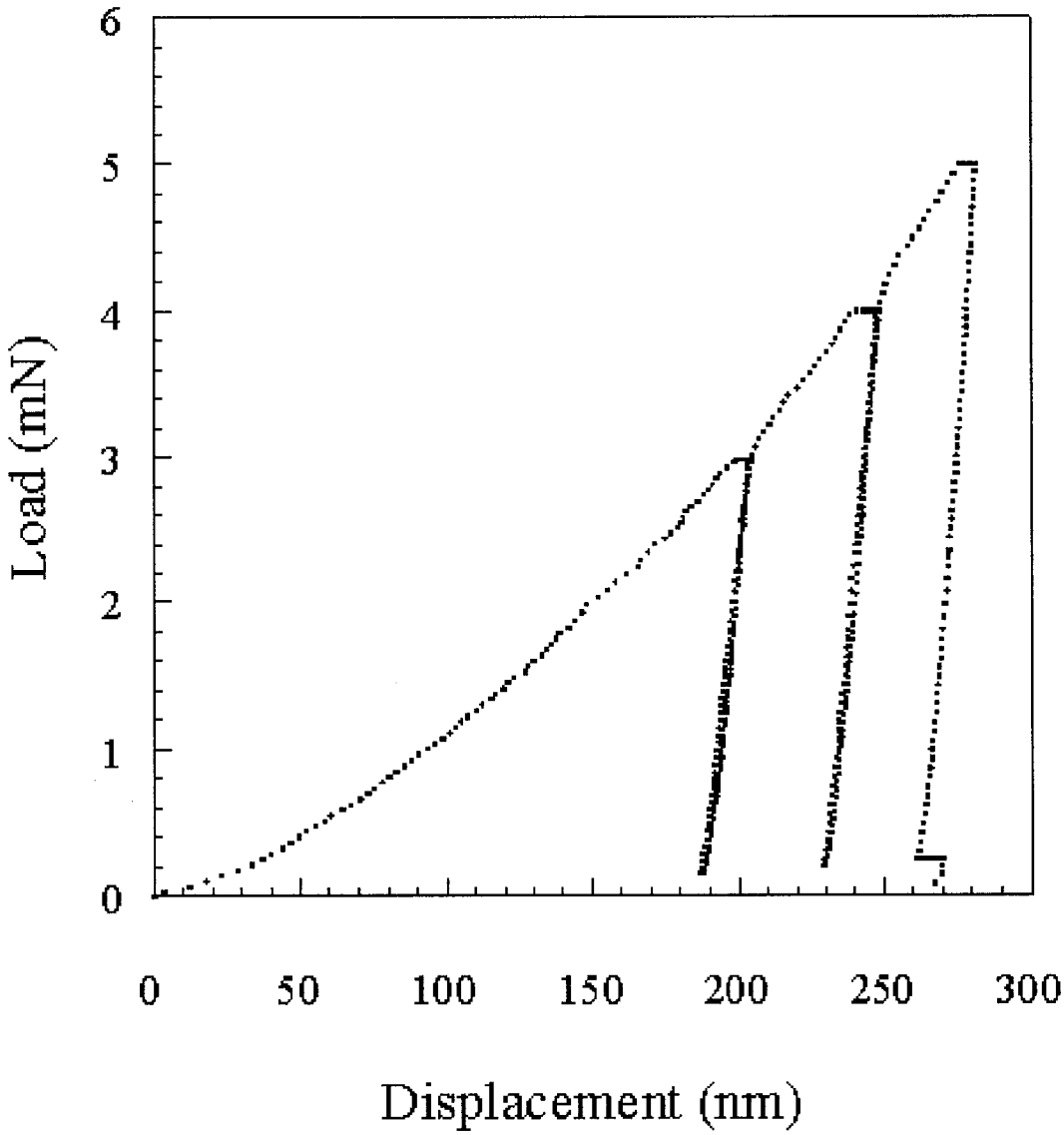

Figure 3.8.1 A typical load vs. displacement curve showing the nano-indentation procedure.

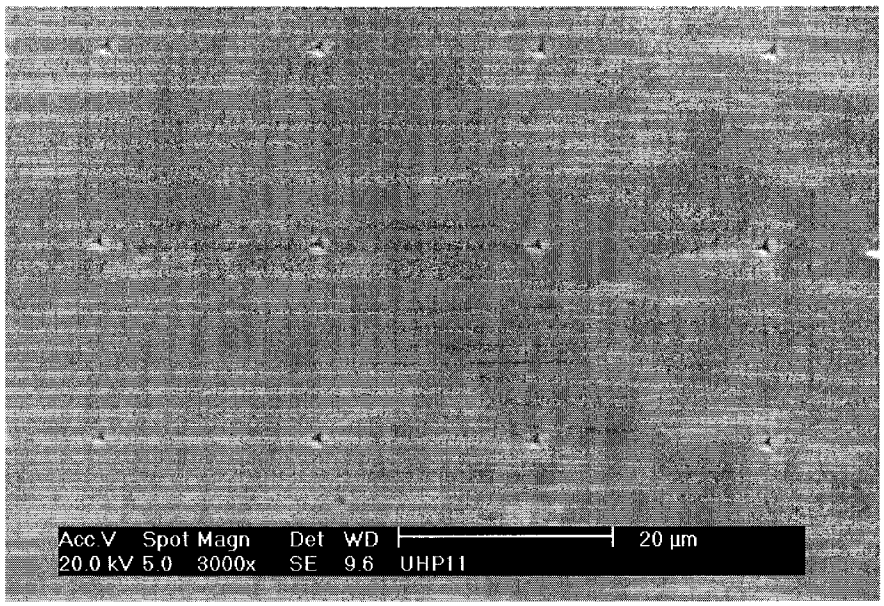

Figure 3.8.2 Patterns of nano-indents performed in a square array on randomly selected areas to determine sample average hardness.

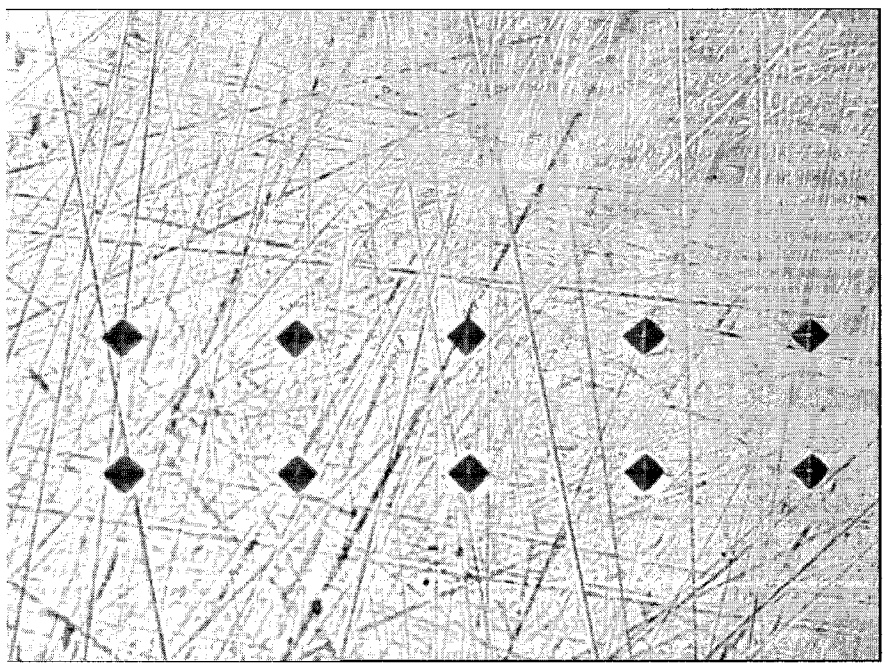

Figure 3.8.3 Patterns of microhardness indents.

CHAPTER 4

RESULTS

This chapter consists of five sections. In the first section, the results from X-ray diffraction are being presented. XRD is one of the most powerful tools in determining the order-disorder transitions. The results obtained in this work show that the transformation can actually take place under irradiation and post-irradiation annealing. The superlattice peaks characteristic to the ordered phases, appear and disappear according to the radiation dose received or to the post-irradiation heat treatment. The second section details the metallographic results. The third part presents the Orientation Imaging Microscopy (OIM) scans. OIM proved to be useful in determining the size and the orientation of the grains. In the fourth section, the RBS spectra are presented. RBS analysis was instrumental in providing information related to the stoichiometry of the alloys before and after the irradiation. These spectra also proved that there was some atomic migration from the surface layers during irradiation. The fifth section reports the results obtained with the micro-indenter and results from the nanoindentation tests.

4.1 Characterization of Irradiated Specimens by XRD.

4.1.1 Influence of the Irradiation

More than 300 XRD spectra were collected and analyzed. The spectra collection procedure was always the same with the initial conditions and the parameters of the XRD instrument kept constant. The surface size and the thickness of each specimen, the mechanical and the electrochemical treatment were identical. All the samples had mirror like finish, were irradiated only on one side and clearly marked on the other side.

For each irradiated set, we had one reference sample that was not subject to any irradiation or annealing treatment. This was marked on each graph as NoI. In the case of irradiation without annealing, the samples were marked NA and in the case of irradiation with annealing the abbreviation is A###. The ### stands for the annealing temperature (for example A250 indicates post irradiation annealing at 250^0 C). After data collection, the spectra were normalized to 100 with respect to the largest peak observed. The form of display used was chosen because allows for easy tracking of the changes from one irradiation condition to the other. Each alloy is presented separate, with the spectra obtained for each of the irradiation dose. In Table 4.1 is given the typical composition of an irradiation batch.

Ni_4Mo	As Cast	A800^0 C 72h	A1000^0 C 72h
Ni_3Mo	As Cast	A800^0 C 72h	A1000^0 C 72h
Ni	pure		

Table 4.1 Composition of each irradiation batch.

No change was observed in the spectra of Ni after H and Ni irradiations as we can see from Figures 4.1.1 and 4.1.2. The next two pages (Figures 4.1.3 and 4.1.4) display the plots obtained from the powder data as graphed by the PowderCell program. The data points are given by the JCPDS file and the indexation shows the angle where each peak appears. This angle positions were used to identify the peaks in the XRD spectra for the irradiated samples.

We expected Ni_4Mo as-cast and Ni_3Mo as-cast to show only the fundamental lines, and this is what we see in Figures 4.1.5 and 4.1.12 in the plot marked NoI. After H irradiation to a dose of 1 DPA, order specific peaks appear for these specimens (Figures 4.1.5 and 4.1.12). The super reflection peaks vanish for Ni_4Mo and Ni_3Mo pre-annealed at 800^0 C when exposed to H irradiation and doses as little as 0.01 DPA (Figures 4.1.17 and 4.1.26). After 1 DPA, we see that most of the peaks are showing up again. Some recovery under H beam is seen in Ni_4Mo pre-annealed at 1000^0 C, but nothing is observed in the case of Ni_3Mo pre-annealed at 1000^0 C (Figures 4.1.31 and 4.1.39).

Ni beam has a different effect. In the case of Ni_4Mo as-cast, there are some changes in the fundamental peak intensities. This may be due to some preferred orientation at the surface (Figure 4.1.7). The change is more obvious in Ni_3Mo as-cast (Figure 4.1.13). We see traces of ordered peaks. In the case of Ni_4Mo and Ni_3Mo pre-annealed at 800^0 C, the ordered structure disappeared after 0.01 DPA. There is very little recovery in Ni_3Mo and we see some preferred orientation (Figures 4.1.18 and 4.1.27). No significant change is noted in Ni_4Mo and Ni_3Mo pre-annealed at 1000^0 C (Figures 4.1.37 and 4.1.40).

If we compare the effects of H, He and Ni beams we note that in Ni_4Mo as-cast, the largest change is induced by the H beam (Figures 4.1.10 and 4.1.11). Ni_4Mo pre-annealed at 800^0 C recovered well in the case of H and He irradiations but did not recover in the case of Ni irradiation (Figures 4.1.24 and 4.1.25). In the case of H irradiation, from the very noisy spectrum, we can deduce that finer structure was achieved. The same noisy spectrum is seen in Ni_4Mo pre-annealed at 1000^0 C, but without order-characteristic peaks (Figure 4.1.38).

4.1.2 Post-Irradiation Annealing

Post-irradiation annealing treatment affected some of the specimens. It was not possible to apply the same treatment to all the samples, simply because there were not enough samples available. Some samples were treated at 100^0 C and then 250^0 C, some at 250^0 C , 350^0 C and at 450^0 C.

If annealing was done first at 100^0 C and then at 250^0 C, we noticed in Ni_3Mo as-cast, that there was finer structure in the specimen after at 250^0 C (spectrum much noisier) than at 100^0 C (Figure 4.1.14 and 4.1.15). This suggests that a post-irradiation annealing at 100^0 C may be a temperature too low to create the fine structure we want. Similar conclusion can be reached in the case of Ni_4Mo (Figures 4.1.8.and 4.1.9) and Ni_4Mo pre-annealed at 800^0 C and post-irradiation annealed at 250^0 C (Figures 4.1.19 and 4.1.20). Ni_3Mo pre-annealed at 800^0 C recovers most the original ordered structure after heat treatment at 250^0 C (Figures 4.1.28, 4.1.29 and 4.1.30).

The specimens annealed at 350^0 C and irradiated with at least 0.5 DPA showed both ordered and fine grain structure, like in the case of Ni_3Mo as-cast and Ni_4Mo pre-annealed at 800^0 C (Figures 4.1.16, 4.1.31, 4.1.32 and 4.1.33). A factor in this outcome must have been the nature of the beam (Ni), because we did not see the same results in case of H irradiation.

In the case of heat treatment at 450^0 C, we saw the recovery of the ordered structure in both Ni_4Mo pre-annealed at 800^0 C (Figures 4.1.21, 4.1.22 and 4.1.23) and Ni_3Mo pre-annealed at 800^0 C (Figures 4.1.34 and 4.1.35).

4.2 Metallographic analysis

The samples were observed in low (50x) and high (500x-2000x) magnification before and after the irradiation. The surface of each sample changed after exposure to irradiation as it can be seen in Figures 4.2.1 through Figure 4.2.8. The defects induced by irradiations appear as small dots at lower dose and then as the dose increased, they became bigger and sometimes more diffuse.

In Figures 4.2.9 through 4.2.18 are presented SEM pics of the surface change under irradiation of the Ni-Mo alloys.

4.3 Orientation Imaging Microscopy

Orientation Imagining Microscopy (OIM) was used to determine the grain size and orientation of the grains with respect with each other in terms of the coincidence site lattice (CSL). The macroscopic structure of grain boundaries is commonly assessed according to the relative orientation between the two neighboring grains [3]. One way to define orientation relationship between two neighboring grains, or "misorientation", is by angle/axis [109]. As such, let us imagine that the two grains (crystals) of Figure 4.3.1 were initially of similar, known, orientation in space. Next, one grain was rotated by an angle θ around a common axis, [*klq*]. In the geometry shown in this figure, the orientation between the two grains is fixed, and in the angle/axis notation is θ / [*klq*]. Further, a cut is performed, such that this will define the adjoining surfaces in both crystals. If we assume that this cut defines the grain boundary plane, then it appears clear that the geometry of a grain boundary can be described by five independent parameters, usually referred to as "degrees of freedom" (DOF):

- Misorientation between the two neighboring grains, commonly described by an angle and axis of rotation – 3 DOF, and
- Inclination of the boundary plane – 2 DOF.

The three degrees of freedom related to the misorientation component of the grain boundary are fixed when the orientations of the two neighboring grains are known. Coincident Site Lattice (CSL) model refers to the 2-D superlattice that forms at certain angle-axis combinations at which some lattice points from one crystal are superimposed on lattice points from the adjacent crystal. Such a case is shown schematically in Figure

4.3.2. In this case, the rotation of one lattice by 36.9° around the common [001] axis causes some of the lattice points to coincide with lattice points from the neighboring crystal. These points, shown with black dots, form the superlattice shown with thick solid lines. It can be observed that in this particular case, one in every five points on either side coincides with a point from the neighboring side. In the terminology of the CSL model, the newly formed superlattice is a Σ5, as the Σ number is the reciprocal of the coincident site fraction, in this case 1/5. As such, the CSL model provides an alternative to angle/axis description for grain boundary misorientations. Clearly, cases of perfect coincidence as shown in Figure 2.2 are most likely rare in polycrystalline materials. To account for this fact, another variable was introduced, the disorientation angle, defined as the difference between the actual misorientation angle and the angle at which the perfect coincidence is achieved. Boundaries with small disorientation angles (LAB) are designated as CSLs provided they satisfy a criterion such that of Brandon, which gives the maximum allowed angular deviation for a given value of Σ[110]:

$$\delta\theta = \theta_0 \Sigma^{-1/2} \tag{4.3.1}$$

where θ_0 =15° is the maximum allowed deviation for a Σ1 boundary, corresponding to the generally accepted transition point from the dislocation sub-boundary to the high angle grain boundary. Boundaries with larger disorientation angle are called high angle boundaries (HAB). These will be marked as such on the OIM plots.

Scans were done for both Ni_4Mo and Ni_3Mo. OIM use is expensive, because requires a large scanning time. A typical 200 μm x 200 μm scan with a step of about .5 μm would take about 5 h. The grain size in some of the scans was in excess of 300 μm. For the scans that were made for areas less than the grain size an incomplete grain

dimensions resulted. Nevertheless, it is possible to estimate the size of the grains even from those scans. The procedure to perform OIM is explained in Appendix A2.

In Figure 4.3.1, is presented an SEM image of one of the Ni-Mo specimens before being OIM scanned, at 0^0 tilt. On the lower part of the picture, the same specimen at different magnification at 70^0 tilt ready for the OIM scan.

In Figures 4.3.2 through 4.3.4 are displayed examples of data "cleaning". In the OIM analysis, the minimum grain size and the error allowed in the calculation of grain disorientation can be input into the main program. In this way, the points where the software is "unsure" can be decisively associated with a grain or another.

OIM scans, inverse pole figures, grain size and orientation data are displayed in the Figures 4.3.5 through 4.3.22 for Ni_3Mo and Ni_4Mo specimens. We notice that the grain size is reduced from about 300 – 400 μm in the as-cast specimens to a submicron range, in the case of specimens post-irradiation annealed at 450^0 C (Figures 4.3.21 and 4.3.22)

4.4 Rutherford Backscattering Spectroscopy (RBS).

This procedure was initially applied to all the as cast samples to confirm the correct stoichiometry. Sample plots are shown in Figures 4.4.1 and Figure 4.4.2. A simulation file data is presented in Figure 4.4.3. The rest of the plots display the spectra in the situations where solute segregation was observed (Figures 4.1.4, 4.1.5, 4.1.6 and 4.1.7). The radiation induced segregation (RIS) is not a new phenomenon but is still not completely understood. Okamoto and Rehn [120] detailed the observed phenomenon of

segregation of alloying elements under irradiation with ions or neutrons, towards and away from the external surface, grain boundaries, dislocations voids or other type of defects. Sometimes, the local compositional change becomes so large that there is phase precipitation in normally stable solid solutions [25 and 65]. The RIS is of a major concern in the wall of a fusion reactor because of radiation damage. Research in this direction done on Ni alloys [3, 6, 43, 45, 111, and 112], indicates that some solute additions (Si, Be, Mo) are effective in inhibiting the void formation but they can also exhibit strong tendencies to segregate to surface or to other defects during irradiation. Oversize solutes such as Ti, Mo, Al, and Cr segregate away from defect sinks while undersize solutes such as Si or Be segregate towards the sinks [65]. This segregation may be large enough to induce the precipitation of other phases near the sinks, such as grain boundaries, external surfaces, dislocations and voids. In two phase alloys, radiation not only enhances coarsening effect but also alters through RIS the spatial distribution of precipitates [39]. RBS is capable of detecting changes in the topmost layers of the alloys. This is what was observed [39 and 114] and this is what we noticed in the RBS spectra. Mo as an oversized solute under heavy ion bombardment may segregate towards the surface leaving a thin layer of about 200-300 nm under the surface with less Mo than in the initial stoichiometry.

4.5 Hardness Measurements

4.5.1 Vickers Hardness Results

The microhardness of all the samples was measured with the Vickers micro-indenter, with a load of 10g to ensure that the penetration is not too deep. The figures at the end of this chapter and in Appendix A3 present the results of the hardness tests on Ni-Mo alloys and the variation with the amount and type of irradiation. In the table on each page, the hardness values are given (in Vickers units) and also the averaged diagonal dimensions for the diamond indentation. Figures 4.5.1 through 4.5.9 present the variation in hardness of Ni-Mo alloys as a function of the beam composition (H, He and Ni). The next plots present the variation of hardness as a function of the post-irradiation annealing treatment (Figures 4.5.10 through 4.5.15). In the Figure 4.5.16 is presented an example of misreading of a hardness indent value. Here, the indenter tip touched an area affected and changed by irradiation.

4.5.2 Nano-Indentation Results

The objectives of this set of experiments were to determine nano-hardness values for Ni-Mo alloys under irradiation and post-annealing conditions and to compare them with the values obtained from micro-hardness tests. It was necessary to use nano-indentation because of the short path of the Ni+ beam through the Ni-Mo alloys. For the nano-hardness experiments, the samples had to be very well polished, with a smooth

surface to avoid erroneous readings. The samples were analyzed for imperfections with the optical microscope prior to testing. When performing nano-hardness testing of poly-crystals where the indent size is usually much smaller than the grain size, several parameters may influence the outcome of the hardness measurements, and therefore, need to be taken into consideration. These are: grain orientation, grain size, and relative position of indents with respect to grain boundaries. A large set of data points had to be taken for each alloy in order to ensure good statistics.

Figures 4.5.17 through 4.5.22 present the nano-indenter measurements of the hardness as a function of the irradiation dose or of the irradiation beam type. The Appendix A3 gives some additional Nano-indenter measurements.

4.6 Tables for Chapter 4

MONI4
source : X-ray Cu-Ka1 1.540598
2Theta : 20.000 - 100.000
geometry : Bragg-Brentano, fixed slit, no anom. disp.

H	K	L	2Theta/deg	d/Å	I/rel.	|F(hkl)|	Mu	FWHM
1	1	0	21.958	4.04465	2.59	24.85	4	0.0707
1	0	1	29.506	3.02488	2.44	23.26	8	0.0707
2	0	0	31.249	2.86000	1.05	22.91	4	0.0707
2	1	1	43.513	2.07817	0.83	20.81	8	0.0707
1	2	1	43.513	2.07817	100.00	228.03	8	0.0707
2	2	0	44.779	2.02233	0.38	20.63	4	0.0707
3	1	0	50.410	1.80882	31.82	214.89	4	0.0707
1	3	0	50.410	1.80882	0.27	19.92	4	0.0707
0	0	2	51.223	1.78200	15.13	213.39	2	0.0707
3	0	1	54.540	1.68120	0.44	19.47	8	0.0707
1	1	2	56.375	1.63074	0.40	19.30	8	0.0707
2	0	2	61.236	1.51244	0.32	18.89	8	0.0707
3	2	1	64.211	1.44934	0.28	18.67	8	0.0707
2	3	1	64.211	1.44934	0.28	18.67	8	0.0707
4	0	0	65.186	1.43000	0.13	18.61	4	0.0707
3	3	0	69.688	1.34822	0.11	18.35	4	0.0707
2	2	2	70.359	1.33700	0.22	18.32	8	0.0707
1	4	1	73.144	1.29201	0.20	18.19	8	0.0707
4	1	1	73.144	1.29201	0.20	18.19	8	0.0707
2	4	0	74.063	1.27903	9.30	176.50	4	0.0707
4	2	0	74.063	1.27903	0.10	18.16	4	0.0707
1	3	2	74.717	1.26944	0.19	18.13	8	0.0707
3	1	2	74.717	1.26944	18.12	175.60	8	0.0707
1	0	3	82.941	1.16318	0.16	17.88	8	0.0707
5	1	0	86.735	1.12178	0.07	17.81	4	0.0707
1	5	0	86.735	1.12178	0.07	17.81	4	0.0707
4	0	2	87.366	1.11530	0.15	17.80	8	0.0707
4	3	1	90.011	1.08926	11.25	157.29	8	0.0707
3	4	1	90.011	1.08926	0.14	17.75	8	0.0707
5	0	1	90.011	1.08926	11.25	157.29	8	0.0707
1	2	3	91.272	1.07747	10.96	155.99	8	0.0707
2	1	3	91.272	1.07747	0.14	17.74	8	0.0707
3	3	2	91.523	1.07517	0.14	17.73	8	0.0707
4	2	2	95.689	1.03908	0.14	17.68	8	0.0707
2	4	2	95.689	1.03908	10.13	151.68	8	0.0707
5	2	1	98.353	1.01793	0.14	17.66	8	0.0707
2	5	1	98.353	1.01793	0.14	17.66	8	0.0707
4	4	0	99.245	1.01116	0.07	17.65	4	0.0707
3	0	3	99.630	1.00829	0.14	17.64	8	0.0707

Table 4.2 Powder XRD lines for Ni_4Mo for 2θ (20 – 100) degrees generated by PowderCell.

NI3MO
source : X-ray Cu-Ka1 1.540598
2Theta : 20.000 - 100.000
geometry : Bragg-Brentano, fixed slit, no anom. disp.

H	K	L	2Theta/deg	d/Å	I/rel.	|F(hkl)|	Mu	FWHM
1	0	1	26.653	3.34190	2.90	19.89	4	0.0707
1	1	0	27.475	3.24371	3.86	23.67	4	0.0707
0	1	1	29.131	3.06295	2.30	19.46	4	0.0707
1	1	1	34.185	2.62083	1.31	12.33	8	0.0707
2	0	0	35.423	2.53200	0.97	22.12	2	0.0707
0	0	2	40.529	2.22400	8.30	74.92	2	0.0707
2	0	1	40.982	2.20046	31.93	105.19	4	0.0707
0	2	0	42.781	2.11200	46.21	187.76	2	0.0707
1	0	2	44.455	2.03628	0.67	19.03	4	0.0707
0	1	2	46.087	1.96790	62.53	167.96	4	0.0707
2	1	1	46.496	1.95153	100.00	151.71	8	0.0707
0	2	1	47.626	1.90786	0.26	11.17	4	0.0707
1	1	2	49.663	1.83426	0.23	7.83	8	0.0707
1	2	1	51.120	1.78535	0.96	16.55	8	0.0707
2	0	2	54.903	1.67095	0.09	7.61	4	0.0707
2	2	0	56.712	1.62185	0.51	19.27	4	0.0707
3	0	1	58.431	1.57818	0.33	15.94	4	0.0707
3	1	0	58.869	1.56747	0.46	19.08	4	0.0707
2	1	2	59.439	1.55379	0.76	17.51	8	0.0707
0	2	2	60.395	1.53147	4.80	63.26	4	0.0707
2	2	1	60.734	1.52372	18.75	88.91	8	0.0707
0	0	3	62.602	1.48267	0.19	18.47	2	0.0707
3	1	1	62.805	1.47836	0.24	10.35	8	0.0707
1	2	2	63.401	1.46590	0.64	17.23	8	0.0707
1	0	3	65.551	1.42293	0.01	3.37	4	0.0707
0	1	3	66.818	1.39899	0.01	3.35	4	0.0707
1	3	0	69.200	1.35654	0.30	18.38	4	0.0707
1	1	3	69.673	1.34847	0.58	18.05	8	0.0707
3	0	2	69.905	1.34457	0.25	16.88	4	0.0707
0	3	1	70.037	1.34235	0.20	15.29	4	0.0707
2	2	2	72.006	1.31042	0.08	7.14	8	0.0707
1	3	1	72.835	1.29754	0.16	10.04	8	0.0707
3	1	2	73.914	1.28123	0.08	7.11	8	0.0707
2	0	3	74.035	1.27945	15.92	142.46	4	0.0707
4	0	0	74.955	1.26600	7.93	143.85	2	0.0707
3	2	1	75.079	1.26421	0.35	15.11	8	0.0707
2	1	3	77.963	1.22451	0.93	25.49	8	0.0707
4	0	1	78.407	1.21764	0.07	9.93	4	0.0707
0	2	3	78.807	1.21350	0.22	17.70	4	0.0707
0	3	2	80.708	1.18963	10.91	126.87	4	0.0707
2	3	1	81.008	1.18599	17.75	114.74	8	0.0707
1	2	3	81.498	1.18009	0.01	3.25	8	0.0707
4	1	1	82.352	1.17000	0.29	14.93	8	0.0707
1	3	2	83.386	1.15811	0.06	7.00	8	0.0707
3	2	2	85.553	1.13423	0.34	16.41	8	0.0707
3	0	3	87.497	1.11397	0.01	3.22	4	0.0707
0	0	4	87.691	1.11200	2.54	91.12	2	0.0707
4	0	2	88.874	1.10023	1.57	51.01	4	0.0707
2	2	3	89.484	1.09431	19.55	127.68	8	0.0707
1	0	4	90.343	1.08612	0.10	12.78	4	0.0707
4	2	0	90.371	1.08586	9.91	129.08	4	0.0707
3	3	0	90.865	1.08124	0.19	17.74	4	0.0707
3	1	3	91.309	1.07714	0.36	17.44	8	0.0707
2	3	2	91.355	1.07671	0.31	16.32	8	0.0707
0	1	4	91.502	1.07536	5.03	92.31	4	0.0707
4	1	2	92.606	1.06470	16.04	117.06	8	0.0707

Table 4.3 Powder XRD lines for Ni_3Mo for 2θ (20 – 100) degrees.

D (Å)	I/Io	hkl	2θ
2.034	100	111	44.51
1.762	42	200	51.81
1.246	21	220	76.41
1.0624	20	311	93.00
1.0172	7	222	98.50

Table 4.4 Powder XRD lines for Ni powder for 2θ (20 – 100) degrees.

4.7 Figures for Chapter 4

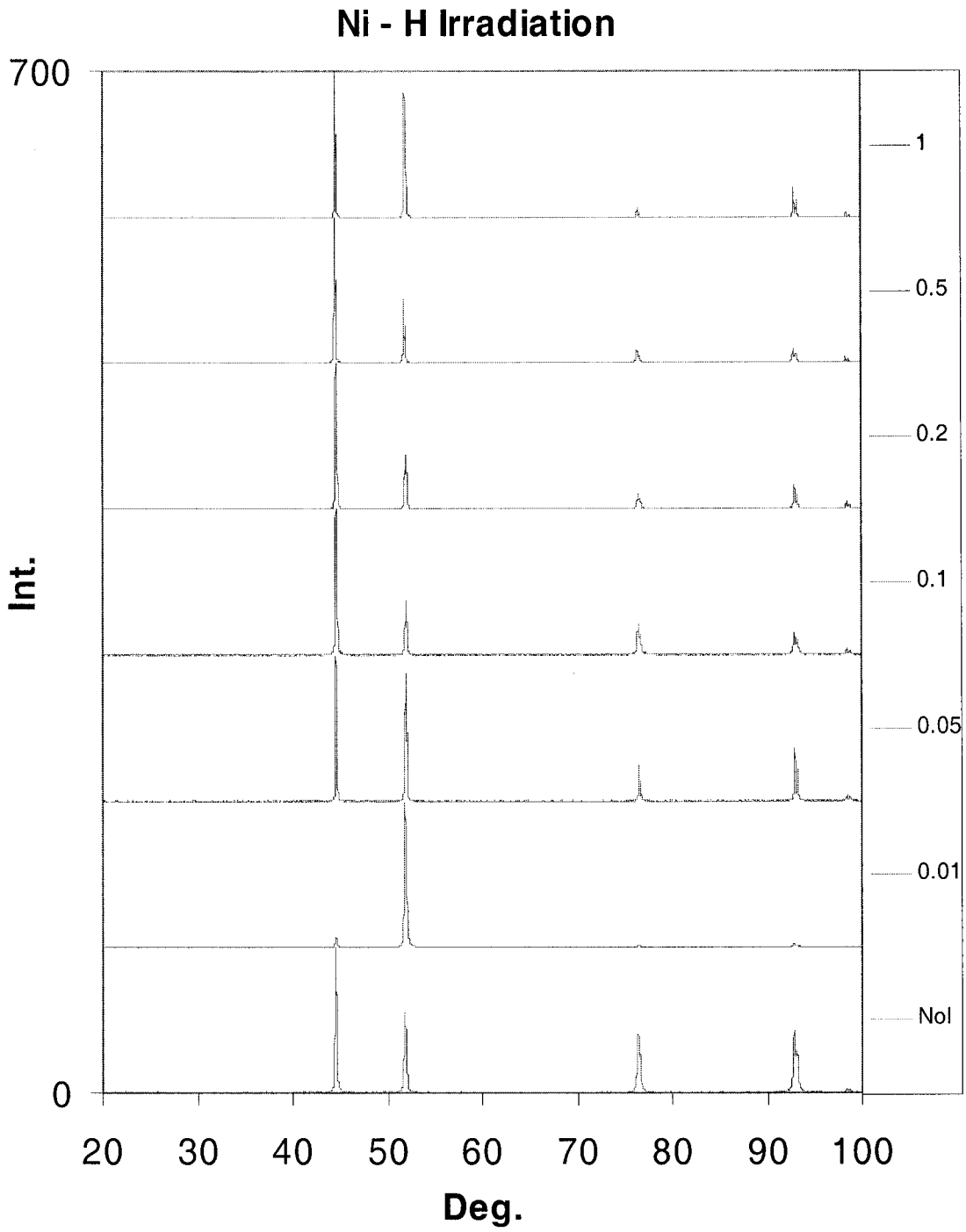

Figure 4.1.1 XRD spectra generated for Ni samples irradiated with an H+ beam with a dose varying from 0.01 DPA to 1 DPA. The Intensity axis is in arbitrary units and is plotted as a function of the angle 2θ.

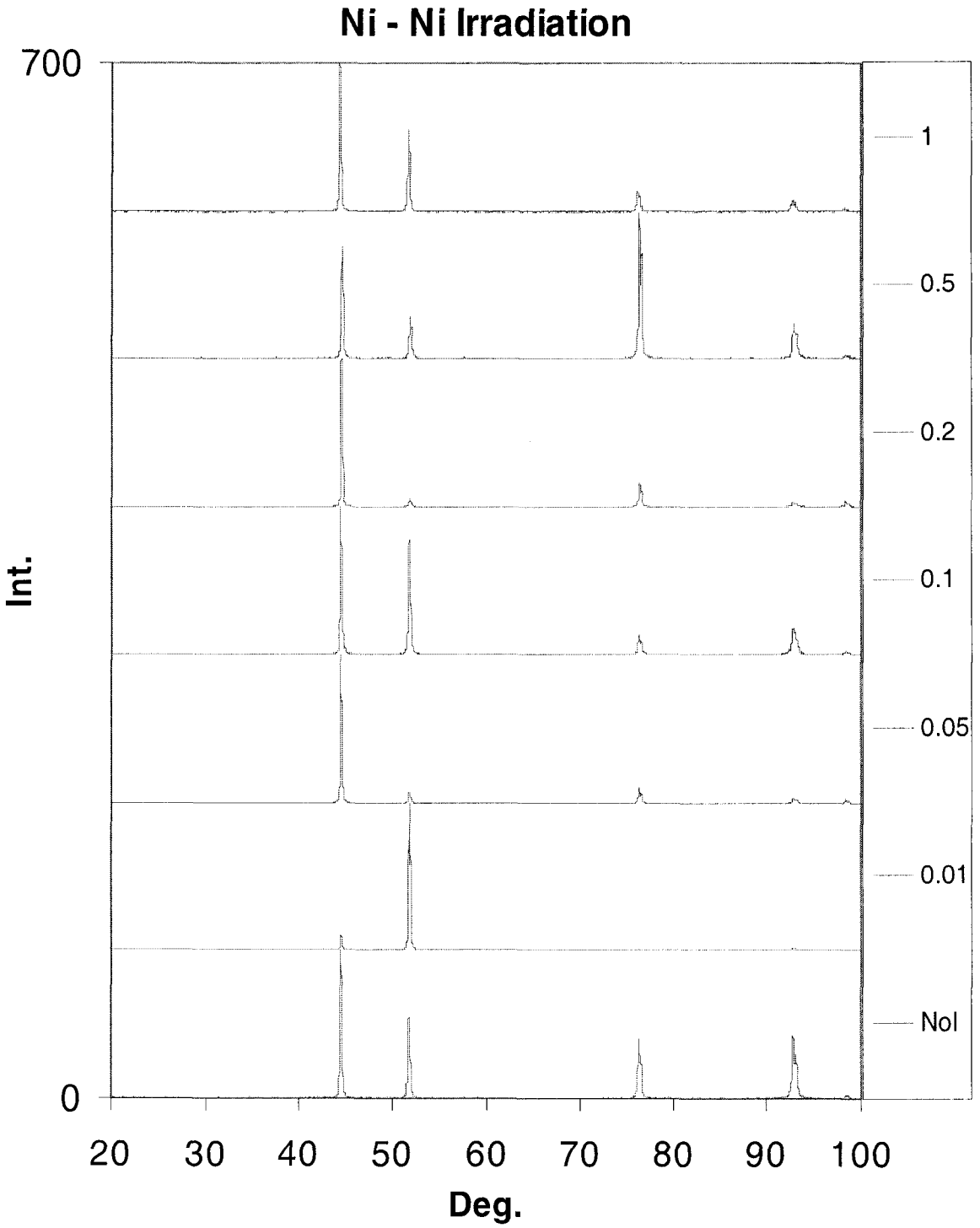

Figure 4.1.2 XRD spectra generated for Ni samples irradiated with a Ni+ beam with a dose varying from 0.01 DPA to 1 DPA. The Intensity axis is in arbitrary units and is plotted as a function of the angle 2θ.

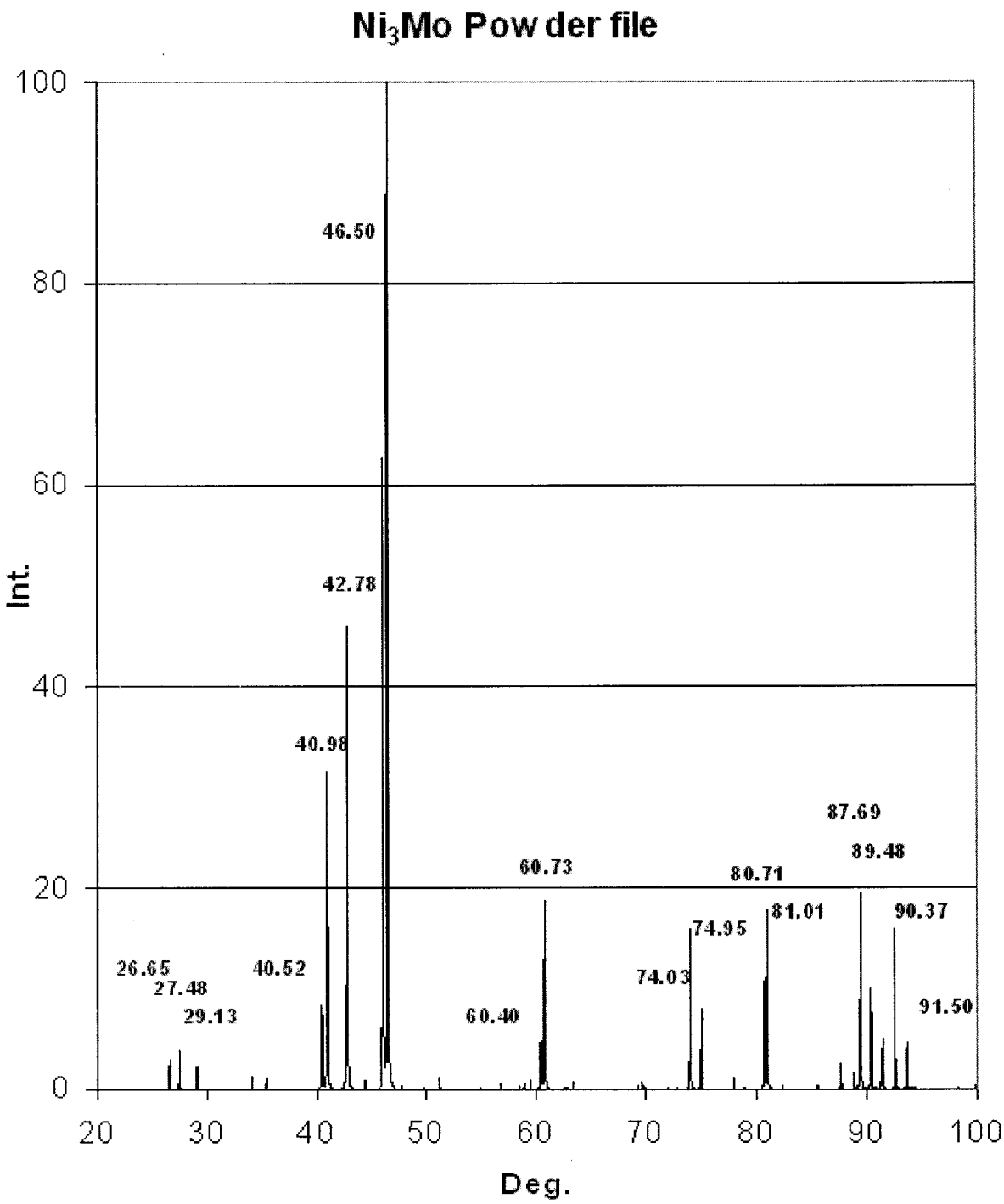

Figure 4.1.3 PowderCell program plot generated for Ni_3Mo. The main peaks are indexed with the corresponding angle values.

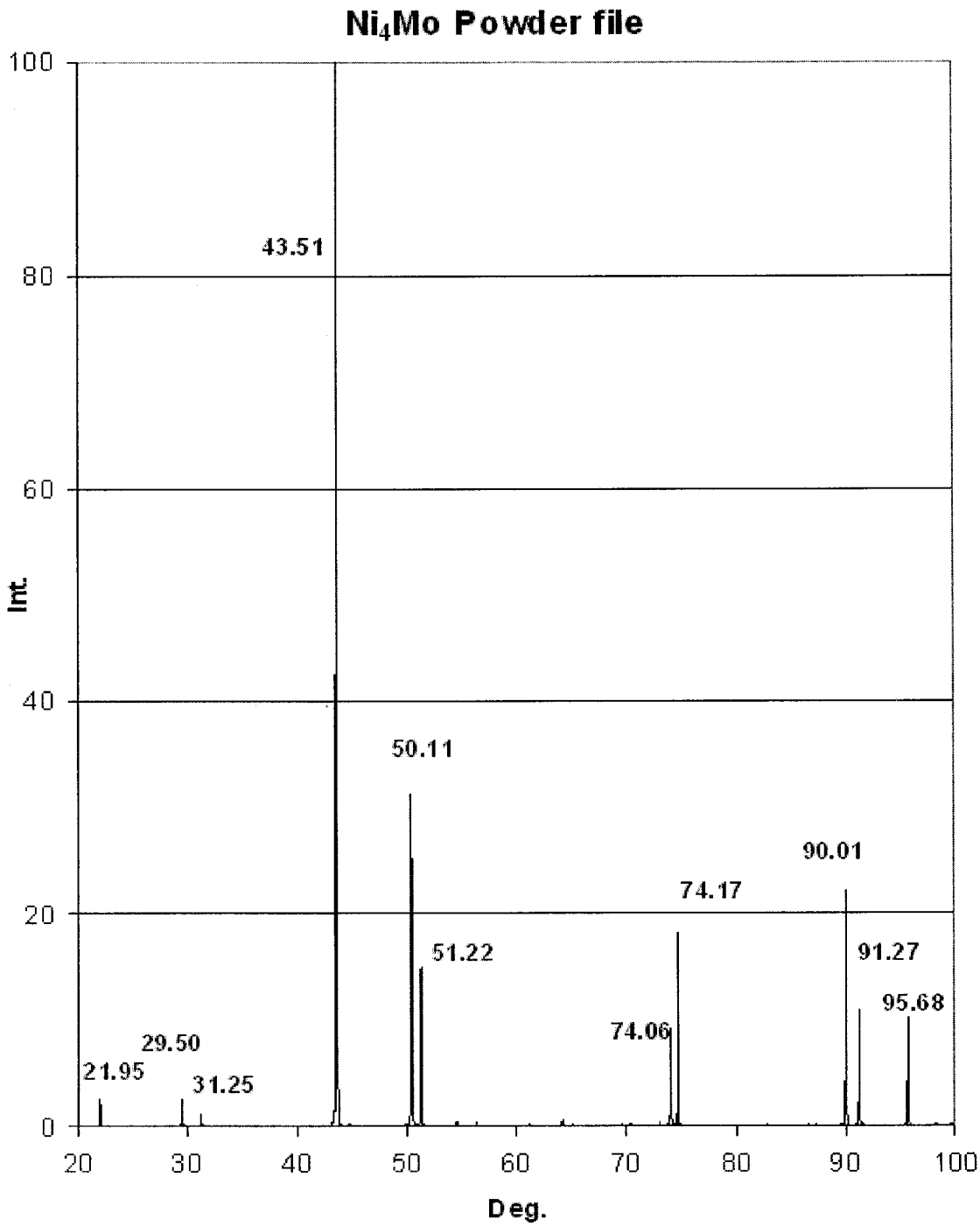

Figure 4.1.4 PowderCell program plot generated for Ni_4Mo. The main peaks are indexed with the corresponding angle values.

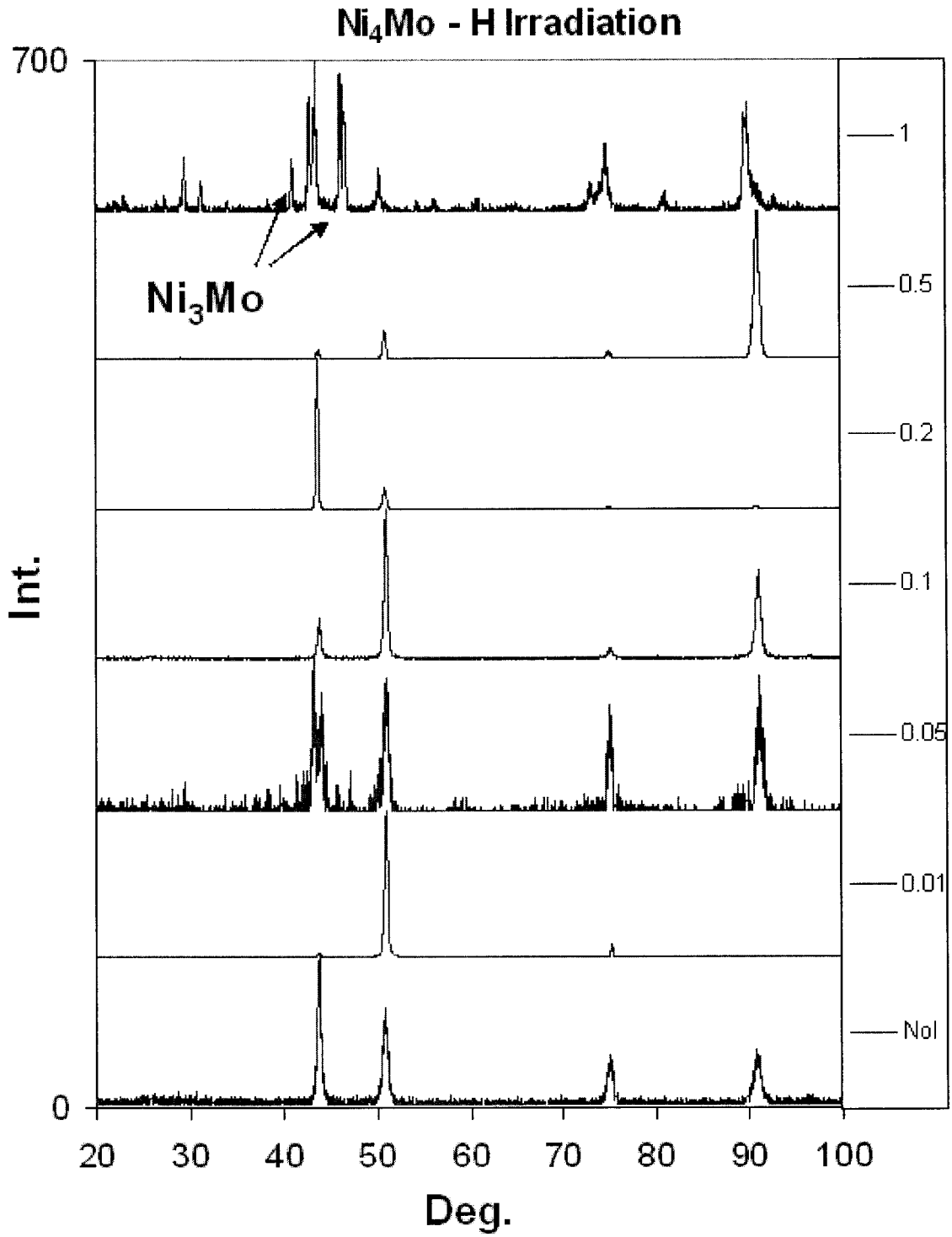

Figure 4.1.5 XRD spectra generated for Ni_4Mo as-cast samples irradiated with an H+ beam with a dose varying from 0.01 DPA to 1 DPA. The Intensity axis is in arbitrary units and is plotted as a function of the angle 2θ.

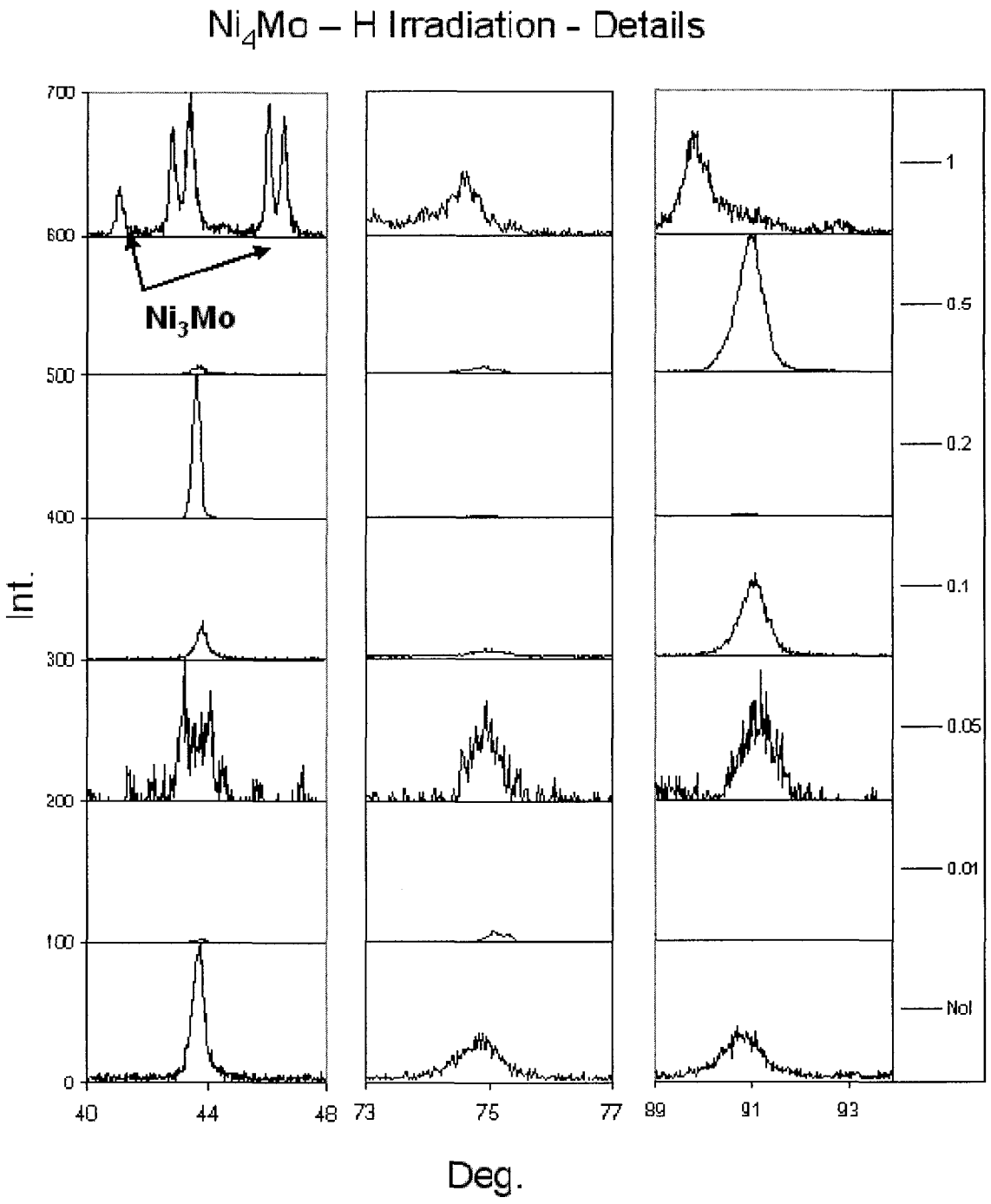

Figure 4.1.6 Detail of the XRD spectra generated for Ni_4Mo as-cast samples irradiated with an H+ beam with a dose varying from 0.01 DPA to 1 DPA. The Intensity axis is in arbitrary units and is plotted as a function of the angle 2θ.

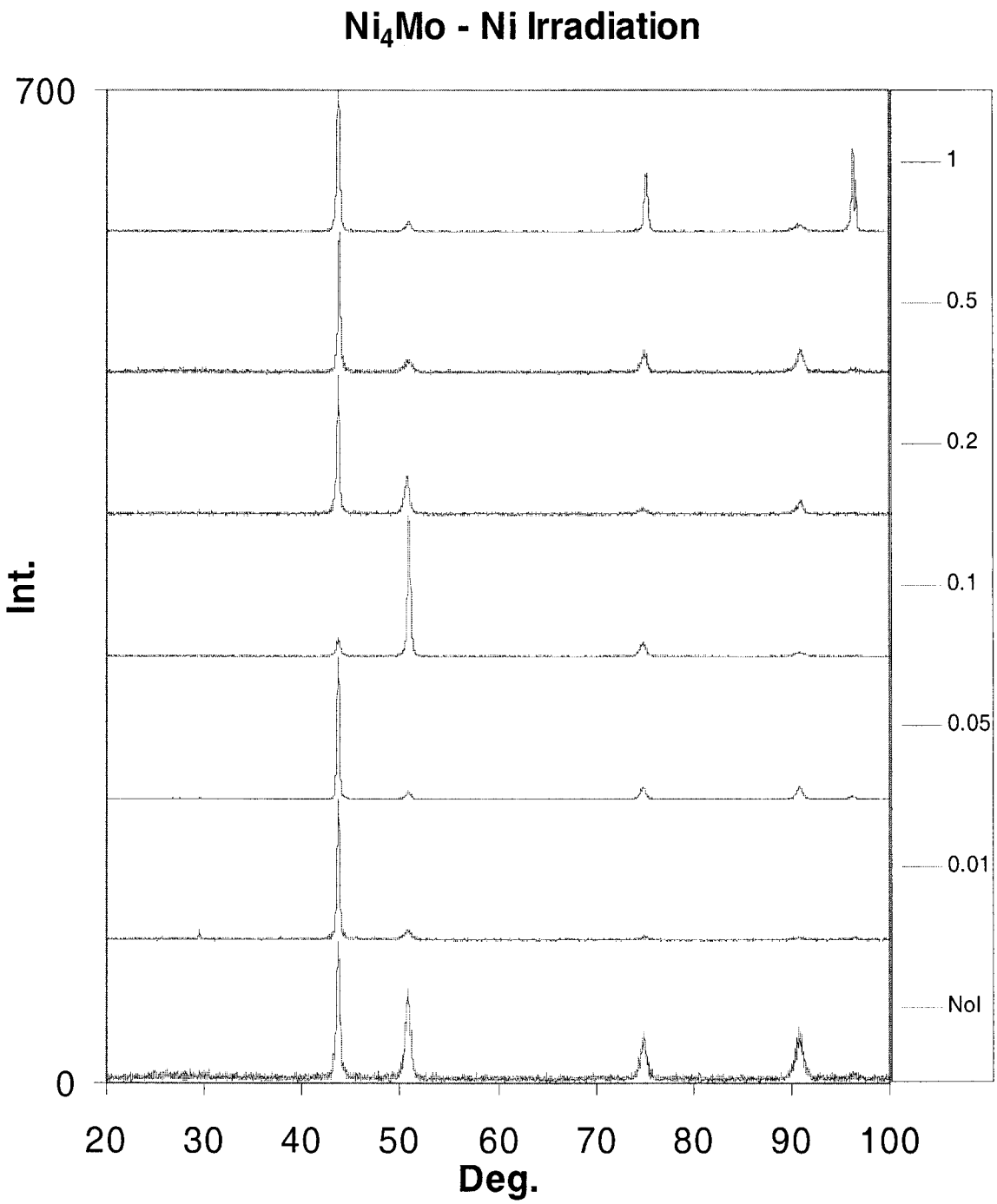

Figure 4.1.7 XRD spectra generated for Ni_4Mo as-cast samples irradiated with a Ni+ beam with a dose varying from 0.01 DPA to 1 DPA. The Intensity axis is in arbitrary units and is plotted as a function of the angle 2θ.

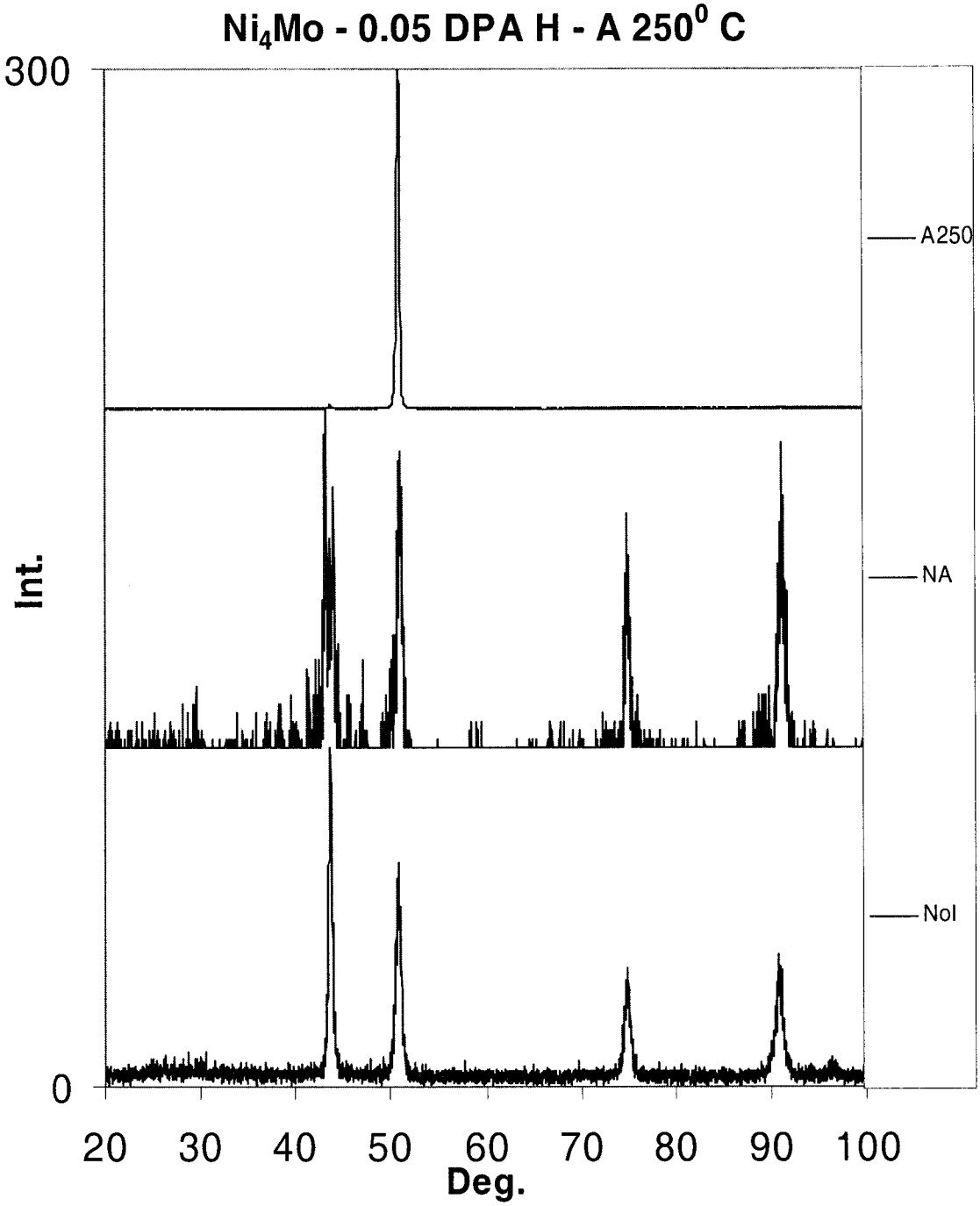

Figure 4.1.8 XRD spectra generated for Ni_4Mo as-cast samples exposed to an H+ beam for a 0.05 DPA dose. After irradiation, the samples were annealed for three hours at 250^0 C. The Intensity axis is in arbitrary units and is plotted as a function of the angle 2θ.

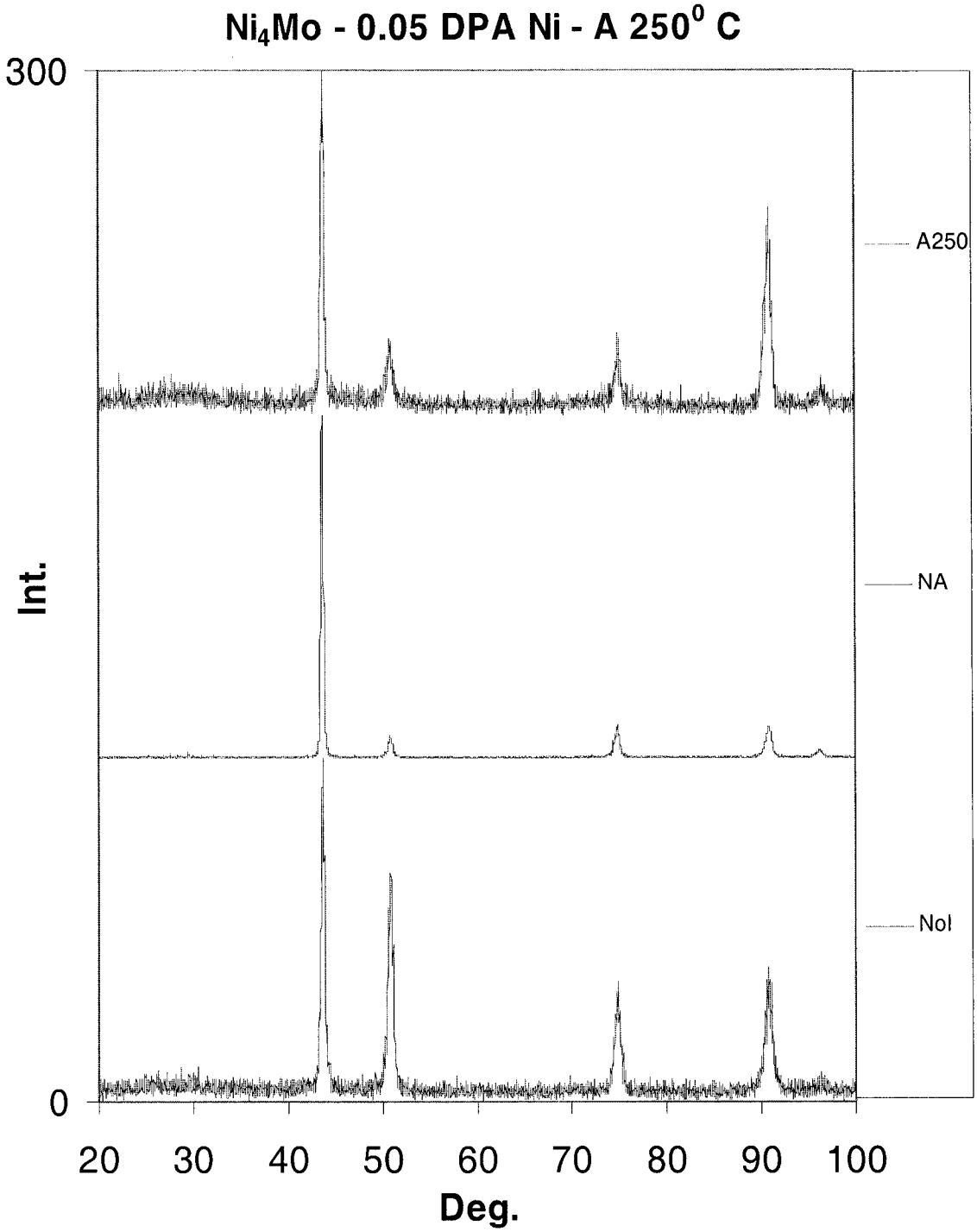

Figure 4.1.9 XRD spectra generated for Ni_4Mo as-cast samples exposed to a Ni+ beam for a 0.05 DPA dose. After irradiation, the samples were annealed for three hours at 250^0 C. The Intensity axis is in arbitrary units and is plotted as a function of the angle 2θ.

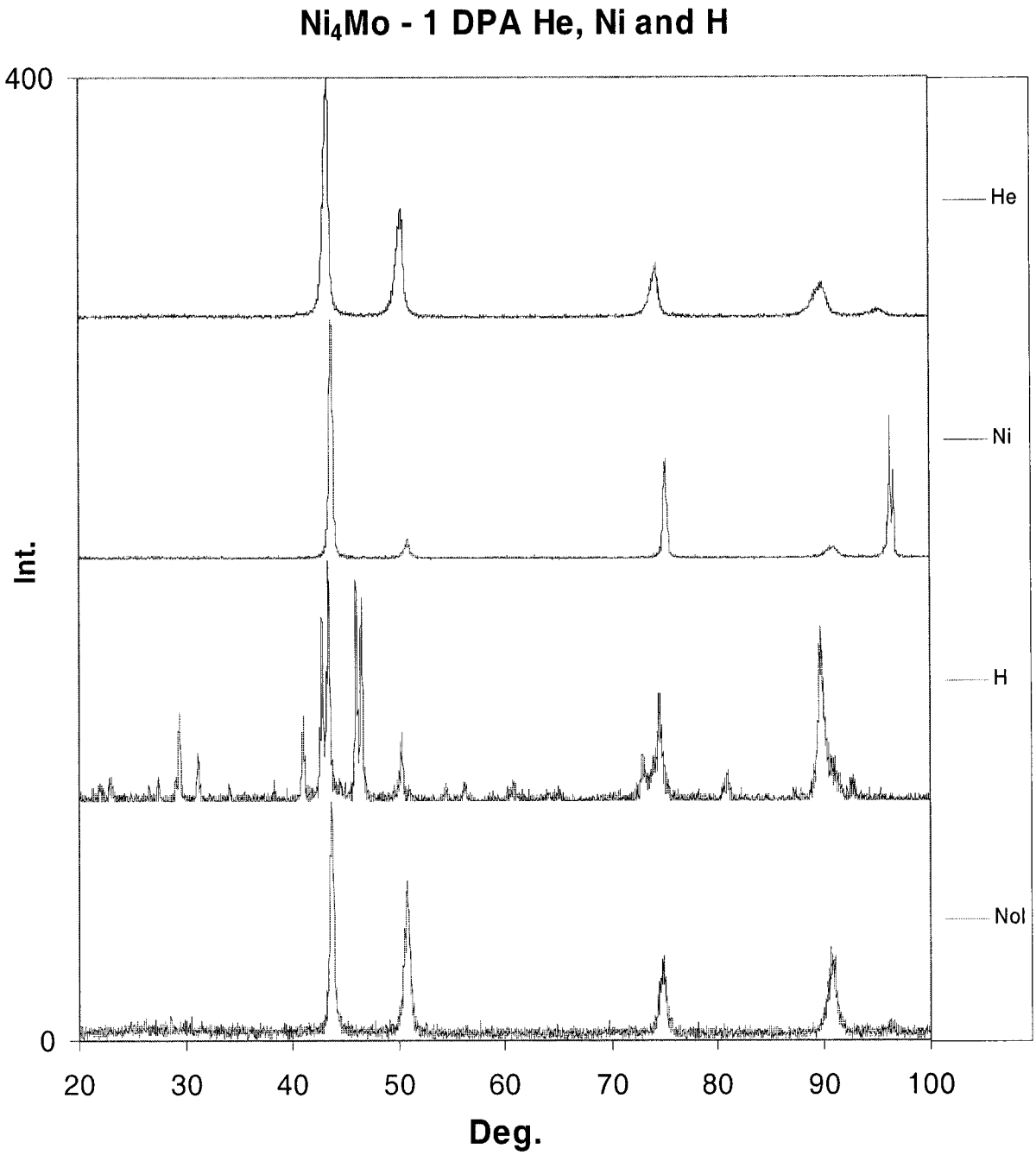

Figure 4.1.10 XRD spectra generated for Ni_4Mo as-cast samples exposed to a He+, Ni+ and an H+ beam for a 1 DPA dose. The Intensity axis is in arbitrary units and is plotted as a function of the angle 2θ.

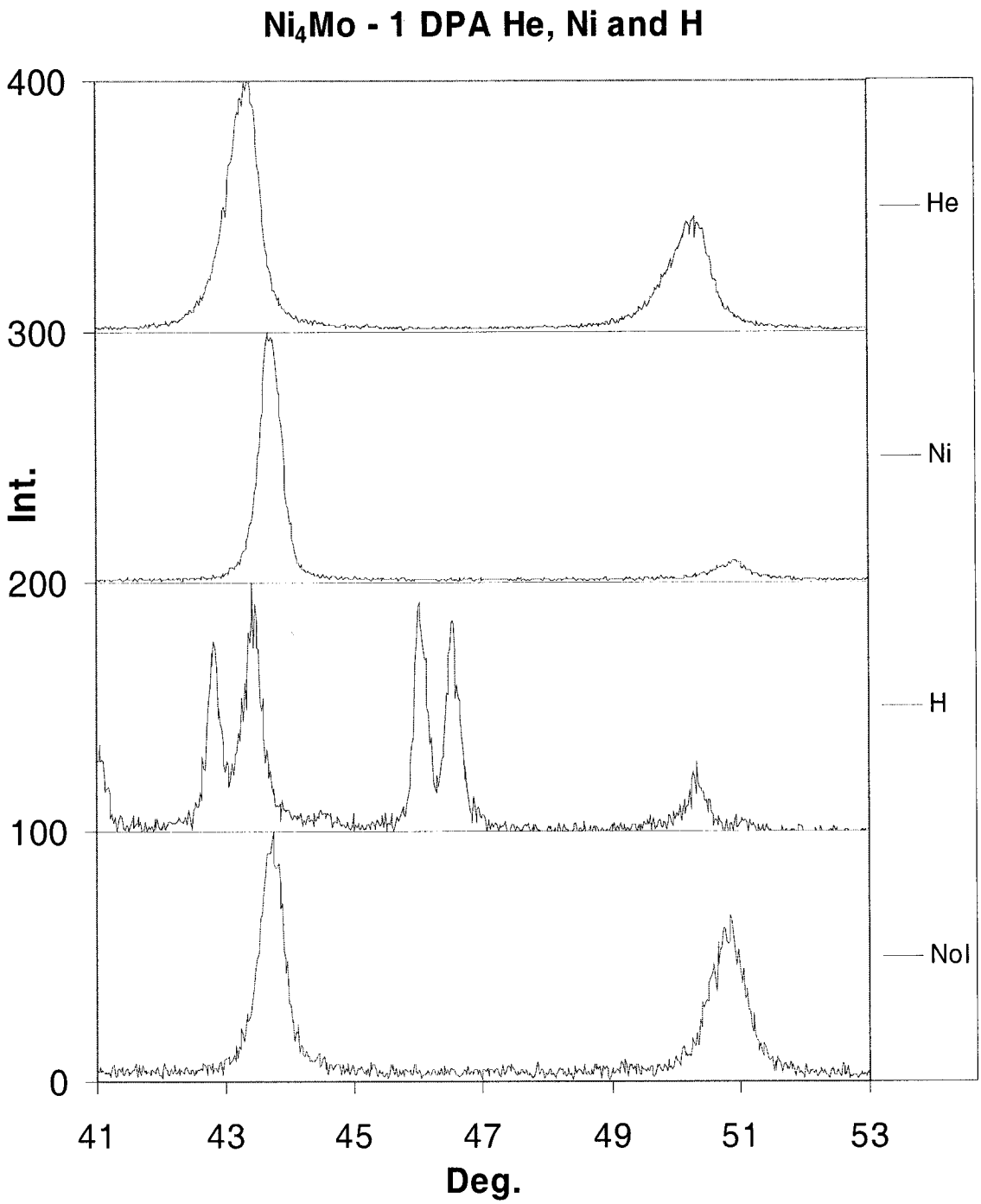

Figure 4.1.11 Detail of the XRD spectra from Figure 4.1.14 generated for Ni_4Mo as-cast samples exposed to a He+, Ni+ and a H+ beam for a 1 DPA dose. The Intensity axis is in arbitrary units and is plotted as a function of the angle 2θ.

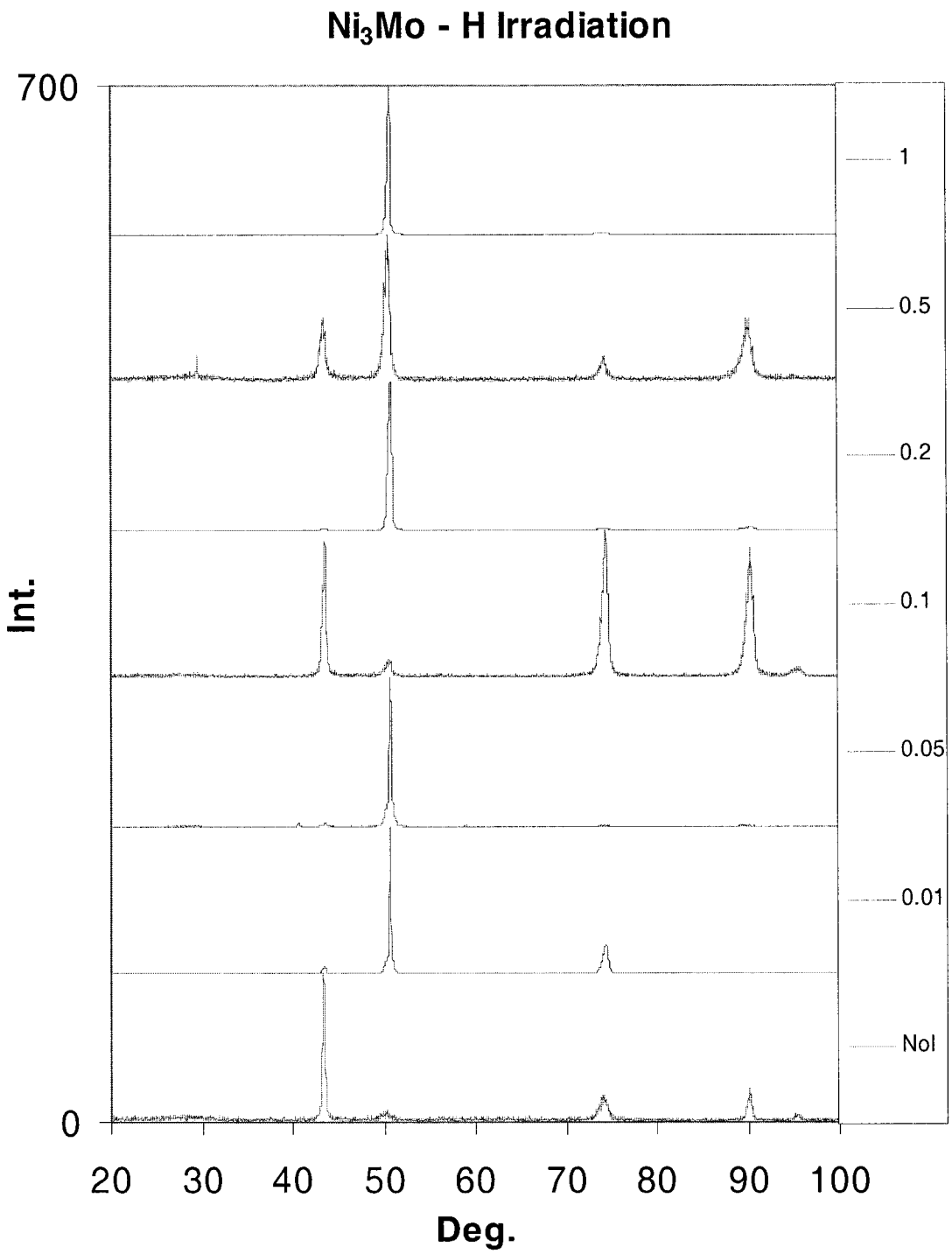

Figure 4.1.12 XRD spectra generated for Ni_3Mo as-cast samples irradiated with an H+ beam with a dose varying from 0.01 DPA to 1 DPA. The Intensity axis is in arbitrary units and is plotted as a function of the angle 2θ.

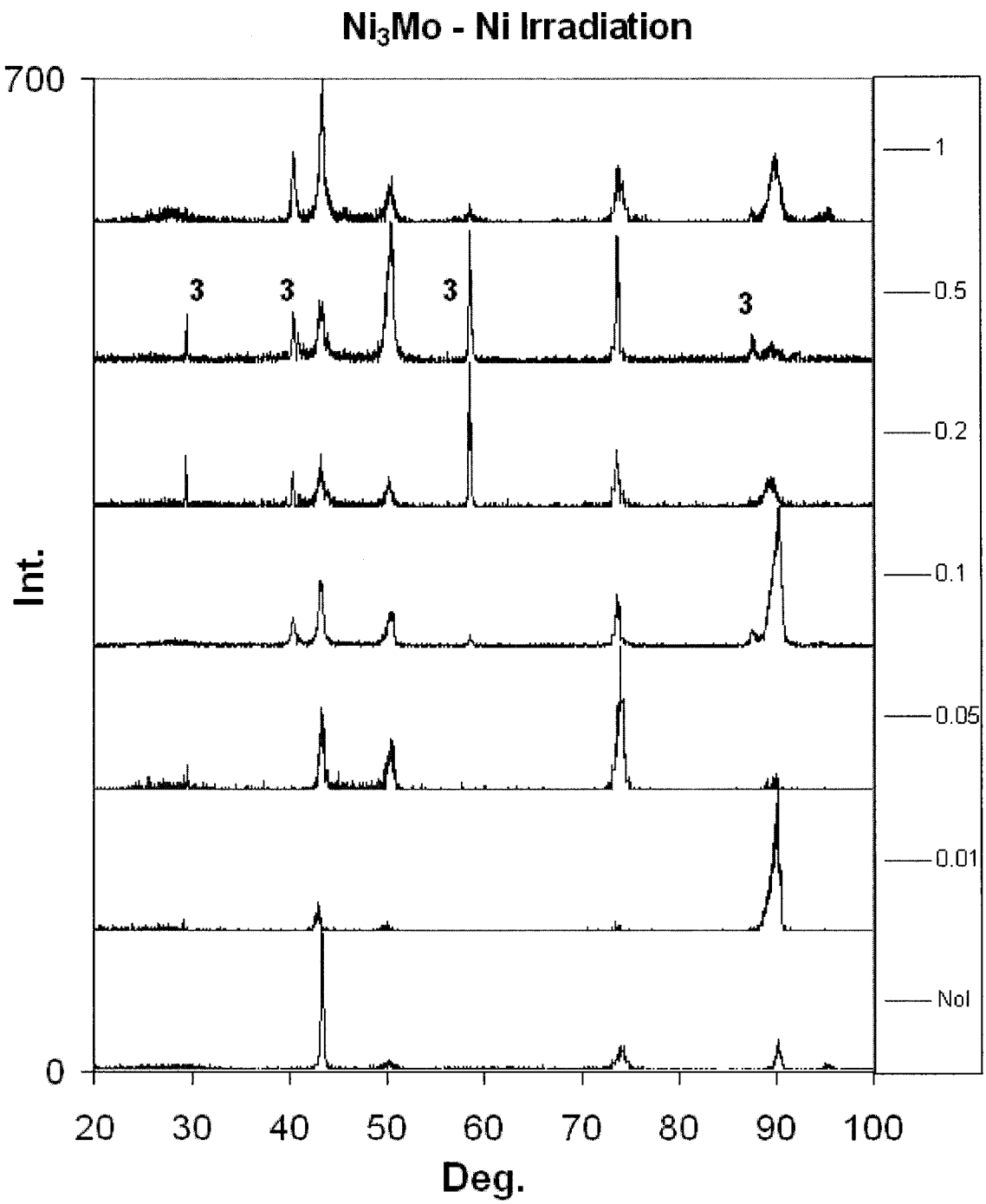

Figure 4.1.13 XRD spectra generated for Ni_3Mo as-cast samples irradiated with a Ni+ beam with a dose varying from 0.01 DPA to 1 DPA. The Intensity axis is in arbitrary units and is plotted as a function of the angle 2θ. The superlattice lines of Ni_3Mo are marked with a "3".

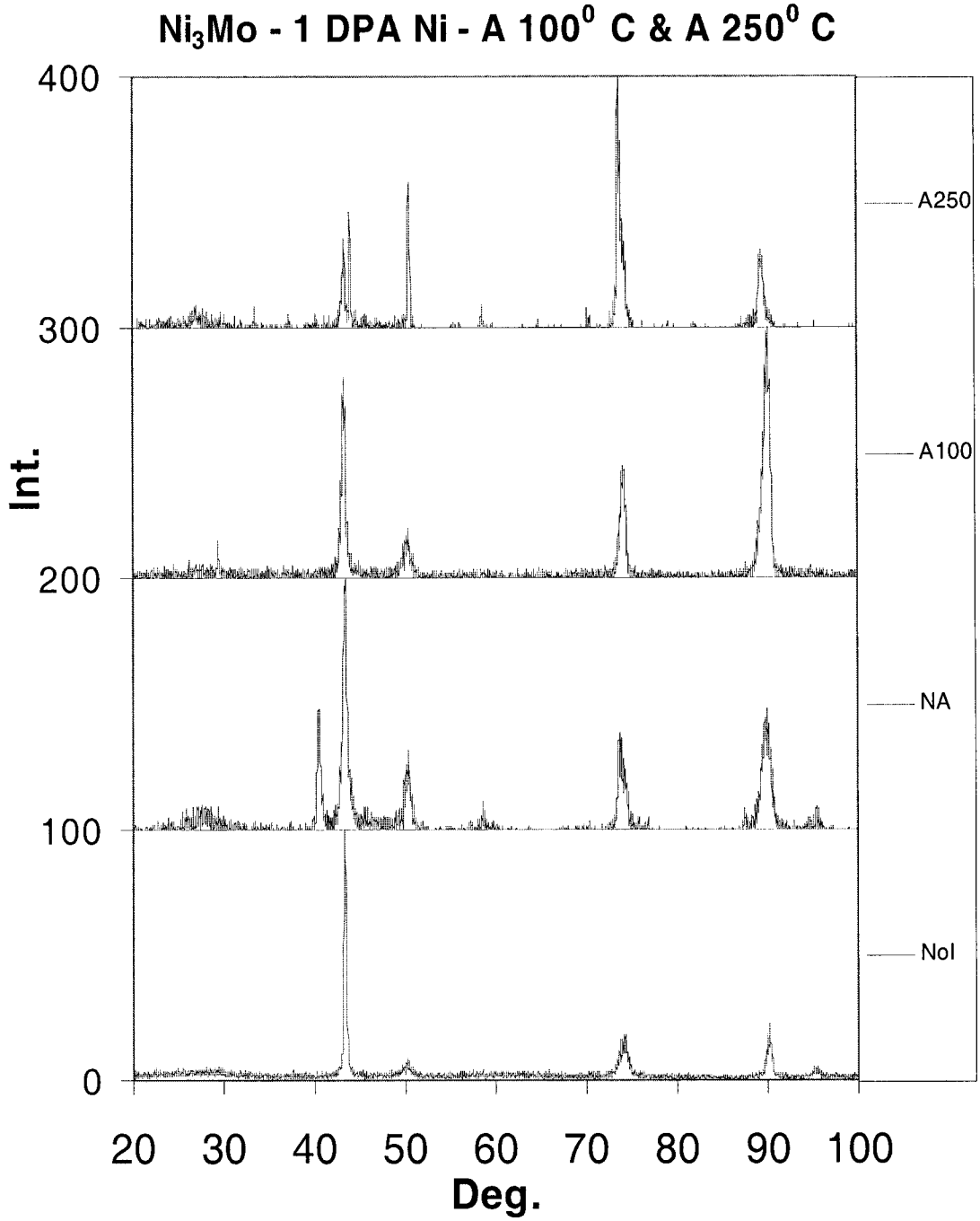

Figure 4.1.14 XRD spectra generated for Ni_3Mo as-cast samples irradiated with a Ni+ beam with a 1 DPA dose. After irradiation, the samples were first annealed for three hours at 100^0 C and then for three hours at 250^0 C. The Intensity axis is in arbitrary units and is plotted as a function of the angle 2θ.

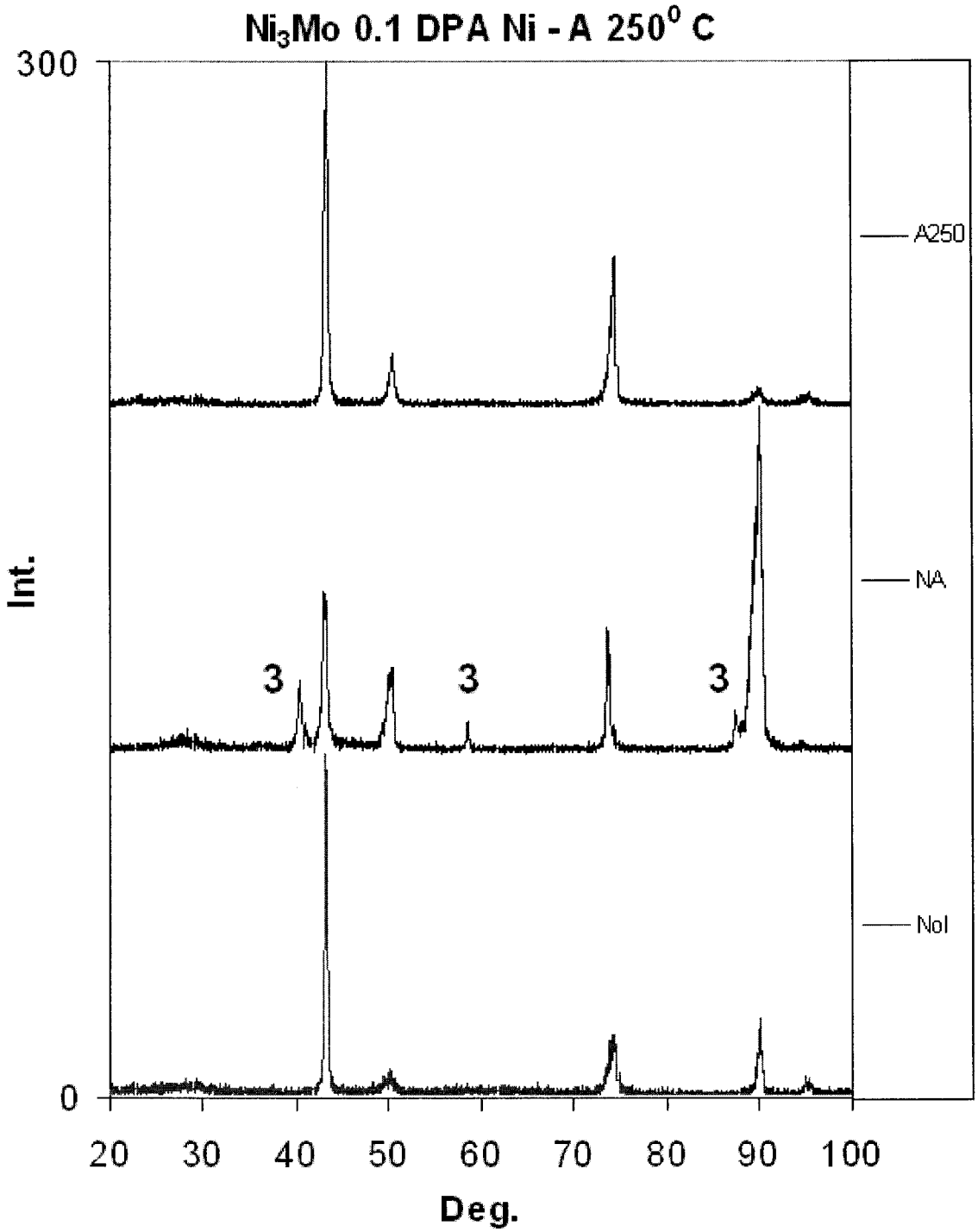

Figure 4.1.15 XRD spectra generated for Ni_3Mo as-cast samples exposed to a Ni+ beam for a 0.1 DPA dose. After irradiation, the samples were annealed for three hours at 250^0 C. The Intensity axis is in arbitrary units and is plotted as a function of the angle 2θ. The superlattice lines of Ni_3Mo are marked with a "3".

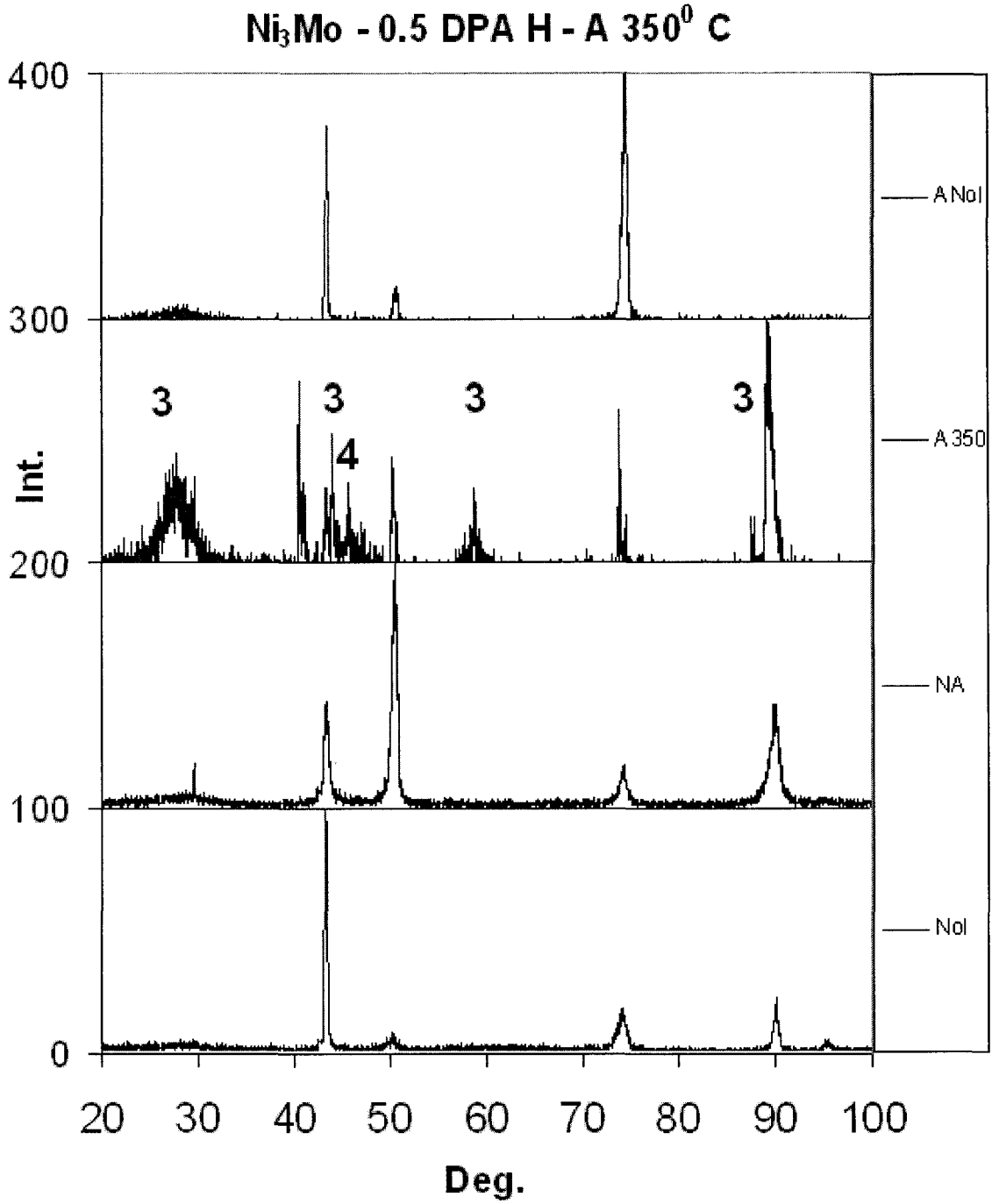

Figure 4.1.16 XRD spectra generated for Ni_3Mo as-cast samples exposed to an H+ beam for a 0.5 DPA dose. After irradiation, the samples were annealed for three hours at 350^0 C. The Intensity axis is in arbitrary units and is plotted as a function of the angle 2θ. Spectra are compared with spectrum from sample with annealing but NoI. The superlattice lines of Ni_3Mo and Ni_4Mo are marked with a "3" and a "4".

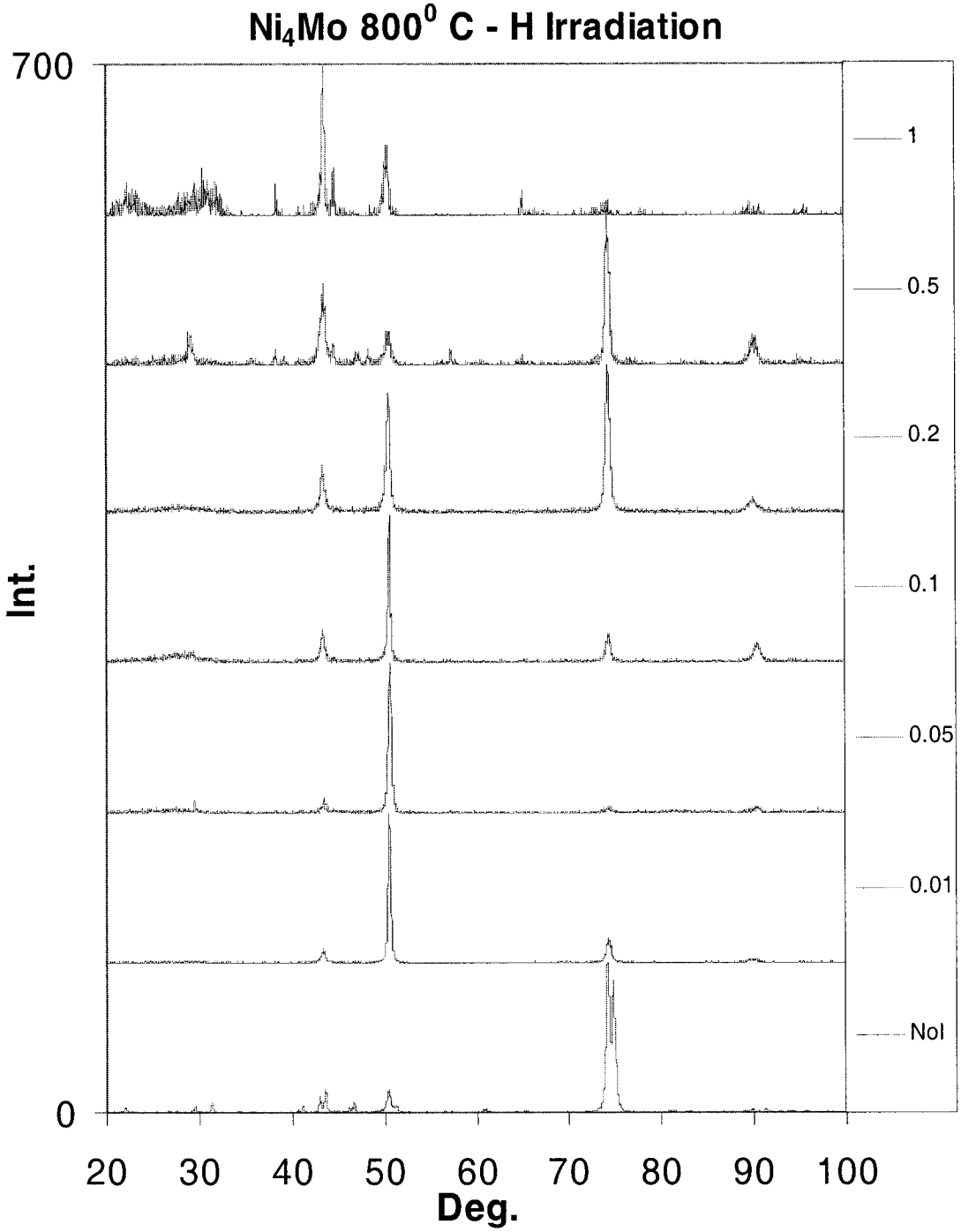

Figure 4.1.17 XRD spectra generated for Ni_4Mo annealed at 800^0 C samples irradiated with an H+ beam with a dose varying from 0.01 DPA to 1 DPA. The Intensity axis is in arbitrary units and is plotted as a function of the angle 2θ.

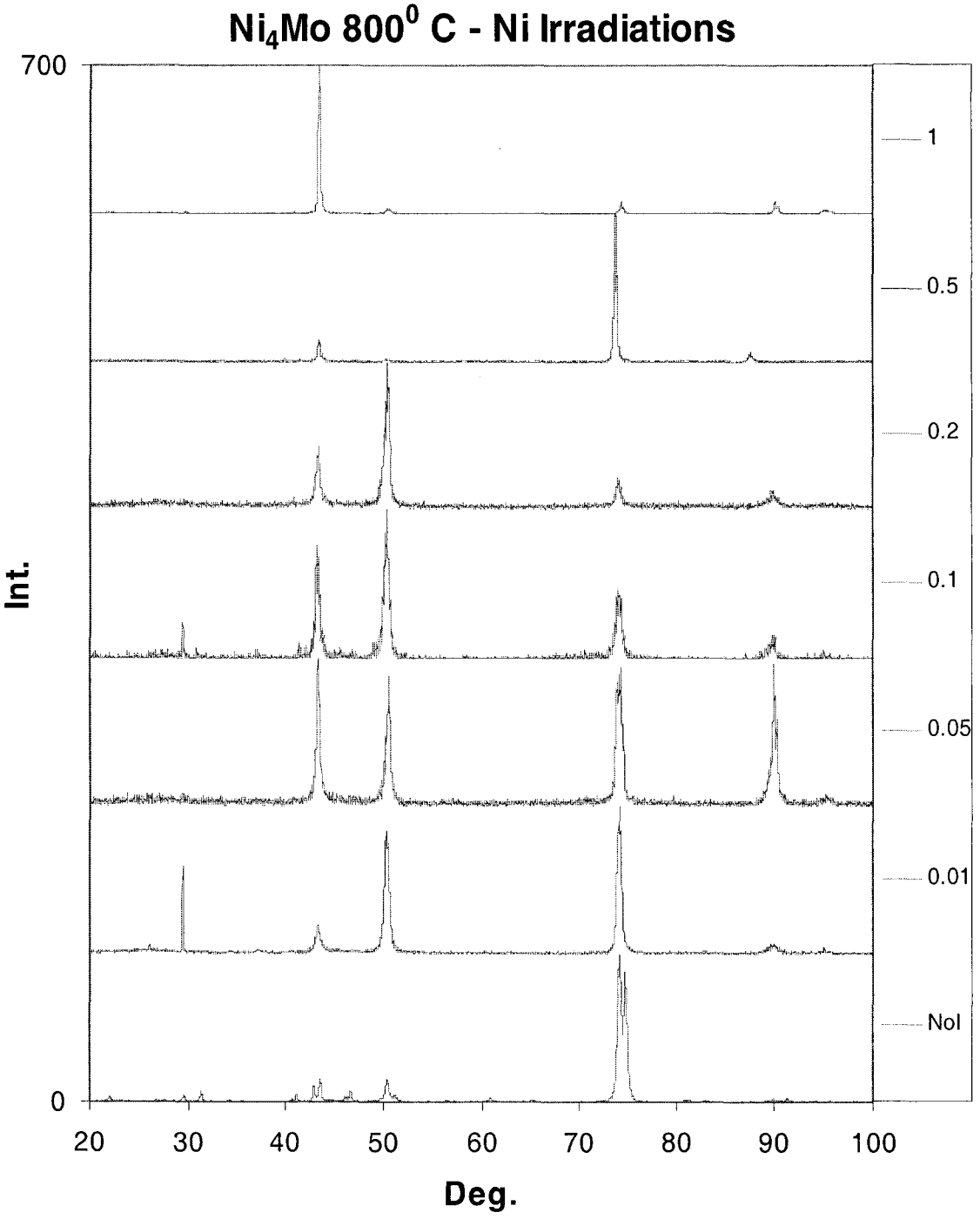

Figure 4.1.18 XRD spectra generated for Ni_4Mo annealed at 800^0 C samples irradiated with a Ni+ beam with a dose varying from 0.01 DPA to 1 DPA. The Intensity axis is in arbitrary units and is plotted as a function of the angle 2θ.

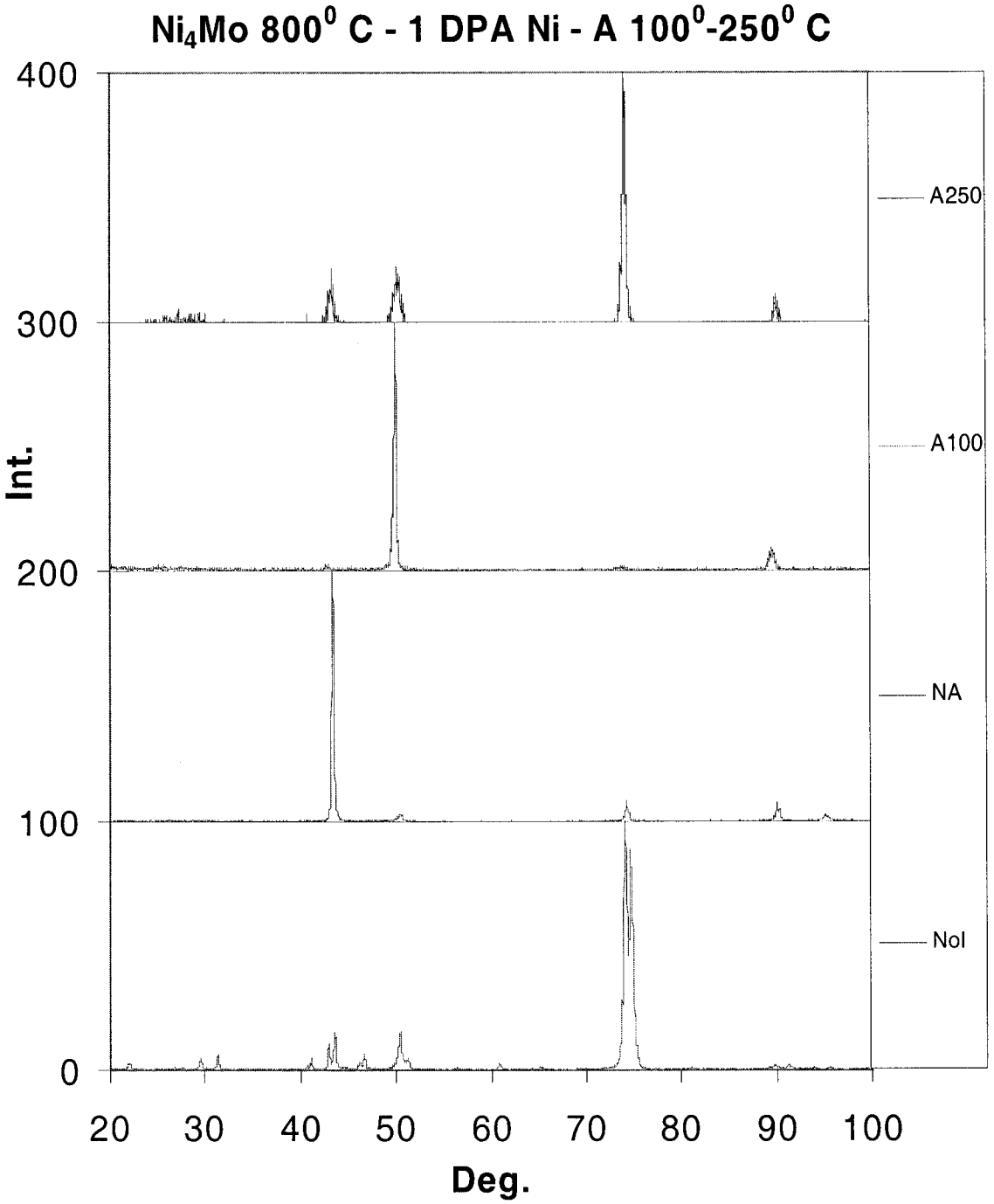

Figure 4.1.19 XRD spectra generated for Ni_4Mo samples annealed at 800^0 C before irradiation and exposed to a Ni+ beam for a 1 DPA dose. After irradiation, the samples were first annealed for three hours at 100^0 C and then for three hours at 250^0 C. The Intensity axis is in arbitrary units and is plotted as a function of the angle 2θ.

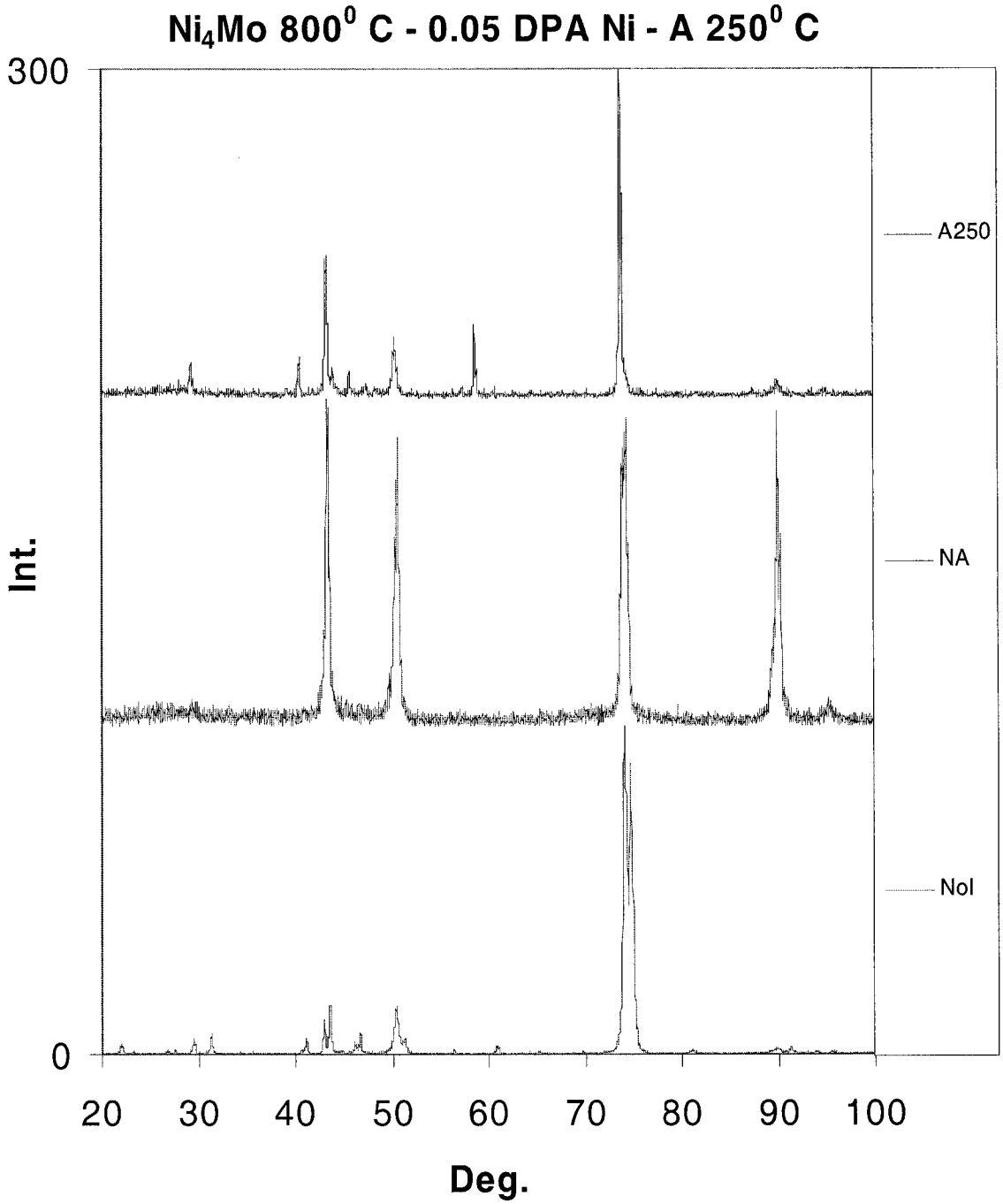

Figure 4.1.20 XRD spectra generated for Ni_4Mo samples annealed at 800^0 C before exposure to a Ni+ beam for a 0.05 DPA dose. After irradiation, the samples were annealed for three hours at 250^0 C. The Intensity axis is in arbitrary units and is plotted as a function of the angle 2θ.

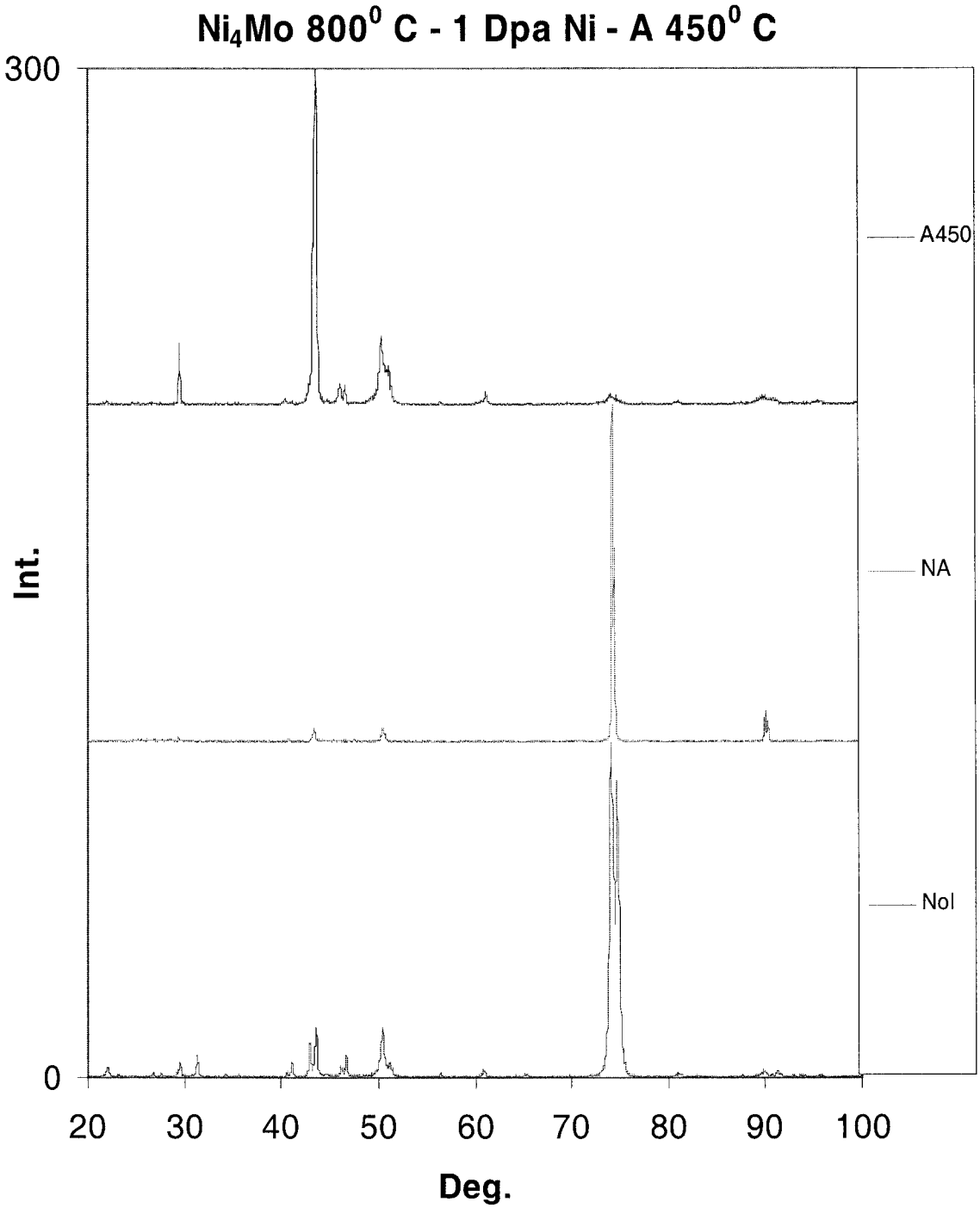

Figure 4.1.21 XRD spectra generated for Ni_4Mo samples annealed at 800^0 C before exposure to a Ni+ beam for a 1 DPA dose. After irradiation, the samples were annealed for three hours at 450^0 C. The Intensity axis is in arbitrary units and is plotted as a function of the angle 2θ.

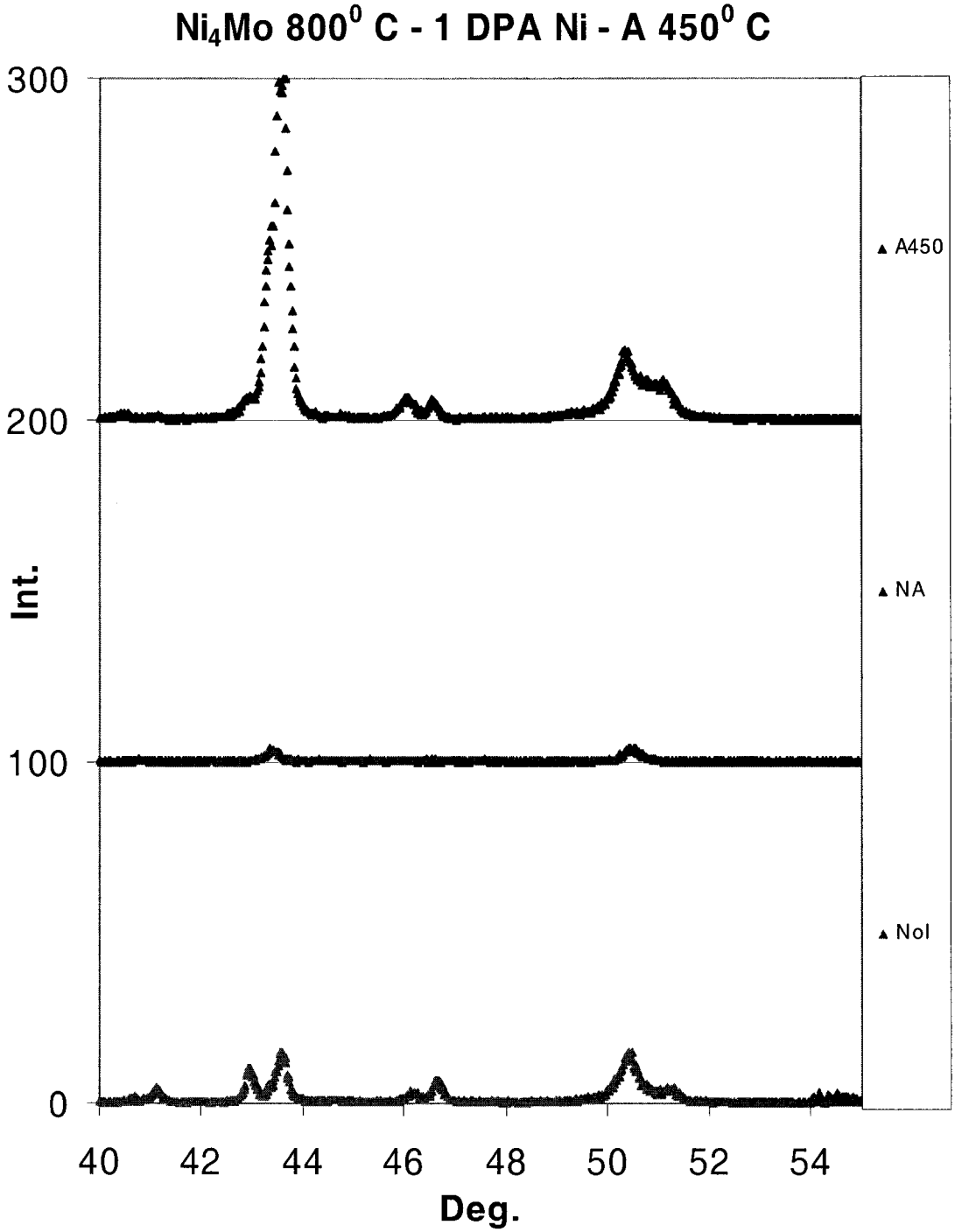

Figure 4.1.22 Detail #1 of the XRD spectra generated for Ni_4Mo samples annealed at 800^0 C before exposure to a Ni+ beam for a 1 DPA dose. After irradiation, the samples were annealed for three hours at 450^0 C. The Intensity axis is in arbitrary units and is plotted as a function of the angle 2θ.

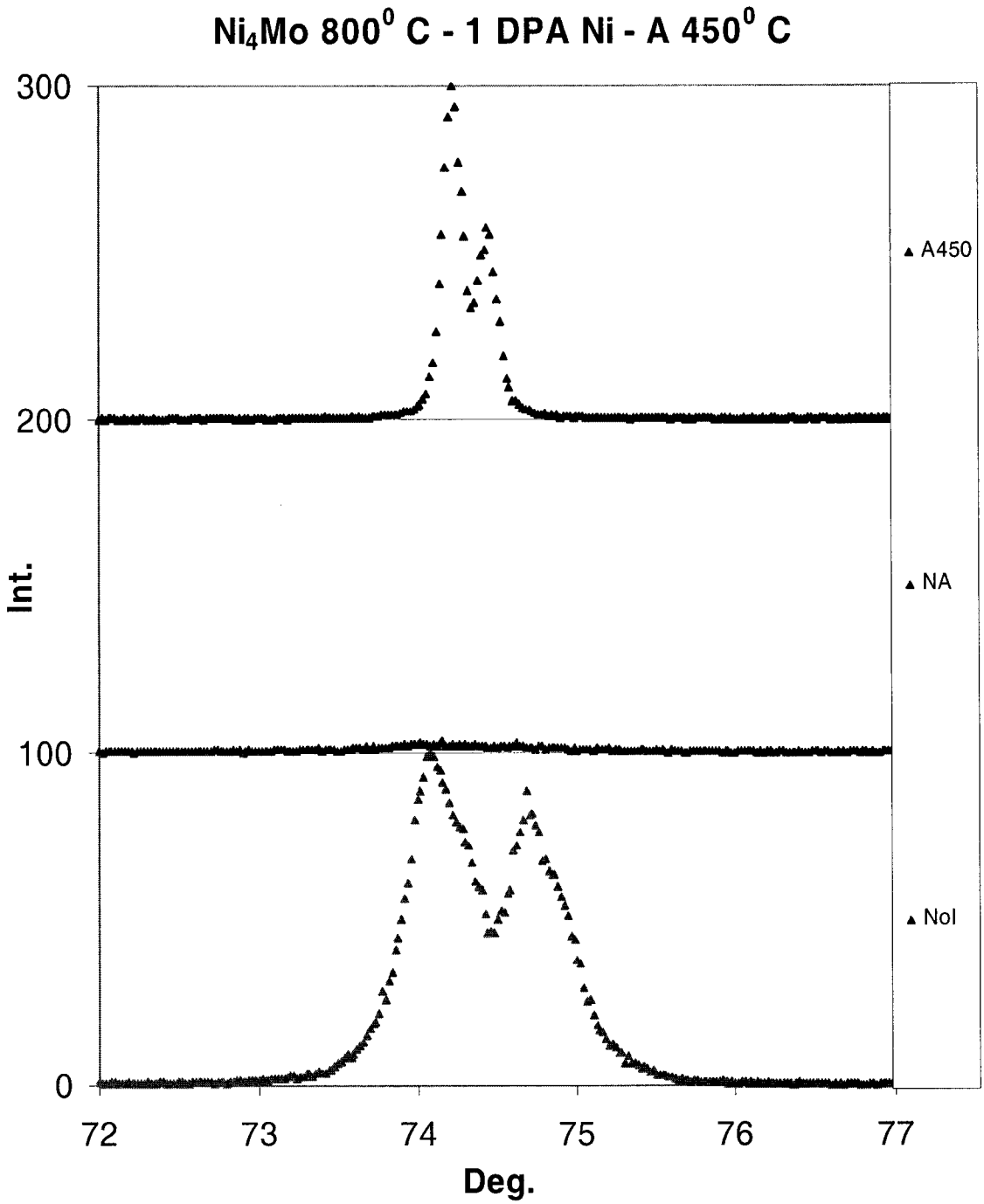

Figure 4.1.23 Detail #2 of the XRD spectra generated for Ni_4Mo samples annealed at 800^0 C before exposure to a Ni+ beam for a 1 DPA dose. After irradiation, the samples were annealed for three hours at 450^0 C. The Intensity axis is in arbitrary units and is plotted as a function of the angle 2θ.

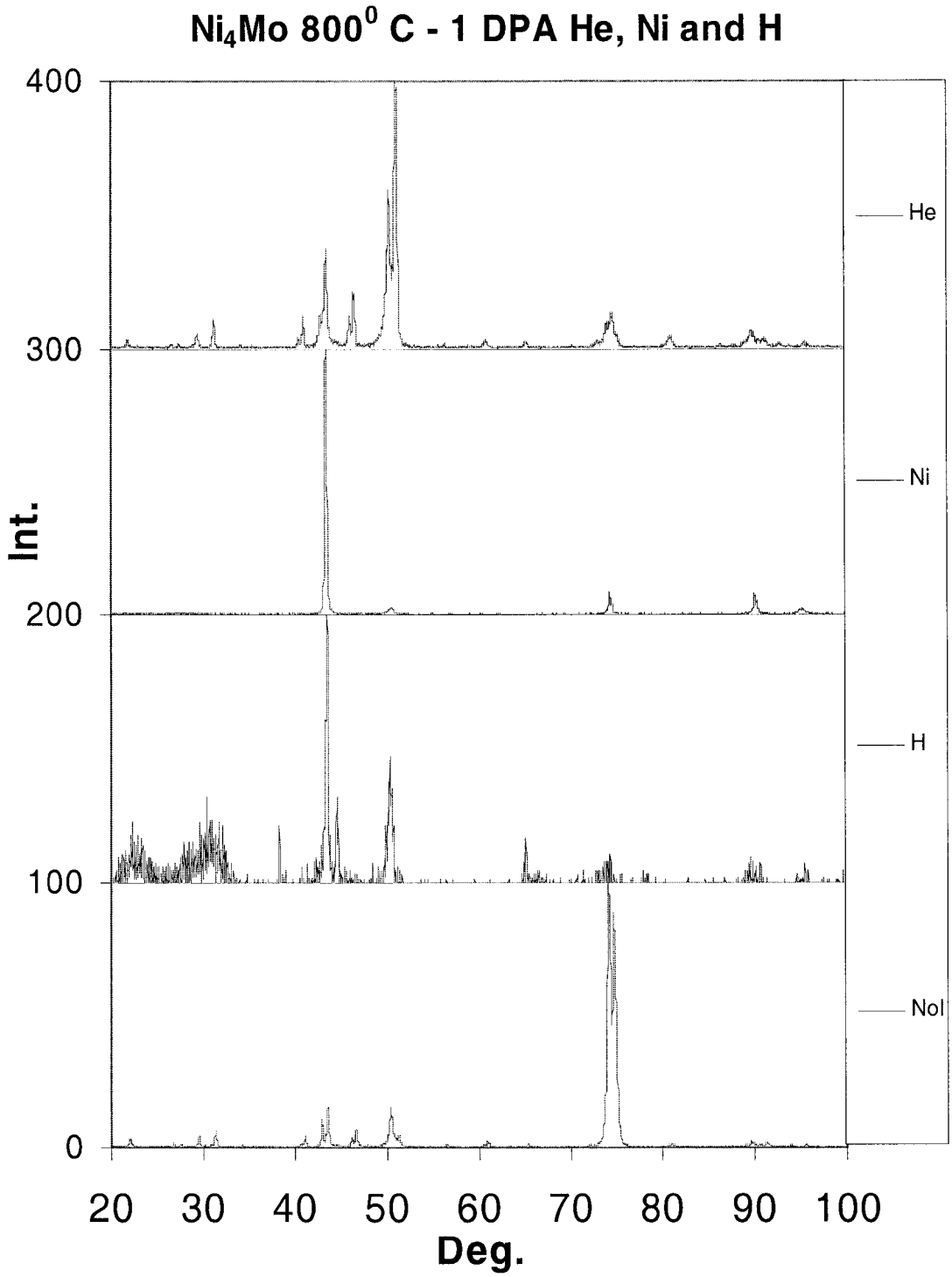

Figure 4.1.24 XRD spectra generated for Ni_4Mo samples annealed at 800^0 C before exposure to a He+, Ni+ and a H+ beam for a 1 DPA dose. The Intensity axis is in arbitrary units and is plotted as a function of the angle 2θ.

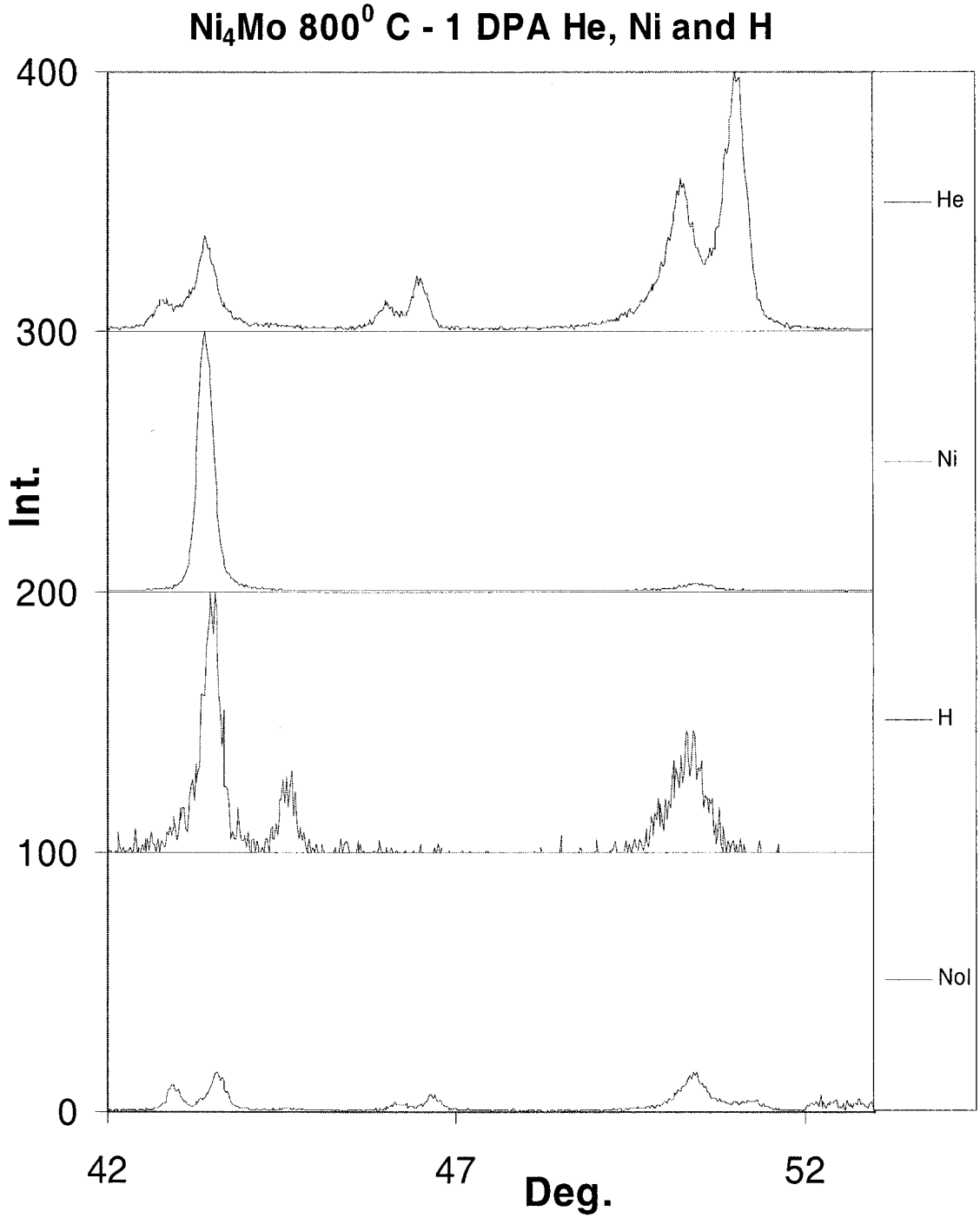

Figure 4.1.25 Detail of the XRD spectra from Figure 4.1.24 generated for Ni_4Mo samples annealed at 800^0 C before exposure to a He+, Ni+ and a H+ beam for a 1 DPA dose. The Intensity axis is in arbitrary units and is plotted as a function of the angle 2θ.

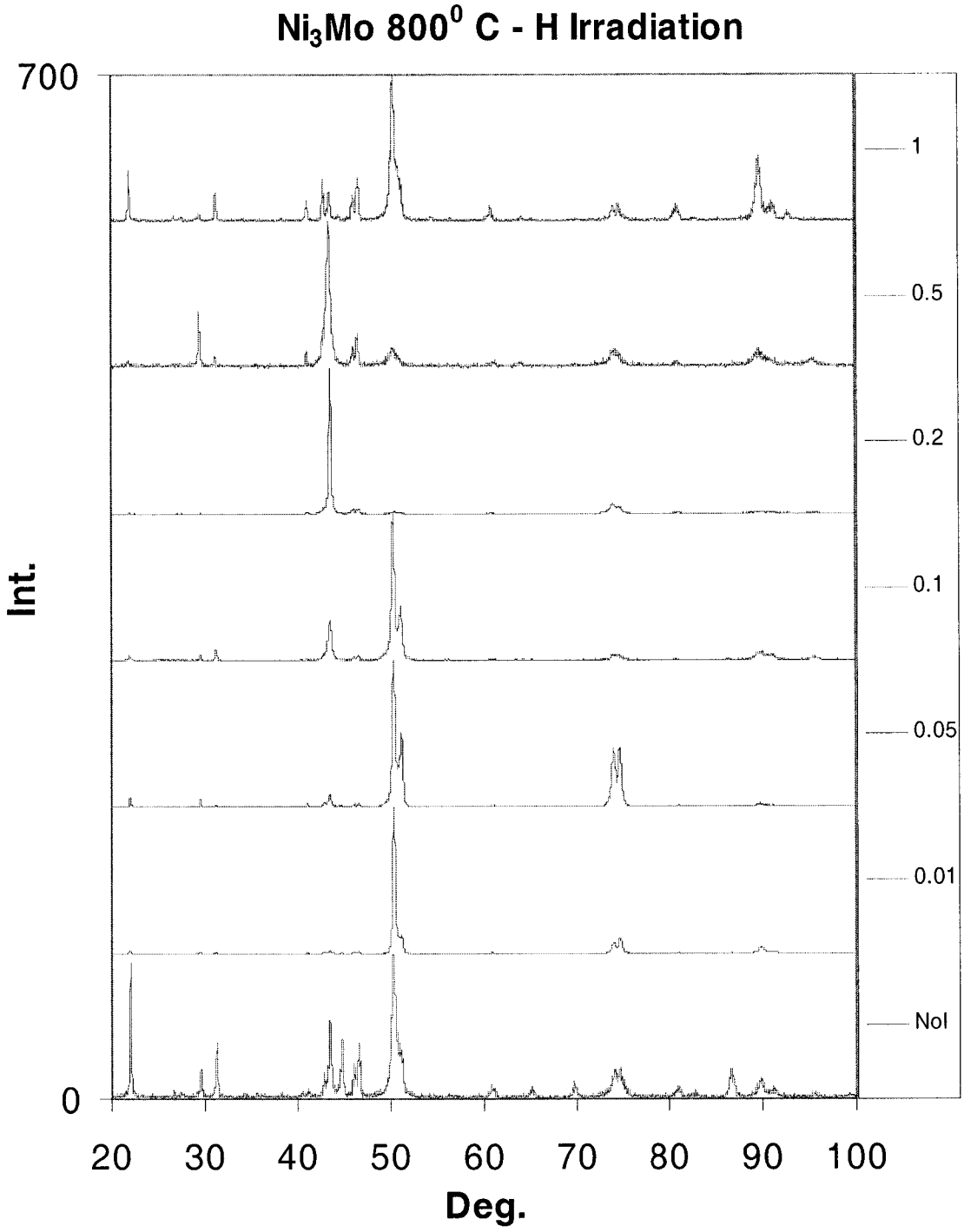

Figure 4.1.26 XRD spectra generated for Ni_3Mo samples annealed at 800^0 C samples irradiated with an H+ beam with a dose varying from 0.01 DPA to 1 DPA. The Intensity axis is in arbitrary units and is plotted as a function of the angle 2θ.

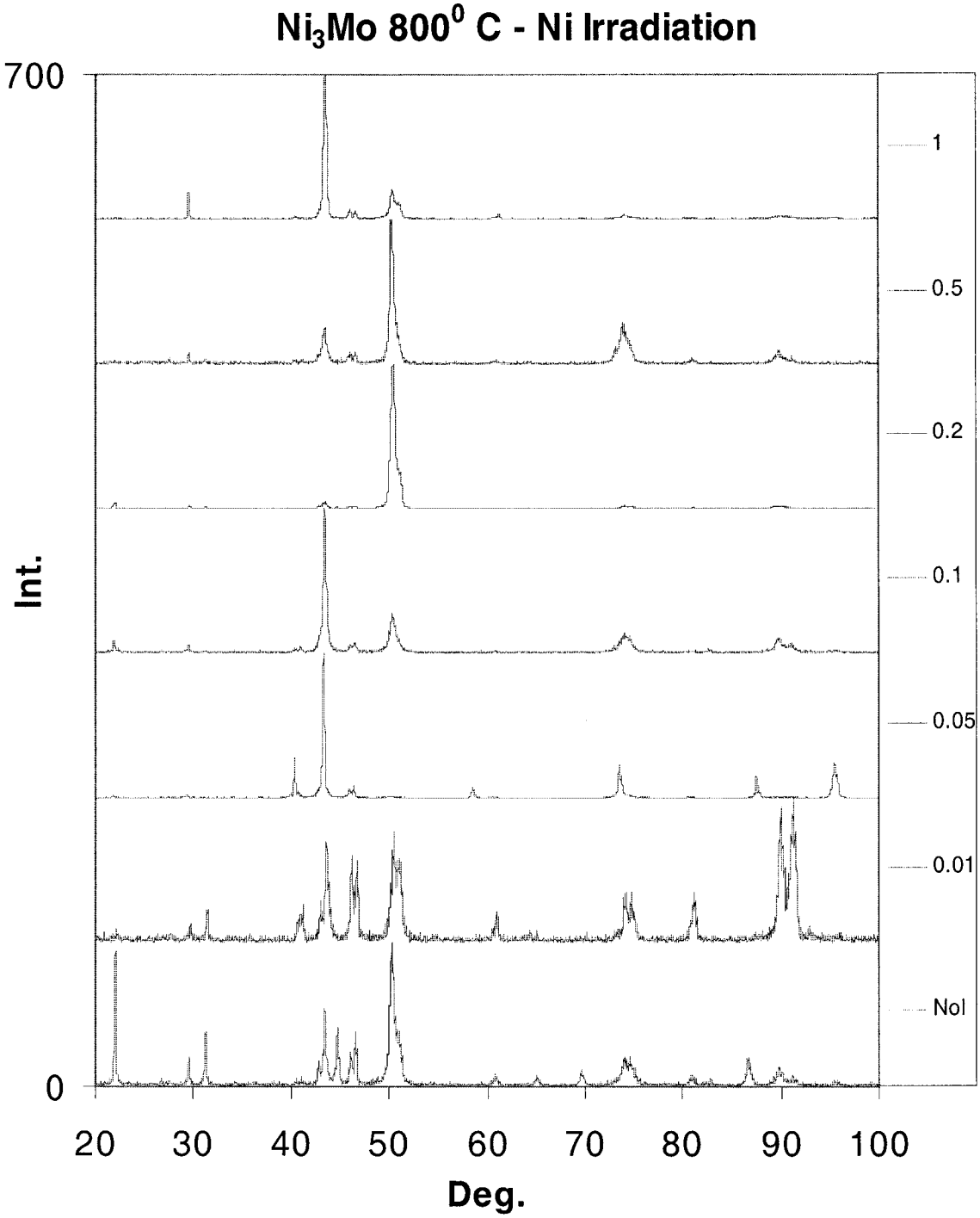

Figure 4.1.27 XRD spectra generated for Ni_3Mo samples annealed at 800^0 C irradiated with a Ni+ beam with a dose varying from 0.01 DPA to 1 DPA. The Intensity axis is in arbitrary units and is plotted as a function of the angle 2θ.

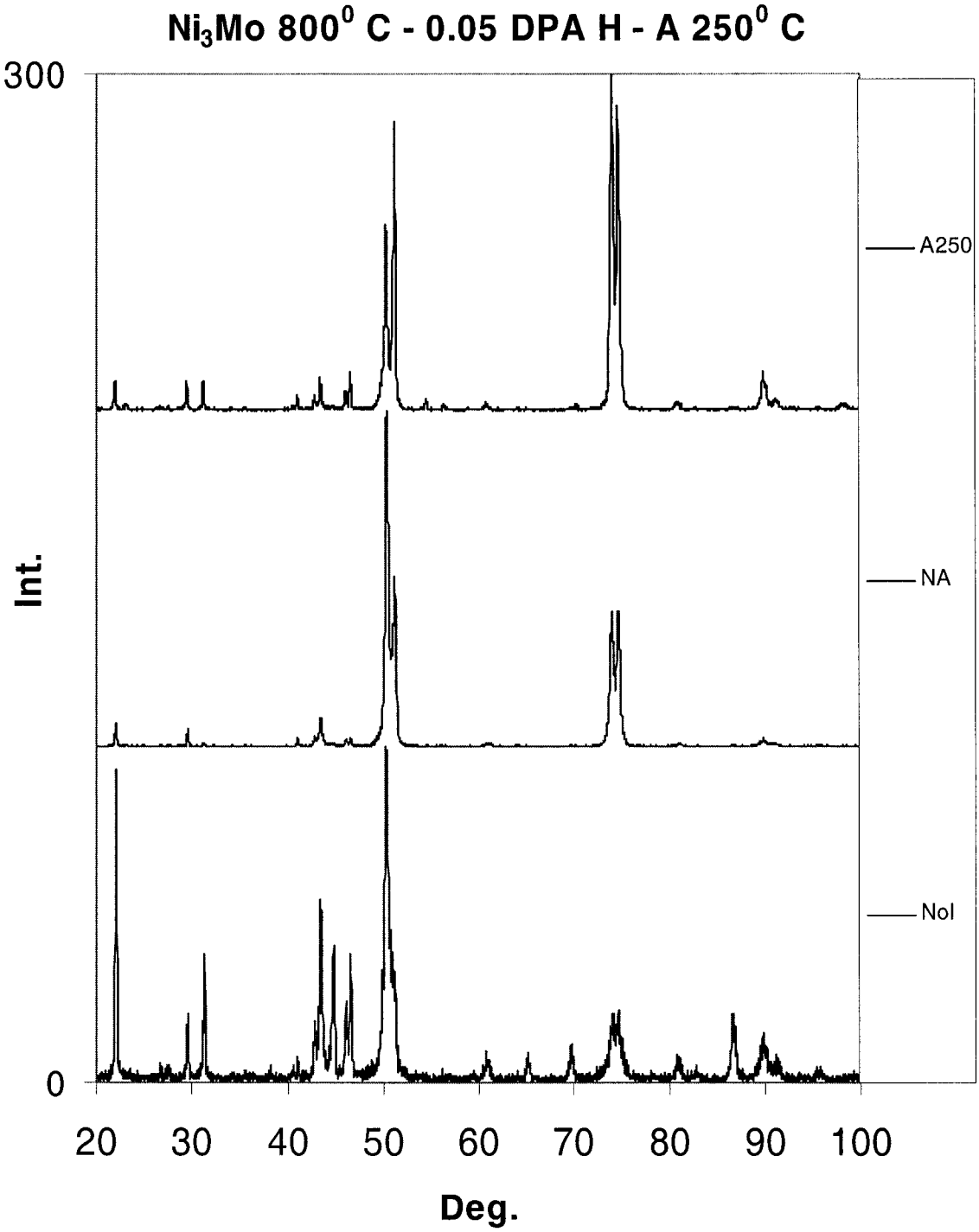

Figure 4.1.28 XRD spectra generated for Ni_3Mo samples annealed at 800^0 C before exposure to an H+ beam for a 0.05 DPA dose. After irradiation, the samples were annealed for three hours at 250^0 C. The Intensity axis is in arbitrary units and is plotted as a function of the angle 2θ.

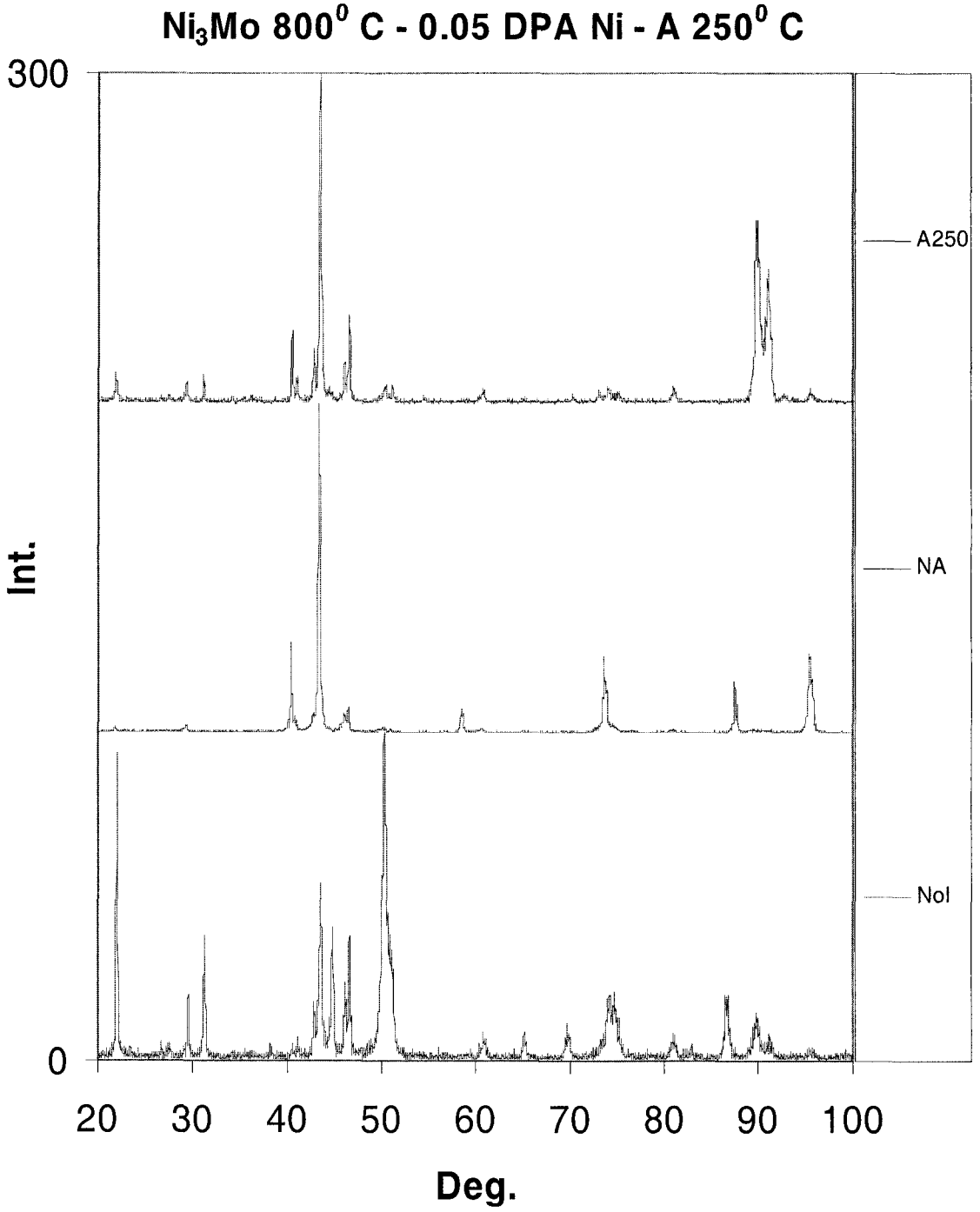

Figure 4.1.29 XRD spectra generated for Ni_3Mo samples annealed at 800^0 C before exposure to a Ni+ beam for a 0.05 DPA dose. After irradiation, the samples were annealed for three hours at 250^0 C. The Intensity axis is in arbitrary units and is plotted as a function of the angle 2θ.

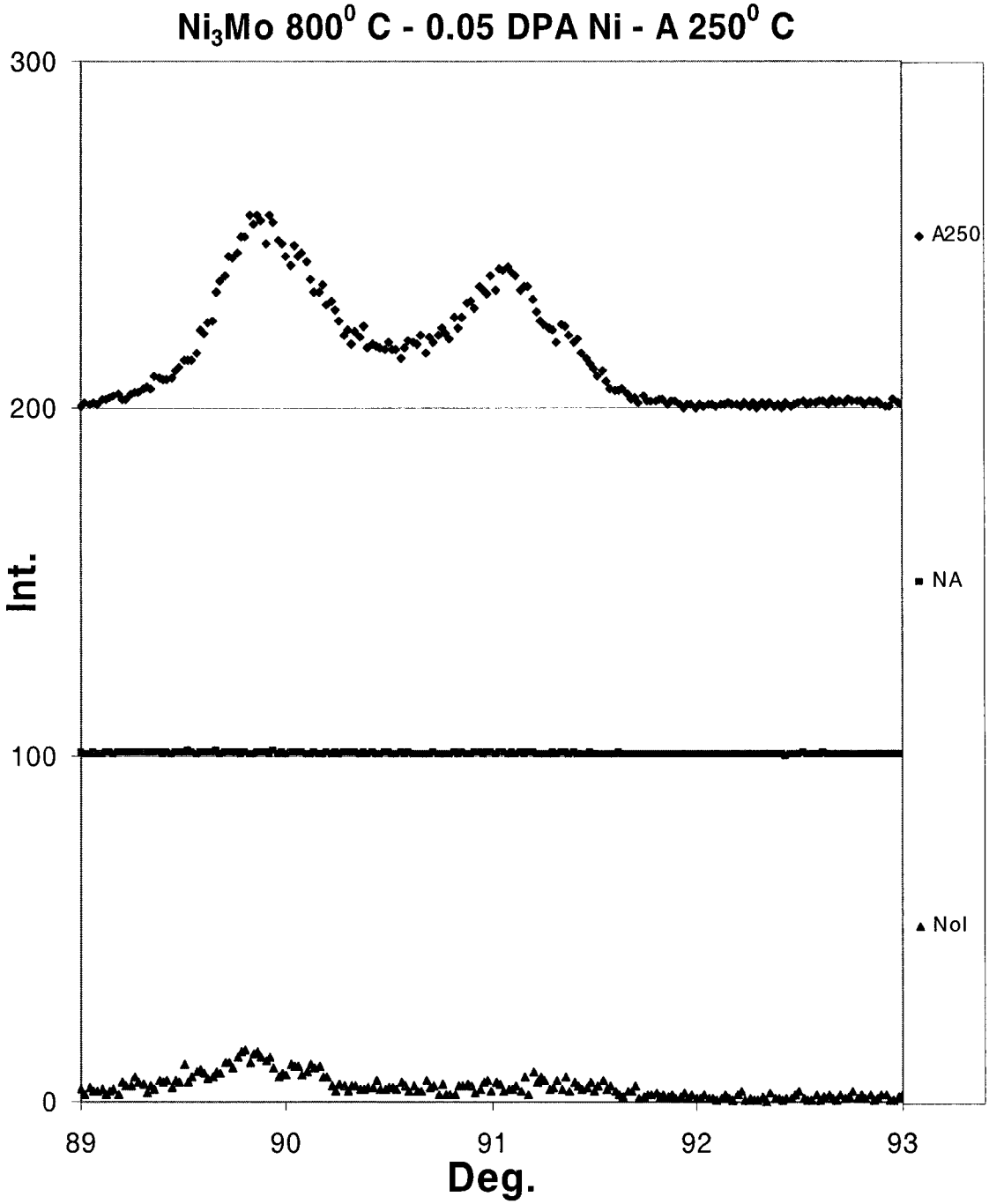

Figure 4.1.30 Detail of the XRD spectra from Figure 4.1.27 generated for Ni_3Mo samples pre-annealed at 800^0 C before exposure to a Ni+ beam for a 0.05 DPA dose. After irradiation, the samples were annealed for three hours at 250^0 C. The Intensity axis is in arbitrary units and is plotted as a function of the angle 2θ.

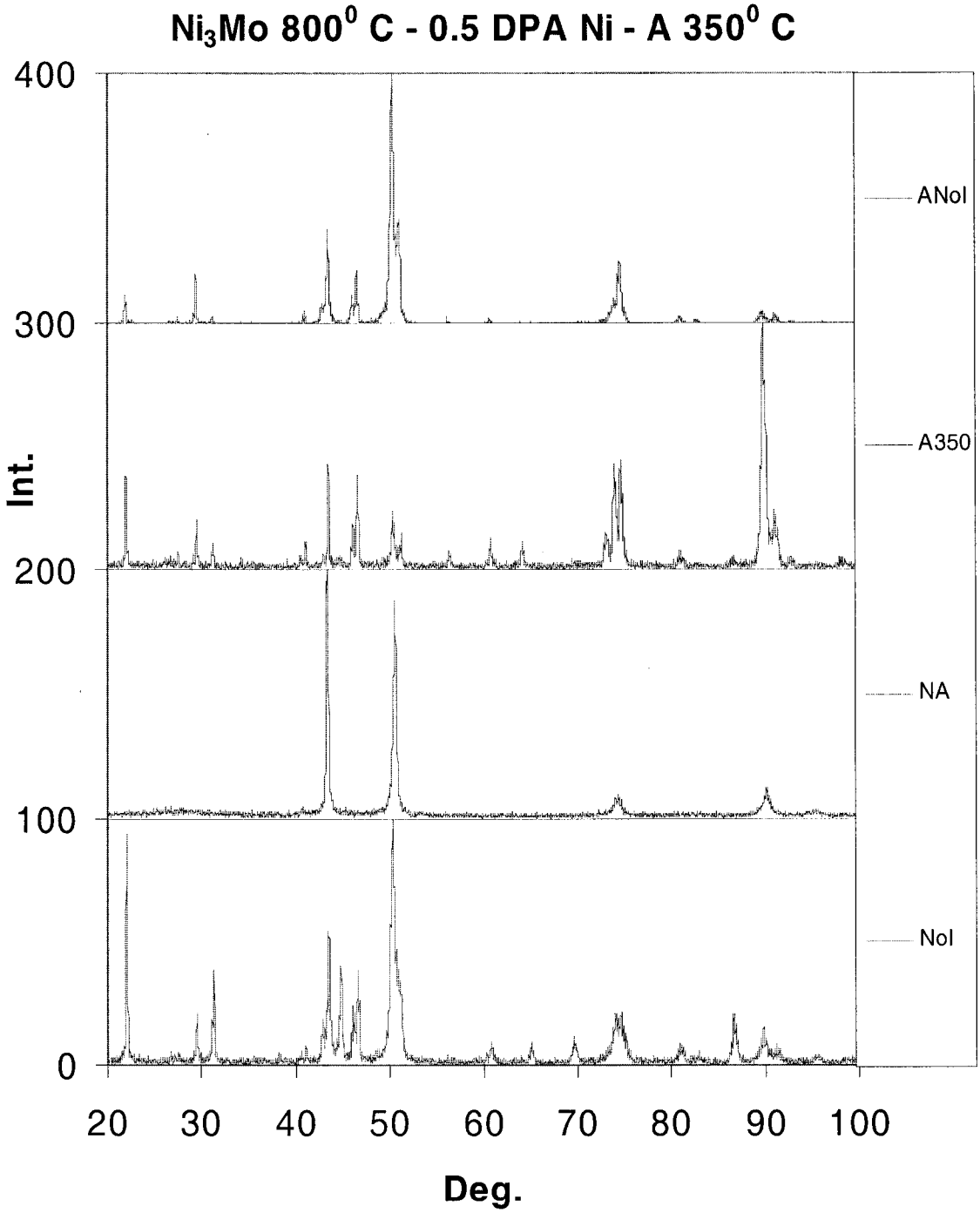

Figure 4.1.31 XRD spectra generated for Ni_3Mo samples annealed at 800^0 C before exposure to a Ni+ beam for a 0.5 DPA dose. After irradiation, the samples were annealed for three hours at 350^0 C. The Intensity axis is in arbitrary units and is plotted as a function of the angle 2θ. Spectra are compared with spectrum from sample with annealing but NoI.

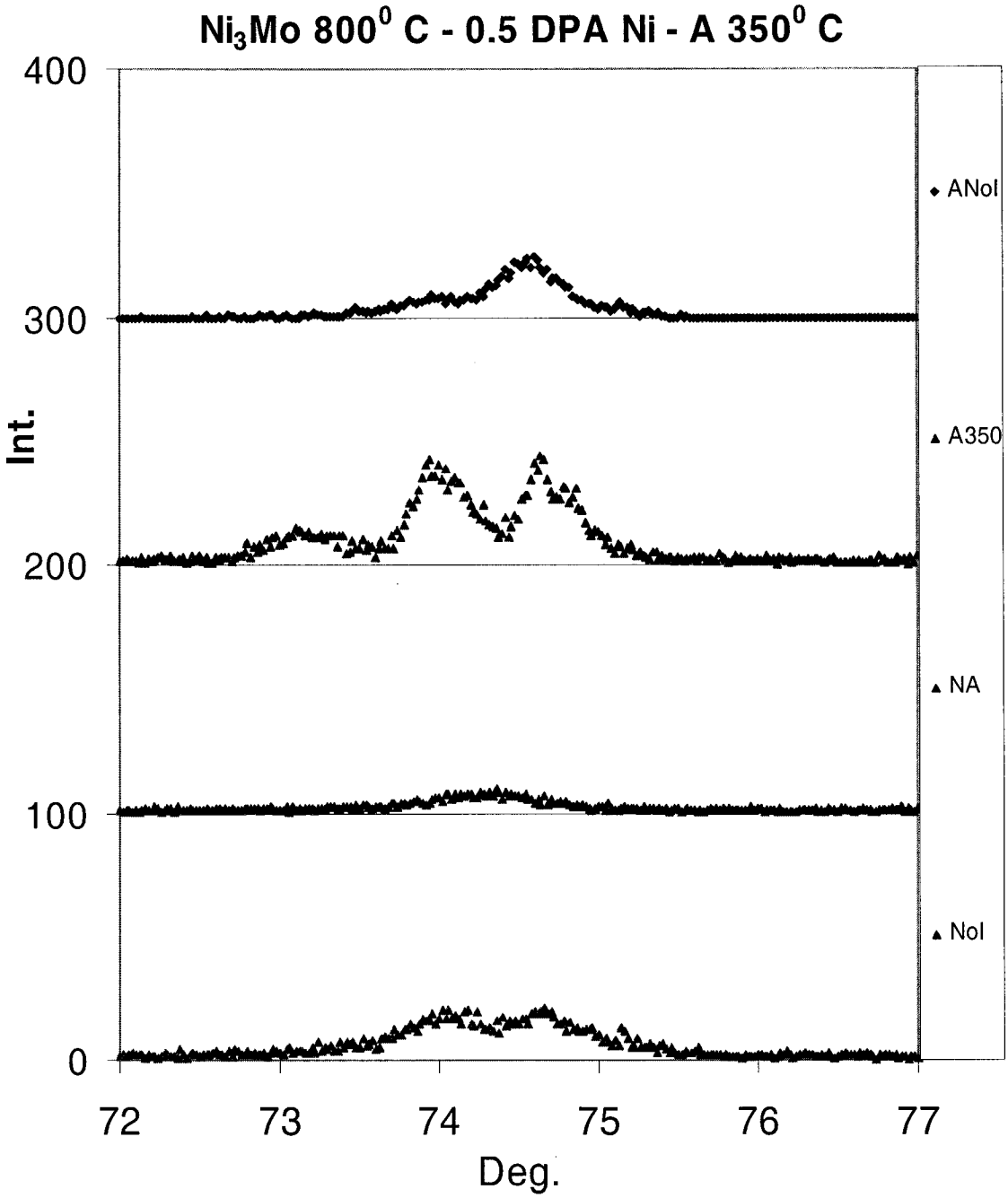

Figure 4.1.32 Detail #1 of the XRD spectra generated for Ni_3Mo samples annealed at 800^0 C before exposure to a Ni+ beam for a 0.5 DPA dose. After irradiation, the samples were annealed for three hours at 350^0 C. The Intensity axis is in arbitrary units and is plotted as a function of the angle 2θ. Spectra are compared with spectrum from sample with annealing but NoI.

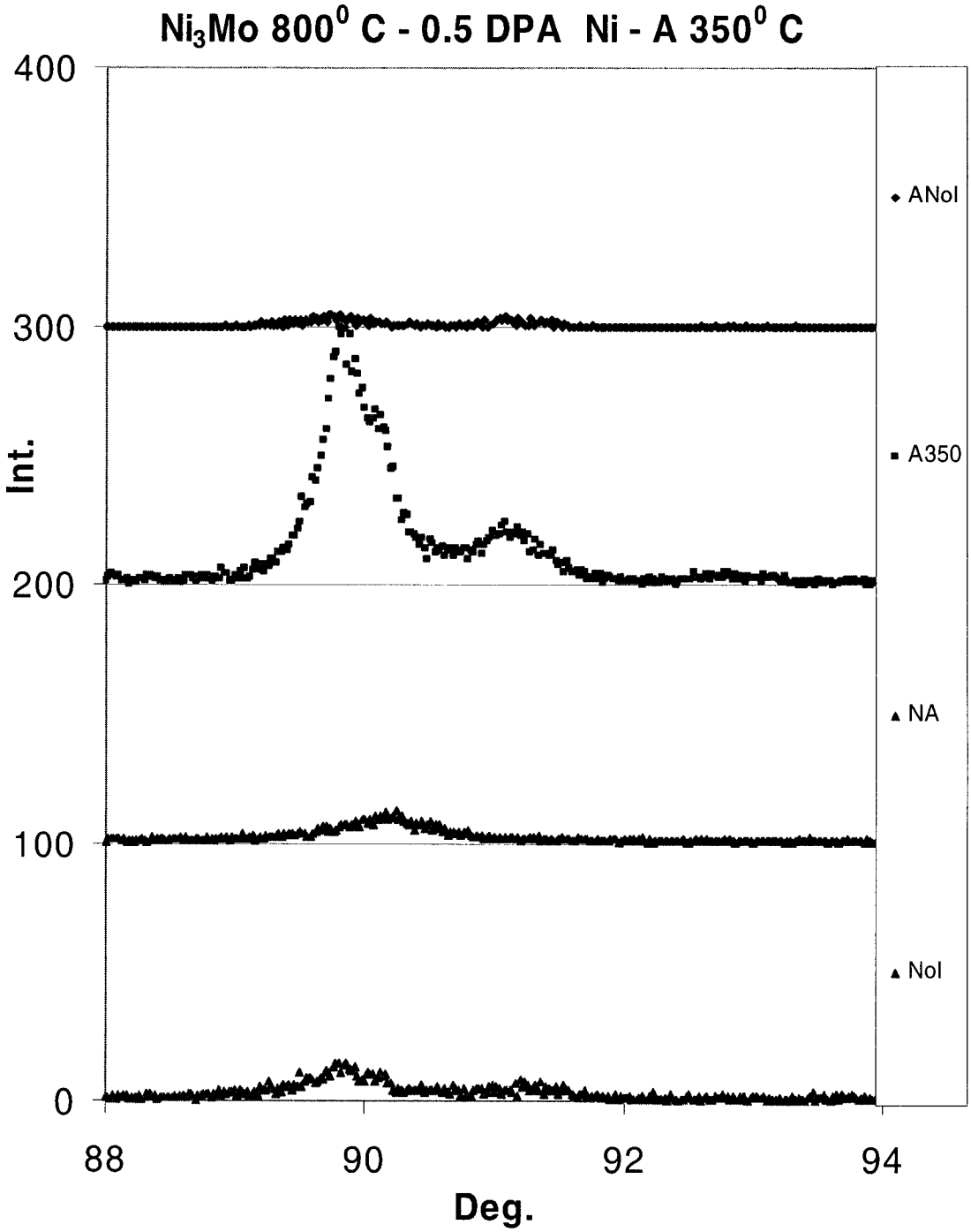

Figure 4.1.33 Detail #2 of the XRD spectra generated for Ni_3Mo samples annealed at 800^0 C before exposure to a Ni+ beam for a 0.5 DPA dose. After irradiation, the samples were annealed for three hours at 350^0 C. The Intensity axis is in arbitrary units and is plotted as a function of the angle 2θ. Spectra are compared with spectrum from sample with annealing but NoI.

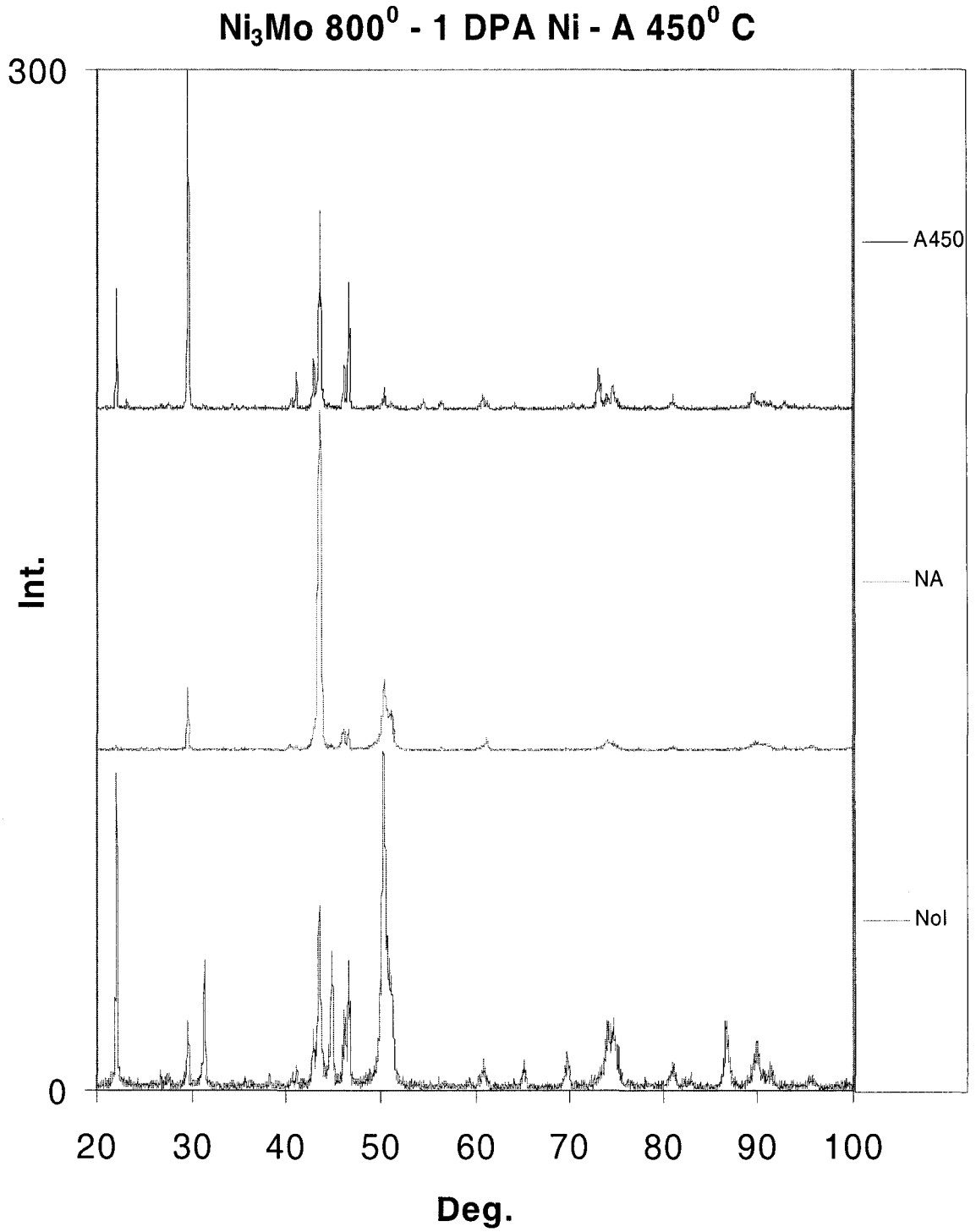

Figure 4.1.34 XRD spectra generated for Ni_3Mo samples annealed at 800^0 C before exposure to a Ni+ beam for a 1 DPA dose. After irradiation, the samples were annealed for three hours at 450^0 C. The Intensity axis is in arbitrary units and is plotted as a function of the angle 2θ.

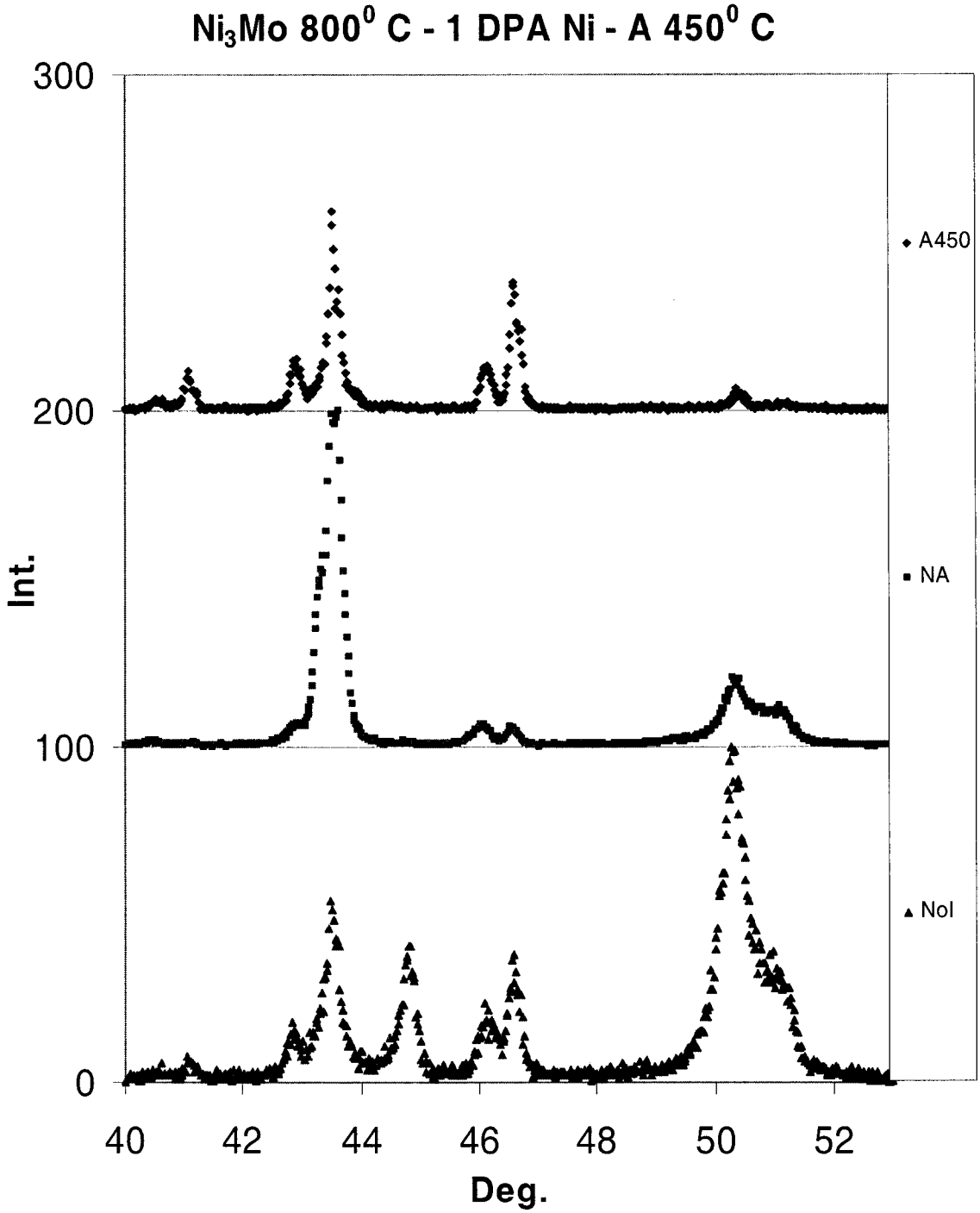

Figure 4.1.35 Detail #1 of the XRD spectra from Figure 4.1.32 generated for Ni_3Mo samples annealed at 800^0 C before exposure to a Ni+ beam for a 1 DPA dose. After irradiation, the samples were annealed for three hours at 450^0 C. The Intensity axis is in arbitrary units and is plotted as a function of the angle 2θ.

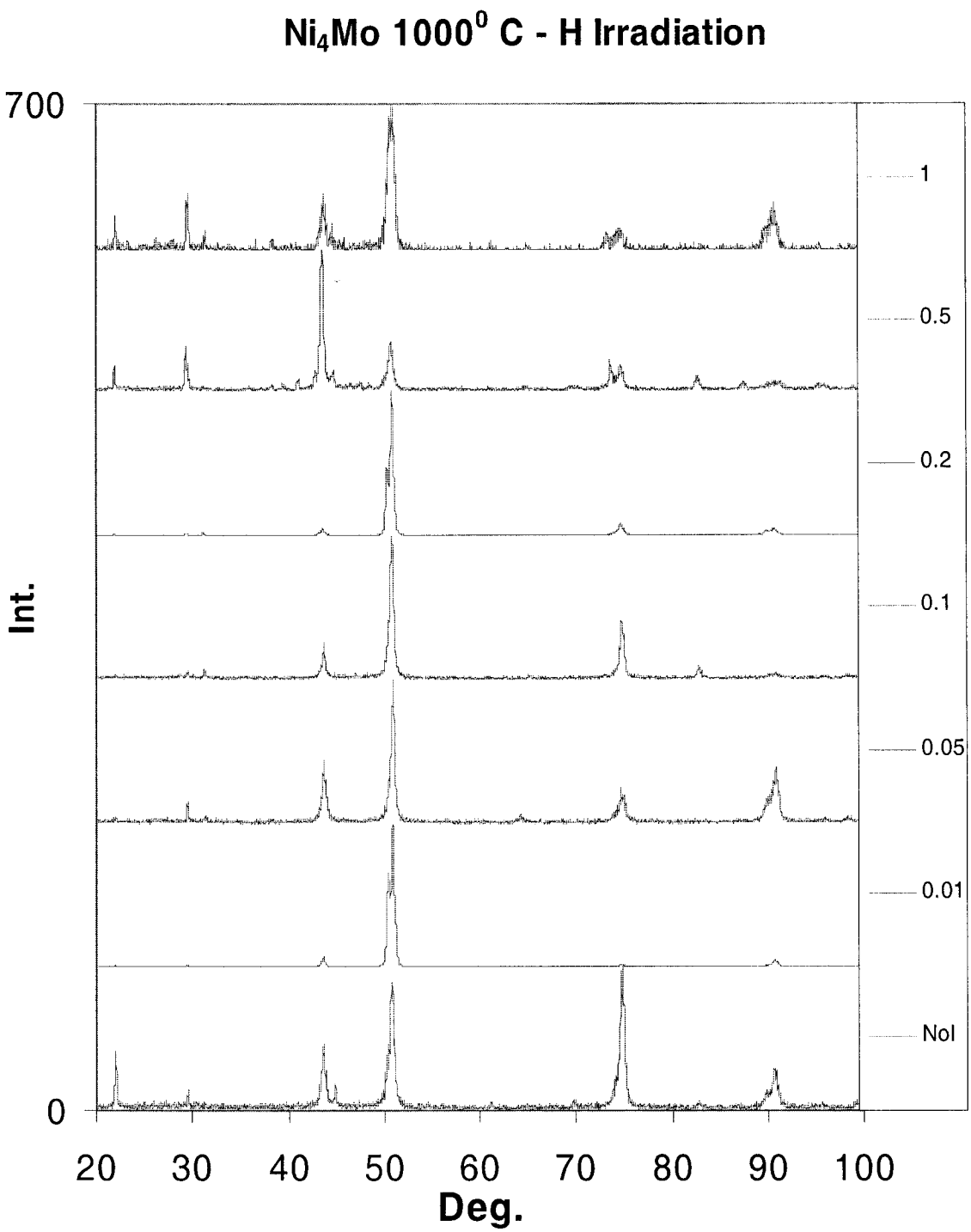

Figure 4.1.36 XRD spectra generated for Ni_4Mo samples annealed at 1000^0 C irradiated with an H+ beam with a dose varying from 0.01 DPA to 1 DPA. The Intensity axis is in arbitrary units and is plotted as a function of the angle 2θ.

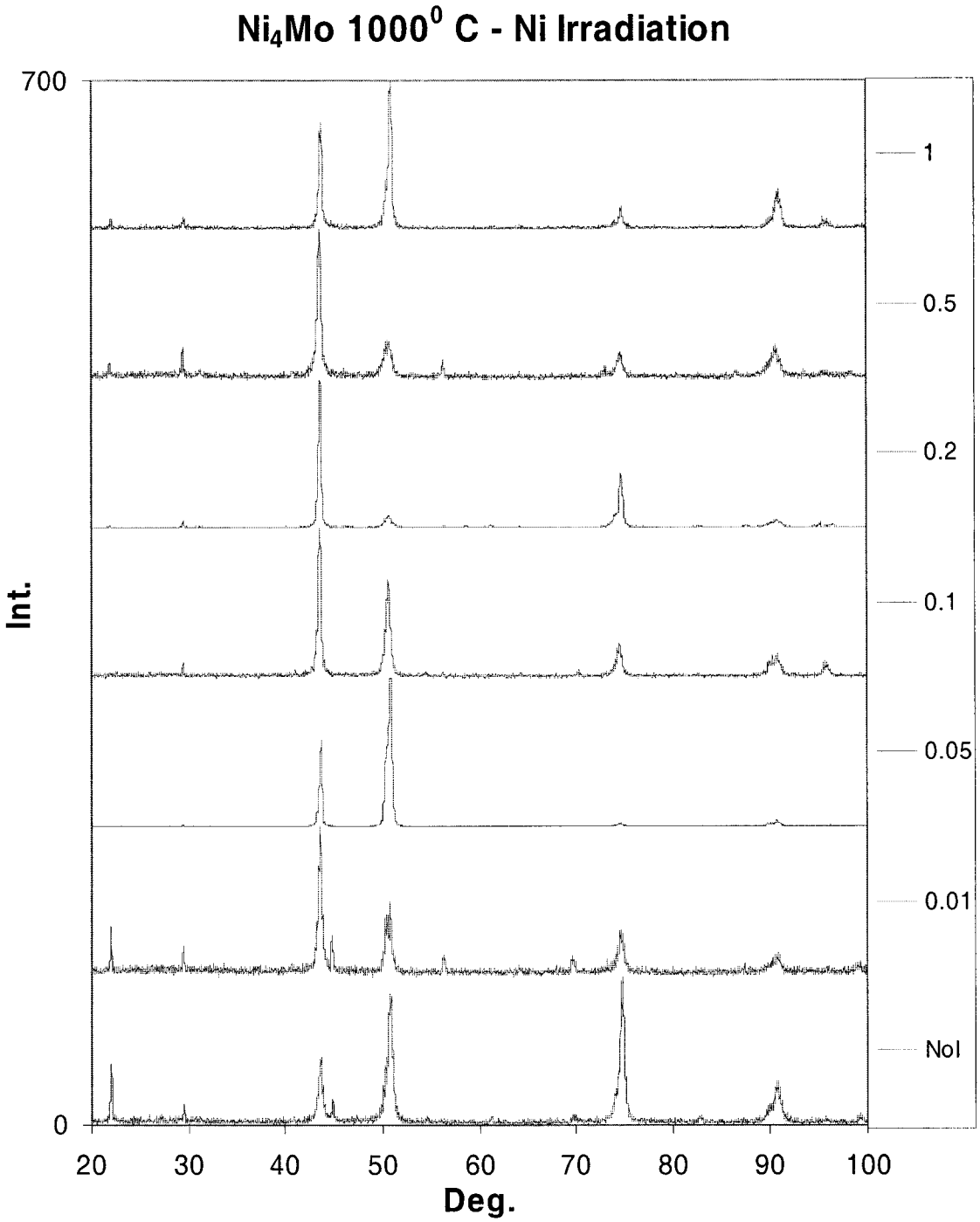

Figure 4.1.37 XRD spectra generated for Ni_4Mo annealed at 1000^0 C samples irradiated with a Ni+ beam with a dose varying from 0.01 DPA to 1 DPA. The Intensity axis is in arbitrary units and is plotted as a function of the angle 2θ.

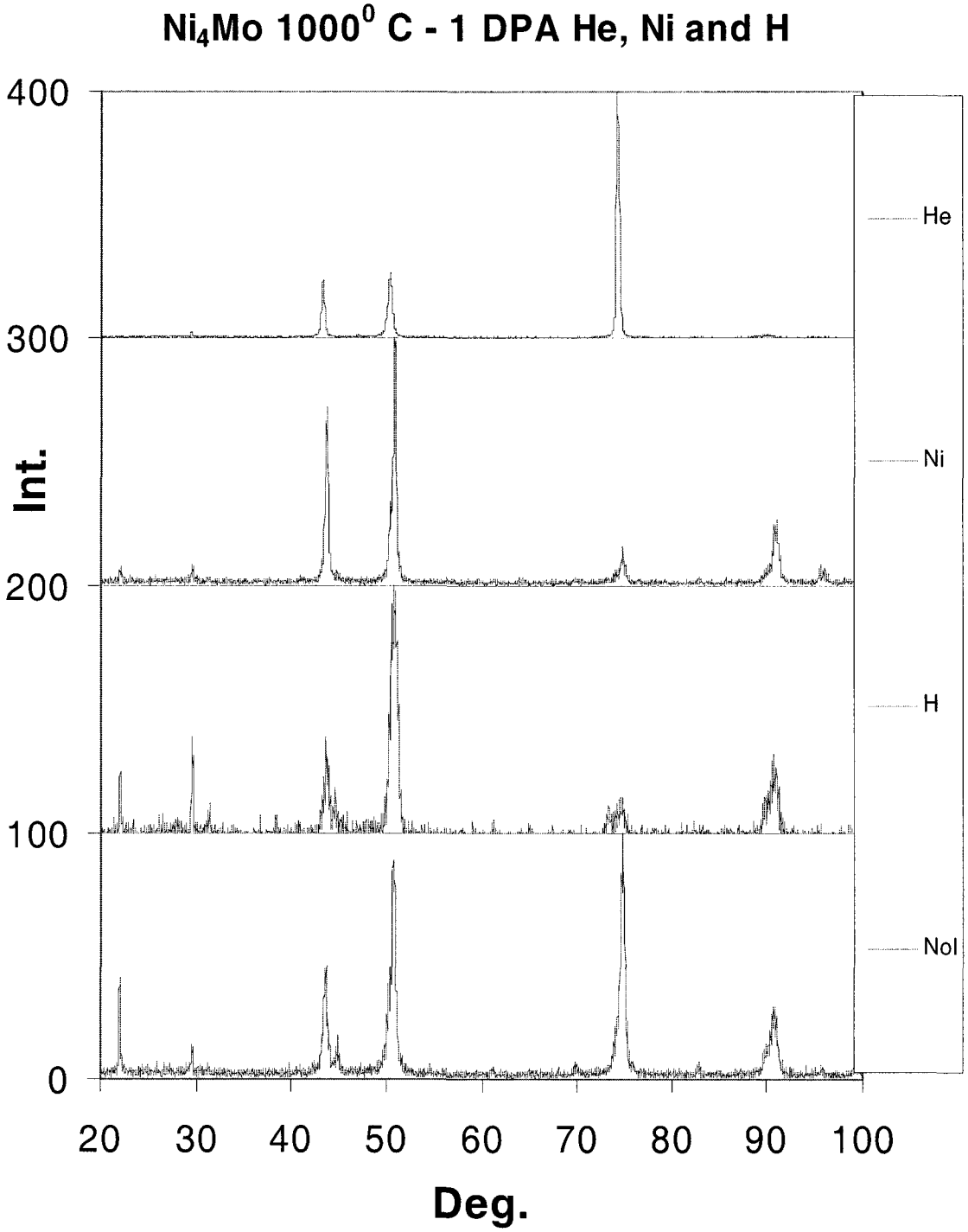

Figure 4.1.38 XRD spectra generated for Ni_4Mo samples annealed at 1000^0 C before exposure to a He+, Ni+ and a H+ beam for a 1 DPA dose. The Intensity axis is in arbitrary units and is plotted as a function of the angle 2θ.

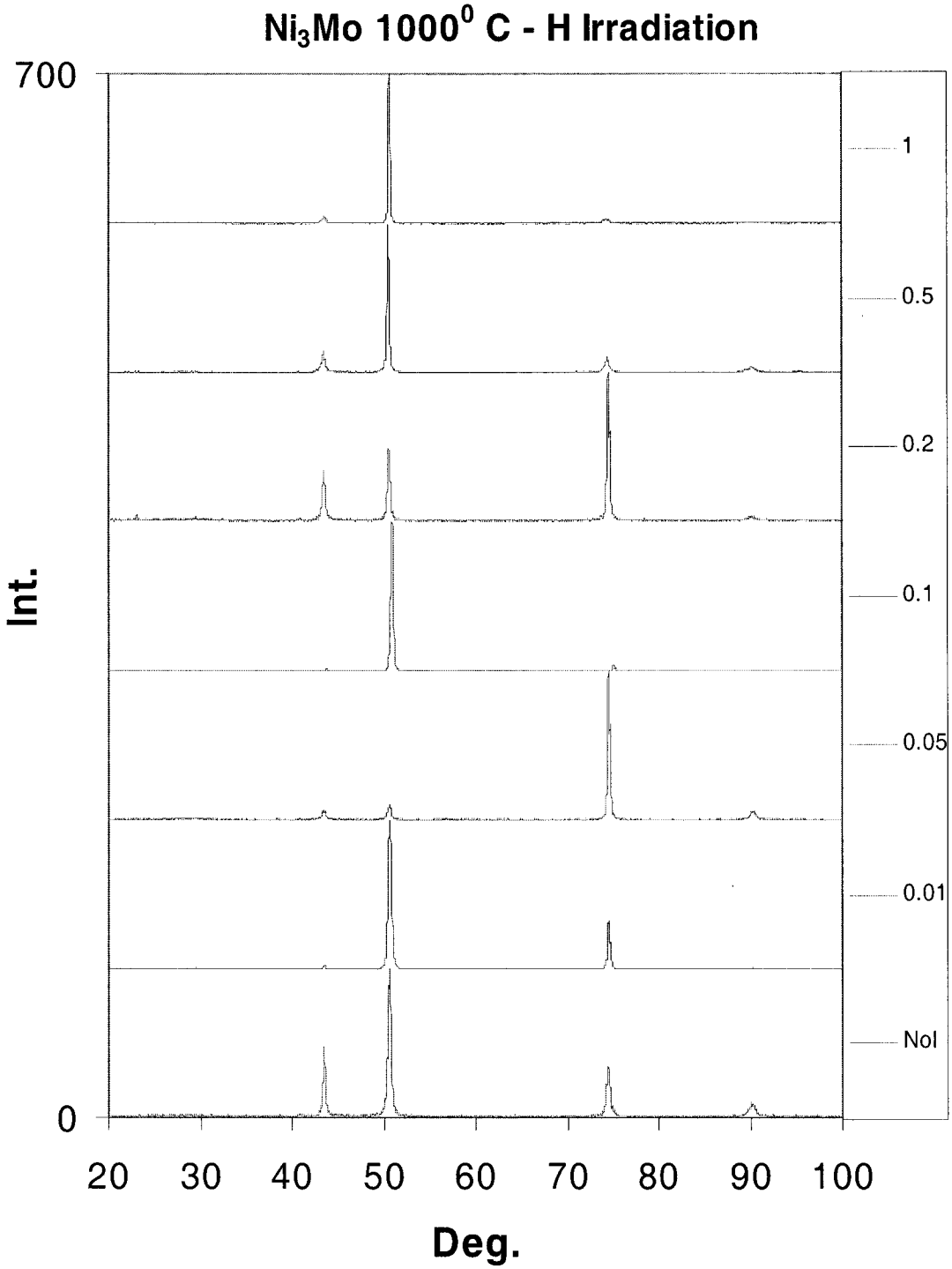

Figure 4.1.39 XRD spectra generated for Ni_3Mo samples annealed at 1000^0 C irradiated with an H+ beam with a dose varying from 0.01 DPA to 1 DPA. The Intensity axis is in arbitrary units and is plotted as a function of the angle 2θ.

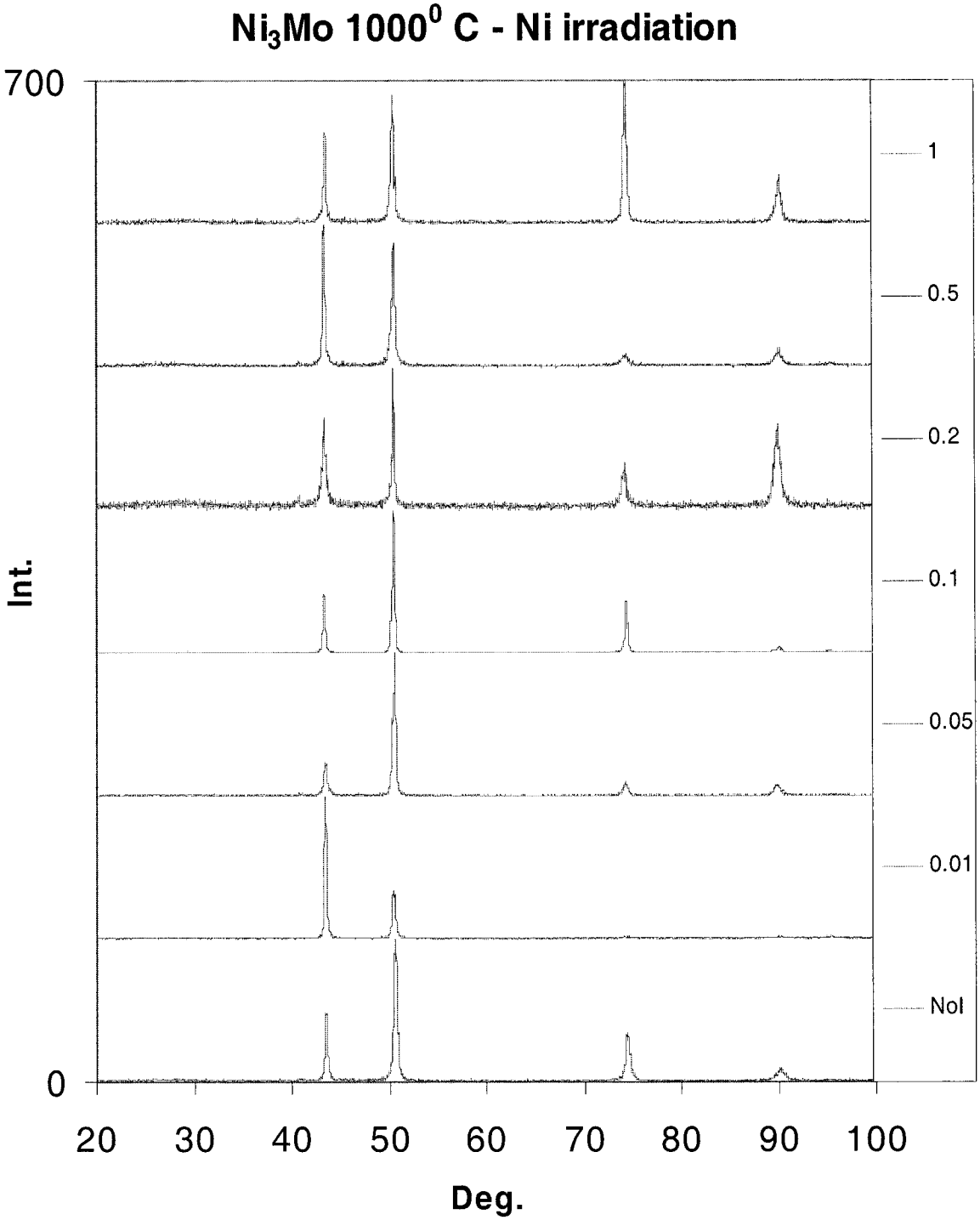

Figure 4.1.40 XRD spectra generated for Ni_3Mo samples annealed at 1000^0 C irradiated with a Ni+ beam with a dose varying from 0.01 DPA to 1 DPA. The Intensity axis is in arbitrary units and is plotted as a function of the angle 2θ.

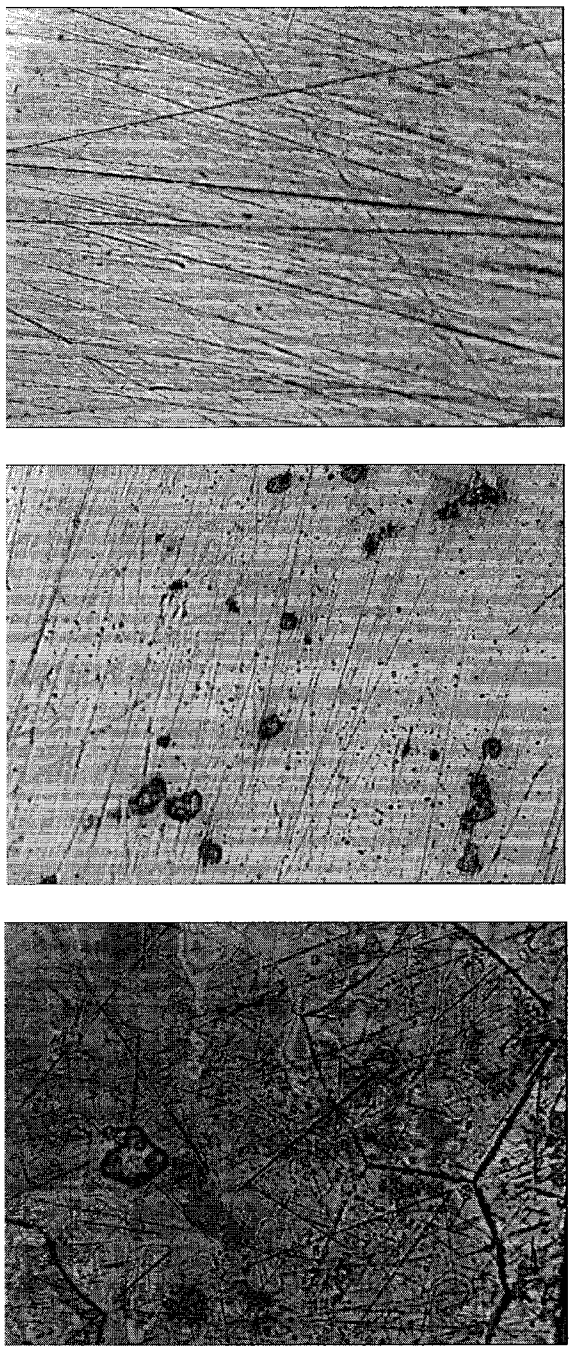

Figure 4.2.1 Surface evolution for Ni irradiation in Ni_4Mo: (A) shows the surface of a sample before irradiation, (B) shows the surface after exposure to 0.1 DPA of Ni beam and (C) after exposure to 0.5 DPA of Ni beam.

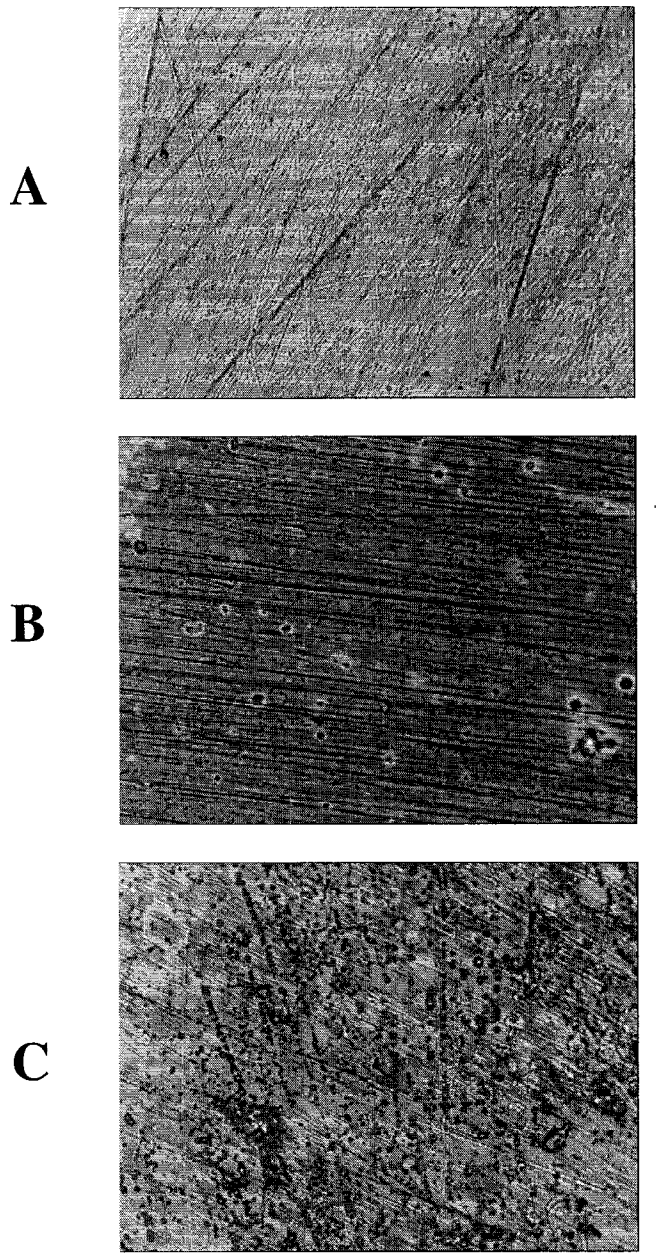

Figure 4.2.2 Surface evolution for Ni^{+} irradiation in Ni_4Mo annealed to 800^0 C prior to irradiation: (A) shows the surface of a sample before irradiation, (B) shows the surface after exposure to 0.1 DPA of Ni beam and (C) after exposure to 1 DPA of Ni beam.

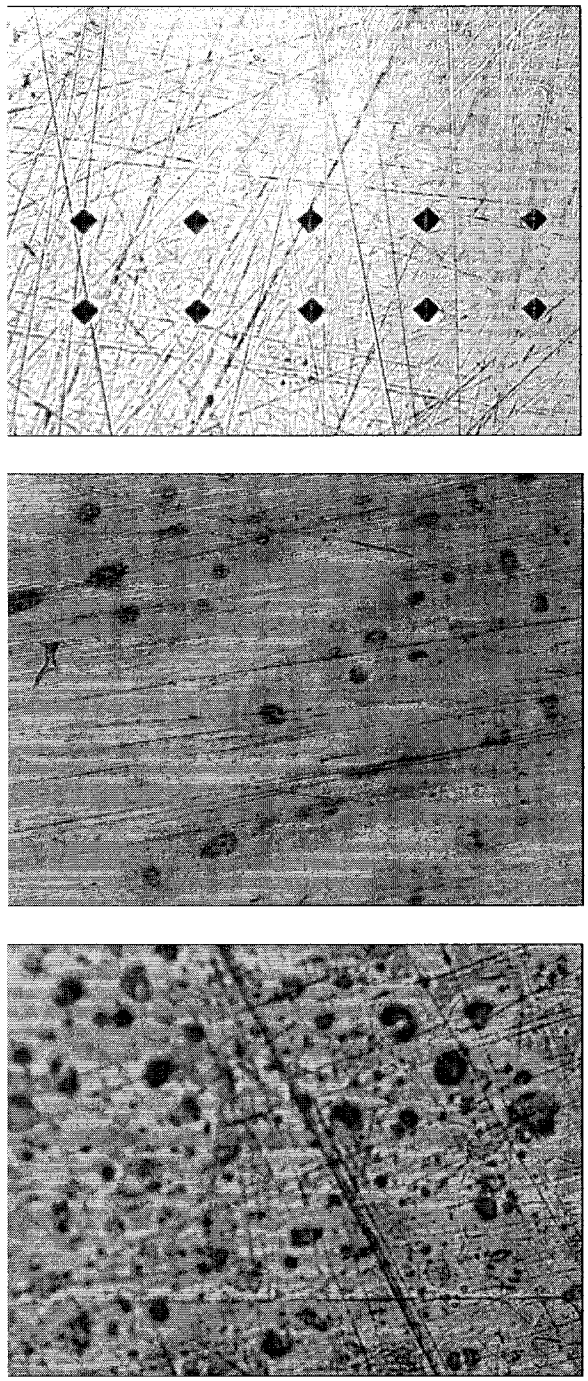

Figure 4.2.3 Surface evolution for Ni irradiation in Ni_3Mo as cast (A) shows the surface of a sample before irradiation (B) shows the surface after exposure to 0.2 DPA of Ni beam and (C) after exposure to 1 DPA of Ni beam.

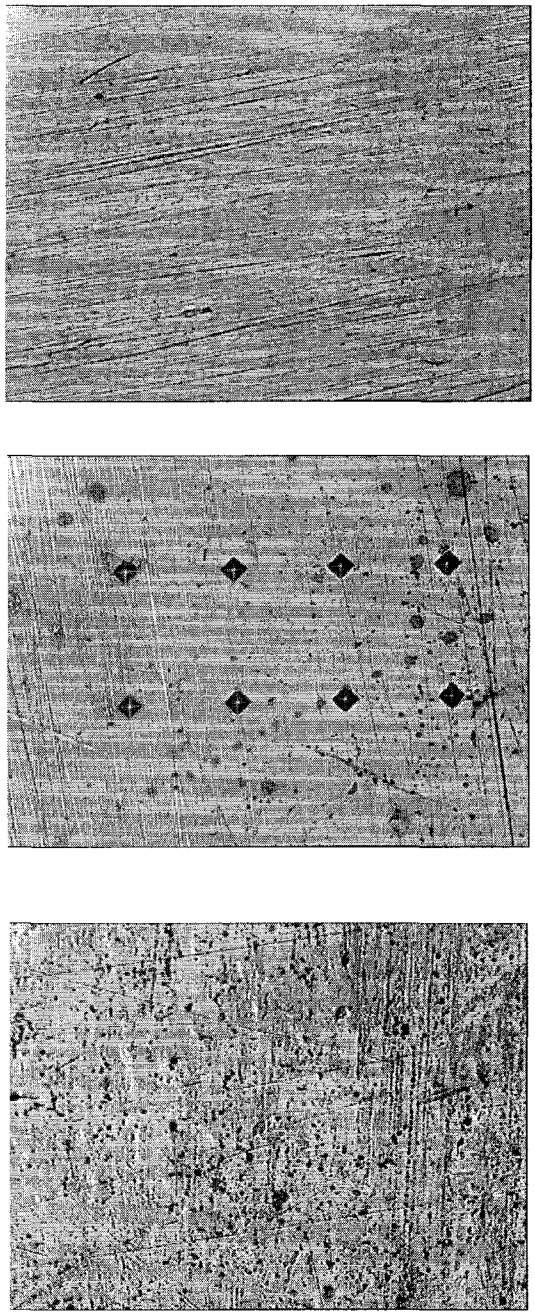

Figure 4.2.4 Surface evolution for H irradiation in Ni_3Mo annealed at 800^0 C prior to irradiation: (A) shows the surface of a sample before irradiation, (B) shows the surface after exposure to 0.2 DPA of Ni beam and (C) after exposure to 1 DPA of Ni beam.

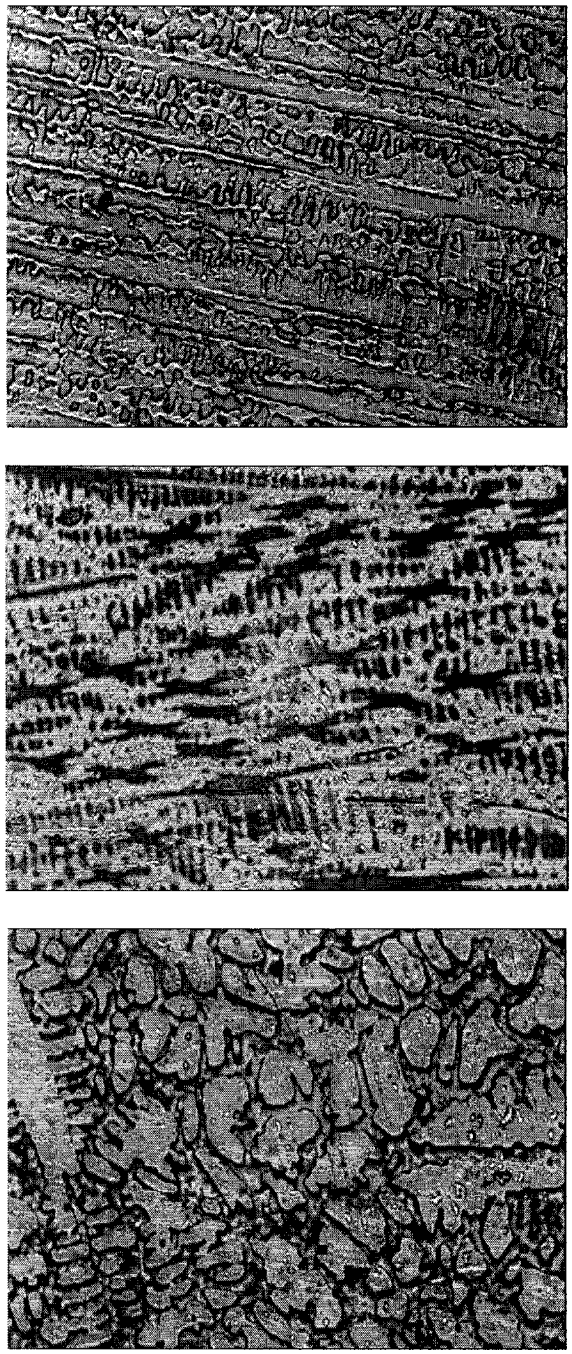

Figure 4.2.5 Surface picture after etching in an acid solution of Ni_3Mo (A) as cast, (B) annealed at 800^0 C prior to irradiation of 0.1 DPA of Ni beam and (C) annealed at 800^0 C prior to irradiation to 1 DPA of Ni beam.

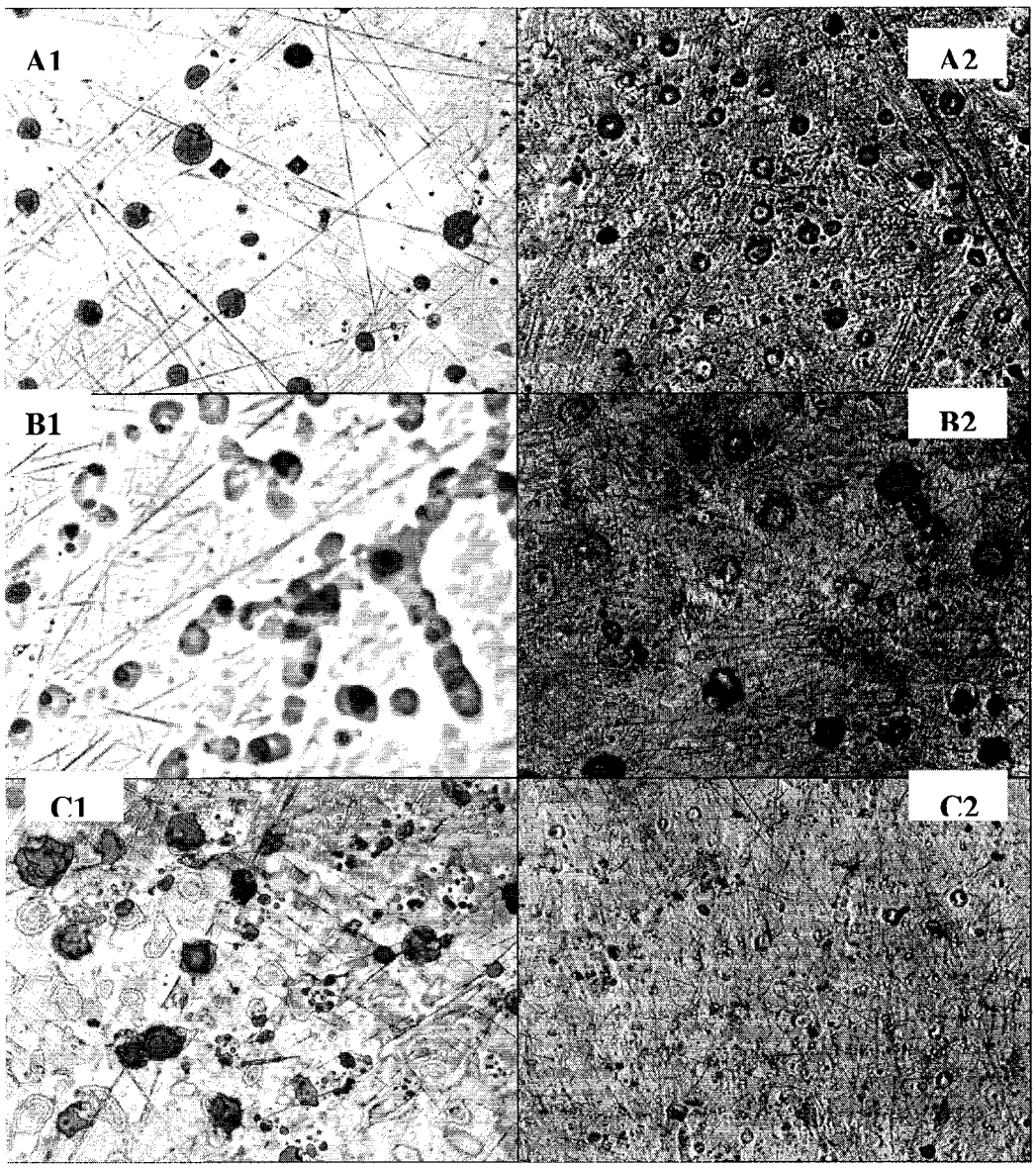

Figure 4.2.6 Surface of samples after Ni^+ (index 1) and H^+ (index 2) irradiations to a dose of 0.5 DPA and annealed at 450^0C after exposure. (A1 – A2) Ni_4Mo as cast, (B1-B2) Ni_4Mo annealed at 800^0 C prior to irradiation and (C1-C2) Ni_4Mo annealed at 1000^0 C prior to irradiation.

A

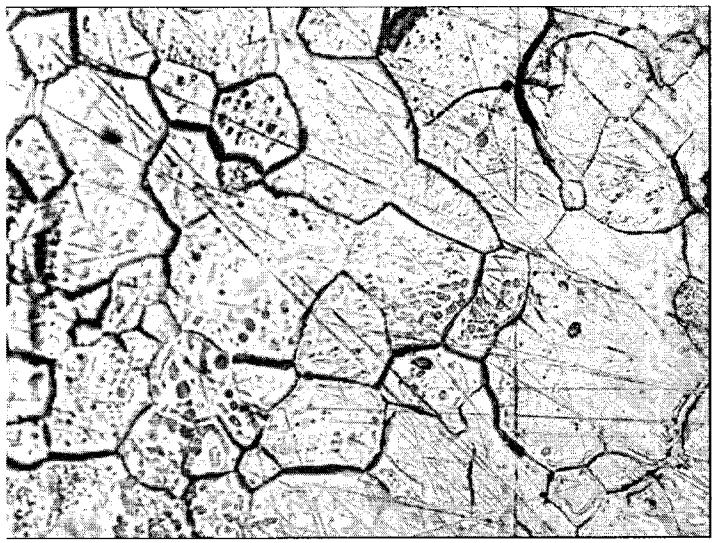

B

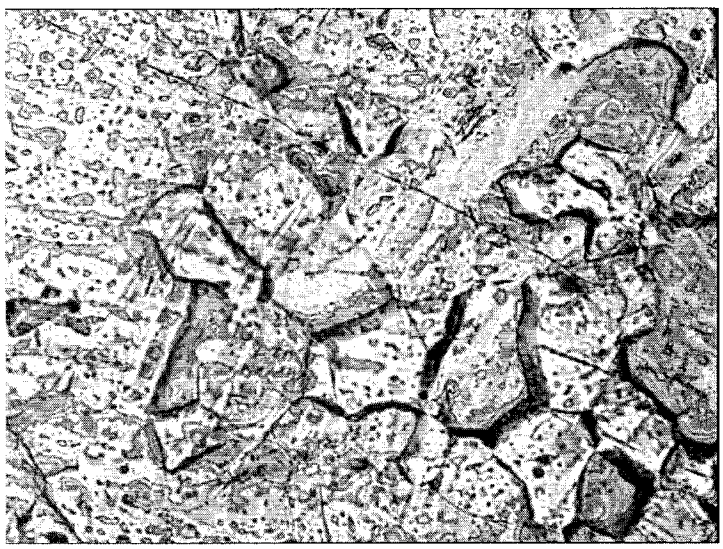

Figure 4.2.7 Surface picture showing the exposed grain boundaries in Ni_4Mo pre-annealed at 800^0 C exposed to (A) 0.5 DPA Ni and (B) 0.5 DPA H and annealed at 350^0 C after irradiation.

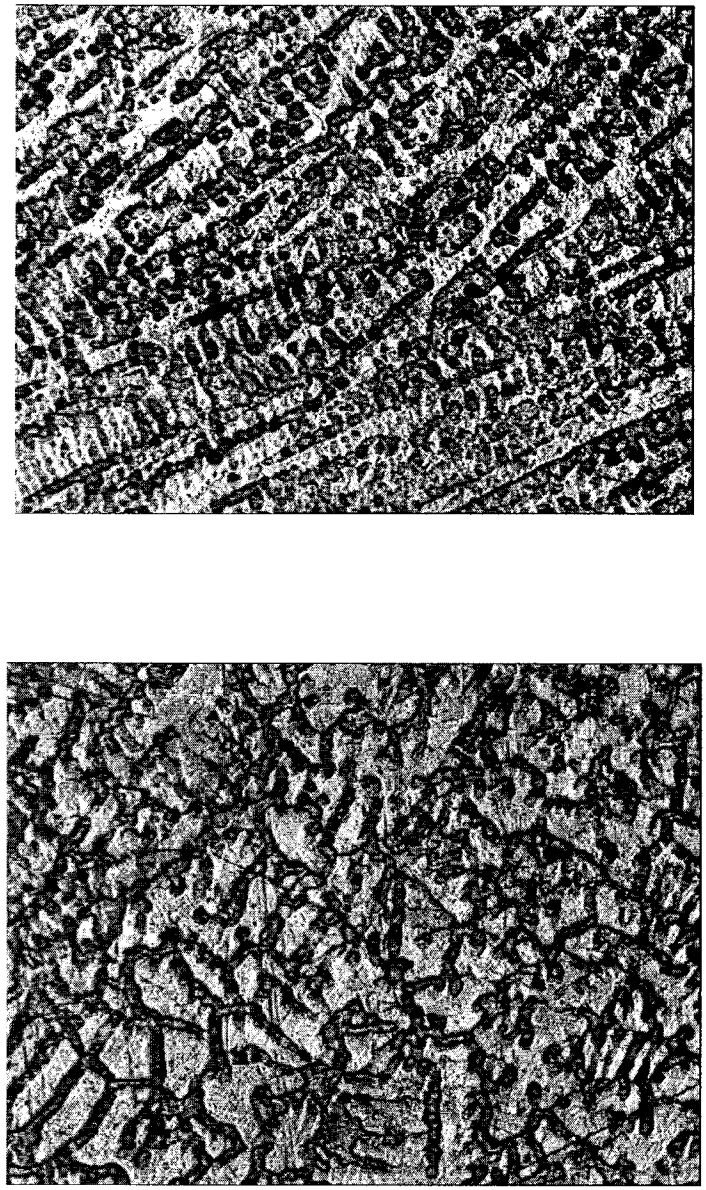

Figure 4.2.8 Surface exposure by acid etching of Ni_4Mo pre-annealed to 1000^0 C prior to irradiation to 1 DPA H. (A) shows the surface before post-irradiation annealing at 350^0 C and (B) after the post-irradiation annealing.

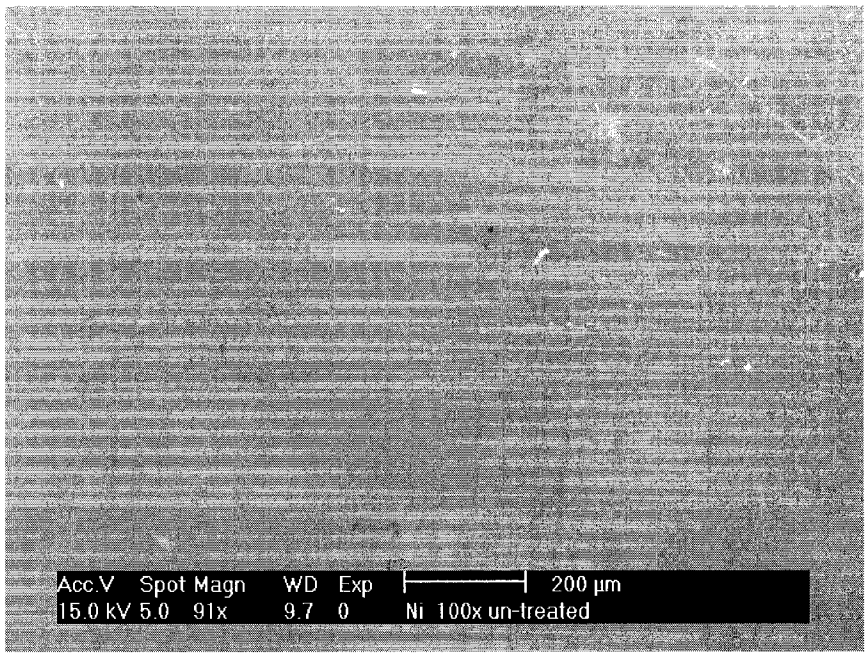

Figure 4.2.9 Surface of Ni before irradiation.

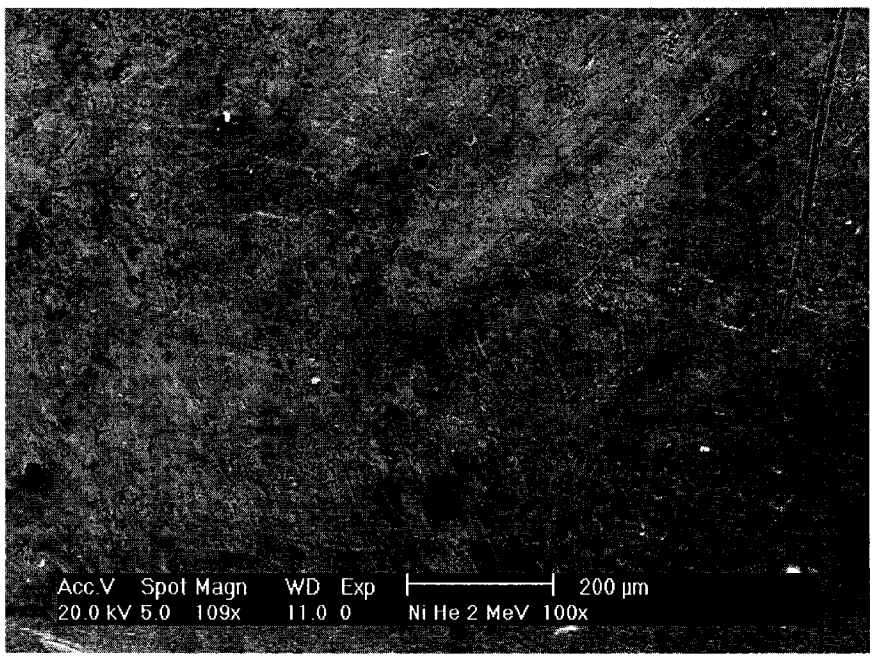

Figure 4.2.10 Surface of Nickel after being irradiated to 1 DPA He+ beam.

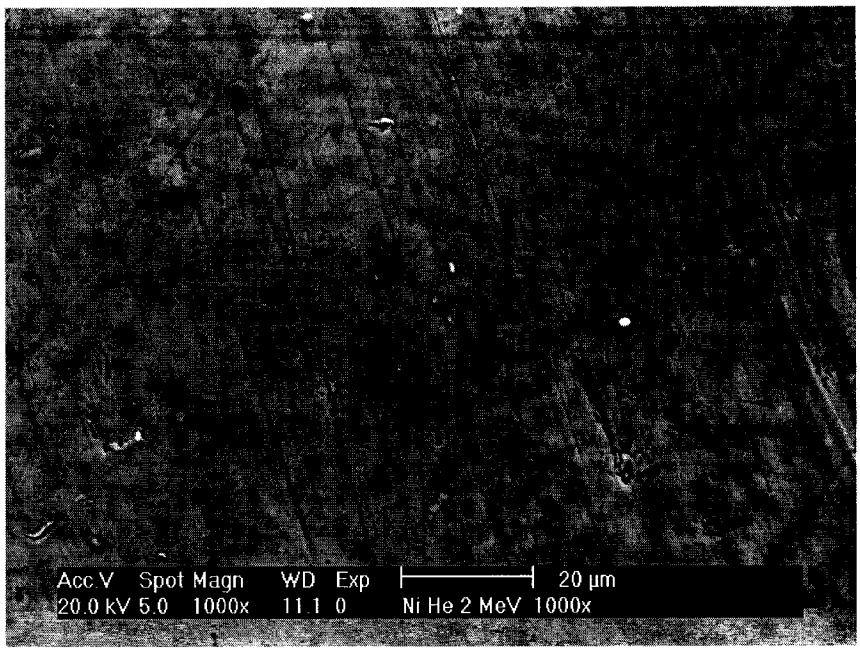

Figure 4.2.11 Surface of Nickel after 1 DPA He^+ in higher magnification.

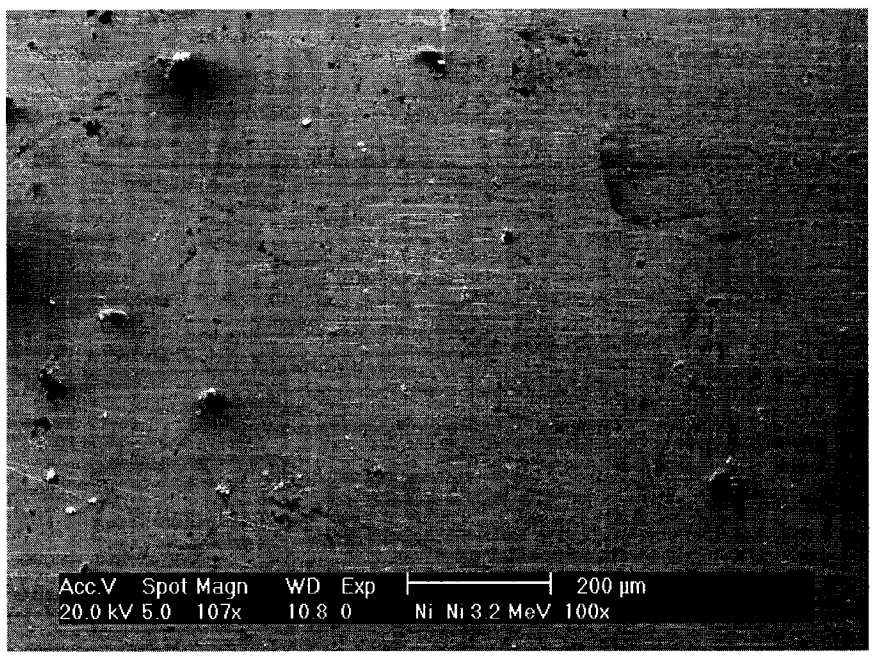

Figure 4.2.12 Surface of Ni after 1 DPA Ni^+ beam irradiation.

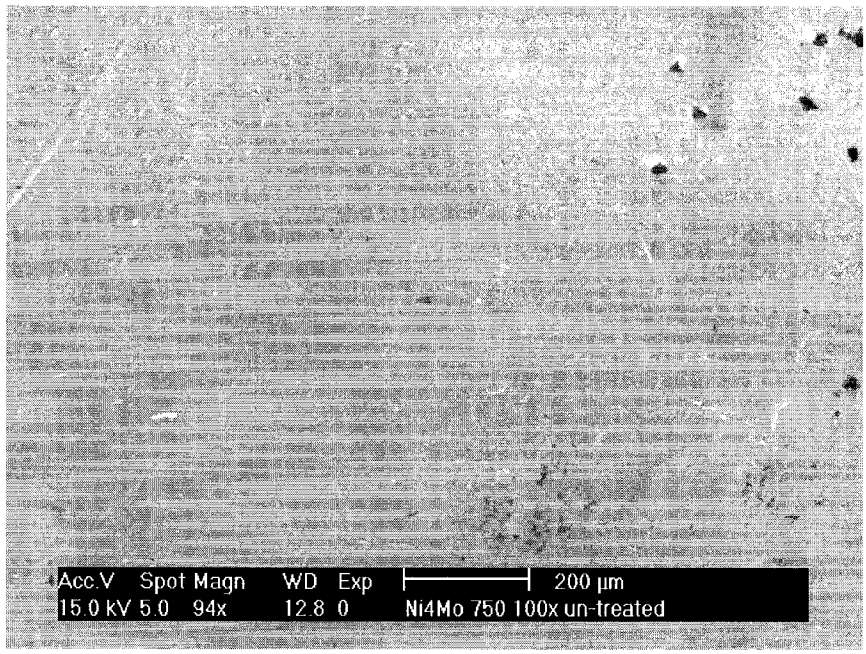

Figure 4.2.13 Surface of Ni_4Mo pre-annealed at 800^0 C with no irradiation applied.

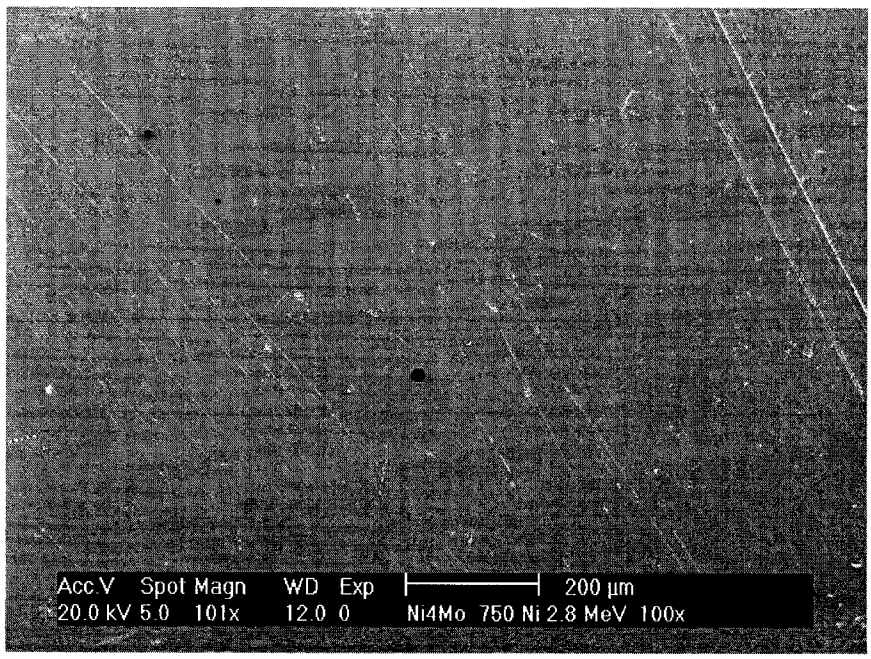

Figure 4.2.14 Surface of Ni_4Mo pre-annealed at 800^0 C with 0.1 DPA of Ni beam applied.

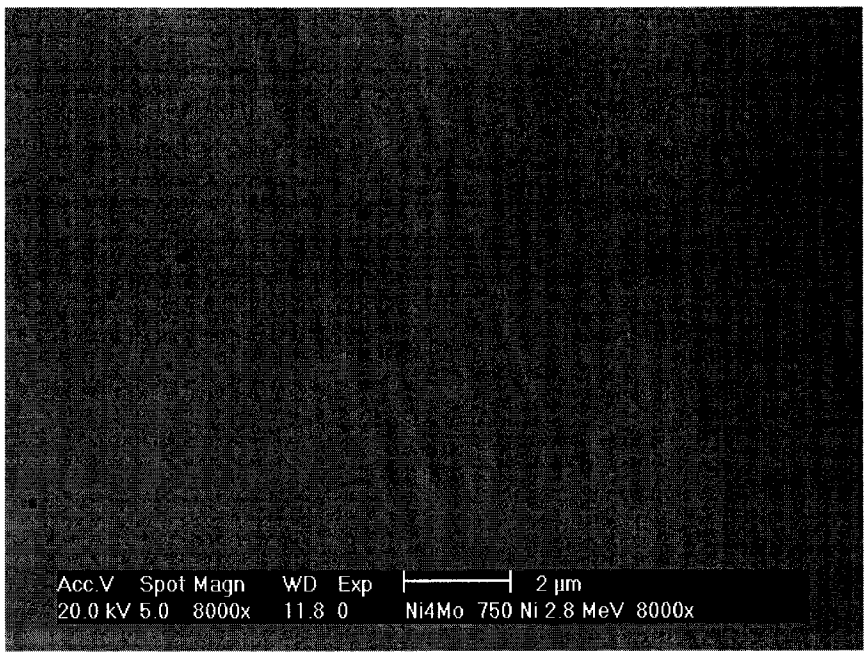

Figure 4.2.15 Surface of Ni_4Mo pre-annealed at 800^0 C with 0.5 DPA of Ni^+ beam applied.

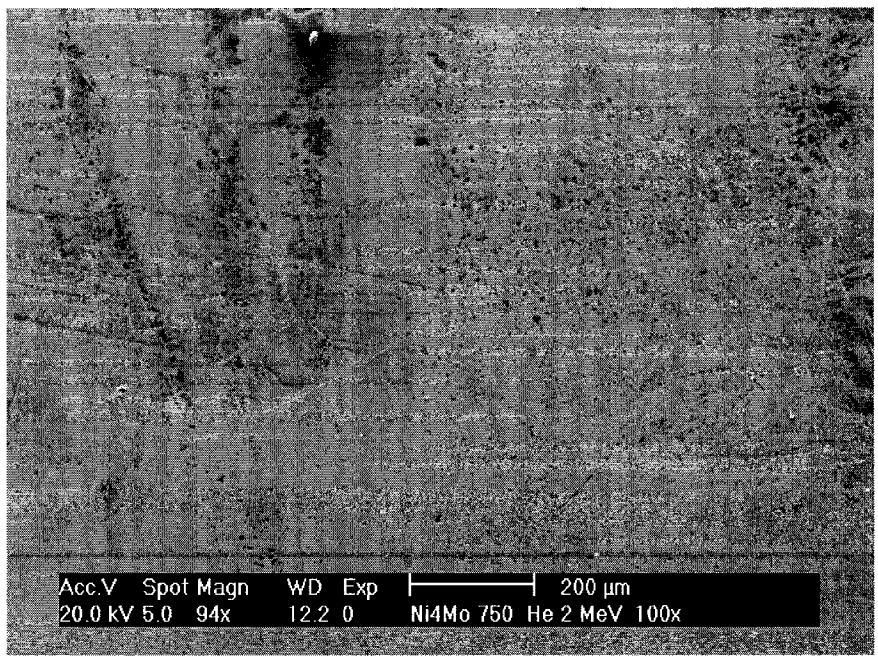

Figure 4.2.16 Surface of Ni_4Mo pre-annealed at 800^0 C with 1 DPA of He^+ beam applied.

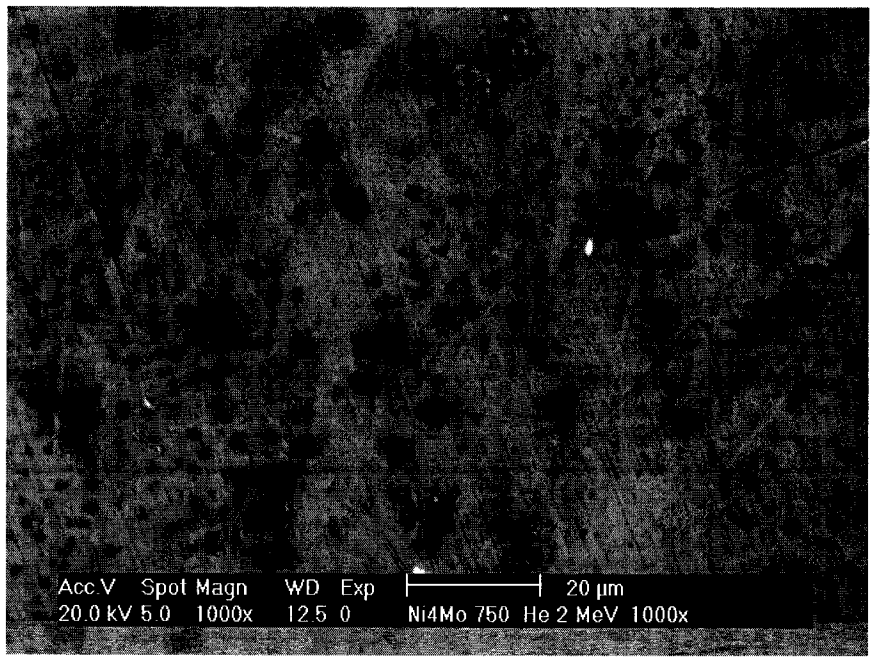

Figure 4.217 Surface of Ni_4Mo pre-annealed at 800^0 C with 1 DPA of He^+ beam applied from Fig. 4.2.15 at higher magnification.

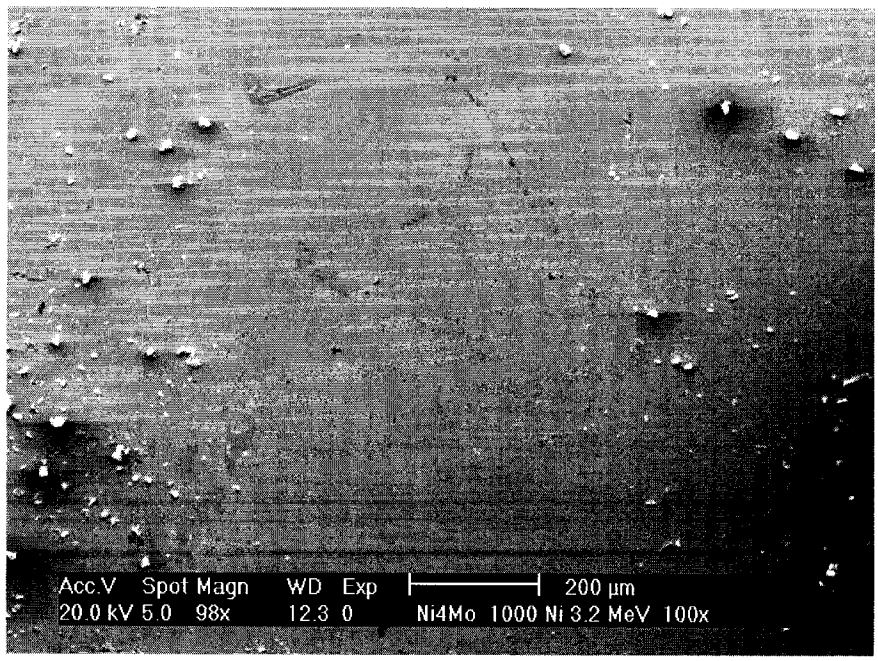

Figure 4.2.18 Surface of Ni_4Mo, pre-annealed at 1000^0 C with 1 DPA of Ni^+ beam applied.

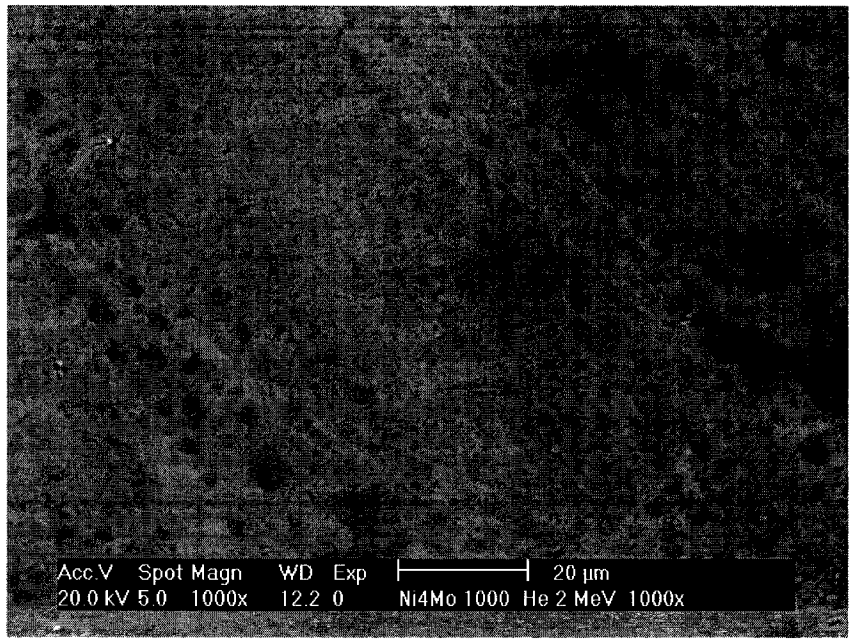

Figure 4.2.19 Surface of Ni_4Mo pre-annealed at 1000^0 with 1 DPA of He^+ beam applied.

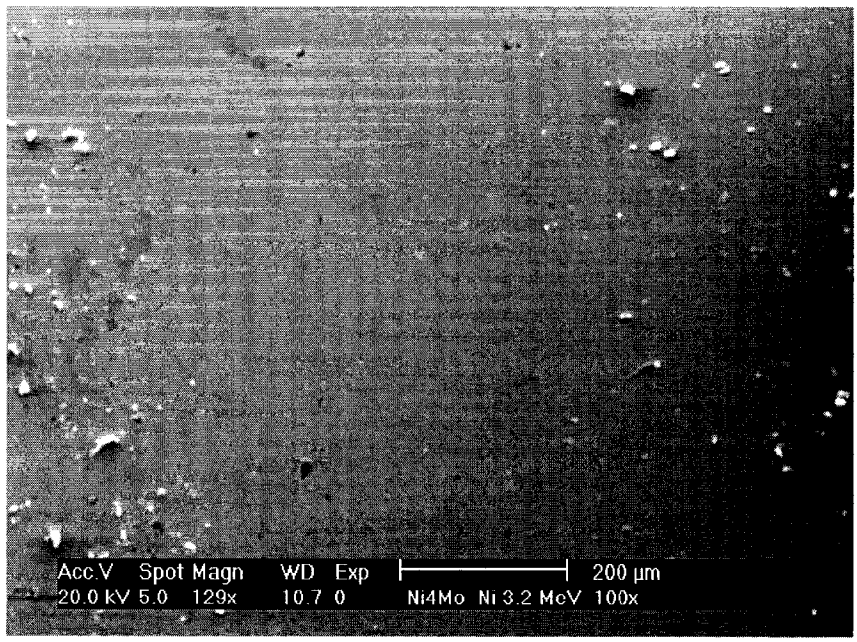

Figure 4.2.20 Surface of Ni_4Mo as-cast with 1 DPA of Ni^+ beam applied.

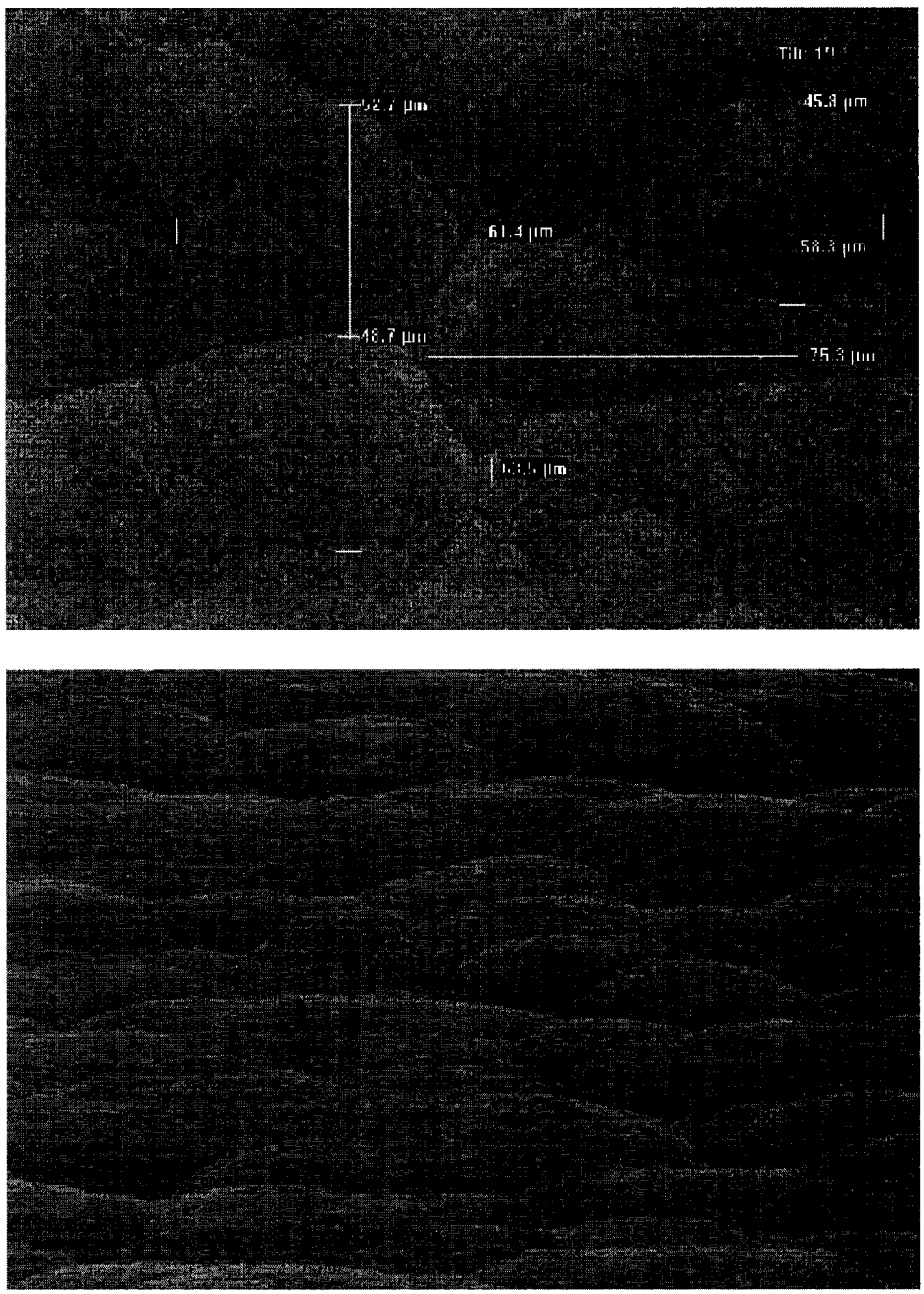

Figure 4.3.1 SEM image of the specimen to be analyzed with OIM. Top: an attempt to measure grains when the sample is horizontal. Bottom: a view of the sample when is rotated at the required 70^0 angle for the OIM data collection.

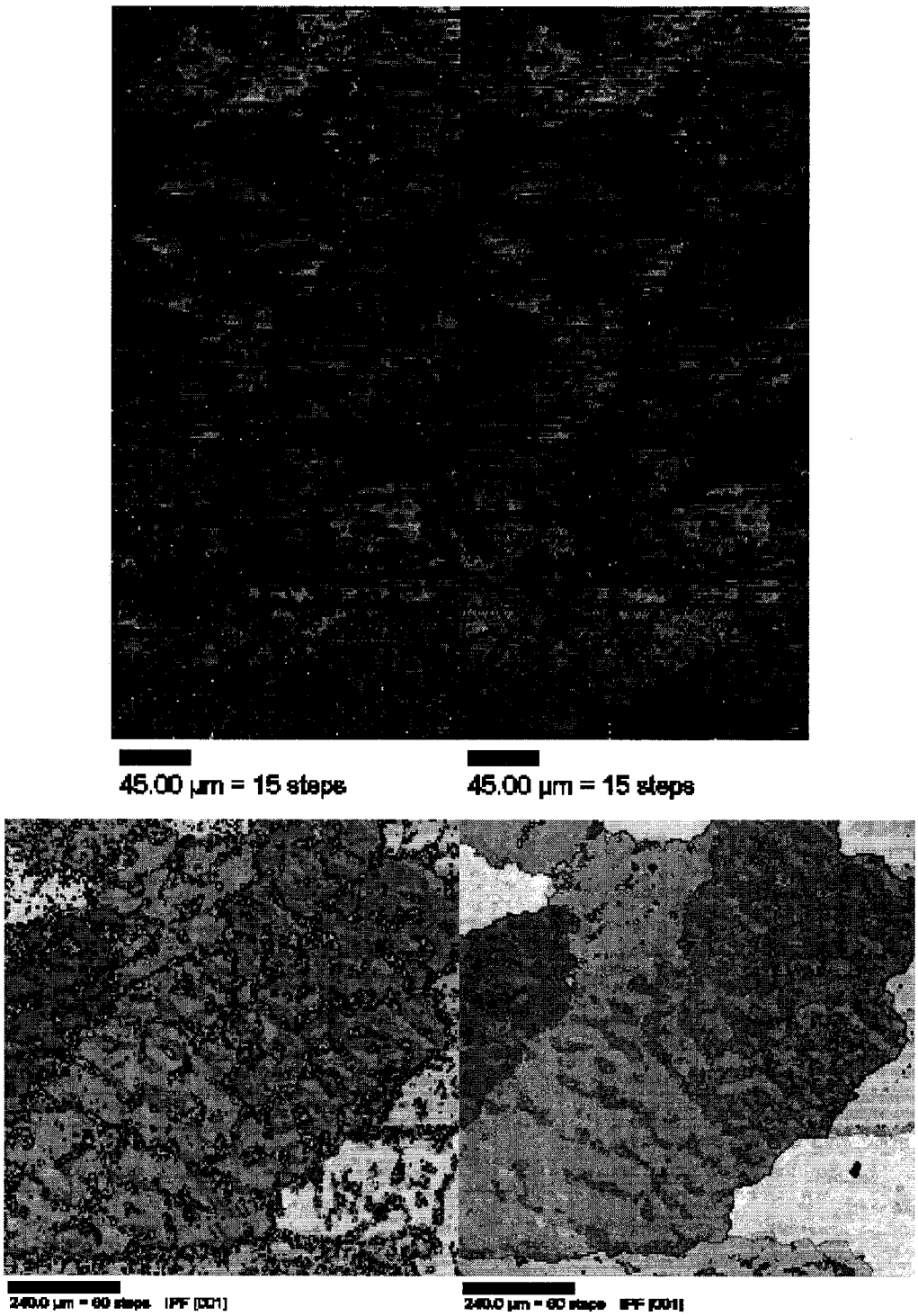

Figure 4.3.2 OIM data cleanup example. Top: OIM scan. Bottom: the inverse pole figure (IPF). The cleanup was performed by increasing the minimum allowed grain size from 2 to 8 and the allowed error for the mis-orientation angle form 5 to 7 degrees.

Gray Scale Map Type: Image Quality
19.7...59.5 (19.7...59.5)

Color Coded Map Type: Crystal Direction

Direction	Min	Max	Total Fraction	Partition Fraction
<1 0 0>||[0 0 1]	0°	15°	0.056	0.056
<0 1 1>||[0 0 1]	0°	15°	0.214	0.214
<1 1 1>||[0 0 1]	0°	15°	0.137	0.137
<1 1 2>||[0 0 1]	0°	15°	0.309	0.309
<1 1 4>||[0 0 1]	0°	15°	0.210	0.210

Boundaries: Rotation Angle

Min	Max	Fraction
15°	180°	0.983

Boundaries: CSL

Sigma	Tolerance	Fraction	Volume	MDF Value
1	15.00	0.017	0.0228	0.74
3	8.66	0.100	0.0176	5.69
5	6.71	0.015	0.0123	1.25
7	5.67	0.005	0.0099	0.53
11	4.52	0.022	0.0075	2.89
13a	4.16	0.001	0.0029	0.47
13b	4.16	0.007	0.0039	1.76
15	3.87	0.007	0.0094	0.72
17a	3.64	0.000	0.0020	0.23
17b	3.64	0.005	0.0039	1.26
19a	3.44	0.014	0.0033	4.11
19b	3.44	0.001	0.0022	0.49
21a	3.27	0.001	0.0019	0.46
21b	3.27	0.002	0.0057	0.35
23	3.13	0.002	0.0050	0.45
25a	3.00	0.001	0.0011	0.84
25b	3.00	0.003	0.0044	0.70
9	5.00	0.038	0.0102	3.78
27a	2.89	0.010	0.0020	5.32
27b	2.89	0.004	0.0039	1.09
summary	-	0.256	0.1317	1.95

*For statistics - any point pair with misorientation exceeding 10° is considered a boundary

Gray Scale Map Type: Image Quality
19.7...59.5 (19.7...59.5)

Color Coded Map Type: Crystal Direction

Direction	Min	Max	Total Fraction	Partition Fraction
<1 0 0>||[0 0 1]	0°	15°	0.058	0.058
<0 1 1>||[0 0 1]	0°	15°	0.189	0.189
<1 1 1>||[0 0 1]	0°	15°	0.097	0.097
<1 1 2>||[0 0 1]	0°	15°	0.360	0.360
<1 1 4>||[0 0 1]	0°	15°	0.187	0.187

Boundaries: Rotation Angle

Min	Max	Fraction
15°	180°	0.951

Boundaries: CSL

Sigma	Tolerance	Fraction	Volume	MDF Value
1	15.00	0.049	0.0228	2.17
3	8.66	0.266	0.0176	15.14
5	6.71	0.004	0.0123	0.32
7	5.67	0.006	0.0099	0.64
11	4.52	0.008	0.0075	1.12
13a	4.16	0.000	0.0029	0.00
13b	4.16	0.001	0.0039	0.24
15	3.87	0.002	0.0094	0.22
17a	3.64	0.001	0.0020	0.36
17b	3.64	0.014	0.0039	3.70
19a	3.44	0.000	0.0033	0.07
19b	3.44	0.002	0.0022	0.95
21a	3.27	0.002	0.0019	1.11
21b	3.27	0.001	0.0057	0.16
23	3.13	0.000	0.0050	0.00
25a	3.00	0.001	0.0011	0.64
25b	3.00	0.005	0.0044	1.06
9	5.00	0.010	0.0102	0.98
27a	2.89	0.000	0.0020	0.00
27b	2.89	0.001	0.0039	0.24
summary	-	0.374	0.1317	2.84

*For statistics - any point pair with misorientation exceeding 10° is considered a boundary

Figure 4.3.3 OIM: Variation in the misorientation angle and its error for the cleanup procedure in Fig. 4.3.2.

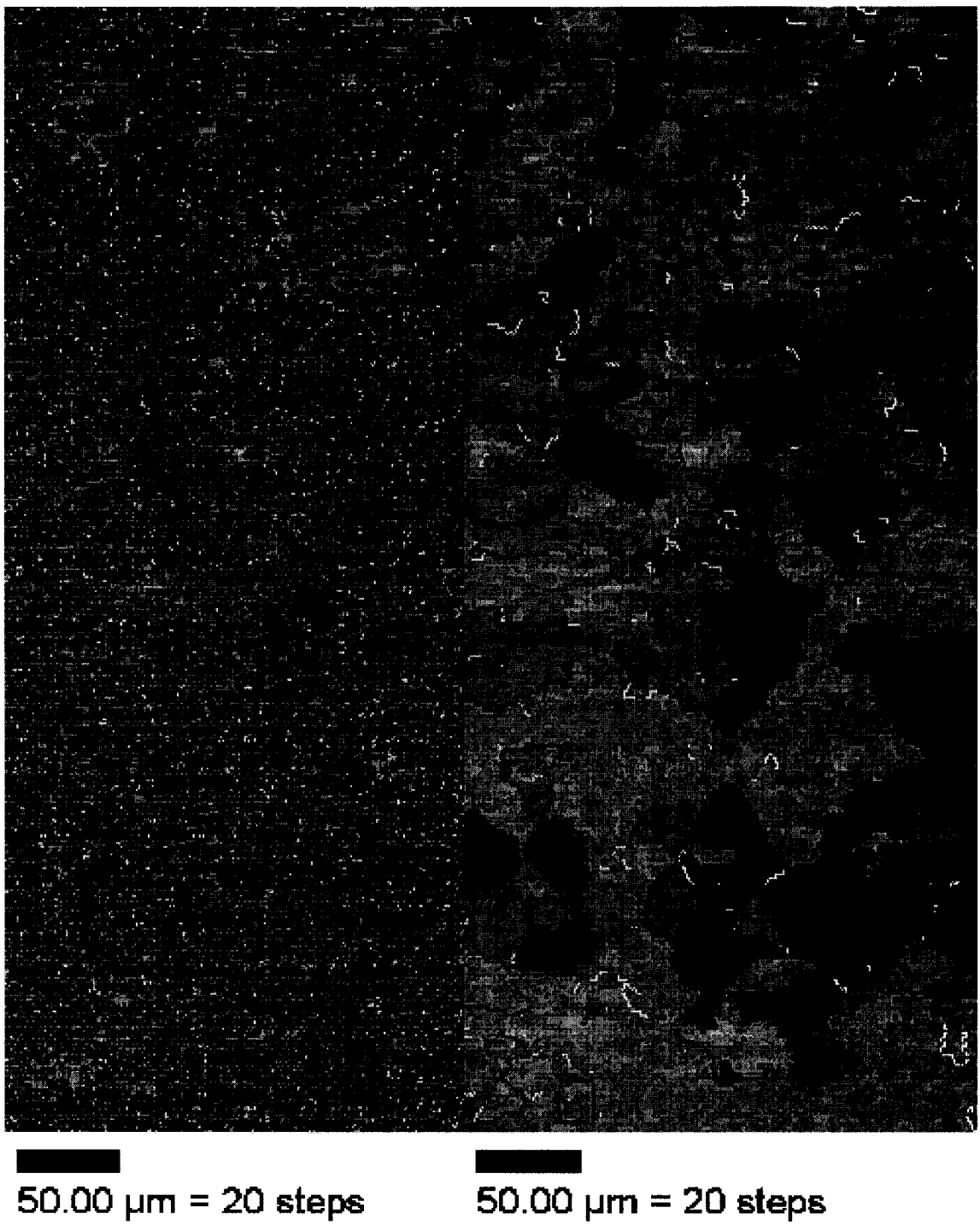

Figure 4.3.4 A second example of OIM data cleanup. The minimum grain size was allowed an increase from 2 µm to 10 µm, and the mis-orientation angle from 5 to 8 degrees.

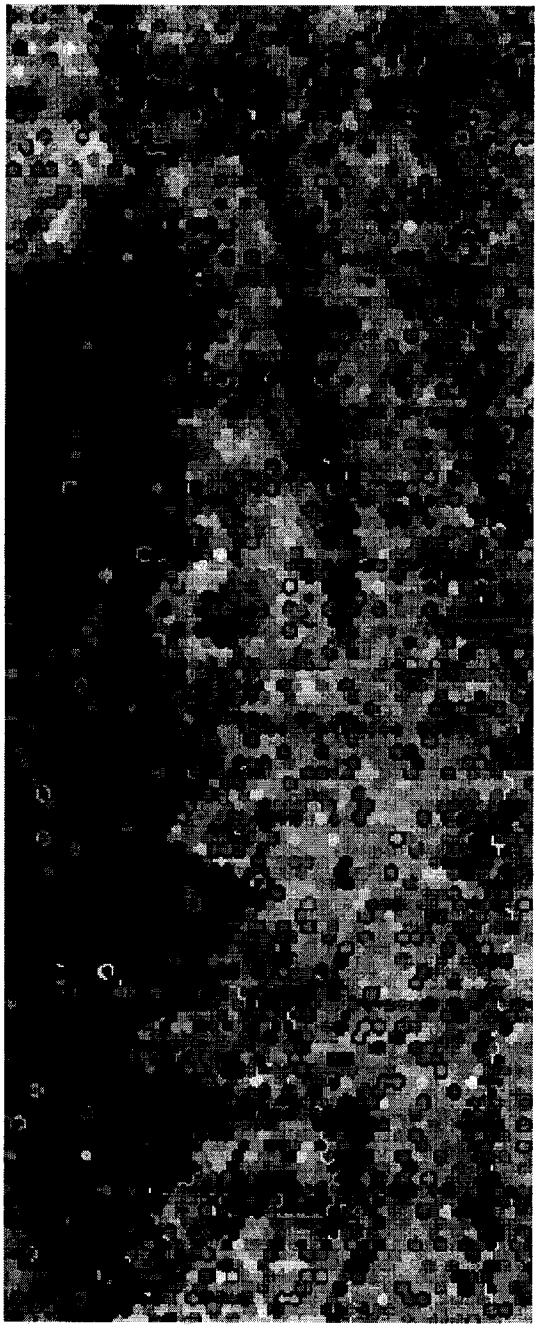

50.00 µm = 10 steps

Gray Scale Map Type: Image Quality
26.6...57.9 (26.6...57.9)

Color Coded Map Type: Crystal Direction

Direction	Min	Max	Total Fraction	Partition Fraction
<1 0 0>||[0 0 1]	0°	15°	0.018	0.018
<0 1 1>||[0 0 1]	0°	15°	0.041	0.041
<1 1 1>||[0 0 1]	0°	15°	0.462	0.462
<1 1 2>||[0 0 1]	0°	15°	0.164	0.164
<1 1 4>||[0 0 1]	0°	15°	0.300	0.300

Boundaries: Rotation Angle

Min	Max	Fraction
15°	180°	0.985

Boundaries: CSL

Sigma	Tolerance	Fraction	Volume	MDF Value
1	15.00	0.015	0.0228	0.65
3	8.66	0.077	0.0176	4.37
5	6.71	0.010	0.0123	0.79
7	5.67	0.003	0.0099	0.34
11	4.52	0.054	0.0075	7.15
13a	4.16	0.001	0.0029	0.21
13b	4.16	0.004	0.0039	1.12
15	3.87	0.007	0.0094	0.73
17a	3.64	0.000	0.0020	0.00
17b	3.64	0.004	0.0039	1.00
19a	3.44	0.005	0.0033	1.55
19b	3.44	0.000	0.0022	0.20
21a	3.27	0.000	0.0019	0.16
21b	3.27	0.001	0.0057	0.21
23	3.13	0.001	0.0050	0.12
25a	3.00	0.000	0.0011	0.27
25b	3.00	0.004	0.0044	0.99
9	5.00	0.081	0.0102	8.00
27a	2.89	0.037	0.0020	18.94
27b	2.89	0.003	0.0039	0.73
summary	-	0.308	0.1317	2.34

*For statistics - any point pair with misorientation exceeding 10° is considered a boundary

Figure 4.3.5 OIM scan and orientation results for Ni_4Mo pre-annealed at 800^0 C.

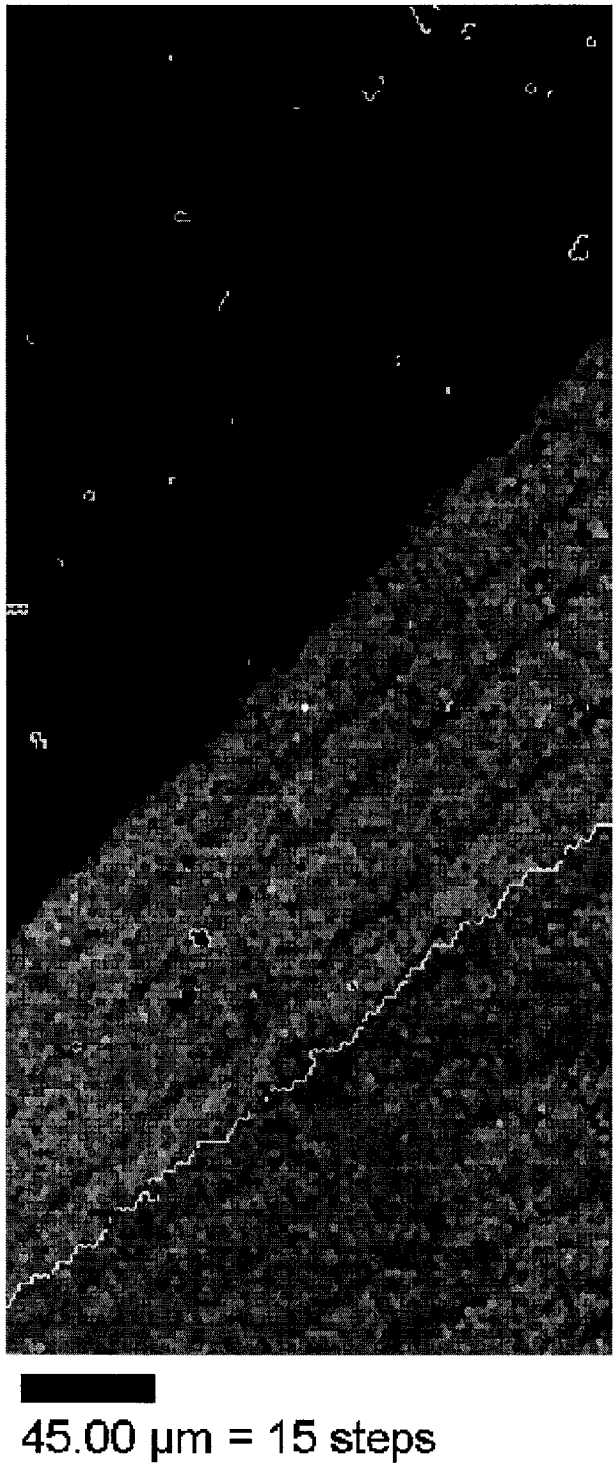

Figure 4.3.6 OIM scan for Ni_3Mo as cast.

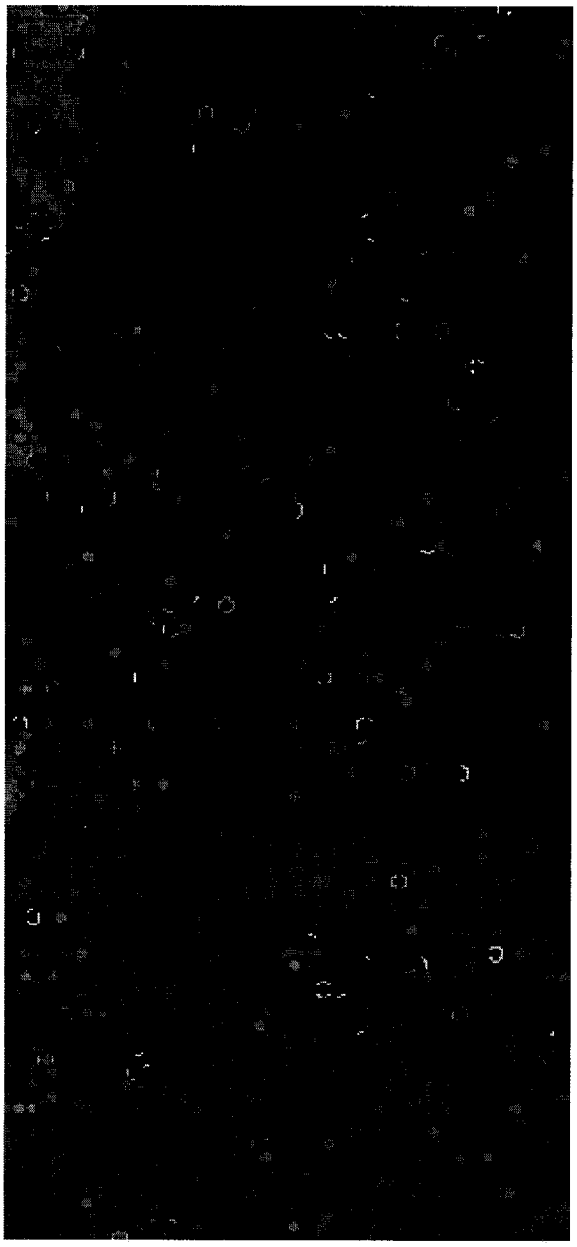

50.00 µm = 10 steps

Gray Scale Map Type: Image Quality
26.1...64 (26.1...64)

Color Coded Map Type: Crystal Direction

Direction	Min	Max	Total Fraction	Partition Fraction
<1 0 0>||[0 0 1]	0°	15°	0.289	0.289
<0 1 1>||[0 0 1]	0°	15°	0.045	0.045
<1 1 1>||[0 0 1]	0°	15°	0.013	0.013
<1 1 2>||[0 0 1]	0°	15°	0.072	0.072
<1 1 4>||[0 0 1]	0°	15°	0.564	0.564

Boundaries: Rotation Angle

Min	Max	Fraction
15°	180°	0.988

Boundaries: CSL

Sigma	Tolerance	Fraction	Volume	MDF Value
1	15.00	0.012	0.0228	0.54
3	8.66	0.042	0.0176	2.38
5	6.71	0.036	0.0123	2.86
7	5.67	0.006	0.0099	0.65
11	4.52	0.018	0.0075	2.43
13a	4.16	0.001	0.0029	0.35
13b	4.16	0.019	0.0039	4.84
15	3.87	0.005	0.0094	0.51
17a	3.64	0.002	0.0020	0.85
17b	3.64	0.005	0.0039	1.38
19a	3.44	0.019	0.0033	5.83
19b	3.44	0.000	0.0022	0.09
21a	3.27	0.002	0.0019	0.87
21b	3.27	0.002	0.0057	0.36
23	3.13	0.002	0.0050	0.46
25a	3.00	0.001	0.0011	0.57
25b	3.00	0.002	0.0044	0.47
9	5.00	0.015	0.0102	1.49
27a	2.89	0.007	0.0020	3.82
27b	2.89	0.002	0.0039	0.42
summary	-	0.199	0.1317	1.51

*For statistics - any point pair with misorientation exceeding 10° is considered a boundary

Figure 4.3.7 OIM scan of the Ni_4Mo pre-annealed at 800^0 C irradiated with .1 dpa Ni^+.

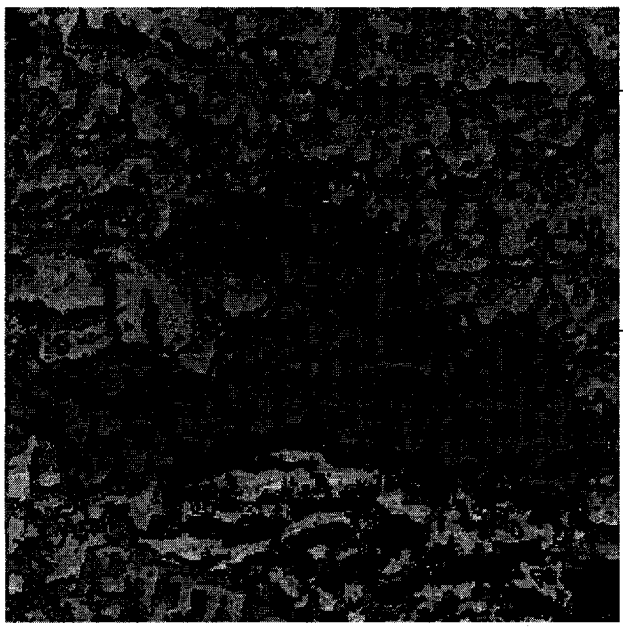

Gray Scale Map Type: Image Quality
0...80.1 (0...80.1)

Color Coded Map Type: Crystal Direction

Direction	Min	Max	Total Fraction	Partition Fraction
<1 0 0>||[0 0 1]	0°	15°	0.000	0.000
<0 1 1>||[0 0 1]	0°	15°	0.549	0.549
<1 1 1>||[0 0 1]	0°	15°	0.000	0.000
<1 1 2>||[0 0 1]	0°	15°	0.280	0.280
<1 1 4>||[0 0 1]	0°	15°	0.078	0.078

Boundaries: Rotation Angle

Min	Max	Fraction
15°	180°	0.685

Boundaries: CSL

Sigma	Tolerance	Fraction	Volume	MDF Value
1	15.00	0.491	0.0228	21.58
3	8.66	0.000	0.0176	0.00
5	6.71	0.000	0.0123	0.00
7	5.67	0.000	0.0098	0.00
11	4.52	0.028	0.0075	3.74
13a	4.16	0.001	0.0028	0.41
13b	4.16	0.000	0.0038	0.00
15	3.87	0.000	0.0094	0.00
17a	3.64	0.000	0.0020	0.00
17b	3.64	0.000	0.0039	0.00
19a	3.44	0.083	0.0033	25.09
19b	3.44	0.000	0.0022	0.00
21a	3.27	0.000	0.0019	0.00
21b	3.27	0.000	0.0057	0.00
23	3.13	0.000	0.0050	0.00
25a	3.00	0.005	0.0011	4.76
25b	3.00	0.000	0.0044	0.00
9	5.00	0.000	0.0102	0.00
27a	2.89	0.000	0.0020	0.00
27b	2.89	0.000	0.0039	0.00
summary	-	0.609	0.1317	4.62

*For statistics - any point pair with misorientation exceeding 10° is considered a boundary

Figure 4.3.8 OIM scan for the Ni_3Mo pre-annealed at 800^0 C irradiated with .1 dpa Ni^+.

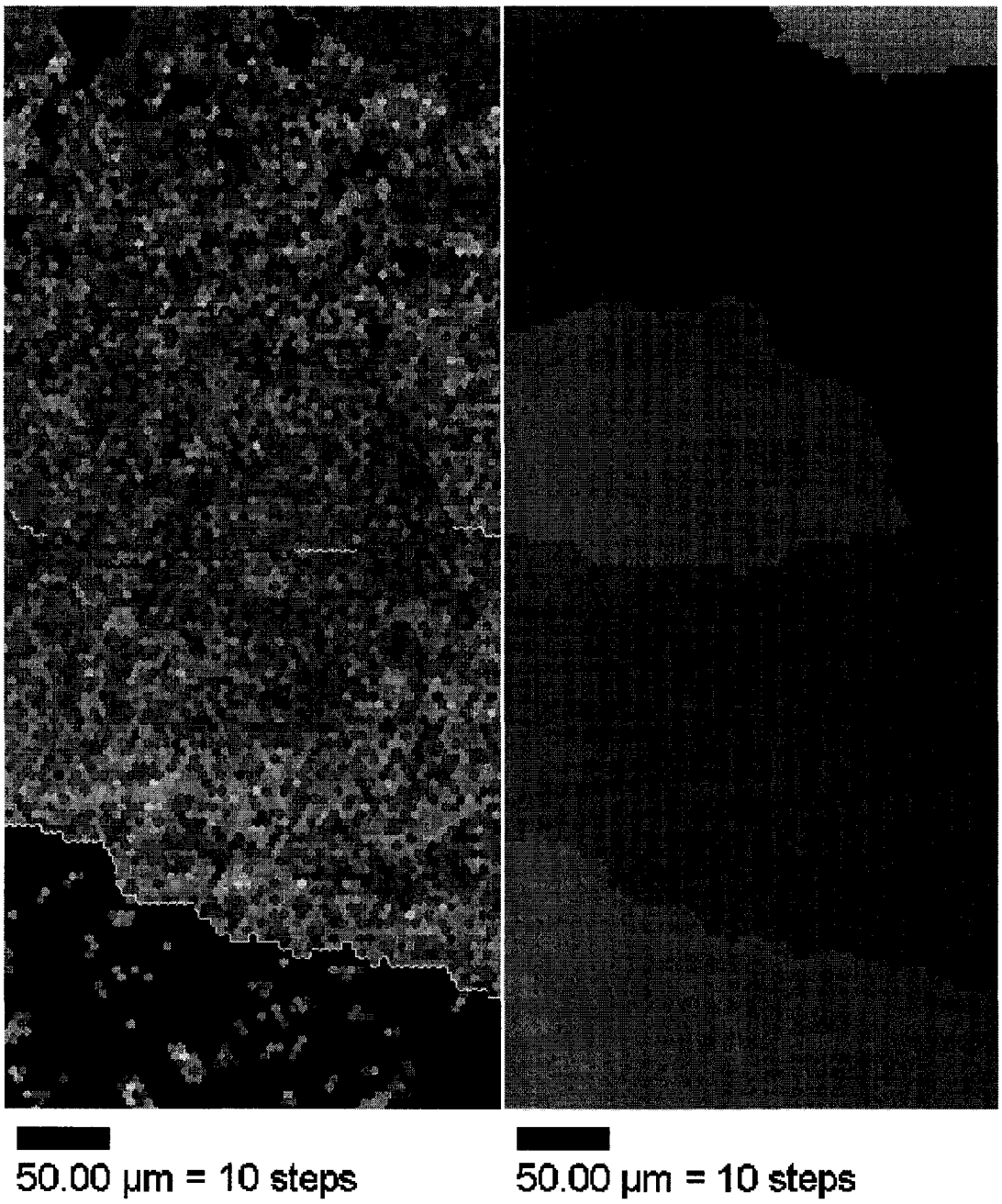

Figure 4.3.9 OIM scan for the Ni_4Mo pre-annealed at 1000 C. In the left side is the actual scan "cleaned up" and at the right is the inverse pole figure (IFP) of the same scan. The code for the IPF is given in the next figure.

Gray Scale Map Type: Image Quality
48.8...98.5 (48.8...98.5)

Color Coded Map Type: Crystal Direction

Direction	Min	Max	Total Fraction	Partition Fraction
<1 0 0>||[0 0 1]	0°	15°	0.000	0.000
<0 1 1>||[0 0 1]	0°	15°	0.496	0.496
<1 1 1>||[0 0 1]	0°	15°	0.000	0.000
<1 1 2>||[0 0 1]	0°	15°	0.033	0.033
<1 1 4>||[0 0 1]	0°	15°	0.189	0.189

Boundaries: Rotation Angle

Min	Max	Fraction
15°	180°	0.624

Boundaries: CSL

Sigma	Tolerance	Fraction	Volume	MDF Value
1	15.00	0.376	0.0228	16.51
3	8.66	0.000	0.0176	0.00
5	6.71	0.000	0.0123	0.00
7	5.67	0.000	0.0099	0.00
11	4.52	0.000	0.0075	0.00
13a	4.16	0.000	0.0029	0.00
13b	4.16	0.000	0.0039	0.00
15	3.87	0.000	0.0094	0.00
17a	3.64	0.000	0.0020	0.00
17b	3.64	0.000	0.0039	0.00
19a	3.44	0.000	0.0033	0.00
19b	3.44	0.000	0.0022	0.00
21a	3.27	0.030	0.0019	15.65
21b	3.27	0.000	0.0057	0.00
23	3.13	0.000	0.0050	0.00
25a	3.00	0.000	0.0011	0.00
25b	3.00	0.000	0.0044	0.00
9	5.00	0.032	0.0102	3.14
27a	2.89	0.000	0.0020	0.00
27b	2.89	0.000	0.0039	0.00
summary	-	0.437	0.1317	3.32

*For statistics - any point pair with misorientation exceeding 10° is considered a boundary

Gray Scale Map Type: <none>

Color Coded Map Type: Inverse Pole Figure [001]

Nickel

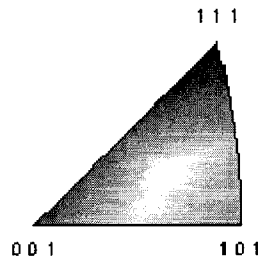

Boundaries: <none>

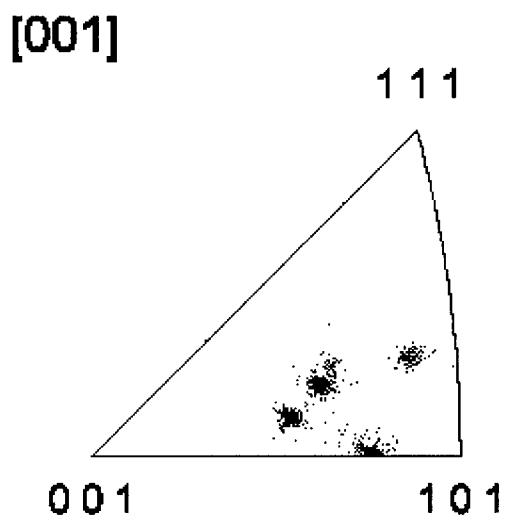

Figure 4.3.10 Data file with the mis-orientation between the grains and the inverse pole figure map for the scan in Figure 4.3.9.

Chart: Grain Size (diameter)

Edge grains excluded from analysis

Diameter [microns]	Area Fraction
6.69893	0.310795
8.51973	0.039819
10.8354	0.0272786
13.7806	0.0155139
17.5262	0.0121526
22.2899	0
28.3483	0.0121526
36.0536	0.0116061
45.8531	0
58.3161	0.0518423
74.1667	0.0477052
94.3256	0
119.964	0
152.57	0
194.04	0
246.781	0.471235
313.857	0
399.164	0
507.659	0
645.643	0
Average Number	6.93664
Area	130.241

Chart: Misorientation Angle

Angle [degrees]	Number Fraction
9.375	0.0403225
18.125	0.0734289
26.875	0.107619
35.625	0.157907
44.375	0.265169
53.125	0.0978259
61.875	0.0642569
70.625	0.0633186
79.375	0.0598031
88.125	0.0618516
96.875	0.00849798
105.625	0
114.375	0
123.125	0
131.875	0
140.625	0
149.375	0
158.125	0
166.875	0
175.625	0
Average Number	46.6853

Figure 4.3.11 Mis-orientation and grain size statistics for the scan in Figure 4.3.9.

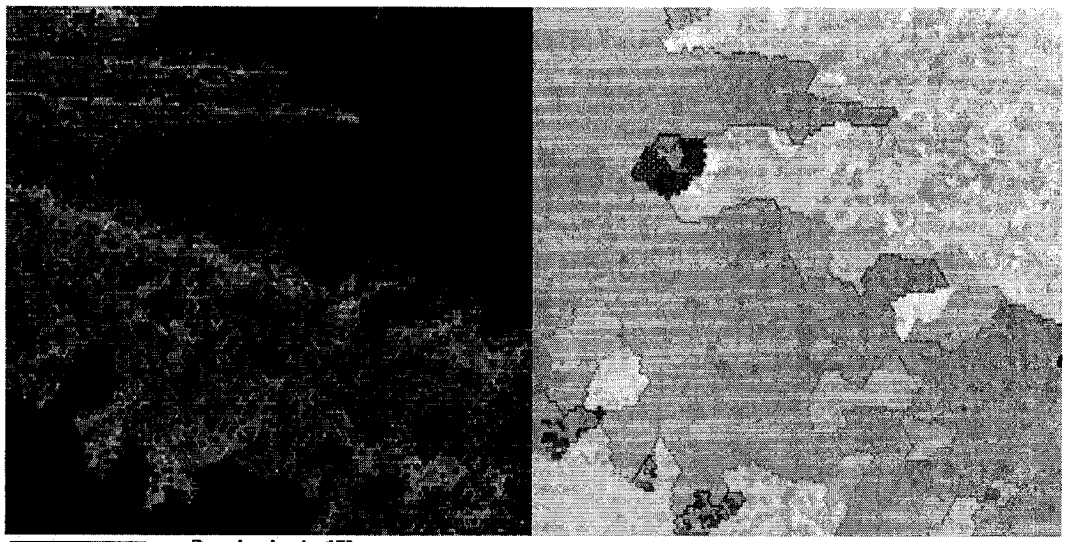

Boundary levels: 15°
50.00 µm = 25 steps IQ 35.3...84.9, Direction

50.00 µm = 25 steps IPF [001]

Gray Scale Map Type: Image Quality
35.3...84.9 (35.3...84.9)

Color Coded Map Type: Crystal Direction

Direction	Min	Max	Total Fraction	Partition Fraction
<1 0 0>||[0 0 1]	0°	15°	0.000	0.000
<0 1 1>||[0 0 1]	0°	15°	0.592	0.592
<1 1 1>||[0 0 1]	0°	15°	0.000	0.000
<1 1 2>||[0 0 1]	0°	15°	0.003	0.003
<1 1 4>||[0 0 1]	0°	15°	0.405	0.405

Boundaries: Rotation Angle

Min	Max	Fraction
15°	180°	1.000

Boundaries: CSL

Sigma	Tolerance	Fraction	Volume	MDF Value
1	15.00	0.000	0.0229	0.00
3	8.66	0.174	0.0176	8.83
5	6.71	0.000	0.0123	0.00
7	5.57	0.000	0.0089	0.00
11	4.52	0.022	0.0075	3.00
13a	4.16	0.000	0.0039	0.00
13b	4.16	0.000	0.0039	0.00
15	3.87	0.000	0.0094	0.00
17a	3.64	0.000	0.0020	0.00
17b	3.64	0.000	0.0039	0.00
19a	3.44	0.000	0.0033	0.00
19b	3.44	0.000	0.0022	0.00
21a	3.27	0.000	0.0019	0.00
21b	3.27	0.000	0.0057	0.00
23	3.13	0.000	0.0050	0.00
25a	3.00	0.000	0.0011	0.00
25b	3.00	0.000	0.0044	0.00
9	3.00	0.000	0.0102	0.00
27a	2.89	0.000	0.0020	0.00
27b	2.89	0.000	0.0039	0.00
summary	-	0.197	0.1317	1.50

*For statistics - any point pair with misorientation exceeding 1.0° is considered a boundary

Gray Scale Map Type: <none>

Color Coded Map Type: Inverse Pole Figure [001]

Nickel

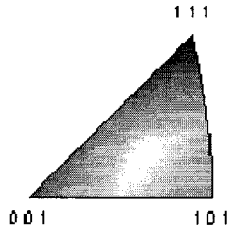

Boundaries: <none>

Figure 4.3.12 OIM scan and IPF for the Ni_3Mo pre-annealed at 1000^0 C irradiated with .1 dpa H^+.

Chart: Grain Size (diameter)

Edge grains excluded from analysis

Diameter [microns]	Area Fraction
10.7972	0.0255556
12.4081	0
14.2594	0
16.3868	0.21
18.8317	0
21.6413	0.247778
24.8701	0.3
28.5806	0.216667
32.8447	0
37.745	0
43.3765	0
49.8481	0
57.2853	0
65.832	0
75.6539	0
86.9412	0
99.9125	0
114.819	0
131.96	0
151.636	0
Average Number	20.2798
Area	22.9415

Chart: Misorientation Angle

Angle [degrees]	Number Fraction
6.5	0.0135635
9.5	0
12.5	0
15.5	0
18.5	0
21.5	0
24.5	0
27.5	0.302096
30.5	0.0838471
33.5	0
36.5	0.00308261
39.5	0
42.5	0
45.5	0.0209618
48.5	0.318126
51.5	0.0739827
54.5	0.0123305
57.5	0.0567201
60.5	0.11529
63.5	0
Average Number	42.2513

Figure 4.3.13 Grain size statistics and mis-orientation data for the scan in Figure 4.3.12.

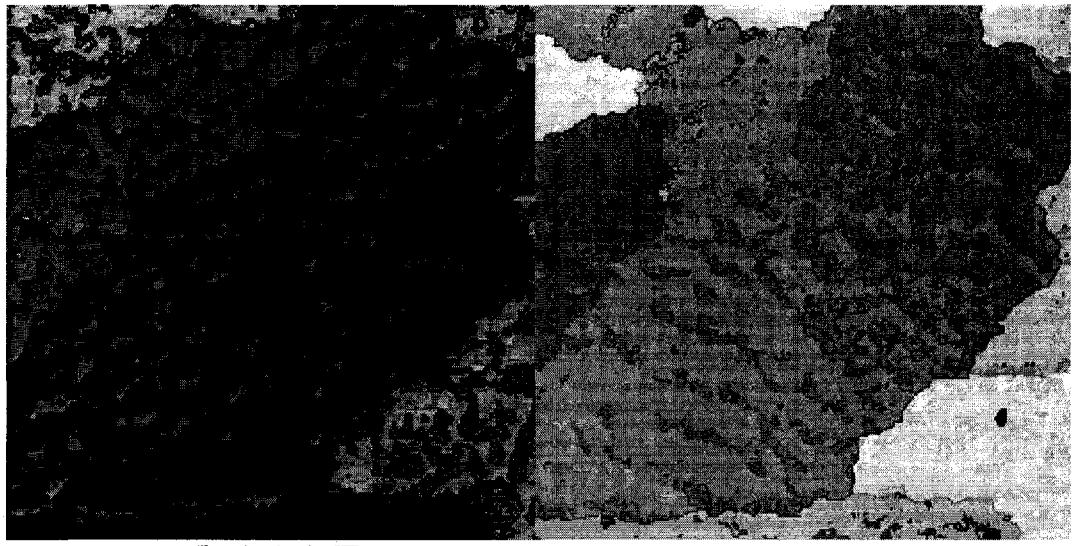

Grey Scale Map Type: Image Quality
0.3...75.6 (0.3...75.6)

Color Coded Map Type: Crystal Direction

Direction	Min	Max	Total Fraction	Partition Fraction
<1 0 0>||[0 0 1]	0°	15°	0.002	0.002
<0 1 1>||[0 0 1]	0°	15°	0.095	0.095
<1 1 1>||[0 0 1]	0°	15°	0.003	0.003
<1 1 2>||[0 0 1]	0°	15°	0.203	0.203
<1 1 4>||[0 0 1]	0°	15°	0.378	0.378

Boundaries: Rotation Angle

Min	Max	Fraction
15°	180°	0.986

Boundaries: CSL

Sigma	Tolerance	Fraction	Volume	MDF Value
1	15.00	0.005	0.0228	0.22
3	8.66	0.020	0.0178	1.13
5	8.71	0.012	0.0123	1.01
7	5.67	0.007	0.0098	0.66
11	4.52	0.038	0.0075	5.05
13a	4.18	0.019	0.0029	6.62
13b	4.18	0.037	0.0039	9.44
15	3.87	0.008	0.0094	0.85
17a	3.64	0.006	0.0020	3.24
17b	3.64	0.003	0.0038	0.81
19a	3.44	0.008	0.0033	2.34
19b	3.44	0.001	0.0022	0.24
21a	3.27	0.001	0.0018	0.37
21b	3.27	0.001	0.0057	0.09
23	3.13	0.003	0.0050	0.67
25a	3.00	0.003	0.0011	1.77
25b	3.00	0.001	0.0044	0.20
9	5.00	0.013	0.0102	1.25
27a	2.89	0.001	0.0020	0.36
27b	2.89	0.001	0.0038	0.27
summary	-	0.187	0.1317	1.42

*For statistics - any point pair with misorientation exceeding 10° is considered a boundary

Figure 4.3.14 OIM scan for Ni_4Mo pre-annealed at 1000^0 C irradiated with 1 dpa H^+.

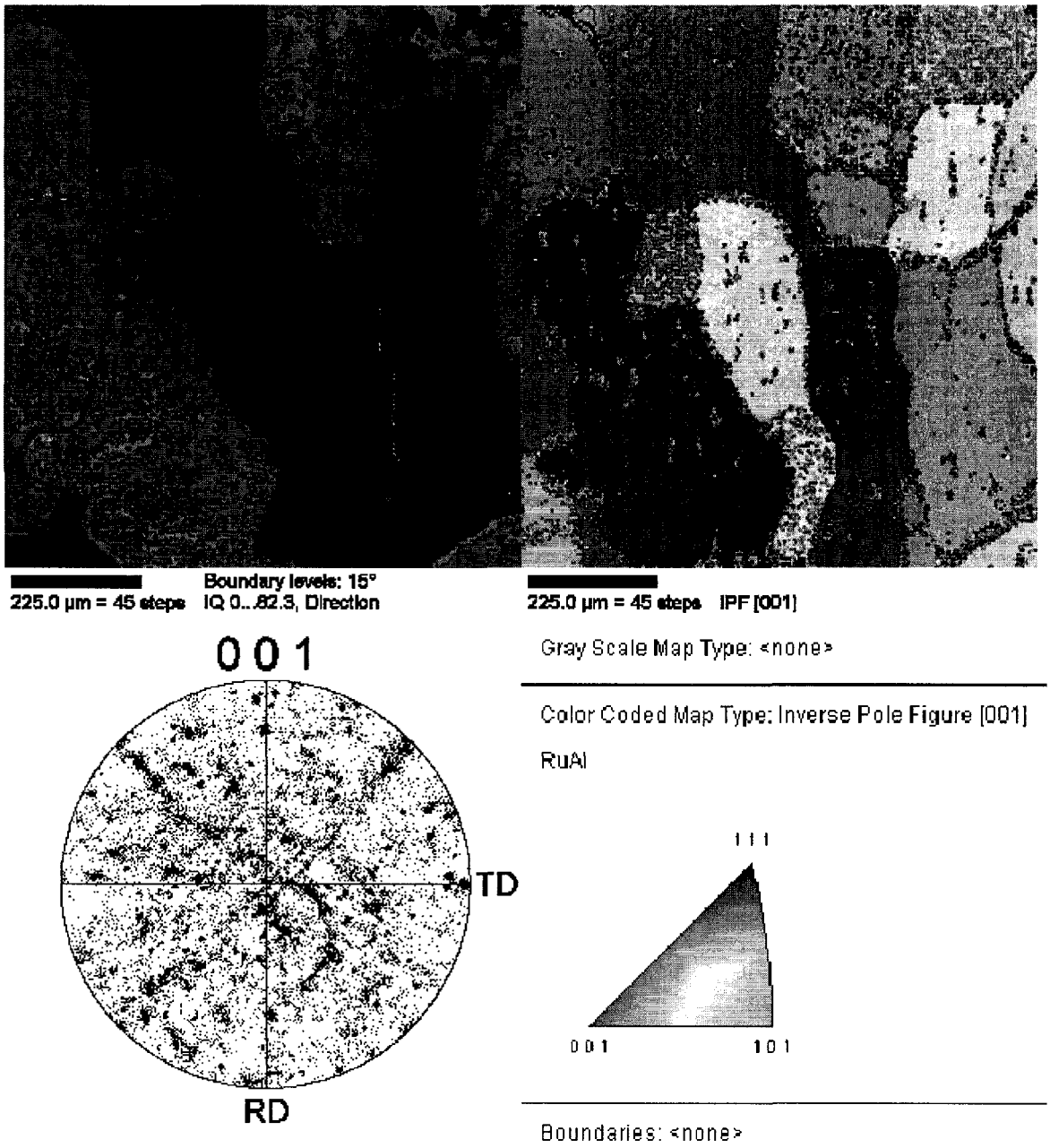

Figure 4.3.15 OIM scan for Ni_4Mo pre-annealed at 1000^0 C irradiated with 1 dpa H^+ and then annealed at 100^0 C.

Gray Scale Map Type: Image Quality
0...82.3 (0...82.3)

Color Coded Map Type: Crystal Direction

Direction	Min	Max	Total Fraction	Partition Fraction
<1 0 0>||[0 0 1]	0°	15°	0.099	0.099
<0 1 1>||[0 0 1]	0°	15°	0.159	0.159
<1 1 1>||[0 0 1]	0°	15°	0.280	0.280
<1 1 2>||[0 0 1]	0°	15°	0.035	0.035
<1 1 4>||[0 0 1]	0°	15°	0.423	0.423

Boundaries: Rotation Angle

Min	Max	Fraction
15°	180°	0.914

Boundaries: CSL

Sigma	Tolerance	Fraction	Volume	MDF Value
1	15.00	0.086	0.0228	3.77
3	8.66	0.121	0.0176	6.89
5	6.71	0.005	0.0123	0.38
7	5.67	0.002	0.0099	0.21
11	4.52	0.003	0.0075	0.40
13a	4.16	0.000	0.0029	0.00
13b	4.16	0.131	0.0039	33.71
15	3.87	0.013	0.0094	1.34
17a	3.64	0.000	0.0020	0.00
17b	3.64	0.009	0.0039	2.30
19a	3.44	0.017	0.0033	5.08
19b	3.44	0.000	0.0022	0.00
21a	3.27	0.000	0.0019	0.00
21b	3.27	0.000	0.0057	0.00
23	3.13	0.001	0.0050	0.28
25a	3.00	0.001	0.0011	1.05
25b	3.00	0.005	0.0044	1.10
9	5.00	0.003	0.0102	0.34
27a	2.89	0.016	0.0020	8.25
27b	2.89	0.005	0.0039	1.24
summary	-	0.418	0.1317	3.18

*For statistics - any point pair with misorientation exceeding 10° is considered a boundary

Chart: Grain Size (diameter)

Edge grains excluded from analysis

Diameter [microns]	Area Fraction
8.22776	0.142547
10.1026	0.0231884
12.4047	0.0307453
15.2313	0.0328157
18.7021	0.0330228
22.9637	0.00517598
28.1964	0.00569358
34.6215	0.00807453
42.5107	0.0057971
52.1976	0.0182195
64.0918	0
78.6963	0.0224638
96.6288	0.071118
118.648	0.110041
145.684	0.0669772
178.88	0
219.642	0.180435
269.691	0.243685
331.146	0
406.604	0
Average	
Number	10.5471
Area	137.193

Figure 4.3.16 Data file showing the mis-orientations between the grains and the grain size statistics from the scan in Figure 4.3.15.

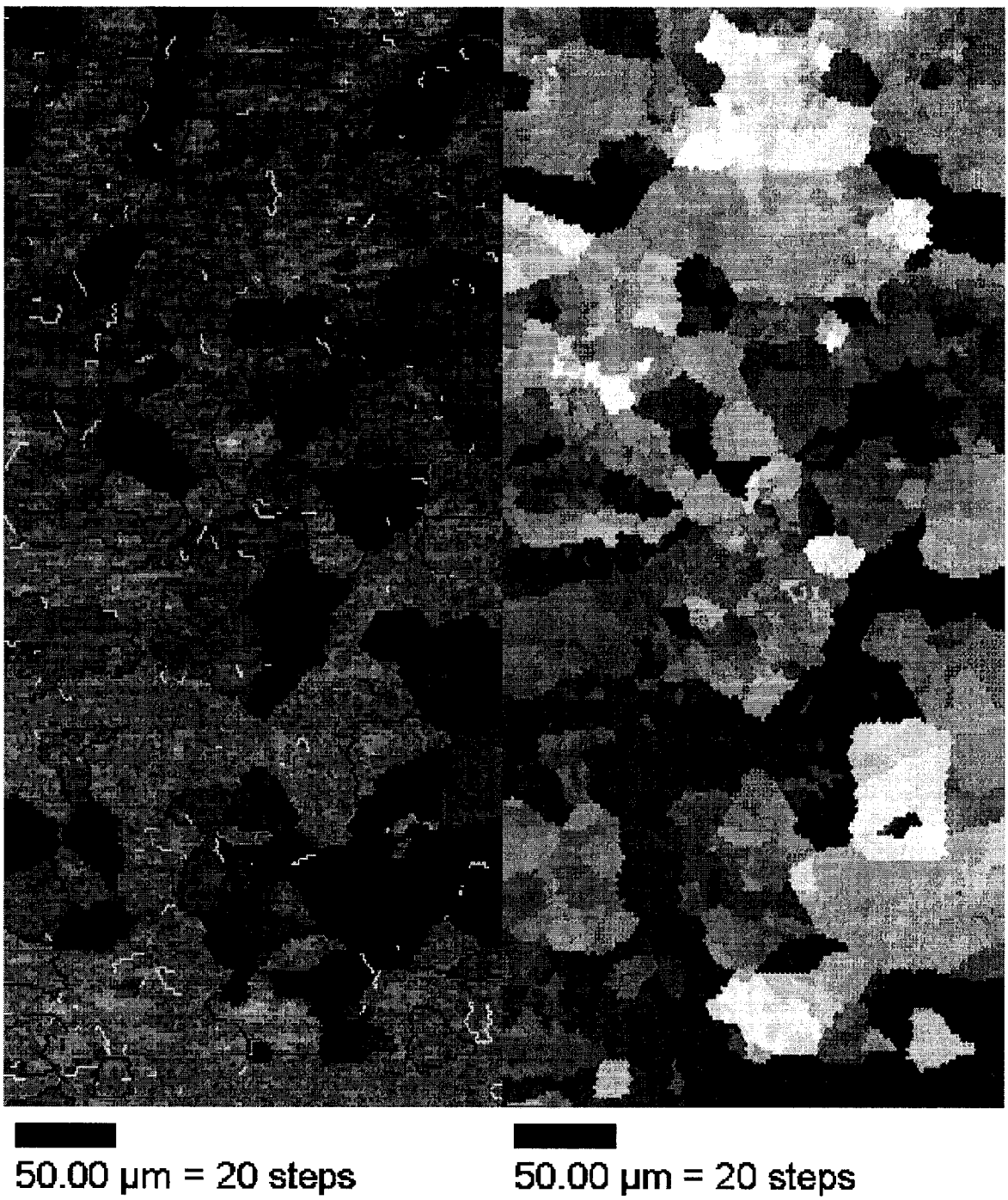

Figure 4.3.17 OIM scan and IPF for the Ni_4Mo pre-annealed at 800^0 C and irradiated with 0.5 dpa H^+ then annealed at 350 C.

Gray Scale Map Type: Image Quality
27.8...58.5 (27.8...58.5)

Color Coded Map Type: Crystal Direction

Direction	Min	Max	Total Fraction	Partition Fraction
<1 0 0>||[0 0 1]	0°	15°	0.033	0.033
<0 1 1>||[0 0 1]	0°	15°	0.160	0.160
<1 1 1>||[0 0 1]	0°	15°	0.343	0.343
<1 1 2>||[0 0 1]	0°	15°	0.213	0.213
<1 1 4>||[0 0 1]	0°	15°	0.215	0.215

Boundaries: Rotation Angle

Min	Max	Fraction
15°	180°	0.892

Boundaries: CSL

Sigma	Tolerance	Fraction	Volume	MDF Value
1	15.00	0.108	0.0228	4.74
3	8.66	0.077	0.0176	4.36
5	6.71	0.011	0.0123	0.91
7	5.67	0.000	0.0099	0.00
11	4.52	0.019	0.0075	2.58
13a	4.16	0.001	0.0029	0.24
13b	4.16	0.002	0.0039	0.50
15	3.87	0.013	0.0094	1.40
17a	3.64	0.002	0.0020	0.79
17b	3.64	0.008	0.0039	2.12
19a	3.44	0.012	0.0033	3.67
19b	3.44	0.002	0.0022	0.96
21a	3.27	0.001	0.0019	0.67
21b	3.27	0.004	0.0057	0.72
23	3.13	0.000	0.0060	0.06
25a	3.00	0.003	0.0011	2.95
25b	3.00	0.008	0.0044	1.80
9	5.00	0.018	0.0102	1.79
27a	2.89	0.006	0.0020	3.09
27b	2.89	0.002	0.0039	0.58
summary	-	0.298	0.1317	2.26

*For statistics - any point pair with misorientation exceeding 10° is considered a boundary

Chart: Grain Size (diameter)

Edge grains excluded from analysis

Diameter [microns]	Area Fraction
4.83221	0.0241193
5.68492	0.00769158
6.68811	0.00781819
7.86832	0.00316526
9.2568	0.00911594
10.8903	0.00870446
12.812	0.0131358
15.0729	0.0212072
17.7327	0.0286456
20.8619	0.0514987
24.5433	0.0421929
28.8743	0.0588738
33.9696	0.0785301
39.964	0.120311
47.0162	0.100782
55.3129	0.0717248
65.0736	0.133606
76.5568	0.08983
90.0663	0.0909695
105.96	0.0380781
Average	
Number	12.6409
Area	48.9708

Figure 4.3.18 Mis-orientation data and grain size statistics for the scan in Figure 4.3.17.

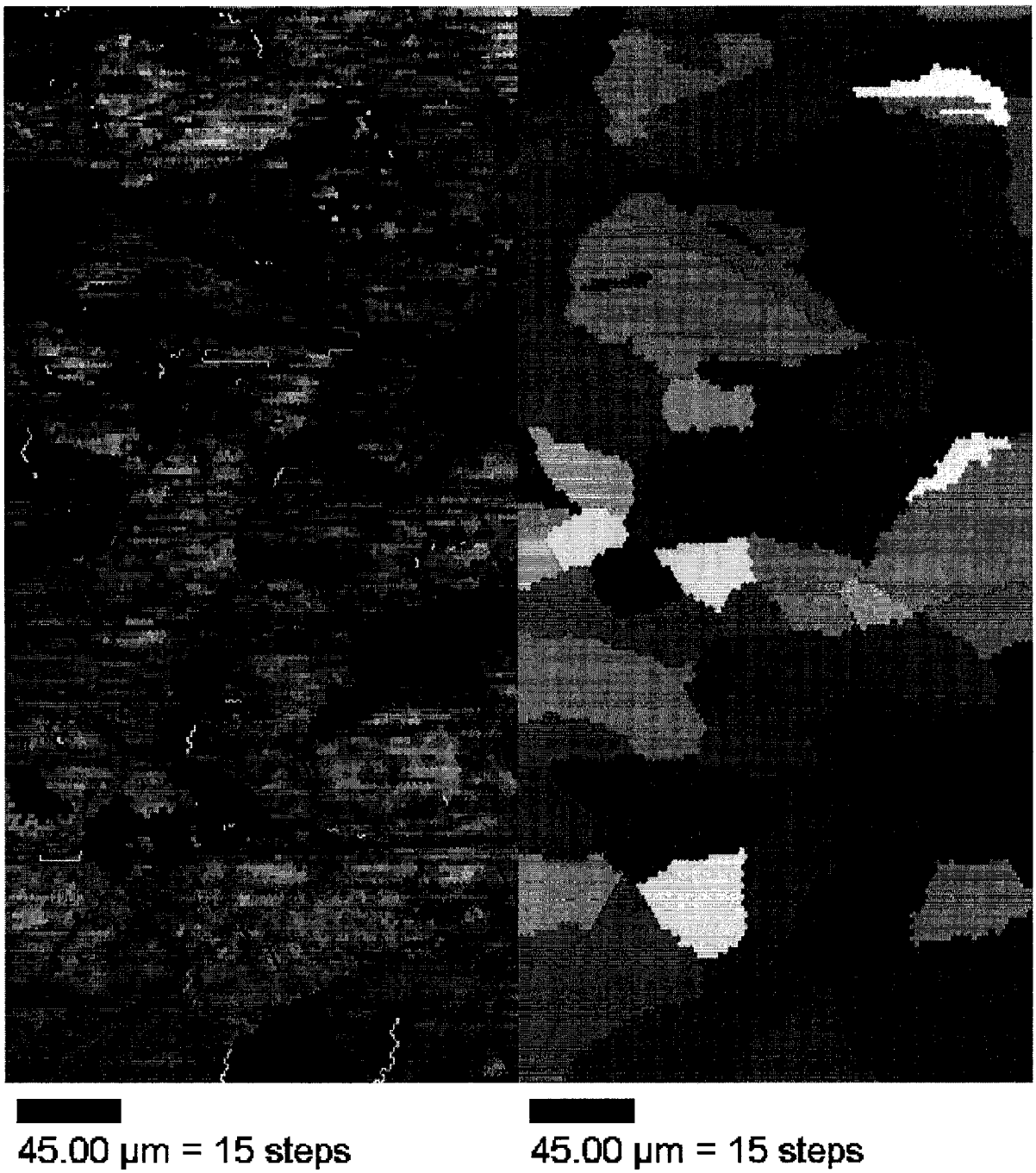

Figure 4.3.19 OIM scan (left) and IPF (right) for the Ni_4Mo pre-annealed at 800^0 C with 0.5 dpa H^+ and post-irradiation annealed at 350^0 C.

Chart: Grain Size (diameter)

Edge grains excluded from analysis

Diameter [microns]	Area Fraction
7.67418	0.238671
8.19757	0
8.75666	0
9.35388	0.124622
9.99182	0
10.6733	0.0876133
11.4012	0.0755287
12.1788	0
13.0094	0.0543807
13.8967	0.0422961
14.8444	0.0483384
15.8569	0.0271903
16.9383	0.0392749
18.0935	0.0181269
19.3275	0.0400302
20.6457	0.0581571
22.0538	0.0400302
23.5579	0.0143505
25.1646	0.070997
26.8808	0.0203927
Average	
Number	9.96412
Area	13.6803

Figure 4.3.20 Grain size statistics for the OIM scan in Figure 4.3.19.

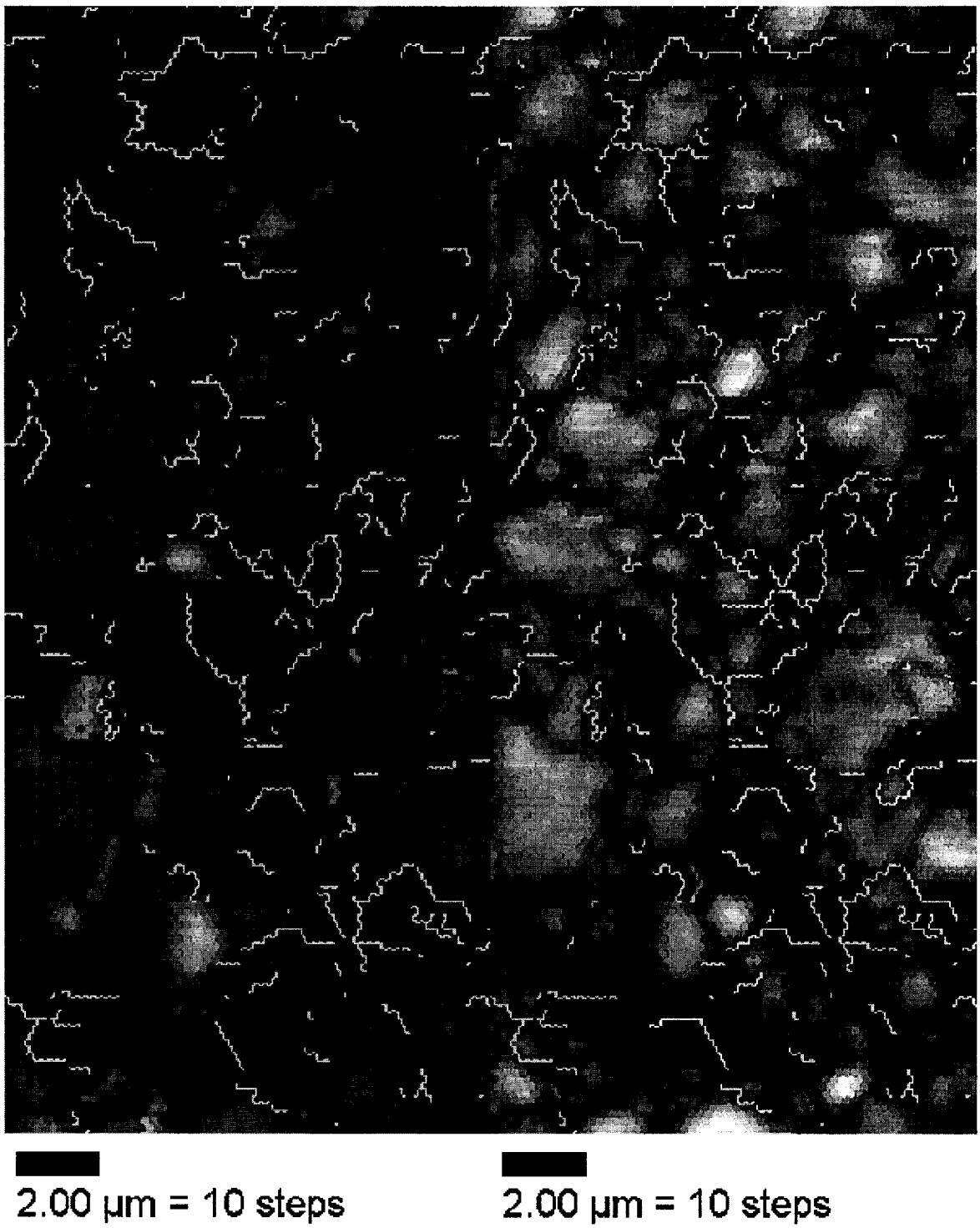

Figure 4.3.21 OIM scan and grain boundary structure for the Ni_4Mo pre-annealed at 800^0 C irradiated at 1 dpa H^+ and annealed at 450^0 C.

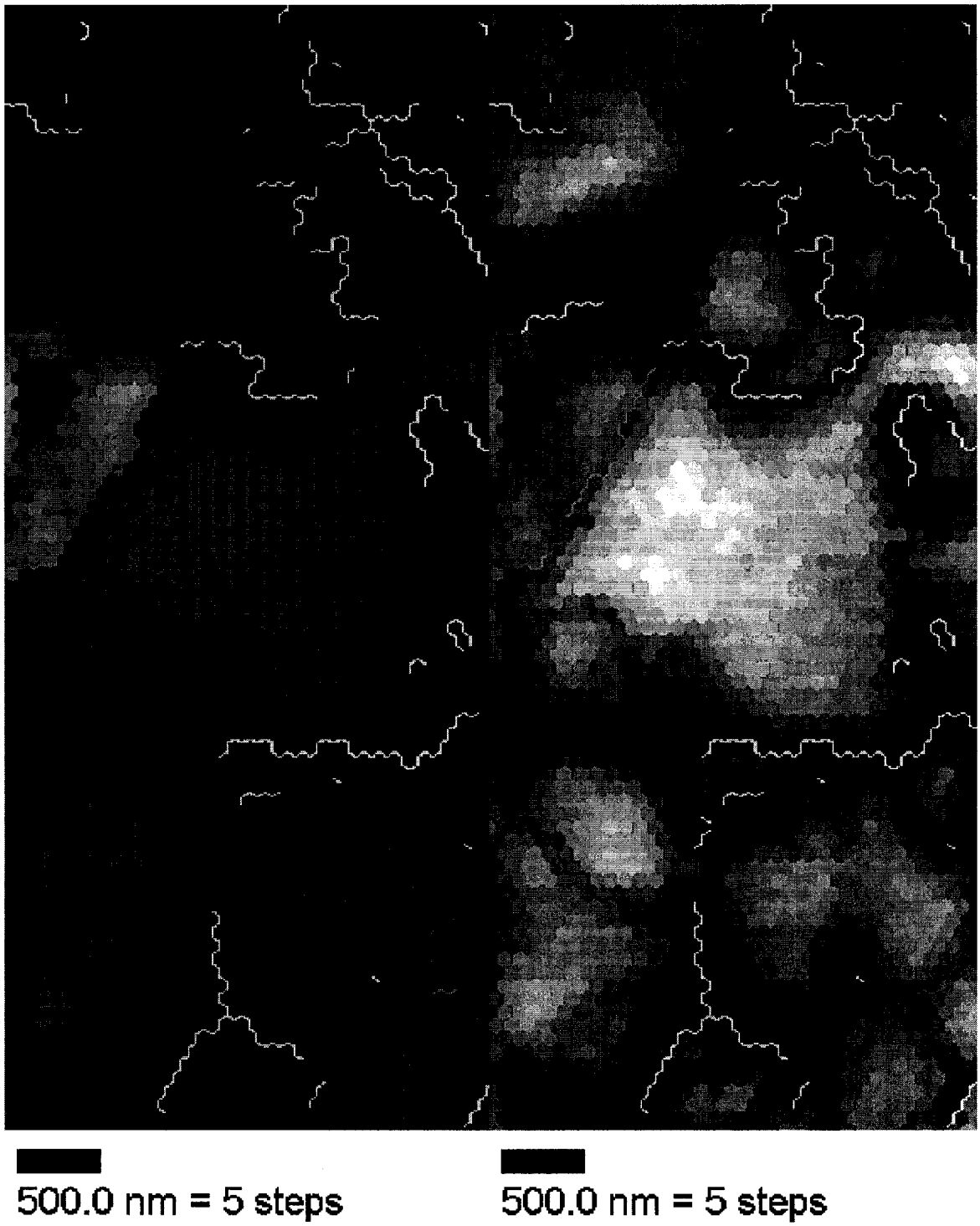

Figure 4.3.22 Detailed OIM scan (smaller step) and grain boundary picture of the scan in Figure 4.3.21.

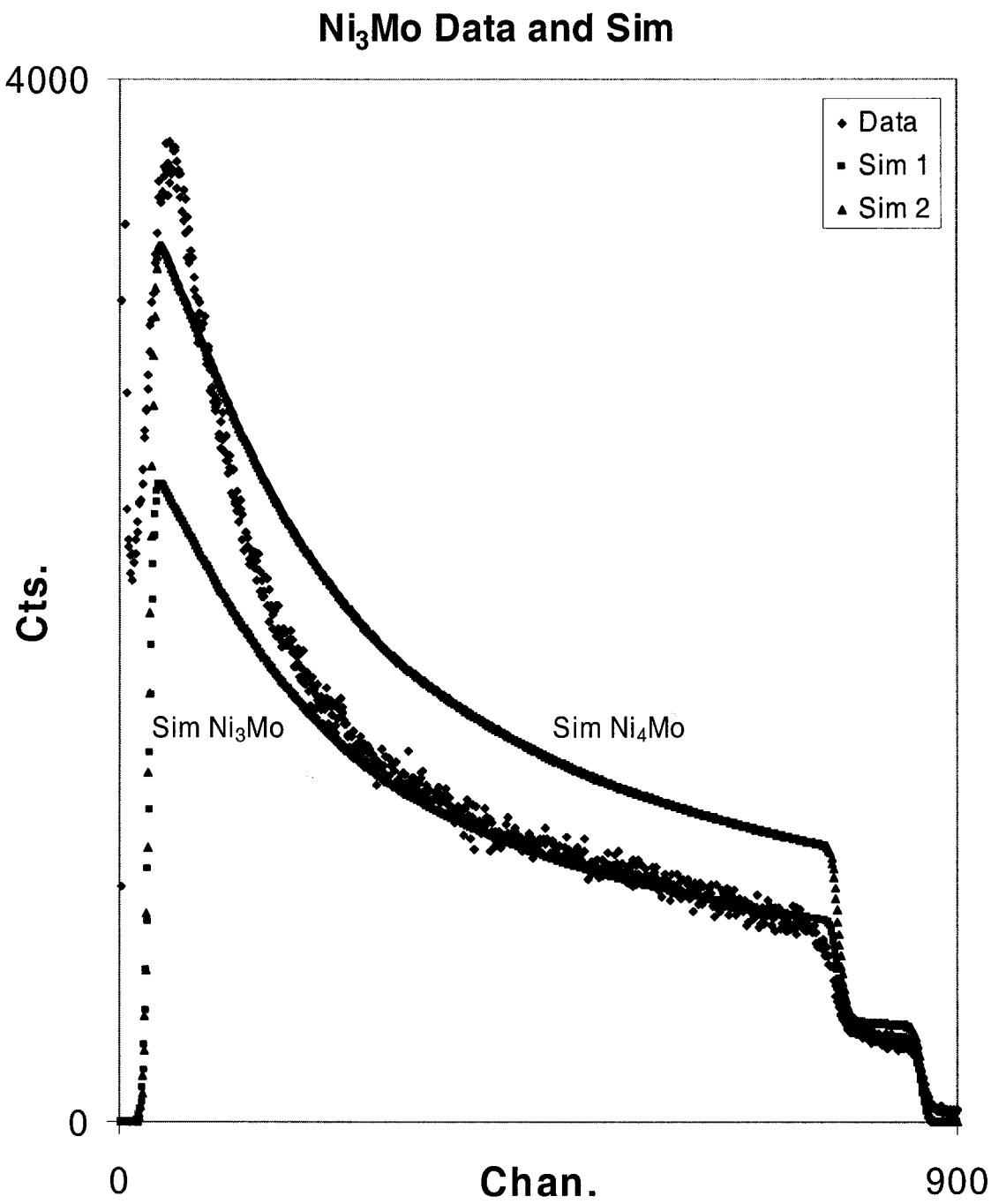

Figure 4.4.1 RBS spectrum with data from a Ni_3Mo sample and two simulated spectra: one for Ni_3Mo and one for Ni_4Mo. This method is successfully used to check if the sample had the desired stoichiometry.

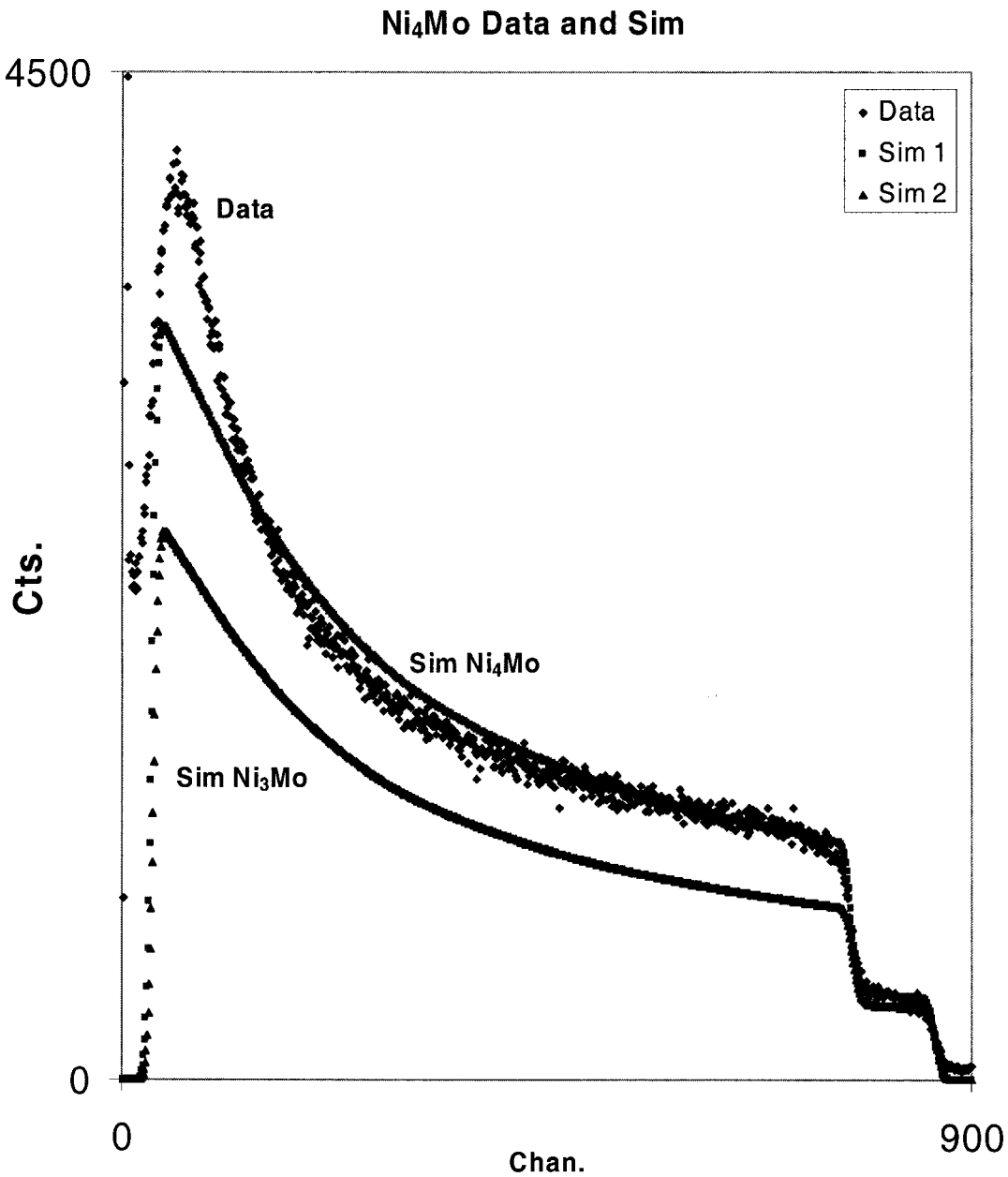

Figure 4.4.2 RBS spectrum with data from a Ni_4Mo sample and two simulated spectra: one for Ni_3Mo and one for Ni_4Mo. This method is successfully used to check if the sample had the desired stoichiometry.

```
Empty File 'f:\a\924files\09240336.rbs                    '
Identier   'Ni4Mo , 0.2H A450                             '
Date       'Spectrum Acquired at 17:56 on 24 September 19031  '
Charge      3.700000     MeV   2.000000
Conversion  1.922000          38.00000
Theta      0.0000000E+00 Phi    10.00000
Omega       5.000000     Corr   1.000000
Choff      0.0000000E+00 FWHM   20.00000
Current    0.0000000E+00
Geometry   IBM      Beam   4He++
Swallow
```

```
Empty File 'f:\a\924files\09240336.rbs                    '
Identier   'Ni4Mo , 0.2H A450                             '
Date       'Spectrum Acquired at 17:56 on 24 September 19031  '
Charge      3.700000     MeV   2.000000
Conversion  1.922000          38.00000
Theta      0.0000000E+00 Phi    10.00000
Omega       5.000000     Corr   1.000000
Choff      0.0000000E+00 FWHM   20.00000
Current    0.0000000E+00
Geometry   IBM      Beam   4He++
Swallow
```

Figure 4.4.3 The data file header from RUMP required to generate the two simulated plots for Ni_3Mo and Ni_4Mo.

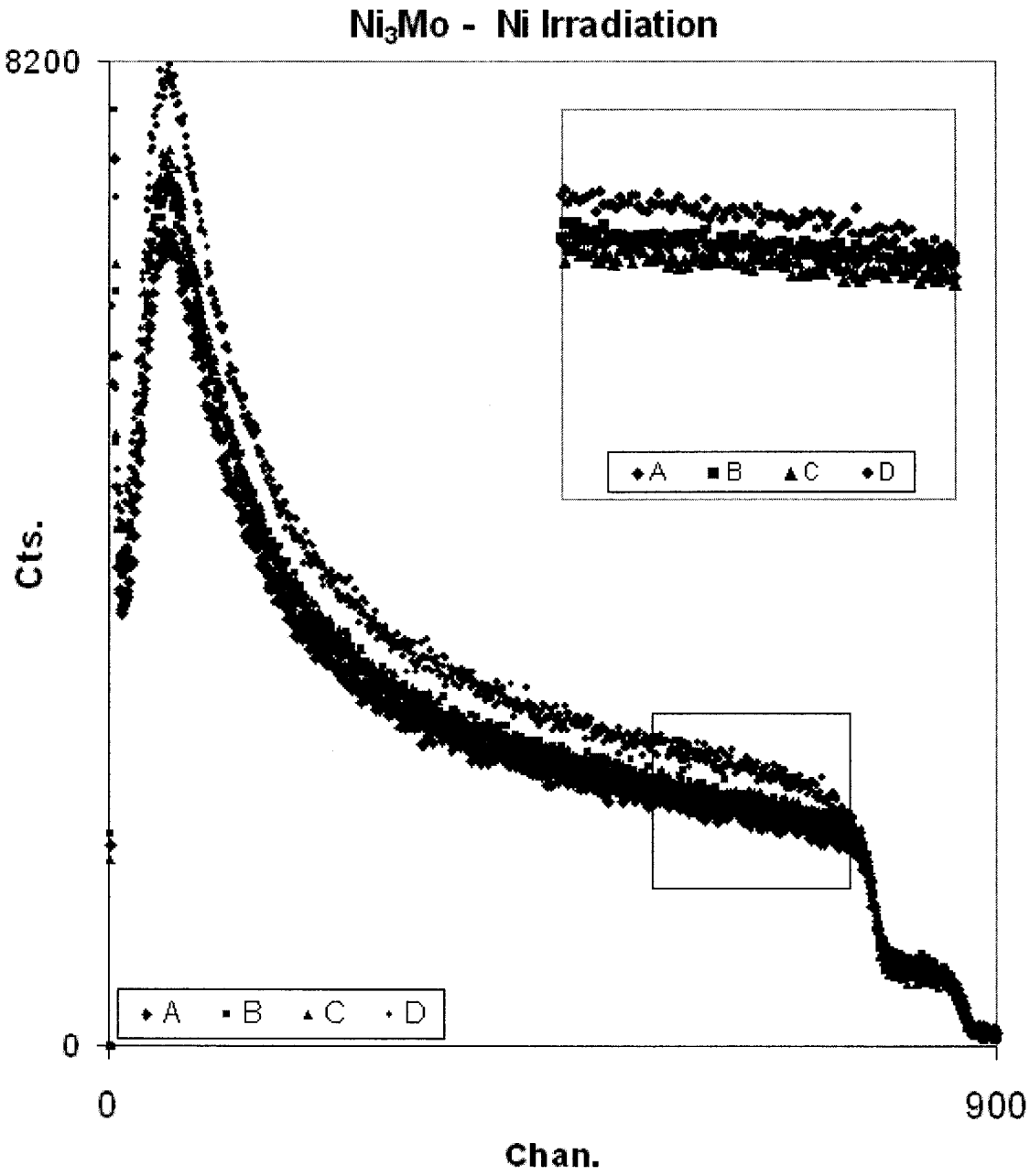

Figure 4.4.4 RBS spectrum for the measurement of Ni_3Mo exposed to Ni^+ irradiation. The doses are A: 0.01 DPA, B: 0.1 DPA, C: 0.5 DPA, D: 1 DPA. We can see some Mo segregation when exposed to higher doses (apparently more Ni than in the 4:1 ratio).

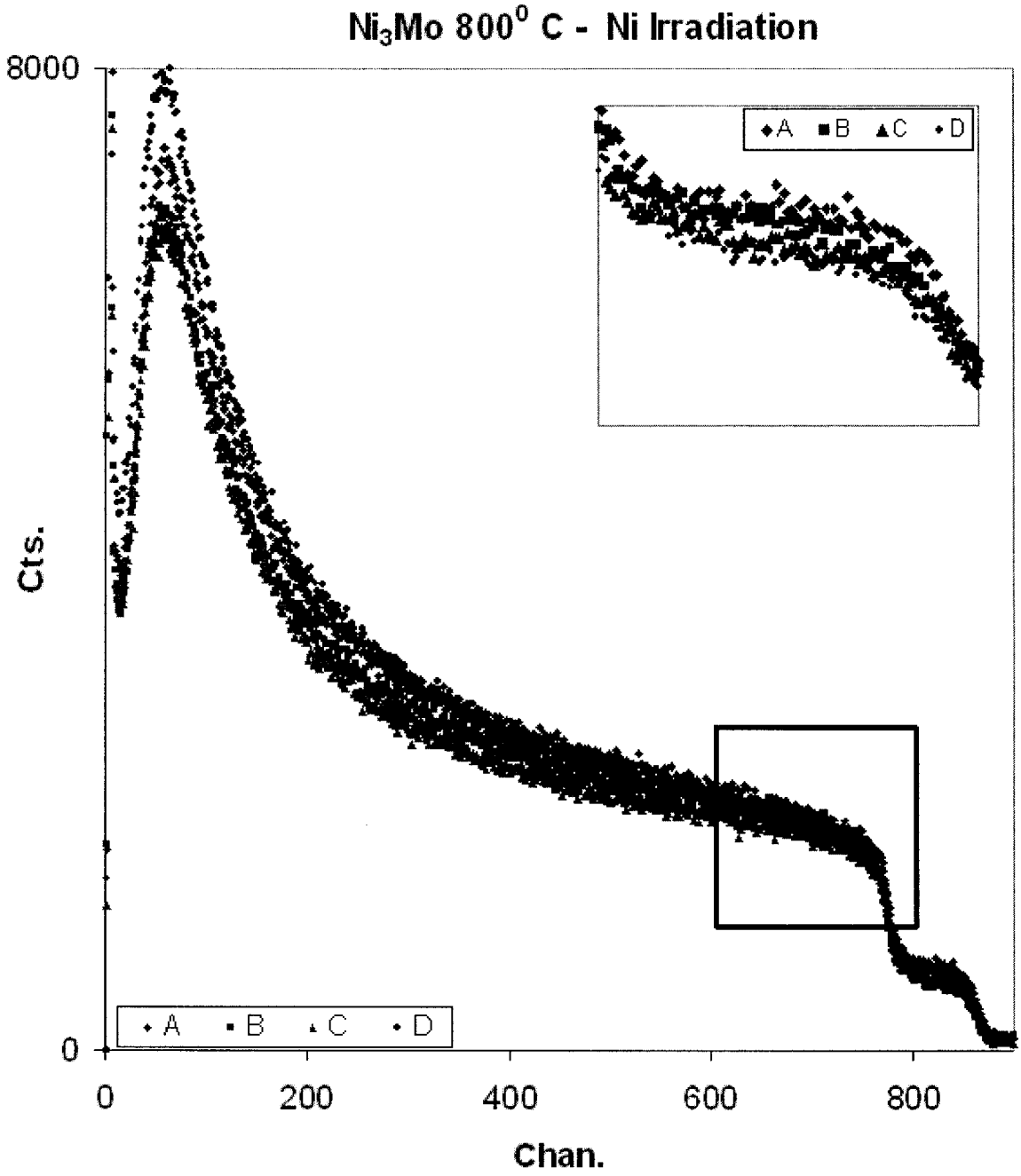

Figure 4.4.5 RBS spectrum for the measurement of Ni_3Mo annealed at 800^0 C before exposed to Ni^+ irradiation. The doses are A: 0.01 DPA, B:0.1 DPA, C:0.5 DPA, D: 1 DPA. No significant difference between the plots.

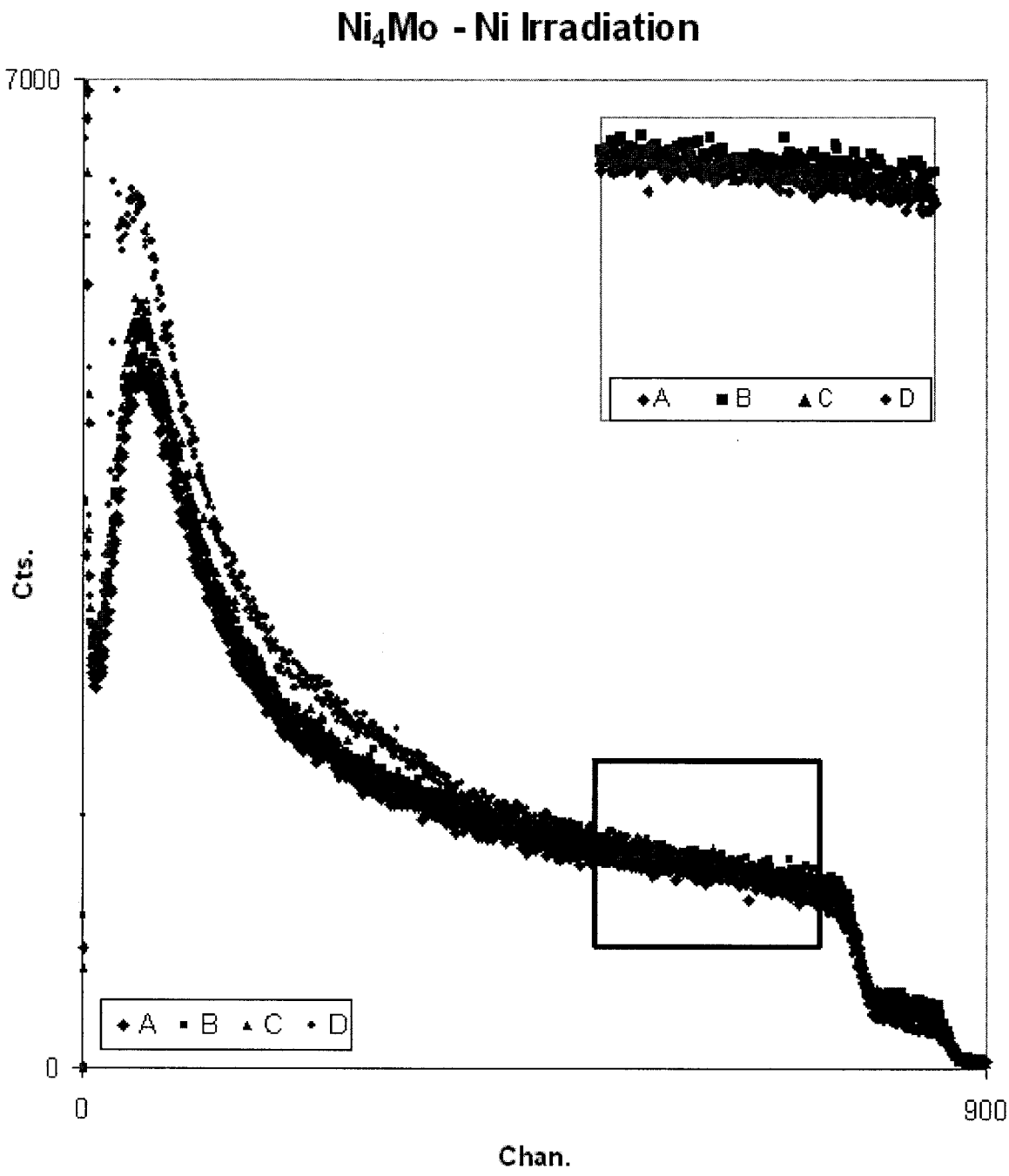

Figure 4.4.6 RBS spectrum for the measurement of Ni_4Mo exposed to H^+ irradiation. The doses are A: 0.01 DPA, B:0.1 DPA, C:0.5 DPA, D: 1 DPA.

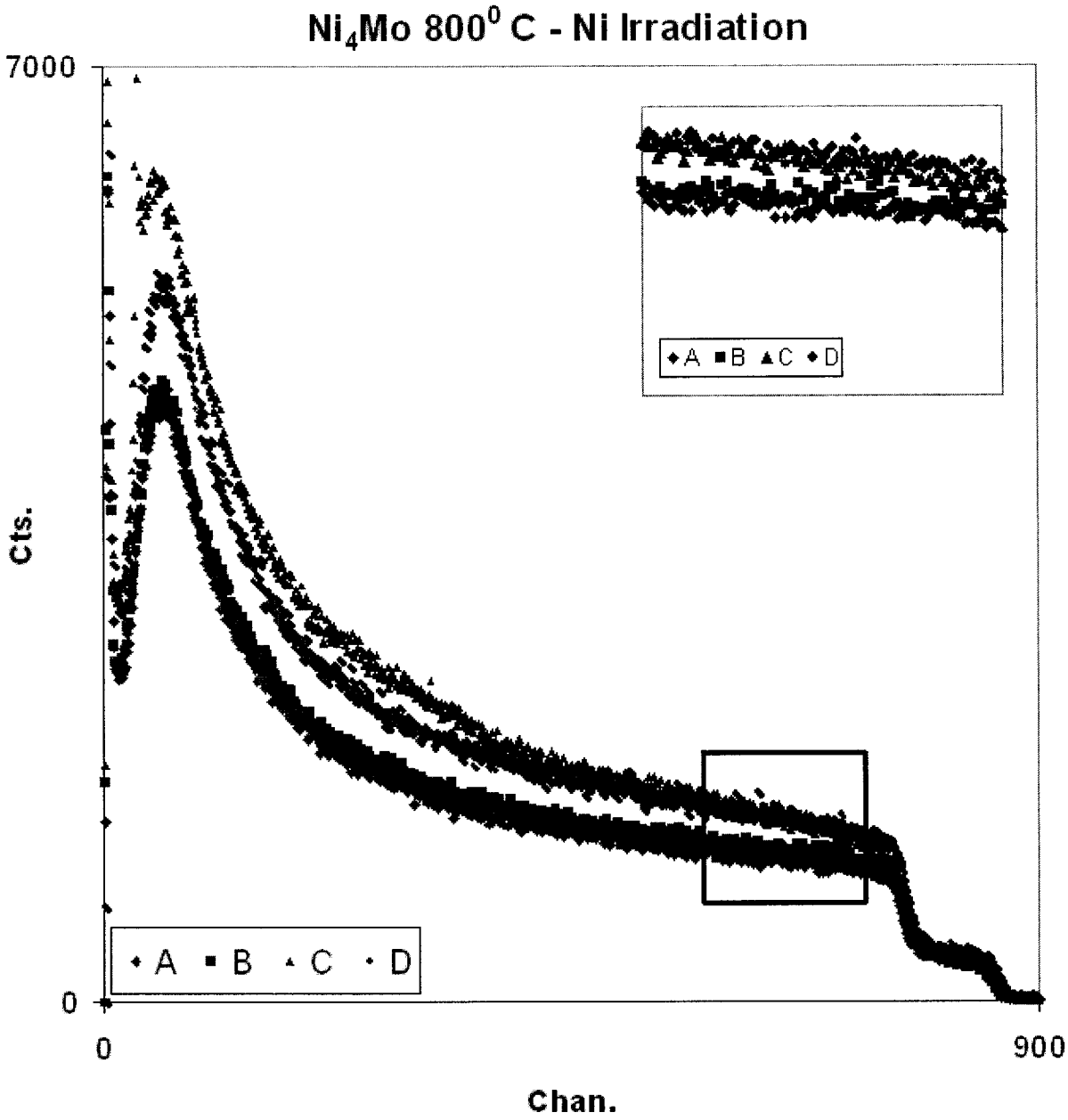

Figure 4.4.7 RBS spectrum for the measurement of Ni_4Mo annealed at 800^0 C before exposed to H^+ irradiation. The doses are A: 0.01 DPA, B:0.1 DPA, C:0.5 DPA, D: 1 DPA. There is a segregation of Mo at the surface of the alloy.

#	Alloy	H (VH)	d1(μm)	d2(μm)
1	Ni	196.37	9.84	9.63
2	NiMo	616.12	5.57	5.45
3	Ni2Mo	253.62	8.73	8.38
4	Ni3Mo	283.48	8.13	8.06
5	Ni3Mo 800 C	454.27	6.45	6.34
6	Ni3Mo 1000 C	253.62	8.73	8.38
7	Ni4Mo	256.19	8.53	8.48
8	Ni4Mo 800 C	268.27	8.46	8.18
9	Ni4Mo 1000 C	262.06	8.51	8.33

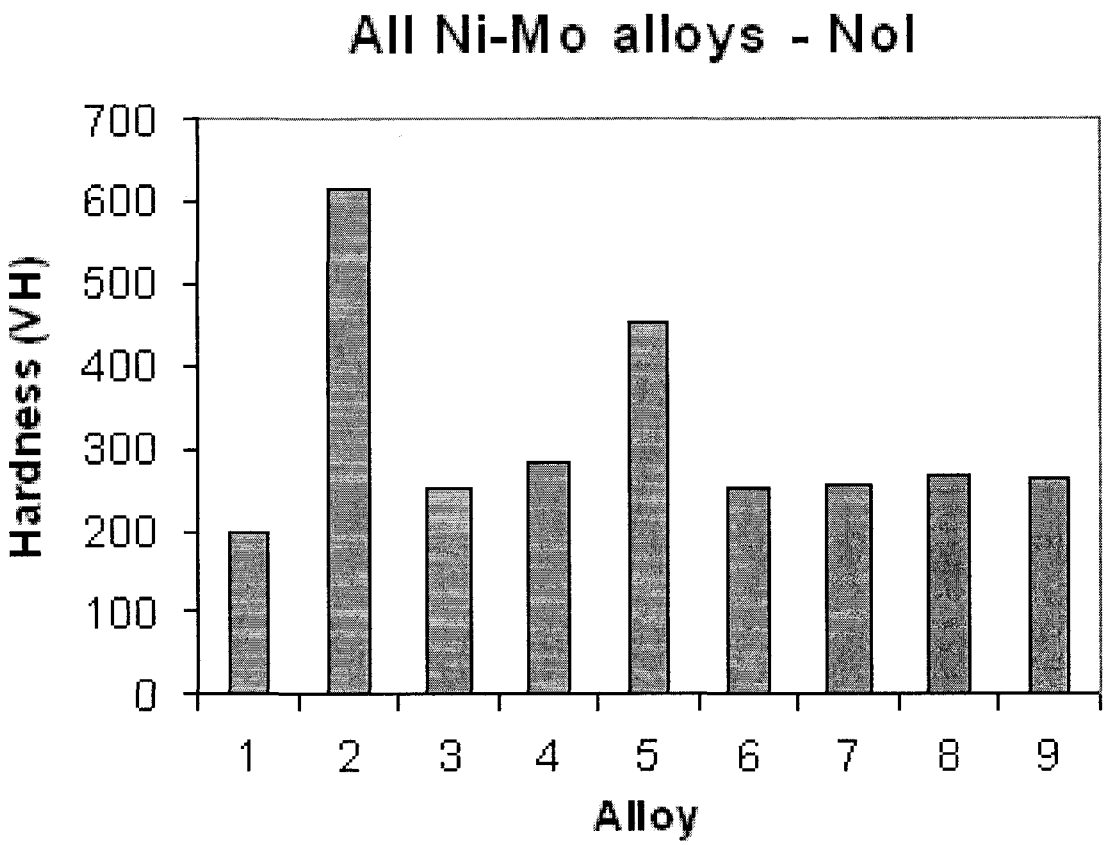

Figure 4.5.1 Hardness values for Ni and all Ni-Mo alloys with no exposure to irradiation. Averaged Vickers hardness values and the averaged dimensions of the indentation are displayed in the table.

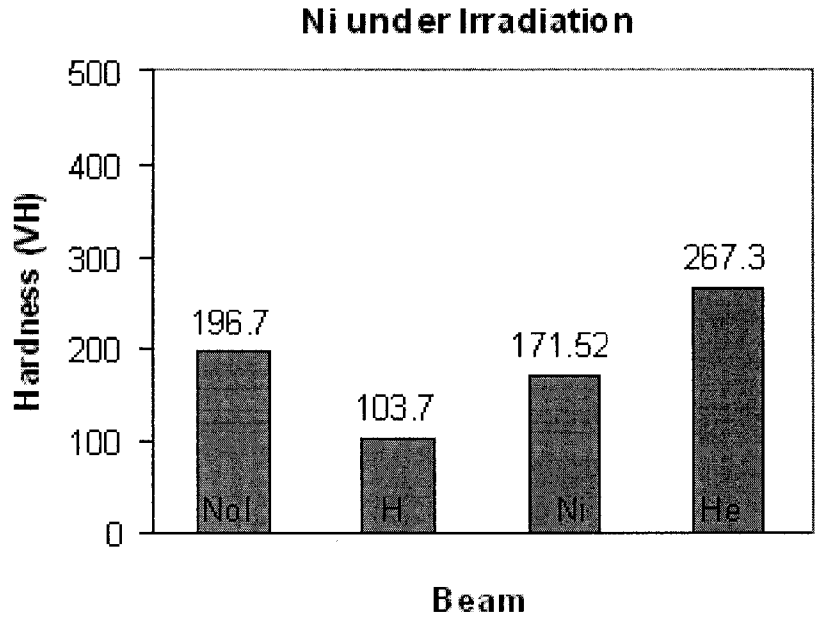

Figure 4.5.2 Hardness values for Ni with irradiation exposure to a dose of 1 DPA. The beams considered are H^+, Ni^+ and He^+.

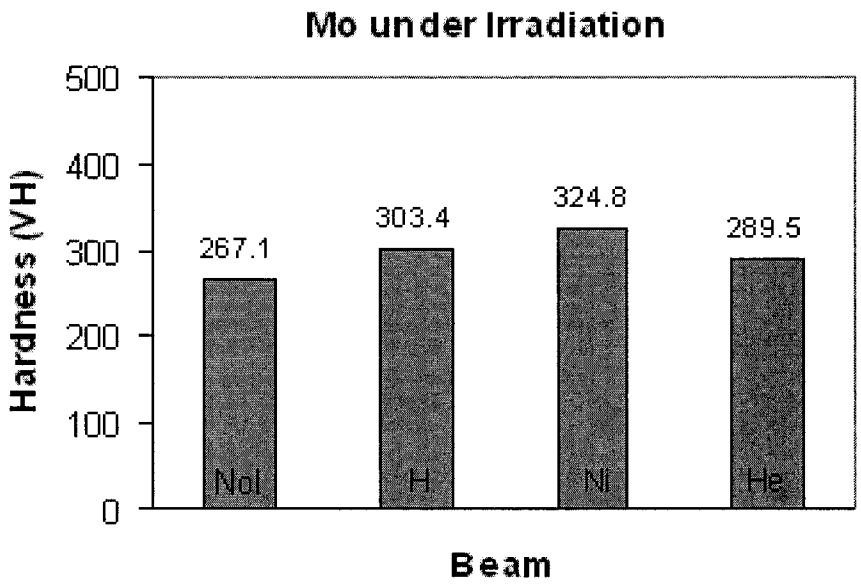

Figure 4.5.3 Hardness values for Ni_3Mo alloy with irradiation exposure to a dose of 1 DPA. The beams considered are H^+ and Ni^+.

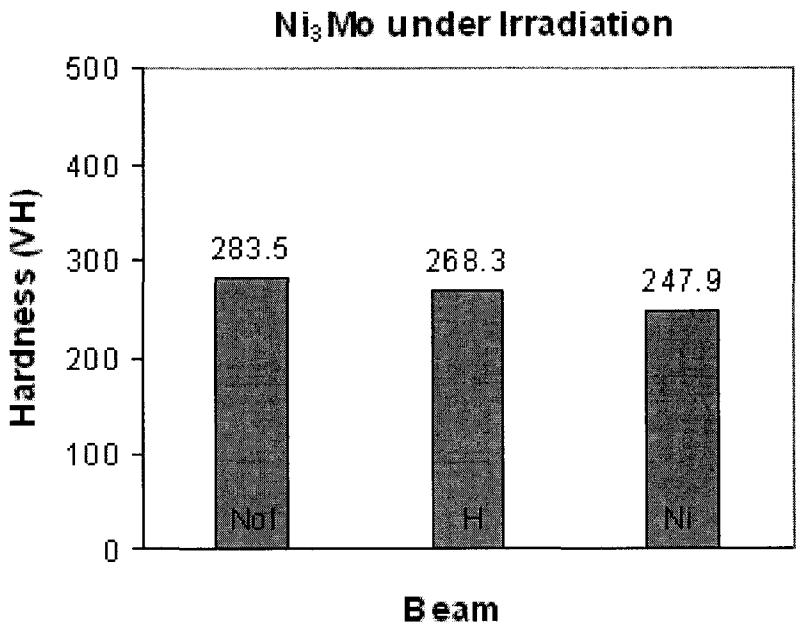

Figure 4.5.4 Hardness values for Ni_3Mo with irradiation exposure to a dose of 1 DPA. The beams considered are H^+ and Ni^+

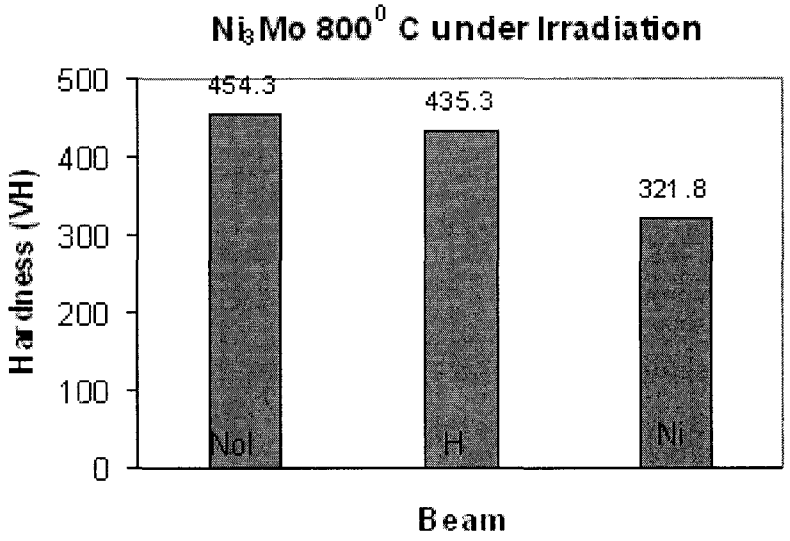

Figure 4.5.5 Hardness values for Ni_3Mo alloy annealed at 800^0 C with irradiation exposure to a dose of 1 DPA. The beams considered are H^+ and Ni^+.

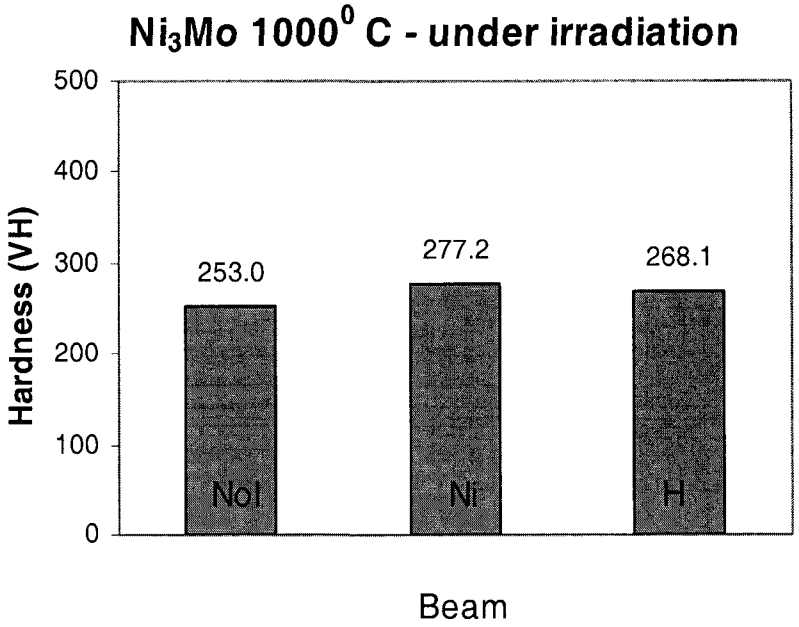

Figure 4.5.6 Hardness values for Ni_3Mo alloy annealed at 1000^0 C with irradiation exposure to a dose of 1 DPA. The beams considered are H^+ and Ni^+.

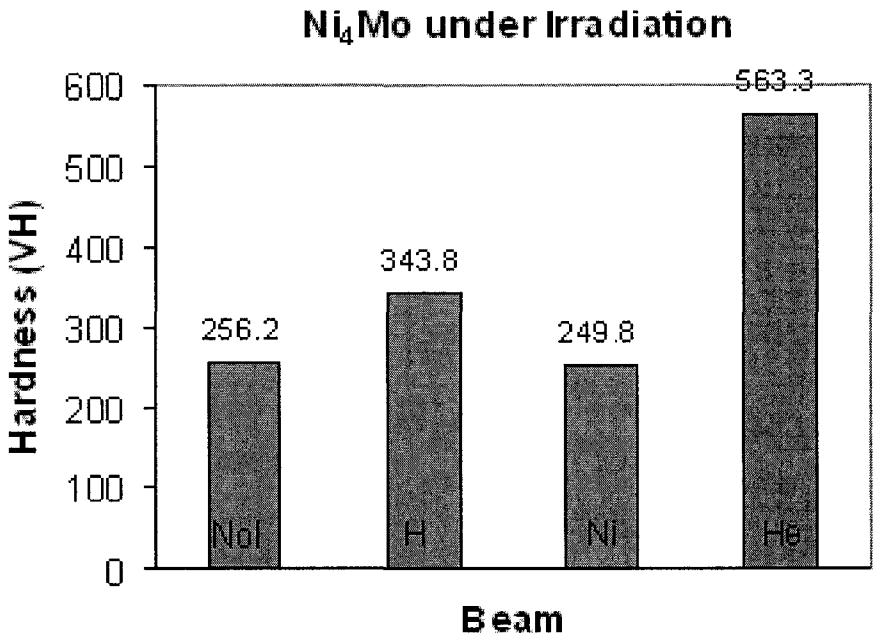

Figure 4.5.7 Hardness values for Ni_4Mo alloy with irradiation exposure to a dose of 1 DPA. The beams considered are H^+, Ni^+ and He^+.

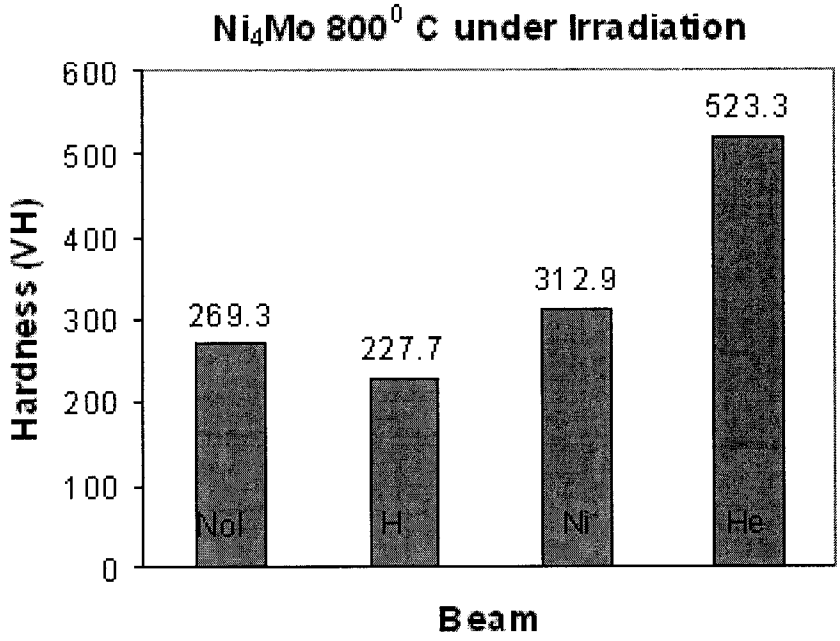

Figure 4.5.8 Hardness values for Ni_4Mo alloy pre-annealed at 800^0 C with irradiation exposure to a dose of 1 DPA. The beams considered are H^+, Ni^+ and He^+.

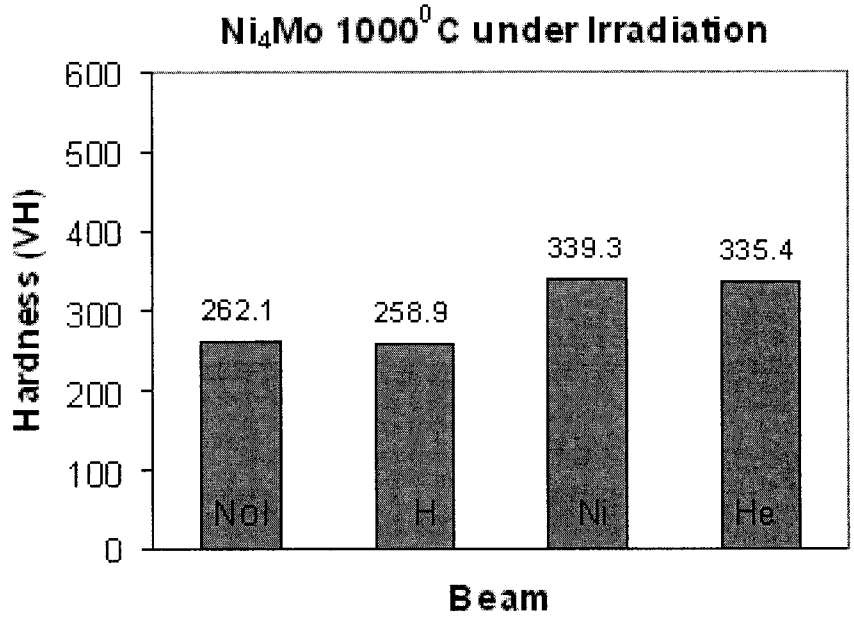

Figure 4.5.9 Hardness values for Ni_4Mo alloy C pre-annealed at 1000^0 C with irradiation exposure to a dose of 1 DPA. The beams considered are H^+, Ni^+ and He^+.

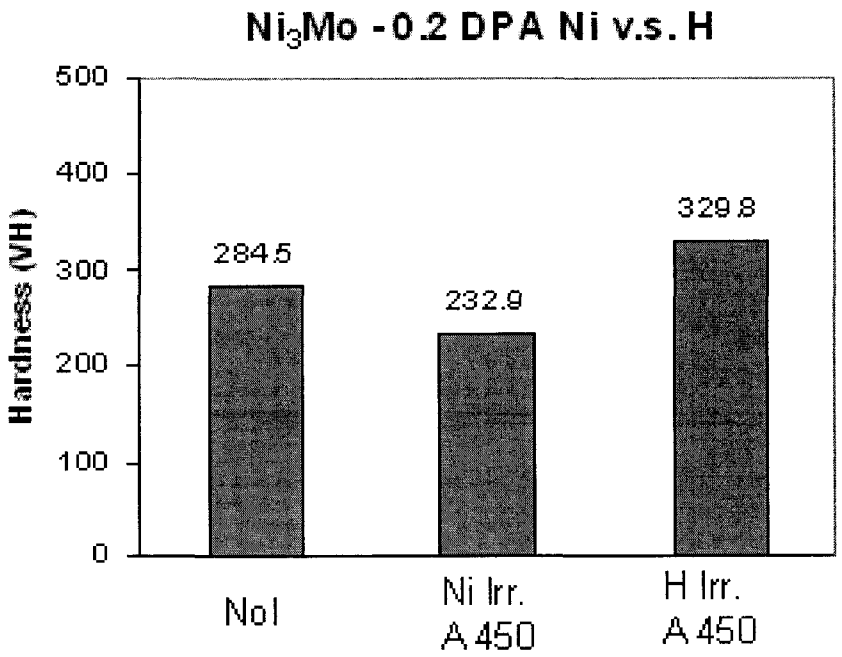

Figure 4.5.10 Ni_3Mo hardness comparison between 0.2 DPA Ni^+ and 0.2 DPA H^+ irradiations. Samples were annealed after irradiation to 450^0 C.

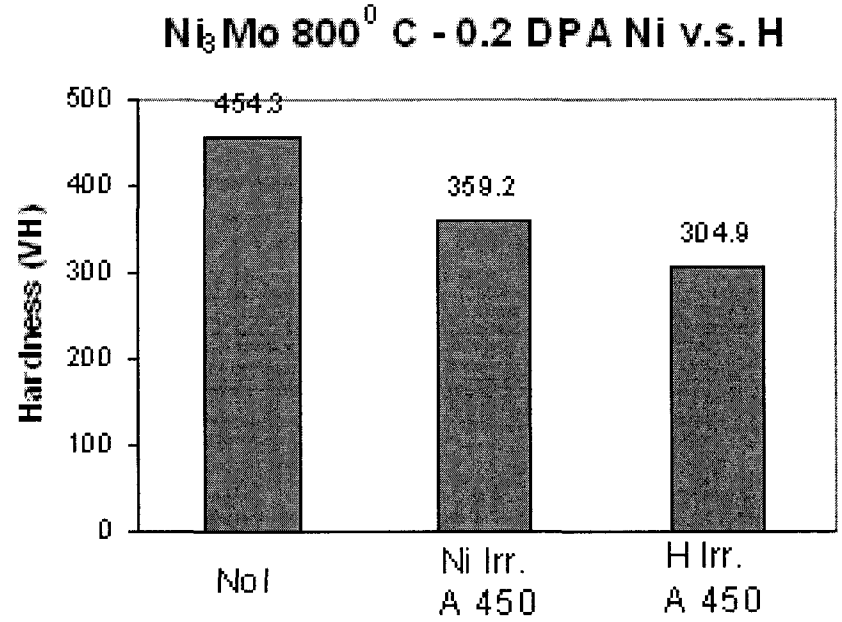

Figure 4.5.11 Ni_3Mo annealed at 800^0 C, hardness comparison between 0.2 DPA Ni^+ and 0.2 DPA H^+ irradiations. Samples were annealed after irradiation to 450^0 C.

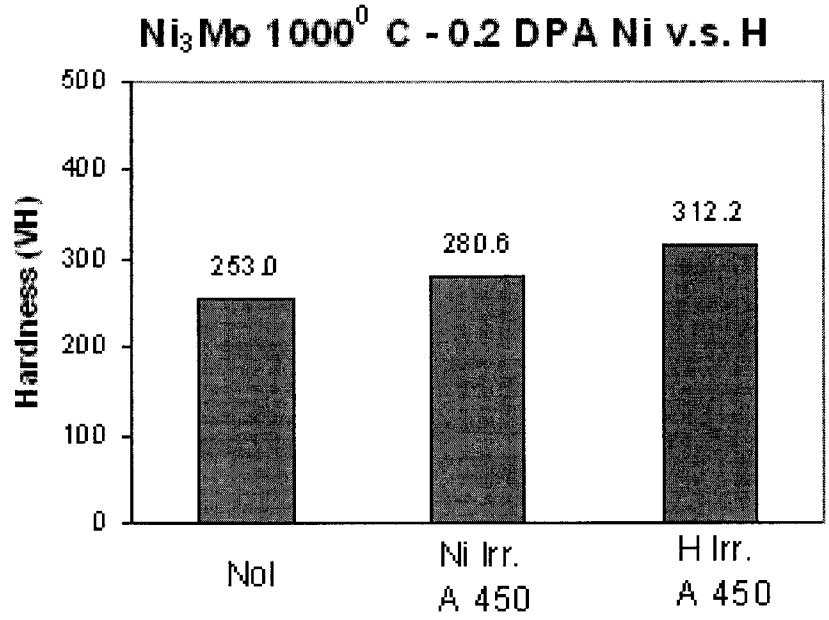

Figure 4.5.12 Ni_3Mo annealed at 1000^0 C. Hardness comparison between 0.2 DPA Ni^+ and 0.2 DPA H^+ irradiations. Samples were annealed after irradiation to 450^0 C.

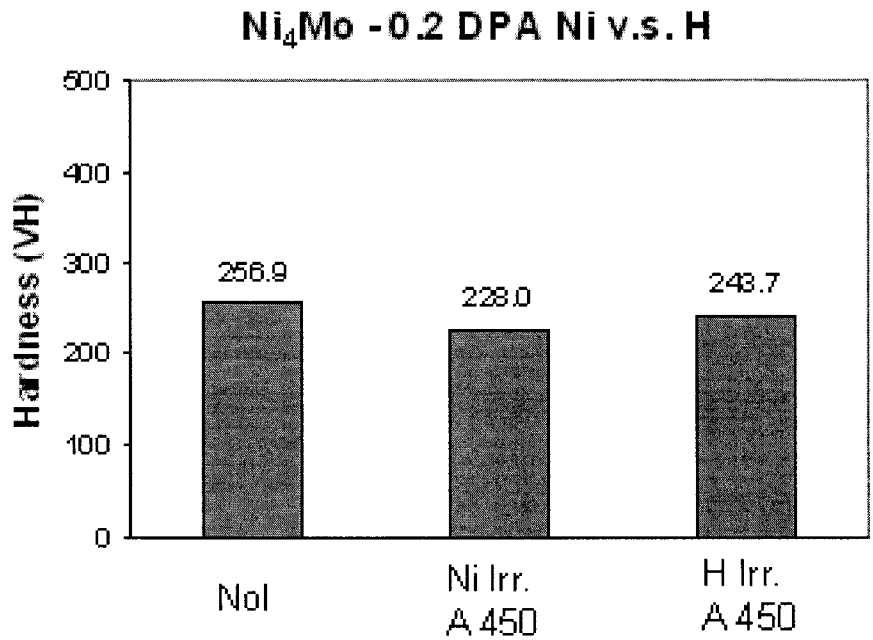

Figure 4.5.13 Ni_4Mo hardness comparison between 0.2 DPA Ni^+ and 0.2 DPA H^+ irradiations. Samples were annealed after irradiation to 450^0 C.

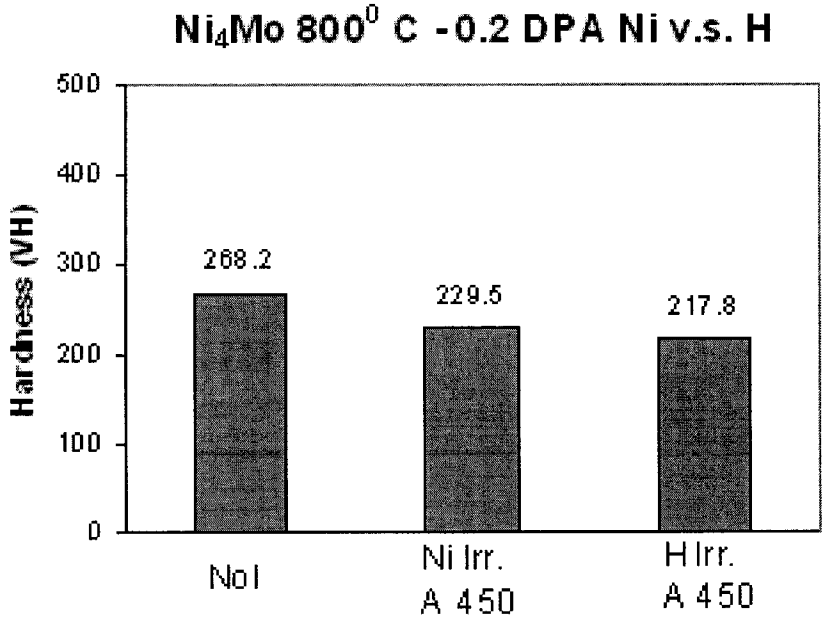

Figure 4.5.14 Ni_4Mo pre-annealed at 800^0 C. Hardness comparison between 0.2 DPA Ni^+ and 0.2 DPA H^+ irradiations. Samples were annealed after irradiation to 450^0 C.

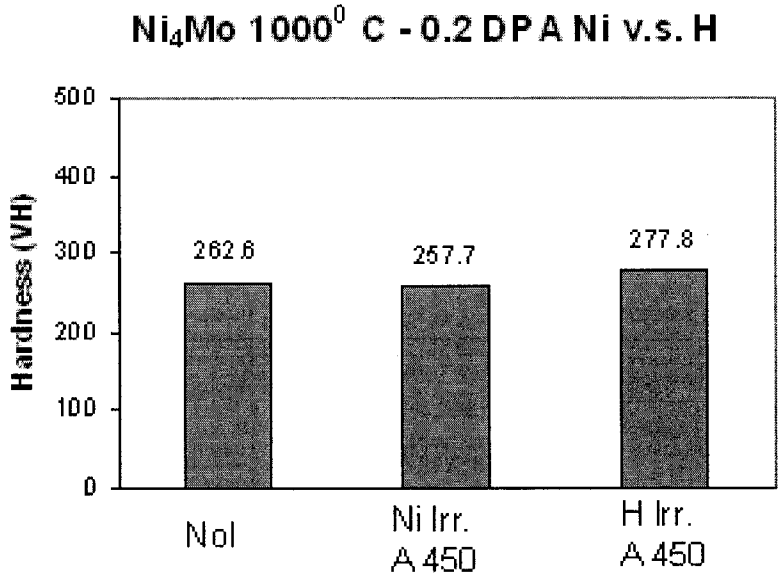

Figure 4.5.15 Ni_4Mo pre-annealed at 1000^0 C, hardness comparison between 0.2 DPA Ni^+ and 0.2 DPA H^+ irradiations. Samples were annealed after irradiation to 450^0 C.

A

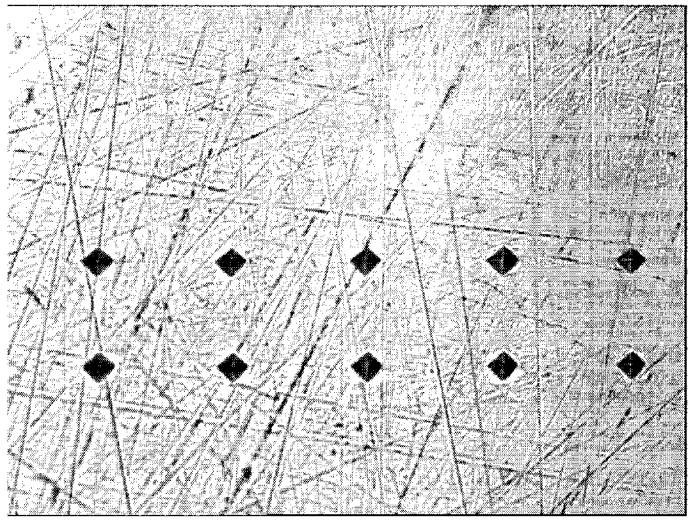

B

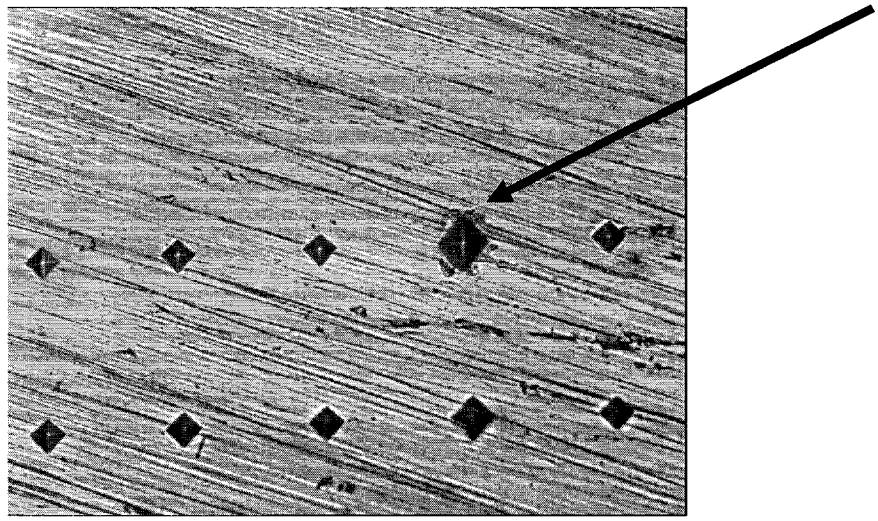

Figure 4.5.16 Indentation examples. In (A) normal indents spread over a 1 mm distance, where the variation in size is minimal. In (B) one of the indents got into one of the defects induced by irradiation, and the hardness reading would be much less (larger indent).

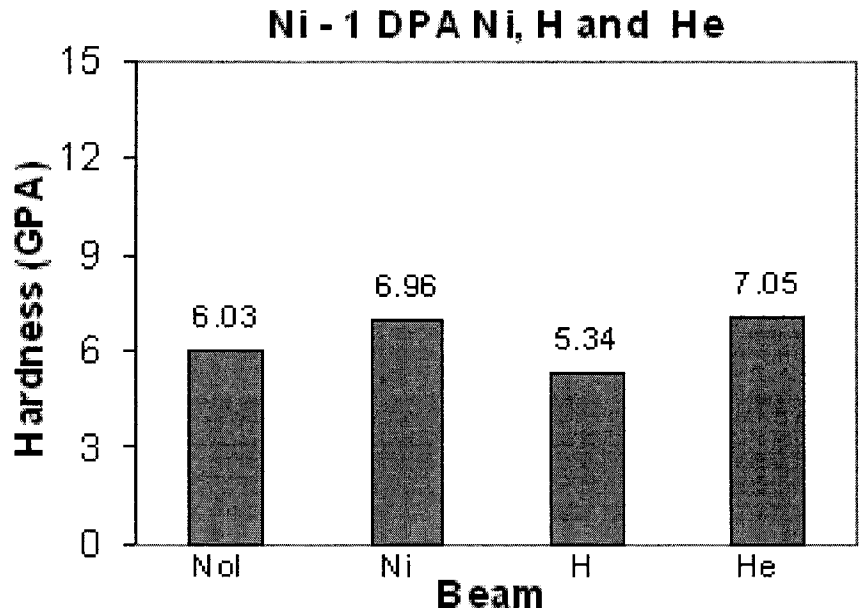

Figure 4.5.17 The hardness of Ni as a function of irradiation beam with the same dose (1 DPA). Measurements by nanoindentation.

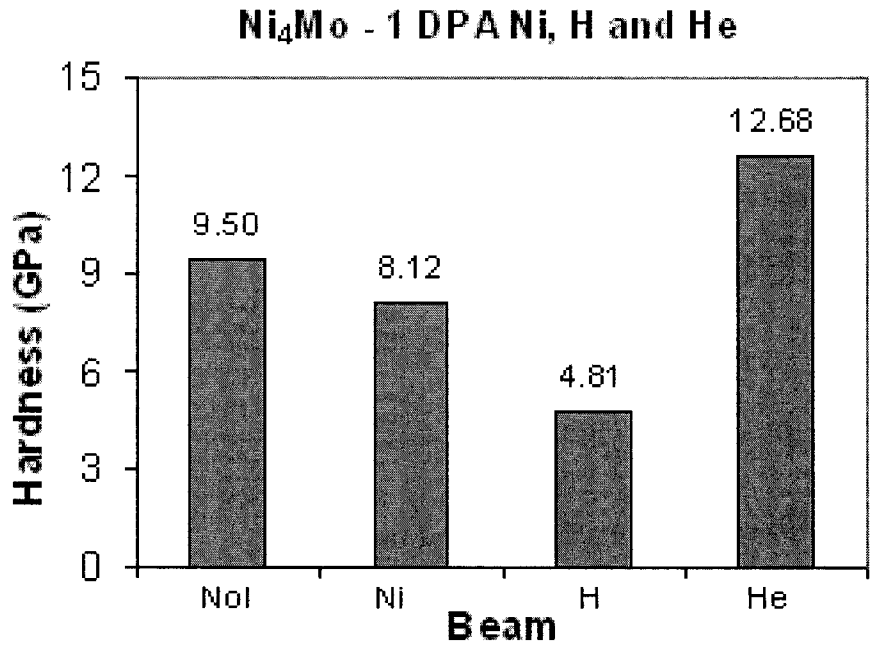

Figure 4.5.18 The hardness of Ni_4Mo as a function of irradiation beam with the same dose (1 DPA). Measurements by nanoindentation.

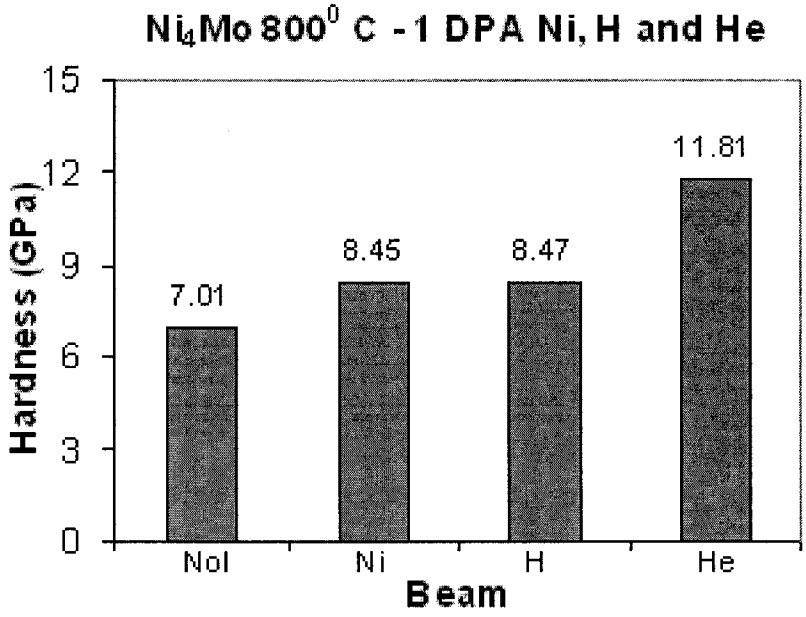

Figure 4.5.19 The hardness of Ni_4Mo pre-annealed at 800^0 C as a function of irradiation beam with the same dose (1 DPA). Measurements by nanoindentation.

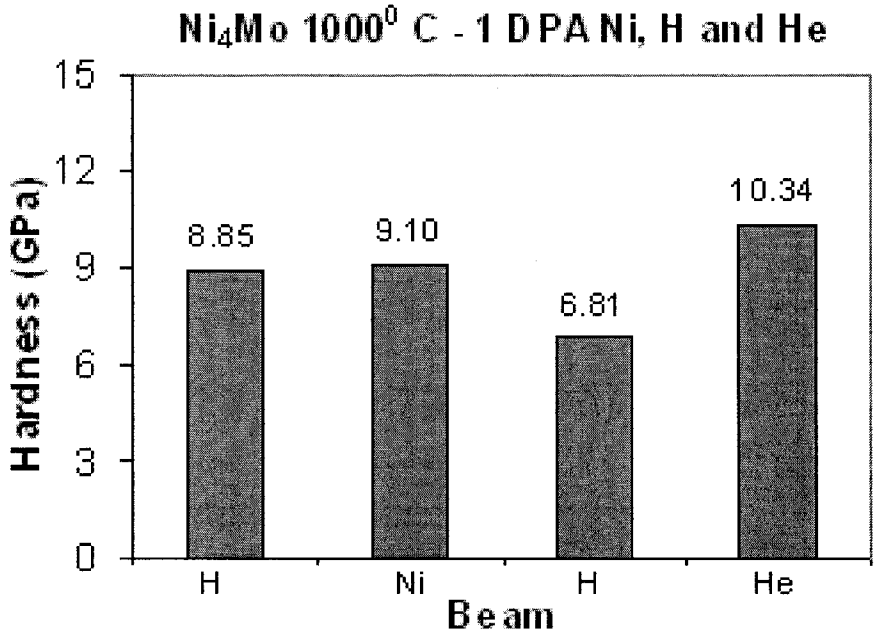

Figure 4.5.20 The hardness of Ni_4Mo pre-annealed at 800^0 C as a function of irradiation beam with the same dose (1 DPA). Measurements by nanoindentation.

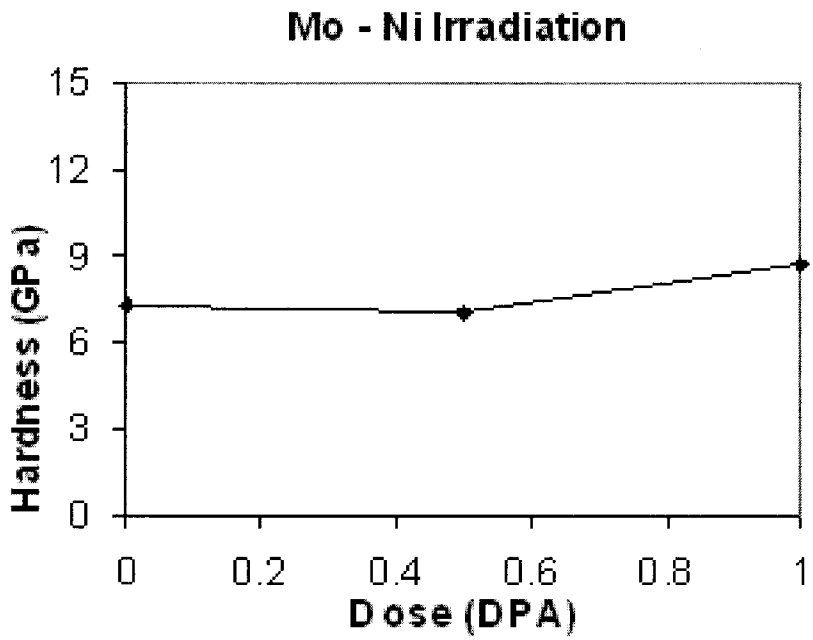

Figure 4.5.21 Mo hardness as a function of Ni^+ irradiation dose. Measurements by nanoindentation.

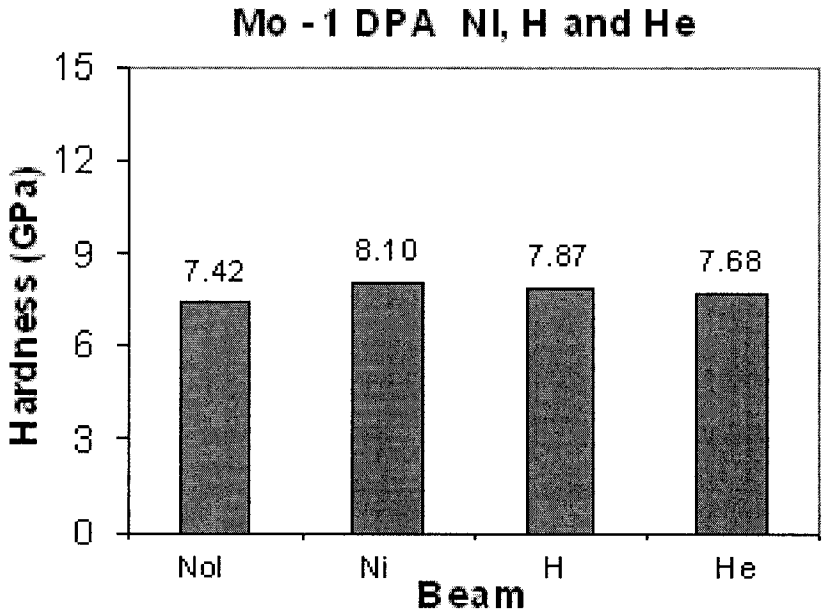

Figure 4.5.22 The hardness of Mo as a function of irradiation beam with the same dose (1 DPA). Measurements by nanoindentation.

CHAPTER 5

DISCUSSION

The irradiation effects on binary alloys can be understood by employing the Thermal Spikes Model (TSM), as presented by Potter [21]. The considerable variation in grain growth observed after irradiation indicates that the collision displacements are not enough to explain the ion-induced grain-size change. However, this model can explain well some of the effects observed in ion-irradiated materials [14, 40, 45 and 65]. During the thermal spike phase of a displacement cascade, the remaining kinetic energy of the recoil atoms is thermalized within the crystal lattice. Because of this thermalization, each primary recoil causes a temperature spike to occur in a small localized region of the lattice. When spikes occur on the grain boundary, atoms can be thermally activated to jump across. If a net number of atom jumps occur in one direction across the boundary, the boundary will be displaced or will migrate in opposite direction. Also diffusion-induced grain boundary migration [115] is a possible effect that could influence the ion-induced grain size change of the alloys during irradiation. The problem with the diffusion is that it cannot offer a complete explanation, as the main driving force in the structural change of the materials subject to irradiation. At low temperature, the diffusion constant is small and the diffusion cannot become the main force behind the observed grain refinement. During the irradiation, the chemical potential could vary a lot.

Changes in material due to the variation of the chemical potential may cause the rapid change observed in low-temperature post-irradiation annealing.

So far, most theories treating the transition order-disorder consider that the intensities of the superlattice peaks are proportional to the square of the degree of order, or S^2 [24]. This parameter can provide a qualitative measure of the degree of order and is at the core of the "The Radiation Disorder Model" (RDM), created by Zee and Wilkes [25]. The parameter (S) is modeled into irradiation effects. First, they consider radiation disordering through local cascade replacements and replacement collision sequences that create point defects. Next, they consider the ordering energy as the energy difference for a wrong pair (right atom on wrong lattice site) and for a right pair (right atom on right lattice site), as Dienes suggested [34]. Ordering proceeds by a vacancy mechanism and the increased ordering under irradiation is a proof of this fact, as we have seen from our results as well. They came up with an equation that describes the actual ordering rate, as a balance between radiation disordering rate and the radiation enhanced ordering:

$$\frac{dS}{dt} = \frac{dS}{dt_{irr}} + \frac{dS}{dt_{thermal}} \tag{5.1}$$

If this equation is plotted for a specific alloy, according to the formulas from the RDM model at high temperatures, radiation does not have too much of an effect when thermal energy dominates. This is due to the fact that at high temperatures there are already a lot of voids. At a low temperature ($<200^0$ C), the enhanced ordering rate is dominant under irradiation. In this case, the mobility of the vacancies decreases and the ordering rate decreases as well. The ordering parameter has, according to most theories, a behavior similar to the one in Figure 5.1.

In the case of Ni^+ irradiations, after times as short as 10 seconds necessary to accumulate 0.01 DPA, detectable changes were observed in the microstructure, reflected in new peaks showing up in the XRD spectra. The main question here is: are we really dealing with an ordering-disordering reaction or a different type of phenomenon? Of course, the interpretation of the results can be done in more than one way. There is also some room for parameter variation or experimental error. Most of the groups researching binary alloys use the terms long-range order or short-range order loosely. Observing superlattice reflection in a spectrum may be enough to conclude that at least SRO could exist in a specific material. The Ni-Mo behavior in pre-irradiation annealing and irradiation experiments has been seen in other binary alloys like Ni-Si, Ni-Al, and Cu-Au [21]. One of the common traits in these alloys is the appearance of dark spots on the surface of the specimens after irradiation. These spots correspond to small volumes or zones of defects. Potter [21] observed these zones in Cu_3Au irradiated with Cu^+ beam. His TEM diffraction proved the fact that these zones have no superlattice reflections. What we observed in Ni-Mo alloys for higher irradiation doses, was observed as well in Cu-Au alloys. The peaks become more and more diffuse and the background stronger, typical to an amorphous state. He concluded that the ordered phase may start developing on dislocation loops, grain boundaries and at the surface of the alloys bombarded with ions.

5.1 Pre-Irradiation Structure

Before considering any specimen for irradiation, I used the Rutherford Backscattering Spectroscopy analysis on Ni_4Mo and Ni_3Mo as-cast to confirm the right stoichiometry, as shown in Figures 4.4.1 and 4.1.2. Ni_4Mo as cast and Ni_3Mo as cast should be in a completely disordered states or contain just a very small fraction of ordered domains. Indeed, as we can see from the no-irradiation (NoI) plots (Figures 4.1.5 and 4.1.12), only the fundamental reflections are present in the spectrum. The Orientation Imaging Microscopy scans of Ni_3Mo and Ni_4Mo as-cast that were performed, revealed an elongated dendritic type grain structure typical to the arc-melting process (Figures 4.3.4, 5, 8, 9, and 10). There is no significant difference between as-cast alloys and the specimens that received pre-irradiation thermal treatment. Surface metallography reveals that there is no significant difference between the surface evolution of Ni_4Mo and Ni_3Mo pre-annealed at 800^0 C or Ni_4Mo and Ni_4Mo as-cast, as we can see from Figures 4.2.1 and 4.2.2. In the NoI spectra of Ni_4Mo and Ni_3Mo pre-annealed at 800^0 C, we can see the peaks specific to an ordered structure (Figures 4.1.17, 4.1.18, 4.1.26 and 4.1.27). The plots of Ni_4Mo and Ni_3Mo pre-annealed at 1000^0 C display few of the superlattice peaks (Figures 4.1.36, 4.1.37, 4.1.39 and 4.1.40). It is possible, that the temperature 1000^0 C was high enough to destroy most of the order in Ni_4Mo. More appropriate would have been a temperature close to 900^0 C.

5.2 The Irradiation Effects

The irradiated only samples will have a small fractional scatter in grain composition than the samples that were also annealed. Okamoto [39] describes the formation of ordered phases during irradiations as resulting from the competition between the induced defect creation and the radiation enhanced diffusive reordering. At room temperature, the disordering process is favored, preventing the formation of the superlattice structures. By applying a certain amount of radiation to an ordered structure, we can cause the appearance of a state of disorder, and the superlattice reflections or peaks would fade away. Interesting enough, at higher irradiation doses and at room temperature due to radiation enhanced diffusion (RED), the reflections (or peaks) start to appear or regain some strength.

As we hypothesized, after the irradiation we observed the amorphization of Ni_3Mo and Ni_4Mo pre-annealed at 800^0 C as we can see from XRD plots (Figures 4.1.17, 4.1.18, 4.1.26 and 4.1.27). In the case of H+ irradiation vs. Ni+ irradiation, the superlattice peaks are much stronger because the affected depth is much larger for H+ than for Ni+. The average penetration depth is about 1.5μm for Ni+ and about 7-10 μm for H+ as determined by SRIM 2003 program (Figures 3.3.1, 3.3.2 and 3.3.3). For doses as small as 0.05 DPA of H+ beam the XRD spectrum becomes very noisy, and the counts for the maximum peak decreases substantially, from 15,000 counts at 0.01 DPA to about 100 counts for the maximum at 0.05 DPA (Figures 4.1.17). The reason for such a behavior is that the specimens became amorphous, with the decrease of the grain size. The phenomenon is not as strong in higher doses of irradiations. The local heating

caused by irradiation might have been enough to allow for recrystallization. The noticeable effect in Ni+ irradiation is the observed preferred orientation in most irradiations. This may have been caused by the formation of a thin film-like layer on the surface of the specimens. From sputtering experiments was observed that Ni films have a strong preferred orientation [65]. We observe a similar effect in Ni_3Mo as-cast. The difference now is that small doses of Ni+ beam cause the appearance of the amorphous state. In higher doses, Ni and Ni_2Mo peaks start appearing in the XRD spectra.

Ni_4Mo pre-annealed at 800^0 C has a slightly different behavior. It forms the thin film-like layer on the surface at lower doses of H+ beam. The process of amorphization begins at doses close to 1 DPA (Figures 4.1.17 – 4.1.18). In high dose ranges, Ni lines become dominant as we expected from the transformation: $Ni_4Mo \rightarrow Ni_3Mo + FCC$. Under Ni+ irradiation, we noticed the process of amorphization starting at about 0.05 DPA.

Ni_3Mo pre-annealed at 800^0 C becomes amorphous at slightly higher doses of H+ and Ni+ irradiation (0.2 DPA) than Ni_4Mo and the spectra become noisier in the high dose irradiation (Figures 4.1.26 – 4.1.27). Similar behavior is noted in Ni_4Mo specimens pre-annealed at 1000^0 C. However, in Ni_3Mo pre-annealed at 1000^0 C and subject to an irradiation dose of 0.05 DPA or higher, the strongly oriented thin film behavior seems to dominate (Figures 4.1.39 – 4.1.40).

We expected that in the lower dose: $Ni_4Mo \rightarrow Ni_3Mo + FCC$ solid solution and in the higher dose $Ni_4Mo \rightarrow FCC +$ amorphous solid solution. Actually, we observed the first reaction in the high dose and the second in the low dose (Figures 4.1.5 and 4.1.6). As we have seen from the XRD spectra, even a dose of 0.05 DPA, could create an

amorphous structure in most of the samples. The XRD spectra become noisier in these situations, due to the reduction in grain size. The OIM scans showed that after casting, we had grains in the range of hundreds of μm (Figures 4.3.5 – 4.3.15). After annealing, we could end up with grains in the sub micron range (Figures 4.3.21 and 4.3.22). We noted that in some cases (XRD spectra after annealing), the increase in irradiation dose created a strong preferred orientation on the surface of the specimens. We observed that the amorphous phase formed in the lower dose. In the higher irradiation doses, we saw indications of ordering in the appearance of superlattice peaks.

5.3 Post-Irradiation Annealing Effects

The irradiation process did not always destroy the ordered structures. The post-annealing treatment re-induced order and reduced the grain size. We observed that a post-irradiation annealing treatment at 100^0 C was not enough for grain refinement. Post-irradiation annealing at 250^0 C treatment could re-order most of the specimens. Annealing performed at 350^0 C and 450^0 C gives even better results.

For Ni_4Mo as-cast, 350^0 C seems to be the temperature for which even in low dose (0.05 DPA), the grain size reduction causes the spectrum to be very noisy (Figure 4.1.8 and 4.1.9). Ni_3Mo as-cast shows some tendency of recrystalization at 250^0 C, but overall is not recovering a whole lot (Figure 4.1.14 and 4.1.16). It may also be a dose dependence, and we did not have enough samples available for a direct comparison.

Ni_4Mo pre-annealed at 800^0 C did not need too much temperature treatment to show the same behavior (Figures 4.1.19 through 4.1.23). At 250^0 C and a dose of at least

0.1 DPA would cause this specimen to undergo the re-crystallization process as expected, to change from the FCC solution and Ni_3Mo back into Ni_4Mo. The OIM shown in 4.3.16 – 21, confirms the great reduction in grain size. This effect seemed to be coupled also with a strong grain orientation effect, as we can see from the grain misorientations.

Not too much change is induced in the samples pre-irradiation annealed at 1000^0 C (Figures 4.1.36 through 4.1.40). From the OIM scan in Figure 4.3.14, we see that there is a reduction in grain size from the 300-500 μm range into the 100 μm range. A much less effect is noted in Ni_3Mo pre-annealed at 1000^0 C.

5.4 Closing Remarks

To the best of my knowledge, there are no experiments in literature that document low temperature irradiation followed by low temperature thermal annealing. We have obtained specimens displaying strong textures in the surface layers, especially in pre-annealed at 800^0 C Ni_4Mo. In the XRD spectra, some fundamental peaks disappeared and the intensity of other peaks increased, signifying a change in texture. The texture formation seemed to be surface related and not the result of channeling effect of the incident ions. Texture appears to result from a reduction in surface energy that accompanies the alignment of the closed packed atom planes with the surface of the specimens [165]. The reason may be the fast kinetics due to the fine mixture of Ni and Ni_2Mo created by the local heating during irradiation. Very probably after irradiation, a structure close to the amorphous structure formed at the surface of some of the samples. After annealing the grain size became small, close to the limit of detection of XRD. We

can assume that this happened, because in the XRD spectrum for these specimens, the background noise became as large as 10 - 20% of the main peak size (Figures 4.1.8, 4.1.14, 4.1.16, 4.1.17, 4.1.27 and 4.1.31). We observed in many irradiated specimens that after the post-irradiation annealing at temperatures as low as 250^0 C, grain size began to decrease. This could be seen in the peak thinning in the XRD spectra. As the boundary migrates, a new alloy or phase forms in its place, especially if there are enough small grains to provide a large amount of grain boundary. Low angle tilt boundaries may be modeled as parallel stacked edge dislocations [29]. The cores of these dislocations, provide a free volume that allows more rapid diffusion parallel to these cores than it would be possible in the lattice [21]. In this manner, the diffusion via dislocation combined with the large amount of grain boundary area in the case of small grains, permitted greater mobility of the atoms inside the alloys causing the rearrangement inside the lattice. The diffusion continued in paths perpendicular to the dislocations along the boundaries of the grains. However, as stated earlier, diffusion can not explain the rapid rate of recovering, observed in low-temperature post-irradiation annealing.

The proton irradiation had a more pronounced effect, in part due to the fact that the path in the material is much longer in the case of protons than in the case of the Ni^+ ions. The XRD spectra may be presenting a depth effect, with the intensities of the peaks getting stronger because the depth affected by protons is a lot larger than the depth affected by Ni^+ beam.

Definitely, more research is needed to establish the temperature dependence of the irradiation disordering mechanisms.

We were able to show that with the appropriate dose and post-irradiation treatment, a coarse grained specimen can be forced to re-crystallize with a small grain size. As mentioned in the literature, the ordered state of Ni_4Mo can be obtained through thermal treatment after many days at about 800^0 C. If the same process is attempted in low temperature range, years may be a reasonable time to wait. Our results indicate that irradiation followed by low-temperature annealing would give almost the same result after just 3 hours of post-irradiation annealing treatment.

5.5 Future Work

First of all, additional OIM scans are required to get a complete picture of the grain boundary orientation in different stages of irradiation and after post-annealing treatments. The OIM could provide detailed information of the orientation and of the texture of the surface layers after irradiation.

Transmission Electron Microscopy (TEM) would be by far the next best tool to evaluate the different stages of order and disorder. Currently, we have all specimens ready to be polished and become TEM disks. I have made an attempt in the preliminary stages of the current work and obtained a diffraction pattern indicating the appearance of superlattice reflections, as well as some dark field images.

Next, improving the RBS data collection we could get more precise information, have better statistics and trace smaller changes in surface composition. By changing the angle of impact of the beam with the surface we can scan thinner regions closer to the

surface and by comparing the spectra at different angles, we could trace changes with the depth.

The infrared emissivity of Ni_3Mo and Ni_4Mo can provide means of monitoring the degree of order. This fact was discovered a while ago while monitoring the irradiation temperature for a Ni_3Si alloy, with an infrared pyrometer [24]. The apparent temperature decreased with time after reaching a steady state. The thermal steady state during irradiation was achieved in the first few minutes that the beam was on, but the temperature seemed to continually decrease after a certain dose. The pyrometer temperature reading was contradicted by spot welded thermocouple readings that indicated that the temperature was stable. The temperature of pure metals does not vary during irradiation [24]. MIBL is equipped now with and infrared thermal imager that is capable of detecting any temperature changes during the irradiation over the entire surface of the specimens. The emissivity of different Ni-Mo alloys and of bulk Ni, can be initially measured with a spectrometer. We can then detect changes in structure by simply noting changes in temperature during irradiation. In this manner, we could determine the dose and the temperature when structural changes would occur in the specimens.

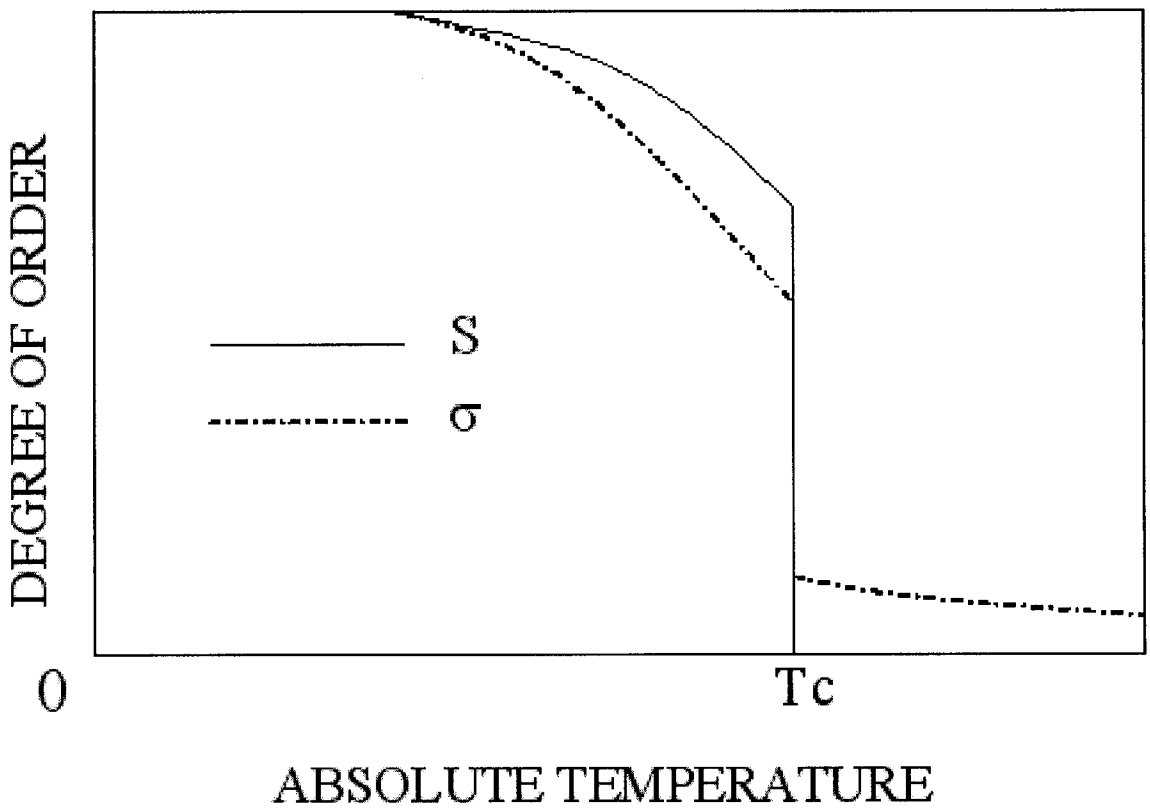

Figure 5.1 The evolution of the long range order parameter. S is the theoretical parameter and σ is the experimental parameter [67].

APPENDIX A1
Additional XRD Spectra

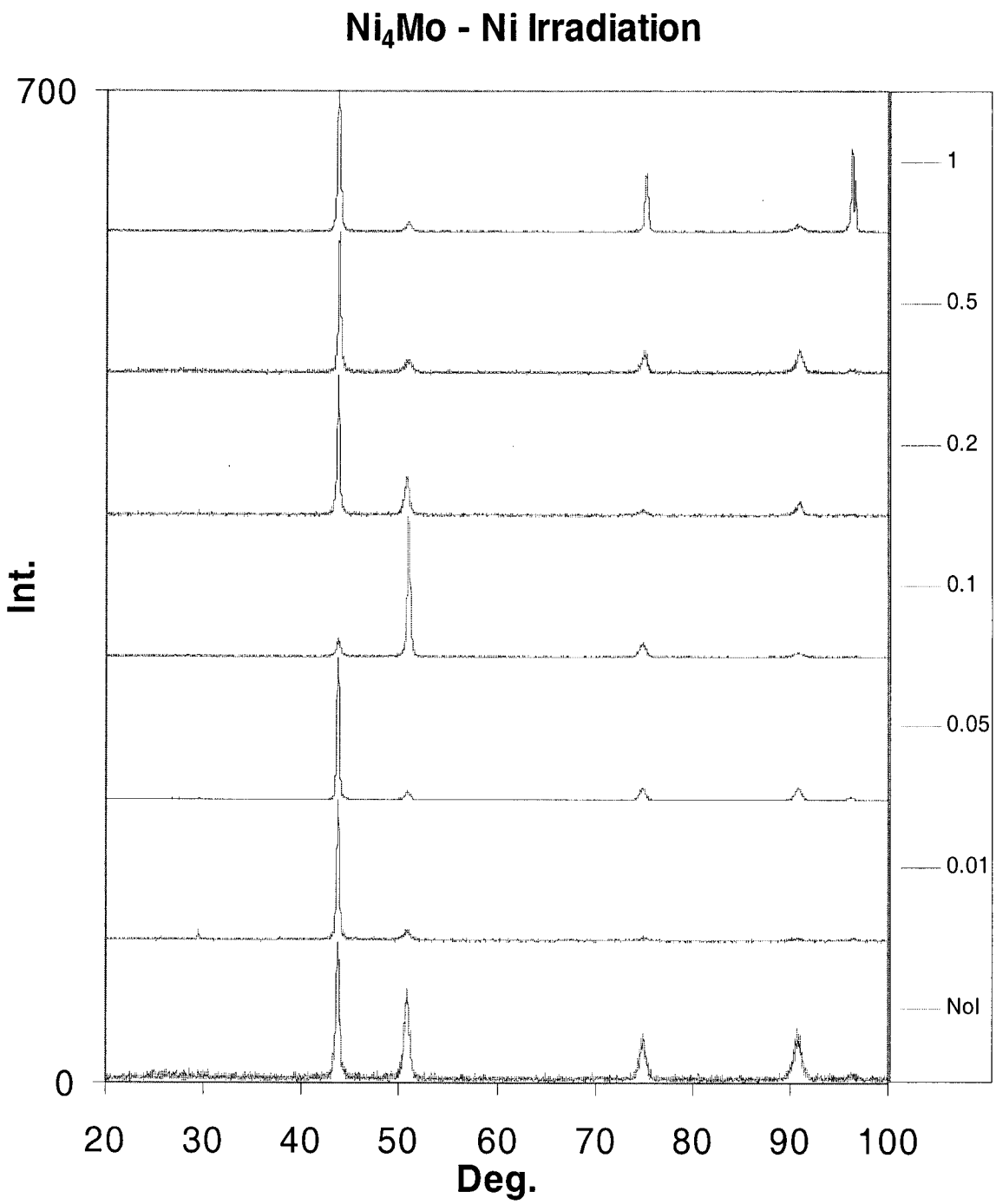

Figure A1.1 XRD spectra generated for Ni_4Mo as-cast samples irradiated with a Ni+ beam with a dose varying from 0.01 DPA to 1 DPA. The Intensity axis is in arbitrary units and is plotted as a function of the angle 2θ.

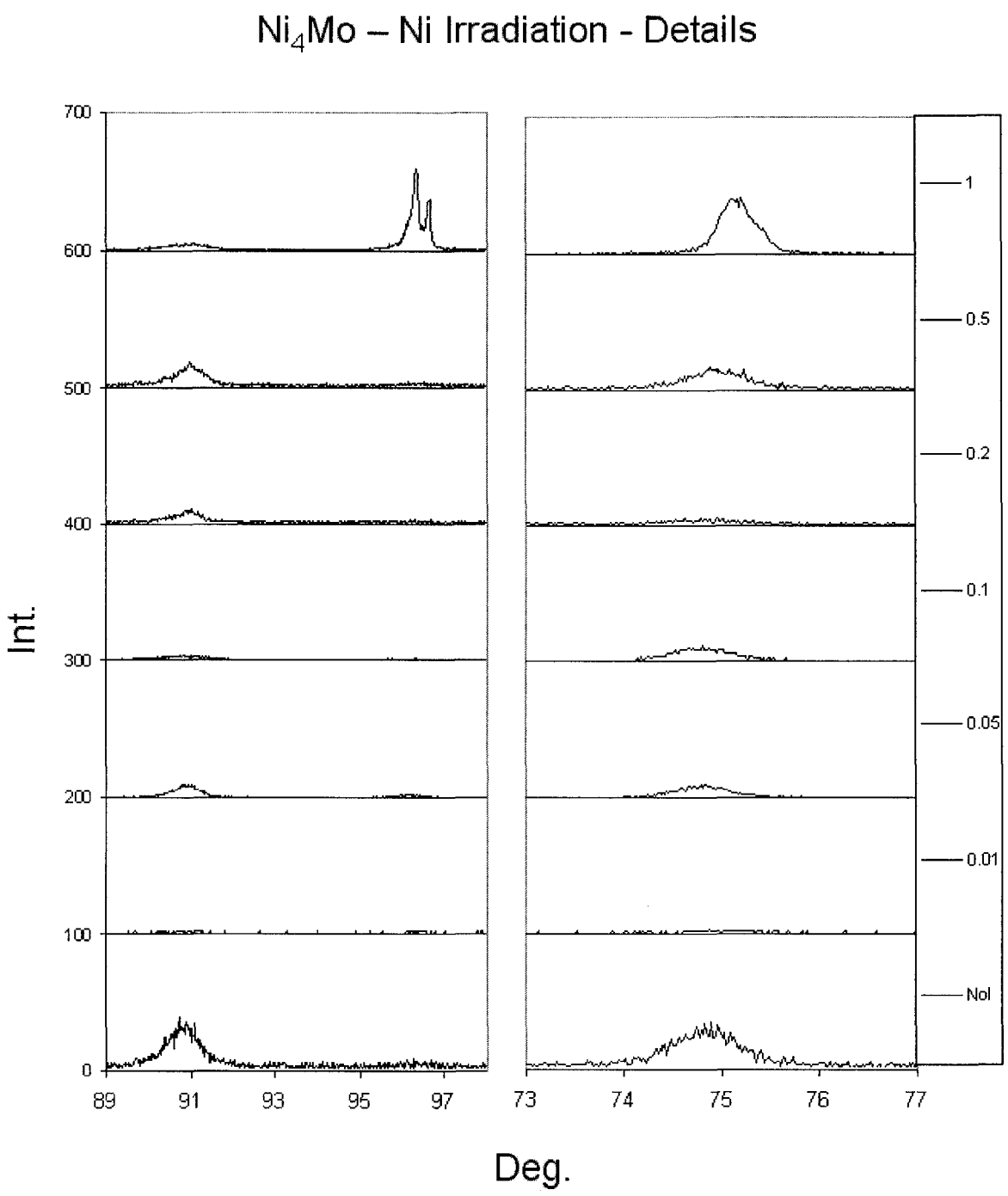

Figure A1.2 Detail of the XRD spectra generated for Ni_4Mo as-cast samples irradiated with a Ni+ beam with a dose varying from 0.01 DPA to 1 DPA. The Intensity axis is in arbitrary units and is plotted as a function of the angle 2θ.

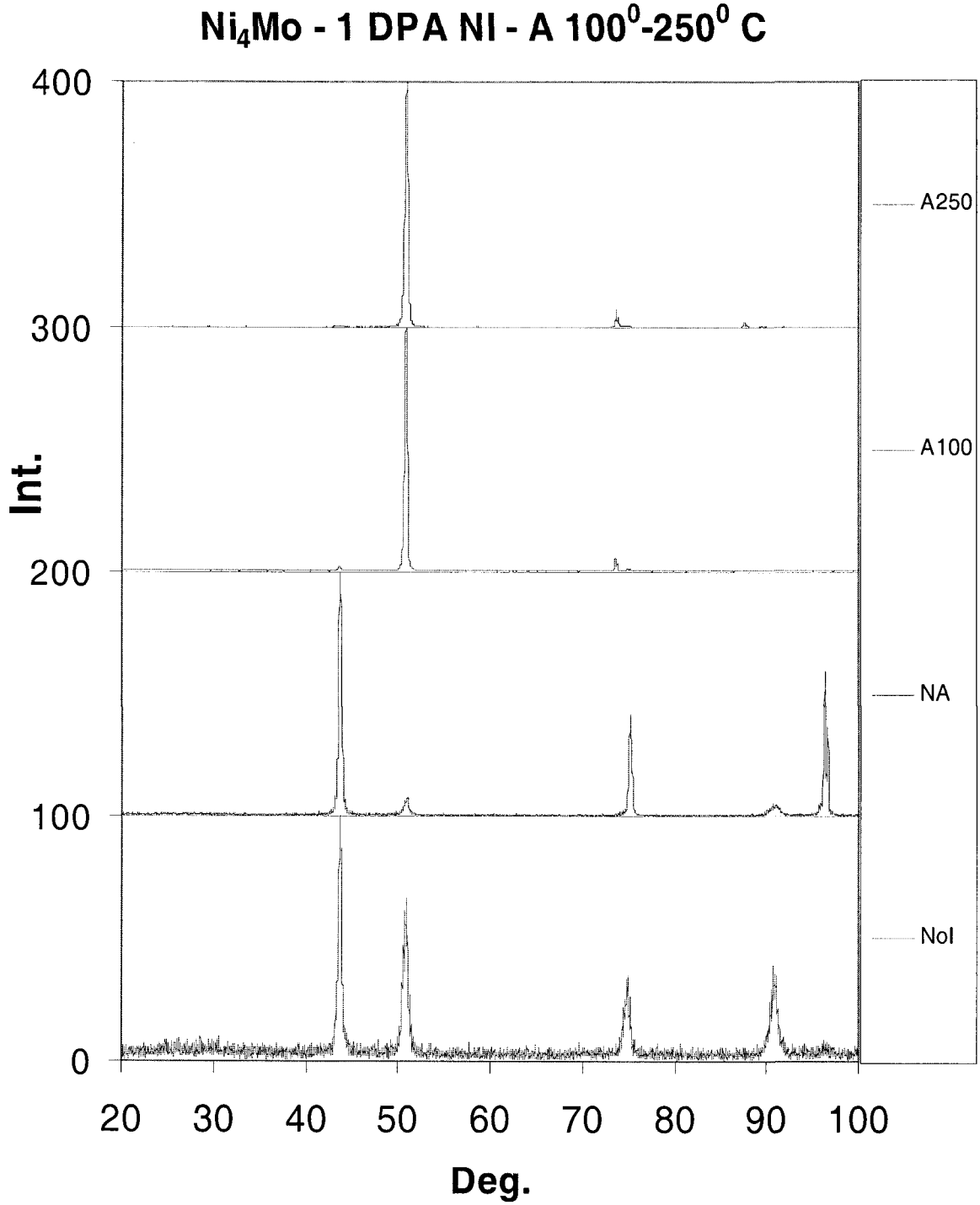

Figure A1.3 XRD spectra generated for Ni_4Mo as-cast samples irradiated with a Ni+ beam with a 1 DPA dose. After irradiation the samples were first annealed for three hours at 100^0 C and then for three hours at 250^0 C. The Intensity axis is in arbitrary units and is plotted as a function of the angle 2θ.

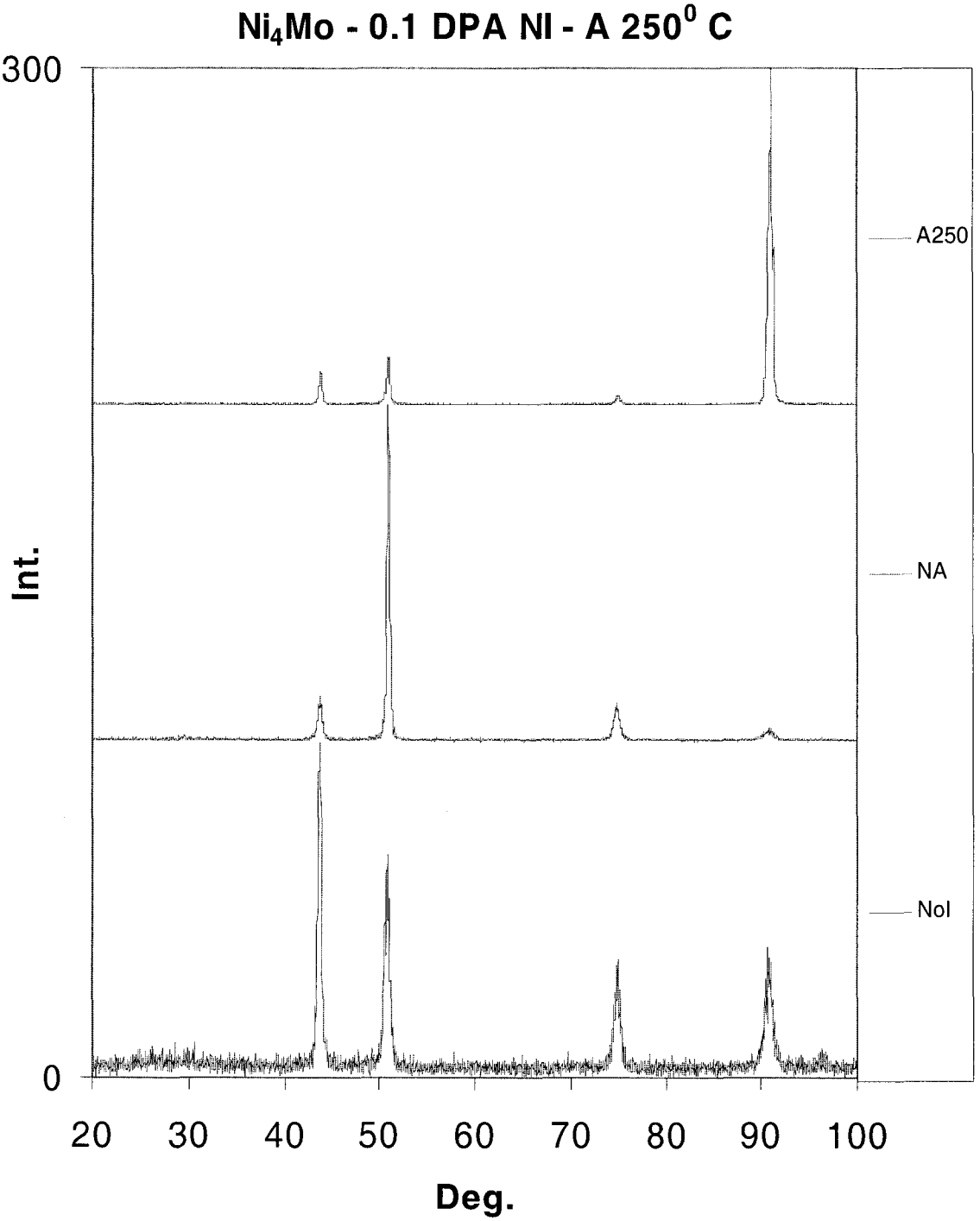

Figure A1.4 XRD spectra generated for Ni_4Mo as-cast samples exposed to a Ni+ beam for a 0.1 DPA dose. After irradiation, the samples were annealed for three hours at 250^0 C. The Intensity axis is in arbitrary units and is plotted as a function of the angle 2θ.

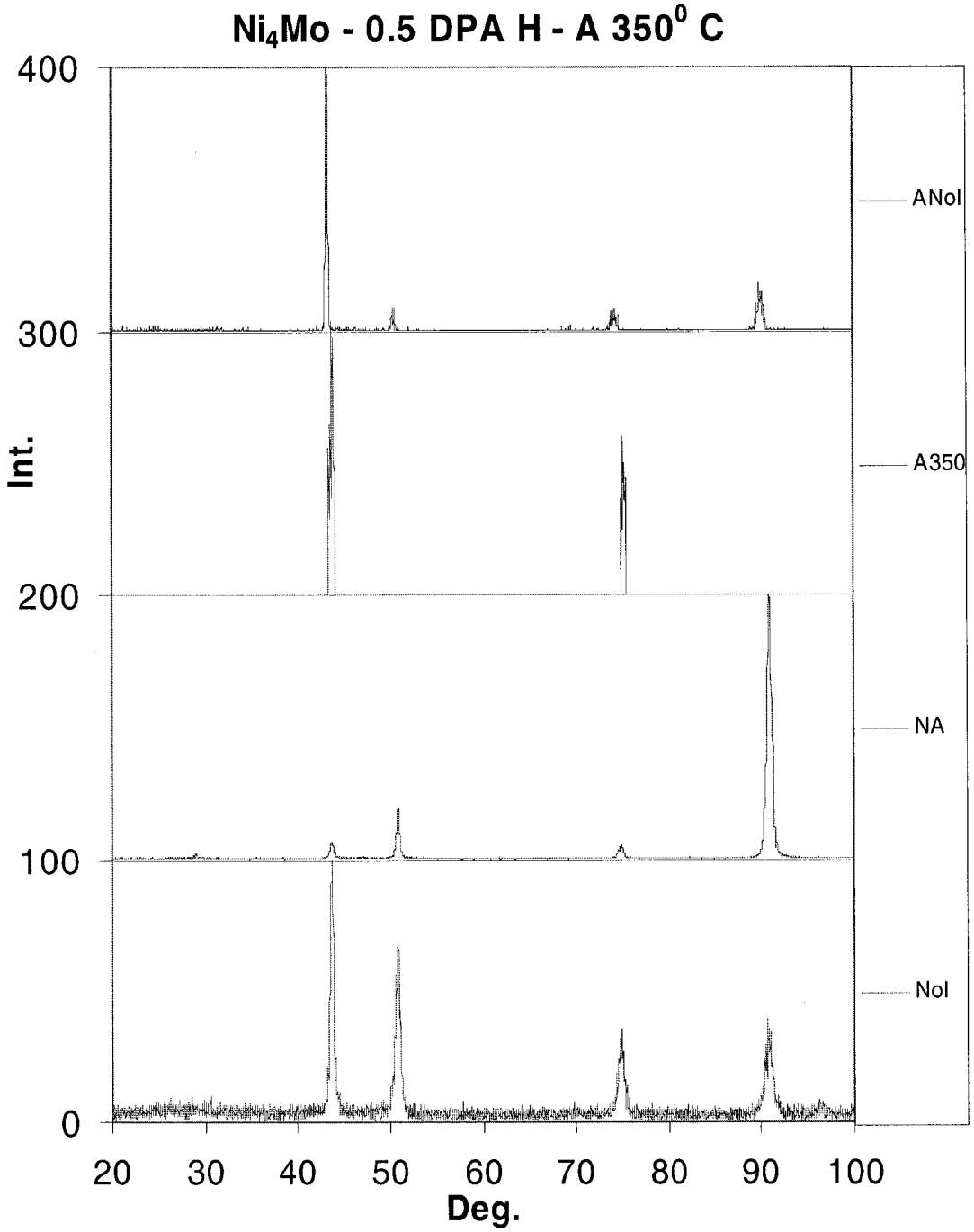

Figure A1.5 XRD spectra generated for Ni_4Mo as-cast samples exposed to an H+ beam for a 0.5 DPA dose. After irradiation, the samples were annealed for three hours at 350^0 C. The Intensity axis is in arbitrary units and is plotted as a function of the angle 2θ. Spectra are compared with spectrum from sample with annealing but NoI.

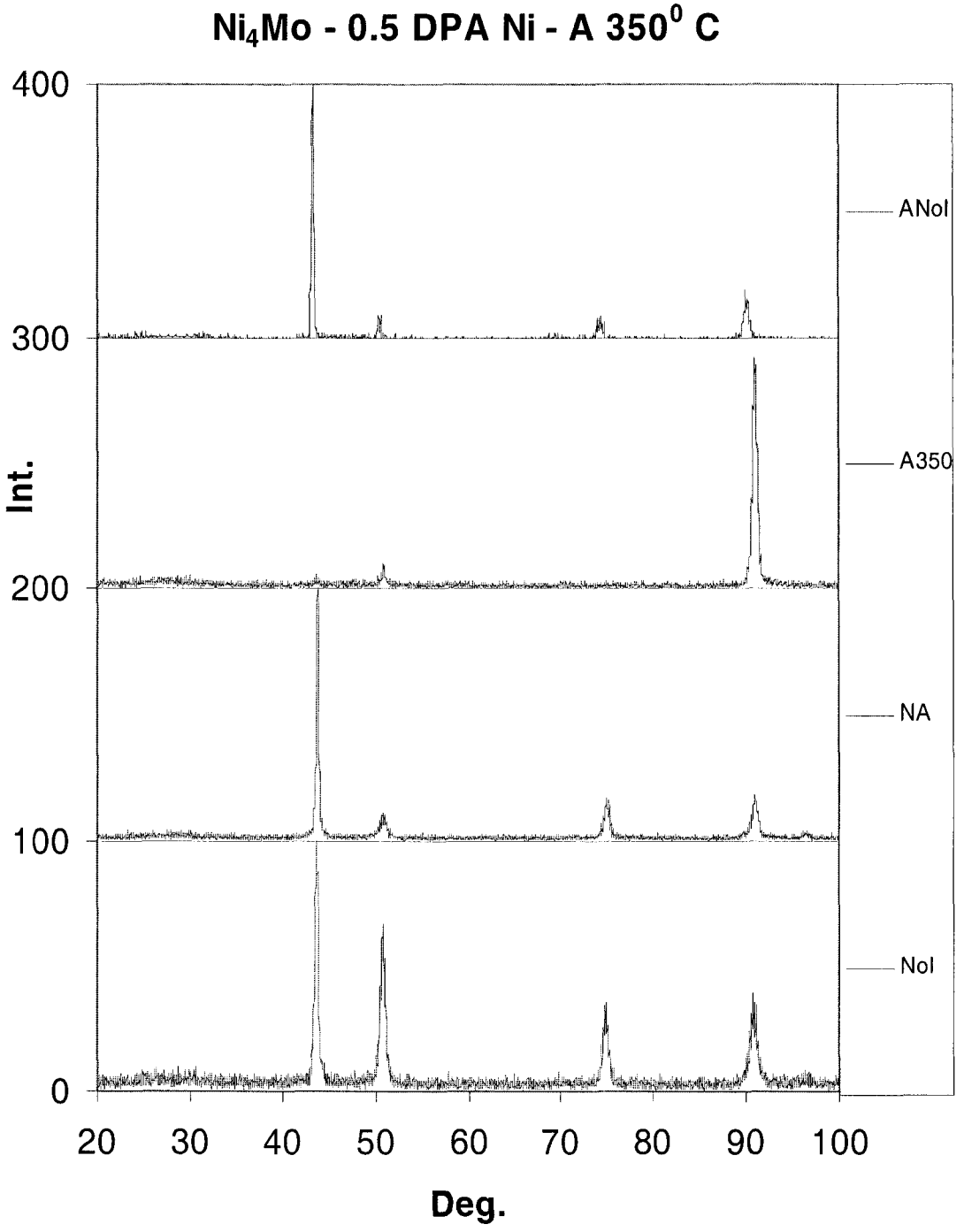

Figure A1.6 XRD spectra generated for Ni_4Mo as-cast samples exposed to a Ni+ beam for a 0.5 DPA dose. After irradiation, the samples were annealed for three hours at 350^0 C. The Intensity axis is in arbitrary units and is plotted as a function of the angle 2θ. Spectra are compared with spectrum from sample with annealing but NoI.

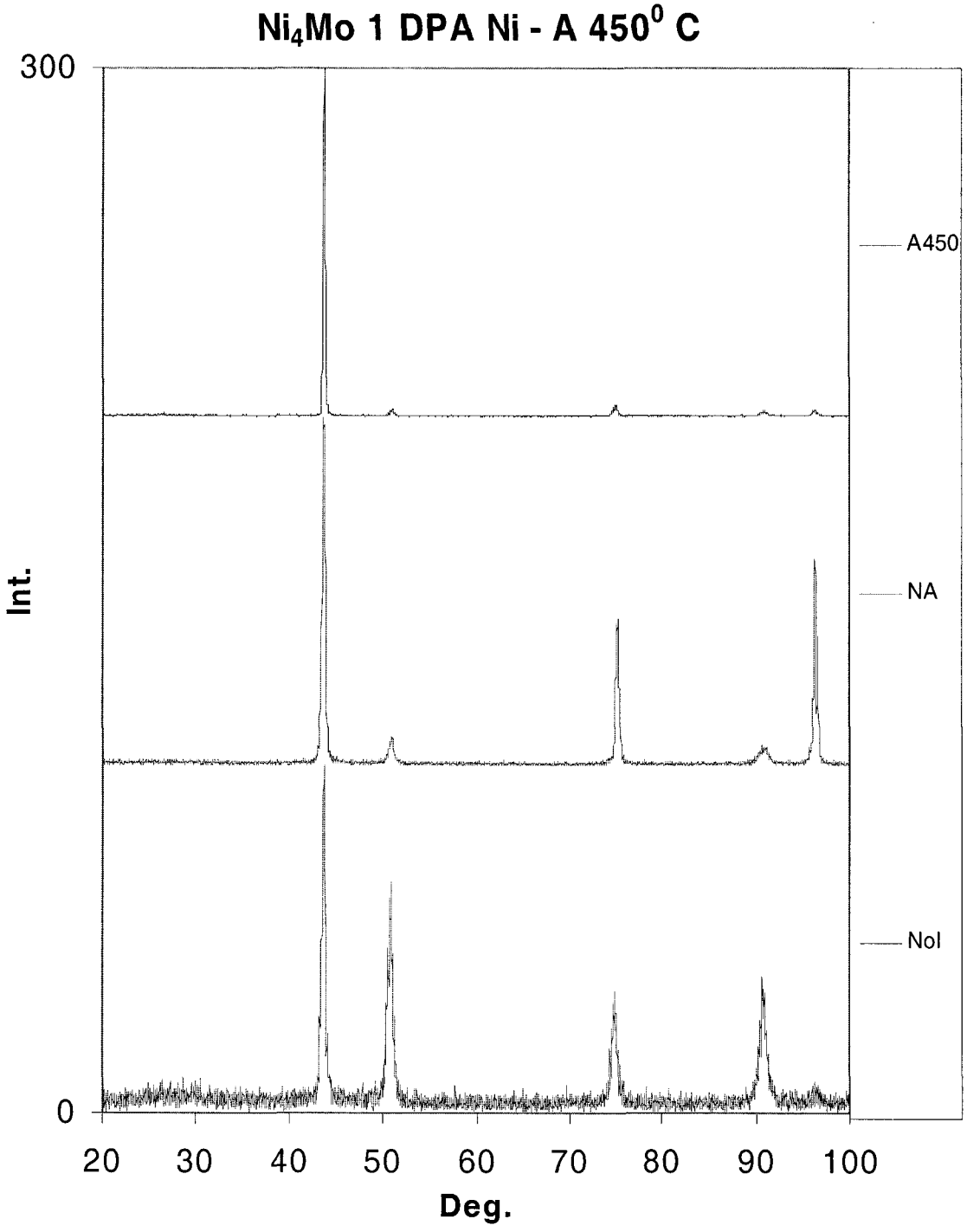

Figure A1.7 XRD spectra for Ni_4Mo as-cast sample exposed to a Ni+ beam for a 1 DPA dose. After irradiation, the samples were annealed for three hours at 450^0 C. The Intensity axis is in arbitrary units and is plotted as a function of the angle 2θ.

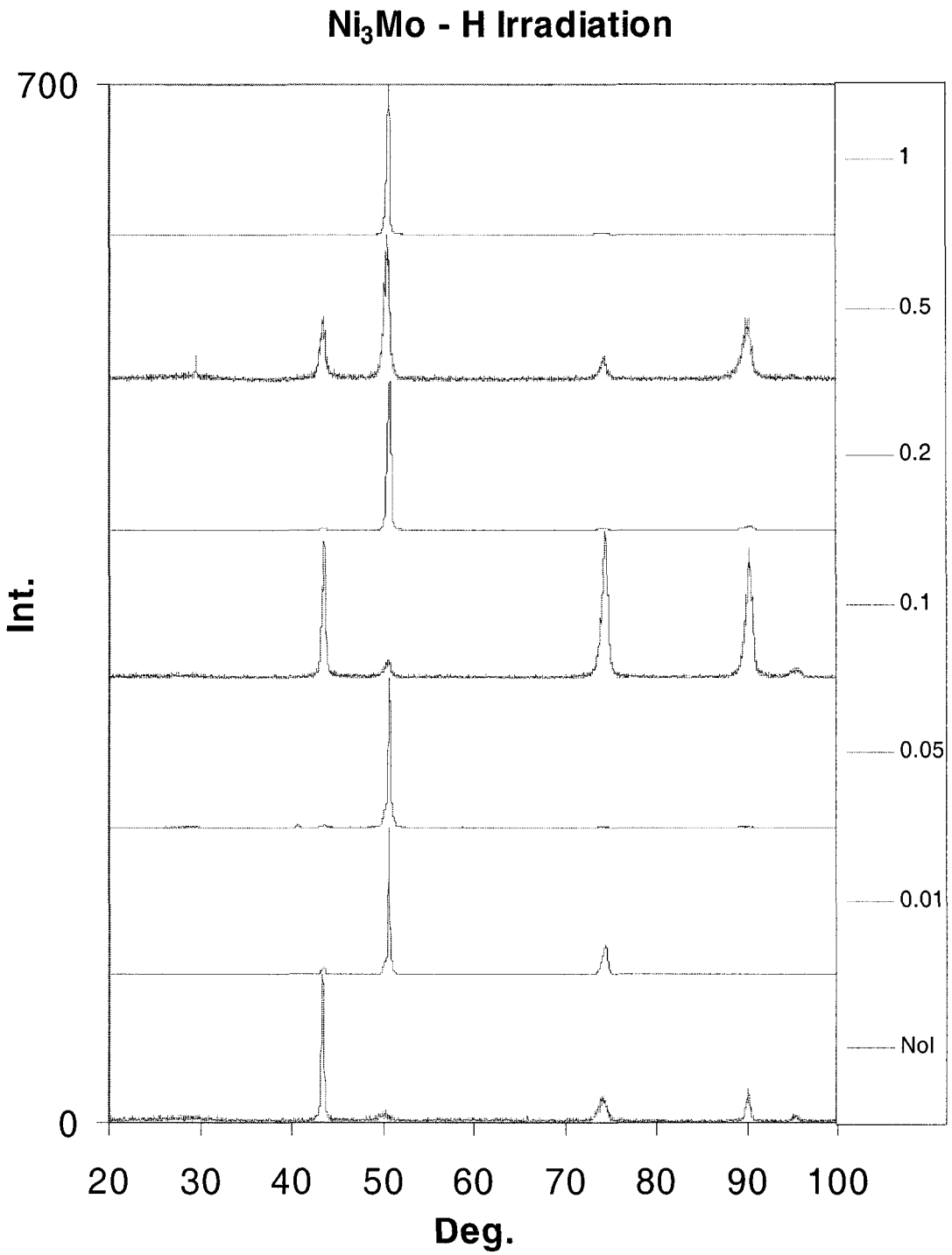

Figure A1.8 XRD spectra generated for Ni_3Mo as-cast samples irradiated with an H+ beam with a dose varying from 0.01 DPA to 1 DPA. The Intensity axis is in arbitrary units and is plotted as a function of the angle 2θ.

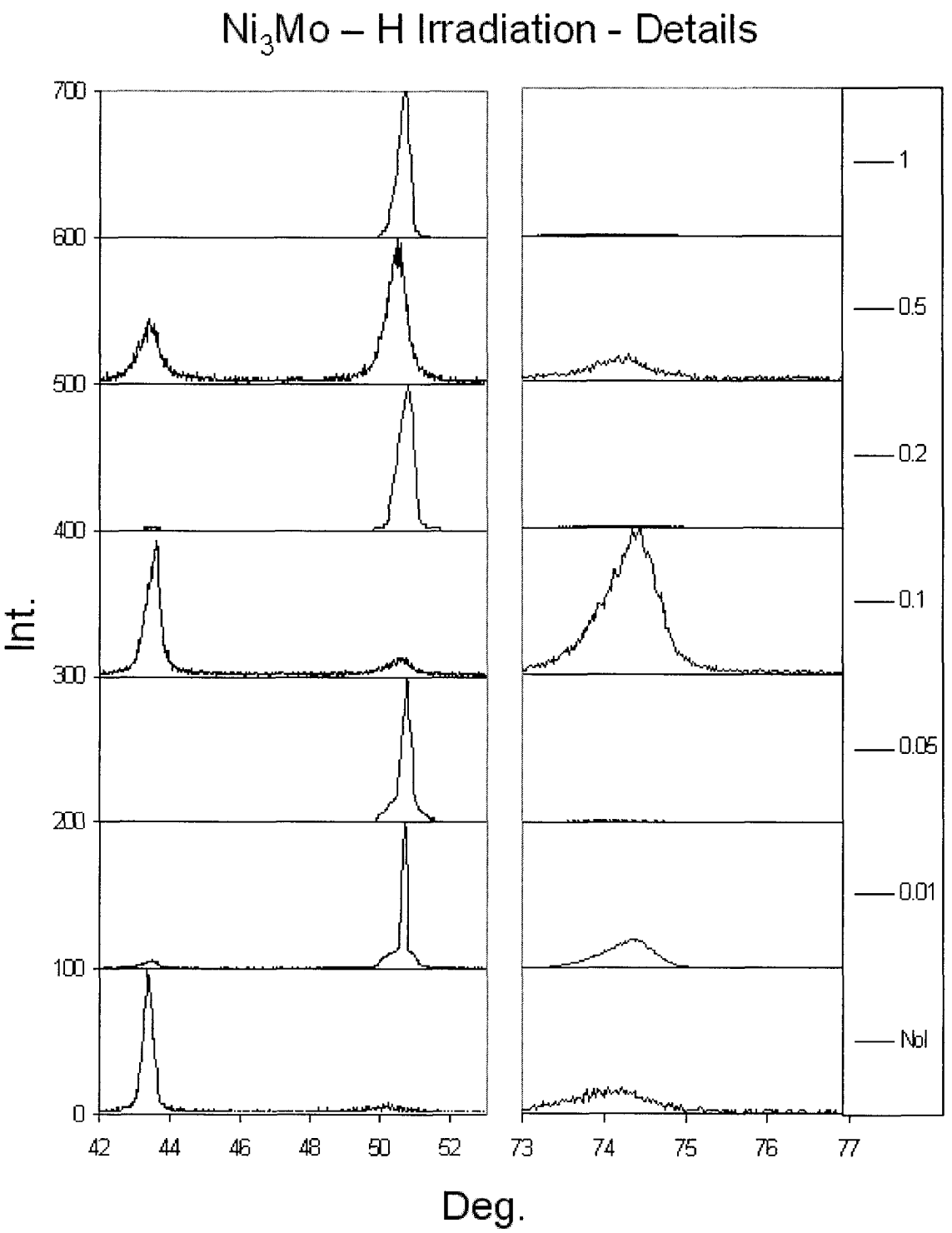

Figure A1.9. Detail of the XRD spectra generated for Ni_3Mo as-cast samples irradiated with an H+ beam with a dose varying from 0.01 DPA to 1 DPA. The Intensity axis is in arbitrary units and is plotted as a function of the angle 2θ.

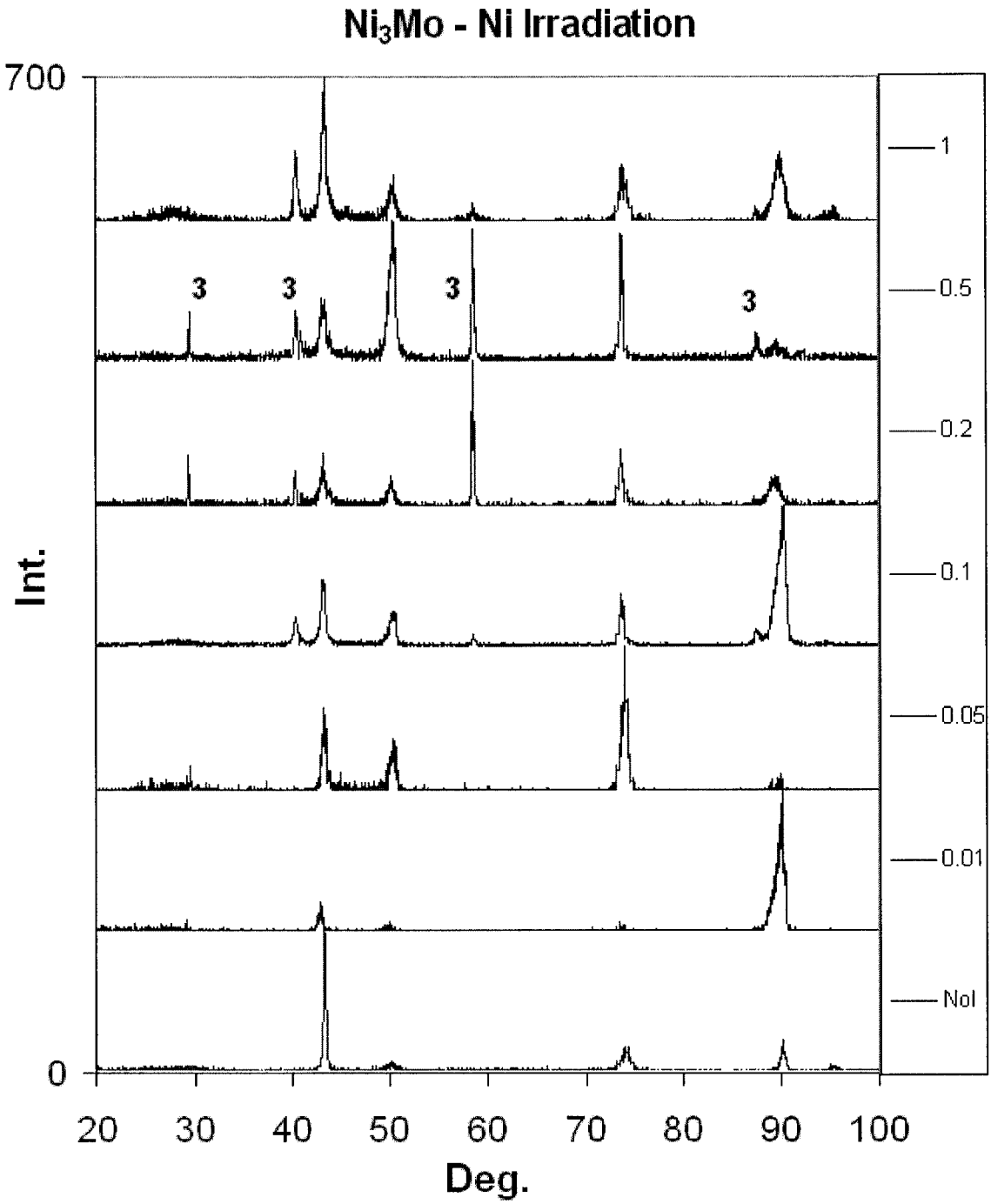

Figure A1.10 XRD spectra generated for Ni_3Mo as-cast samples irradiated with a Ni+ beam with a dose varying from 0.01 DPA to 1 DPA. The Intensity axis is in arbitrary units and is plotted as a function of the angle 2θ. The superlattice lines of Ni_3Mo are marked with a "3".

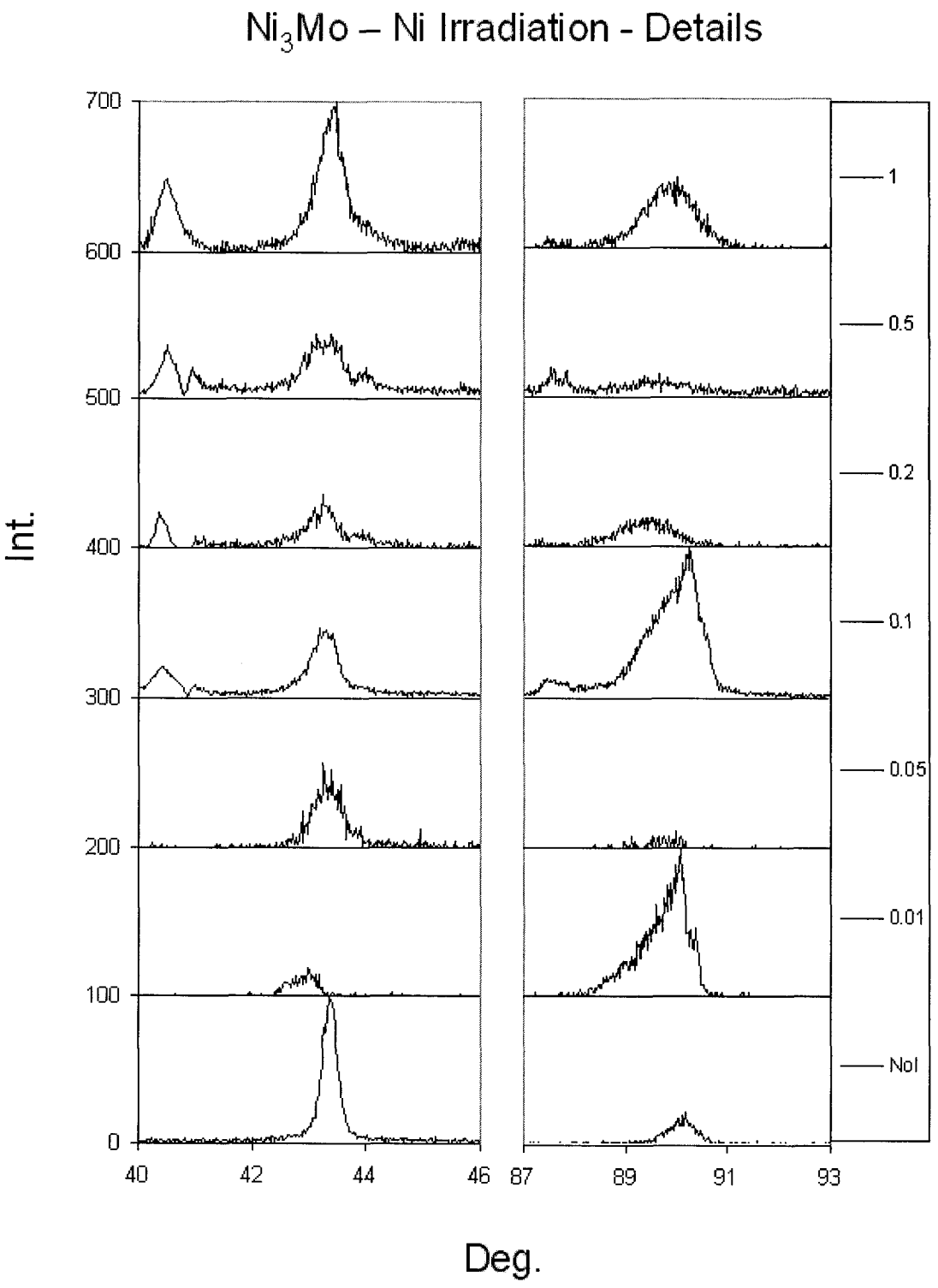

Figure A1.11 Detail of the XRD spectra generated for Ni_3Mo as-cast samples irradiated with a Ni+ beam with a dose varying from 0.01 DPA to 1 DPA. The Intensity axis is in arbitrary units and is plotted as a function of the angle 2θ.

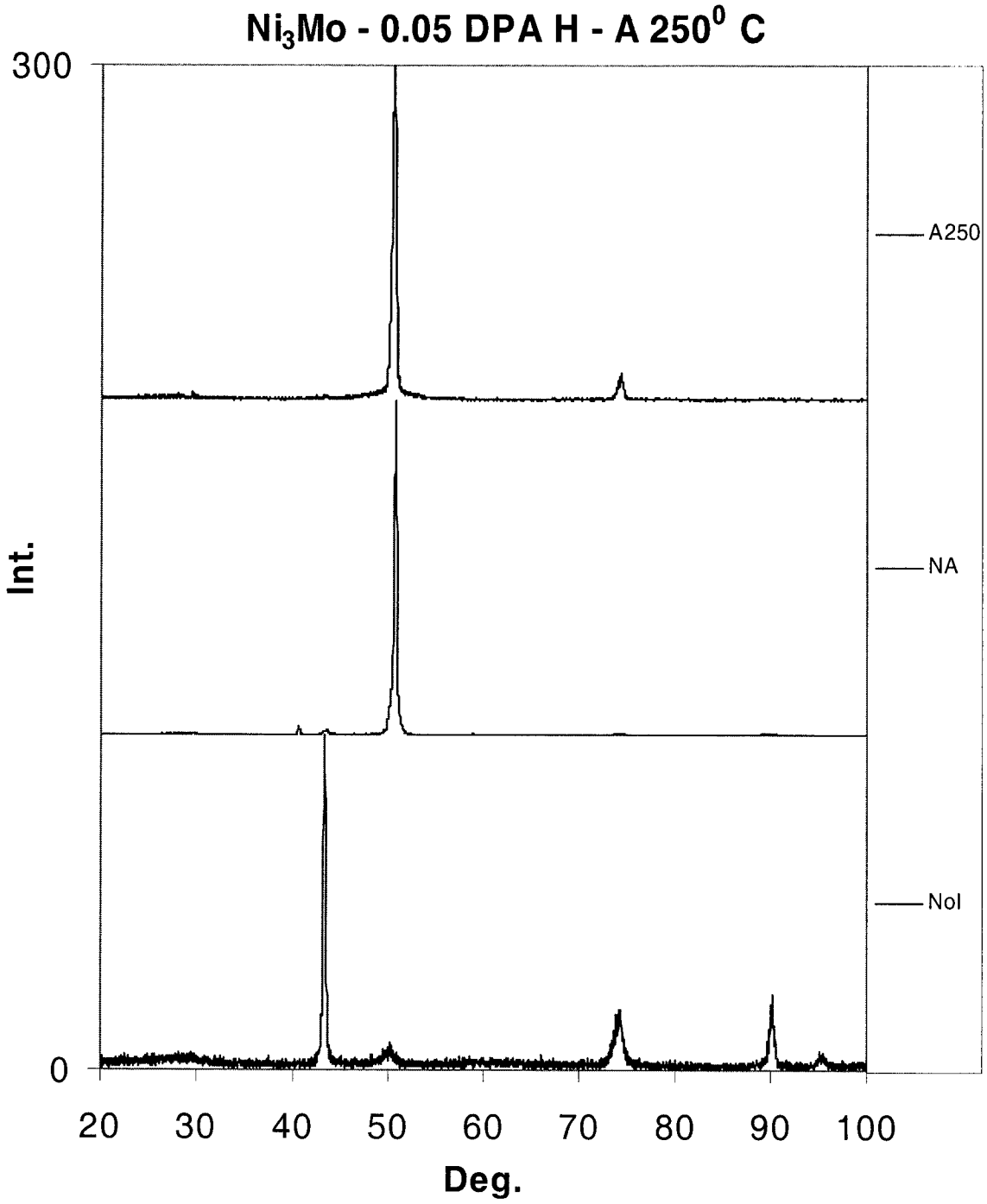

Figure A1.12 XRD spectra generated for Ni_3Mo as-cast samples exposed to an H+ beam for a 0.05 DPA dose. After irradiation, the samples were annealed for three hours at 250^0 C. The Intensity axis is in arbitrary units and is plotted as a function of the angle 2θ.

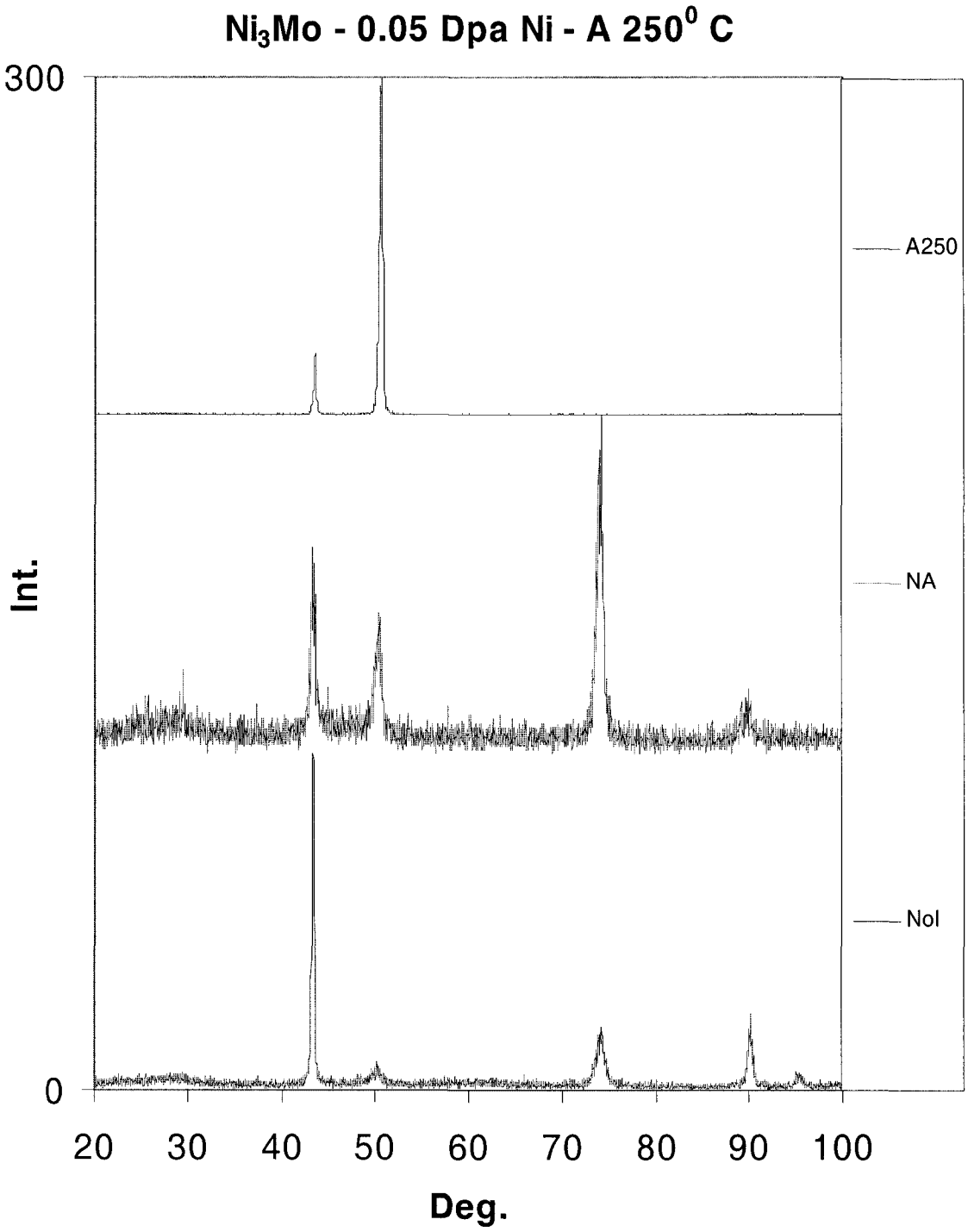

Figure A1.13 XRD spectra generated for Ni_3Mo as-cast samples exposed to a Ni+ beam for a 0.05 DPA dose. After irradiation, the samples were annealed for three hours at 250^0 C. The Intensity axis is in arbitrary units and is plotted as a function of the angle 2θ.

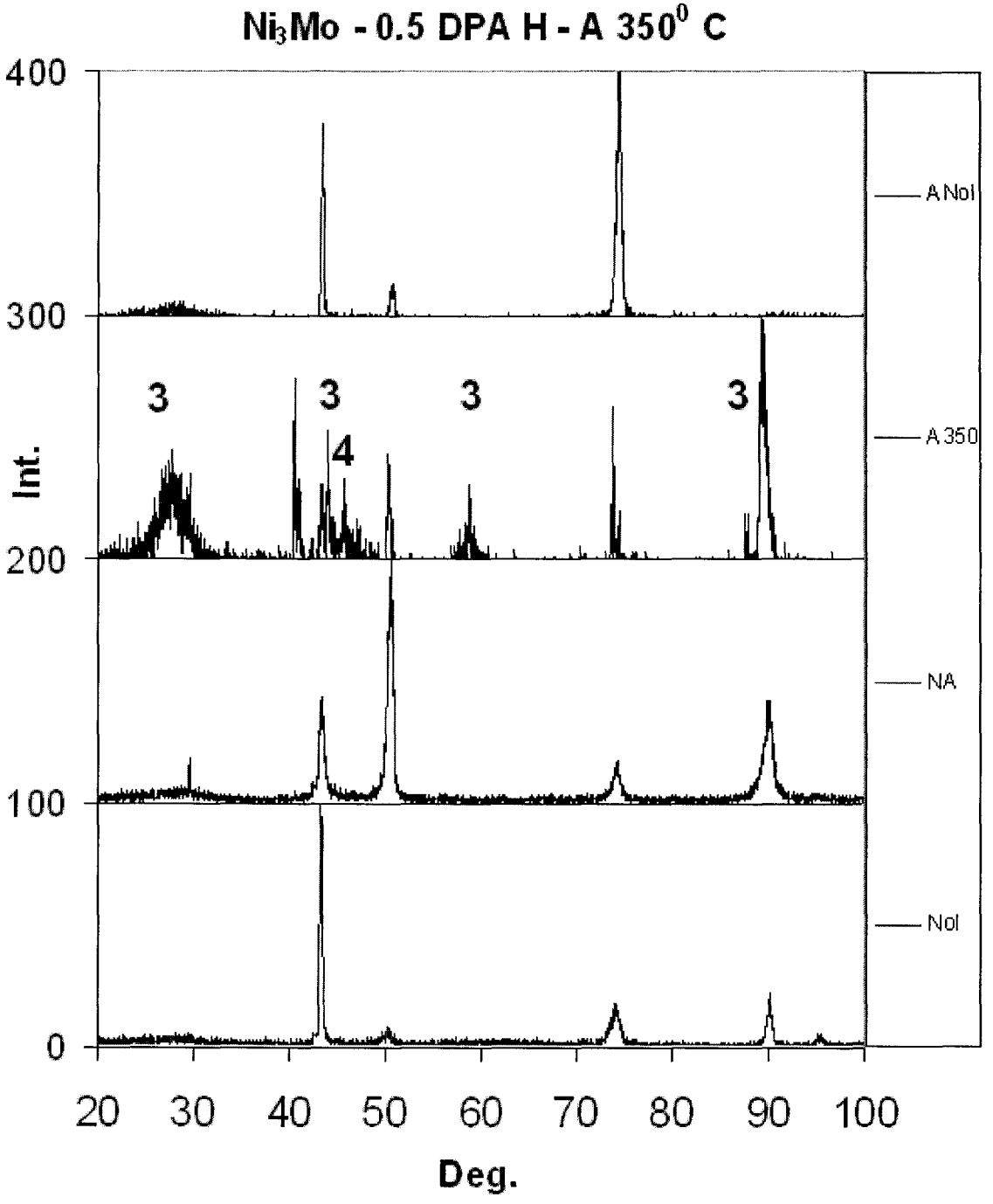

Figure A1.14 XRD spectra generated for Ni_3Mo as-cast samples exposed to an H+ beam for a 0.5 DPA dose. After irradiation, the samples were annealed for three hours at 350^0 C. The Intensity axis is in arbitrary units and is plotted as a function of the angle 2θ. Spectra are compared with spectrum from sample with annealing but NoI. The superlattice lines of Ni_3Mo and Ni_4Mo are marked with a "3" and a "4".

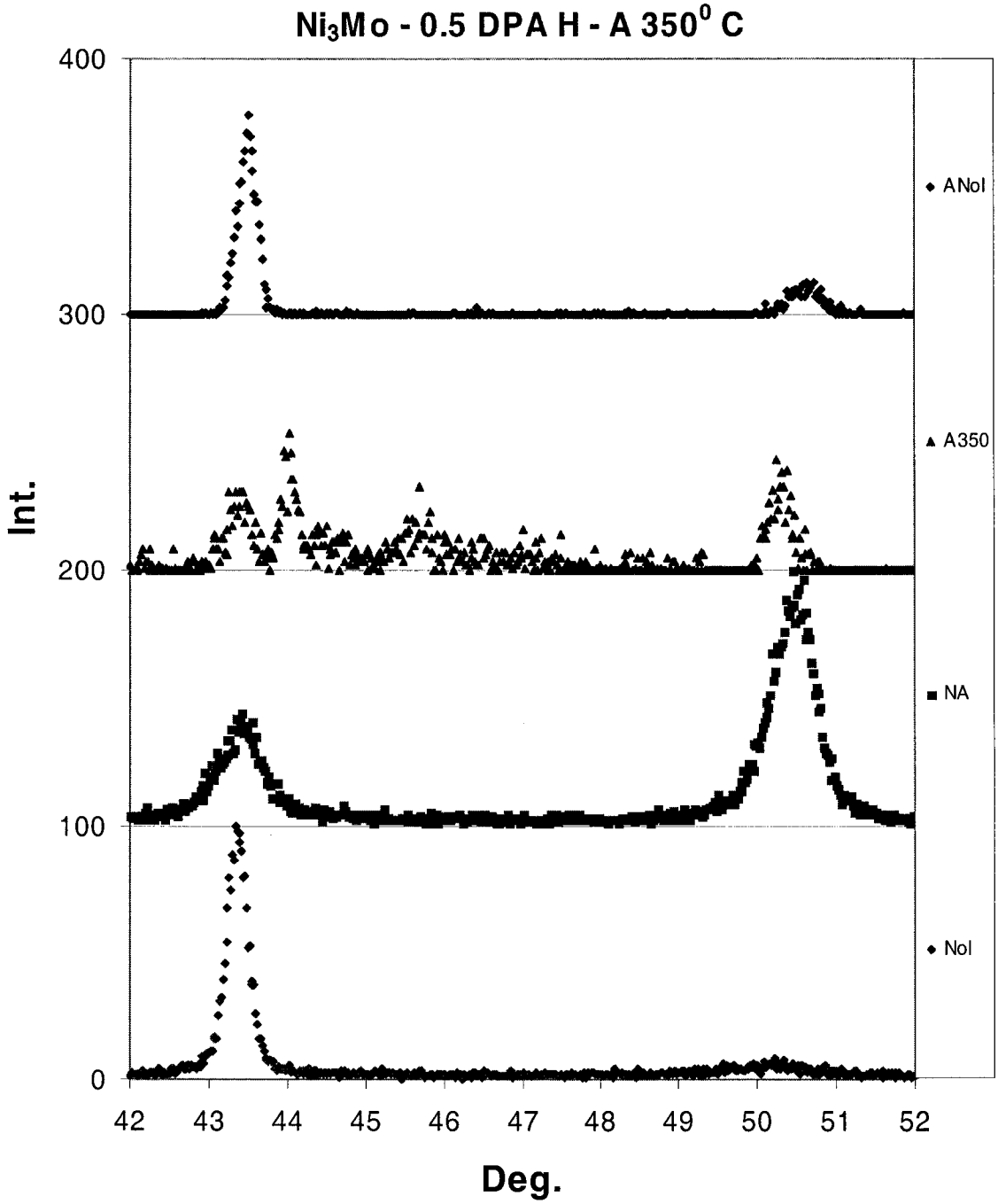

Figure A1.15 Detail#1 of XRD spectra generated for Ni_3Mo as-cast samples exposed to an H+ beam for a 0.5 DPA dose. After irradiation, the samples were annealed for three hours at 350^0 C. The Intensity axis is in arbitrary units and is plotted as a function of the angle 2θ. Spectra are compared with spectrum from sample with annealing but NoI.

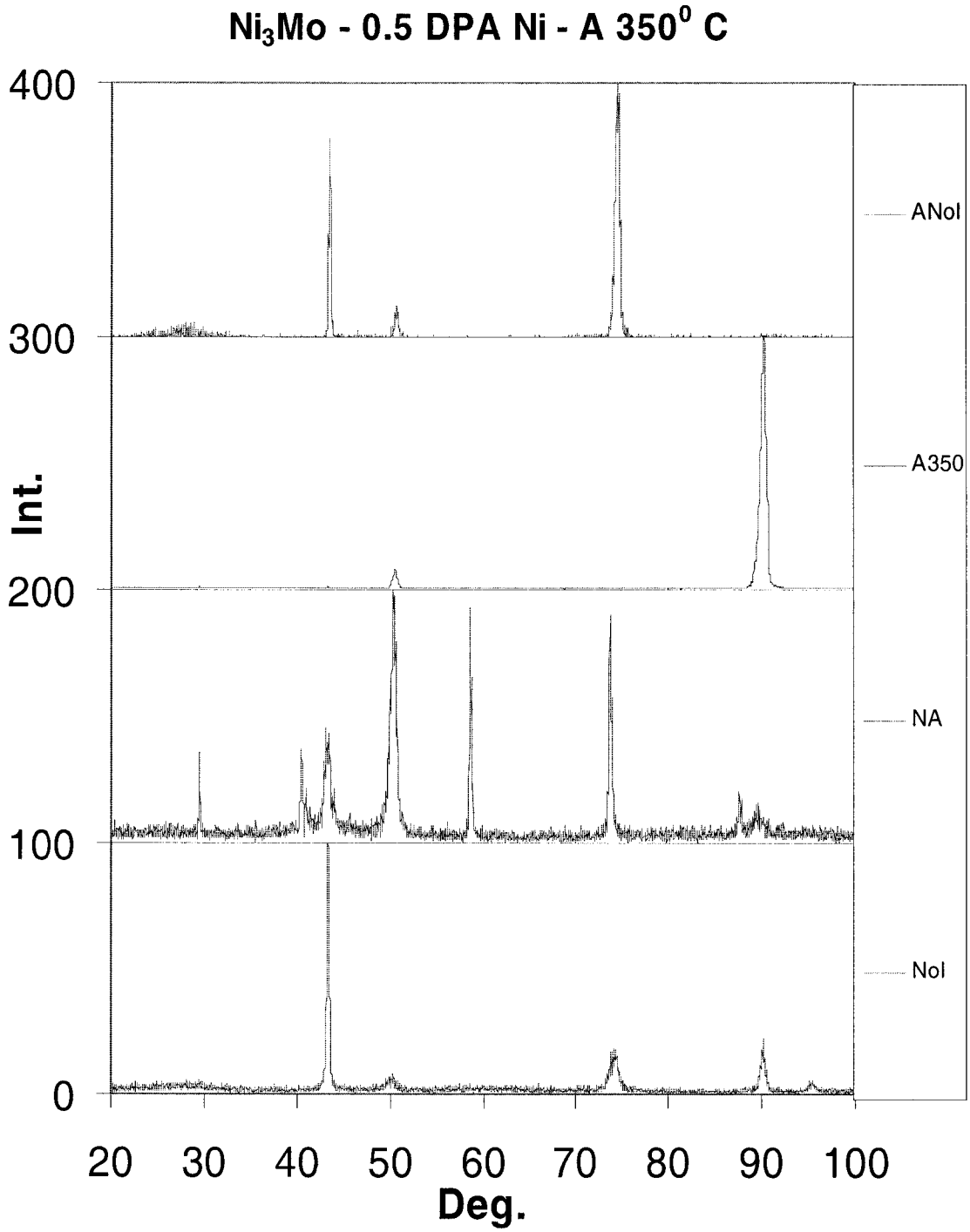

Figure A1.16 XRD spectra generated for Ni_3Mo as-cast samples exposed to a Ni+ beam for a 0.5 DPA dose. After irradiation, the samples were annealed for three hours at 350^0 C. The Intensity axis is in arbitrary units and is plotted as a function of the angle 2θ. Spectra are compared with spectrum from sample with annealing but NoI.

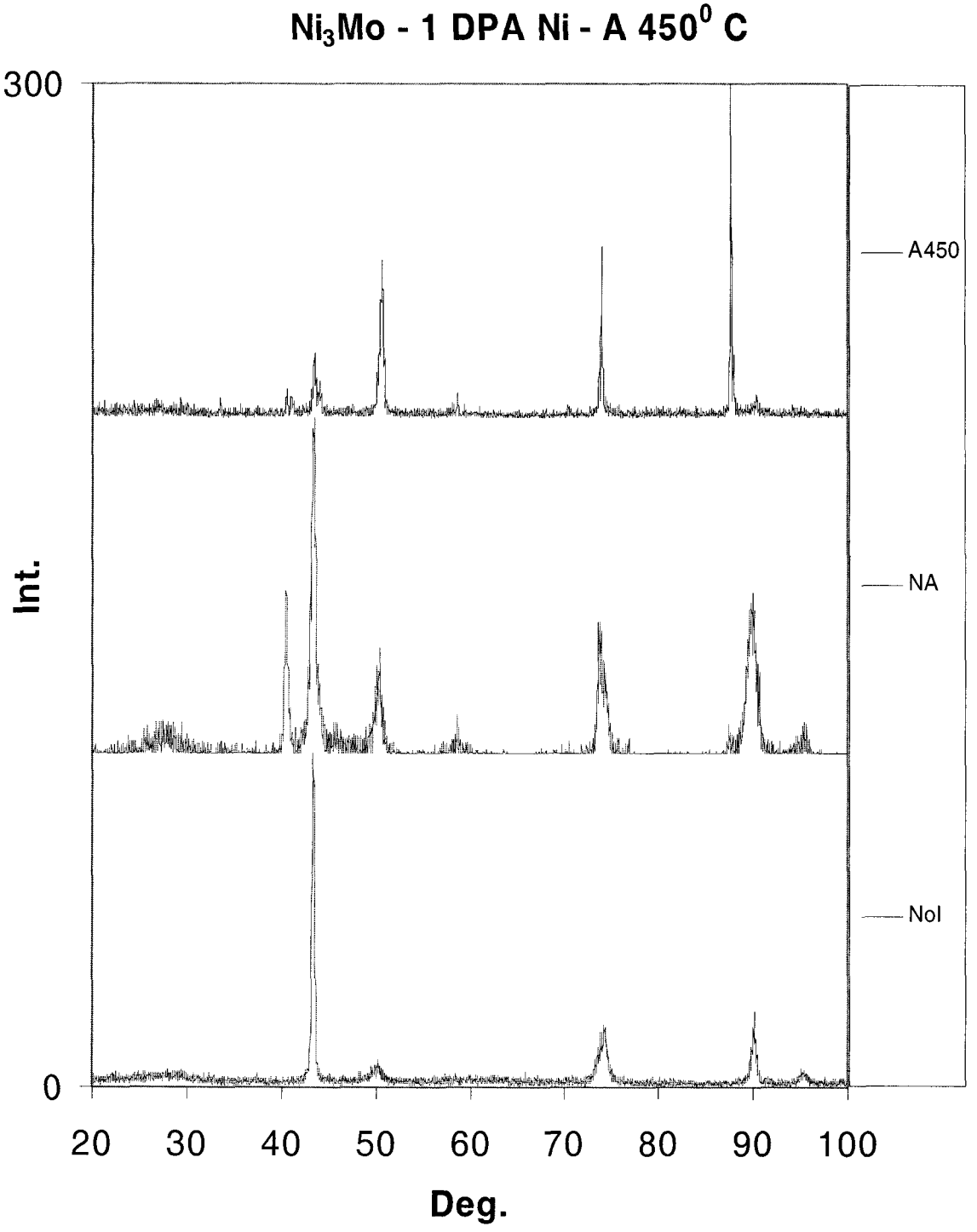

Figure A1.17 XRD spectra for Ni_3Mo as-cast sample exposed to a Ni+ beam for a 1 DPA dose. After irradiation, the samples were annealed for three hours at 450⁰ C. The Intensity axis is in arbitrary units and is plotted as a function of the angle 2θ.

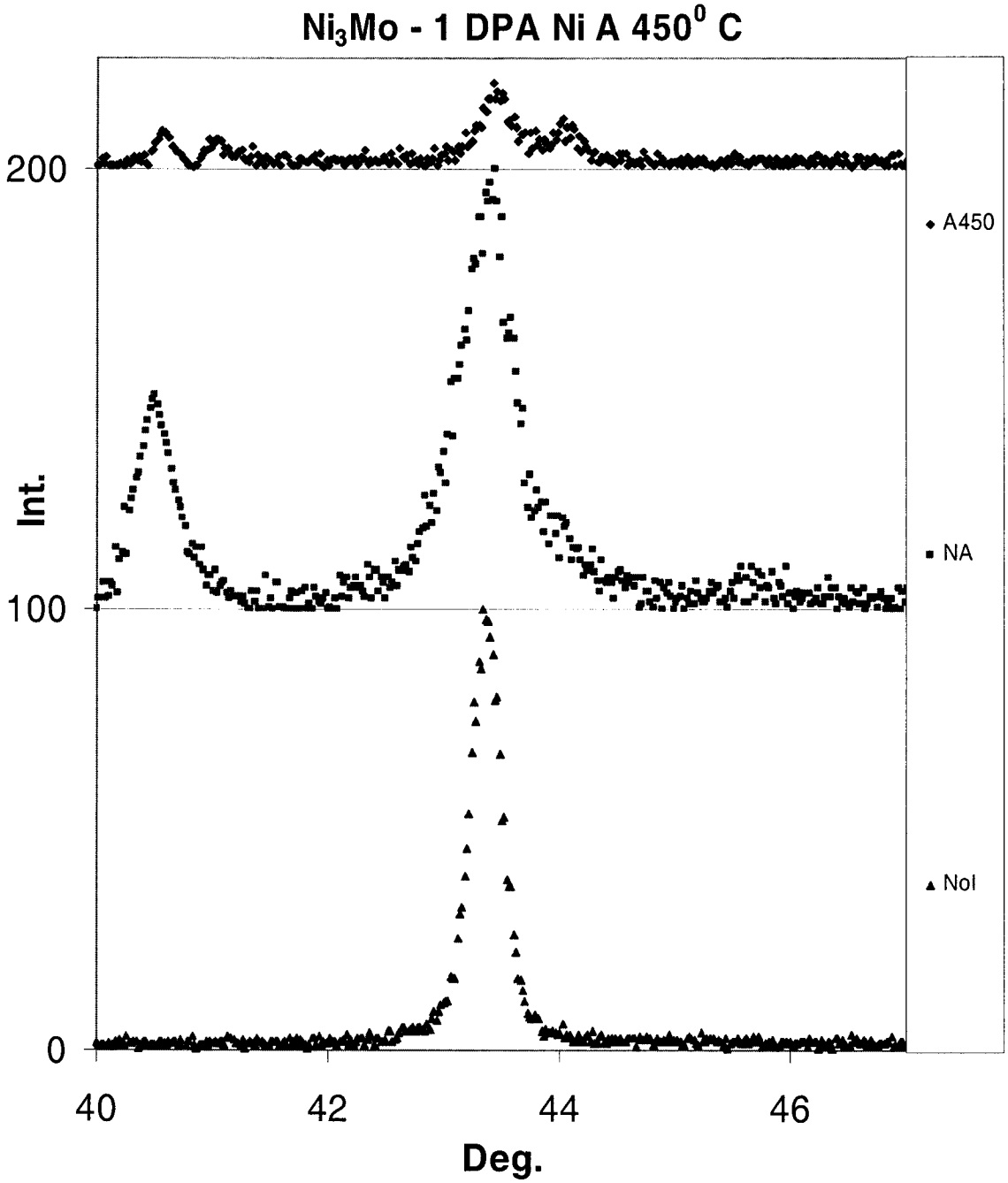

Figure A1.18 Detail #1 of the XRD spectra for Ni_3Mo as-cast sample exposed to a Ni+ beam for a 1 DPA dose. After irradiation, the samples were annealed for three hours at 450^0 C. The Intensity axis is in arbitrary units and is plotted as a function of the angle 2θ.

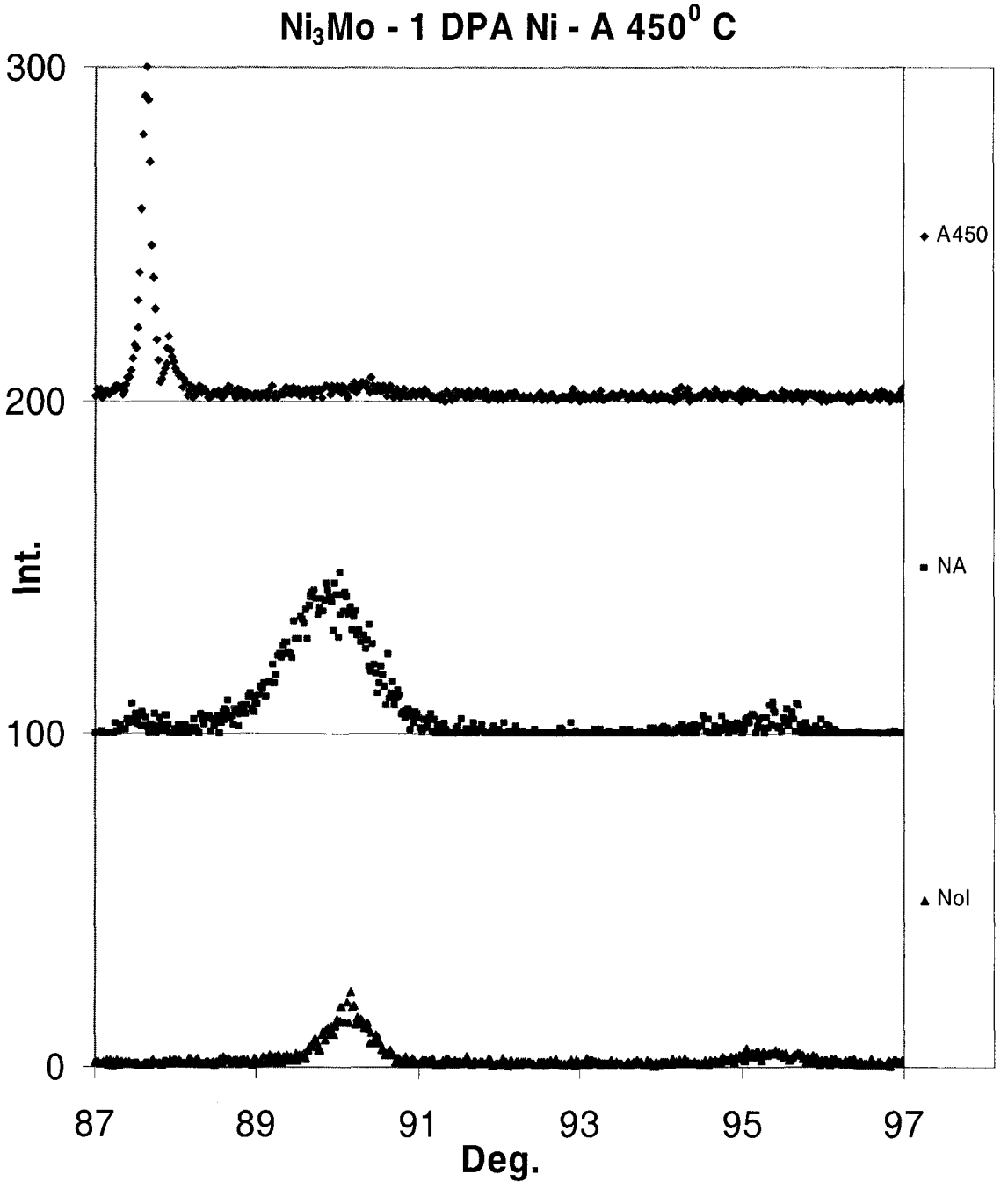

Figure A1.19 Detail #2 of the XRD spectra for Ni_3Mo as-cast sample exposed to a Ni+ beam for a 1 DPA dose. After irradiation, the samples were annealed for three hours at 450^0 C. The Intensity axis is in arbitrary units and is plotted as a function of the angle 2θ.

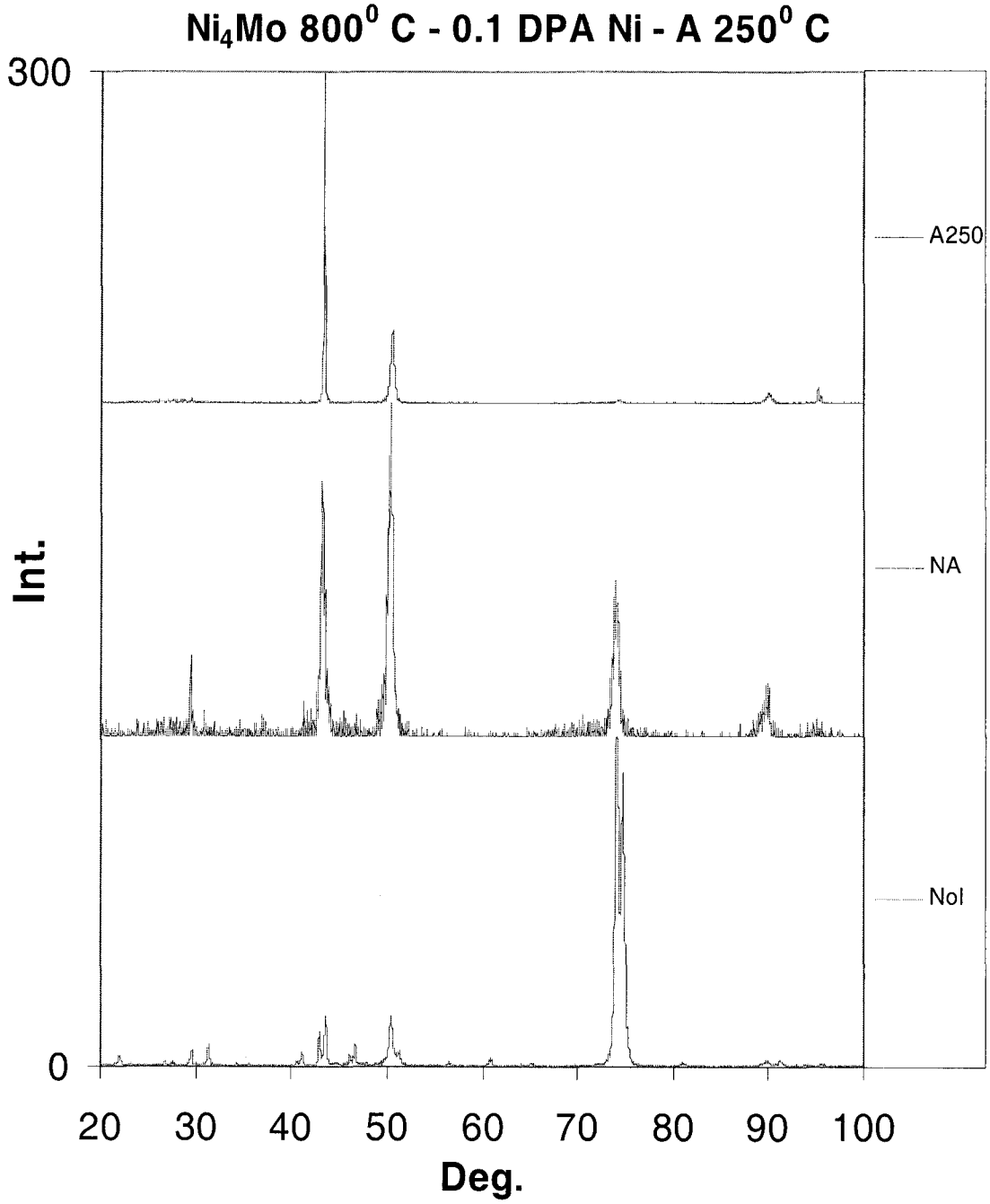

Figure A1.20 XRD spectra generated for Ni_4Mo samples annealed at 800^0 C before exposure to a Ni+ beam for a 0.1 DPA dose. After irradiation, the samples were annealed for three hours at 250^0 C. The Intensity axis is in arbitrary units and is plotted as a function of the angle 2θ.

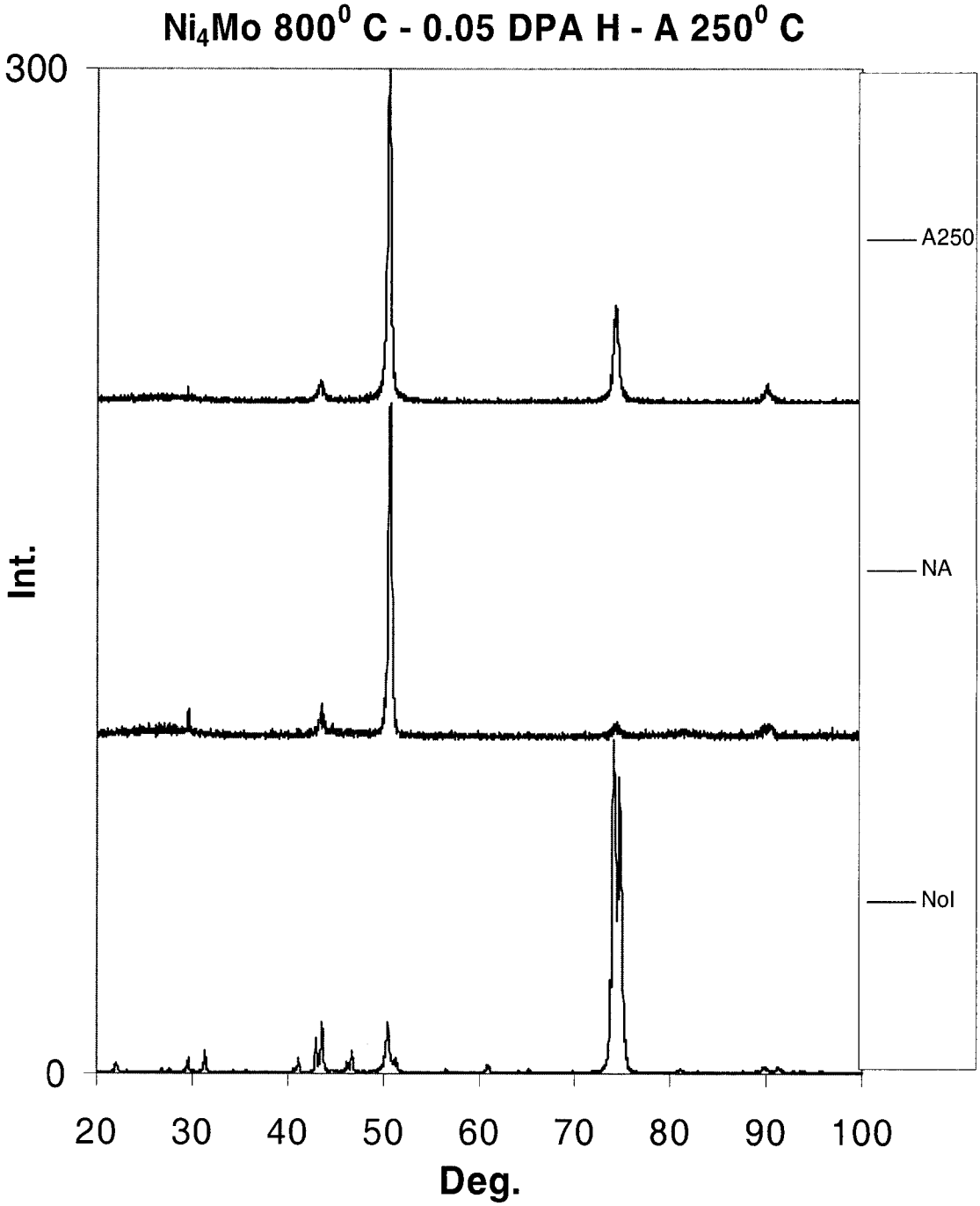

Figure A1.21 XRD spectra generated for Ni_3Mo samples annealed at 800^0 C before exposure to an H+ beam for a 0.05 DPA dose. After irradiation, the samples were annealed for three hours at 250^0 C. The Intensity axis is in arbitrary units and is plotted as a function of the angle 2θ.

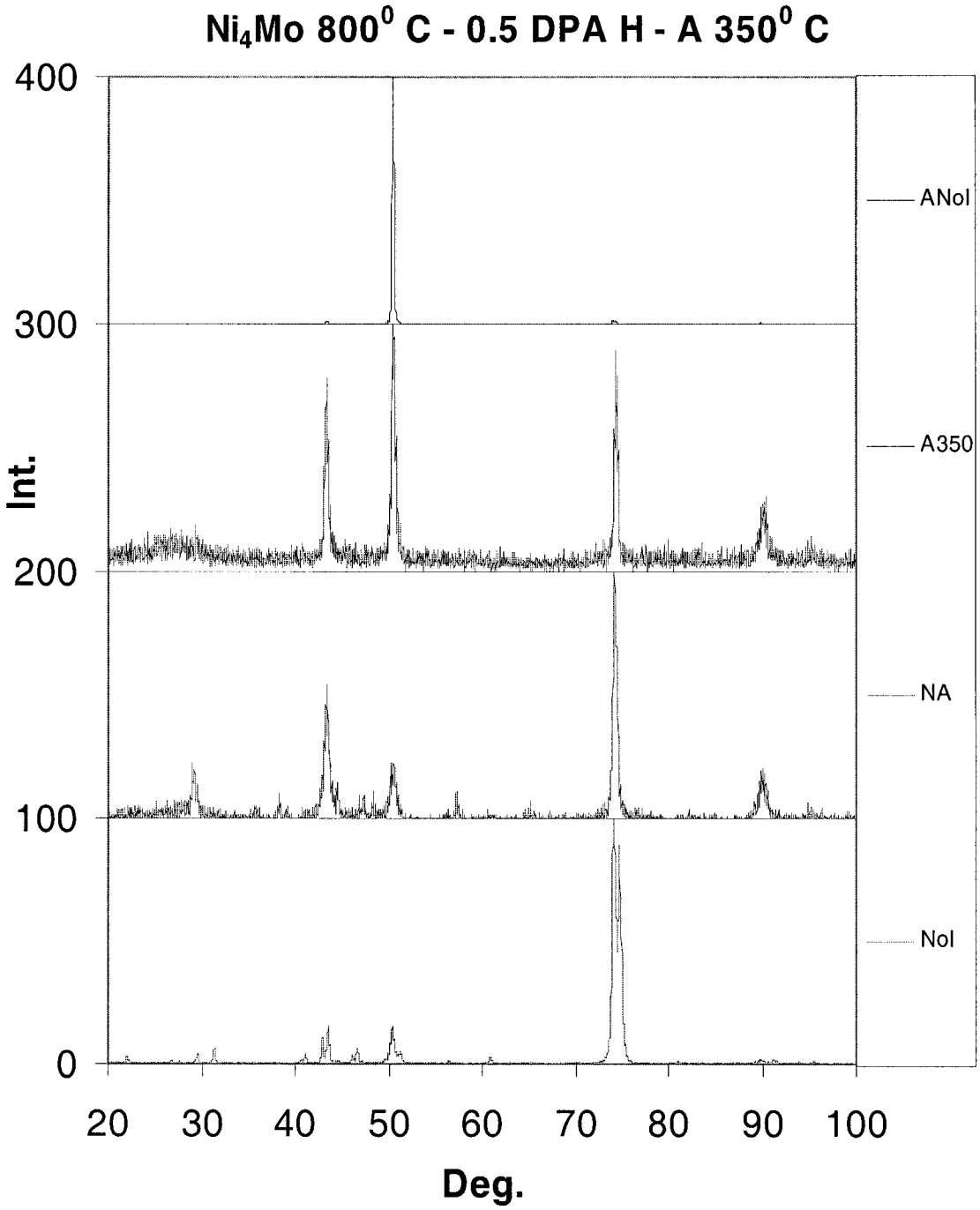

Figure 4.1.22 XRD spectra generated for Ni_4Mo samples annealed at 800^0 C before exposure to an H+ beam for a 0.5 DPA dose. After irradiation, the samples were annealed for three hours at 350^0 C. The Intensity axis is in arbitrary units and is plotted as a function of the angle 2θ. Spectra are compared with spectrum from sample with annealing but NoI.

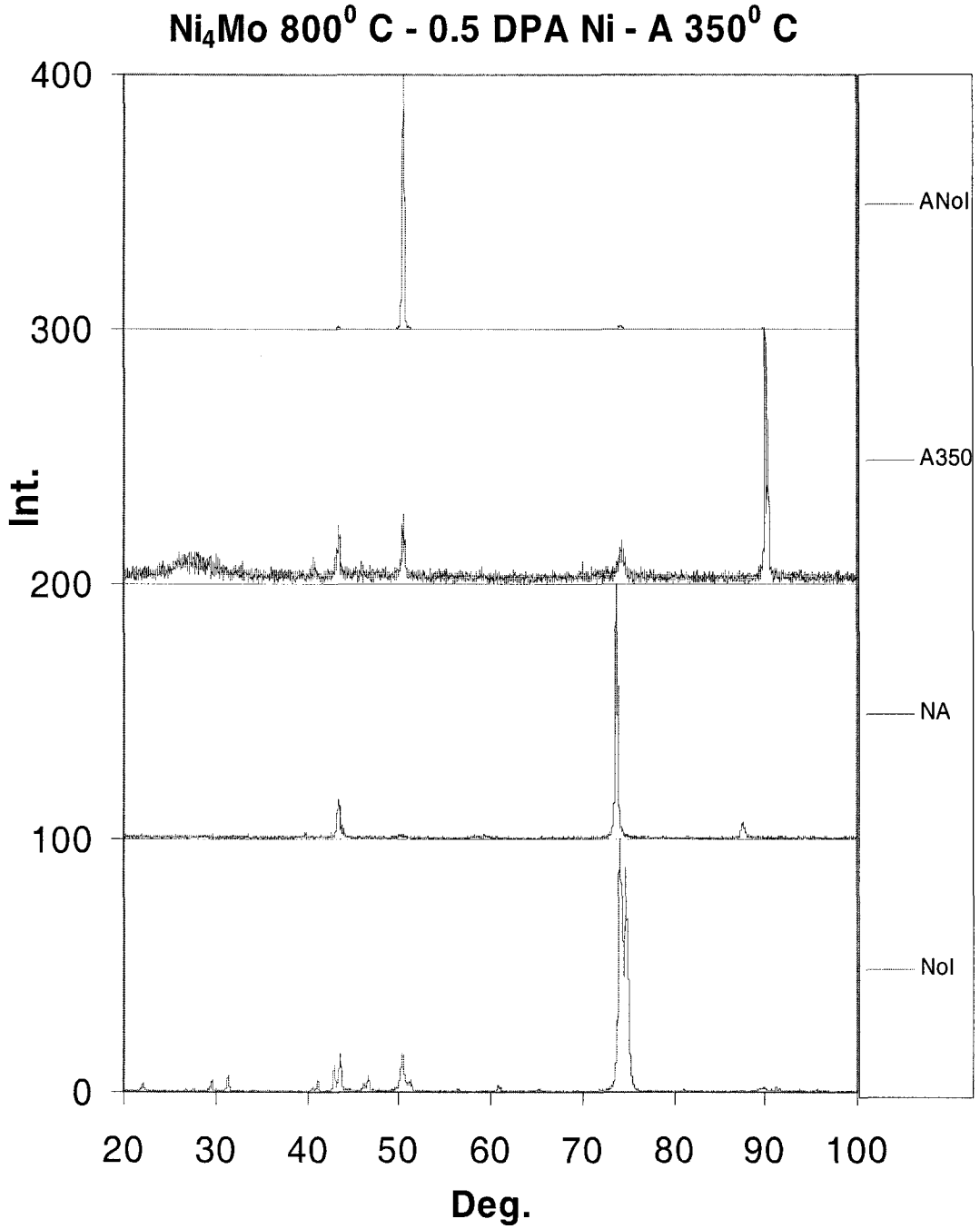

Figure A1.23 XRD spectra generated for Ni_4Mo samples annealed at 800^0 C before exposure to a Ni+ beam for a 0.5 DPA dose. After irradiation, the samples were annealed for three hours at 350^0 C. The Intensity axis is in arbitrary units and is plotted as a function of the angle 2θ. Spectra are compared with spectrum from sample with annealing but NoI.

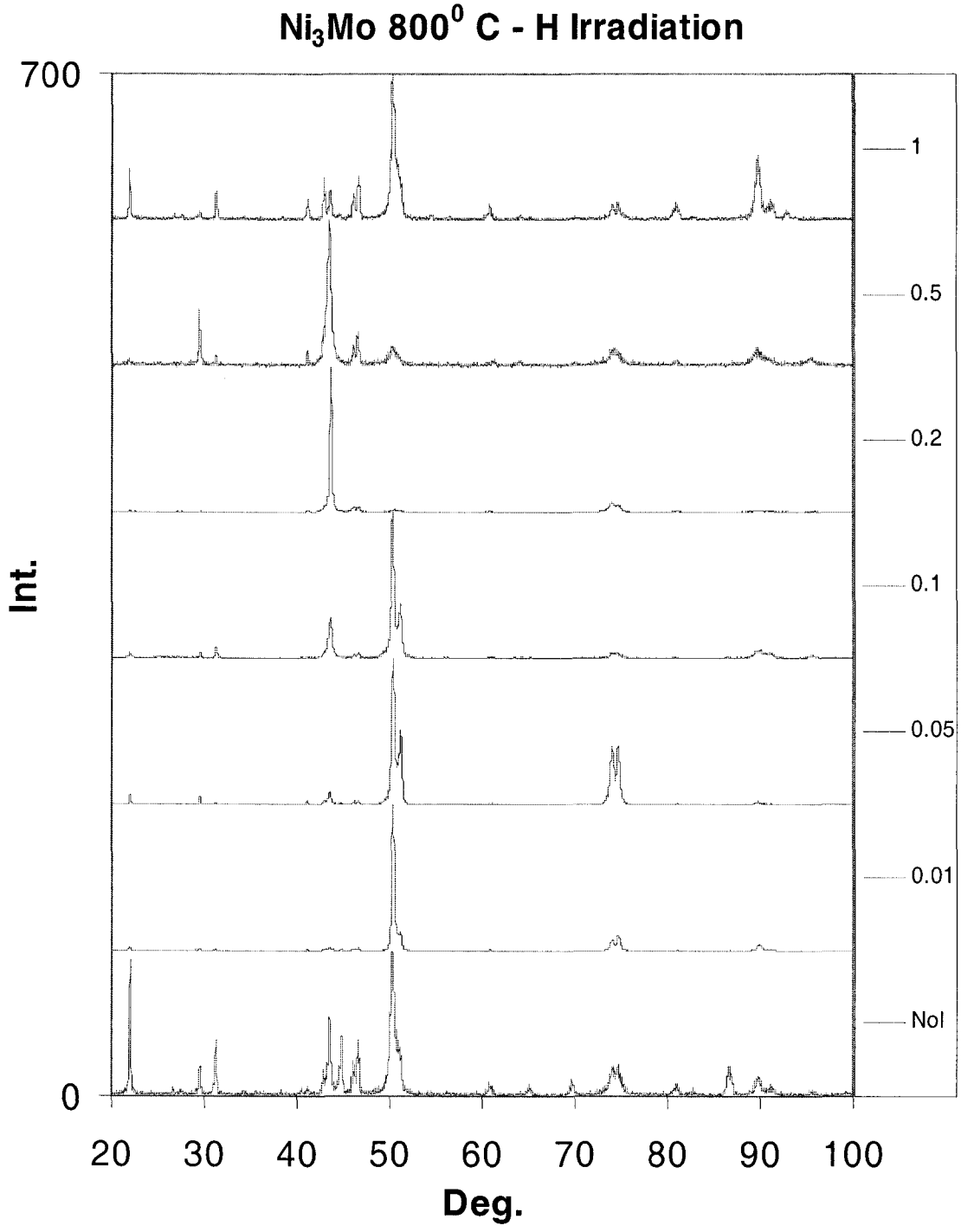

Figure A1.24 XRD spectra generated for Ni_3Mo samples annealed at 800^0 C samples irradiated with an H+ beam with a dose varying from 0.01 DPA to 1 DPA. The Intensity axis is in arbitrary units and is plotted as a function of the angle 2θ.

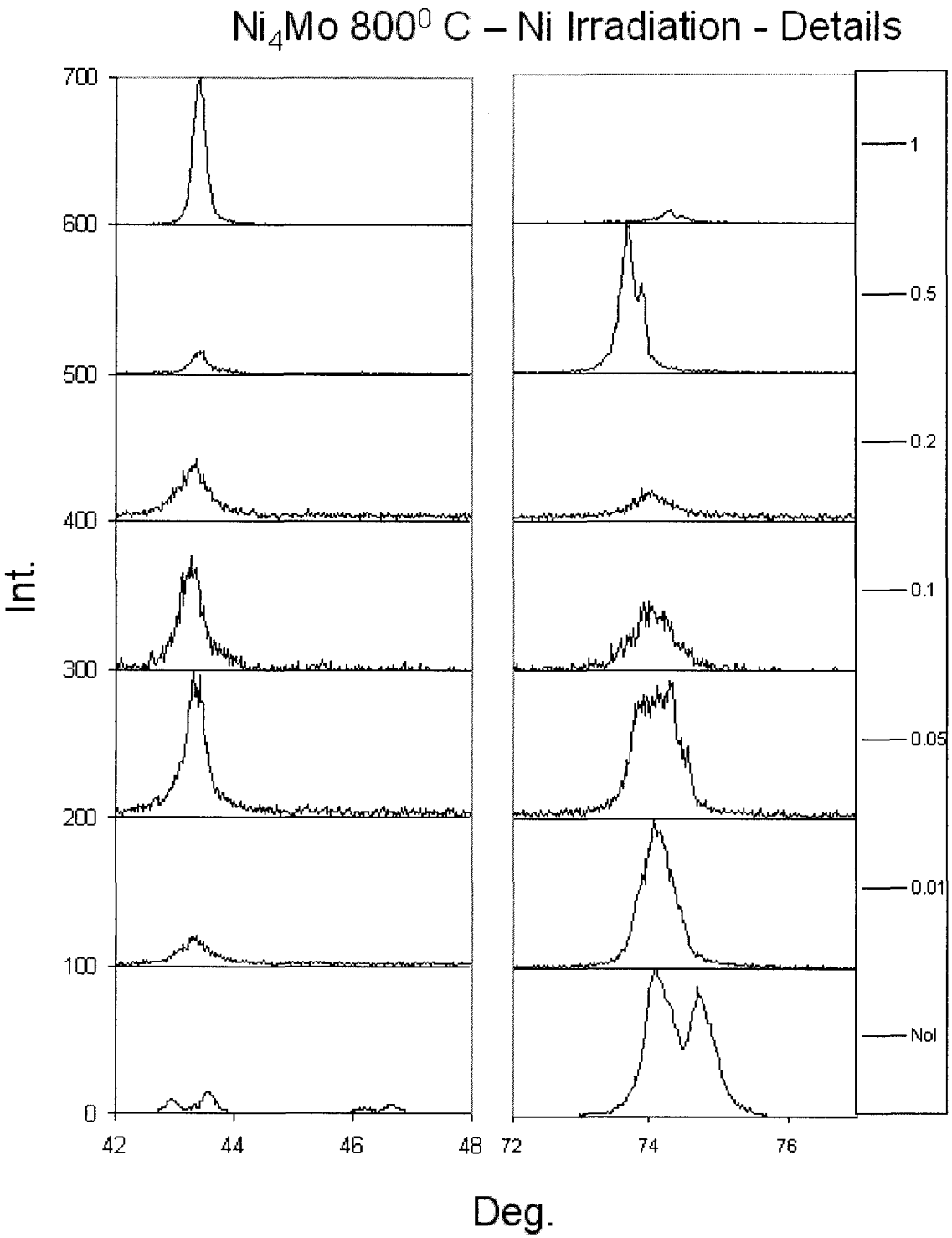

Figure A1.25 Detail of the XRD spectra generated for Ni_3Mo annealed at 800^0 C samples irradiated with a H+ beam with a dose varying from 0.01 DPA to 1 DPA. The Intensity axis is in arbitrary units and is plotted as a function of the angle 2θ.

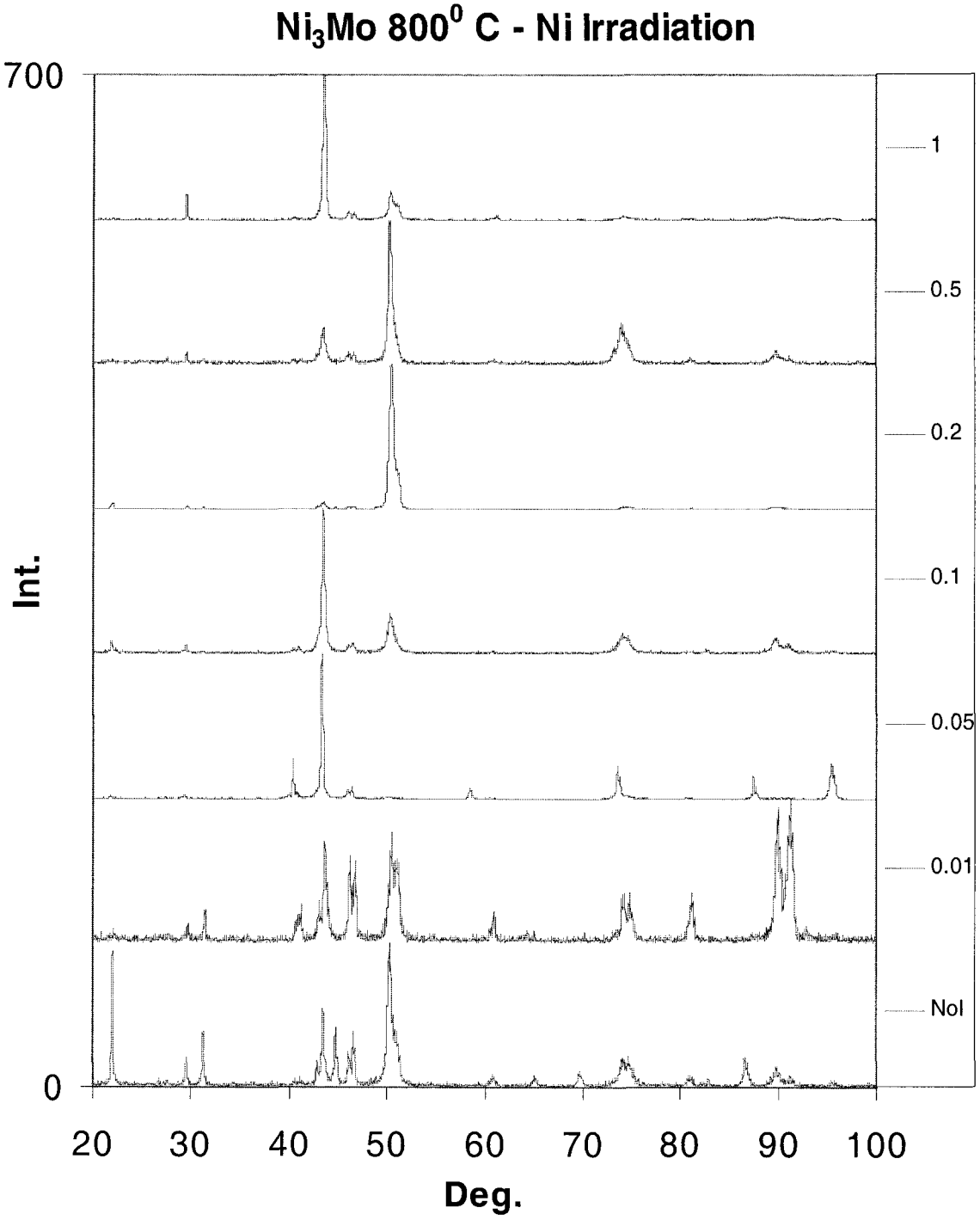

Figure A1.26 XRD spectra generated for Ni_3Mo samples annealed at 800^0 C irradiated with a Ni+ beam with a dose varying from 0.01 DPA to 1 DPA. The Intensity axis is in arbitrary units and is plotted as a function of the angle 2θ.

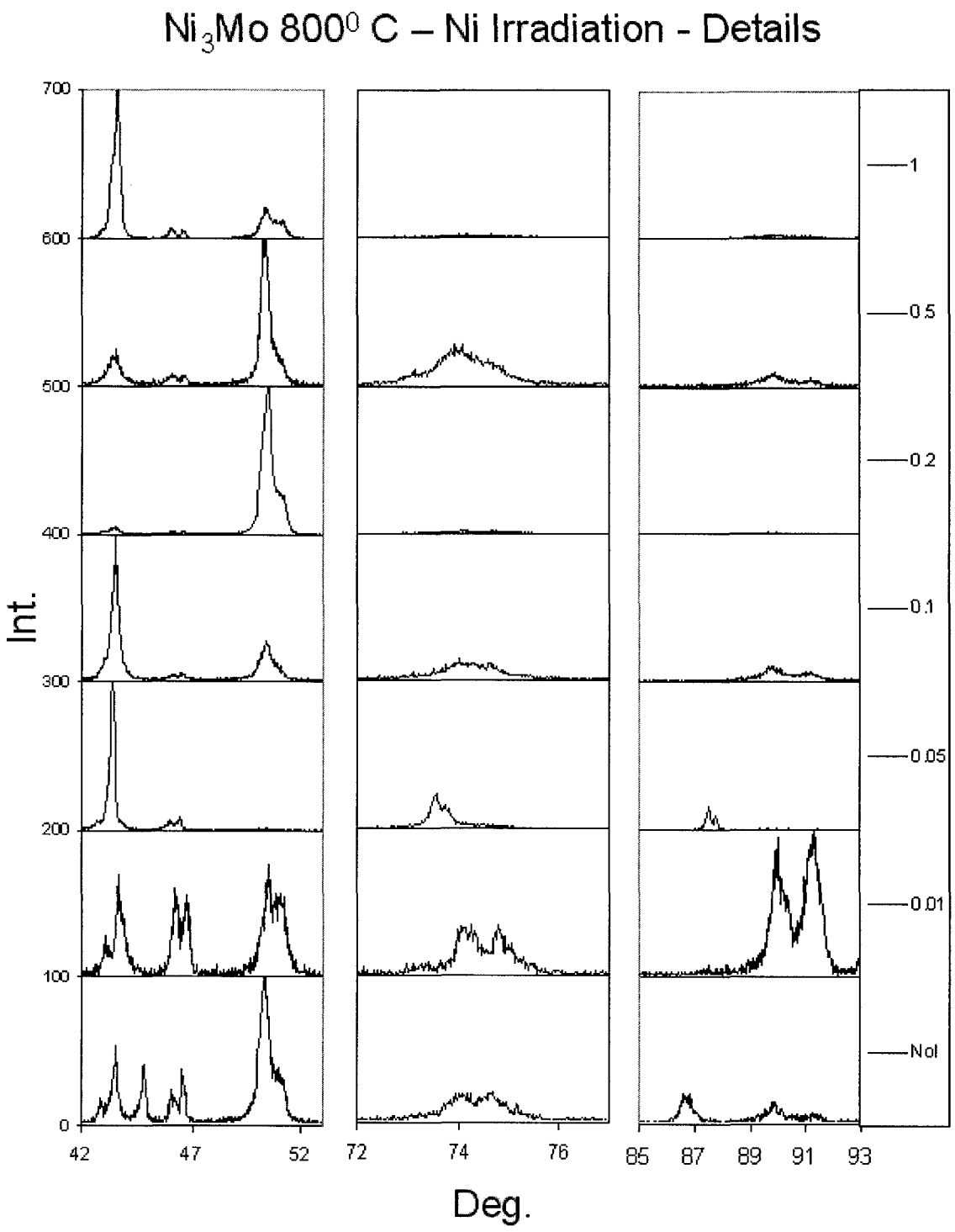

Figure A1.27 Detail of the XRD spectra generated for Ni_3Mo annealed at 800^0 C samples irradiated with a Ni+ beam with a dose varying from 0.01 DPA to 1 DPA. The Intensity axis is in arbitrary units and is plotted as a function of the angle 2θ.

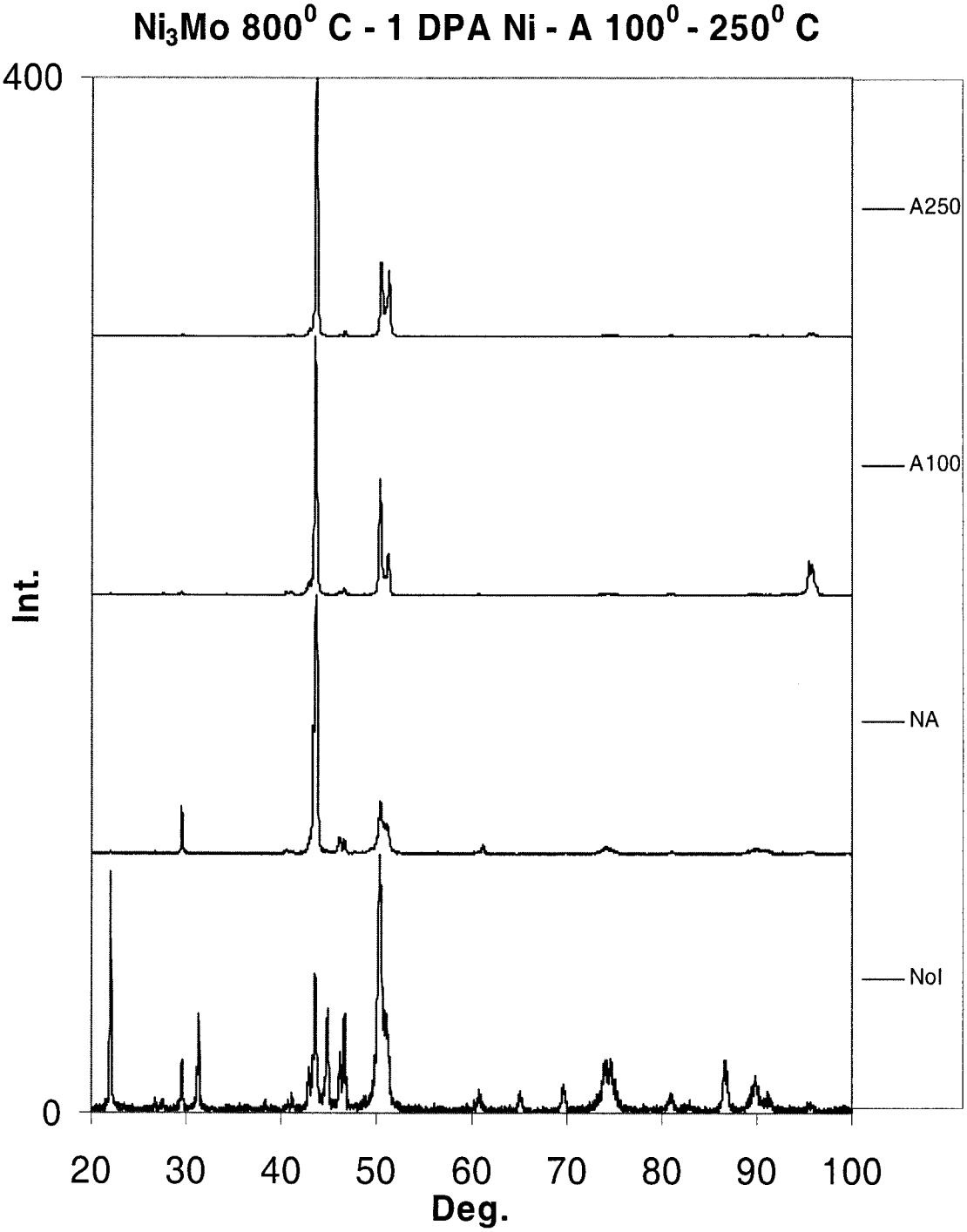

Figure A1.28 XRD spectra generated for Ni_3Mo samples annealed at 800^0 C before irradiation and exposed to a Ni+ beam for a 1 DPA dose. After irradiation the samples were first annealed for three hours at 100^0 C and then for three hours at 250^0 C. The Intensity axis is in arbitrary units and is plotted as a function of the angle 2θ.

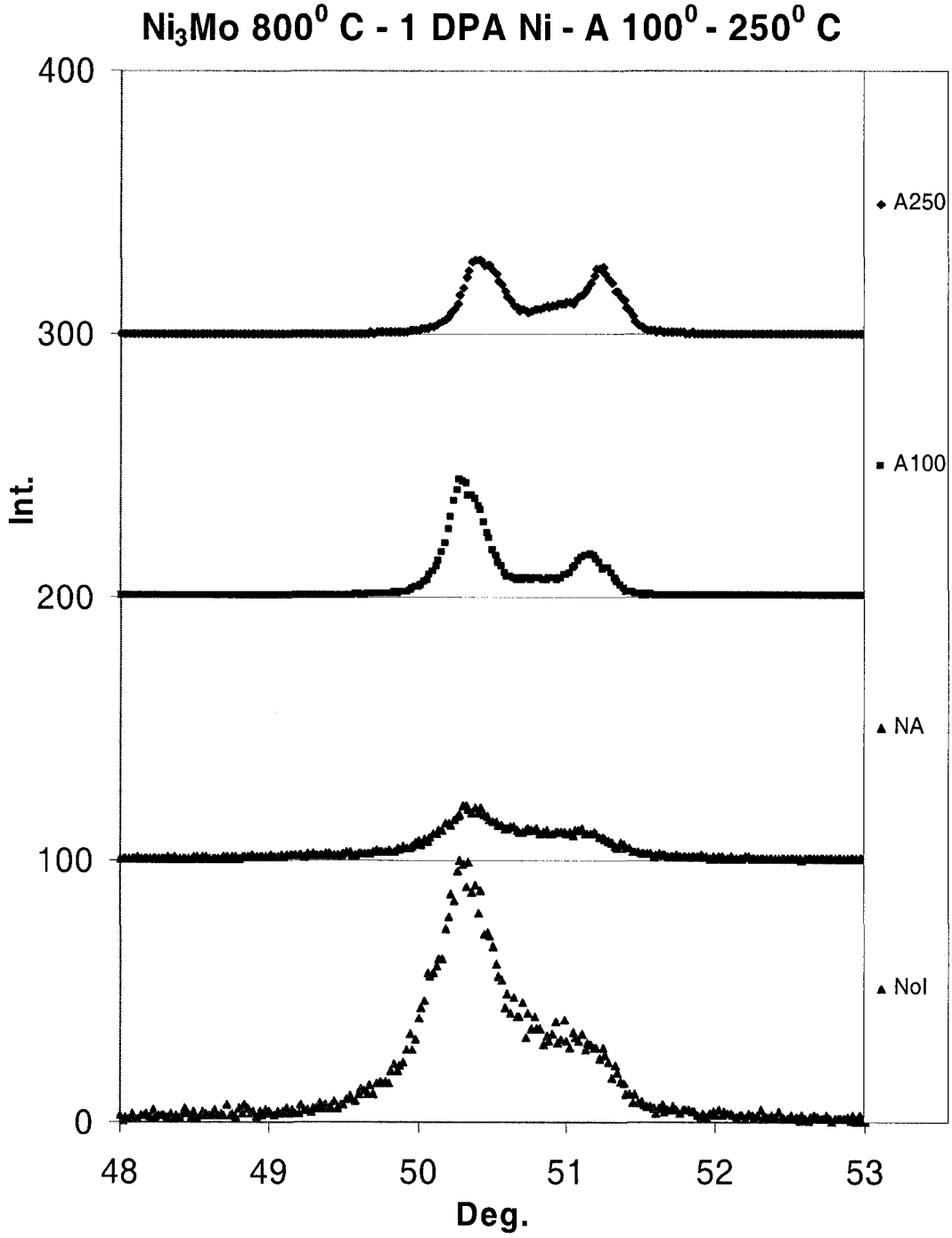

Figure A1.29 Detail #1 of the XRD spectra generated for Ni_3Mo samples annealed before irradiation at 800^0 C irradiated with a Ni+ beam with a 1 DPA dose from Figure A1.28. The Intensity axis is in arbitrary units and is plotted as a function of the angle 2θ.

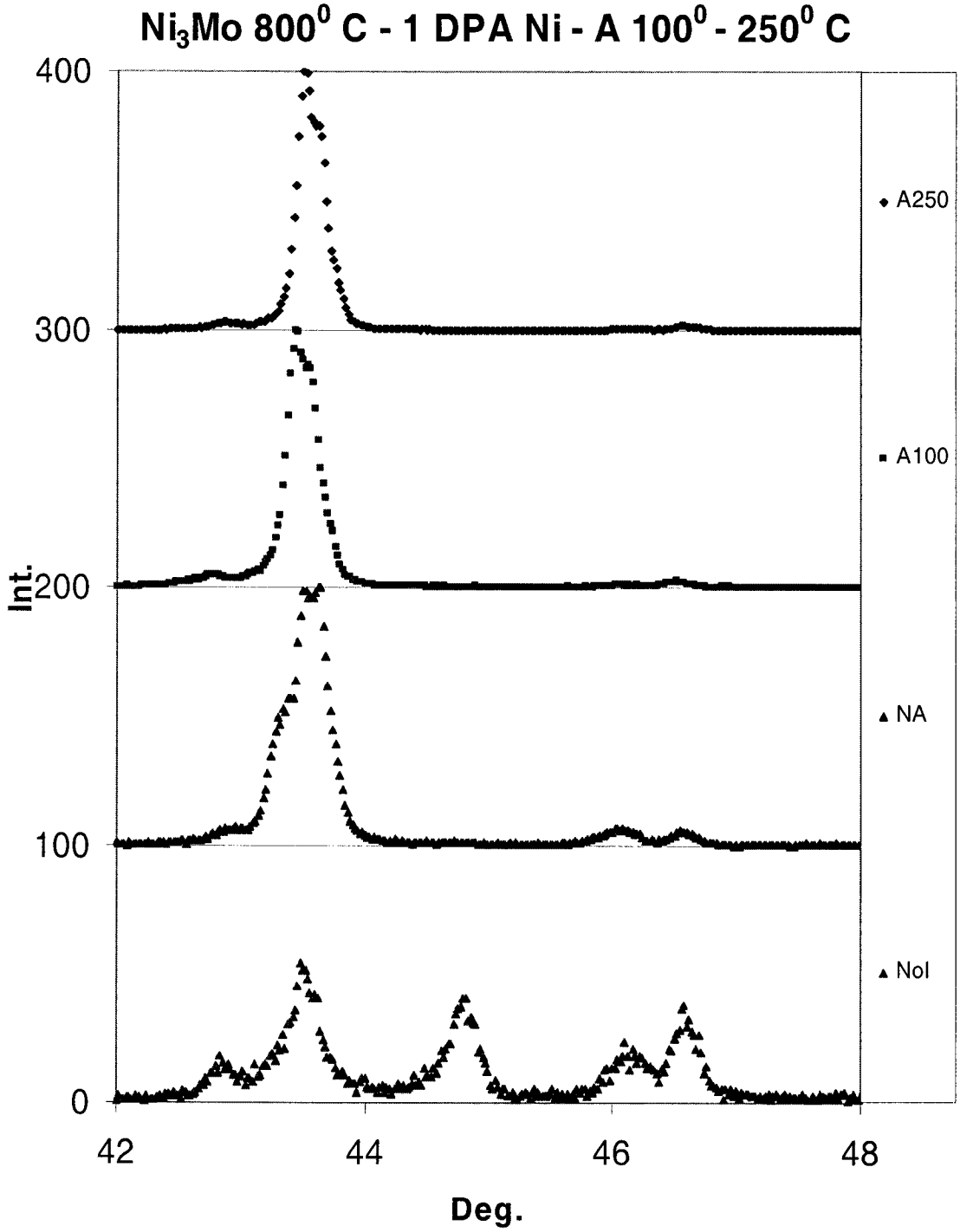

Figure A1.30 Detail #2 of the XRD spectra generated for Ni_3Mo samples annealed before irradiation at 800^0 C irradiated with a Ni+ beam with a 1 DPA dose from Figure A1.28. The Intensity axis is in arbitrary units and is plotted as a function of the angle 2θ.

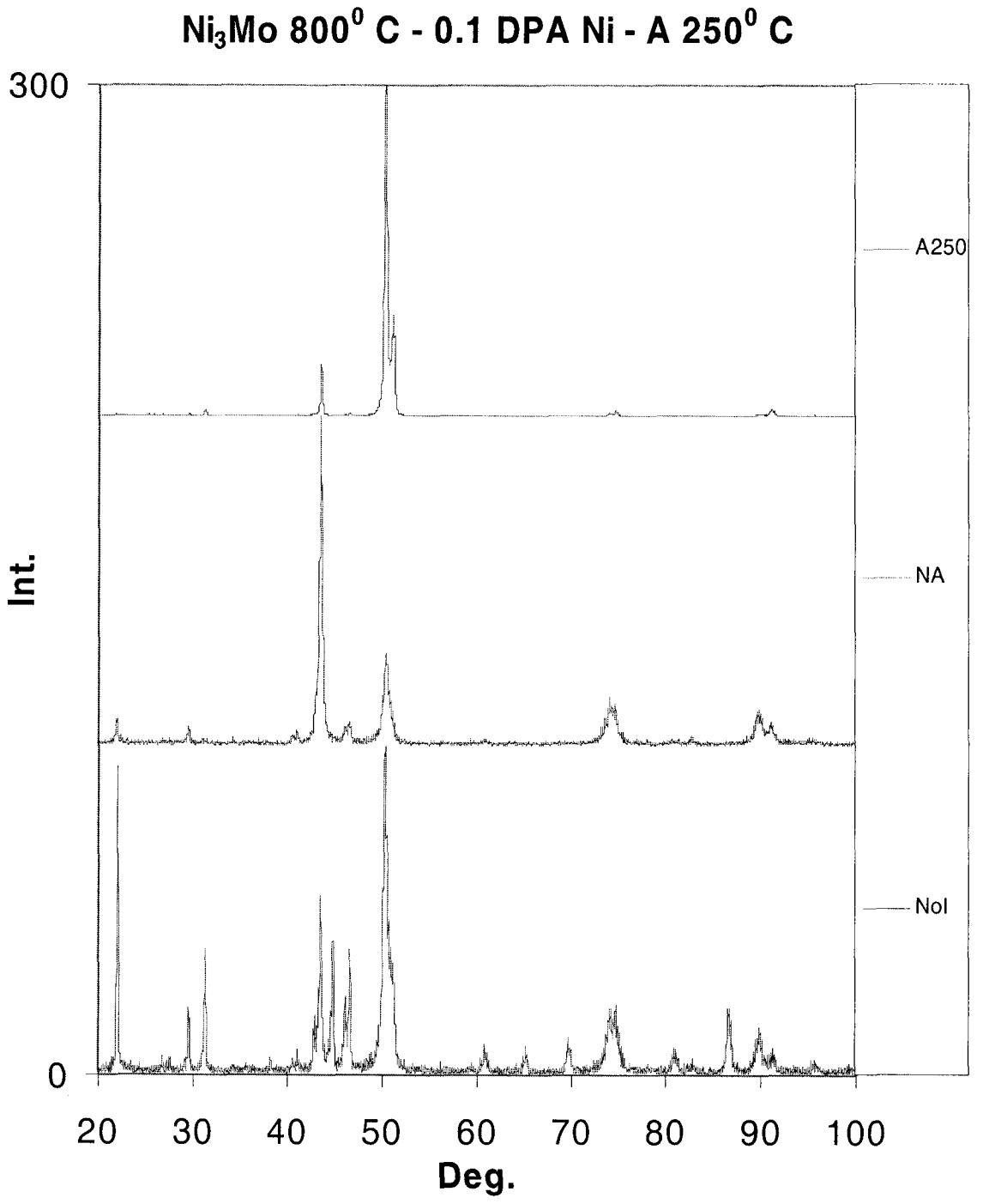

Figure A1.31 XRD spectra generated for Ni_3Mo samples annealed at 800^0 C before exposure to a Ni+ beam for a 0.1 DPA dose. After irradiation, the samples were annealed for three hours at 250^0 C. The Intensity axis is in arbitrary units and is plotted as a function of the angle 2θ.

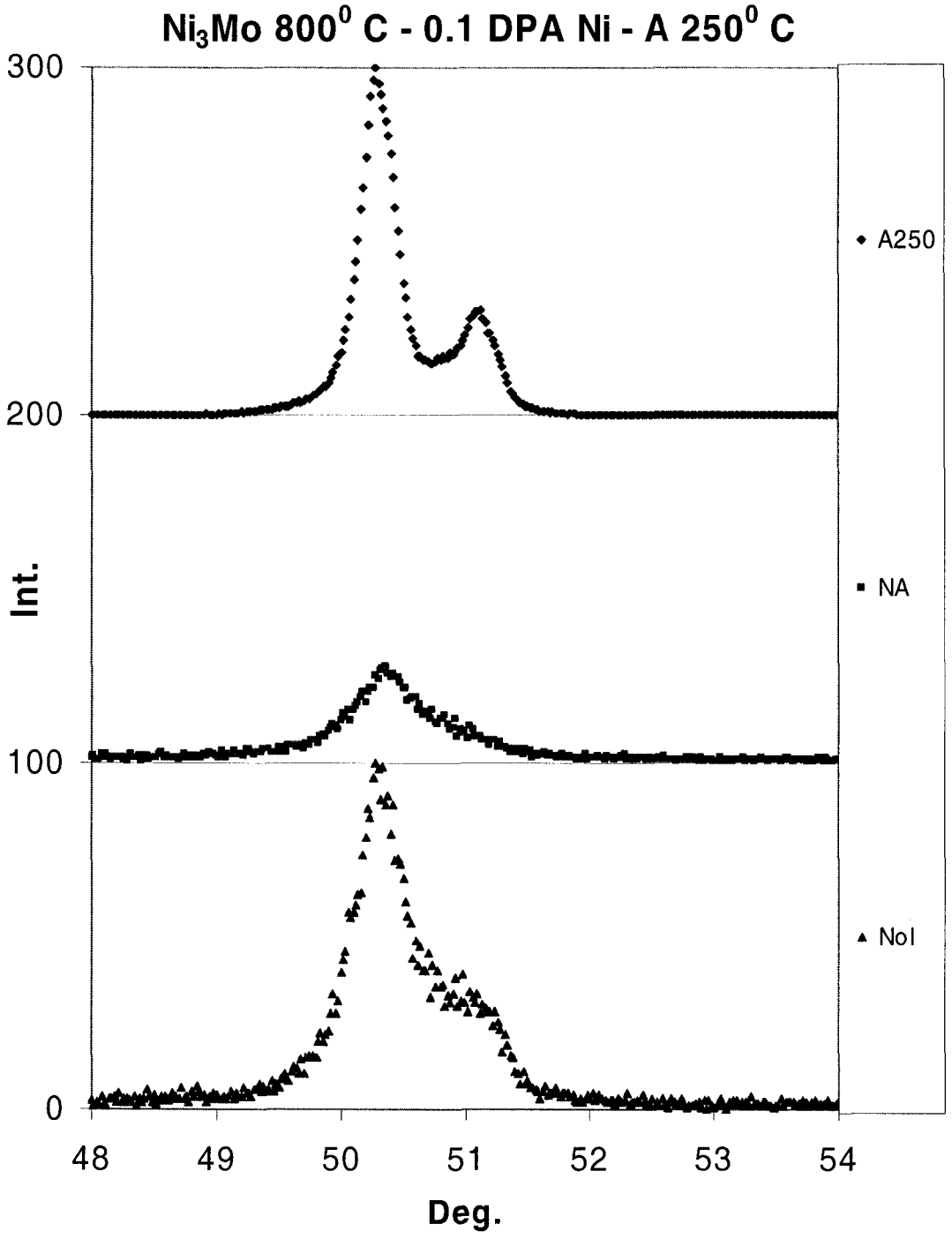

Figure A1.32 Detail#1 of XRD spectra generated for Ni_3Mo samples annealed at 800^0 C before exposure to a Ni+ beam for a 0.1 DPA dose. After irradiation, the samples were annealed for three hours at 250^0 C. The Intensity axis is in arbitrary units and is plotted as a function of the angle 2θ.

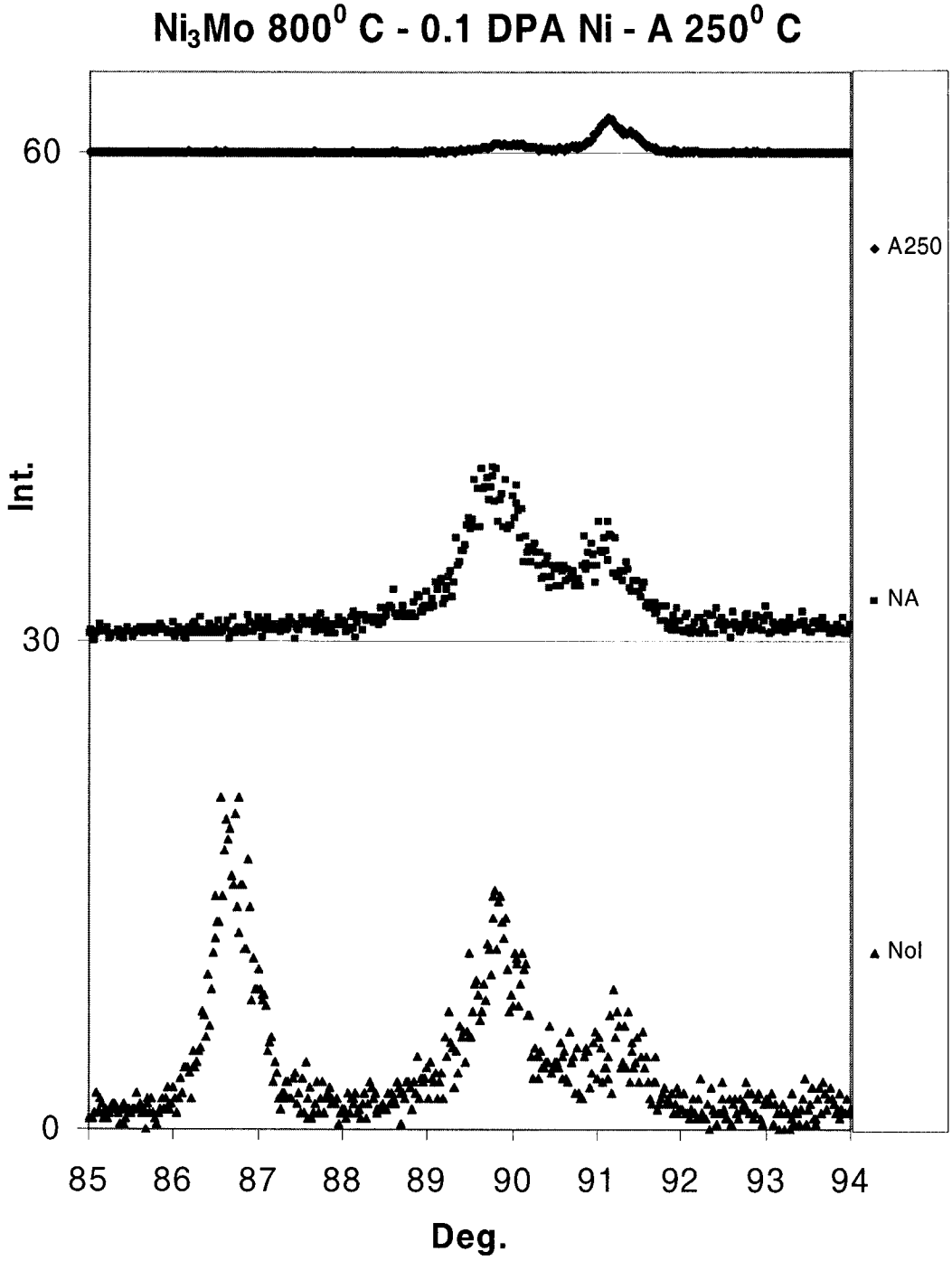

Figure A1.33 Detail#2 of XRD spectra generated for Ni_3Mo samples annealed at 800^0 C before exposure to a Ni+ beam for a 0.1 DPA dose. After irradiation, the samples were annealed for three hours at 250^0 C. The Intensity axis is in arbitrary units and is plotted as a function of the angle 2θ.

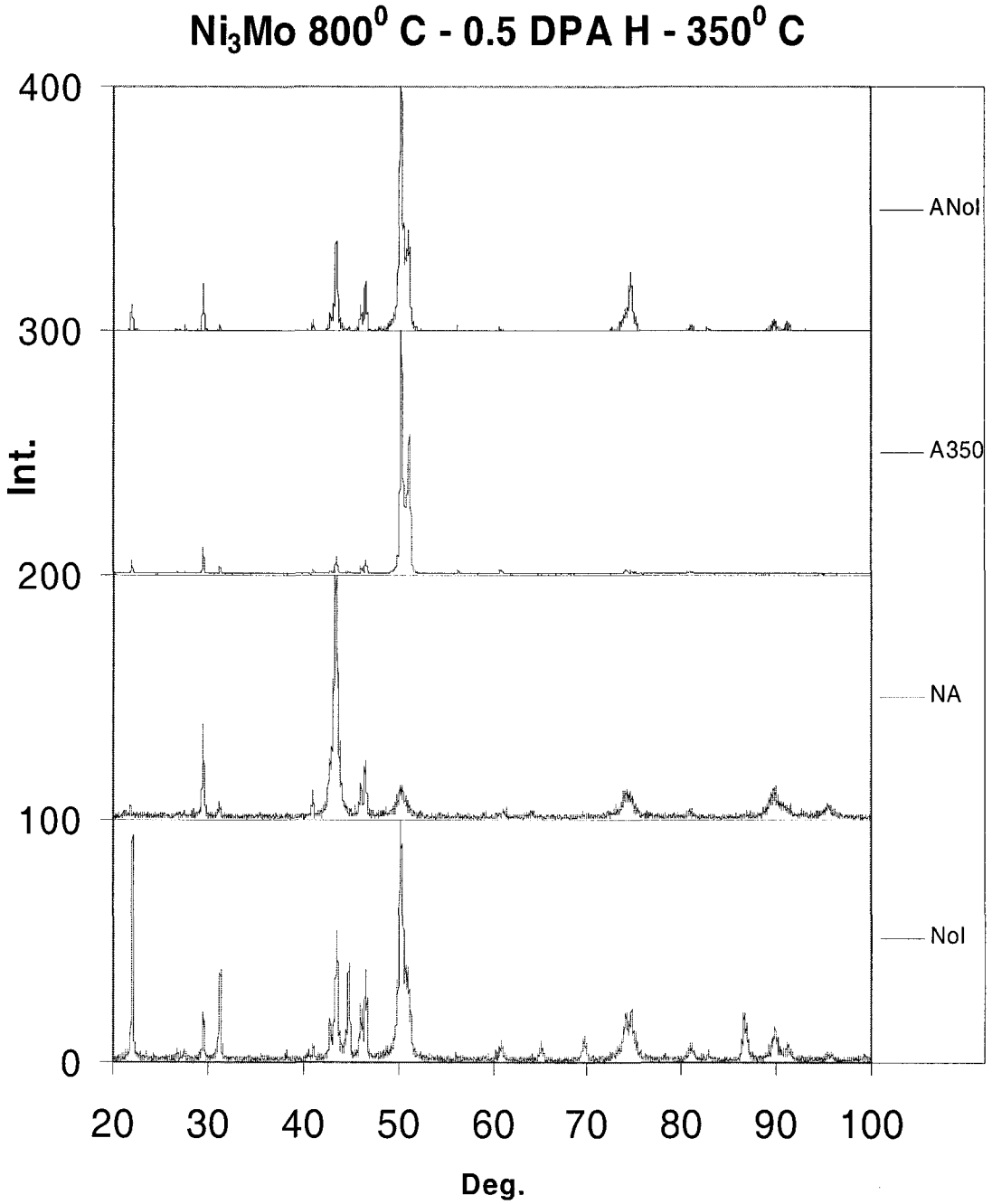

Figure A1.34 XRD spectra generated for Ni_3Mo samples annealed at 800^0 C before exposure to an H+ beam for a 0.5 DPA dose. After irradiation, the samples were annealed for three hours at 350^0 C. The Intensity axis is in arbitrary units and is plotted as a function of the angle 2θ. Spectra are compared with spectrum from sample with annealing but NoI.

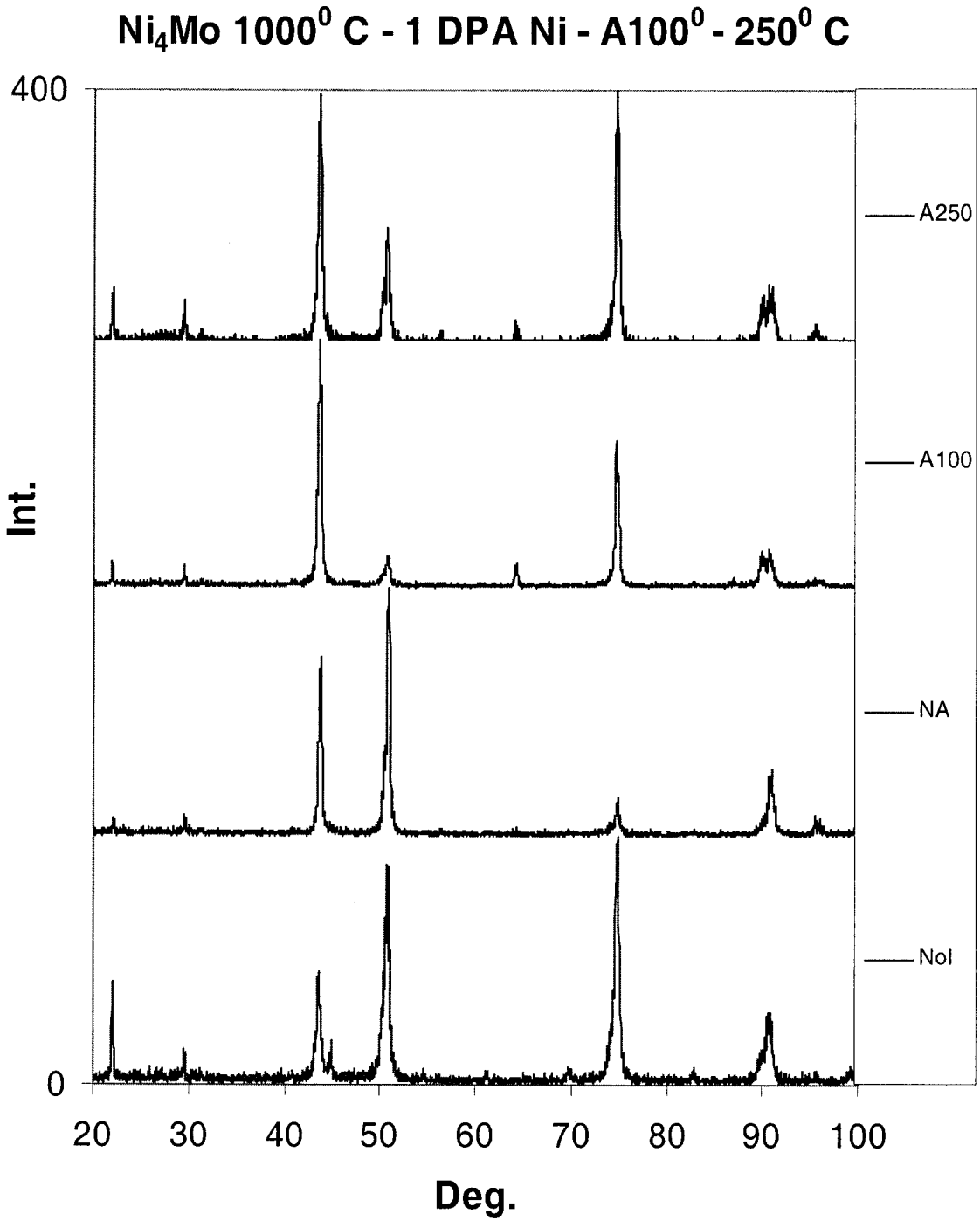

Figure A1.35 XRD spectra generated for Ni_4Mo samples annealed at 1000^0 C before irradiation and exposed to a Ni+ beam for a 1 DPA dose. After irradiation the samples were first annealed for three hours at 100^0 C and then for three hours at 250^0 C. The Intensity axis is in arbitrary units and is plotted as a function of the angle 2θ.

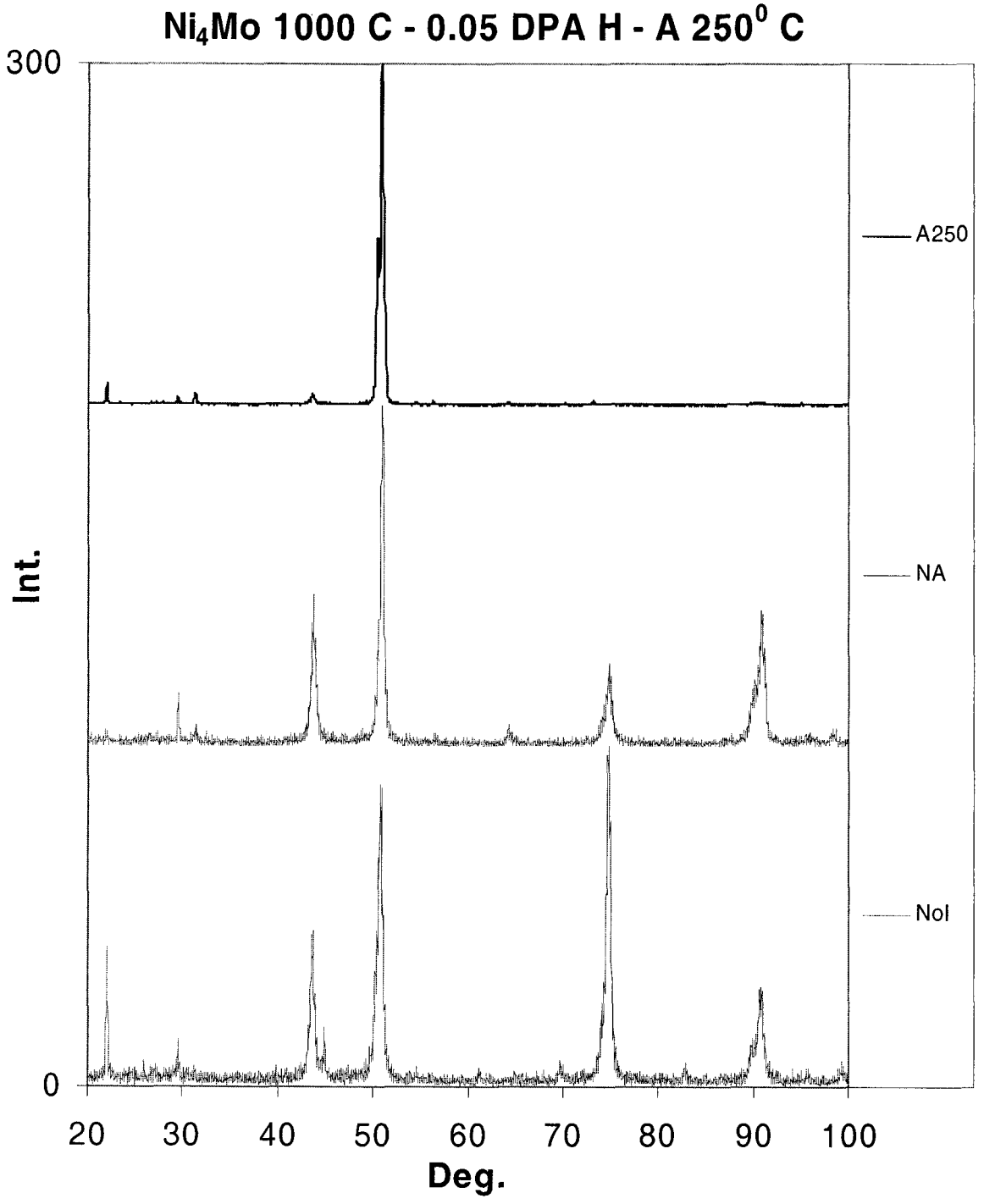

Figure A1.36 XRD spectra generated for Ni_4Mo samples annealed at 1000^0 C before exposure to an H+ beam for a 0.05 DPA dose. After irradiation, the samples were annealed for three hours at 250^0 C. The Intensity axis is in arbitrary units and is plotted as a function of the angle 2θ.

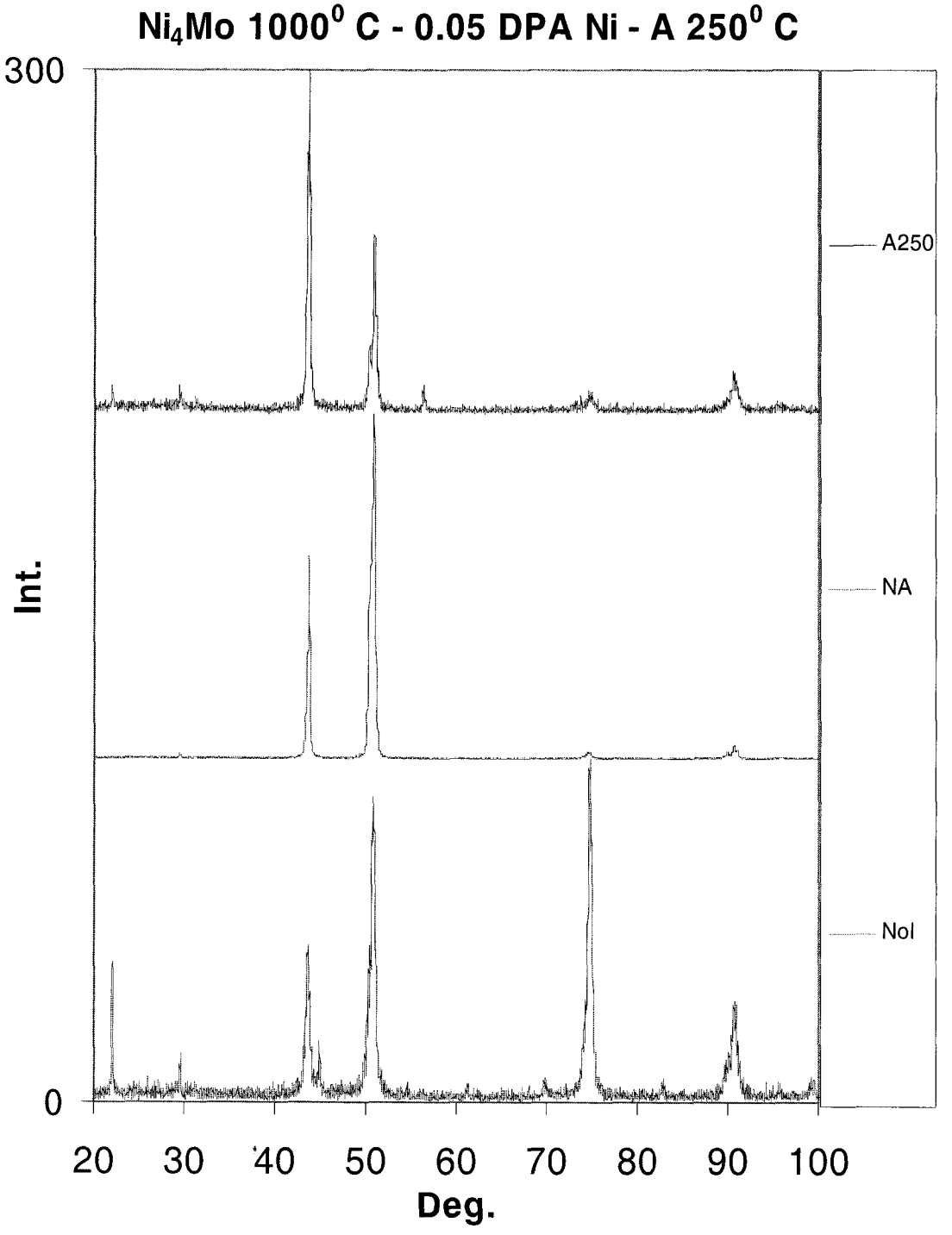

Figure A1.37 XRD spectra generated for Ni_4Mo samples annealed at 1000^0 C before exposure to a Ni+ beam for a 0.05 DPA dose. After irradiation, the samples were annealed for three hours at 250^0 C. The Intensity axis is in arbitrary units and is plotted as a function of the angle 2θ.

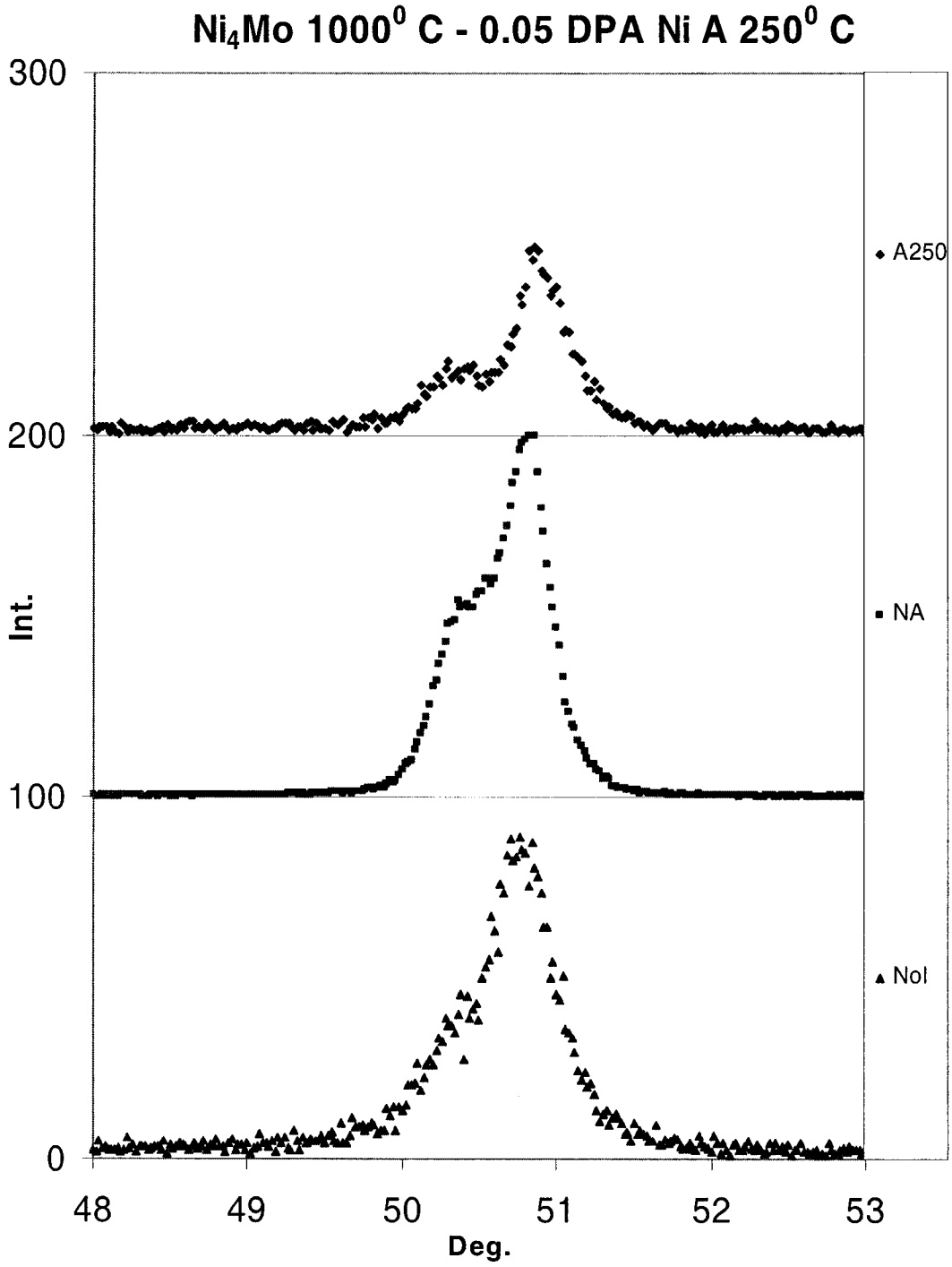

Figure A1.38 Detail#1 of the XRD spectra from Figure A1.37 generated for Ni_4Mo samples annealed at 1000^0 C before exposure to a Ni+ beam for a 0.05 DPA dose. After irradiation, the samples were annealed for three hours at 250^0 C. The Intensity axis is in arbitrary units and is plotted as a function of the angle 2θ.

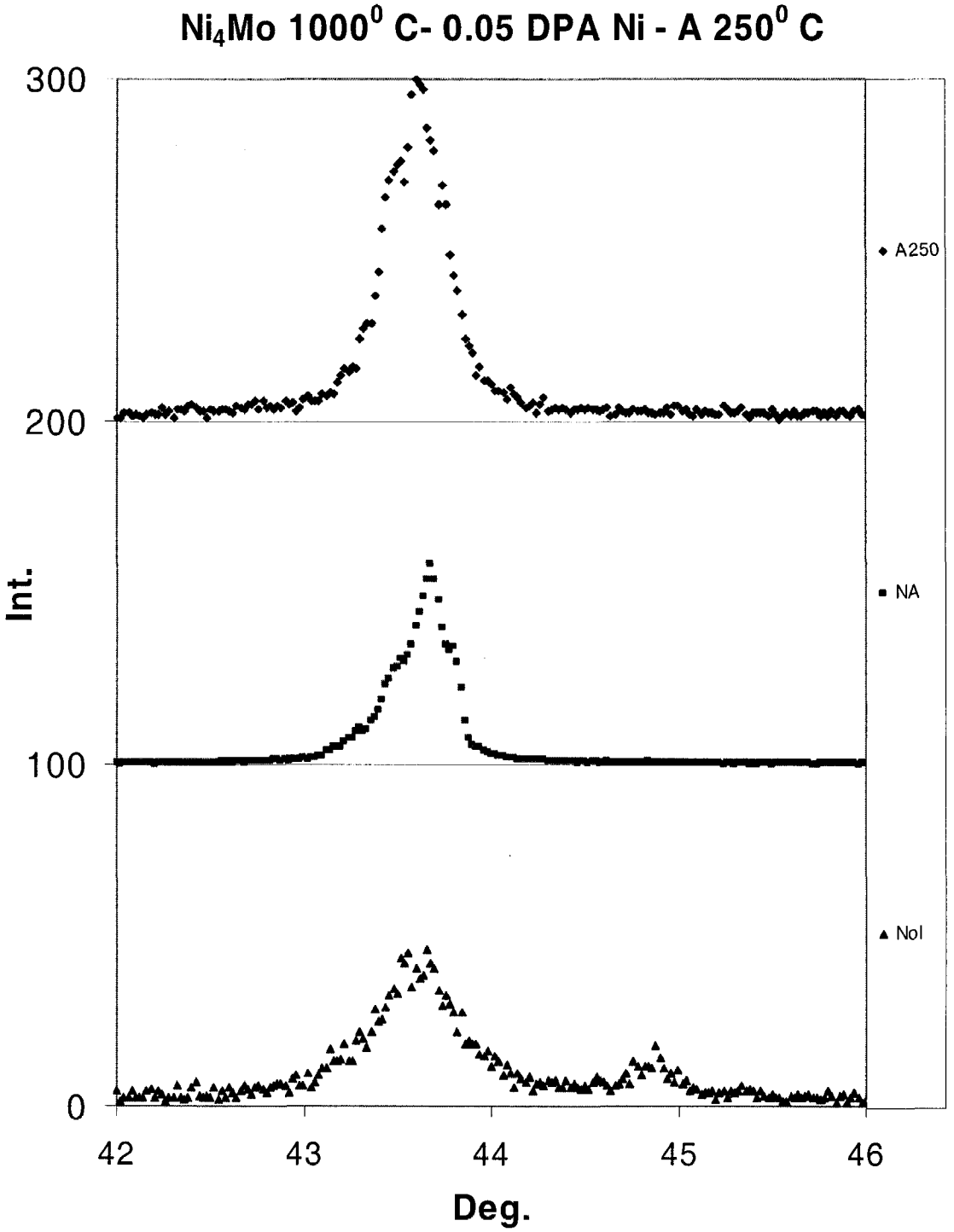

Figure A1.39 Detail#2 of the XRD spectra from Figure A1.37 generated for Ni_4Mo samples annealed at 1000^0 C before exposure to a Ni+ beam for a 0.05 DPA dose. After irradiation, the samples were annealed for three hours at 250^0 C. The Intensity axis is in arbitrary units and is plotted as a function of the angle 2θ.

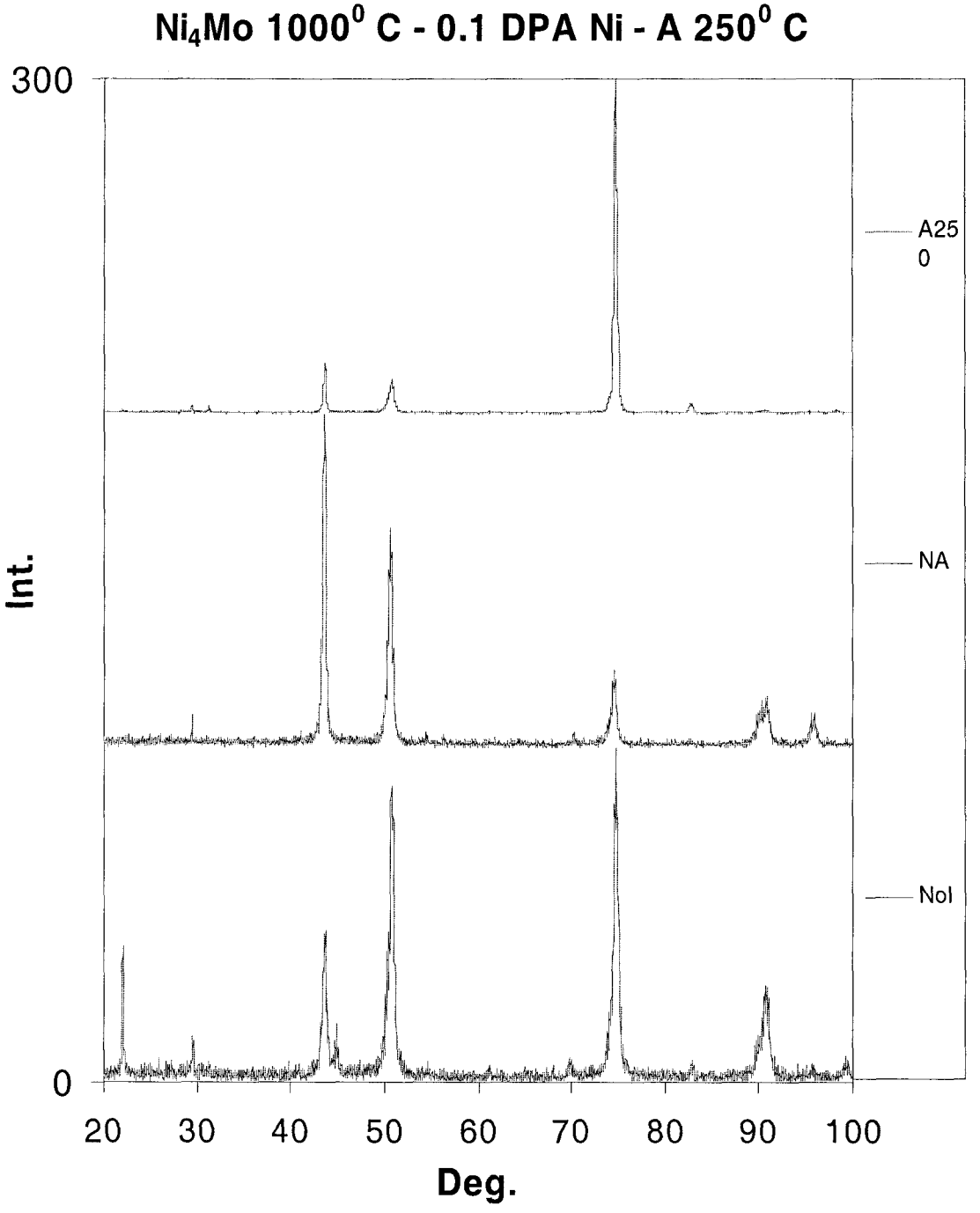

Figure A1.40 XRD spectra generated for Ni_4Mo samples annealed at 1000^0 C before exposure to a Ni+ beam for a 0.1 DPA dose. After irradiation, the samples were annealed for three hours at 250^0 C. The Intensity axis is in arbitrary units and is plotted as a function of the angle 2θ.

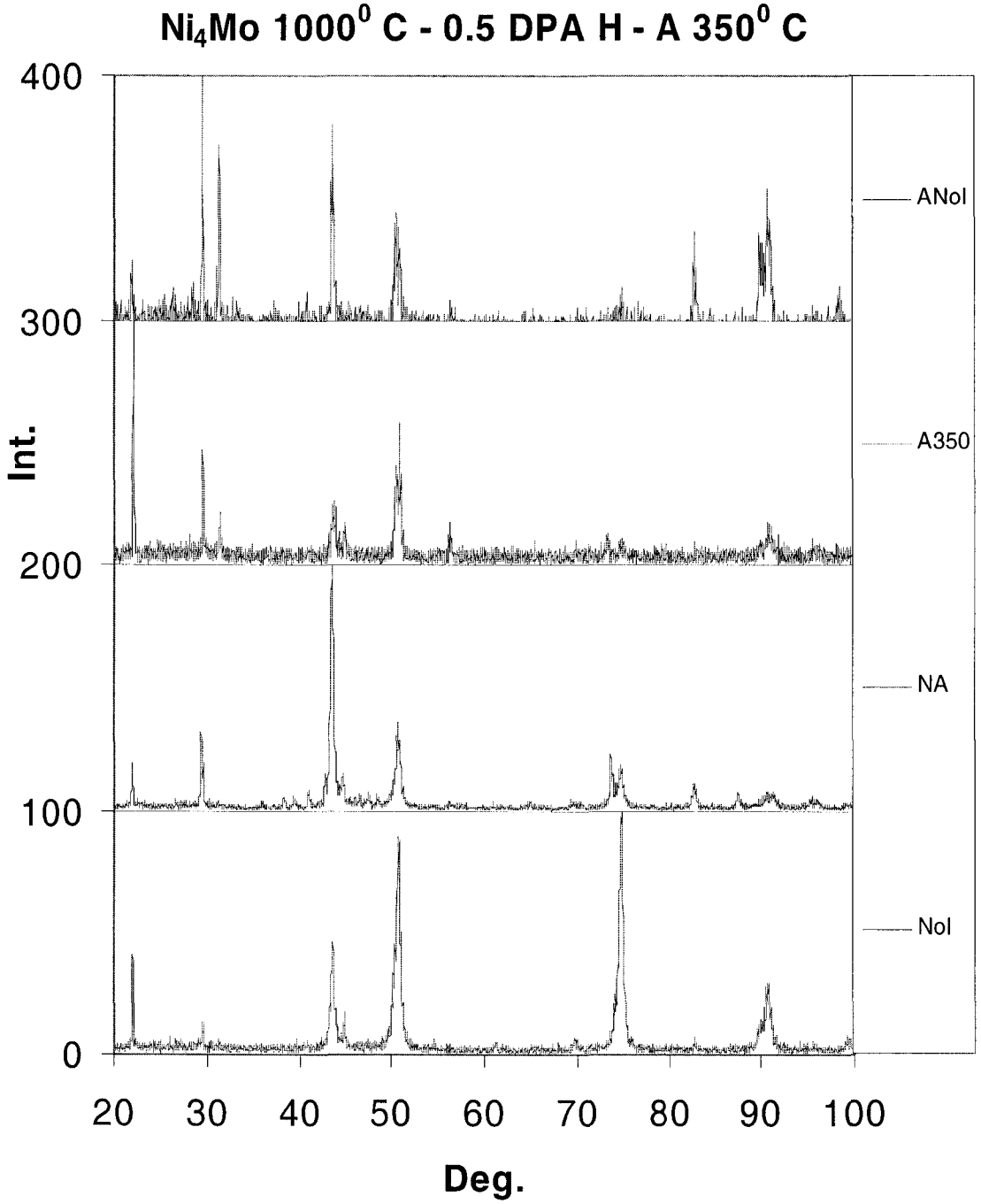

Figure A1.41 XRD spectra generated for Ni_4Mo samples annealed at 1000^0 C before exposure to an H+ beam for a 0.5 DPA dose. After irradiation, the samples were annealed for three hours at 350^0 C. The Intensity axis is in arbitrary units and is plotted as a function of the angle 2θ. Spectra are compared with spectrum from sample with annealing but NoI.

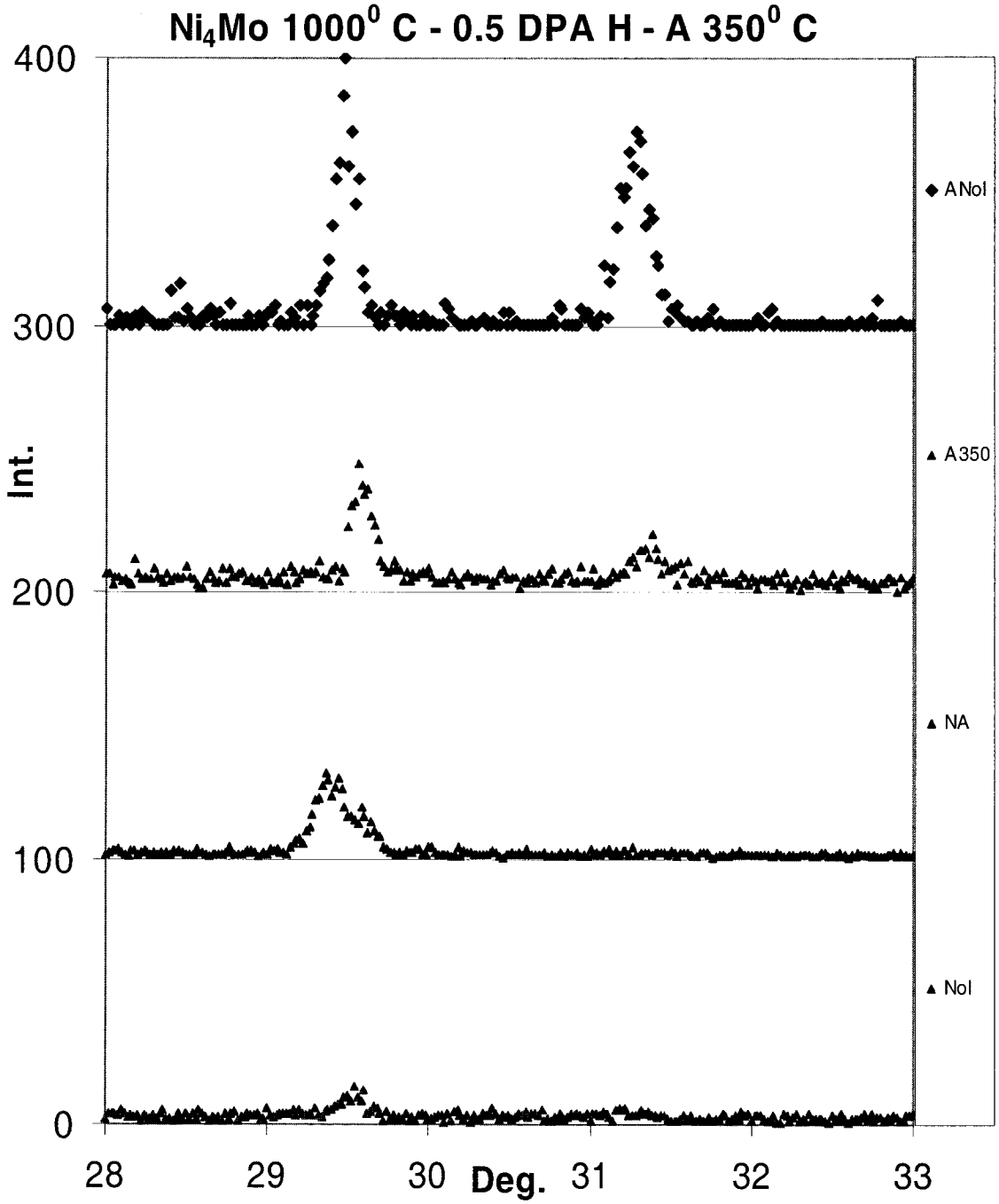

Figure A1.42 Detail#1 of XRD spectra generated for Ni_4Mo samples annealed at 1000 C before exposure to an H+ beam for a 0.5 DPA dose. After irradiation, the samples were annealed for three hours at 350^0 C. The Intensity axis is in arbitrary units and is plotted as a function of the angle 2θ. Spectra are compared with spectrum from sample with annealing but NoI.

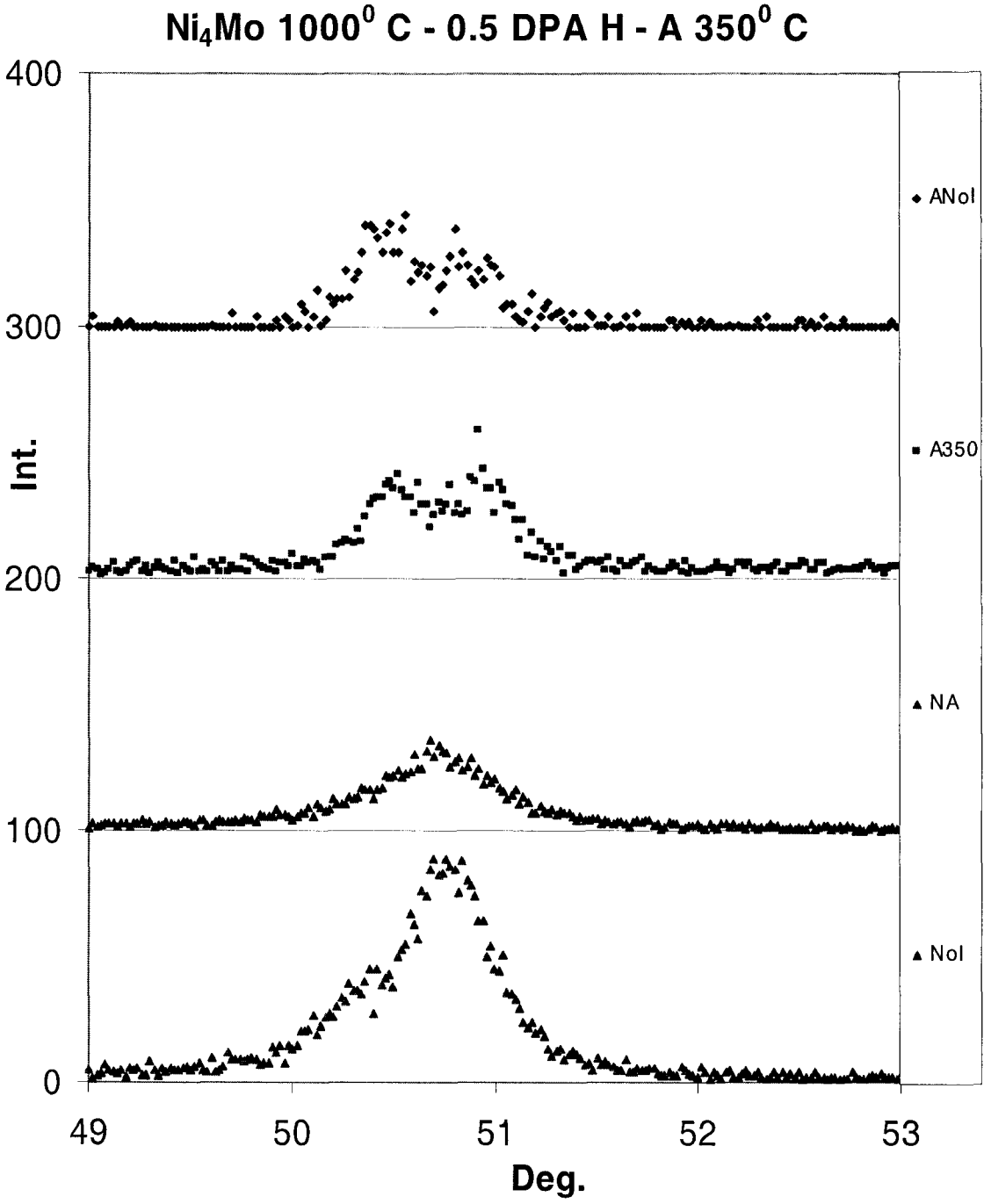

Figure A1.43 Detail#2 of XRD spectra generated for Ni_4Mo samples annealed at 1000 C before exposure to an H+ beam for a 0.5 DPA dose. After irradiation, the samples were annealed for three hours at 350^0 C. The Intensity axis is in arbitrary units and is plotted as a function of the angle 2θ. Spectra are compared with spectrum from sample with annealing but NoI.

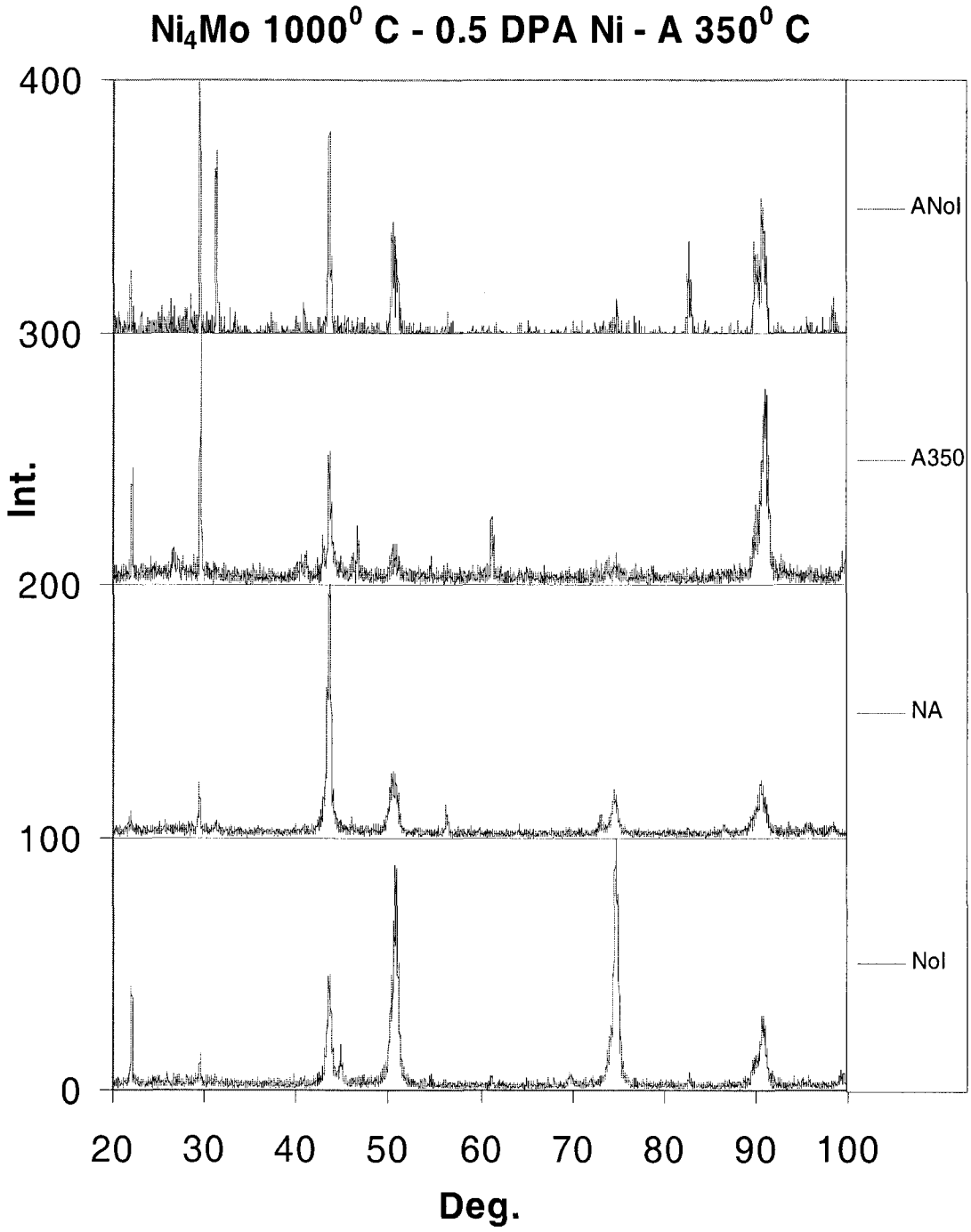

Figure A1.44 XRD spectra generated for Ni_4Mo samples annealed at 1000^0 C before exposure to a Ni+ beam for a 0.5 DPA dose. After irradiation, the samples were annealed for three hours at 350^0 C. The Intensity axis is in arbitrary units and is plotted as a function of the angle 2θ. Spectra are compared with spectrum from sample with annealing but NoI.

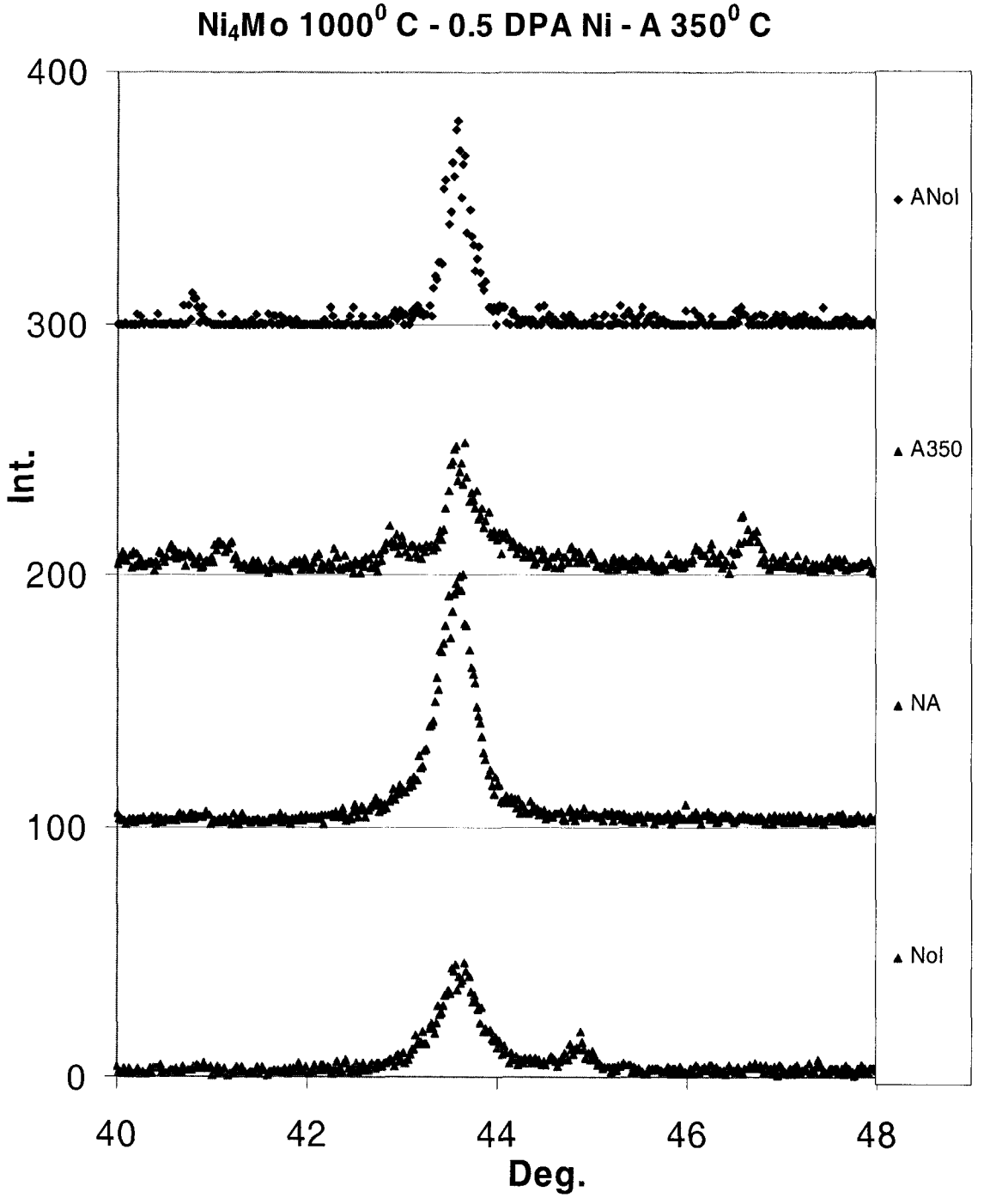

Figure A1.45 Detail #1 of the XRD spectra from Figure A1.44, generated for Ni_4Mo samples annealed at 1000^0 C before exposure to a Ni+ beam for a 0.5 DPA dose. After irradiation, the samples were annealed for three hours at 350^0 C. The Intensity axis is in arbitrary units and is plotted as a function of the angle 2θ. Spectra are compared with spectrum from sample with annealing but NoI.

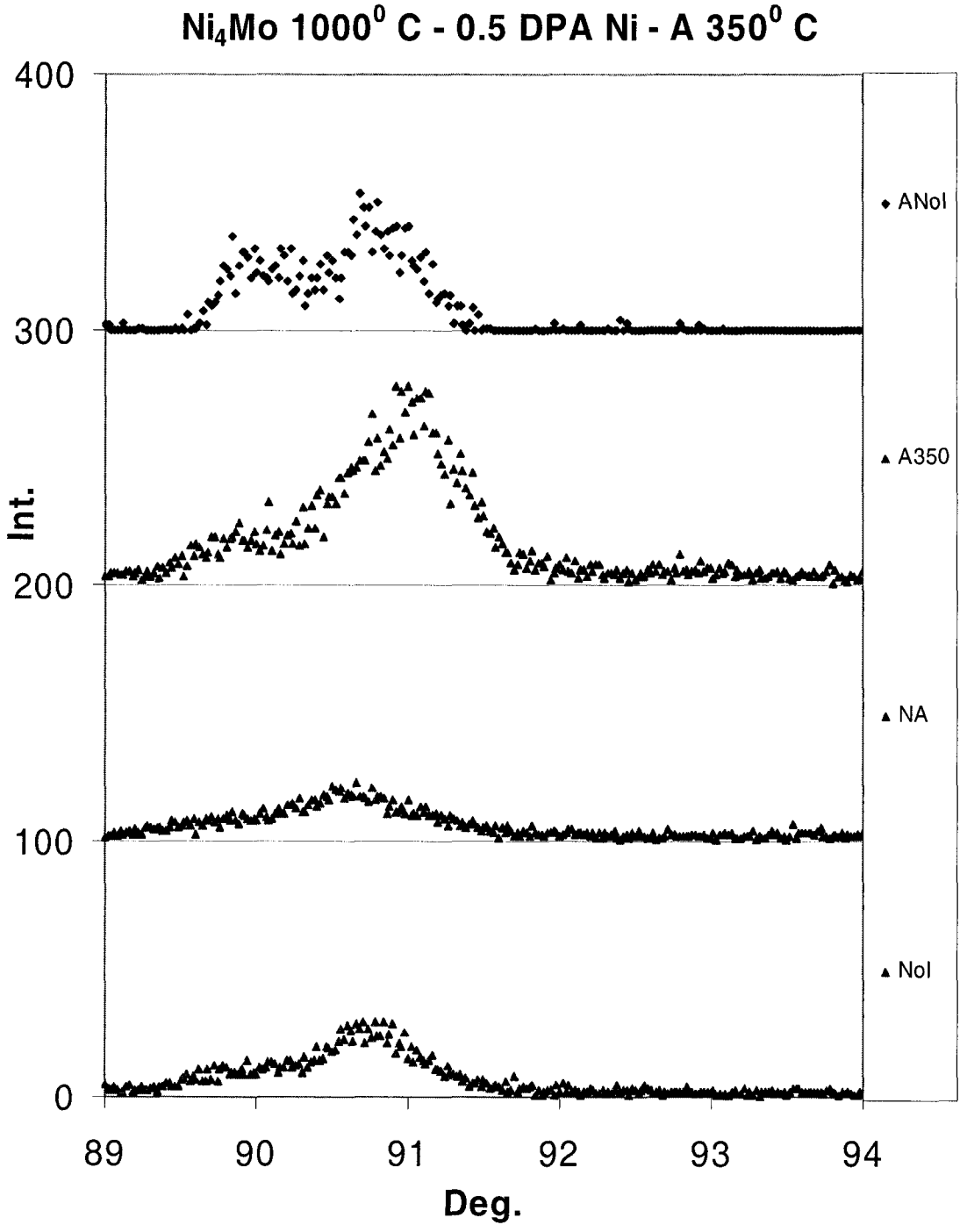

Figure A1.46 Detail #2 of the XRD spectra from Figure A1.44, generated for Ni_4Mo samples annealed at 1000^0 C before exposure to a Ni+ beam for a 0.5 DPA dose. After irradiation, the samples were annealed for three hours at 350^0 C. The Intensity axis is in arbitrary units and is plotted as a function of the angle 2θ. Spectra are compared with spectrum from sample with annealing but NoI.

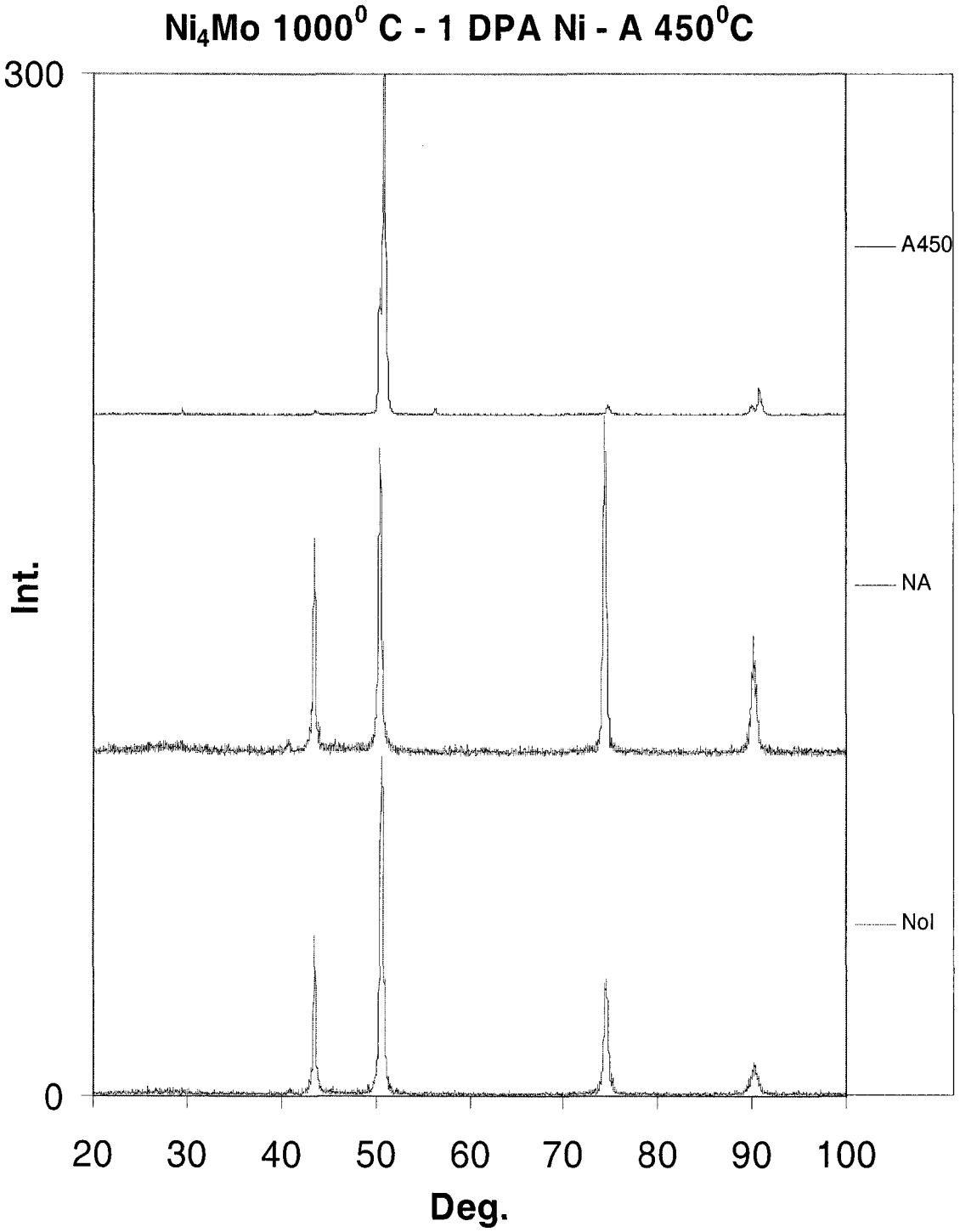

Figure A1.47 XRD spectra generated for Ni_4Mo samples annealed at 1000^0 C before exposure to a Ni+ beam for a 1 DPA dose. After irradiation, the samples were annealed for three hours at 450^0 C. The Intensity axis is in arbitrary units and is plotted as a function of the angle 2θ.

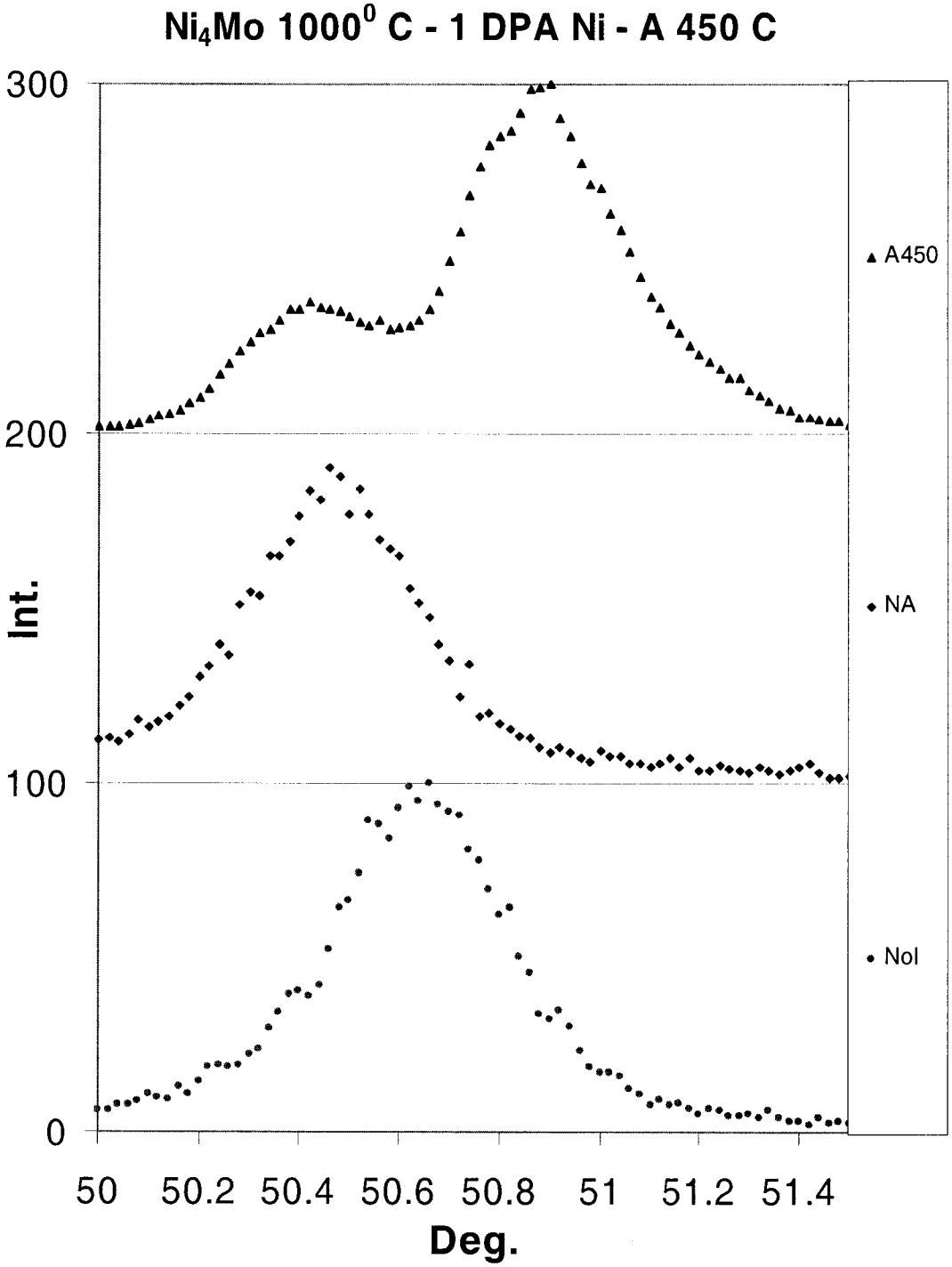

Figure A1.48 Detail #1 of the XRD spectra from Figure A1.46 generated for Ni_4Mo samples annealed at 1000^0 C before exposure to a Ni+ beam for a 1 DPA dose. After irradiation, the samples were annealed for three hours at 450^0 C. The Intensity axis is in arbitrary units and is plotted as a function of the angle 2θ.

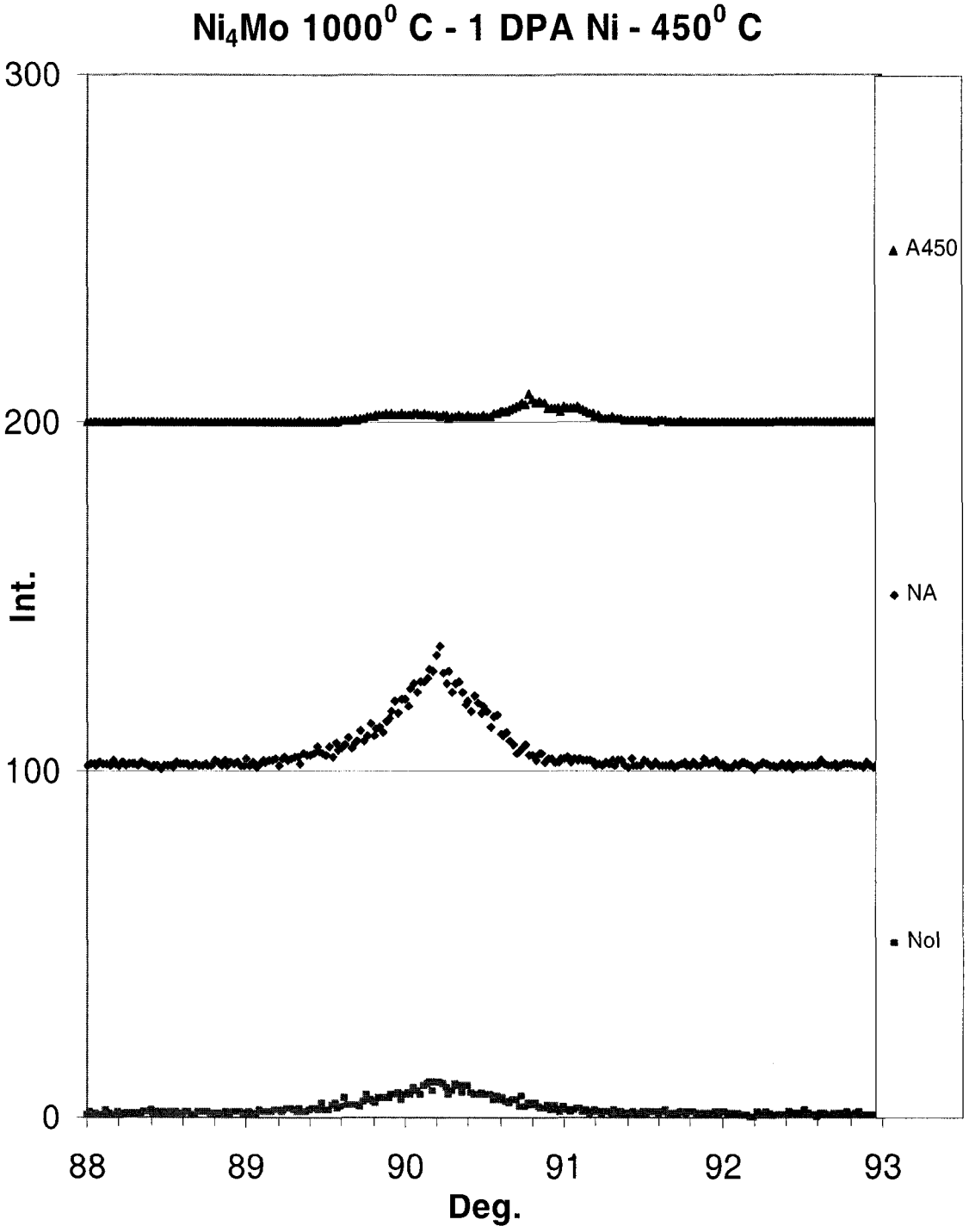

Figure A1.49 Detail #2 of the XRD spectra from Figure A1.47 generated for Ni_4Mo samples annealed at 1000^0 C before exposure to a Ni+ beam for a 1 DPA dose. After irradiation, the samples were annealed for three hours at 450^0 C. The Intensity axis is in arbitrary units and is plotted as a function of the angle 2θ.

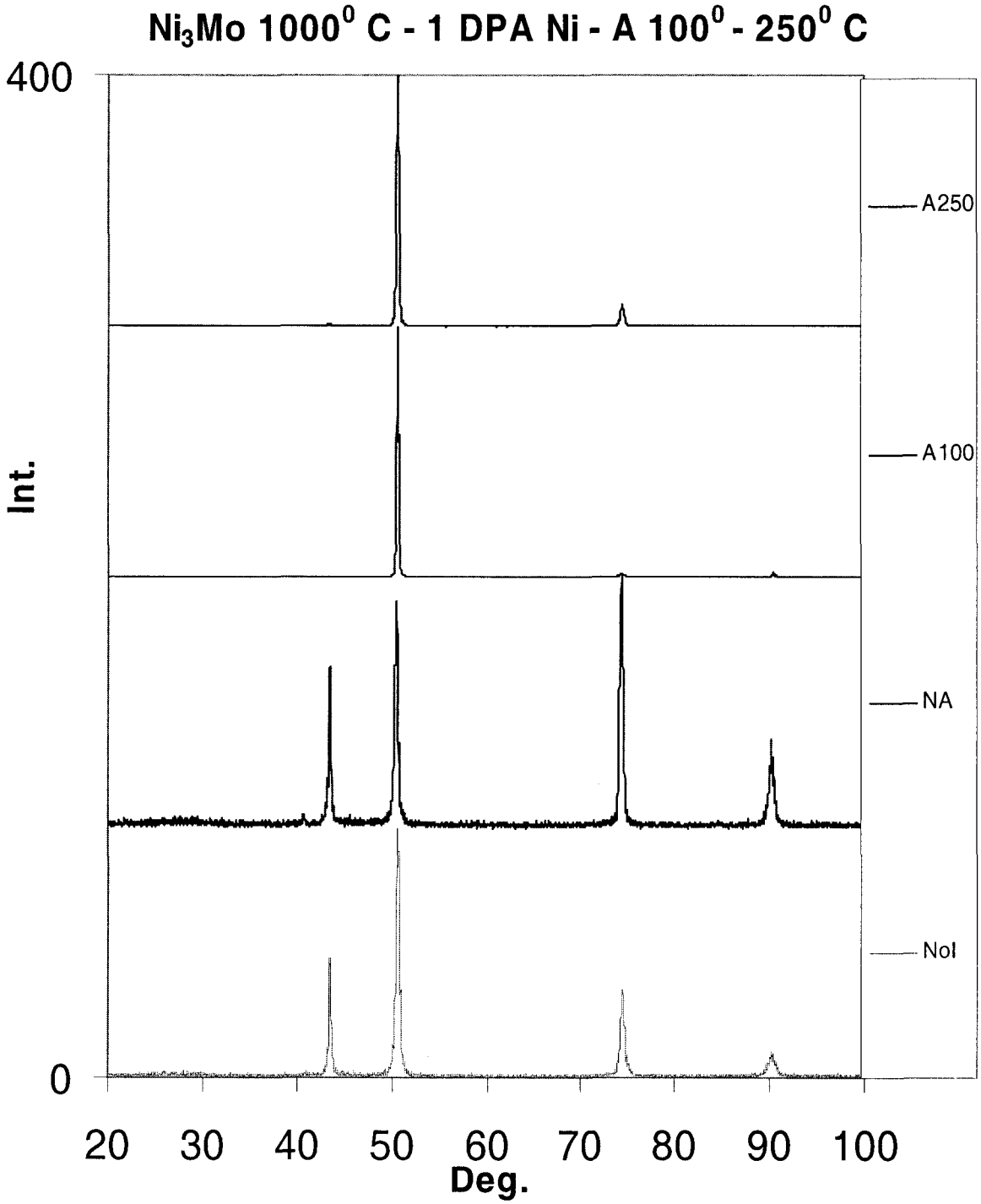

Figure A1.50 XRD spectra generated for Ni_3Mo samples annealed at 1000^0 C before irradiation and exposed to a Ni+ beam for a 1 DPA dose. After irradiation the samples were first annealed for three hours at 100^0 C and then for three hours at 250^0 C. The Intensity axis is in arbitrary units and is plotted as a function of the angle 2θ.

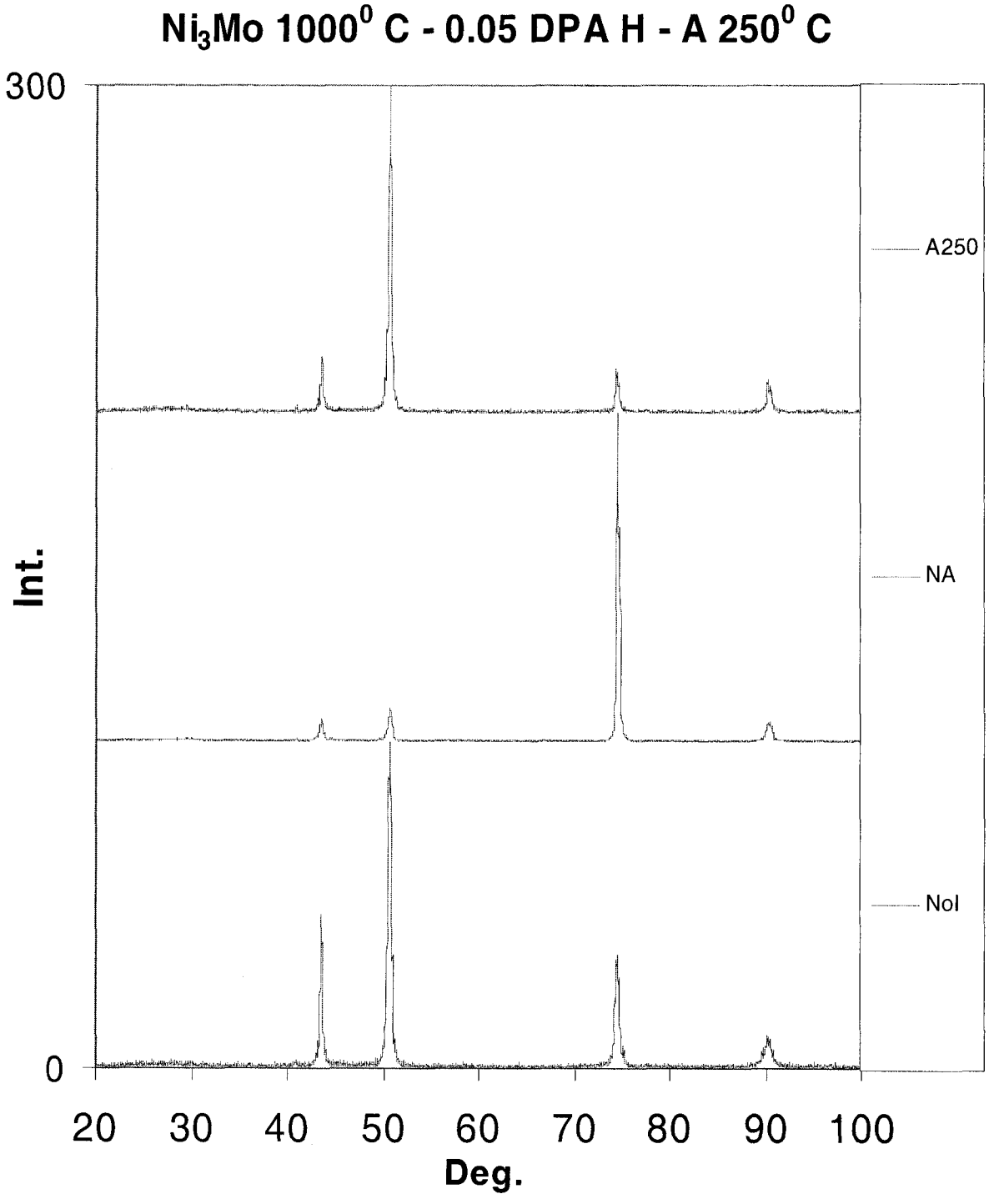

Figure A1.51 XRD spectra generated for Ni_3Mo samples annealed at 1000^0 C before exposure to an H+ beam for a 0.05 DPA dose. After irradiation, the samples were annealed for three hours at 250^0 C. The Intensity axis is in arbitrary units and is plotted as a function of the angle 2θ.

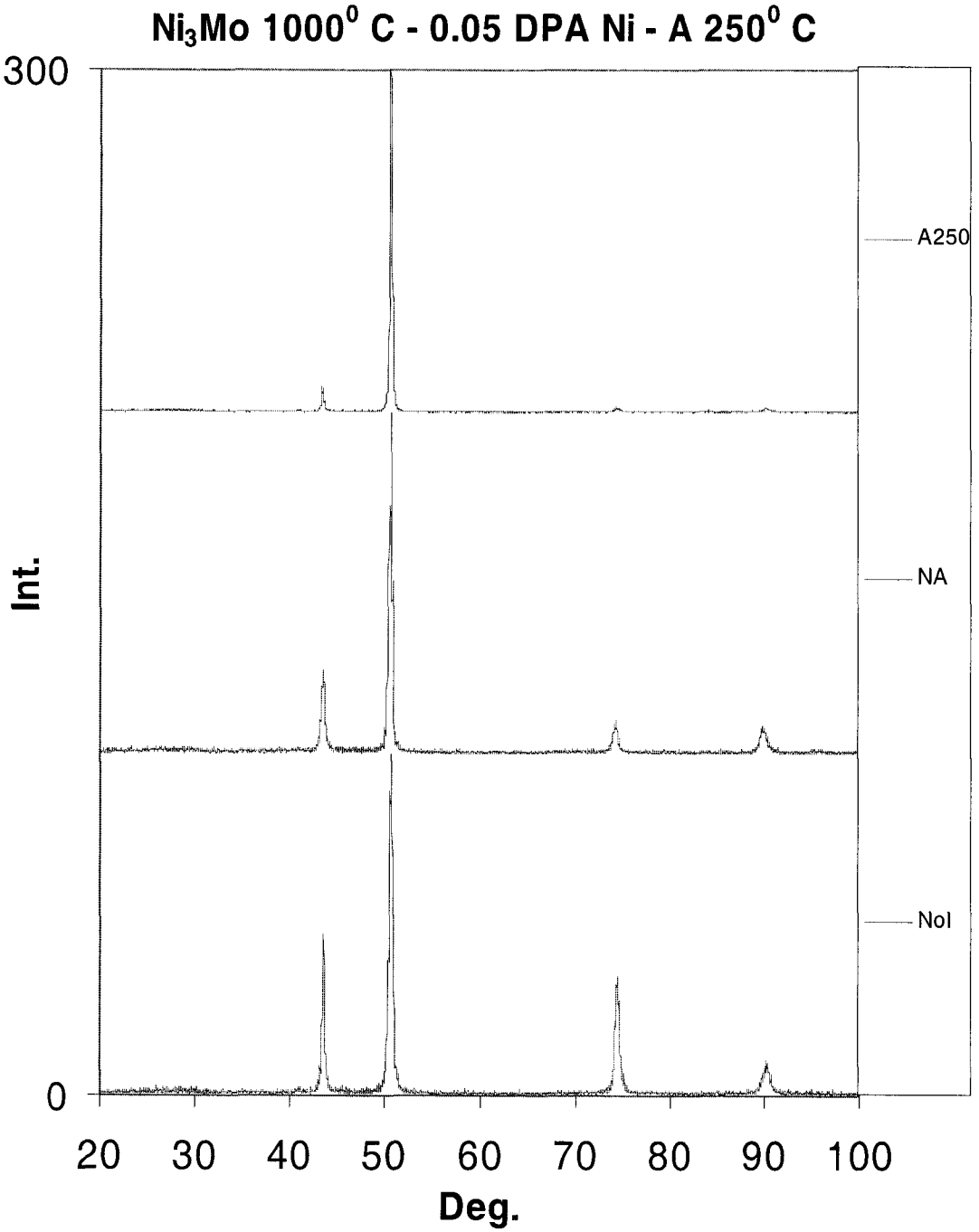

Figure A1.52 XRD spectra generated for Ni_3Mo samples annealed at 1000^0 C before exposure to a Ni+ beam for a 0.05 DPA dose. After irradiation, the samples were annealed for three hours at 250^0 C. The Intensity axis is in arbitrary units and is plotted as a function of the angle 2θ.

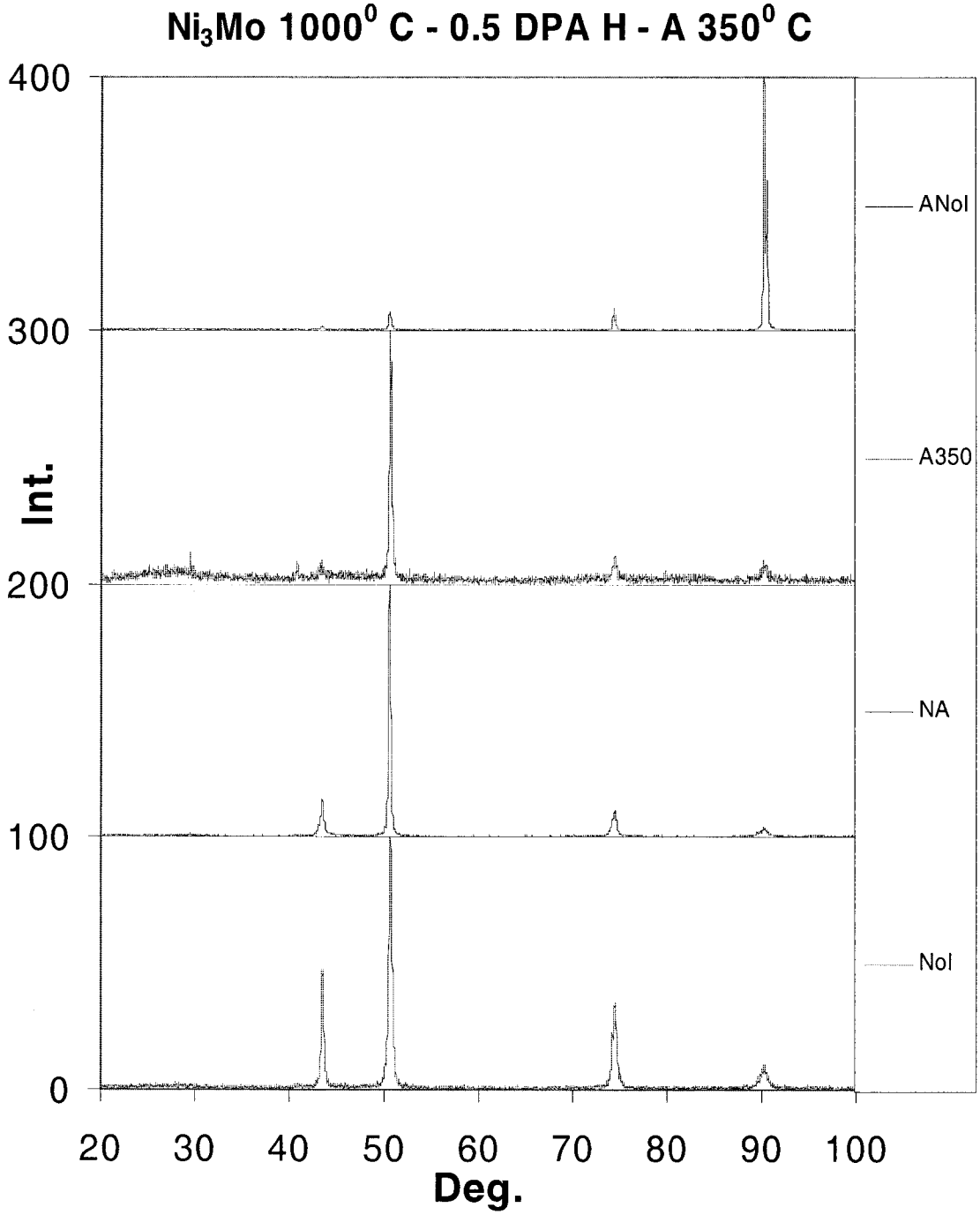

Figure A1.53 XRD spectra generated for Ni_3Mo samples annealed at 1000 C before exposure to an H+ beam for a 0.5 DPA dose. After irradiation, the samples were annealed for three hours at 350^0 C. The Intensity axis is in arbitrary units and is plotted as a function of the angle 2θ. Spectra are compared with spectrum from sample with annealing but NoI.

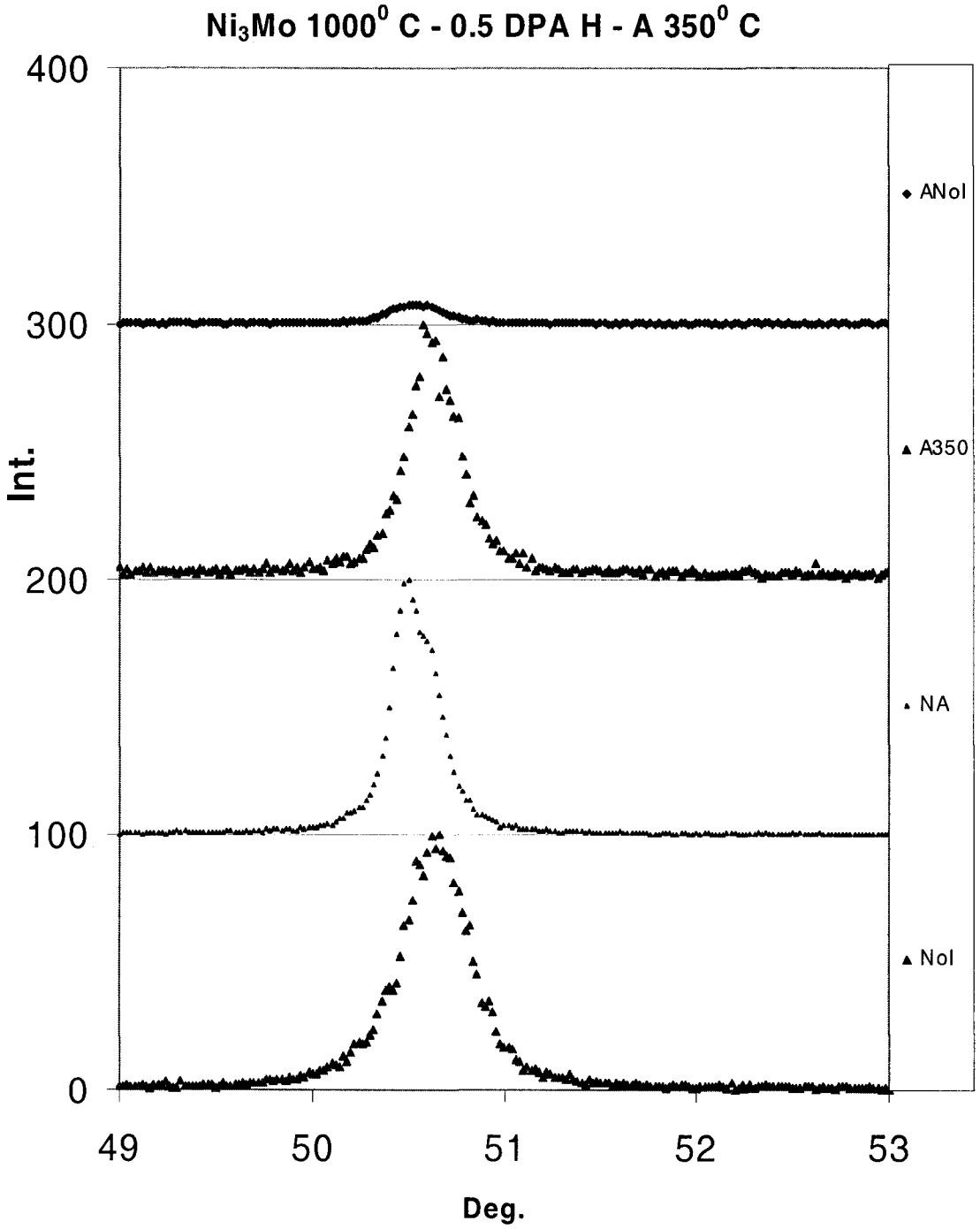

Figure A1.54 Detail#2 of XRD spectra generated for Ni_3Mo samples annealed at 1000 C before exposure to an H+ beam for a 0.5 DPA dose. After irradiation, the samples were annealed for three hours at 350^0 C. The Intensity axis is in arbitrary units and is plotted as a function of the angle 2θ. Spectra are compared with spectrum from sample with annealing but NoI.

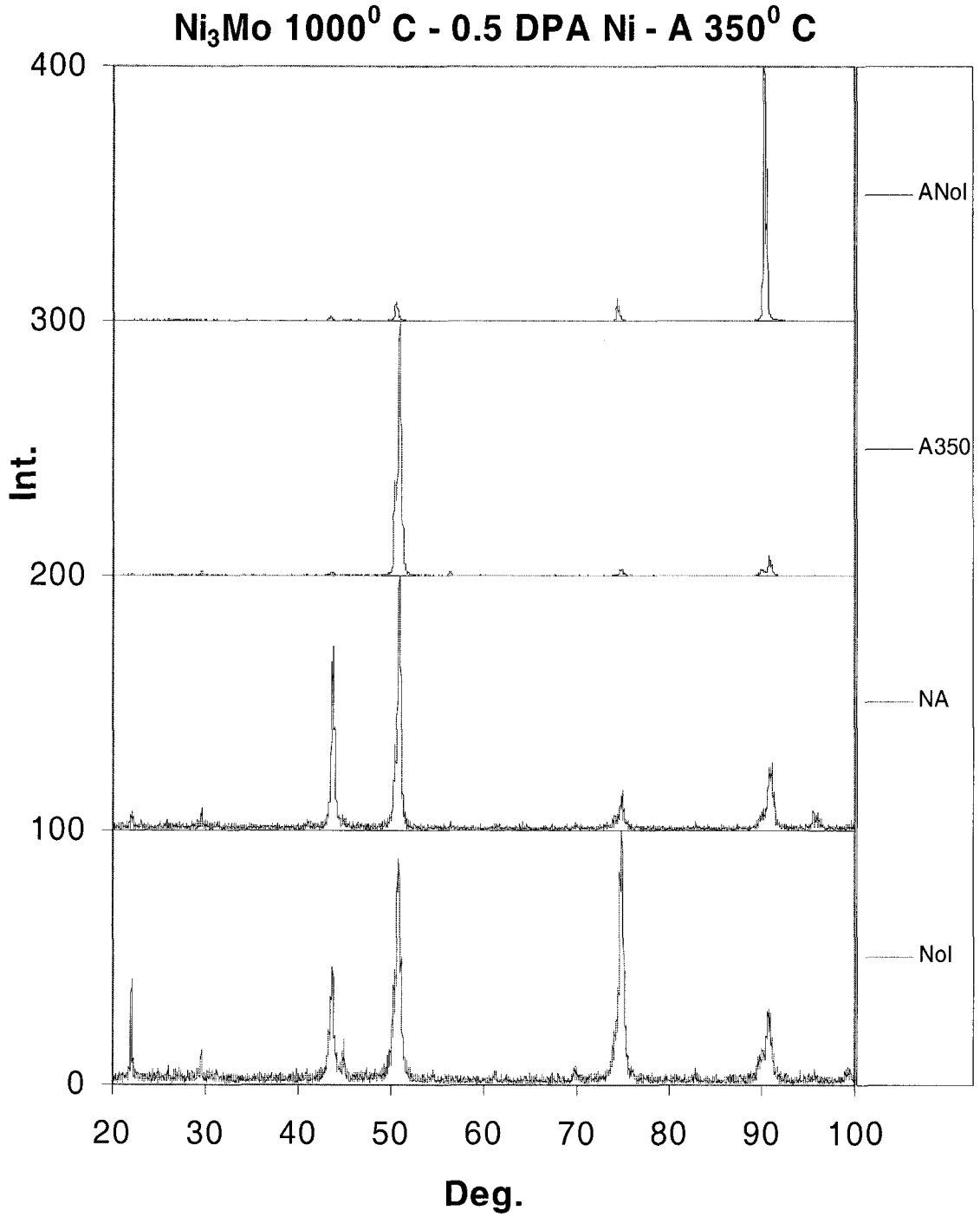

Figure A1.55 XRD spectra generated for Ni_3Mo samples annealed at 1000^0 C before exposure to a Ni+ beam for a 0.5 DPA dose. After irradiation, the samples were annealed for three hours at 350^0 C. The Intensity axis is in arbitrary units and is plotted as a function of the angle 2θ. Spectra are compared with spectrum from sample with annealing but NoI.

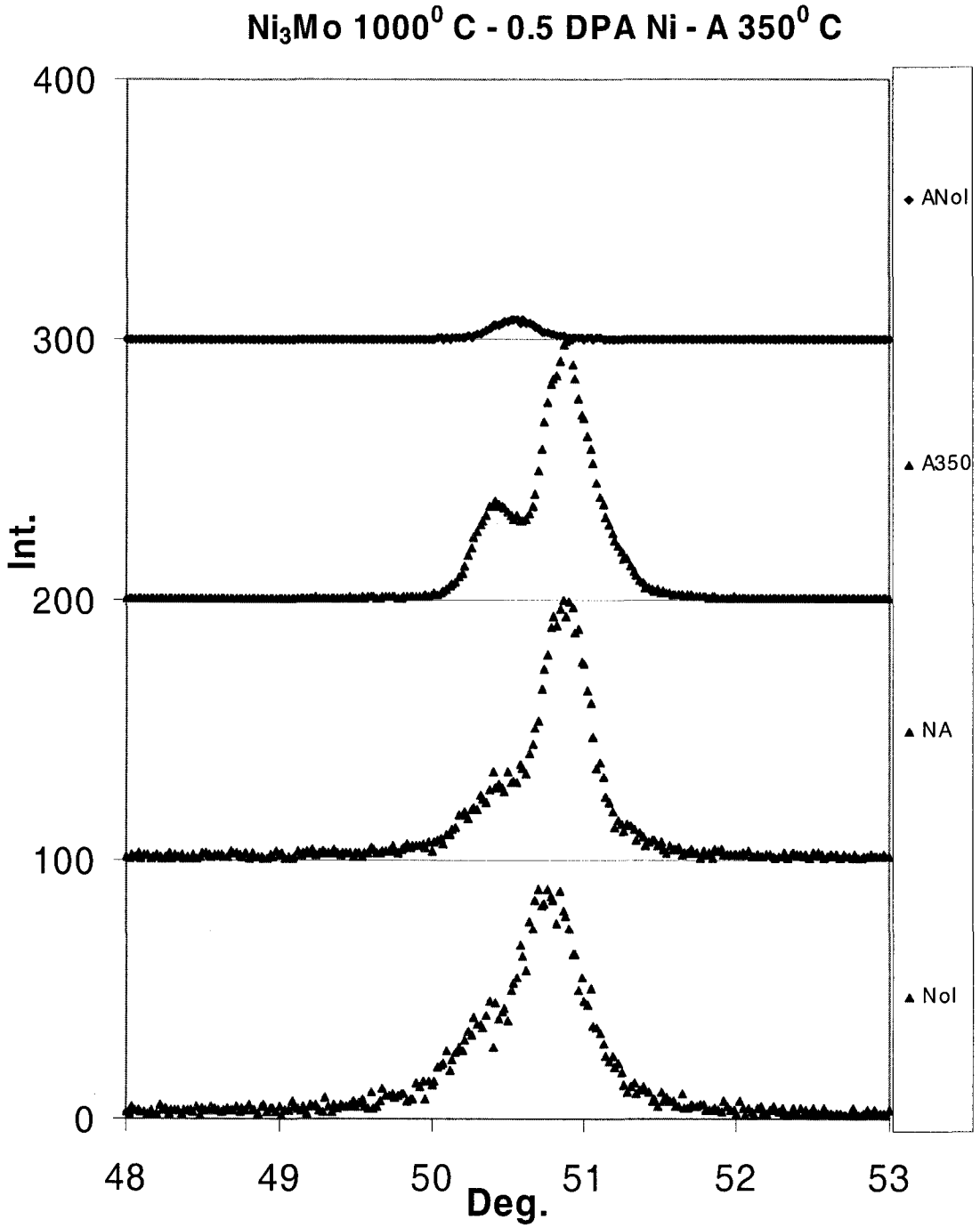

Figure A1.56 Detail #1 of the XRD spectra from Figure A1.55, generated for Ni_3Mo samples annealed at 1000^0 C before exposure to a Ni+ beam for a 0.5 DPA dose. After irradiation, the samples were annealed for three hours at 350^0 C. The Intensity axis is in arbitrary units and is plotted as a function of the angle 2θ. Spectra are compared with spectrum from sample with annealing but NoI.

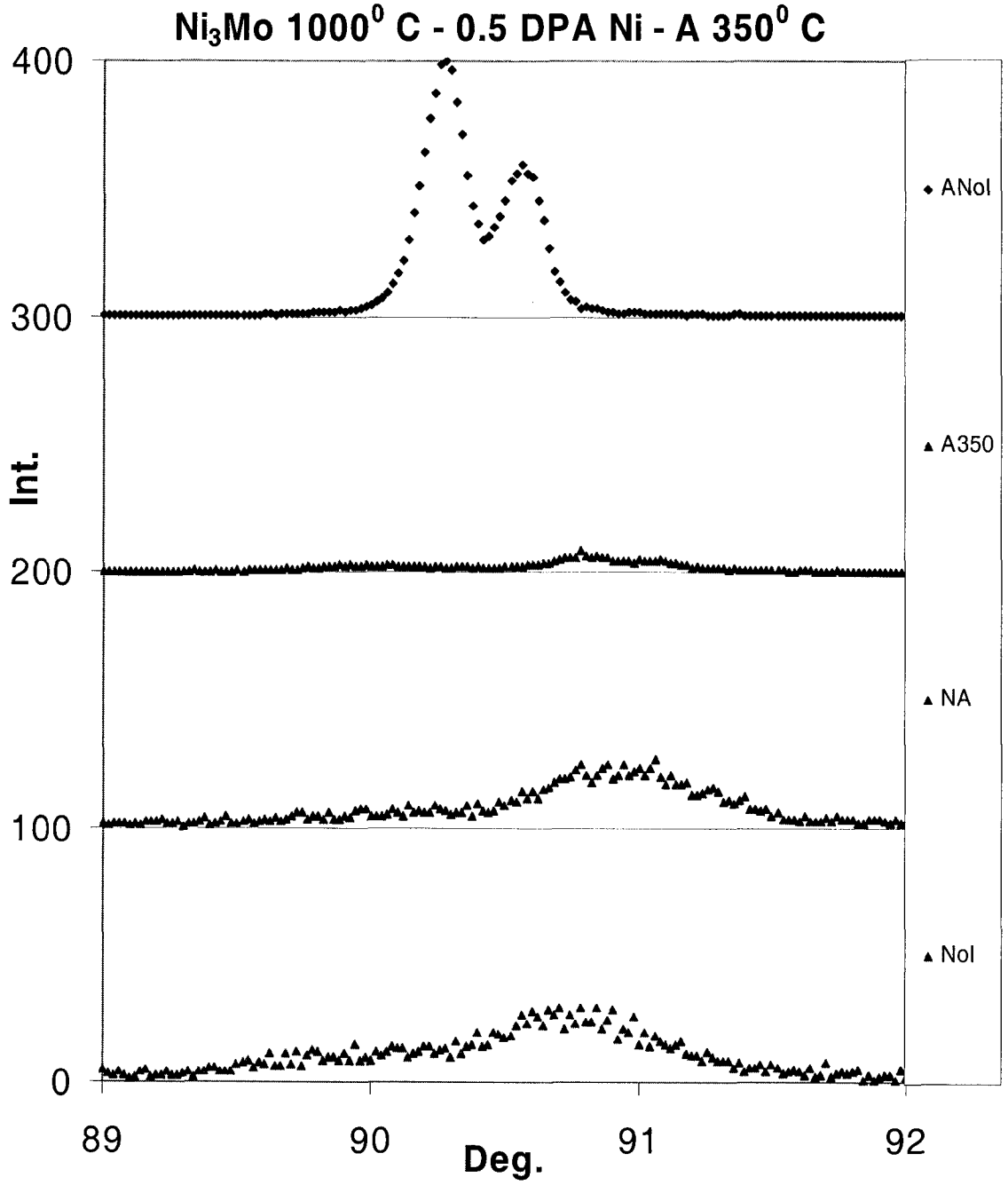

Figure A1.57 Detail #2 of the XRD spectra from Figure A1.55, generated for Ni_3Mo samples annealed at 1000^0 C before exposure to a Ni+ beam for a 0.5 DPA dose. After irradiation, the samples were annealed for three hours at 350^0 C. The Intensity axis is in arbitrary units and is plotted as a function of the angle 2θ. Spectra are compared with spectrum from sample with annealing but NoI.

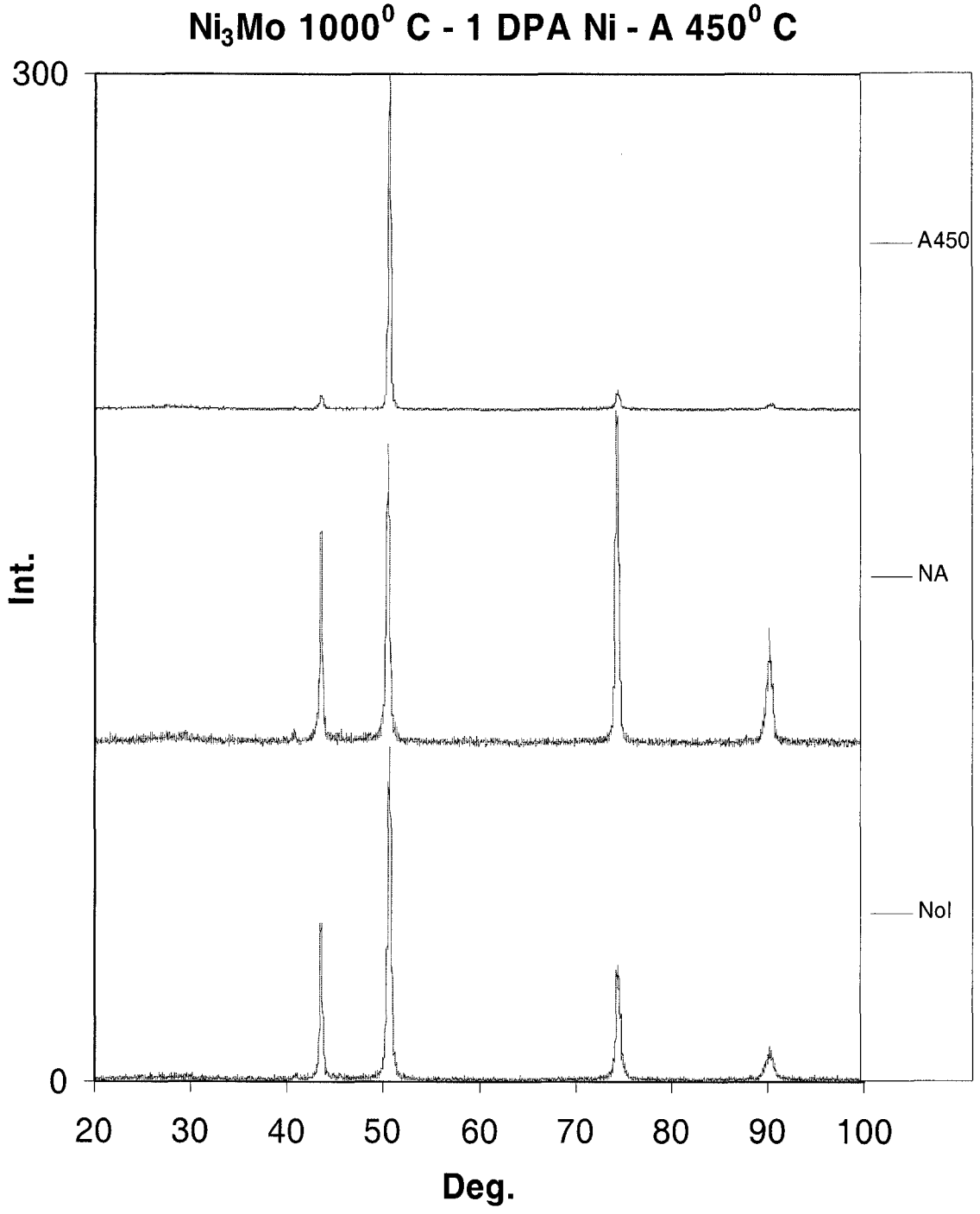

Figure A1.58 XRD spectra generated for Ni_3Mo samples annealed at 1000^0 C before exposure to a Ni+ beam for a 1 DPA dose. After irradiation, the samples were annealed for three hours at 450^0 C. The Intensity axis is in arbitrary units and is plotted as a function of the angle 2θ.

APPENDIX A2
Instructions for Operating the OIM System

INSTRUCTIONS FOR OPERATING THE OIM® SYSTEM

This appendix contains the steps necessary to perform an OIM scan. The assumptions are that 1) the user has an electropolished sample, 2) the user is familiar with the operation of the Philips XL30 FEG SEM.

1) Loading the sample

1.1. The loading of the sample in the SEM is important only in cases where the user wishes to return (and relocate) the areas scanned by OIM. In such a case, if possible, the sample should be marked. For example, a tensile bar could be marked on one of the shoulders, this way, designating the face on which the OIM analysis will be performed. Further, since the analysis will be performed with the sample tilted at 70°, a tensile bar can be accommodated in this geometry only if it is perpendicular to sliding door of the SEM vacuum chamber. The known position of the marked shoulder will aid with future attempts at relocating the scanned areas. After positioning the sample, the SEM chamber can be pumped down.

1.2. The OIM electronics should also be turned on at this stage.

2) Obtaining and optimizing the EBSP pattern

2.1. Select CCD camera on the SEM, and tilt the sample 70°.

2.2. Turn the beam ON and set the voltage to 25 kV, and the spot size to 5.

2.2. Select SE imaging and obtain an SEM image of the sample and focus to determine the working distance, WD. The system is currently calibrated for WD = 20 mm.

2.1. If WD is not 20 mm, return to CCD imaging and adjust sample position by "Y" and "Z" knobs controlling the movement of the stage. Check WD again.

2.2. Only when WD=20 (and sample is below the gun), insert the Phosphor screen – SIT camera assembly form the "Camera control unit" of the OIM system.

2.6. Return to SEM SE imaging and select the area to be scanned. Adjust magnification such that the desired area occupies most part of the SEM monitor. This will be the image that the OIM PC computer will receive, and on which the area to be scanned will be selected. (Usually, for a material having the grain size 35 μm, a tensile bar will be scanned at a magnification 500×, but the area surrounding the hole in a TEM disk will be scanned at magnification 2000×).

2.7. Change the SEM scan to "spot" mode. A Kikuchi pattern will be visible on the OIM monitor. Return to SEM "scan" mode and acquire the background. Return to "spot" mode and capture a processed pattern. Adjust brightness and contrast on the OIM monitor as necessary.

2.8. Place the SEM on "external". From now, the SEM will be controlled by the OIM PC.

3) Setting up a scan

3.1. Launch the "OIM Data Collection" program on the OIM PC.

3.2. Capture the Kikuchi pattern from the OIM monitor, and test the calibration.

3.2. Capture the SEM image (shown on the SEM monitor).

3.3. Select the desired scan area, and set the step size. (For a tensile bar (35 μm grain size), a scan area 400 μm × 700 μm with step size of 4-6 μm gives a good reproduction of the microstructure, but for a TEM specimen the scan area will most likely be 100 μm ×100 μm, and thus the step size may be set to 0.5-1 μm for a better description on the microstructure).

4) Finishing up the session

4.1. Return the SEM to SE imaging.

4.2. Turn the beam OFF.

4.3. Capture the sample image on the CCD camera.

4.4. Retract the Phosphor screen – SIT camera assembly CDD form the "Camera control unit" of the OIM system.

4.5. Turn the OIM system OFF.

4.6. Bring the sample to normal position.

4.7. Vent the SEM chamber and remove the specimen.

APPENDIX A3
Additional Hardness Results

Dose (DPA)	H(VH)	d1(μm)	d2(μm)
0.00	283.48	8.13	8.06
0.01	308.50	8.03	7.48
0.05	313.58	7.86	7.51
0.10	287.32	7.99	8.00
0.20	288.90	8.07	7.96
0.50	285.10	8.01	8.23
1.00	247.85	8.83	8.56

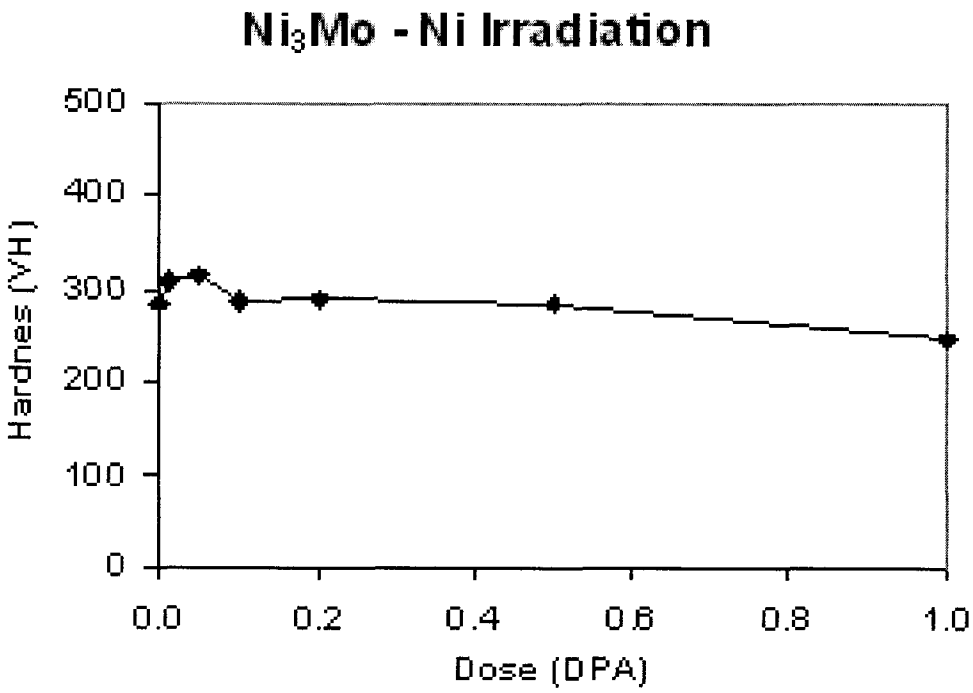

Figure A3.1 Hardness values for Ni_3Mo alloy under Ni^+ irradiation. Irradiation doses are given in the table, as well as averaged Vickers hardness values and the averaged dimensions of the indent.

Dose (DPA)	H(VH)	d1(μm)	d2(μm)
0.00	283.48	8.13	8.06
0.01	257.70	8.73	8.20
0.05	253.31	8.65	8.51
0.10	247.01	8.85	8.48
0.20	264.10	8.28	8.41
0.50	260.20	8.52	8.26
1.00	268.34	8.29	8.34

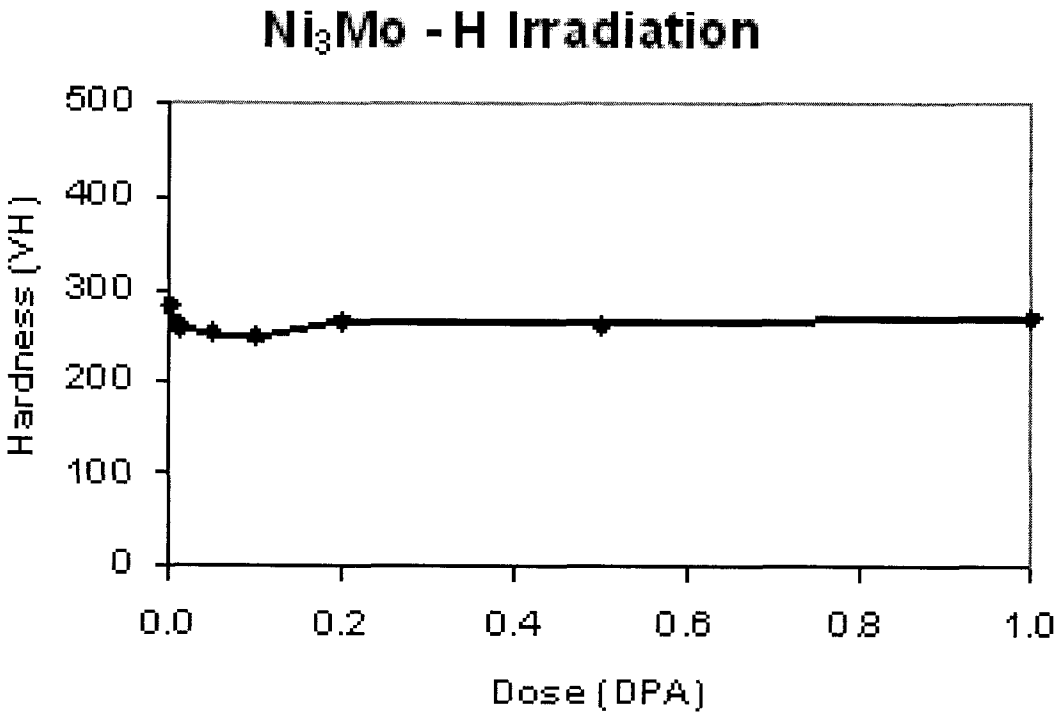

Figure A3.2 Hardness values for Ni_3Mo alloy under H^+ irradiation. Irradiation doses are given in the table, as well as averaged Vickers hardness values and the averaged dimensions of the indentation.

Dose(DPA)	H(VH)	d1(μm)	d2(μm)
0.00	454.27	6.45	6.34
0.01	439.33	6.82	6.19
0.05	440.25	6.54	6.53
0.10	448.40	6.37	6.56
0.20	444.22	6.49	6.44
0.50	334.54	7.69	7.21
1.00	321.81	7.64	7.58

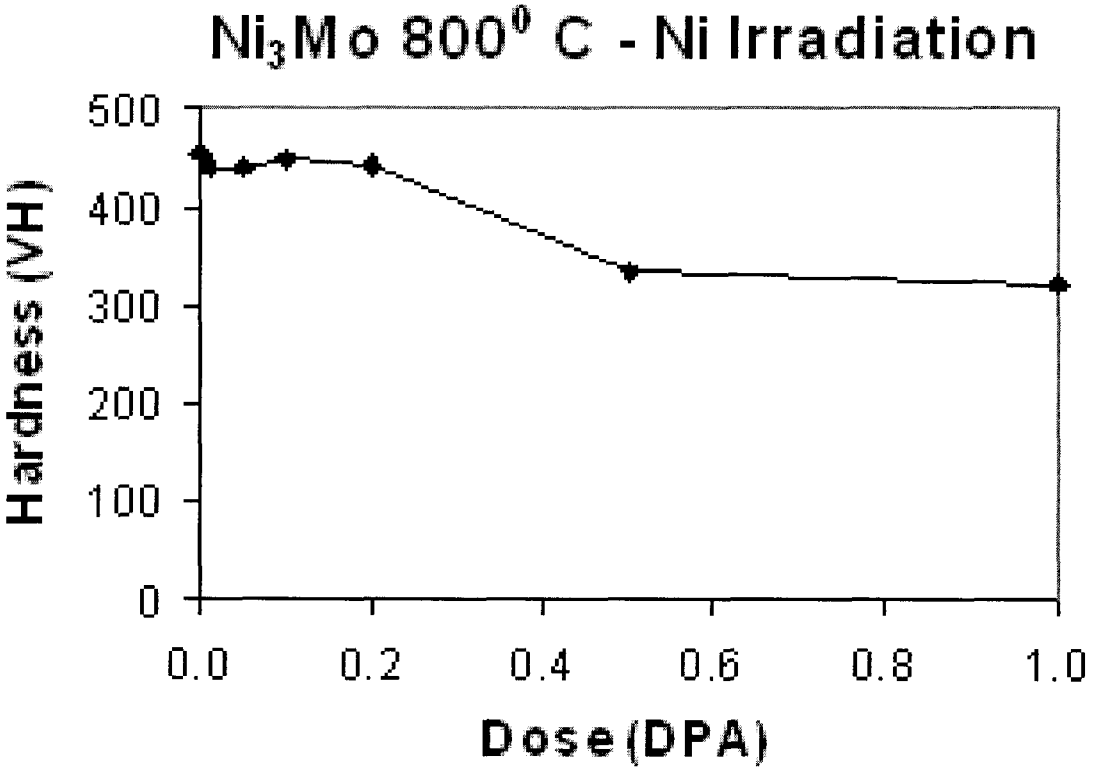

Figure A3.3 Hardness values for Ni_3Mo alloy annealed before irradiation at 800^0 C exposed to Ni^+ irradiation. Irradiation doses are given in the table, as well as averaged Vickers hardness values and the averaged dimensions of the indentation.

Dose(DPA)	H(VH)	d1(μm)	d2(μm)
0.00	454.27	6.45	6.34
0.01	442.05	6.45	6.53
0.05	451.82	6.27	6.68
0.10	448.99	6.65	6.26
0.20	438.33	6.52	6.53
0.50	430.27	6.67	6.46
1.00	435.27	6.64	6.43

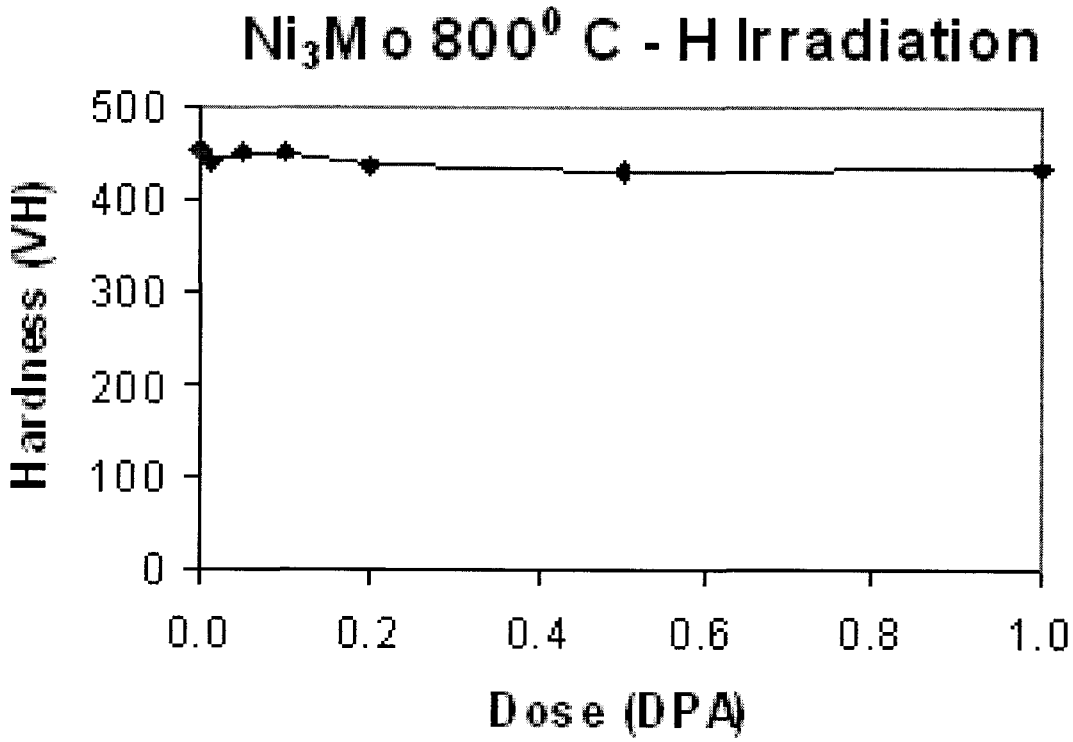

Figure A3.4 Hardness values for Ni_3Mo alloy annealed before irradiation at 800^0 C exposed to H^+ irradiation. Irradiation doses are given in the table, as well as averaged Vickers hardness values and the averaged dimensions of the indentation.

Dose(DPA)	H(VH)	d1(μm)	d2(μm)
0.00	253.00	8.68	8.48
0.01	277.27	8.38	7.98
0.05	248.65	8.88	8.45
0.10	269.18	8.38	8.23
0.20	255.82	8.63	8.41
0.50	271.70	8.41	8.13
1.00	277.22	8.38	7.98

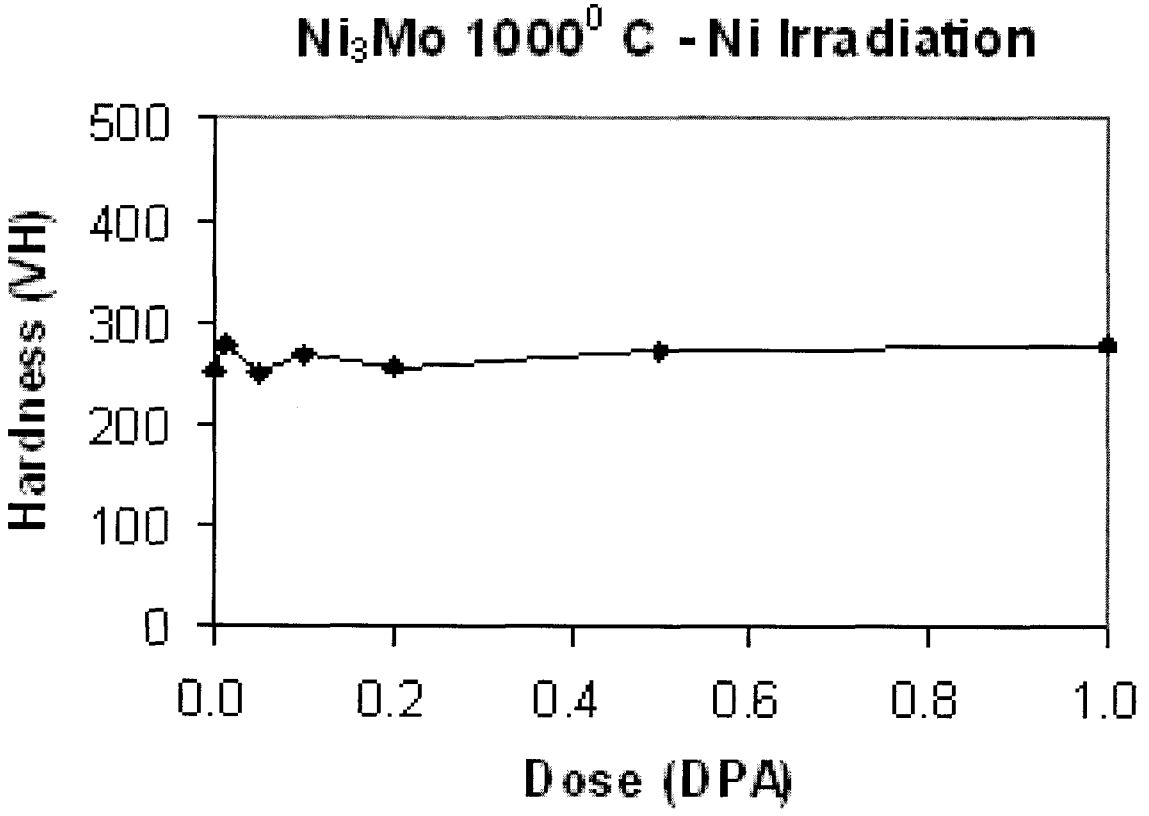

Figure A3.5 Hardness values for Ni_3Mo alloy annealed before irradiation at 1000^0 C exposed to Ni^+ irradiation. Irradiation doses are given in the table, as well as averaged Vickers hardness values and the averaged dimensions of the indentation.

Dose (DPA)	H(VH)	d1(μm)	d2(μm)
0.00	253.00	8.68	8.48
0.01	262.36	8.46	8.33
0.05	253.19	8.56	8.59
0.10	258.79	8.66	8.26
0.20	280.59	8.33	7.83
0.50	279.54	8.19	8.06
1.00	268.10	8.43	8.21

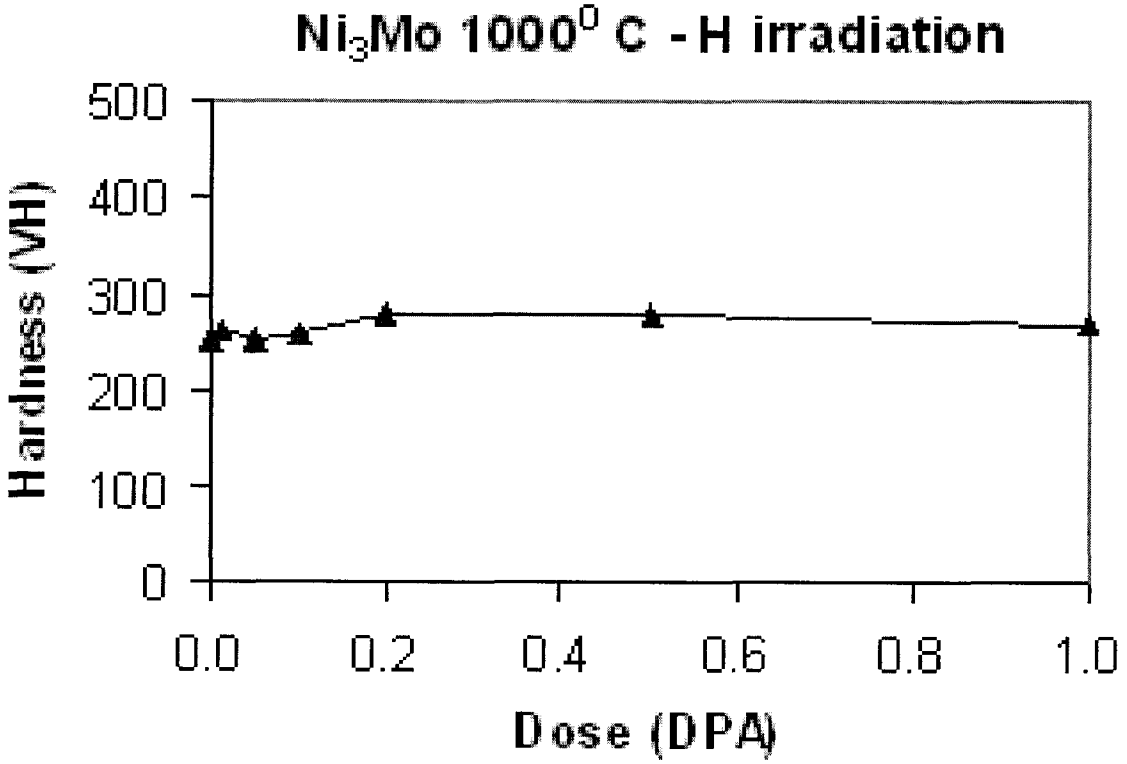

Figure A3.6 Hardness values for Ni_3Mo alloy annealed before irradiation at 1000^0 C exposed to H^+ irradiation. Irradiation doses are given in the table, as well as averaged Vickers hardness values and the averaged dimensions of the indentation.

Dose(DPA)	H(VH)	d1(μm)	d2(μm)
0	256.19	8.53	8.48
0.01	301.51	7.96	7.73
0.05	244.41	9.17	8.47
0.1	248.60	8.75	8.56
0.2	268.26	8.36	8.28
0.5	270.18	8.36	8.23
1	249.48	8.70	8.56

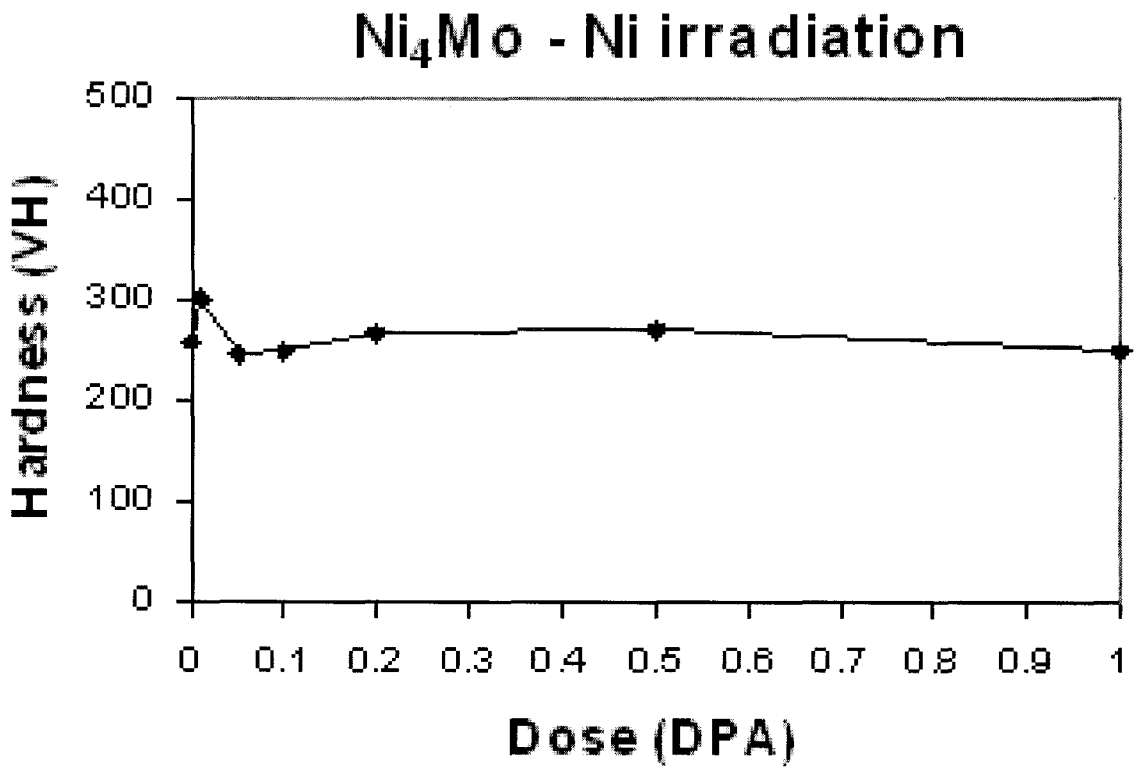

Figure A3.7 Hardness values for Ni_4Mo alloy exposed to Ni^+ irradiation. Irradiation doses are given in the table, as well as averaged Vickers hardness values and the averaged dimensions of the indentation.

Dose(DPA)	H(VH)	d1(μm)	d2(μm)
0	256.19	8.53	8.48
0.01	192.95	9.80	9.83
0.05	236.97	8.70	8.96
0.1	211.12	9.49	9.29
0.2	247.80	8.85	8.46
0.5	232.70	9.30	8.63
1	343.82	7.54	7.15

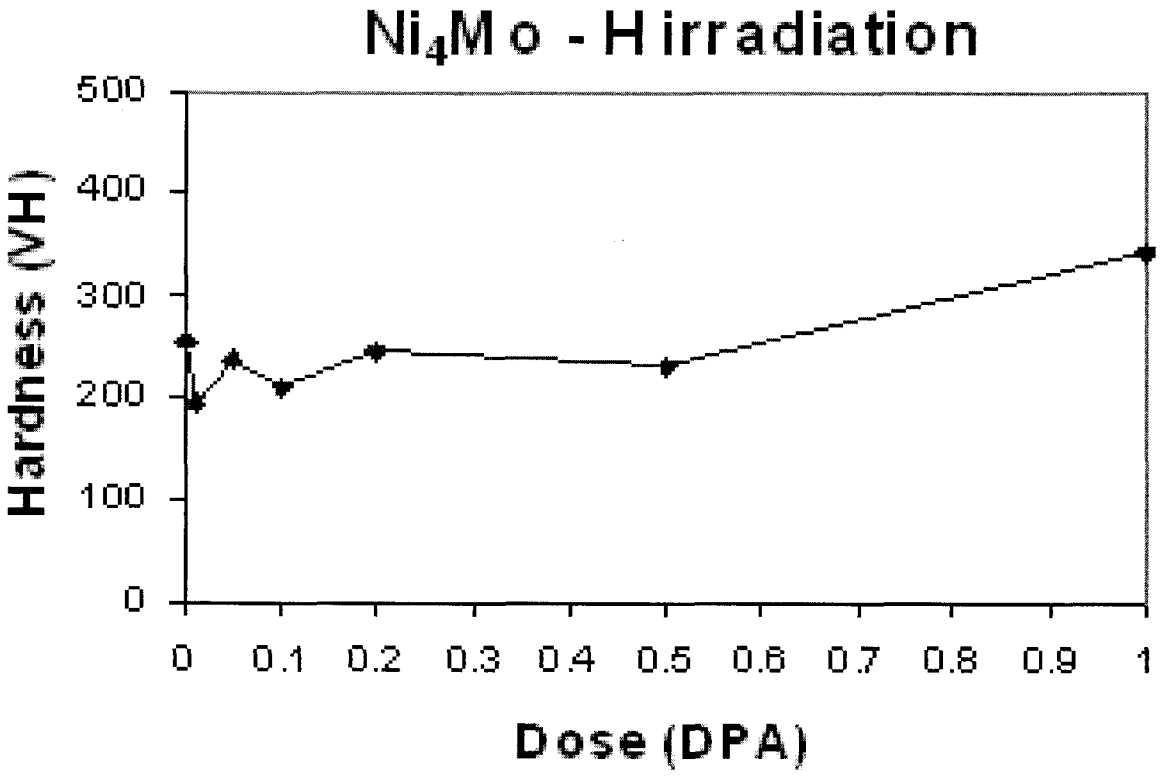

Figure A3.8 Hardness values for Ni_4Mo alloy exposed to H^+ irradiation. Irradiation doses are given in the table, as well as averaged Vickers hardness values and the averaged dimensions of the indentation.

Dose(DPA)	H(VH)	d1(μm)	d2(μm)
0	268.27	8.46	8.18
0.01	268.35	8.55	8.08
0.05	277.51	8.21	8.11
0.1	295.72	7.86	7.98
0.2	299.56	7.96	7.78
0.5	258.32	8.48	8.28
1	312.90	7.76	7.88

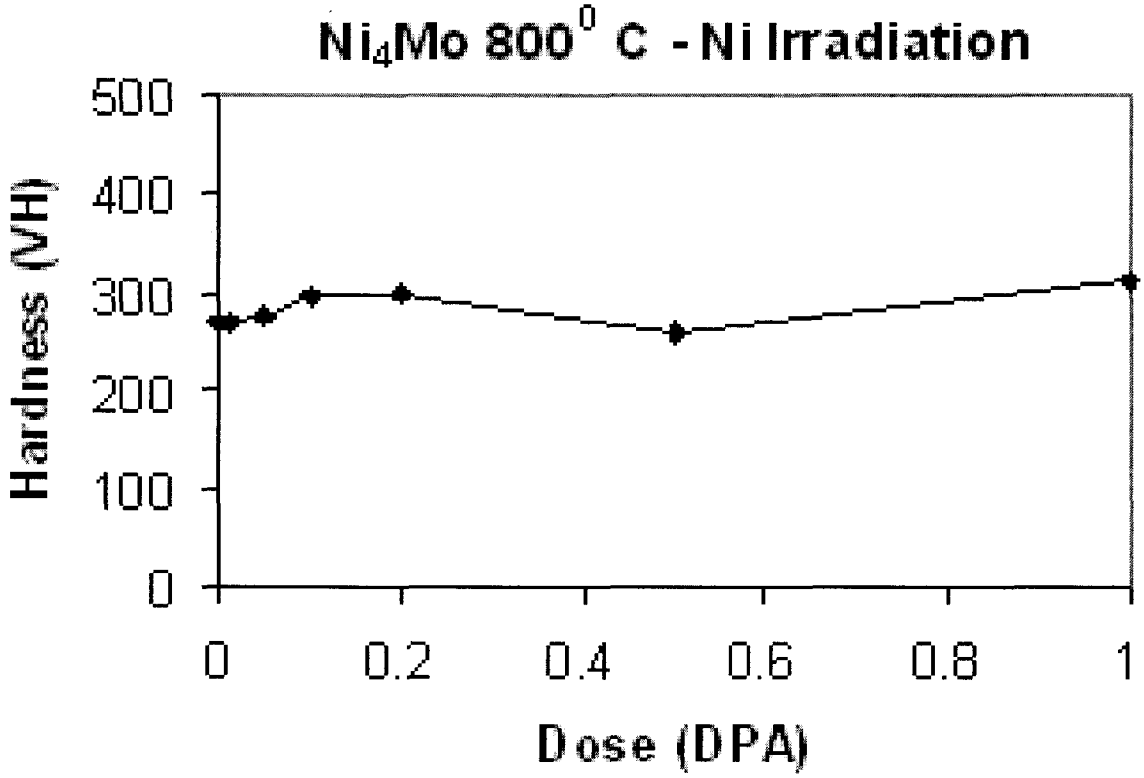

Figure A3.9 Hardness values for Ni_4Mo alloy pre-annealed at 1000^0 C exposed to Ni^+ irradiation. Irradiation doses are given in the table, as well as averaged Vickers hardness values and the averaged dimensions of the indentation.

Dose(DPA)	H(VH)	d1(μm)	d2(μm)
0	268.27	8.46	8.18
0.01	295.88	8.08	7.76
0.05	280.23	8.07	8.08
0.1	293.04	8.06	7.86
0.2	274.70	8.43	7.91
0.5	237.39	9.03	8.67
1	227.74	9.15	8.91

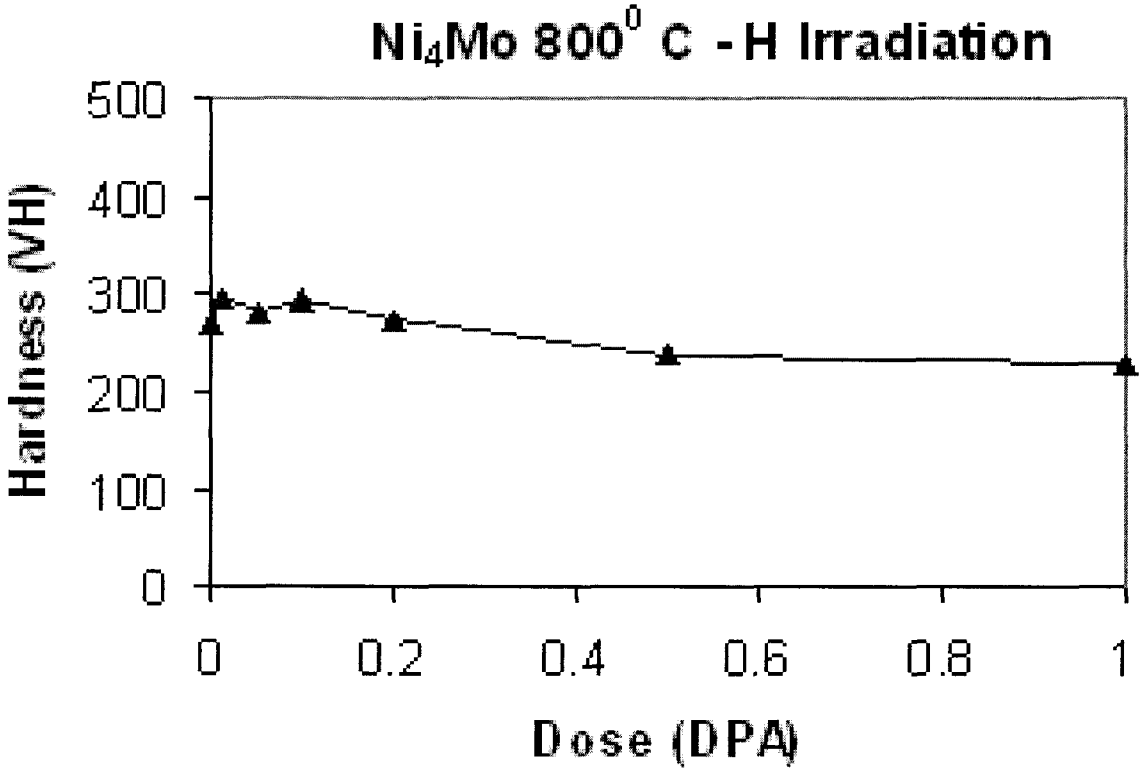

Figure A3.10 Hardness values for Ni_4Mo alloy pre-annealed at 800^0 C exposed to H^+ irradiation. Irradiation doses are given in the table, as well as averaged Vickers hardness values and the averaged dimensions of the indentation.

Dose(DPA)	H(VH)	d1(μm)	d2(μm)
0	256.19	8.53	8.48
0.01	301.51	7.96	7.73
0.05	244.41	9.17	8.47
0.1	248.60	8.75	8.56
0.2	268.26	8.36	8.28
0.5	270.18	8.36	8.23
1	249.48	8.70	8.56

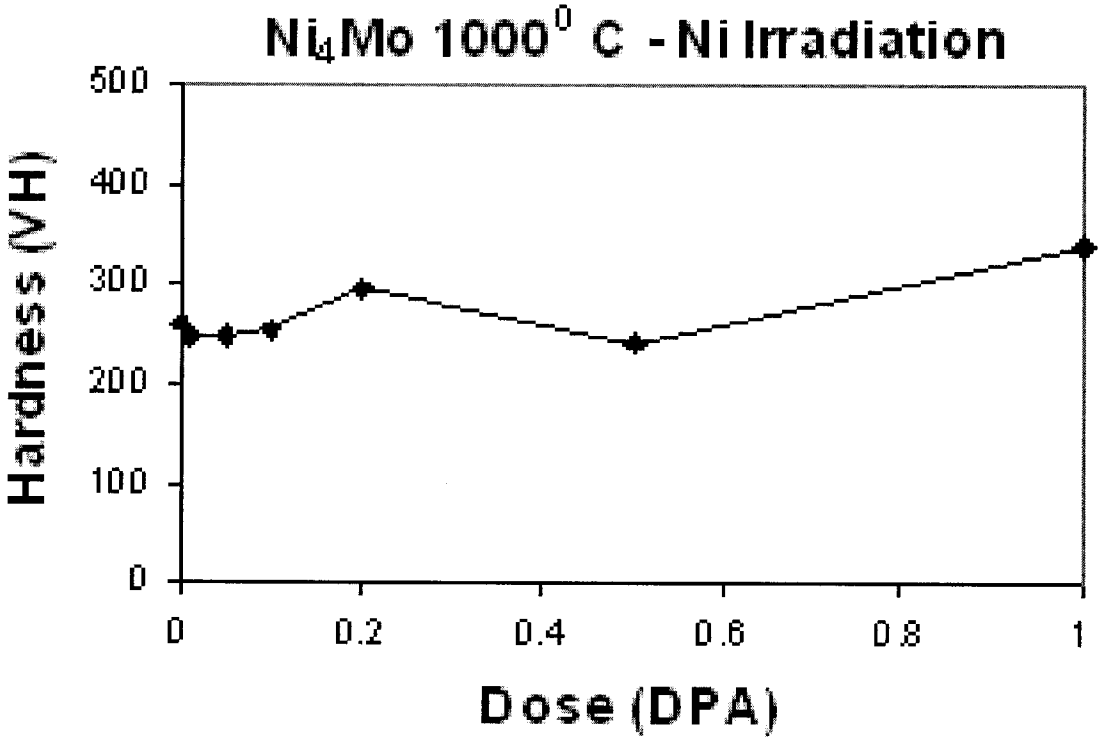

Figure A3.11 Hardness values for Ni_4Mo alloy pre-annealed at 1000^0 C exposed to Ni^+ irradiation. Irradiation doses are given in the table, as well as averaged Vickers hardness values and the averaged dimensions of the indentation.

Dose(DPA)	H(VH)	d1(μm)	d2(μm)
0	262.06	8.51	8.33
0.01	321.40	7.51	7.68
0.05	318.73	7.66	7.51
0.1	301.77	7.79	7.88
0.2	395.70	6.96	6.92
0.5	344.27	7.54	7.30
1	258.88	8.56	8.38

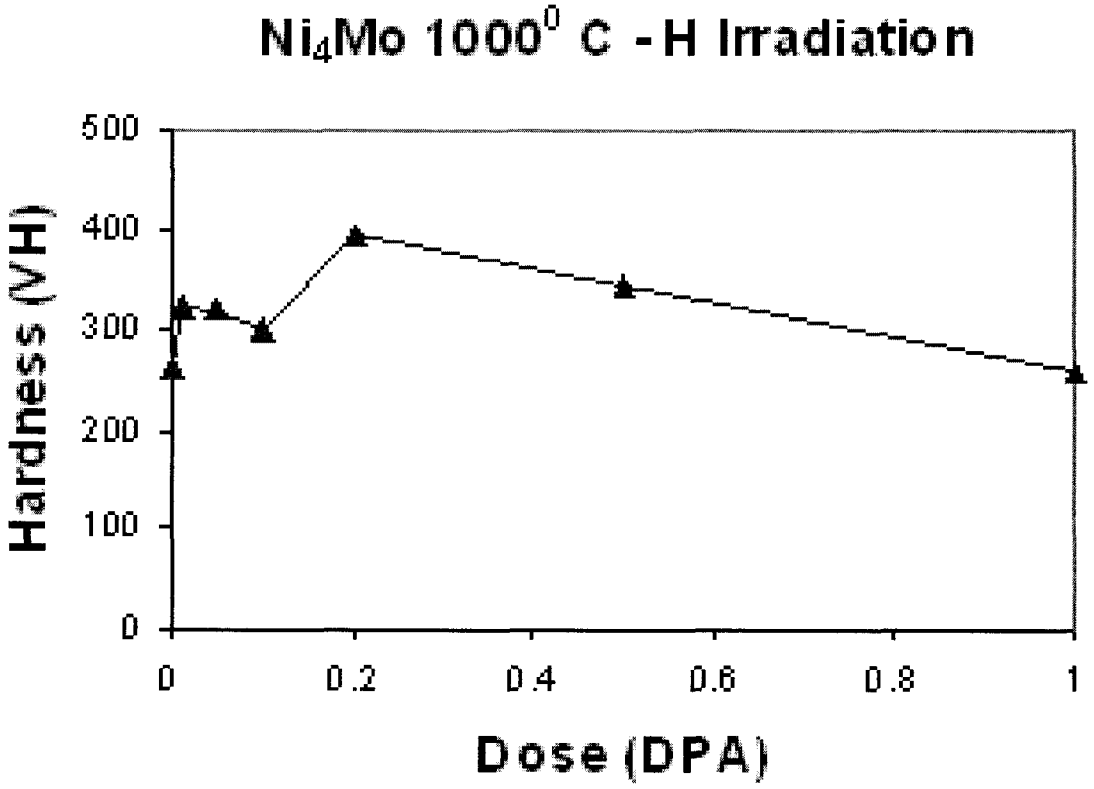

Figure A3.2 Hardness values for Ni_4Mo alloy pre-annealed at 1000^0 C exposed to H^+ irradiation. Irradiation doses are given in the table, as well as averaged Vickers hardness values and the averaged dimensions of the indentation.

Dose(DPA)	H (VH)	d1(μm)	d2(μm)
0	196.37	9.84	9.63
0.01	178.46	10.39	10.03
0.05	121.94	13.07	11.62
0.1	139.74	11.65	11.39
0.2	173.52	10.76	9.96
0.5	180.20	10.20	10.11
1	171.52	10.46	10.23

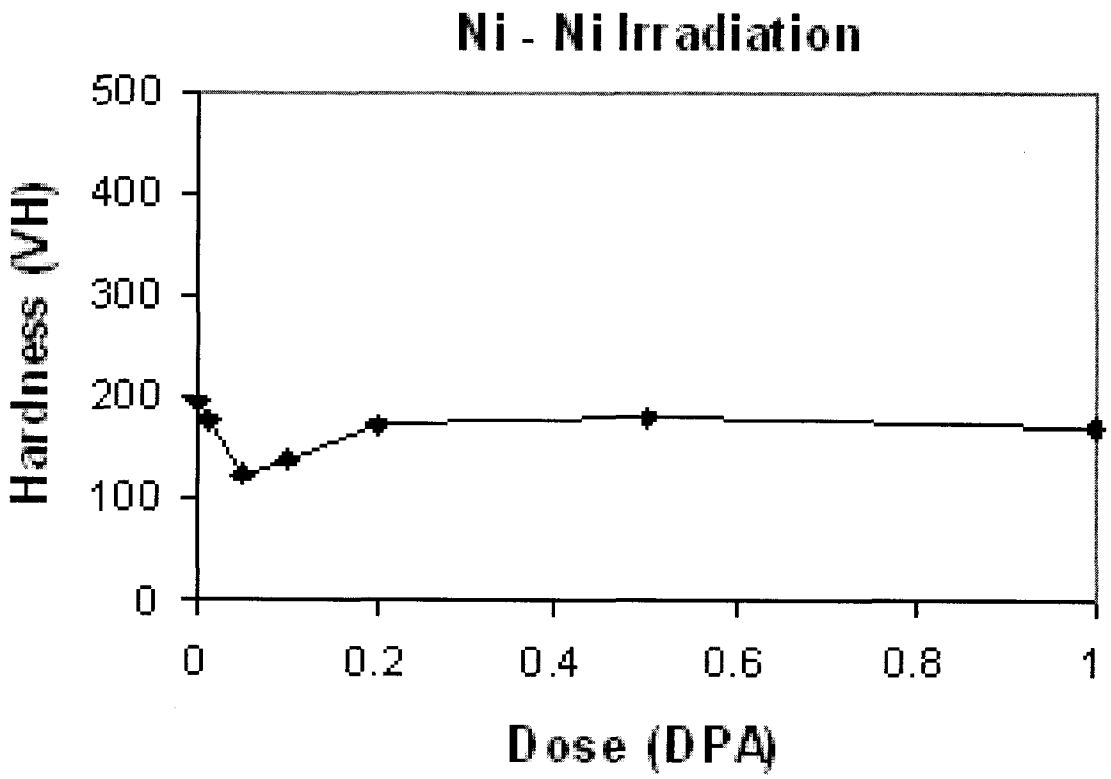

Figure A3.13 Hardness values for Ni exposed to Ni^+ irradiation. Irradiation doses are given in the table, as well as averaged Vickers hardness values and the averaged dimensions of the indentation

Dose(DPA)	H(VH)	d1(μm)	d2(μm)
0	196.37	9.84	9.63
0.01	114.21	12.45	12.86
0.05	133.03	11.9	11.66
0.1	120.21	12.16	12.63
0.2	121.32	12.82	11.75
0.5	88.45	14.09	15.09
1	103.25	12.84	13.75

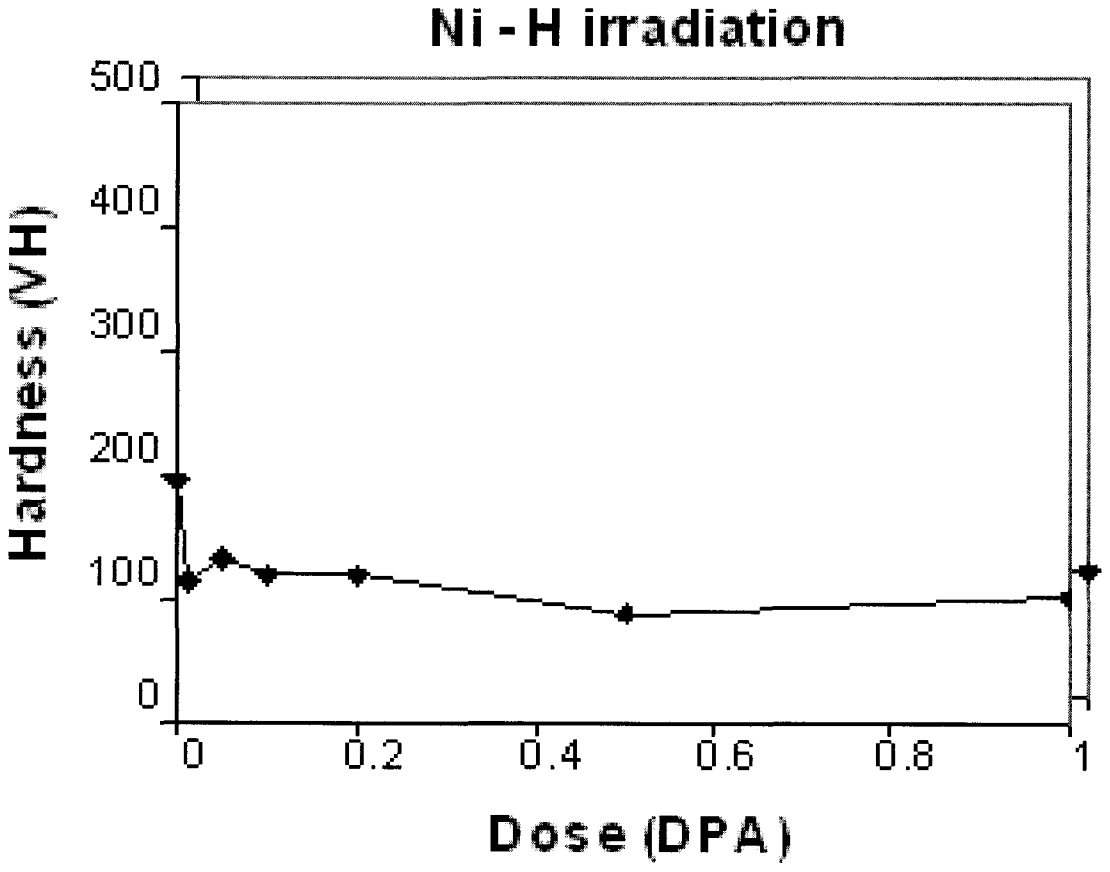

Figure A3.14 Hardness values for Ni exposed to H^+ irradiation. Irradiation doses are given in the table, as well as averaged Vickers hardness values and the averaged dimensions of the indentation

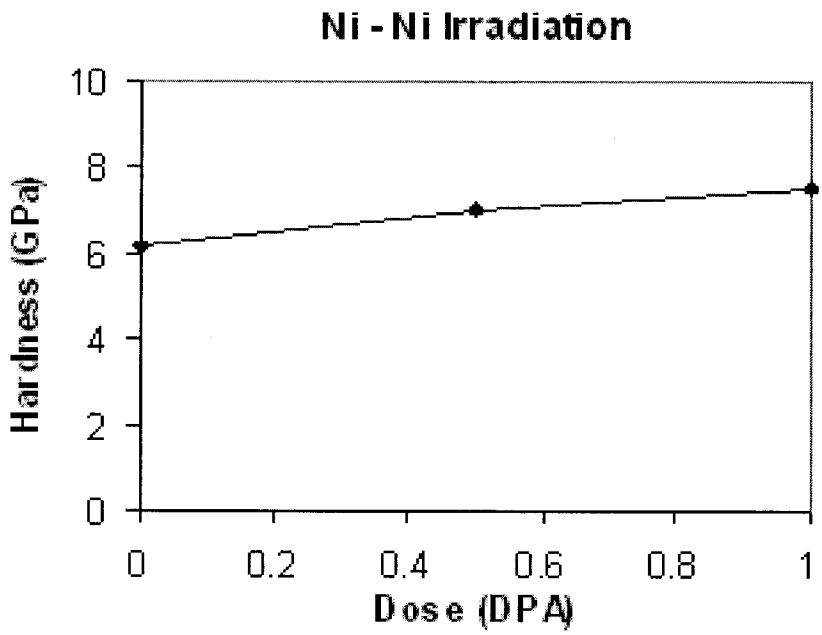

Figure A3.15 Ni hardness as a function of Ni^+ irradiation dose. Measurements by nanoindentation.

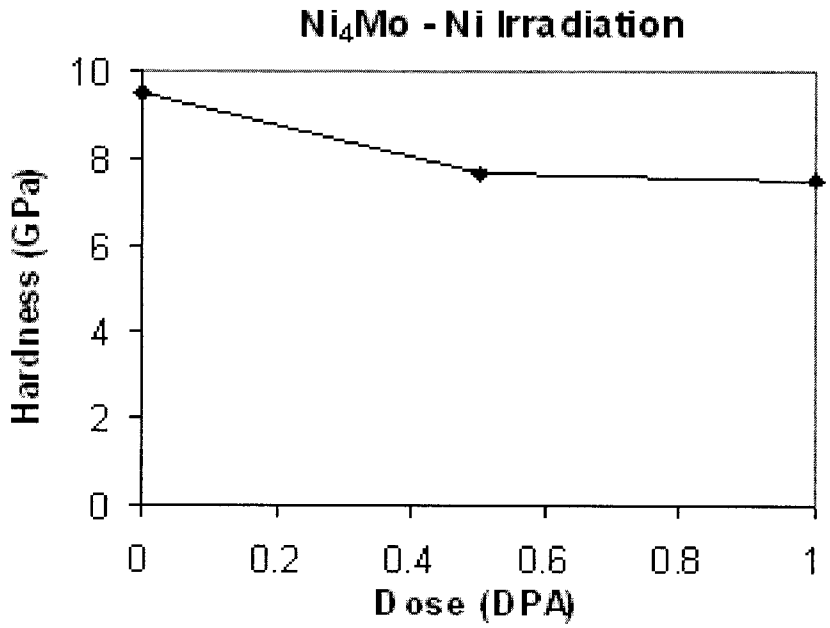

Figure A3.16 Ni_4Mo hardness as a function of Ni^+ irradiation dose. measurements by nanoindentation.

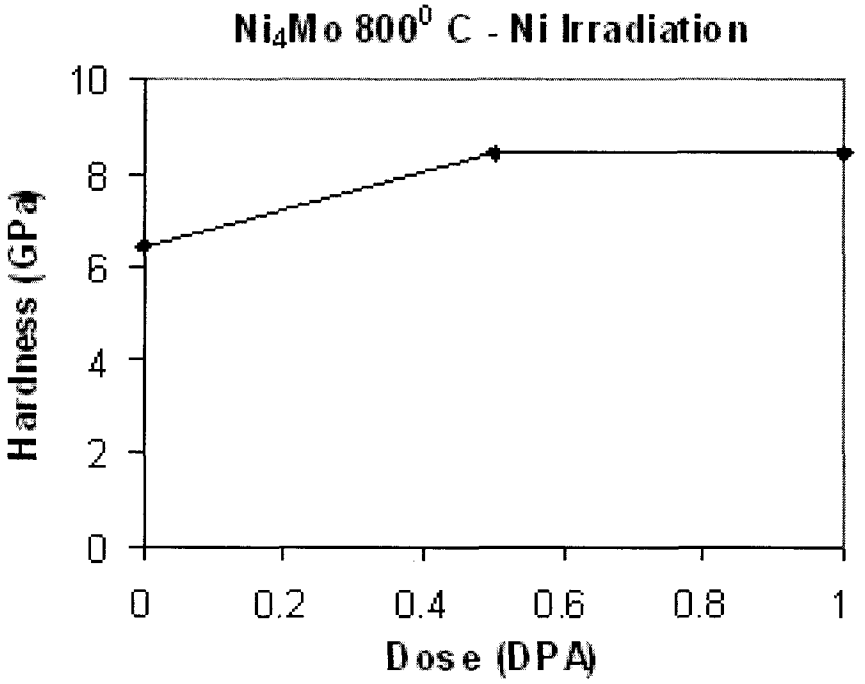

Figure A3.17 Ni_4Mo pre-annealed at 800^0 C; hardness as a function of Ni^+ irradiation dose. measurements by nanoindentation.

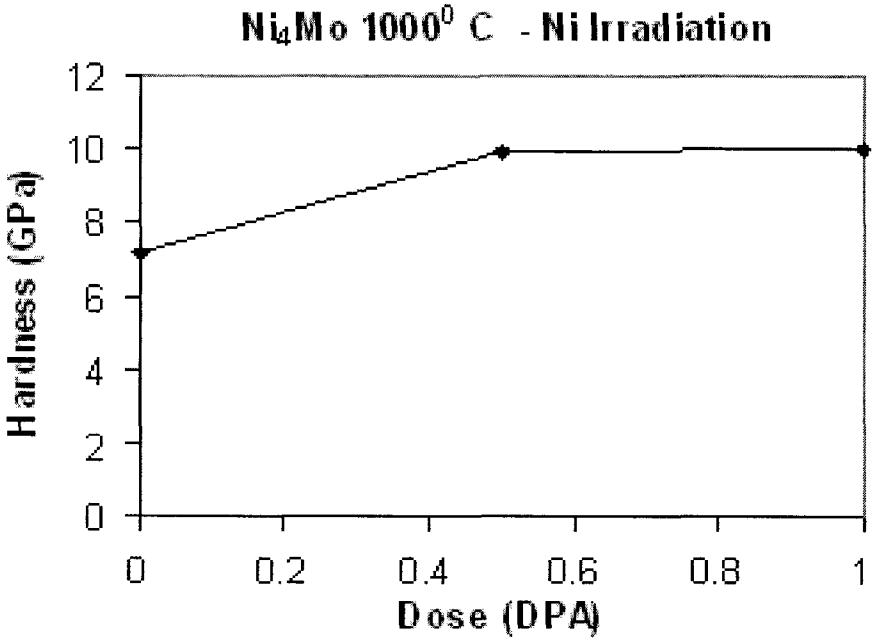

Figure A3.18 Ni_4Mo pre-annealed at 1000^0 C hardness as a function of Ni^+ irradiation dose. measurements by nanoindentation.

BIBLIOGRAPHY

01. Banerjee, S., Arya, A., Das, G. P., "Replacive ordering in alloys", *Physica A, **270,** 215-225, (1999).*

02. Bellon, P., Okamoto, P.R., Schumacher, D., "Non-equilibrium structures induced by ion irradiation in Ni_4Mo", *Journal of Nuclear Materials, **205,** 438-444, (1993).*

03. Bellon, P. and Martin, G., "Irradiation-induced formation of metastable phases, a master-equation approach", *Physical Review B Vol.**38**, No.**4**, (1988).*

04. Bullough, R. and Wood, M. H. "Theory of Microstructural Evolution", *Physics of Radiation Effects in Crystals, eds. R.A. Johnson and A.N. Orlov, 189, (1986).*

05. Jena, A.K. and Chaturvedi, M.C., "Phase Transformations in Materials", Prentice Hall, New Jersey, (1992).

06. Brinkman, J.A., "Production of atom displacements by high-energy particles", *Am. J. Phys., **24**, 246, (1956).*

07. Clausing, R.E., Patriarca, P. and Manly, W.D. *Trans. Am. Soc. Metals **51**, 123 (1959).*

08. Ruedl, E., Delavignette, P. and Amelinckx, S., "Electron diffraction and electron microscopic study of LRO and SRO in Ni_4Mo and of the substructure resulting from ordering", *Phys. Stat. Sol. **28**, 305-28, (1968).*

09. Brooks, C.R., Sanganeria, M., "Intergranular fracture along migrated boundaries in ordered Ni_4Mo", *Scripta Metall., Vol.**22**, 1683-1688, (1988).*

10. Cao, S., Brooks, C.R., Allard L.F., "Characterization of domain boundaries in Ni4Mo by convergent electron beam diffraction", *Materials Characterization, **36**, 73-81, (1996).*

11. Kinchin, G.H. and Pease, J., "The mechanism of the irradiation disordering of alloys", *J. Nucl. Energy, **1**, 200-2, (1955).*

12. Mhatre, U., Kale, A., Kothari, D., Sundararaman, M., Banerjee, S., Kanjilal, D., "TEM investigation of Ni_4Mo LRO and SRO after MeV irradiation", *Nuclear Instruments and Methods in Physics Research, B **100**, 191-195, (1995).*

13. Okamoto, P.R. and Thomas, G., "On SRO and Micro Domains in the Ni_4Mo System", *Acta Metallurgica, Vol.**19**, (1971).*

14. Matveeva, N.M. and Kazlov, E.V., "Ordered phases in metallic systems", Nova Science Publishers, Inc., New York, (1996).

15. Bellon, P., Okamoto, P.R., Schumacher, D., "Non-equilibrium structures induced by ion irradiation in Ni_4Mo", *Journal of Nuclear Materials, **205,** 438-444, (1993).*

16. Bellon, P. and Martin, G., "Cascade effects in a nonequilibrum phase transition with metallurgical relevance", *Physical Review B, Vol.**39**, No.**4**, (1989).*

17. Blaschko, O., Fratzl, P., Klemencic, R., "Model for the structural changes occurring at low temperatures in PdD_x ", *Physical Review B, Vol.**24**, No.**1**, (1981).*

18. Brooks, C.R., Spruelli, J.E. and Stansbury, E.E., "Physical metallurgy of nickel-molybdenum alloys", *Int. Metals Rev.* ***29****, 210-248, (1984).*

19. Irani, R.S., Ling, F.W. and Cahn, R.W., "Domain structures and hardening in ordered Ni_4Mo", *Metallography, No.* ***6****, 141-153, (1973).*

20. Jenkins, M.L., Katerbau, K.H. and Wilkens, M., "Transmission Electron Microscope studies of displacement cascades in Cu_3Au – The diffraction contrast of the disordered zones", *Phil. Mag.,* ***34****, 1141-53, (1976)*

21. Potter, D.I., Irradiation of Alloys Containing Ordered Phases", *Phase Transformations during Irradiation", edited by Nolfi, F.V., Applied Sciences Publishers, Essex, England, (1983).*

22. Schulson, E.M., "The ordering and disordering of solid solutions under irradiation", *J. Nucl. Mater.,* ***83****, 239-64, (1979).*

23. Sundararaman, M., Banerjee, S. and Wollenberger, H., "Order-disorder transformations in Ni_4Mo under self ion irradiation", *Acta Metallurgica Materialia, Vol.****43****, No.****1****, 107-119, (1995).*

24. Wiedersich, H. and Okamoto, P.R., "Effects of radiation-induced segregation on phase stability", *In Phase Stability during irradiation, Eds. Holland, J.R., Mansur, L.K. and Potter, D.I., Met. Soc. AIME, 23-41, (1981).*

25. Zee, R. and Wilkes, P., "The irradiation induced order-disorder transformation in Cu_3Au", *Phil. Mag. A* ***42,*** *463-82, (1980).*

26. Banerjee, S. and Sundararaman, M., "Comparison of electron and ion irradiation effects on order-disorder transition in Ni_4Mo" Journal *of Nuclear Materials,* ***233-237****, 1223-1228, (1996).*

27. Banerjee, S., Urban, K., Wilkens, M., "Order-disorder transformation in Ni4Mo under electron irradiation in a high-voltage electron microscope", *Acta Metall., Vol.**32**, No. **3** ,299 -311, (1984)*

28. Bellon, P., Grandjean, I., Przybylowicz, M., Soisson, F. and Martin, G, "Phase evolution under irradiation, Monte Carlo and mean-field modeling", *Nucl. Instr. And Methods in Phys. Res. B, **102**, 72-76, (1995).*

29. Birtcher, R.C., Richardson, J.W. and Mueller, M.H., "Amorphisation of U_3Si by ion or neutron irradiation", *J. of Nucl. Mater., No.**244**, 251-257, (1997).*

30. Hastings, I.J., "Burnup and temperature dependence of swelling in U_3Si", *J. of Nucl. Mater. , **41**, 195-202, (1971)*

31. Bethune, B., "Transmission electron microscopy of U_3Si effect of irradiation", *J. Nucl. Mater., No.**40**, 205-212, (1971).*

32. Banerjee, S., Kulkarni, U. D., Urban, K., "Initial stages of ordering in Ni_3Mo – Thermal and irradiation ordering", *Acta Metallurgica, Vol. **37**, No. **1**, 35-48, (1989).*

33. Wilkes, P., Liou, K.Y. and Lott, R.G., "Comments on Radiation Induced Phase Instability", *Radiation Effects **29**, 249, (1976).*

34. Dienes, D.J., "Kinetics of order-disorder transformations", *Acta Metall., **3**, 549-57, (1955).*

35. Liou, K.Y. and Wilkes, P., "The irradiation disorder model of phase stability", *J. Nucl. Mater., **87**, 317-30, (1979).*

36. Dubinko, V.I., Tur, A.V., Turkin, A.A., Yanovskij, V.V., "A mechanism of formation and properties of the void lattice in metals under irradiation", *Journal of Nuclear Materials* ***161****, 57-71, (1989).*

37. Kirk, M.A., Blewitt, T.H. and Scott, T.L., "Irradiation disordering of Ni_3Mn by replacement collision sequences", *Phys. Rev.* ***15****, 2914-22, (1977)*

38. Meulanere, de, P., Tendeloo, van, P., Landuyt, van, J., "Radiation defects and ordered radiation patterns in Ni and Ni_4Mo. A study by electron microscopy", *Phil. Mag.* ***A****, Vol.****67****, No.****3****, 745-756, (1993).*

39. Okamoto, P.R. and Rehn, L.E., "Radiation-induced segregation in binary and ternary alloys", *J. Nucl. Mater.* ***83****, 2-23, (1979).*

40. Ossi, P.M., "Phase formation and amorphisation processes under high-energy ion bombardment", *Surface and Coatings Technology,* ***83,*** *22-29, (1996).*

41. Brimhall, J.L., Kissinger, H.E. and Charlot, L.A., "Amorphous Phase Formation in Irradiated Intermetallic Compounds", *Radiation Effects* ***77****, 45, (1983).*

42. Chen, K.C., Ling, F.W. and Starke, E.A.: "Structure and mechanical properties of stress-ordered Ni_4Mo", *Mat. Sci. and Eng.* ***13****, 255-62, (1974).*

43. Nolfi, F.V. "Phase transformations during irradiation", *Applied Science Publishers, London, (1983).*

44. Fontaine, de-, D., "k-space symmetry rules for order-disorder reactions", *Acta Metall., Vol.****23****, 553-71, (1975).*

45. Nastasi, M. and Mayer, J.W., "Thermodynamics and Kinetics of Phase Transformations Induced by Ion Irradiation", *Mat. Sci. Rep.* ***6****, 1-51, (1991).*

46. Ducastelle, F., "Order and phase stability in alloys", North Holland Press, (1991).

47. Russell, K.C., "Phase Stability under Irradiation", Progr. Mat. Sci. **28**, (1984)

48. Martin, G., Soisson, F., Bellon, P., "Phase Stability in Microstructural Evolution in Concentrated Alloys under Irradiation", *Journal of Nuclear Materials* ***205,*** *301-311, (1993).*

49. Johnson, R.A., Lam, N.Q., "Solute segregation in metals under irradiation", *Physical Revue B*, V*ol.**13**, No. **10**, (1976).*

50. Johnson, R.A., Lam, N.Q., "Solute segregation to voids during irradiation", *Physical Revue B*, V*ol.**15**, No. **4**, (1977).*

51. Cauvin, R. and Martin, G., "Solid solutions under irradiation", *Phys. Rev. B, Vol.**25**, No.**5**, 3385-88, (1982).*

52. Lamond, S.P. and Potter, D.I., "Ion mass effects on bombardment-induced disordering of □-Ni_3Si", *J. Nucl. Mat., **117**, 64-69, (1983).*

53. Meulanere, de, P., Tendeloo, van, P., Landuyt, van, J., "Radiation Defects and Ordered Radiation patterns in Ni and Ni_4Mo. A Study by Electron Microscopy", *Philosophical Magazine A, Vol.**67**, No.**3**, 745-756, (1993).*

54. Wollenberger, H.J., "Production Rates of Frenkel Defects During Low-temperature Irradiations", *Vacancies and Iinterstitials in Metals, eds. Seeger et al. (1970).*

55. Tawancy, H., "Effect of chemical composition on the mechanical properties and ordering behavior of a Ni-Mo alloy", *Scripta Metallurgica et Materialia, Vol.**32**, No.**10**, 1525-1531, (1995).*

56. Spruielli, J. and Stansbury, E., "X-ray study of SRO Ni alloys containing 20 at % Mo", *Journal of Physical Chemical Solids, Vol.**26**, 811-822, (1965).*

57. Tanner, L.E., *Acta Metall., **20**, 1197, (1972).*

58. Tanner, L.E., *Phys. Stat. Sol. **30**, 685, (1968).*

59. Hata, S., Mitate, T., Kuwano, N., Matsumura, S., Shindo, D., Oki, K., "Short range order structures in fcc-based Ni-Mo studied by HRTEM with image processing", *Material Science and Engineering, A **312**, 160-167, (2001).*

60. Chen, C.W., Silvent, A., Sainfort, G.: "Remarques sur la formation de cavites dans le nickel par bombardment d'ions Ni++ de 100 KeV", *Journal of Nuclear Materials, **46**, 353-355, (1973).*

61. Menzinger, F. and Sacchetti F., "Dose-rate dependence of swelling and damage in ion irradiated nickel", *J. Nucl. Mater., **57**, 193-197, (1975).*

62. Makin, M.J. and Minter, F.J. "Irradiation Hardening in Copper and Nickel", *Acta Met., 8, (1960).*

63. Wilsdorf, H.H.F., "Nature of radiation damage in Ni", *Phys. Rev. Letters **3**, (1959).*

64. Ardell, A.J. and Janghorban, K., "Irradiation-induced phase transformations in Binary Nickel and Palladium based alloys", *edited by Nolfi, F.V., Applied Sciences Publishers, Essex, England, (1983).*

65. Nastasi, M., Mayer, J.W. and Hirvonen, J.K. "Ion-Solid Interactions", Cambridge University Press, (1996).

66. Tendeloo, van G., Amelinckx, S. and Fontaine, de, D., "On the nature of the SRO in 1 ½ 0 alloys", *Acta Cryst. B **41**, 281-292, (1985).*

67. LeFevre, B.G., Guy, A.G. and Gould, R.W., *Trans. Am. Inst. Min. Eng. 242-788, (1968).*

68. Das, S.K., Okamoto, P.R., Fisher, P.M., Thomas, G., "SRO in Ni-Mo, Au-Cr, Au-V and Au-Mn Alloys", *Acta Metallurgica, Vol.**21**, 913-28, (1973).*

69. Christian, J.W. "The theory of phase transformations in metals and alloys", *433, Pergamon Press, Oxford (1965).*

70. Ridder, de R. van Tendeloo, G., and Amelinckx, G., *Acta Cryst., A **32**, 216, (1976).*

71. Jin, Y., Han, Y.F. and Chaturvedi, M.C., "Electron microscopy study of the ⊔ NiMo phase in a binary Ni-Mo alloy", *Mat. Let., **23**, 21-25, (1995).*

72. Chevalier, J.P. and Stobbs, W.M.: "SRO and the disorder-order transformation in stoichiometric Ni_4Mo", *Acta Metall. Vol.**27**, 1197-1217, (1979).*

73. Landau L.D. and Lifshitz E.M. :"Statistical Physics", Addison Wesley Press, (1958).

74. Khanchaturian, A.G., "The problem of symmetry in statistical thermodynamics of substitutional and interstitial ordered solid solutions", *Phys. Stat. Sol. B, **60**, 9-37, (1973).*

75. Satoshi H., Matsumura S., Kuwano N. and Oki K., "Short range order and its transformation to long range order in Ni_4Mo", *Acta Materialia, Vol.**46**, No.**3**, 881-892, (1998).*

76. Beeler, J.R., "Intermetallics compounds", *Addison Wesley, (1967).*

77. Pfeiler, W. and Sprusil, B, "Atomic ordering in alloys, stable states and kinetics", *Mat. Sci. and Eng. A **324**, 34-42, (2002).*

78. Fournet, G., "Order-disorder phenomena and solid solutions", Phase stability in metals and alloys", *edited by Rudman, P., McGraw Hill, NY, (1966).*

79. Sharkeev, Y., Kozlov, E., Didenko, A., Kolupaeva, S.N., Vihor, N.A., "The mechanisms of the long-range effect in metals and alloys by ion implantation", *Surface and Coatings Technology, **83**, **15**-21, (1996).*

80. Cowley, J.M., J. Appl. Phys, 21-24, (1950).

81. Aubauer, H.P., Acta Met., **20,**165-173, (1972).

82. Aubauer, H.P., Warlimont, H.Z. Metallkd., **65**, 297, (1974).

83. Greenholz, M. and Kidron A., *Acta Cryst., A **26**, 306, (1970).*

84. Hashimoto S., *Acta Cryst. , A **30**, 792, (1974).*

85. Hashimoto S., *Acta Cryst., A **37**, 511, (1981).*

86. Tendeloo, van-, G., "SRO considerations and development of LRO in different Ni-Mo alloys", *Mat. Sci. and Eng., **26,** 209-220, (1976).*

87. Meulanere, de, P., Tendeloo, van, P., Landuyt, van, J., Dyck, van J., "On the interpretation of HREM images of partially ordered alloys", *Ultramicroscopy **60**, 265-282, (1995).*

88. Warren, B.E., "X-ray Diffraction", *Addison Wesley Pub., (1969).*

89. Sharkeev, Y., Kozlov, E., Didenko, A., "Defect structures in metals exposed to irradiation of different nature", *Surface and coatings technology, **96**, 95-102, (1997).*

90. Cullity, B.O., "Elements of X-Ray Diffraction", *McGraw Hill, (1989).*

91. Guinier, A., "X-ray Diffraction", *Freeman and Co., San Francisco, (1963).*

92. Ling, F.W., Irani, R.S. and Cahn, R.W., "Ordering kinetics of cold-worked Ni_4Mo", *Mat. Sci. and Eng., **15**, 181-86, (1974).*

93. Ling, F.W. and Starke, E.A., "The development of LRO and the resulting strengthening effect in Ni_4Mo", *Acta Metall., **19**, 759-68, (1971).*

94. Chu, W. K., Mayer, J. W. and Nicolet, M., Backscattering Spectrometry, *Academic Press, New York, (1978).*

95. Feldman, L.C. and Mayer, J.W., "Fundamentals of surface and thin film analysis", *Prentice Hall, NJ, (1986).*

96. Tesmer, R.T. and Nastasi, M., "Handbook of modern ion beam materials analysis", *MRS, (1995).*

97. Doolittle, L.R., *Nuclear Instruments and Methods, B **9**, 506, (1985).*

98. Sarholt-Kristensen, L., Andreev, A., Johansen, A., Andersen, H.H.,Johnson, E., "Sputtering and RBS Investigations of Ordered and Disordered Ni_4Mo", *Nuclear Instruments and Methods in Physics Research , B **68**, 258-261, (1992).*

99. Tawancy, H., "Deformation behavior of ordered Ni-Mo and Ni-Mo-Cr alloys", *Scripta Metall. Mater., Vol.**32**, No.**12**, 2055-2060, (1978).*

100. Shanshoury, El-, I.A., Gadallah, F.I. and Hammad, A.M., "Effect of neutron irradiation and extension rate on the elevated temperature mechanical properties of Ni and Ni based alloys", *J. of Nucl. Mater., **42**, 203-211, (1972).*

101. Chakravarti, B., Starke, E.A., Lefevre, B.G., "Order-Induced Strengthening in Ni4Mo", *Journal of Materials Science **5**, 394-40, (1970).*

102. Kulkarni, U.D., "FCC Superlattice Structure, A Novel Quasiperiodic Structure without Forbidden Symmetries", *Physical Revue Letters, Vol. **63, No. 22, 27**, (1989).*

103. Hata, S., T., Kuwano, N., Matsumura, S., Shindo, D., Oki, K., "SRO in NI_4Mo and its HRTEM images", *Acta Materialia, Vol.**46**, No **14**, 4955-4961, (1998).*

104. Hata, S., Kuwano, N., Matsumura, S., Oki, K., "SRO and its transformation to LRO in Ni_4Mo", *Acta Mater., Vol.**46**, No. **3**, 881-892, (1998).*

105. Busby, J.T., PhD Thesis, University of Michigan, (2001).

106. Rotberg, V.H., Toader, O. and Was, G.S., "A high intensity radiation effects facility", *CAARI, edited by J. Duggan and L. Morgan, (2000).*

107. Toader, O.F., Rotberg, V.H. and Was, G.S. "Remote control of irradiation experiments", CAARI, edited by J. Duggan and L. Morgan (2002).

108. Ziegler, H., "Stopping and Ion Ranges in Materials", Pergamon Press New York, (1980).

109. Alexandreanu, B., Ph.D. Thesis, University of Michigan, (2003).

110. Brandon, D.G: "The structure of high-angle grain boundaries", *Acta Metallurgica,* 14 (1966) 1479-1484.

111. Bragg, W.L. and Williams, E.J., "The effects of thermal agitation on atomic arrangements of alloys", Proc. Royal Soc., A **145**, 699, (1934).

112. Friedland, E., Berg, van der, N.G., Hanssman, J. and Meyer, O., "Damage ranges in metals after ion implantation", *Surface and Coatings Technology, **83**, 10-14, (1996).*

113. Kircher, J. and Bowman, R., "Effects of radiation on Materials and Components", *Addison-Wesley, 1989.*

114. Schonfeld, B., "Local atomic arrangements in binary alloys", *Progress in Materials Science, **44**, 453-543, (1999).*

115. Pumphrey, P.H.,"Grain boundary structure and properties", *edited by Chadwick, G.A and Smith, D.A., New York, Academic Press, (1976).*